CRYOGEN-FREE ZEEMAN-PERTURBED NQR AND GREEN MECHANOCHEMISTRY FOR HALOGEN AND CHALCOGEN BONDING IN MOLECULAR SOLIDS

A thesis submitted to the University of Ottawa in partial fulfillment of the requirements for the Doctorate in Philosophy degree in Chemistry

Alireza Nari

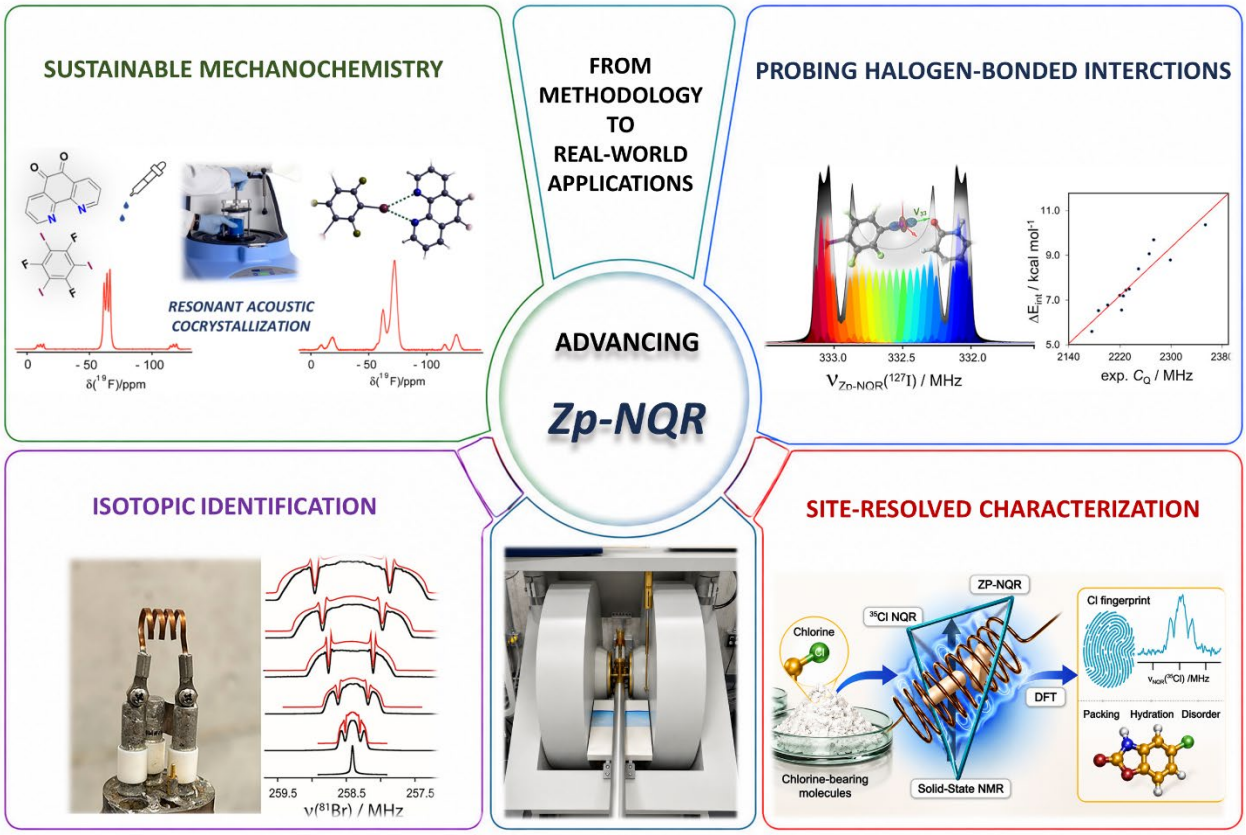
Department of Chemistry and Biomolecular Sciences

Faculty of Science

University of Ottawa

© Alireza Nari, Ottawa, Canada, 2026

Graphical Abstract



Abstract

Understanding the relationships between crystal structure, local electronic environment, and intermolecular interactions is fundamental to the rational design of molecular solids for applications in pharmaceuticals, supramolecular chemistry, and functional materials. This dissertation presents complementary advances in the sustainable characterization and synthesis of molecular solids through the development of cryogen-free Zeeman-perturbed nuclear quadrupole resonance (Zp-NQR) spectroscopy, integrated multimodal structural analysis, and mechanochemical synthesis.

The primary contribution of this work is the development of a practical and versatile cryogen-free Zp-NQR methodology for investigating quadrupolar nuclei in molecular solids. By introducing a weak magnetic field, generated by an adjustable electromagnet, to perturb the pure quadrupolar energy levels and analyzing the resulting spectral line shapes using exact Hamiltonian simulations, a robust experimental workflow was established for accurately determining the complete electric field gradient (EFG) tensor directly from powder samples. This approach eliminates the need for superconducting magnets and liquid-helium cryogens, significantly lowering the experimental barriers associated with quadrupolar spectroscopy while providing a more sustainable and accessible alternative to conventional high-field magnetic resonance techniques.

Building upon this methodological foundation, the analytical capabilities of Zp-NQR were further expanded. Zeeman perturbation was shown to enable direct experimental identification of quadrupolar isotopes by measuring their characteristic Zeeman response to an applied magnetic field. Analysis of the resulting spectral splitting allows the corresponding Larmor frequency and

gyromagnetic ratio (γ), which is unique to each isotope, to be determined experimentally, thereby enabling unambiguous isotopic assignment and the identification of overlapping resonance lines in complex, and multicomponent, molecular solids without isotopic enrichment or prior structural information. The methodology was subsequently extended to demonstrate that experimentally determined quadrupolar interaction parameters serve as sensitive reporters of halogen bond strength. By combining Zp-NQR with relativistic density functional theory (DFT) calculations, strong correlations were established between quadrupolar coupling constants, electric field gradient tensors, electronic structure descriptors, and halogen-bond interaction energies, providing a direct experimental approach for quantifying halogen-bond strength in molecular solids.

The versatility of the methodology was further demonstrated through the site-resolved characterization of chlorine-bearing pharmaceutical materials. An integrated approach combining ^{35}Cl Zp-NQR, zero-field NQR, high-field solid-state NMR (SSNMR), three-dimensional electron diffraction 3D ED, and first-principles calculations enabled the structural characterization of pharmaceutical cocrystals, hydration-dependent materials, degradation products, and conformationally disordered systems directly from powder samples. The combined methodology resolved chemically inequivalent chlorine environments and provided detailed insight into crystal packing, hydration, disorder, and local electronic structure, establishing a multimodal framework for pharmaceutical solid-state characterization.

Complementary studies expanded the scope of this dissertation beyond quadrupolar resonance spectroscopy. Combined ^{77}Se magic-angle spinning (MAS) SSNMR spectroscopy and first-principles quantum chemical calculations were employed to investigate selenium-centred non-covalent interactions, providing detailed insight into the amphiphilic behaviour of selenium and its participation in halogen and chalcogen bonding. In parallel, resonant acoustic mixing

(RAM) was demonstrated as a gentle, scalable, and solvent-efficient mechanochemical route for the synthesis of halogen-bonded cocrystals. RAM successfully produced phase-pure materials, enabled the discovery of previously unknown crystal forms, and expanded accessible polymorphic and stoichiometric landscapes beyond those attainable by conventional ball milling.

Overall, this dissertation demonstrates how advances in cryogen-free magnetic resonance spectroscopy, complementary crystallographic and computational techniques, and sustainable mechanochemical synthesis can be integrated into a unified framework for molecular solid research. Beyond expanding the analytical capabilities and accessibility of quadrupolar resonance spectroscopy, this work establishes experimentally grounded approaches for probing local electronic structure, intermolecular interactions, and structural complexity while promoting more sustainable practices in the characterization and synthesis of molecular materials.

Acknowledgements

The completion of this dissertation marks the end of an unforgettable chapter of my life. First and foremost, I would like to express my deepest gratitude to my supervisor, Professor David L. Bryce. It is difficult to fully convey how grateful I am for his mentorship over the past several years. Dave has been far more than a research supervisor; he has been an exceptional teacher and mentor. Under his supervision, I became not only a better scientist, but also a better writer, and a more confident presenter. His passion for science, attention to detail, and dedication to his students continue to inspire me. Thank you, Dave, for believing in me, for always encouraging me to aim higher, and for serving as a guiding light throughout my doctoral journey. I sincerely hope to carry forward the values and scientific integrity that you have instilled in me throughout my future career.

I am sincerely grateful to the members of my Thesis Advisory Committee—Professor Abdel Sayari, Professor Darrin Richeson, and Dr. Saman Alavi—for their valuable advice, constructive discussions, and thoughtful feedback throughout my doctoral studies.

I would also like to acknowledge my lab mates, past and present (Bryce Nation), for creating such an enjoyable and collaborative research environment.

This dissertation would not have been possible without the outstanding technical support provided by the staff of the Department of Chemistry and Biomolecular Sciences and the University of Ottawa research facilities. I am especially grateful to Dr. Jeffrey S. Ovens, former manager of the X-ray Diffraction facility, for his expertise in crystallography and his assistance with numerous diffraction experiments. I would also like to thank Dr. Patrick M. J. Szell, former manager of the NMR facility, for many valuable discussions and for his contributions to several

collaborative projects that became an important part of this dissertation. My sincere thanks also go to Dr. Scott A. Southern, the manager of the NMR Facility, for his support, and to our dedicated NMR technician, Volodymyr Semeniuchenko (Vova), whose technical expertise, enthusiasm, and willingness to help were invaluable throughout this work.

I would also like to acknowledge Professor J. C. (Tito) Scaiano. Receiving the graduate scholarship established in his name provided important financial support during my doctoral studies and was a tremendous encouragement. I am sincerely grateful for this recognition.

I gratefully acknowledge the financial support provided by the Natural Sciences and Engineering Research Council of Canada (NSERC) and the University of Ottawa, whose funding made this research possible. Computational resources and technical support were provided by the Digital Research Alliance of Canada (Compute Canada), for which I am sincerely thankful.

Finally, I would like to express my deepest gratitude to my family. Pursuing a PhD abroad has meant spending several years away from those who have always been my greatest source of encouragement. To my parents, thank you for your unconditional love, constant support, and unwavering belief in me, despite the distance that separated us throughout this journey.

To my beloved wife, Farzaneh, thank you for standing beside me through every challenge and every success. Your patience, understanding, encouragement, and endless support made this journey possible. You celebrated every achievement with me, carried me through the difficult moments, and reminded me to keep moving forward whenever the path seemed uncertain. This accomplishment is as much yours as it is mine, and I will always be grateful for having you by my side.

Statement of Originality

I certify that the research presented in this thesis is my own work or work to which I have made substantial contributions, and that all referenced work performed by others is explicitly acknowledged using standard scholarly citation practices. This thesis contains six scientific articles/manuscripts (five published and one in final preparation for submission). Artificial intelligence (AI)-assisted writing tools were used in selected instances to improve the clarity, grammar, and readability of my original drafts. All scientific content, experimental work, data analysis, interpretation, conclusions, and final editorial decisions remain entirely my own.

List of Works Included in This Thesis and Author Contributions:

1. A. Nari, P. M. J. Szell, and D. L. Bryce, "Isotopic Identification of Quadrupolar Spin Resonance Lines by Zeeman Perturbation", J. Phys. Chem. Lett. **2025**, *16*, 8752–8757.

Role: First author; responsible for conceptualization, experimental work, data analysis, and manuscript preparation.

2. A. Nari, S. J. Thomas, D. L. Bryce, and B. Thomas, "Understanding Non-Covalent Interactions in Diphenyldiselenide and Diphenylselenide Cocrystals Using a Combined ^{77}Se Magic-Angle Spinning Solid-State NMR and Quantum Chemical Analysis Approach", J. Phys. Chem. C **2025**, *129*, 13299–13311.

Role: First author; responsible for conceptualization, experimental work, data analysis, and manuscript preparation.

3. A. Nari, P. M. J. Szell, and D. L. Bryce, "Practical Aspects of Zeeman-Perturbed NQR Spectroscopy Using an Adjustable Electromagnet", Solid State Nucl. Magn. Reson. **2025**, *138*, 102014.

Role: First author; responsible for conceptualization, experimental work, data analysis, and manuscript preparation.

4. A. Nari, M. Rahman, P. M. J. Szell, V. Semeniuchenko, and D. L. Bryce, “Halogen Bond Strength in Solids Quantified via Zeeman-Perturbed Nuclear Quadrupole Resonance Spectroscopy”, J. Am. Chem. Soc. **2025**, *147*, 9528–9543.

Role: First author; responsible for conceptualization, experimental work, data analysis, and manuscript preparation.

5. A. Nari, J. S. Ovens, and D. L. Bryce, “Halogen-Bonded Cocrystals via Resonant Acoustic Mixing”, RSC Mechanochem. **2024**, *1*, 50–62 (Cover article).

Role: First author; responsible for conceptualization, experimental work, data analysis, and manuscript preparation

.

6. A. Nari, J. N. Rusimovic, P. M. J. Szell, M. Jasil, V. Terskikh, D. L. Bryce, B. Thomas, “Resolving Chlorine Sites in Pharmaceuticals by Integrated Site-Resolved Zeeman-Perturbed NQR, Solid-State NMR, and Electron Diffraction Crystallography.” J. Am. Chem. Soc. **2026,** Revised and resubmitted October 2026 following peer review.

Role: First author; responsible for conceptualization, experimental work, data analysis, and manuscript preparation.

Table of Contents

Graphical Abstract ii

Abstract iii

Acknowledgements vi

Statement of Originality viii

Table of Contents xi

List of Figures xiv

List of Symbols and Abbreviations xvi

Part 1 – Non-Covalent Interactions, Quadrupolar Spectroscopy, and Sustainable Molecular Solid Research **1**

Chapter 1 – Halogen and Chalcogen Bonds as Versatile Tools in Supramolecular Chemistry: Opportunities and Challenges for Green and Sustainable Practices 3

Chapter 2 – Theoretical Principles of Quadrupolar Interactions and the Evolution of Zeeman-Perturbed NQR (Zp-NQR) as a Cryogen-Free Technique 21

Chapter 3 – Mechanochemistry and Sustainable Molecular Solid Preparation: Integrating Green Synthesis with Cryogen-Free Characterization 59

Part 2 – Methodological Development and Applications of Cryogen-Free Zeeman-Perturbed Nuclear Quadrupole Resonance **78**

Chapter 4 – Practical Aspects of Zeeman-Perturbed NQR Spectroscopy Using an Adjustable Electromagnet: Establishing a Routine, Cryogen-Free Laboratory Workflow 80

Chapter 5 – Isotopic Identification of Quadrupolar Spin Resonance Lines by Zeeman Perturbation: Enabling Analysis of Complex, Impure, and Multi-Component Systems 93

Chapter 6 – Direct Quantification of Halogen Bond Strength in Solids via Zeeman-Perturbed NQR: The Electric Field Gradient as a Reporter of Interaction Energetics 102

Chapter 7 –Integrated Site-Resolved Zp-NQR, SSNMR, and 3D Electron Diffraction Crystallography of Chlorine-Bearing Molecules in Powders..... 121

Summary of Part 2 168

Part 3 – Complementary Solid-State Characterization by Solid-State NMR and First-Principles Calculations 169

Chapter 8 – Unraveling the Amphiphilic Nature of Selenium in Non-Covalent Interactions: Combined ^{77}Se MAS SSNMR and Quantum Chemical Analysis of Se–I Halogen and Chalcogen Bonds 169

Summary of Part 3 185

Part 4 – Sustainable Mechanochemical Synthesis of Halogen-Bonded Molecular Solids..186

Chapter 9 – Resonant Acoustic Mixing as a Gentle, Scalable, and Solvent-Efficient Route to Halogen-Bonded Cocrystals: Accessing Novel Polymorphs and Stoichiometries... 186

Part 5 – Conclusions and Future Outlook 203

5.1 Summary of Major Scientific Contributions..... 203

5.2 Assessing the Green Chemistry Footprint of This Thesis..... 204

5.3 Zp-NQR in the Post-Helium Era: A Practical Model for Sustainable Magnetic Resonance 205

5.4 The Realized Synergy: Green Mechanochemistry + Cryogen-Free Zp-NQR 206

5.5 Limitations and Critical Reflections 207

5.6 Future Directions 208

5.7 Final Remarks 210

Appendix I – List of Publications and Conference Presentations 212

Appendix II – Supporting Information 232

II.1 Supporting Information for Chapter 5 215

II.2 Supporting Information for Chapter 6 233

II.3 Supporting Information for Chapter 7 256

II.3 Supporting Information for Chapter 8 272

II.5 Supporting Information for Chapter 9 286

List of Figures

Part 1 – Non-Covalent Interactions, Quadrupolar Spectroscopy, and Sustainable Molecular Solid Research

Figure 1.1.1. Comparison of halogen and chalcogen bonding interactions relevant to the molecular solids investigated throughout this thesis..... 5

Figure 1.1.2. Electrostatic potential of representative halogen-bond donor molecules…..... 6

Figure 1.1.3. Representative examples of directional non-covalent interactions commonly employed in crystal engineering and supramolecular chemistry.. 8

Figure 1.1.4. Selected examples illustrating the diverse roles of halogen and chalcogen bonding across different areas of chemistry..... 10

Figure 1.1.5. Schematic comparison of conventional and sustainable methodologies for studying molecular solids.. 13

Figure 1.2.1. Schematic representation of nuclear charge distributions and their associated nuclear quadrupole moments.. 26

Figure 1.2.2. EFG tensor surfaces calculated for the ^{127}I nucleus in *p*-DITFB 28

Figure 1.2.3. Comparison of the energy-level splitting of a spin-*I*=3/2 nucleus in NMR and NQR.. 33

Figure 1.2.4. Comparison of high-field SSNMR and pure NQR for a spin-5/2 nucleus.. 38

Figure 1.2.5. Energy-level diagram illustrating the effect of a weak magnetic field on a spin-3/2 nucleus in Zp-NQR.. 46

Figure 1.2.6. Representative workflow for the modern analysis of Zp-NQR spectra.. 49

Figure 1.3.1. Overview of the principal green chemistry metrics used to evaluate the sustainability of synthetic processes..... 63

Figure 1.3.2. General concept of mechanochemical synthesis.. 64

Figure 1.3.3. Mechanochemical synthesis platforms used throughout this thesis.. 69

Figure 2.7.1. Site-resolved chlorine spectroscopy for pharmaceutical compounds..... 126

Figure 2.7.2. Molecular structures of the Cl containing compounds investigated in chapter 7..127

Figure 2.7.3. ^{35}Cl NQR, Zp-NQR, and SSNMR spectra of KTZ powder.. 133

Figure 2.7.4. ^{35}Cl NQR, Zp-NQR, and WURST-QCPMG SSNMR spectra of CAT.. 138

Figure 2.7.5. TGA and DSC thermograms of commercial CAT.. 140

Figure 2.7.6. ^{35}Cl NQR and Zp-NQR spectra of CHZ and its series of cocrystals..... 145

Figure 2.7.7. The static ^{35}Cl WURST-QCPMG SSNMR spectra of CHZ and its cocrystals.... 147

Figure 2.7.8. Crystal packing diagrams of the CHZ series.. 148

Figure 2.7.9. Correlation between experimental and GIPAW-DFT calculated ^{35}Cl C_Qs.. 151

Figure 2.7.10. NCI plots for CHZ and its cocrystals.. 153

Figure 5.1. Integrated workflow developed throughout this thesis..... 207

List of Symbols and Abbreviations

3D ED	3D electron diffraction
a, b, c	Crystallographic unit cell lengths
ADF	Amsterdam density functional
CASTEP	Cambridge sequential total energy package
ChB	Chalcogen bond
CPMAS	Cross-polarization magic angle spinning
C_Q	Quadrupolar coupling constant
CSA	Chemical shift anisotropy
CSD	Cambridge structural database
DFT	Density functional theory
$d_{x\cdots y}$	Halogen bond length
d_{vdW}	van der Waals radius
EFG	Electric field gradient
ESP	Electrostatic potential
ETS-NOCV	Extended transition state–natural orbitals for chemical valence
FWHM	Full width at half maximum
GIPAW	Gauge including projector augmented wave
h	Planck constant
HB	Hydrogen bond
IR	Infrared
IQA	Interacting quantum atoms
NCI	Non-covalent interaction
QCPMG	Quadrupolar Carr-Purcell-Meiboom-Gill
QTAIM	Quantum theory of atoms in molecules
RAM	Resonant acoustic mixing
VMD	Visual molecular dynamics

WURST-QCPMG	wideband uniform rate smooth truncation QCPMG
XB	Halogen bond
PXRD	Powder X-ray diffraction
Zp-NQR	Zeeman-perturbed nuclear quadrupole resonance
α, β, γ	Crystallographic unit cell angles
γ_L	Gyromagnetic ratio
δ_{iso}	Isotropic chemical shift
δ^+, δ^-	Partial positive and negative charge, respectively
η	Quadrupolar asymmetry parameter
$\theta_{R\text{-}X\cdots Y}$	Halogen bond angle relative to the R-X···Y axis
κ	Chemical shift tensor skew
λ	Wavelength
ν_L	Larmor frequency
ν_{MAS}	Magic angle spinning frequency
ν_Q	Quadrupolar coupling frequency
σ_{CS}	Nuclear shielding
σ-hole	Area of positive electrostatic potential associated with the halogen, or chalcogen bond donor

Part 1 – Non-Covalent Interactions, Quadrupolar Spectroscopy, and Sustainable Molecular Solid Research

The rational design of molecular solids relies on a detailed understanding of the non-covalent interactions[1] that govern crystal packing, supramolecular assembly, and material properties. Among these interactions, halogen bonds (XBs)[2] and chalcogen bonds (ChBs)[3] have emerged as powerful and highly directional tools in crystal engineering, enabling the controlled construction of functional materials, pharmaceutical cocrystals, molecular recognition systems, and supramolecular architectures.[4–6] Owing to their tunable strength, geometric predictability, and compatibility with a broad range of chemical environments, these σ-hole interactions[7] (*vide infra*) have become increasingly important in modern materials chemistry and solid-state science.

At the same time, growing attention is being directed toward the sustainability of chemical research and manufacturing. Traditional approaches to cocrystal synthesis frequently rely on large volumes of organic solvents, while advanced characterization techniques often depend on expensive infrastructure and finite resources.[8] In magnetic resonance spectroscopy, concerns regarding the availability and cost of liquid helium[9] have motivated renewed interest in alternative methodologies capable of providing high-quality structural information with reduced resource demands. These challenges create opportunities to develop more sustainable workflows for both the preparation and characterization of molecular solids.

This thesis explores the intersection of supramolecular chemistry, magnetic resonance spectroscopy, and sustainable materials research. The work combines mechanochemical synthesis through resonant acoustic mixing (RAM), a solvent-minimized approach to cocrystal preparation, with cryogen-free Zeeman-perturbed nuclear quadrupole resonance (Zp-NQR), an emerging

technique capable of probing strongly quadrupolar nuclei under ambient laboratory conditions. Together with complementary solid-state NMR spectroscopy and quantum chemical calculations, these approaches provide new opportunities to investigate halogen and chalcogen bonding in molecular solids while reducing reliance on traditional solvent-intensive and resource-intensive methodologies.

Part 1 establishes the theoretical and conceptual foundations required for the remainder of this thesis. Chapter 1 introduces the fundamental principles and applications of halogen and chalcogen bonding while discussing the growing need for sustainable practices in supramolecular chemistry. Chapter 2 provides the theoretical framework of quadrupolar interactions and the development of Zp-NQR spectroscopy as an accessible characterization method. Chapter 3 introduces mechanochemistry as a green synthetic platform and discusses its integration with resource-efficient analytical techniques. These chapters establish the scientific context for the methodological developments and applications presented in the subsequent parts of this thesis.

Chapter 1 – Halogen and Chalcogen Bonds as Versatile Tools in Supramolecular Chemistry: Opportunities and Challenges for Green and Sustainable Practices

The title of this chapter reflects two complementary themes that underpin this thesis. The first is the growing importance of halogen and chalcogen bonding as versatile design elements in supramolecular chemistry, crystal engineering, and materials science. Over the past two decades, these highly directional non-covalent interactions have evolved from relatively specialized concepts into widely employed tools for controlling molecular assembly, tuning solid-state properties, and constructing functional materials. Their influence now extends across fields ranging from pharmaceutical sciences and catalysis to molecular electronics and energy-related materials.[6,10]

The second theme concerns sustainability. While advances in crystal engineering have enabled increasingly sophisticated molecular design strategies, many synthesis and characterization approaches remain resource intensive. Conventional solution-based cocrystallization often consumes substantial quantities of organic solvents, while state-of-the-art magnetic resonance techniques frequently depend on superconducting magnets and liquid helium infrastructure. The increasing economic and environmental costs associated with solvent use and helium consumption have motivated the search for more sustainable alternatives.[11,12]

This chapter establishes both the scientific and societal motivations for the research presented throughout this thesis. It begins by introducing the fundamental concepts of σ-hole interactions and their manifestation in halogen and chalcogen bonding. The discussion then expands to the broad applications of these interactions in crystal engineering and functional

materials. Finally, current challenges associated with sustainability, resource consumption, and experimental accessibility are examined, providing the rationale for the development of the mechanochemical and cryogen-free characterization methodologies described in subsequent chapters.

1.1 The σ-Hole and Directional Non-Covalent Interactions

The organization of molecules within crystalline solids is governed by a complex interplay of intermolecular forces. While hydrogen bonding[13] (HB) has historically dominated discussions of supramolecular chemistry and crystal engineering, increasing attention has been devoted to a broader family of highly directional interactions known as σ-hole interactions.[7] These interactions arise when an atom covalently bonded to an electron-withdrawing substituent exhibits an anisotropic distribution of electron density, creating a localized region of positive electrostatic potential along the extension of the covalent bond. This electron-deficient region, commonly termed a σ-hole because it occurs along the extension of the covalent σ bond (Figure 1.1), can interact attractively with electron-rich species such as lone pairs, anions, π-systems, or other nucleophilic regions.[2,14]

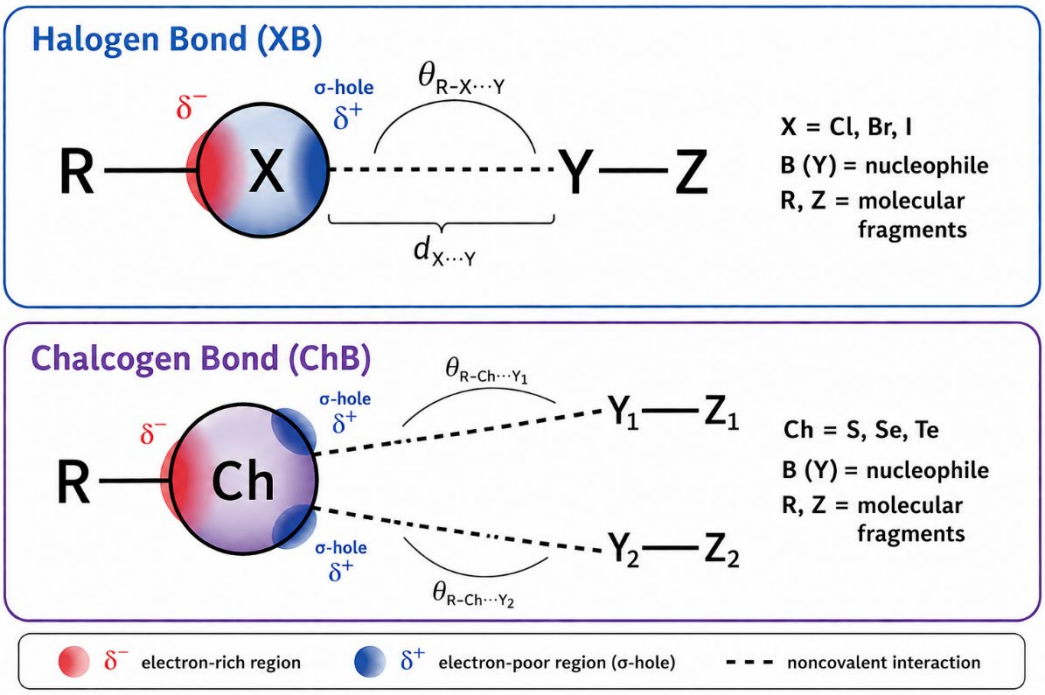


Figure 1.1.1. Comparison of halogen and chalcogen bonding interactions relevant to the molecular solids investigated throughout this thesis. The σ-hole located on a halogen (Cl, Br, or I) or chalcogen (S, Se, or Te) atom acts as an electrophilic site capable of interacting with electron-rich acceptors. Chalcogen atoms may possess two σ-holes, although the presence and participation of one or both interaction sites depend on the molecular and crystallographic environment.

As illustrated in Figure 1.1.2, the anisotropic distribution of electron density around covalently bound iodine atoms produces a localized region of positive electrostatic potential, commonly referred to as a σ-hole, which serves as the electrophilic site responsible for halogen bonding interactions.[15] The presence of a positive electrostatic potential region opposite a covalent bond gives rise to interactions such as halogen bonding (Group 17), chalcogen bonding (Group 16)[16–18], pnictogen bonding (Group 15)[19,20], and tetrel bonding (Group 14)[21–23], each of which exhibits distinct geometric and electronic characteristics. Although the magnitude and spatial distribution of the σ-hole depend on the identity of the atom involved and its chemical environment, these interactions share common characteristics including high directionality,

tunable strength, and predictable geometries. Such features make σ-hole interactions particularly attractive for the rational design of molecular assemblies and functional materials.[24]

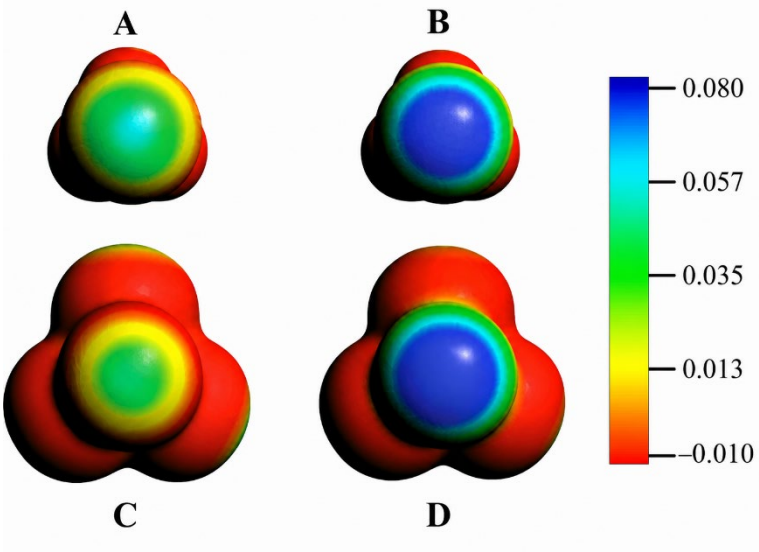


Figure 1.1.2. Electrostatic potential maps projected onto the 0.001 e Bohr^{-3} electron-density isosurface of representative halogen-bond donor molecules. Panels A and C show the electrostatic potential surfaces of CF_3I and CI_4, respectively, illustrating the anisotropic electron-density distribution around iodine and the formation of a positive electrostatic potential region (σ-hole) along the extension of the C–I bond. Panels B and D show the corresponding electrostatic potential distributions in the presence of a −1.0 point charge, highlighting the polarization and enhancement of the σ-hole region. Red regions correspond to the most negative electrostatic potentials, whereas blue regions indicate the most positive electrostatic potentials. Reproduced from Ref. 15 with permission from The Royal Society of Chemistry.

Among σ-hole interactions, halogen bonding has become one of the most extensively studied. A halogen bond (XB) is commonly defined as the net attractive interaction between an electrophilic region associated with a halogen atom and a nucleophilic region in another, or the same, molecular entity.[13] The interaction typically involves chlorine, bromine, or iodine atoms

acting as electron-deficient donors, with iodine generally producing the strongest halogen bonds due to its greater polarizability and larger σ-hole.[14]

XBs possess several features that make them particularly useful in crystal engineering. The interactions are highly directional, with preferred bond angles approaching 180° relative to the R–X covalent bond axis. Furthermore, their strengths can range from a few kilojoules per mole to values approaching those associated with moderate HBs.[10] The strength and geometry of the interaction can be systematically tuned through chemical substitution, particularly through the incorporation of electron-withdrawing groups such as fluorinated aromatic rings.[25,26]

A closely related class of interactions is provided by chalcogen bonds (ChBs). In these systems, sulfur, selenium, or tellurium atoms serve as σ-hole donors. Unlike halogen atoms, divalent chalcogens often possess two σ-holes (Figure 1.1.1), creating opportunities for more diverse supramolecular architectures and multidirectional interactions.[27] ChBs share many characteristics with XBs but frequently display greater structural diversity owing to the electronic complexity of the chalcogen atom.

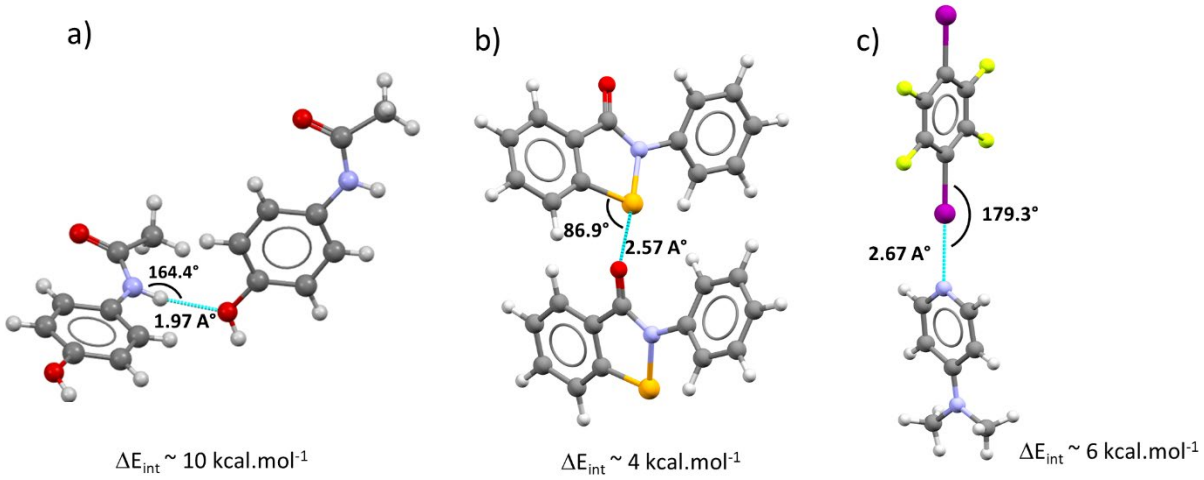


Figure 1.1.3. Representative examples of directional non-covalent interactions commonly employed in crystal engineering and supramolecular chemistry. (a) Intermolecular N–H···O HB in crystalline paracetamol (Form I), illustrating the characteristic short donor–acceptor distance and near-linear geometry. (b) Intermolecular Se···O ChB in crystalline Ebselen, arising from the interaction of an oxygen lone pair with a σ-hole on selenium. (c) Intermolecular I···N halogen bond in the cocrystal of 1,4-diiodotetrafluorobenzene and 4-dimethylaminopyridine, demonstrating the highly directional nature of halogen bonding. Selected intermolecular distances and bond angles are indicated. Approximate interaction energies are shown for comparison and are based on representative literature values for analogous systems.

The ability to predict and manipulate these interactions has transformed the field of crystal engineering. Through deliberate selection of donor and acceptor molecules, researchers can influence crystal packing motifs, molecular recognition events, and material properties. Consequently, halogen and chalcogen bonding now occupy central positions within modern supramolecular chemistry.

1.2 Scope and Applications in Crystal Engineering, Pharmaceuticals, and Functional Materials

The growing interest in halogen and chalcogen bonding stems from their broad applicability across numerous scientific disciplines. Their highly directional nature enables precise control over molecular assembly, allowing crystal structures to be designed with increasing levels of predictability. As a result, these interactions have become valuable tools in crystal engineering, where the relationship between molecular structure and crystal packing is exploited to achieve targeted physical and chemical properties.[28]

One of the most prominent applications of halogen bonding is the construction of cocrystals.[29] In cocrystal design, complementary donor and acceptor molecules self-assemble through predictable intermolecular interactions to produce new crystalline phases possessing distinct physicochemical properties. Halogen bonding has proven particularly useful in this context because the interaction strength and geometry can often be tuned independently of the molecular framework.[30] Such flexibility has enabled the preparation of numerous cocrystals exhibiting modified melting points, solubilities, mechanical properties, and optical behavior.[31,32]

In pharmaceutical science, crystal engineering has emerged as an important strategy for improving drug performance.[33] Many active pharmaceutical ingredients suffer from poor aqueous solubility, limited bioavailability, or undesirable mechanical properties.[34] Pharmaceutical cocrystals provide a means of modifying these characteristics without altering the molecular structure of the active ingredient itself.[35] While hydrogen bonding has traditionally dominated pharmaceutical cocrystal design, halogen bonding has increasingly been explored as an alternative supramolecular synthon capable of generating novel crystal forms and improved solid-state properties.[36,37]

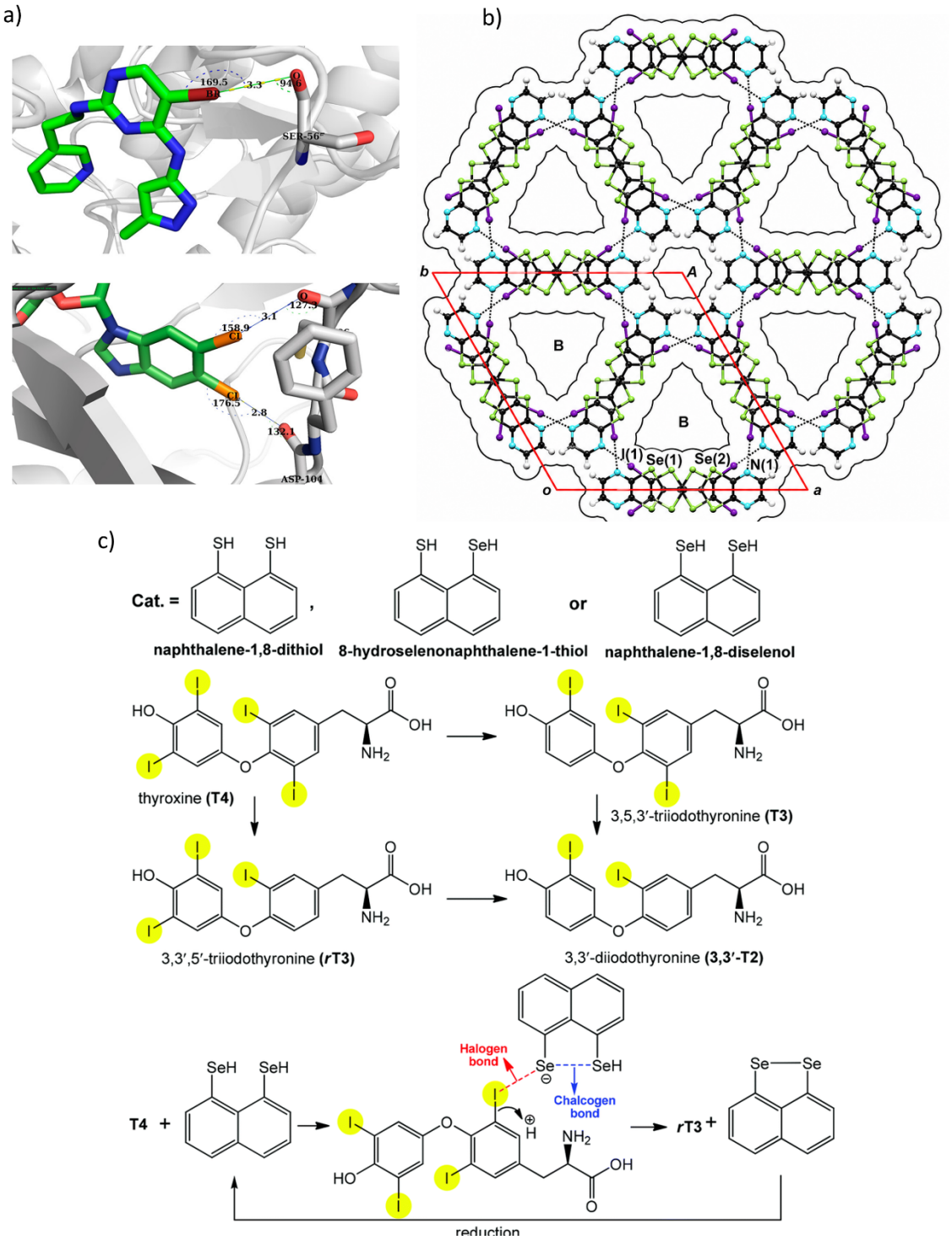


Figure 1.1.4. Selected examples illustrating the diverse roles of halogen and chalcogen bonding across different areas of chemistry. (a) Halogen bonding interactions observed in protein–ligand complexes, demonstrating their importance in biomolecular recognition and rational drug design.

(Reprinted with permission from Ref.38, American Chemical Society) (b) Halogen-bonded supramolecular framework constructed through directional I···N interactions, highlighting the utility of halogen bonding in crystal engineering and the formation of porous molecular materials. (Reproduced with permission from Ref. 39, Wiley-VCH) (c) Examples of chemical transformations in which halogen and chalcogen bonding have been implicated in substrate activation and catalytic processes, including the activation of carbon–iodine bonds through cooperative σ-hole interactions. (Adapted with permission from Ref. 40, American Chemical Society)

Beyond pharmaceutical applications, halogen and chalcogen bonds play important roles in functional materials. Examples include liquid crystals, molecular conductors, porous solids, luminescent materials, and responsive supramolecular assemblies. The directionality of these interactions allows the formation of extended one-, two-, and three-dimensional architectures with tailored electronic and structural properties.[42,43]

In recent years, chalcogen bonding has emerged as a particularly attractive interaction for the development of advanced materials. Selenium- and tellurium-containing systems exhibit strong and highly tunable σ-hole interactions, enabling applications in molecular electronics, photophysical materials, catalysis, and anion recognition. Furthermore, the ability of chalcogen atoms to function both as Lewis acids and Lewis bases introduces additional complexity and versatility into supramolecular design strategies.[41,44]

The studies presented in this thesis focus primarily on halogen- and chalcogen-bonded molecular solids. These systems provide ideal model platforms for investigating the relationships between intermolecular interactions, crystal structure, and local electronic environments using advanced spectroscopic techniques.

1.3 Current Bottlenecks—Solvent-Intensive Synthesis and Cryogen Dependence

Despite significant advances in supramolecular chemistry and crystal engineering, important challenges remain regarding the sustainability and accessibility of experimental methodologies. Two issues are particularly relevant to the work presented in this thesis: the extensive use of organic solvents in crystal preparation and the dependence of many advanced characterization techniques on liquid-helium-based infrastructure.

Traditional cocrystal synthesis often relies on solution crystallization methods, including slow evaporation, cooling crystallization, slurry conversion, and solvent-mediated transformations. While these approaches are highly effective, they frequently require large solvent volumes and extensive optimization. Solvent consumption contributes substantially to the environmental footprint of chemical manufacturing and remains one of the largest contributors to waste generation in both academic and industrial laboratories.[12]

Mechanochemistry has emerged as an attractive alternative capable of reducing or eliminating solvent requirements.[45,46] By utilizing mechanical energy to induce solid-state transformations, mechanochemical methods often achieve rapid synthesis with reduced waste generation and improved atom economy. Nevertheless, the adoption of mechanochemical methodologies remains incomplete, and further development of scalable, reproducible, and gentle mechanochemical approaches remains an active area of research.[47]

A second challenge concerns structural characterization. Modern solid-state characterization increasingly relies on advanced magnetic resonance techniques. High-resolution SSNMR spectroscopy often requires superconducting magnets operating at cryogenic temperatures, which depend on liquid helium as a cooling medium. The finite global supply of

helium, together with increasing costs and periodic supply disruptions, has raised concerns regarding the long-term sustainability of helium-dependent technologies.[48–50]

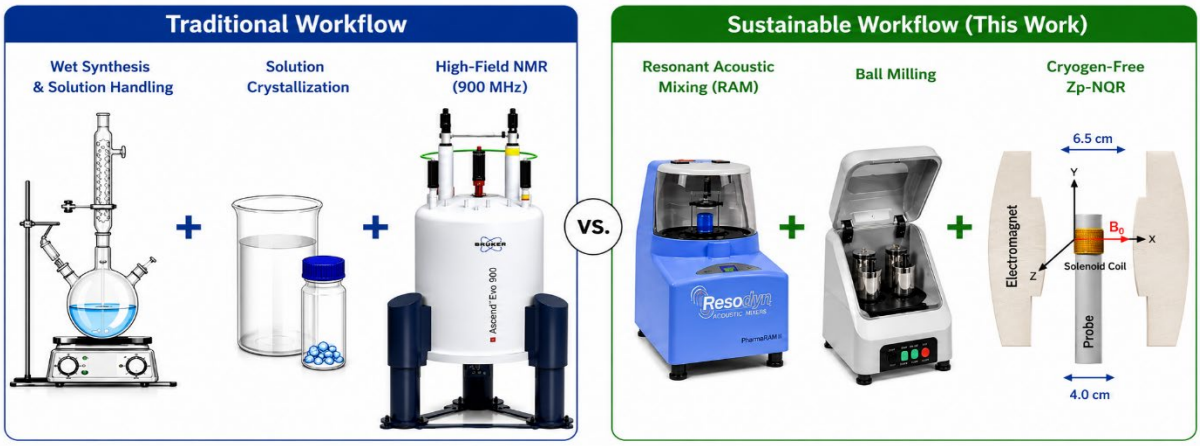


Figure 1.1.5. Comparison of conventional and sustainable workflows for studying molecular solids. The traditional workflow combines solution-based synthesis and crystallization with high-field NMR spectroscopy, whereas the sustainable workflow developed in this thesis integrates mechanochemical synthesis via RAM and ball milling with cryogen-free Zp-NQR spectroscopy. Images of the RAM, ball mill, and NMR spectrometer were adapted from the official websites of Resodyn Acoustic Mixers, MSE Supplies, and Bruker Corporation, respectively.

The challenge is particularly pronounced for strongly quadrupolar nuclei such as ^{79}Br, ^{81}Br, and ^{127}I. Their large quadrupolar interactions frequently render conventional high-field NMR approaches difficult or impractical.[51,52] Consequently, alternative characterization methodologies capable of providing local structural information without reliance on ultrahigh magnetic fields are highly desirable.

These considerations motivate the central themes of this thesis: the development of resource-efficient characterization methods through Zp-NQR spectroscopy and the implementation of solvent-minimized mechanochemical synthesis routes based on resonant acoustic mixing.

References for Chapter 1.

(1) Title Page. In Non-Covalent Interactions in Quantum Chemistry and Physics; Otero de la Roza, A., DiLabio, G. A., Eds.; *Elsevier*, **2017**; pp i–iii. https://doi.org/10.1016/B978-0-12-809835-6.00018-9.

(2) Politzer, P.; Murray, J. S. Halogen Bonding: An Interim Discussion. *ChemPhysChem* **2013**, *14* (2), 278–294. https://doi.org/10.1002/cphc.201200799.

(3) Murray, J. S.; Lane, P.; Clark, T.; Politzer, P. σ-Hole Bonding: Molecules Containing Group VI Atoms. *J. Mol. Model.* **2007**, *13* (10), 1033–1038. https://doi.org/10.1007/s00894-007-0225-4.

(4) Berger, G.; Soubhye, J.; Meyer, F. Halogen Bonding in Polymer Science: From Crystal Engineering to Functional Supramolecular Polymers and Materials. *Polym. Chem.* **2015**, *6* (19), 3559–3580. https://doi.org/10.1039/C5PY00354G.

(5) Erdélyi, M. Halogen Bonding in Solution. *Chem. Soc. Rev.* **2012**, *41* (9), 3547–3557. https://doi.org/10.1039/C2CS15292D.

(6) Gilday, L. C.; Robinson, S. W.; Barendt, T. A.; Langton, M. J.; Mullaney, B. R.; Beer, P. D. Halogen Bonding in Supramolecular Chemistry. *Chem. Rev.* **2015**, *115* (15), 7118–7195. https://doi.org/10.1021/cr500674c.

(7) Politzer, P.; Murray, J. S.; Clark, T.; Resnati, G. The σ-Hole Revisited. *Phys. Chem. Chem. Phys.* **2017**, *19* (48), 32166–32178. https://doi.org/10.1039/C7CP06793C.

(8) Tundo, P.; Anastas, P.; Black, D. S.; Breen, J.; Collins, T. J.; Memoli, S.; Miyamoto, J.; Polyakoff, M.; Tumas, W. Synthetic Pathways and Processes in Green Chemistry. Introductory Overview. *Pure Appl. Chem.* **2000**, *72* (7), 1207–1228. https://doi.org/10.1351/pac200072071207.

(9) Hu, Z.; Li, J. A Review of Helium Resources and Development. *Nat. Gas Ind. B* **2025**, *12* (3), 356–367. https://doi.org/10.1016/j.ngib.2025.05.008.

(10) Cavallo, G.; Metrangolo, P.; Milani, R.; Pilati, T.; Priimagi, A.; Resnati, G.; Terraneo, G. The Halogen Bond. *Chem. Rev.* **2016**, *116* (4), 2478–2601. https://doi.org/10.1021/acs.chemrev.5b00484.

(11) Anastas, P. T.; Warner, J. C. Green Chemistry: Theory and Practice; *Oxford University Press* **2000**. https://doi.org/10.1093/oso/9780198506980.001.0001.

(12) Martínez, J.; Cortés, J. F.; Miranda, R. Green Chemistry Metrics, A Review. *Processes* **2022**, *10* (7), 1274. https://doi.org/10.3390/pr10071274.

(13) Arunan, E.; Desiraju, G. R.; Klein, R. A.; Sadlej, J.; Scheiner, S.; Alkorta, I.; Clary, D. C.; Crabtree, R. H.; Dannenberg, J. J.; Hobza, P.; Kjaergaard, H. G.; Legon, A. C.; Mennucci, B.; Nesbitt, D. J. Definition of the Hydrogen Bond (IUPAC Recommendations 2011). **2011**, *83* (8), 1637–1641. https://doi.org/10.1351/PAC-REC-10-01-02.

(14) Clark, T.; Hennemann, M.; Murray, J. S.; Politzer, P. Halogen Bonding: The σ-Hole. *J. Mol. Model.* **2007**, *13* (2), 291–296. https://doi.org/10.1007/s00894-006-0130-2.

(15) Huber, S. M.; Jimenez-Izal, E.; Ugalde, J. M.; Infante, I. Unexpected Trends in Halogen-Bond Based Noncovalent Adducts. *Chem. Commun.* **2012**, *48* (62), 7708–7710. https://doi.org/10.1039/C2CC33304J.

(16) Benz S.; López-Andarias J.; Mareda J.; Sakai N.; Matile S. Catalysis with Chalcogen Bonds; *Angew. Chem*. **2017**, 56 (3), 812-815. https://doi.org/10.1002/anie.201611019.

(17) Jason Y. C. Lim, Igor Marques, Amber L. Thompson, Kirsten E. Christensen, Vítor Félix, and Paul D. Beer Chalcogen Bonding Macrocycles and [2]Rotaxanes for Anion Recognition *J. Am. Chem. Soc.* **2017** 139 (8), 3122-3133. https://doi.org/10.1021/jacs.6b12745.

(18) Pascoe, D. J.; Ling, K. B.; Cockroft, S. L. The Origin of Chalcogen-Bonding Interactions. *J. Am. Chem. Soc.* **2017**, *139* (42), 15160–15167. https://doi.org/10.1021/jacs.7b08511.

(19) Yang, M.; Tofan, D.; Chen, C.-H.; Jack, K. M.; Gabbaï, F. P. Digging the Sigma-Hole of Organoantimony Lewis Acids by Oxidation. *Angew. Chem. Int. Ed.* **2018**, *57* (42), 13868–13872. https://doi.org/10.1002/anie.201808551.

(20) Zahn, S.; Frank, R.; Hey-Hawkins, E.; Kirchner, B. Pnicogen Bonds: A New Molecular Linker? *Chem. – Eur. J.* **2011**, *17* (22), 6034–6038. https://doi.org/10.1002/chem.201002146.

(21) Bauzá, A.; Mooibroek, T. J.; Frontera, A. Tetrel-Bonding Interaction: Rediscovered Supramolecular Force? *Angew. Chem. Int. Ed.* **2013**, *52* (47), 12317–12321. https://doi.org/10.1002/anie.201306501.

(22) Mani, D.; Arunan, E. The X–C···Y (X = O/F, Y = O/S/F/Cl/Br/N/P) 'Carbon Bond' and Hydrophobic Interactions. *Phys. Chem. Chem. Phys.* **2013**, *15* (34), 14377–14383. https://doi.org/10.1039/C3CP51658J.

(23) Mundlapati, V. R.; Sahoo, D. K.; Bhaumik, S.; Jena, S.; Chandrakar, A.; Biswal, H. S. Noncovalent Carbon-Bonding Interactions in Proteins. *Angew. Chem. Int. Ed.* **2018**, *57* (50), 16496–16500. https://doi.org/10.1002/anie.201811171.

(24) Kumar, V.; Pilati, T.; Terraneo, G.; Meyer, F.; Metrangolo, P.; Resnati, G. Halogen Bonded Borromean Networks by Design: Topology Invariance and Metric Tuning in a Library of Multi-Component Systems. *Chem. Sci.* **2017**, *8* (3), 1801–1810. https://doi.org/10.1039/C6SC04478F.

(25) Riley, K. E.; Murray, J. S.; Fanfrlík, J.; Řezáč, J.; Solá, R. J.; Concha, M. C.; Ramos, F. M.; Politzer, P. Halogen Bond Tunability I: The Effects of Aromatic Fluorine Substitution on the

Strengths of Halogen-Bonding Interactions Involving Chlorine, Bromine, and Iodine. *J. Mol. Model.* **2011**, *17* (12), 3309–3318. https://doi.org/10.1007/s00894-011-1015-6.

(26) Riley, K.E., Murray, J.S., Fanfrlík, J. et al. Halogen bond tunability II: the varying roles of electrostatic and dispersion contributions to attraction in halogen bonds. *J Mol Model* **2013**, 19, 4651–4659. https://doi.org/10.1007/s00894-012-1428-x.

(27) Nari, A.; Thomas, S. P.; Bryce, D. L.; Thomas, B. Understanding Non-Covalent Interactions in Diphenyldiselenide and Diphenylselenide Cocrystals Using a Combined ^{77}Se Magic-Angle Spinning Solid-State NMR and Quantum Chemical Analysis Approach. *J. Phys. Chem. C* **2025**, *129* (29), 13299–13311. https://doi.org/10.1021/acs.jpcc.5c01979.

(28) Hein, R.; Beer, P. D. Halogen Bonding and Chalcogen Bonding Mediated Sensing. *Chem. Sci.* **2022**, *13* (24), 7098–7125. https://doi.org/10.1039/D2SC01800D.

(29) Nari, A.; Ovens, J. S.; Bryce, D. L. Halogen-Bonded Cocrystals via Resonant Acoustic Mixing. *RSC Mechanochemistry* **2024**, 1 (1), 50–62. https://doi.org/10.1039/D3MR00028A.

(30) Priimagi, A.; Cavallo, G.; Metrangolo, P.; Resnati, G. The Halogen Bond in the Design of Functional Supramolecular Materials: Recent Advances. *Acc. Chem. Res.* **2013**, *46* (11), 2686–2695. https://doi.org/10.1021/ar400103r.

(31) Chen, Y.-H.; Zhang, G.-Z.; Chen, F.-H.; Zhang, S.-Q.; Fang, X.; Chen, H.-M.; Lin, M.-J. Halogen-Bonded Charge-Transfer Co-Crystal Scintillators for High-Resolution X-Ray Imaging. *Chem. Sci.* **2024**, *15* (20), 7659–7666. https://doi.org/10.1039/D4SC00735B.

(32) Christopherson, J.-C.; Topić, F.; Barrett, C. J.; Friščić, T. Halogen-Bonded Cocrystals as Optical Materials: Next-Generation Control over Light–Matter Interactions. *Cryst. Growth Des.* **2018**, *18* (2), 1245–1259. https://doi.org/10.1021/acs.cgd.7b01445.

(33) Bolla, G.; Nangia, A. Pharmaceutical Cocrystals: Walking the Talk. *Chem. Commun.* **2016**, *52* (54), 8342–8360. https://doi.org/10.1039/C6CC02943D.

(34) Blagden, N.; de Matas, M.; Gavan, P. T.; York, P. Crystal Engineering of Active Pharmaceutical Ingredients to Improve Solubility and Dissolution Rates. *Adv. Drug Deliv. Rev.* **2007**, *59* (7), 617–630. https://doi.org/10.1016/j.addr.2007.05.011.

(35) Bolla, G.; Sarma, B.; Nangia, A. K. Crystal Engineering of Pharmaceutical Cocrystals in the Discovery and Development of Improved Drugs. *Chem. Rev.* **2022**, *122* (13), 11514–11603. https://doi.org/10.1021/acs.chemrev.1c00987.

(36) Lu, Y.; Liu, Y.; Xu, Z.; Li, H.; Liu, H.; Zhu, W. Halogen Bonding for Rational Drug Design and New Drug Discovery. *Expert Opin. Drug Discov.* **2012**, *7* (5), 375–383. https://doi.org/10.1517/17460441.2012.678829.

(37) Lu, Y.; Shi, T.; Wang, Y.; Yang, H.; Yan, X.; Luo, X.; Jiang, H.; Zhu, W. Halogen Bonding—A Novel Interaction for Rational Drug Design? *J. Med. Chem.* **2009**, *52* (9), 2854–2862. https://doi.org/10.1021/jm9000133.

(38) Sirimulla, S.; Bailey, J. B.; Vegesna, R.; Narayan, M. Halogen Interactions in Protein–Ligand Complexes: Implications of Halogen Bonding for Rational Drug Design. *J. Chem. Inf. Model.* **2013**, *53* (11), 2781–2791. https://doi.org/10.1021/ci400257k.

(39) Metrangolo, P.; Meyer, F.; Pilati, T.; Resnati, G.; Terraneo, G. Halogen Bonding in Supramolecular Chemistry. *Angew. Chem. Int. Ed.* **2008**, *47* (33), 6114–6127. https://doi.org/10.1002/anie.200800128.

(40) Manna, D.; Mugesh, G. Regioselective Deiodination of Thyroxine by Iodothyronine Deiodinase Mimics: An Unusual Mechanistic Pathway Involving Cooperative Chalcogen

and Halogen Bonding. *J. Am. Chem. Soc.* **2012**, *134* (9), 4269–4279. https://doi.org/10.1021/ja210478k.

(41) Mahmudov, K. T.; Kopylovich, M. N.; Silva, M. F. C. G. da; Pombeiro, A. J. L. Chalcogen Bonding in Synthesis, Catalysis and Design of Materials. *Dalton Trans.* **2017**, *46* (31), 10121–10138. https://doi.org/10.1039/C7DT01685A.

(42) Frumar, M.; Wagner, T.; Shimakawa, K.; Frumarova, B. Crystalline and Amorphous Chalcogenides, High-Tech Materials with Structural Disorder and Many Important Applications. In Nanomaterials and Nanoarchitectures; Bardosova, M., Wagner, T., Eds.; *Springer Netherlands: Dordrecht*, **2015**; pp 151–238. https://doi.org/10.1007/978-94-017-9921-8_7.

(43) Saccone, M.; Catalano, L. Halogen Bonding beyond Crystals in Materials Science. *J. Phys. Chem. B* **2019**, *123* (44), 9281–9290. https://doi.org/10.1021/acs.jpcb.9b07035.

(44) Vogel, L.; Wonner, P.; Huber, S. M. Chalcogen Bonding: An Overview. *Angew. Chem. Int. Ed.* **2019**, *58* (7), 1880–1891. https://doi.org/10.1002/anie.201809432.

(45) Friščić, T.; Mottillo, C.; Titi, H. M. Mechanochemistry for Synthesis. *Angew. Chem.* **2020**, *132* (3), 1030–1041. https://doi.org/10.1002/ange.201906755.

(46) L. James, S.; J. Adams, C.; Bolm, C.; Braga, D.; Collier, P.; Friščić, T.; Grepioni, F.; M. Harris, K. D.; Hyett, G.; Jones, W.; Krebs, A.; Mack, J.; Maini, L.; Guy Orpen, A.; P. Parkin, I.; C. Shearouse, W.; W. Steed, J.; C. Waddell, D. Mechanochemistry: Opportunities for New and Cleaner Synthesis. *Chem. Soc. Rev.* **2012**, *41* (1), 413–447. https://doi.org/10.1039/C1CS15171A.

(47) Fantozzi, N.; Volle, J.-N.; Porcheddu, A.; Virieux, D.; García, F.; Colacino, E. Green Metrics in Mechanochemistry. *Chem. Soc. Rev.* **2023**, *52* (19), 6680–6714. https://doi.org/10.1039/D2CS00997H.

(48) Anderson, S. T. Economics, Helium, and the U.S. Federal Helium Reserve: Summary and Outlook. *Nat. Resour. Res.* **2018**, *27* (4), 455–477. https://doi.org/10.1007/s11053-017-9359-y.

(49) Kouzes, R. T. *The 3He Supply Problem*; PNNL-18388; Pacific Northwest National Laboratory (PNNL), Richland, WA (US), 2009. https://doi.org/10.2172/956899.

(50) Shea, D. A.; Morgan, D. The Helium-3 Shortage: Supply, Demand, and Options for Congress. **2011**.

(51) Bryce, D. L. Chapter One - Solid-State NMR of Quadrupolar Nuclei: Selected New Methods and Applications. In *Annual Reports on NMR Spectroscopy*; Webb, G. A., Ed.; Academic Press, 2022; Vol. 107, pp 1–46. https://doi.org/10.1016/bs.arnmr.2022.06.001.

(52) Bryce, D. L. New Frontiers for Solid-State NMR across the Periodic Table: A Snapshot of Modern Techniques and Instrumentation. *Dalton Trans.* **2019**, *48* (23), 8014–8020. https://doi.org/10.1039/C9DT01801H.

Chapter 2 – Theoretical Principles of Quadrupolar Interactions and the Evolution of Zeeman-Perturbed NQR (Zp-NQR) as a Cryogen-Free Technique

Nuclear quadrupole resonance (NQR) spectroscopy is a powerful solid-state spectroscopic technique for probing the local electronic environments of quadrupolar nuclei in crystalline materials.[1] Unlike conventional nuclear magnetic resonance (NMR), which relies on a strong external magnetic field to generate nuclear spin transitions, NQR exploits the interaction between the nuclear electric quadrupole moment and the electric field gradient (EFG) produced by the surrounding electronic charge distribution. Because the resonance frequencies arise solely from this interaction, NQR provides direct insight into local bonding environments, intermolecular interactions, crystal packing, and structural disorder without the need for an applied magnetic field.

The research presented in this thesis is centered on the development and application of Zeeman-perturbed nuclear quadrupole resonance (Zp-NQR), a methodology that extends the capabilities of conventional NQR by introducing a weak, controllable magnetic field as a perturbation to the dominant quadrupolar interaction.[2] The additional spectroscopic information generated by this perturbation enables complete characterization of the EFG tensor, determination of nuclear gyromagnetic ratios, isotopic assignment of resonance lines, and site-resolved analysis of complex molecular solids. Importantly, these measurements are performed using compact adjustable electromagnets rather than superconducting magnets, providing a practical cryogen-free alternative for extracting quadrupolar interaction parameters that are often inaccessible by conventional NQR alone.

Beyond introducing the theoretical basis of quadrupolar spectroscopy, this chapter establishes the conceptual framework that underpins the experimental developments presented

throughout the remainder of this thesis. The discussion begins with the origin of the electric field gradient and the nuclear quadrupolar interaction before introducing the fundamental principles of pure NQR spectroscopy. The limitations of conventional NQR, particularly for spin-3/2 nuclei, are then examined to motivate the development of Zp-NQR. Finally, the theoretical foundations, historical evolution, and modern implementation of Zp-NQR are presented, providing the basis for the experimental methodologies and applications described in the subsequent chapters.

2.1 The Electric Field Gradient and Quadrupolar Hamiltonian

2.1.1 Nuclear Spin and the Electric Quadrupole Moment

NMR and NQR spectroscopy are founded on the interactions between atomic nuclei and their surrounding electromagnetic environments. The spectroscopic behaviour of a nucleus is governed primarily by its nuclear spin quantum number, *I*, an intrinsic quantum mechanical property that gives rise to both an angular momentum (*J*) and, for nuclei with non-zero spin, a magnetic moment (μ). These quantities form the basis of all magnetic resonance phenomena and determine how a nucleus responds to external magnetic fields and local electromagnetic interactions.[3,4]

The nuclear angular momentum, *J*, is quantized and is related to the nuclear spin according to

$$J = \hbar I \qquad Eq.\,2.1$$

where $\hbar$ is the reduced Planck constant and *I* is nuclear spin quantum number. The magnitude of the angular momentum is therefore given by

$$|J| = \hbar\sqrt{I(I+1)} \qquad Eq.\,2.2$$

while its projection along an arbitrary quantization axis is restricted to the discrete values

$$J_z = m_I \qquad Eq.2.3$$

where the magnetic quantum number m_I assumes the $2I$+1allowed values

$$m_I = -I, -I + 1, \ldots, +I \qquad Eq.2.4$$

The existence of these discrete spin states gives rise to the quantized energy levels observed in magnetic resonance spectroscopy.

Associated with the nuclear angular momentum is the nuclear magnetic moment, μ, which originates from the motion and intrinsic spin of protons within the nucleus. The magnetic moment is proportional to the angular momentum,

$$\mu = \gamma J \qquad Eq.2.5$$

where γ is the gyromagnetic ratio, a fundamental nuclear constant that relates magnetic moment to angular momentum. The magnitude of the magnetic moment is therefore

$$|\mu| = \gamma\hbar\sqrt{I(I+1)} \qquad Eq.2.6$$

and its component along the quantization axis is

$$\mu_z = \gamma\hbar m_I \qquad Eq.2.7$$

The gyromagnetic ratio is characteristic of each isotope and determines the strength of its interaction with an external magnetic field. In conventional NMR spectroscopy, it directly governs the Larmor frequency according to

$$\nu_0 = \frac{\gamma B_0}{2\pi} \qquad Eq.2.8$$

where B_0 is the applied magnetic field. Although pure NQR experiments are performed in the absence of an external magnetic field, the gyromagnetic ratio remains an important nuclear property because it determines the magnitude of the Zeeman perturbation introduced in Zp-NQR experiments. As demonstrated in later sections of this chapter, one of the distinctive capabilities of Zp-NQR is the direct experimental determination of nuclear gyromagnetic ratios from powder samples.

Nuclei with $I = 1/2$, such as ^{1}H, ^{13}C, and ^{19}F, possess spherically symmetric charge distributions and therefore interact exclusively through their magnetic dipole moments. In contrast, nuclei with $I > 1/2$ exhibit non-spherical distributions of nuclear charge and possess an additional property known as the nuclear electric quadrupole moment (Q). These nuclei, commonly referred to as quadrupolar nuclei, account for approximately 75% of all NMR-active isotopes in the periodic table. Their interaction with the surrounding electric field gradient gives rise to the quadrupolar effects that dominate both NQR spectroscopy and many solid-state NMR experiments. table.[5,6]

Table 2.1. Selected quadrupolar nuclei commonly encountered in NMR and NQR spectroscopy.[7]

Nucleus	Natural abundance(%)	Spin (I)	$\gamma/2\pi$ (kHz G^{-1})	Q (10^{-24} cm^2) = 1 barn
^{2}H	0.015	1	0.654	+0.00286
^{6}Li	7.4	1	0.626	−0.0008
^{7}Li	92.6	3/2	1.655	−0.040
^{10}B	19.6	3	0.458	+0.085
^{11}B	80.4	3/2	1.366	+0.041
^{14}N	99.6	1	0.308	+0.019
^{17}O	0.048	5/2	−0.577	−0.26
^{23}Na	100	3/2	1.126	+0.10
^{27}Al	100	5/2	1.109	+0.14

Nucleus	Natural abundance(%)	Spin (*I*)	γ/2π (kHz G^{-1})	*Q* (10^{-24} cm^2) = 1 barn
^{35}Cl	75.5	3/2	0.417	−0.082
^{37}Cl	24.5	3/2	0.347	−0.064
^{50}V	0.25	6	0.425	+0.21
^{51}V	99.8	7/2	1.119	−0.05
^{55}Mn	100	5/2	1.050	+0.33
^{59}Co	100	7/2	1.005	+0.40
^{63}Cu	69.1	3/2	1.128	−0.21
^{65}Cu	30.9	3/2	1.209	−0.195
^{69}Ga	60.4	3/2	1.022	+0.17
^{71}Ga	39.6	3/2	1.298	+0.10
^{75}As	100	3/2	0.729	+0.31
^{79}Br	50.5	3/2	1.067	+0.33
^{81}Br	49.5	3/2	1.150	+0.28
^{85}Rb	72	5/2	0.411	+0.23
^{87}Rb	28	3/2	1.393	+0.13
^{93}Nb	100	9/2	1.041	−0.32
^{113}In	4.3	9/2	0.931	+0.8
^{115}In	95.7	9/2	0.933	+0.8
^{121}Sb	57.3	5/2	1.019	−0.4
^{123}Sb	42.7	7/2	0.552	−0.5
^{127}I	100	5/2	0.852	−0.7
^{139}La	0.1	5	0.564	+0.4
^{181}Ta	99.9	7/2	0.606	+0.2
^{201}Bi	100	9/2	0.684	−0.4
^{235}U	0.72	7/2	−0.076	+5

Note: The quadrupole moment *Q* can be either positive or negative, depending on the anisotropy of the nuclear charge distribution. A positive *Q* corresponds to a predominantly prolate (elongated) charge distribution, whereas a negative *Q* corresponds to an oblate (flattened) distribution.

The quadrupolar nuclei investigated throughout this thesis include ^{35}Cl, ^{121}Sb, ^{123}Sb, ^{79}Br, ^{81}Br, and ^{127}I, all of which possess non-zero quadrupole moments and therefore exhibit strong

quadrupolar interactions in the solid state. Because these interactions are governed by the local distribution of electronic charge, they provide exceptionally sensitive probes of chemical bonding, intermolecular interactions, crystal packing, and local structural symmetry.

The nuclear quadrupole moment originates from deviations of the nuclear charge distribution from spherical symmetry. Depending on the nucleus, the charge distribution may adopt either a prolate (elongated) or oblate (flattened) shape (Figure 1.2.1). When such an anisotropic charge distribution is placed within an inhomogeneous electric field, an electrostatic interaction arises between the nuclear quadrupole moment and the local electric field gradient (EFG). This interaction forms the physical basis of NQR spectroscopy and contributes significantly to the spectra of quadrupolar nuclei observed by solid-state NMR.

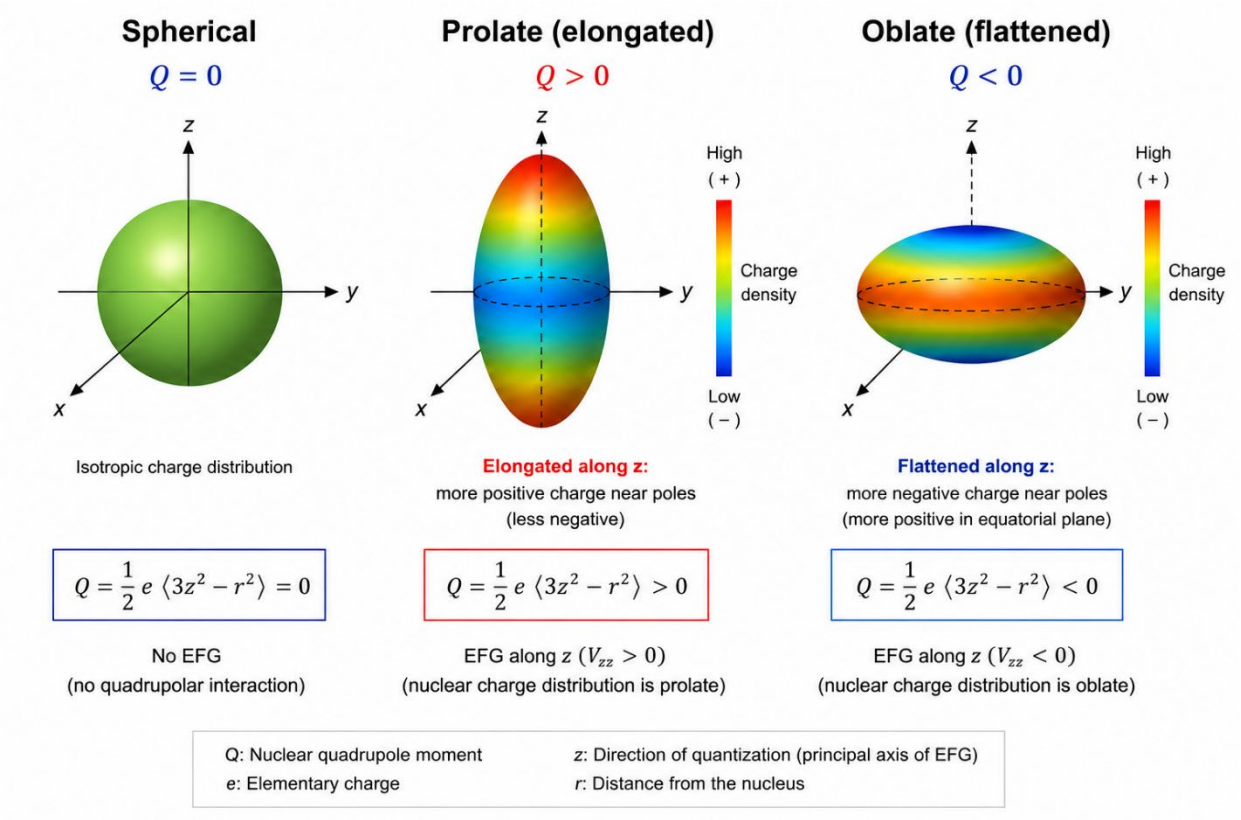


Figure 1.2.1. Schematic representation of nuclear charge distributions and their associated nuclear quadrupole moments (Q). A spherically symmetric charge distribution possesses no quadrupole moment ($Q = 0$), whereas non-spherical distributions give rise to finite quadrupole moments. A prolate (elongated) charge distribution corresponds to a positive quadrupole moment ($Q > 0$), while an oblate (flattened) charge distribution corresponds to a negative quadrupole moment ($Q < 0$). Nuclei with spin quantum number $I > 1/2$ may possess a non-zero quadrupole moment and can interact with the EFG generated by the surrounding electronic environment.

2.1.2 The Electric Field Gradient Tensor

The EFG describes the spatial variation of the electric field surrounding a nucleus and is the fundamental quantity responsible for the nuclear quadrupolar interaction. Mathematically, the EFG is a second-rank tensor defined as the matrix of second derivatives of the electrostatic potential, V, with respect to the Cartesian coordinates,

$$Vij = \frac{\partial^2 V}{\partial x_i \, \partial x_j} \qquad Eq.2.9$$

where (V) is the electrostatic potential and (x_i) and (x_j) correspond to Cartesian coordinates. Unlike the electric field itself, which vanishes at the position of the nucleus according to electrostatic equilibrium, the second derivatives of the electrostatic potential are generally non-zero and provide a measure of the anisotropy of the surrounding charge distribution. Consequently, the EFG reflects the combined influence of the local electronic structure and the arrangement of neighbouring atoms and ions.

Diagonalization of the EFG tensor yields three mutually orthogonal principal components, conventionally denoted $(V_{XX}), (V_{YY})$, and (V_{ZZ}) , which define the principal-axis system (PAS). By convention, the components are ordered according to

$$|V_{ZZ}| \geq |V_{YY}| \geq |V_{XX}| \qquad Eq.2.10$$

Because the electrostatic potential satisfies Laplace's equation in regions free of charge, the EFG tensor is traceless,

$$V_{XX} + V_{YY} + V_{ZZ} = 0 \qquad Eq. 2.11$$

As a result, only two independent tensor components are required to completely describe the EFG. These are commonly expressed through the quadrupolar coupling constant, which reflects the magnitude of the interaction, and the asymmetry parameter, which describes the deviation of the tensor from axial symmetry. These parameters are introduced in Section 2.1.4.

In molecular solids, the EFG is highly sensitive to the distribution of electronic charge surrounding the nucleus. Contributions arise from covalent bonding electrons, lone-pair electrons, core electrons, and the electrostatic influence of neighbouring atoms. Consequently, hydrogen bonding, halogen bonding, chalcogen bonding, crystal packing, and other intermolecular interactions can significantly modify both the magnitude and symmetry of the EFG. This exceptional sensitivity makes quadrupolar spectroscopy a powerful probe of local structure in crystalline materials.

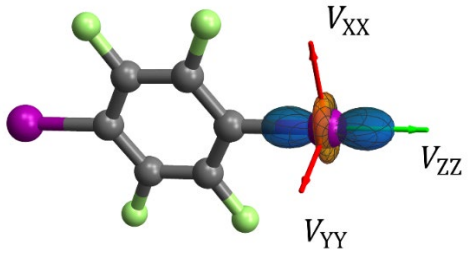


Figure 1.2.2. EFG tensor surfaces calculated for the ^{127}I nucleus in 1,4-diiodotetrafluorobenzene. The EFG tensor is represented in its principal-axis system by the components V_{XX} , V_{YY} , and V_{ZZ} , which satisfy the relation $V_{XX} + V_{YY} + V_{ZZ} = 0$. The tensor surfaces were visualized using a custom Mathematica Version 14 notebook.[8] The EFG tensor is displayed as a three-dimensional surface to illustrate both its sign and symmetry, with blue regions corresponding to positive EFG

values and orange regions corresponding to negative EFG values. The pronounced anisotropy of the tensor reflects the highly directional electronic environment surrounding the iodine nucleus arising from the covalent C–I bond and intermolecular interactions.

Throughout this thesis, variations in the EFG are used to investigate changes in the electronic environments of chlorine, bromine, iodine, and antimony nuclei resulting from non-covalent interactions in molecular solids. As demonstrated in the following chapters, subtle changes in bonding often produce measurable changes in the EFG, allowing quadrupolar spectroscopy to distinguish crystallographically inequivalent sites and quantify the effects of intermolecular interactions.

2.1.3 The Quadrupolar Hamiltonian

The interaction between the nuclear electric quadrupole moment and the electric field gradient is described by the quadrupolar Hamiltonian, which forms the theoretical foundation of both NQR spectroscopy and the quadrupolar interactions observed in SSNMR. In quantum mechanics, the nuclear spin is represented by the vector spin operator

$$\hat{\mathrm{I}} = \left(\hat{\mathrm{I}_\mathrm{X}}, \hat{\mathrm{I}_\mathrm{Y}}, \hat{\mathrm{I}_\mathrm{Z}}\right) \qquad Eq.\,2.12$$

Where $\widehat{I_X}$, $\widehat{I_Y}$, and $\widehat{I_Z}$ are the Cartesian components of the nuclear spin angular momentum operator. In the principal-axis system of the EFG tensor, the Hamiltonian is conventionally given by Eq. 2.13 and follows the convention established by Das and Hahn and later summarized in standard NMR texts.[1,9]

$$\widehat{H_Q} = \frac{eQV_{ZZ}}{4I(2I-1)}\left[3\widehat{I_Z^2} - \widehat{I^2} + \eta\left(\widehat{I_X^2} - \widehat{I_Y^2}\right)\right] \qquad Eq.\,2.13$$

where e is the elementary charge, Q is the nuclear electric quadrupole moment, V_{ZZ} is the largest principal component of the electric field gradient tensor, I is the nuclear spin quantum number, $\widehat{I^2}$ is the total nuclear spin angular momentum operator, and η is the electric field gradient asymmetry parameter.

This Hamiltonian describes the electrostatic interaction between the non-spherical nuclear charge distribution and the surrounding electric field gradient. The resulting quadrupolar interaction removes the degeneracy of the nuclear spin states, producing the discrete energy levels observed in NQR spectroscopy and contributing to the broad powder patterns characteristic of quadrupolar nuclei in SSNMR.

The magnitude of the quadrupolar interaction depends directly on both the nuclear quadrupole moment and the local EFG. Consequently, nuclei possessing large quadrupole moments and highly anisotropic electronic environments often exhibit quadrupolar coupling constants corresponding to resonance frequencies ranging from several megahertz to hundreds of megahertz.

For the nuclei investigated throughout this thesis, the quadrupolar interaction is substantially larger than the Zeeman interaction produced by the weak magnetic fields employed in Zp-NQR experiments. The quadrupolar Hamiltonian therefore remains the dominant contribution to the nuclear spin Hamiltonian, while the magnetic field acts only as a perturbation. This distinction forms the basis of the weak-field treatment discussed in Section 2.3.

2.1.4 Quadrupolar Coupling Constant and Asymmetry Parameter

The magnitude and symmetry of the electric field gradient are commonly described by two experimentally accessible parameters: the quadrupolar coupling constant, C_Q, and the asymmetry parameter, η. Together, these quantities provide a complete description of the EFG tensor and constitute the principal observables obtained from NQR and quadrupolar NMR experiments.

The quadrupolar coupling constant is defined as

$$C_Q = \frac{\mathrm{eQV_{ZZ}}}{\mathrm{h}} \qquad Eq.\,2.14$$

where (h) is Planck's constant.

Because C_Q is directly proportional to both the nuclear quadrupole moment and the largest principal component of the EFG tensor, it reflects the overall strength of the quadrupolar interaction. Changes in chemical bonding, molecular geometry, crystal packing, and intermolecular interactions alter the local electron density and therefore modify the quadrupolar coupling constant. As a result, C_Q serves as a sensitive indicator of changes in the local electronic structure.[10]

The deviation of the EFG tensor from axial symmetry is quantified by the asymmetry parameter,

$$\eta = \frac{V_{XX} - V_{YY}}{V_{ZZ}} \qquad Eq.\,2.15$$

which ranges from

$$0 \leq \eta \leq 1 \qquad Eq.\,2.16$$

An axially symmetric EFG corresponds to η=0 whereas increasing values of η indicate progressively greater deviations from cylindrical symmetry. Since many intermolecular interactions perturb the electronic structure asymmetrically, the asymmetry parameter often provides structural information complementary to that obtained from the quadrupolar coupling constant alone.

Throughout this thesis, simultaneous determination of C_Q and η forms the basis for quantifying changes in local electronic structure and identifying crystallographically distinct quadrupolar sites. One of the principal objectives of the Zp-NQR methodology developed in this work is the accurate extraction of these two parameters from powdered molecular solids.

2.1.5 Energy Levels of Quadrupolar Nuclei

The quadrupolar Hamiltonian lifts the degeneracy of the nuclear spin states and produces discrete energy levels that depend on the spin quantum number, quadrupolar coupling constant, and asymmetry parameter. The number of energy levels increases with nuclear spin according to the 2I+1 allowed magnetic quantum states.

For a spin 3/2 nucleus, such as ^{35}Cl, ^{79}Br, and ^{81}Br, four magnetic sublevels exist corresponding to

$$m_I = +\frac{3}{2}, +\frac{1}{2}, -\frac{1}{2}, -\frac{3}{2} \qquad Eq.\,2.17$$

In the absence of an external magnetic field, the quadrupolar interaction alone determines the energy-level structure. Under these conditions, the $+m_I$ and $-m_I$ states remain degenerate, giving rise to a single allowed NQR transition between the ±1/2 and ±3/2 levels, as illustrated in Figure 1.2.3.

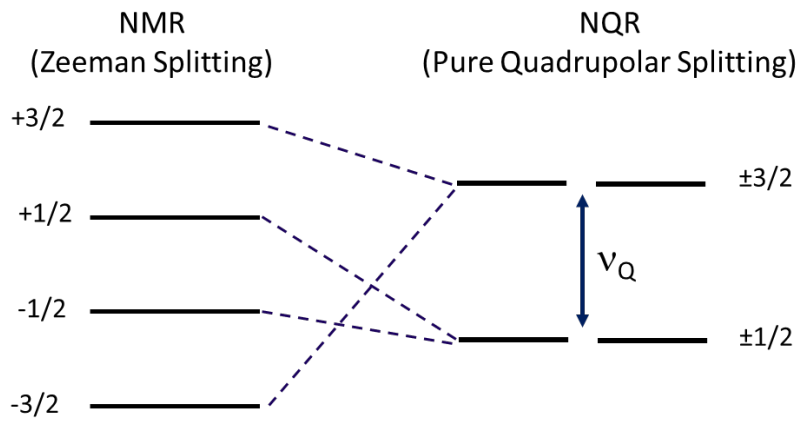


Figure 1.2.3. Comparison of the energy-level splitting of a spin-*I*=3/2 nucleus in NMR and NQR. In the presence of an external magnetic field (B_0), the Zeeman interaction splits the nuclear spin states into four equally spaced levels. In contrast, in zero magnetic field the nuclear quadrupole interaction with the EFG produces two doubly degenerate energy levels, $|m_I| = 1/2$ and $|m_I| = 3/2$, separated by the NQR transition frequency ν_Q.

This degeneracy represents one of the fundamental limitations of conventional NQR for spin-3/2 nuclei. Because only a single transition frequency is observed, the experiment provides insufficient information to determine both the quadrupolar coupling constant and the asymmetry parameter independently. As discussed in the following section, overcoming this limitation has been a major motivation for the development of Zeeman-perturbed NQR spectroscopy.

2.2 Pure Nuclear Quadrupole Resonance

2.2.1 Principles of Pure Nuclear Quadrupole Resonance

NQR is a radiofrequency spectroscopic technique that probes the interaction between the nuclear electric quadrupole moment and the electric field gradient surrounding a quadrupolar nucleus in the absence of an externally applied magnetic field.[11] Unlike conventional NMR spectroscopy, where resonance frequencies are primarily determined by the Zeeman interaction,

the NQR spectrum arises exclusively from the quadrupolar interaction. Consequently, the observed resonance frequencies directly reflect the magnitude and symmetry of the local electric field gradient and are therefore highly sensitive to the electronic structure of crystalline solids.[12]

Because the quadrupolar interaction originates from the local distribution of electronic charge, NQR is exceptionally responsive to changes in chemical bonding, molecular geometry, crystal packing, polymorphism, molecular dynamics, and non-covalent interactions, including hydrogen, halogen, and chalcogen bonding.[13–17] Even subtle structural perturbations that produce only minor changes in diffraction data can generate measurable shifts in NQR frequencies, making the technique an exceptionally sensitive local structural probe.

The nuclear spin Hamiltonian describing a pure NQR experiment contains only the quadrupolar interaction,

$$\hat{\mathrm{H}} = \widehat{\mathrm{H_Q}} \qquad Eq.\,2.18$$

where $\widehat{\mathrm{H_Q}}$ is the quadrupolar Hamiltonian introduced in Section 2.1.3. Since no external magnetic field is present, the resonance frequencies depend entirely on the electric field gradient generated by the surrounding electronic environment.

An important consequence of this dependence is that every crystallographically distinct quadrupolar nucleus experiences a unique electric field gradient and therefore gives rise to its own characteristic resonance frequency. NQR is therefore inherently site-specific and can distinguish chemically inequivalent atomic sites without isotopic enrichment or an externally applied magnetic field. This capability has made NQR an important tool for the characterization of molecular crystals, pharmaceuticals, energetic materials, perovskites, and other functional solids.

Throughout this thesis, pure NQR serves as the experimental foundation upon which Zeeman-perturbed NQR is built. Understanding both the capabilities and the intrinsic limitations of conventional NQR is therefore essential for appreciating the motivation behind the methodology developed in the following sections.

2.2.2 NQR Transition Frequencies

The resonance frequencies observed in NQR depend on the nuclear spin quantum number and the magnitude and symmetry of the electric field gradient tensor. For a spin-3/2 nucleus, which includes the isotopes ^{35}Cl, ^{79}Br, and ^{81}Br investigated throughout this thesis, only a single transition is allowed under pure quadrupolar coupling. The transition frequency is given by

$$\nu_Q = \frac{C_Q}{2}\sqrt{1+\frac{\eta^2}{3}} \qquad Eq.\,2.19$$

demonstrating that the observed resonance depends simultaneously on both the quadrupolar coupling constant and the asymmetry parameter.

Because both quantities are influenced by the local electronic structure, variations in chemical bonding, intermolecular interactions, crystal packing, temperature, and pressure all lead to measurable changes in the NQR frequency. Consequently, the resonance frequency provides a direct spectroscopic fingerprint of the crystallographic environment surrounding the quadrupolar nucleus.

The situation differs for nuclei with higher spin quantum numbers, such as ^{127}I (I = 5/2). Multiple allowed transitions are observed, providing sufficient experimental observables to determine both C_Q and η directly from pure NQR measurements. In contrast, only a single

transition is available for spin-3/2 nuclei, fundamentally limiting the structural information that can be extracted from conventional NQR experiments.

This distinction has important practical consequences because chlorine and bromine nuclei—the primary nuclei investigated throughout this thesis—both possess $I = 3/2$. As discussed in the following sections, overcoming this limitation is one of the principal motivations for the development of Zp-NQR.

2.2.3 Advantages of Pure NQR

Pure NQR possesses several unique advantages that distinguish it from other solid-state spectroscopic techniques. Since no external magnetic field is required, NQR instrumentation is considerably simpler than conventional superconducting NMR spectrometers and operates without cryogenic cooling or liquid helium. Measurements can therefore be performed using compact, comparatively inexpensive instrumentation at room temperature, making the technique both accessible and operationally efficient.

Perhaps the greatest strength of NQR lies in its exceptional sensitivity to the local electronic structure. Because resonance frequencies are governed directly by the electric field gradient, they respond strongly to subtle changes in chemical bonding and intermolecular interactions. Consequently, NQR has proven particularly valuable for identifying polymorphs, monitoring phase transitions, characterizing pharmaceutical solids, detecting energetic materials, and investigating non-covalent interactions in crystalline systems.[18–20]

Another important advantage is its intrinsic site selectivity. Each crystallographically distinct quadrupolar nucleus generally produces an individual resonance frequency, enabling local structural information to be obtained without isotopic enrichment or chemical labeling. As a result,

NQR provides information that is highly complementary to diffraction techniques, particularly in systems where local structural variations are not readily apparent from average crystallographic structures.[14,16]

Although these advantages make NQR a powerful structural characterization tool, the technique also possesses several important limitations that restrict its ability to uniquely determine quadrupolar interaction parameters for many nuclei. These limitations are discussed in the following section and ultimately motivate the development of Zeeman-perturbed NQR.

2.2.4 Limitations of Pure NQR

Despite its many advantages, pure NQR possesses several important limitations that restrict its ability to fully characterize quadrupolar nuclei. The most significant limitation arises for spin-3/2 nuclei, including ^{35}Cl, ^{79}Br, and ^{81}Br, which constitute the primary nuclei investigated throughout this thesis.

The most fundamental limitation arises from the number of experimentally observable transitions. As discussed in Section 2.2.2, a spin-3/2 nucleus exhibits only a single allowed NQR transition in the absence of an external magnetic field. The corresponding resonance frequency is described by Eq. 2.18 which is determined by both the C_Q , and the η,

Consequently, one experimental observable depends on two independent unknowns. An infinite number of (C_Q, η) combinations can therefore reproduce the same resonance frequency, preventing the unique determination of the complete electric field gradient tensor from pure NQR measurements alone. For spin-3/2 nuclei, this ambiguity represents a fundamental limitation of the technique rather than an instrumental constraint.

Figure 1.2.4 illustrates this distinction by comparing the information available from pure NQR and high-field solid-state NMR for a representative spin-5/2 nucleus. Whereas multiple NQR transitions are observed for higher-spin nuclei such as ^{127}I, allowing both C_Q and η to be determined directly, only a single transition is available for spin-3/2 nuclei. As a result, conventional NQR cannot uniquely characterize the quadrupolar interaction for many technologically and chemically important isotopes, including chlorine and bromine.

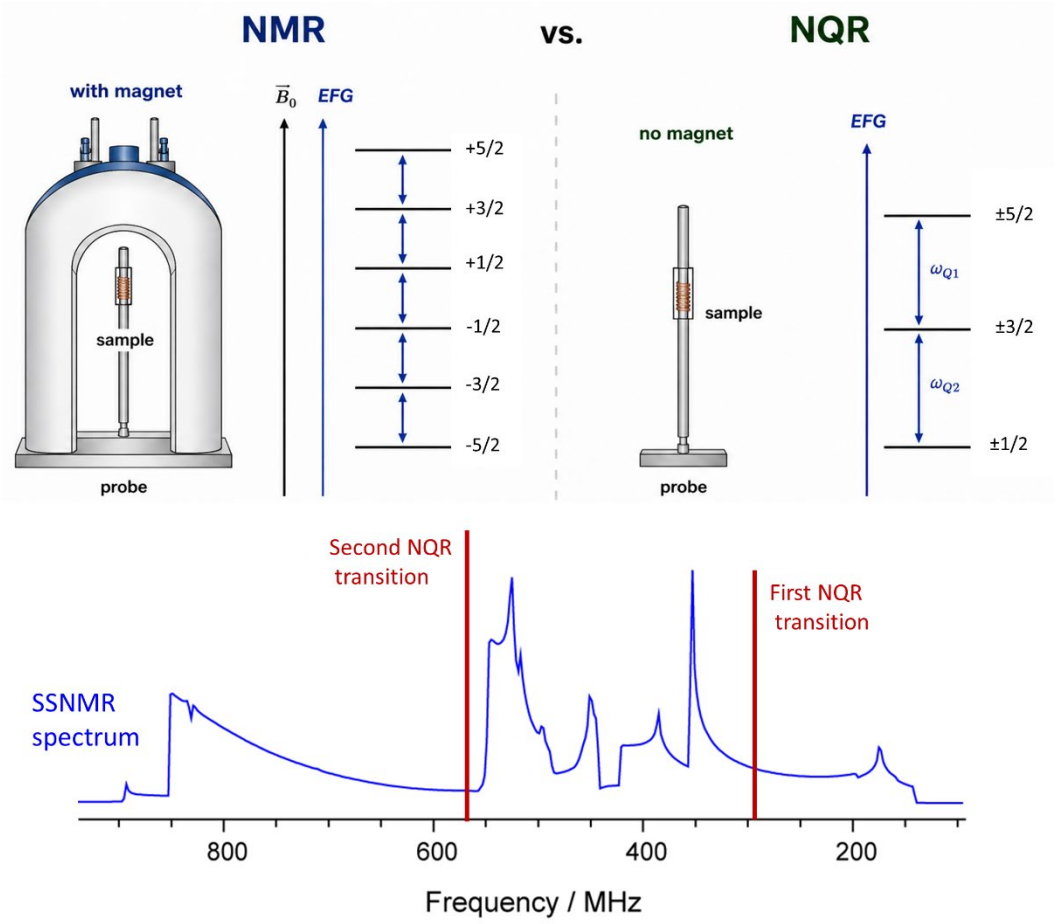


Figure 1.2.4. Comparison of high-field SSNMR and pure NQR for a spin-5/2 nucleus, illustrated using parameters representative of ^{127}I ($C_Q = 2000$ MHz and $\eta = 0.12$). *Top:* Schematic comparison of the experimental configurations and corresponding energy-level diagrams. In conventional SSNMR (left), the sample is positioned within a superconducting magnet, where the external magnetic field (B_0) dominates the nuclear spin Hamiltonian, producing six Zeeman-split energy

levels. In pure NQR (right), no external magnetic field is applied (B_0=0), and the energy levels arise solely from the interaction between the nuclear electric quadrupole moment and the local EFG, resulting in three doubly degenerate quadrupolar energy levels. *Bottom:* Simulated spectra illustrating the corresponding resonance frequencies. The SSNMR powder pattern spans a broad frequency range owing to the large second-order quadrupolar interaction at 21.1 T, whereas pure NQR exhibits two discrete resonance lines corresponding to the ±1/2↔±3/2 and ±3/2↔±5/2 transitions.

Beyond this intrinsic limitation, pure NQR also presents several practical experimental challenges. Unlike conventional NMR spectroscopy, where resonance frequencies are largely determined by the applied magnetic field, NQR frequencies depend entirely on the local electric field gradient and therefore vary widely from one compound to another. Consequently, the resonance frequency of an unknown material is rarely known *a priori*. Locating an NQR signal often requires scanning broad frequency ranges in small increments while repeatedly retuning the probe, making resonance searches both time-consuming and experimentally demanding.

Recent developments have substantially improved this process. First-principles electronic structure calculations, particularly density functional theory (DFT), can provide reliable estimates of quadrupolar coupling constants and expected resonance frequencies before an experiment is performed. Likewise, automated frequency-search systems employing robotic probe tuning have significantly accelerated resonance detection by enabling autonomous tuning and frequency scanning across broad spectral ranges with minimal operator intervention. [21]

Additional challenges arise for higher-spin nuclei, where multiple NQR transitions are theoretically available. In many iodine-containing molecular solids, for example, one of the ^{127}I transitions occurs above 600 MHz.[10] Such frequencies exceed the operating range of many commercial NQR spectrometers and require specialized broadband radiofrequency probes capable

of efficient operation over an exceptionally wide frequency range. Consequently, although the complete quadrupolar interaction is theoretically accessible for these nuclei, instrumental limitations may prevent observation of all required transitions in practice.

Considerable progress has also been made in the development of broadband pulse sequences for quadrupolar spectroscopy. In particular, Rossini and co-workers introduced the combination of Wideband Uniform Rate Smooth Truncation (WURST) pulses with the Quadrupolar Carr–Purcell–Meiboom–Gill (QCPMG) echo train, enabling the efficient acquisition of ultra-wide quadrupolar NMR and NQR spectra that would otherwise require prohibitively long acquisition times.[22] By combining broadband excitation with the sensitivity enhancement afforded by QCPMG echo trains, the WURST-QCPMG experiment has become a widely adopted method for the characterization of quadrupolar nuclei exhibiting broad resonance patterns.[23] Although this development substantially improved the experimental efficiency of broadband quadrupolar spectroscopy, it does not overcome the fundamental limitation of pure NQR for spin-3/2 nuclei, namely that only a single zero-field transition is available for determining the quadrupolar interaction parameters.

These considerations illustrate that the principal obstacle is not the sensitivity of NQR, but rather the limited amount of information available from the zero-field experiment. The technique provides an exceptionally sensitive probe of local electronic structure, yet for spin-3/2 nuclei it lacks sufficient experimental observables to uniquely determine the complete electric field gradient tensor. Overcoming this limitation while preserving the intrinsic advantages of NQR constitutes the central motivation for the Zeeman-perturbed methodology developed throughout this thesis.

2.2.5 Overcoming the Limitations of Pure NQR: Motivation for Zeeman-Perturbed Nuclear Quadrupole Resonance

The limitations discussed in the previous section arise not because NQR lacks sensitivity to local structure, but because the zero-field experiment provides an insufficient number of independent observables for many quadrupolar nuclei. This distinction is particularly important for spin-3/2 nuclei, where a single resonance frequency must simultaneously describe both the magnitude and symmetry of the electric field gradient. Consequently, additional experimental information is required to uniquely determine the complete quadrupolar interaction.

A straightforward approach to obtaining this information is to perturb the quadrupolar energy levels by introducing an external magnetic field. If the applied field is sufficiently weak that the quadrupolar interaction remains the dominant contribution to the nuclear spin Hamiltonian, the degeneracy of the quadrupolar energy levels is partially lifted without fundamentally altering the character of the spectrum. The resulting Zeeman splitting generates additional resonance transitions whose positions depend not only on the quadrupolar coupling constant and asymmetry parameter, but also on the nuclear gyromagnetic ratio and the orientation of the electric field gradient relative to the applied magnetic field.

This weak-field regime forms the basis of Zp-NQR. By introducing a controlled magnetic perturbation while preserving the intrinsic sensitivity of NQR to the electric field gradient, Zp-NQR provides the additional experimental observables required to determine quadrupolar interaction parameters that are inaccessible from conventional NQR measurements alone.

It is important to emphasize that Zp-NQR does not replace conventional NQR or high-field solid-state NMR. Rather, it occupies an intermediate regime in which the quadrupolar interaction

remains the dominant term in the spin Hamiltonian, while the Zeeman interaction provides complementary information through controlled perturbation of the energy levels. This operating principle distinguishes Zp-NQR fundamentally from conventional NMR and defines its unique role within the family of quadrupolar spectroscopic techniques.

The following section introduces the theoretical framework of Zeeman perturbation and traces the historical development of the technique from its early applications to single crystals through its modern implementation for polycrystalline powders using exact Hamiltonian simulations.

2.3.1 Principles and Historical Development of Zeeman-Perturbed Nuclear Quadrupole Resonance

Zp-NQR extends conventional NQR by introducing a weak static magnetic field while maintaining the quadrupolar interaction as the dominant contribution to the nuclear spin Hamiltonian. Under these conditions, the applied field acts as a perturbation that partially removes the degeneracy of the quadrupolar energy levels, generating additional resonance transitions without fundamentally changing the quadrupolar nature of the spectrum. The resulting transition frequencies and intensities depend on the quadrupolar coupling constant, the asymmetry parameter, the nuclear gyromagnetic ratio, and the orientation of the electric field gradient relative to the applied magnetic field. Collectively, these additional observables provide sufficient information to characterize quadrupolar interactions that cannot be uniquely determined by pure NQR alone.

The theoretical basis of Zeeman perturbation emerged during the 1950s and 1960s, when several groups recognized that the Zeeman interaction could be treated as a small perturbation to

the dominant quadrupolar Hamiltonian in weak magnetic fields. This operating regime is fundamentally different from that of conventional high-field NMR, where the Zeeman interaction dominates and quadrupolar effects are treated as perturbations. Early theoretical treatments by Dean, Toyama, Morino, and co-workers established the mathematical framework describing the Zeeman splitting of quadrupolar energy levels and predicted the characteristic spectral features observed experimentally.[24,25]

Early experimental studies were performed primarily on single crystals, where rotating the crystal with respect to the applied magnetic field enabled the complete electric field gradient tensor and its orientation relative to the crystallographic axes to be determined.[26,27] Although these experiments demonstrated the considerable structural information obtainable from Zeeman perturbation, they required high-quality single crystals and precise goniometric instrumentation, limiting their applicability to many chemically relevant materials.

A major advance was achieved through the work of Morino and Toyama, who demonstrated that Zeeman-perturbed spectra acquired from polycrystalline powders also contain sufficient structural information for quantitative analysis.[28] Rather than relying on measurements from individual crystal orientations, they showed that the singularities characteristic of powder spectra could be used to determine the asymmetry parameter directly from randomly oriented samples. This development significantly broadened the applicability of Zp-NQR to systems for which suitable single crystals were unavailable, including pharmaceuticals, molecular crystals, and many inorganic solids.

While these pioneering studies relied primarily on first-order perturbation theory and analytical interpretation of characteristic spectral features,[29,24,28] modern Zp-NQR has evolved substantially through advances in computational methods and instrumentation. Exact numerical

diagonalization of the complete nuclear spin Hamiltonian now permits direct simulation of the full powder spectrum without the approximations inherent in perturbation theory. This approach provides significantly improved accuracy and enables quantitative analysis of higher-spin nuclei, multiple crystallographic sites, overlapping resonances, and experimentally complex line shapes.[30,31]

The methodology employed throughout this thesis builds upon these developments by combining adjustable electromagnets, cryogen-free instrumentation, and exact Hamiltonian simulations implemented through the QUadrupolar Exact SofTware (QUEST).[32] This combination enables quantitative analysis of polycrystalline molecular solids without the need for superconducting magnets or single crystals, forming the experimental foundation for the studies presented in the following chapters.

2.3.2 Weak-Field Hamiltonian and Zeeman Splitting

The defining characteristic of Zeeman-perturbed nuclear quadrupole resonance is that the quadrupolar interaction remains the dominant contribution to the nuclear spin Hamiltonian while the externally applied magnetic field acts only as a perturbation. This operating regime distinguishes Zp-NQR fundamentally from conventional high-field SSNMR, where the Zeeman interaction dominates and quadrupolar effects are treated as comparatively small perturbations.

The total nuclear spin Hamiltonian describing a quadrupolar nucleus in the presence of both an electric field gradient and an external magnetic field is given by

$$\widehat{\mathrm{H}} = \widehat{\mathrm{H_Q}} + \widehat{\mathrm{H_Z}} \qquad Eq.\,2.20$$

where $\widehat{H_Q}$ is the quadrupolar Hamiltonian introduced in Section 2.1.3 and $\widehat{H_Z}$ is the Zeeman Hamiltonian,

$$\widehat{\mathrm{H_Z}} = -\gamma\hbar B_0 \cdot \hat{\mathrm{I}} \qquad Eq.\,2.21$$

where γ is the nuclear gyromagnetic ratio, $\hbar$ is the reduced Planck constant, B_0 is the externally applied magnetic field, and $\hat{\mathrm{I}}$ is the nuclear spin operator.

The relative magnitudes of these two interactions determine the spectroscopic regime. In conventional solid-state NMR, magnetic fields of several tesla produce Zeeman energies that greatly exceed the quadrupolar interaction,

$$\left|\widehat{\mathrm{H_Z}}\right| \gg \left|\widehat{\mathrm{H_Q}}\right| \qquad Eq.\,2.22$$

so that the Zeeman interaction defines the primary nuclear energy levels and the quadrupolar interaction introduces relatively small corrections to the resonance frequencies.

Zp-NQR operates in the opposite limit. Magnetic fields are typically only a few tens of millitesla, such that

$$\left|\widehat{\mathrm{H_Q}}\right| \gg \left|\widehat{\mathrm{H_Z}}\right| \qquad Eq.\,2.23$$

Under these conditions, the electric field gradient continues to govern the energy-level structure, while the applied magnetic field produces only a controlled perturbation of the quadrupolar states. This weak-field regime preserves the intrinsic sensitivity of NQR to the local electronic environment while simultaneously generating additional spectroscopic observables.

For a spin-3/2 nucleus, the quadrupolar interaction alone produces two doubly degenerate energy levels corresponding to the $m_Q = \pm 1/2$ and $m_Q = \pm 3/2$ states (Figure 1.2.5). Application of

a weak magnetic field lifts the $\pm m_Q$ degeneracy, splitting each quadrupolar level into two Zeeman sublevels. Consequently, the single resonance observed in pure NQR evolves into four allowed transitions that are distributed symmetrically about the zero-field resonance frequency.

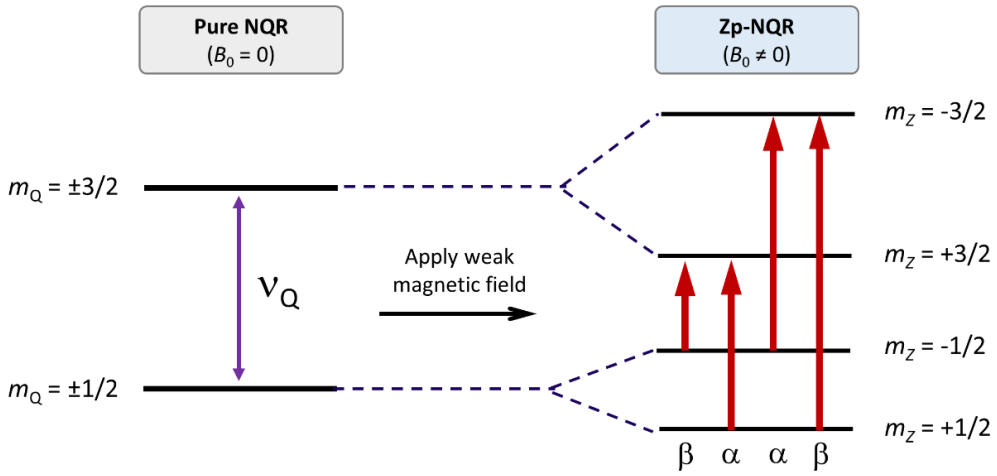


Figure 1.2.5. Energy-level diagram illustrating the effect of a weak magnetic field on a spin-3/2 nucleus in Zp-NQR. Under pure NQR conditions (B_0= 0), the quadrupolar interaction produces two doubly degenerate energy levels, denoted by the quadrupolar quantum number $m_Q = \pm 1/2$ and $m_Q = \pm 3/2$, resulting in a single resonance transition with frequency ν_Q. Upon application of a weak static magnetic field ($B_0 \neq 0$), the Zeeman interaction lifts the $\pm m_Q$ degeneracy, splitting each quadrupolar level into two Zeeman sublevels labeled by the magnetic quantum number m_Z . Consequently, the single NQR transition is transformed into four allowed Zeeman-perturbed transitions, conventionally designated as the α and β transition pairs, which form the characteristic four-line Zeeman-perturbed spectrum of a spin-3/2 nucleus.

The magnitude of the splitting is governed primarily by the nuclear gyromagnetic ratio and the strength of the applied magnetic field. To first order, the separation between adjacent Zeeman components is proportional to the nuclear Larmor frequency,

$$\nu_0 = \frac{\gamma B_0}{2\pi} \qquad Eq.\,2.24$$

although exact transition frequencies depend on the complete nuclear spin Hamiltonian and therefore require numerical diagonalization for accurate analysis. As the magnetic field is increased, the Zeeman components become progressively more separated. In practice, the applied field must remain sufficiently weak that the quadrupolar interaction continues to dominate the Hamiltonian, thereby preserving the validity of the weak-field approximation that defines Zp-NQR.

The fundamental distinction between conventional high-field solid-state NMR and Zeeman-perturbed NQR lies in the relative magnitudes of the Zeeman and quadrupolar interactions. Whereas the Zeeman interaction dominates the spin Hamiltonian in high-field NMR, the quadrupolar interaction remains the principal interaction in Zp-NQR. The key differences between these two regimes are summarized in Table 2.2.

Table 2.2. Comparison of the operating regimes of conventional high-field SSNMR and Zp-NQR. The two techniques differ fundamentally in the relative magnitudes of the Zeeman and quadrupolar interactions. In high-field SSNMR, the Zeeman interaction dominates the nuclear spin Hamiltonian and the quadrupolar interaction is treated as a perturbation. In contrast, Zp-NQR operates in the weak-field regime, where the quadrupolar interaction remains the dominant term and the applied magnetic field acts only as a small perturbation.

Feature	***High-Field SSNMR***	***Zeeman-Perturbed NQR***
Dominant interaction	Zeeman interaction	Quadrupolar interaction
Typical magnetic field	Several tesla	Tens of millitesla
Hamiltonian relationship	$\lvert\widehat{H_Z}\rvert \gg \lvert\widehat{H_Q}\rvert$	$\lvert\widehat{H_Q}\rvert \gg \lvert\widehat{H_Z}\rvert$
Role of quadrupolar interaction	Perturbation to the Zeeman interaction	Principal interaction

Feature	*High-Field SSNMR*	*Zeeman-Perturbed NQR*
Primary experimental observable	Zeeman transitions modified by quadrupolar effects	Quadrupolar transitions perturbed by the Zeeman interaction

2.3.3 Zeeman-Perturbed Powder Spectra

Although the earliest Zp-NQR experiments were performed on single crystals, the technique has become particularly valuable for the characterization of polycrystalline powders, which represent the form of many pharmaceuticals, molecular crystals, energetic materials, and functional solids. In powder samples, the crystallites are randomly oriented with respect to the applied magnetic field, so each crystallite experiences a different Zeeman perturbation depending on the orientation of its electric field gradient tensor.

Rather than producing discrete resonance lines characteristic of a single crystal, the superposition of all crystallite orientations gives rise to a broadened powder spectrum. The resulting spectral envelope contains a wealth of structural information because different crystallite orientations contribute with different transition frequencies and probabilities. Consequently, the overall line shape reflects both the quadrupolar interaction and the orientational distribution of crystallites within the sample.

The asymmetry parameter, η, exerts a particularly strong influence on the appearance of Zeeman-perturbed powder spectra. For axially symmetric electric field gradients ($\eta = 0$), the spectrum exhibits a comparatively simple and symmetric line shape. As the asymmetry increases, the positions and relative intensities of the characteristic singularities evolve systematically, producing increasingly complex spectral envelopes. These relationships formed the basis of the pioneering work by Morino and Toyama, who demonstrated that powder spectra could be used to determine the asymmetry parameter directly without requiring single crystals.[2,24,28,33]

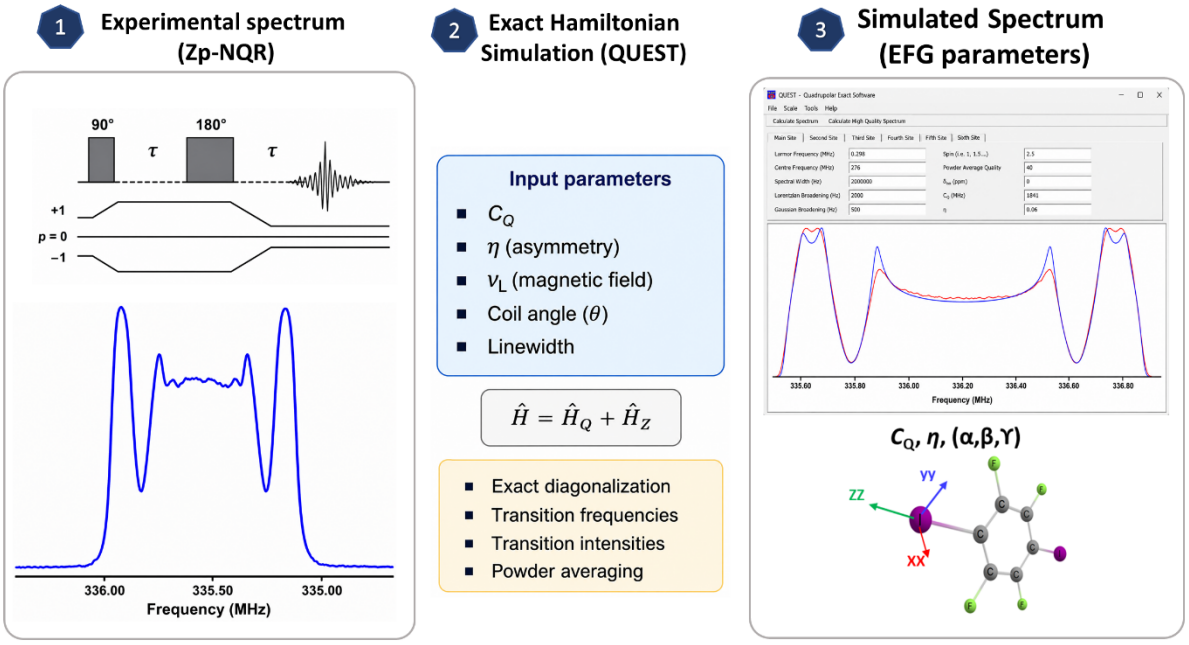


Figure 1.2.6. Representative workflow for the modern analysis of Zp-NQR spectra using exact Hamiltonian simulations. The experimental spectrum is compared with a simulated powder spectrum generated by exact numerical diagonalization of the complete nuclear spin Hamiltonian. Through iterative whole-spectrum fitting, C_Q, η, and other relevant spectroscopic parameters are optimized to achieve the best agreement between the experimental and simulated spectra. This fitting strategy, implemented in the QUEST, enables accurate and reliable extraction of quadrupolar interaction parameters from polycrystalline samples.

Modern Zp-NQR analysis no longer relies solely on identifying individual spectral singularities. Instead, the entire experimental powder spectrum is compared with spectra generated by exact numerical diagonalization of the complete nuclear spin Hamiltonian. This whole-spectrum fitting approach exploits all available experimental information simultaneously, providing improved precision, greater robustness toward spectral overlap, and applicability to increasingly complex molecular systems.

2.3.4 Exact Hamiltonian Simulations and Whole-Spectrum Fitting

Early analyses of Zeeman-perturbed NQR spectra relied primarily on first-order perturbation theory and graphical interpretation of characteristic spectral features. Although these methods provided valuable physical insight, their applicability is limited to relatively weak magnetic fields and simple systems containing isolated quadrupolar sites.

Advances in computational power have fundamentally changed the analysis of Zp-NQR spectra. Rather than approximating the energy levels using perturbation theory, the complete nuclear spin Hamiltonian can now be diagonalized exactly for every crystallite orientation. This approach permits direct calculation of transition frequencies and intensities without invoking analytical approximations, providing accurate simulations over a broad range of magnetic fields and asymmetry parameters.

Throughout this thesis, simulated spectra were generated using the QUEST, which implements exact Hamiltonian calculations for quadrupolar nuclei in both NMR and NQR experiments. Rather than analysing only selected spectral features, the complete experimental powder spectrum is fitted iteratively to the simulated spectrum until optimal agreement is achieved. This whole-spectrum fitting procedure enables simultaneous determination of the quadrupolar coupling constant, the asymmetry parameter, the nuclear gyromagnetic ratio where appropriate, and additional experimental parameters describing line broadening and magnetic field strength.

The transition from analytical interpretation to exact Hamiltonian simulations has substantially expanded the scope of Zp-NQR by enabling quantitative analysis of systems containing multiple crystallographic sites, overlapping resonances, and higher-spin quadrupolar

nuclei. This computational framework forms the basis of all spectral analyses presented in the following chapters.

2.3.5 Advantages and Scope of Zeeman-Perturbed NQR

Zeeman-Zeeman-perturbed NQR occupies a unique position among quadrupolar spectroscopic techniques by combining the intrinsic sensitivity of conventional NQR with the additional structural information provided by a weak magnetic perturbation. Operating in the weak-field regime allows the technique to retain the direct relationship between resonance frequencies and the local electric field gradient while overcoming the principal ambiguity associated with pure NQR measurements of spin-3/2 nuclei.

An important practical advantage of Zp-NQR is its applicability to polycrystalline powders, eliminating the requirement for large, well-ordered single crystals that are frequently unavailable for pharmaceutical solids and many molecular materials. Furthermore, the modest magnetic fields required for Zeeman perturbation can be generated using compact adjustable electromagnets, avoiding the need for superconducting magnets, cryogenic infrastructure, or liquid helium. These characteristics make the technique both experimentally accessible and well suited for routine investigations of quadrupolar materials.

Rather than replacing conventional solid-state NMR, Zp-NQR should be regarded as a complementary method. High-field NMR provides extensive information through chemical shifts, dipolar couplings, and a wide range of magnetic interactions, whereas Zp-NQR offers direct access to the electric field gradient and is particularly advantageous for nuclei with large quadrupole moments that are difficult to study by conventional NMR. Together, the two techniques provide

complementary views of local structure, electronic environments, and intermolecular interactions in molecular solids.

The theoretical concepts introduced throughout this chapter establish the framework for the experimental studies presented in the remainder of this thesis. The following chapters build upon these principles to develop a modern implementation of Zp-NQR based on cryogen-free instrumentation, exact Hamiltonian simulations, and whole-spectrum analysis, before demonstrating its application to the site-resolved characterization of halogen- and antimony-containing molecular solids.

2.4 Chapter Summary

This chapter has established the theoretical framework that underpins the experimental methodologies and analyses presented throughout this thesis. Beginning with the fundamental properties of quadrupolar nuclei, the discussion introduced the origin of the nuclear electric quadrupole moment, the electric field gradient tensor, and the quadrupolar Hamiltonian, illustrating how these interactions determine the energy levels and resonance frequencies observed in quadrupolar magnetic resonance spectroscopy. The quadrupolar coupling constant and asymmetry parameter were presented as the principal descriptors of the electric field gradient and, consequently, of the local electronic environment surrounding quadrupolar nuclei.

The principles, capabilities, and limitations of conventional nuclear quadrupole resonance were then examined. Pure NQR was shown to provide exceptional sensitivity to local electronic structure, making it a powerful technique for probing chemical bonding, crystal packing, polymorphism, and non-covalent interactions in crystalline solids. However, its application to spin-3/2 nuclei is fundamentally limited by the availability of only a single experimental

observable, preventing the unique determination of both the quadrupolar coupling constant and the asymmetry parameter from zero-field measurements alone. Although recent advances in instrumentation and computational methods have significantly improved the efficiency of NQR experiments, these developments do not overcome this intrinsic limitation.

These considerations provide the scientific motivation for Zeeman-perturbed nuclear quadrupole resonance. By introducing a weak, controlled magnetic field while preserving the quadrupolar interaction as the dominant contribution to the nuclear spin Hamiltonian, Zp-NQR generates additional spectroscopic observables that enable quantitative characterization of quadrupolar interactions beyond the capabilities of conventional NQR. The historical development of the technique, together with advances in exact Hamiltonian simulations and whole-spectrum fitting, has transformed Zp-NQR from a specialized experimental method into a practical approach for the quantitative analysis of polycrystalline molecular solids.

The methodology adopted throughout this thesis builds upon these theoretical developments by combining adjustable electromagnets with exact Hamiltonian simulations implemented through the QUEST. This modern, cryogen-free implementation enables accurate determination of quadrupolar interaction parameters directly from powdered samples and extends the applicability of Zp-NQR to chemically and structurally complex materials that are difficult to investigate using conventional approaches.

The theoretical concepts presented in this chapter provide the foundation for the experimental investigations described in the remainder of this thesis. Part 2 focuses on the development and validation of the modern Zp-NQR methodology, including experimental design, instrumentation, and spectral analysis using exact Hamiltonian simulations. Part 3 then demonstrates the application of these methods to the site-resolved characterization of halogen- and

antimony-containing molecular solids, highlighting the ability of Zp-NQR to provide detailed insight into local electronic structure, non-covalent interactions, and crystallographically distinct atomic environments. Collectively, these studies illustrate how the integration of modern computation with cryogen-free quadrupolar spectroscopy expands the capabilities of magnetic resonance for the structural characterization of molecular materials.

References for Chapter 2.

(1) Das, T.; Hahn, E. NQR Spectroscopy, Supplement 1 of Solid State Physics. *Seitz F. & Turnbull D. (eds) (New York, Academic)***1958**.

(2) Nari, A.; Szell, P. M. J.; Bryce, D. L. Practical Aspects of Zeeman-Perturbed NQR Spectroscopy Using an Adjustable Electromagnet. *Solid State Nucl. Magn. Reson.* **2025**, *138*, 102014. https://doi.org/10.1016/j.ssnmr.2025.102014.

(3) Das, T. P.; Hahn, E. L. Solid State Physics: Supplement; *Academic Press,* **1958**.

(4) Semin, G. K.; Babushkina, T. A.; ÏAkobson, G. G. Nuclear Quadrupole Resonance in Chemistry. *Wiley, New York*, **1975**.

(5) Pound, R. V. Nuclear Electric Quadrupole Interactions in Crystals. *Phys. Rev.* **1950**, *79* (4), 685–702. https://doi.org/10.1103/PhysRev.79.685.

(6) Suits, B. H. Nuclear Quadrupole Resonance Spectroscopy. In *Handbook of Applied Solid State Spectroscopy*; Vij, D. R., Ed.; Springer US: Boston, MA, 2006; pp 65–96. https://doi.org/10.1007/0-387-37590-2_2.

(7) Pyykkö, P. Year-2017 Nuclear Quadrupole Moments. *Mol. Phys.* **2018**, *116* (10), 1328–1338. https://doi.org/10.1080/00268976.2018.1426131.

(8) Inc, W. R. Mathematica, Version 15.0. https://www.wolfram.com/mathematica. (Accessed **2026**)

(9) Abragam, A. *Principles of Nuclear Magnetism*; International Series of Monographs on Physics; *Oxford University Press: Oxford, New York*, **1983**.

(10) Nari, A.; Rahman, M.; Szell, P. M. J.; Semeniuchenko, V.; Bryce, D. L. Halogen Bond Strength in Solids Quantified via Zeeman-Perturbed Nuclear Quadrupole Resonance Spectroscopy. *J. Am. Chem. Soc.* **2025**, *147* (11), 9528–9543. https://doi.org/10.1021/jacs.4c17321.

(11) Cohen, M. H.; Reif, F. Quadrupole Effects in Nuclear Magnetic Resonance Studies of Solids. In Solid State Physics; *Seitz, F., Turnbull, D., Eds.; Academic Press*, **1957**; Vol. 5, pp 321–438. https://doi.org/10.1016/S0081-1947(08)60105-8.

(12) Nierenberg, W. A.; Ramsey, N. F.; Brody, S. B. Measurements of Nuclear Quadrupole Moment Interactions. *Phys. Rev.* **1946**, *70* (9–10), 773–775. https://doi.org/10.1103/PhysRev.70.773.2.

(13) Leroy, C.; Johannson, R.; Bryce, D. L. $^{121/123}$Sb Nuclear Quadrupole Resonance Spectroscopy: Characterization of Non-Covalent Pnictogen Bonds and NQR Crystallography. *J. Phys. Chem. A* **2019**, *123* (5), 1030–1043. https://doi.org/10.1021/acs.jpca.8b11490.

(14) Aebli, M.; Porenta, N.; Aregger, N.; Kovalenko, M. V. Local Structure of Multinary Hybrid Lead Halide Perovskites Investigated by Nuclear Quadrupole Resonance Spectroscopy. *Chem. Mater.* **2021**, *33* (17), 6965–6973. https://doi.org/10.1021/acs.chemmater.1c01945.

(15) Scarperi, A.; Landi, N.; Costamagna, M.; Taddei, M.; Carignani, E.; Geppi, M.; Borsacchi, S. Probing Photoinduced Halide Segregation in $CH_3NH_3Pb(Br_xI_{1-x})_3$ Perovskites via in Situ Nuclear Quadrupole Resonance Spectroscopy. *J. Am. Chem. Soc.* **2025**, *147* (37), 33799–33811. https://doi.org/10.1021/jacs.5c10094.

(16) Szell, P. M. J.; Grébert, L.; Bryce, D. L. Rapid Identification of Halogen Bonds in Co-Crystalline Powders via ^{127}I Nuclear Quadrupole Resonance Spectroscopy. *Angew. Chem.* **2019**, *131* (38), 13613–13619. https://doi.org/10.1002/ange.201905788.

(17) Piveteau, L.; Morad, V.; Kovalenko, M. V. Solid-State NMR and NQR Spectroscopy of Lead-Halide Perovskite Materials. *J. Am. Chem. Soc.* **2020**, *142* (46), 19413–19437. https://doi.org/10.1021/jacs.0c07338.

(18) Szell, P. M. J.; Grébert, L.; Bryce, D. L. Rapid Identification of Halogen Bonds in Co-Crystalline Powders via ^{127}I Nuclear Quadrupole Resonance Spectroscopy. *Angew. Chem. Int. Ed.* **2019**, *58* (38), 13479–13485. https://doi.org/10.1002/anie.201905788.

(19) Piveteau, L.; Morad, V.; Kovalenko, M. V. Solid-State NMR and NQR Spectroscopy of Lead-Halide Perovskite Materials. *J. Am. Chem. Soc.* **2020**, *142* (46), 19413–19437. https://doi.org/10.1021/jacs.0c07338.

(20) Aebli, M.; Porenta, N.; Aregger, N.; Kovalenko, M. V. Local Structure of Multinary Hybrid Lead Halide Perovskites Investigated by Nuclear Quadrupole Resonance Spectroscopy. *Chem. Mater.* **2021**, *33* (17), 6965–6973. https://doi.org/10.1021/acs.chemmater.1c01945.

(21) Wolffs, J. W.; Gómez, J. S.; Janssen, G. E.; de Wijs, G. A.; Kentgens, A. P. M. Automated Wide-Line Nuclear Quadrupole Resonance of Mixed-Cation Lead-Halide Perovskites. *Magn. Reson.* **2025**, *6* (2), 143–155. https://doi.org/10.5194/mr-6-143-2025.

(22) Rossini, A. J.; Hamaed, H.; Schurko, R. W. The Application of Frequency Swept Pulses for the Acquisition of Nuclear Quadrupole Resonance Spectra. *J. Magn. Reson.* **2010**, *206* (1), 32–40. https://doi.org/10.1016/j.jmr.2010.05.018.

(23) O'Dell, L. A. The WURST Kind of Pulses in Solid-State NMR. *Solid State Nucl. Magn. Reson.* **2013**, *55–56*, 28–41. https://doi.org/10.1016/j.ssnmr.2013.10.003.

(24) Dean, C. Zeeman Splitting of Nuclear Quadrupole Resonances. *Phys. Rev.* **1954**, *96* (4), 1053–1059. https://doi.org/10.1103/PhysRev.96.1053.

(25) Toyama, M. Relative Intensities of Zeeman Components in Nuclear Quadrupole Resonance Spectrum. *J. Phys. Soc. Jpn.* **1959**, *14* (12), 1727–1738. https://doi.org/10.1143/JPSJ.14.1727.

(26) Meal, H. C. Zeeman Quadrupole Spectra of p-Chloroaniline and p-Chlorobenzylchloride. *J. Chem. Phys.* **1956**, *24* (5), 1011–1017. https://doi.org/10.1063/1.1742668.

(27) Morino, Y.; Chiba, T.; Shimozawa, T.; Toyama, M. Zeeman Effect of Nuclear Quadrupole Resonance Spectrum in Cyanuryl Chloride. *J. Phys. Soc. Jpn.* **1958**, *13* (8), 869–879. https://doi.org/10.1143/JPSJ.13.869.

(28) Morino, Y.; Toyama, M. Zeeman Effect of the Nuclear Quadrupole Resonance Spectrum in Crystalline Powder. *J. Chem. Phys.* **1961**, *35* (4), 1289–1296. https://doi.org/10.1063/1.1732041.

(29) Brooker, H. R.; Creel, R. B. Zeeman Nuclear Quadrupole Resonance Line Shapes in Powders (I = 3/2). *J. Chem. Phys.* **1974**, *61* (9), 3658–3664. https://doi.org/10.1063/1.1682549.

(30) Creel, R. B.; Drabold, D. A. Exact Analytic Solution of the Spin 3/2 Combined Zeeman-Quadrupole Hamiltonian. *J. Mol. Struct.* **1983**, 111, 85–90. https://doi.org/10.1016/0022-2860(83)85101-1.

(31) Muha, G. M. Exact Solution of the Eigenvalue Problem for a Spin 3/2 System in the Presence of a Magnetic Field. *J. Magn. Reson. 1969* **1983**, 53 (1), 85–102. https://doi.org/10.1016/0022-2364(83)90073-2.

(32) Perras, F. A.; Widdifield, C. M.; Bryce, D. L. QUEST—QUadrupolar Exact SofTware: A Fast Graphical Program for the Exact Simulation of NMR and NQR Spectra for Quadrupolar Nuclei. *Solid State Nucl. Magn. Reson.* **2012**, *45–46*, 36–44. https://doi.org/10.1016/j.ssnmr.2012.05.002.

(33) Bucci, P.; Cecchi, P.; Colligiani, A. The Zeeman Effect of Nuclear Quadrupole Resonance in Single Crystals of Sodium Bromate and P-Dibromobenzene. *J. Am. Chem. Soc.* **1964**, *86* (12), 2513–2514. https://doi.org/10.1021/ja01066a040.

.

Chapter 3 – Mechanochemistry and Sustainable Molecular Solid Preparation: Integrating Green Synthesis with Cryogen-Free Characterization

This chapter marks a transition in the thesis from the theoretical foundations established in Chapters 1 and 2 to the experimental methodologies employed throughout the remainder of this work. While Chapter 1 introduced halogen and chalcogen bonding as versatile supramolecular interactions and Chapter 2 established the theoretical basis of quadrupolar spectroscopy and Zp-NQR, the present chapter focuses on how molecular solids are prepared in a manner consistent with the objective of sustainable materials research.

The development of new functional molecular materials depends not only on advanced characterization techniques but also on synthetic methodologies that minimize waste, reduce resource consumption, and facilitate scalable preparation. Among the emerging approaches that address these challenges, mechanochemistry has become one of the most promising alternatives to conventional solution-based synthesis. By using mechanical energy to promote chemical transformations, mechanochemical methods substantially reduce or eliminate solvent consumption while frequently providing rapid, efficient, and highly reproducible access to crystalline materials. These advantages have led to widespread application of mechanochemistry in crystal engineering, pharmaceutical solid-form development, metal-organic frameworks, and supramolecular chemistry.[1,2]

The emphasis on sustainability extends beyond synthesis to include the analytical techniques used to characterize the resulting materials. Conventional solid-state characterization often relies on resource-intensive instrumentation, particularly high-field solid-state NMR spectrometers that require superconducting magnets, continuous cryogenic cooling, and

significant electrical infrastructure. In contrast, the cryogen-free Zp-NQR methodology developed throughout this thesis provides a complementary approach for investigating quadrupolar nuclei while substantially reducing reliance on liquid-helium-based instrumentation. Together, mechanochemical synthesis and cryogen-free magnetic resonance spectroscopy establish a resource-efficient workflow that addresses sustainability across both material preparation and structural characterization.

This chapter introduces the fundamental principles of mechanochemistry and briefly reviews the quantitative metrics commonly used to evaluate the environmental performance of synthetic methodologies. Particular emphasis is placed on ball milling and resonant acoustic mixing (RAM), the two mechanochemical techniques employed throughout this thesis, with special attention given to the practical advantages that motivated the selection of RAM for the preparation of halogen- and chalcogen-bonded molecular solids. Finally, the complementary relationship between mechanochemistry and cryogen-free Zp-NQR is examined, establishing the integrated experimental strategy that underpins the research presented in the subsequent chapters.

3.1 Evaluating Sustainability in Chemical Synthesis

The transition toward more sustainable chemical manufacturing has created a need for objective methods to assess the environmental performance of synthetic processes. Although the principles of green chemistry provide the conceptual foundation for reducing waste and improving resource efficiency, quantitative metrics are required to compare different synthetic methodologies in a consistent and reproducible manner. Such metrics enable researchers to evaluate not only chemical yield, but also the broader environmental footprint associated with reagent consumption, solvent use, and energy requirements.[3]

Among the twelve principles of green chemistry proposed by Anastas and Warner, several are particularly relevant to the mechanochemical methodologies employed throughout this thesis, including waste prevention, the reduction or elimination of auxiliary solvents, improved energy efficiency, and the development of inherently safer synthetic processes.[3,4] These principles have become especially important in pharmaceutical manufacturing, where solvent consumption frequently dominates both process cost and environmental impact.[5,6]

Several complementary metrics have therefore been developed to quantify the sustainability of chemical syntheses. Rather than relying on a single parameter, these metrics evaluate different aspects of process efficiency, allowing meaningful comparison between conventional solution-based synthesis and mechanochemical approaches.

The E-factor expresses the mass of waste generated per unit mass of product,

$$E\text{-factor} = \frac{\text{Mass of waste}}{\text{Mass of product}} \qquad Eq.\,3.1$$

and remains one of the most widely used indicators of process sustainability. Lower E-factor values correspond to more resource-efficient syntheses, with an ideal process approaching zero waste generation.

The process mass intensity (PMI) extends this concept by considering the total mass of all materials consumed during synthesis, including reactants, solvents, and auxiliary materials,

$$PMI = \frac{\text{Total mass of materials used}}{\text{Mass of product}} \qquad Eq.\,3.2$$

Because PMI accounts for the complete material input, it has become a standard metric for evaluating pharmaceutical manufacturing processes and large-scale synthetic routes.

Since solvent use often represents the largest contributor to both waste generation and environmental burden, solvent intensity (SI) is frequently reported as an additional measure of sustainability,

$$SI = \frac{\text{Mass of solvent}}{\text{Mass of product}} \qquad Eq.3.3$$

Mechanochemical methods typically exhibit substantially lower solvent intensities than conventional solution-based syntheses because reactions are performed either in the complete absence of solvent or using only catalytic quantities of liquid additives.

Finally, energy intensity (EI) provides a measure of the electrical energy required to produce a given quantity of material,

$$EI = \frac{\text{Energy consumed}}{\text{Mass of product}} \qquad Eq.3.4$$

Although energy consumption is often overlooked in laboratory-scale experiments, it becomes increasingly significant when considering process scale-up and industrial implementation.

These metrics provide a quantitative framework for assessing the environmental performance of synthetic methodologies. Throughout the experimental chapters of this thesis, they are used to compare conventional solution-based synthesis with ball milling and resonant acoustic mixing, demonstrating the advantages of mechanochemical approaches for the preparation of molecular solids while providing an objective basis for evaluating improvements in sustainability.

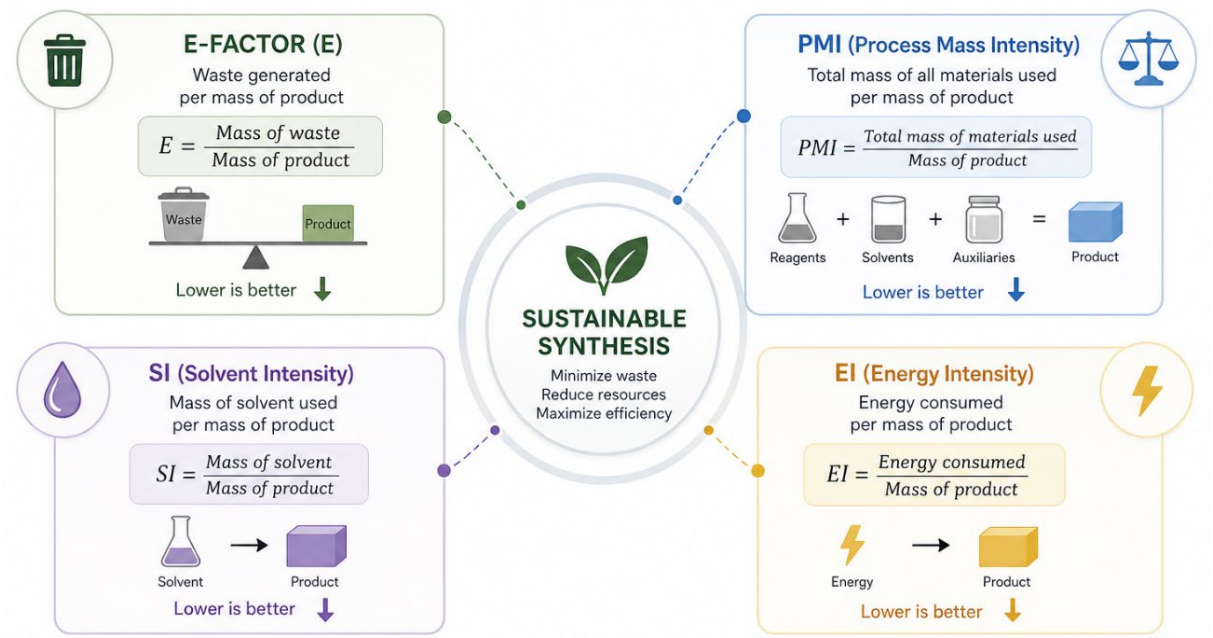


Figure 1.3.1. Overview of the principal green chemistry metrics used to evaluate the sustainability of synthetic processes. The E-factor (E) quantifies the mass of waste generated per unit mass of product, while the process mass intensity (PMI) measures the total mass of all materials consumed relative to the product obtained. Solvent intensity (SI) and energy intensity (EI) assess the solvent and energy requirements, respectively, normalized to the mass of product. These complementary metrics provide a quantitative framework for comparing the environmental performance of conventional solution-based synthesis and mechanochemical approaches, including ball milling and RAM, as discussed in this thesis.

3.2 Mechanochemistry as a Modern Synthetic Strategy

Mechanochemistry encompasses a broad class of synthetic methodologies in which chemical transformations are driven by the direct application of mechanical energy rather than by dissolution, heating, or conventional solution-phase reaction pathways. Although mechanochemical processes have long been employed in mineral processing and metallurgy, their application to molecular synthesis has expanded rapidly over the past two decades, establishing mechanochemistry as one of the most significant advances in sustainable synthetic chemistry.[7–9]

Unlike conventional solution-based synthesis, mechanochemical reactions are typically performed in the solid state, where mechanical forces continuously generate fresh reactive surfaces, promote intimate contact between reactants, and facilitate bond formation through repeated compression, friction, and shear. As a consequence, many reactions proceed rapidly with little or no solvent, substantially reducing chemical waste while simplifying product isolation and purification.[2,10] These characteristics have positioned mechanochemistry as a practical alternative to traditional solution-phase synthesis for a wide range of molecular materials.

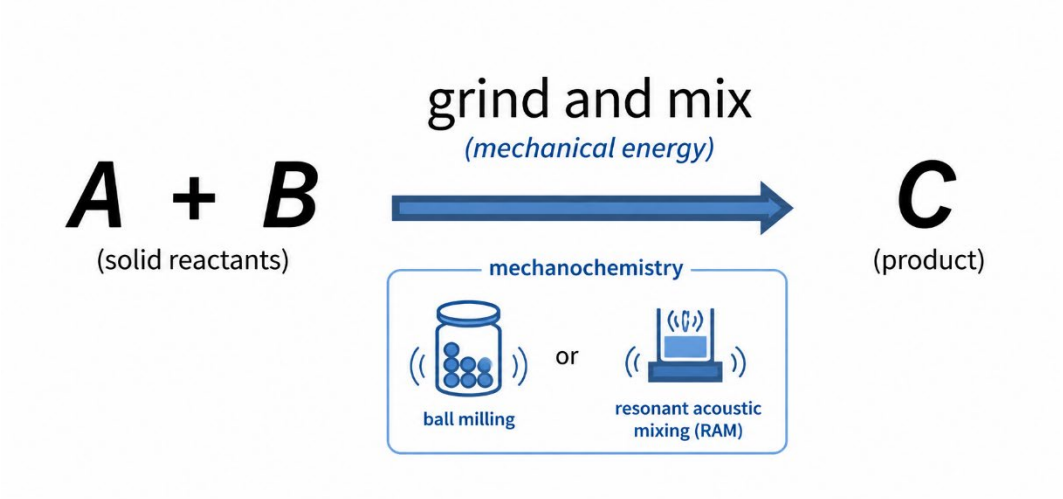


Figure 1.3.2. General concept of mechanochemical synthesis, where mechanical energy drives chemical transformations between solid reactants to form the desired product. Throughout this thesis, mechanochemical reactions were performed using ball milling or RAM.

The impact of mechanochemistry has been particularly pronounced in crystal engineering, where precise control over intermolecular interactions is essential for constructing functional molecular solids. One of the longstanding challenges in crystal engineering is the reproducible preparation of cocrystals with high phase purity while maintaining scalability for future applications. Conventional solution crystallization often depends strongly on solvent choice, evaporation conditions, supersaturation, and crystallization kinetics, factors that can complicate

reproducibility and frequently require extensive optimization. In contrast, mechanochemical synthesis provides a robust and highly reproducible route to cocrystal formation by promoting direct solid-state contact between reactants while minimizing solvent-related variables. Consequently, mechanochemistry has become an increasingly important platform for screening supramolecular synthons and preparing multicomponent crystalline materials.[11,12]

For suitability of mechanochemistry for supramolecular synthesis has been demonstrated extensively for hydrogen-bonded**,** halogen-bonded, and, more recently, chalcogen-bonded molecular solids. Numerous studies have shown that mechanochemical methods efficiently promote non-covalent assembly while requiring substantially smaller quantities of organic solvent than conventional crystallization techniques.[13,14] In many cases, liquid-assisted grinding (LAG), in which only catalytic amounts of solvent are added to the reaction mixture, further enhances reaction kinetics while preserving the environmental advantages of mechanochemical synthesis.[15,16] These developments have established mechanochemistry as a powerful synthetic methodology for crystal engineering and pharmaceutical solid-form screening.[17]

Much of the modern development of mechanochemistry has been driven by the pioneering contributions of Tomislav Friščić, Dominik Cinčić, and their co-workers, who demonstrated the broad applicability of mechanochemical methods to supramolecular chemistry and crystal engineering. Their work has shown that mechanochemistry provides efficient access to a wide range of halogen-bonded cocrystals, including pharmaceutical cocrystals and systems based on classical perfluorinated halogen-bond donors and related electrophilic halogen-bond donors. These studies established mechanochemistry not only as a greener alternative to solution synthesis but also as an effective strategy for rapidly discovering and optimizing supramolecular materials.[18–20]

Beyond its synthetic efficiency, mechanochemistry offers several practical advantages that are directly relevant to this thesis. The substantial reduction in solvent consumption lowers both waste generation and purification requirements while shortening reaction times and simplifying experimental workflows. Furthermore, recent advances in in-situ powder X-ray diffraction (PXRD) have enabled mechanochemical reactions to be monitored in real time, providing valuable insight into reaction pathways, intermediate phases, and cocrystal formation mechanisms.[15] Such developments have significantly improved the fundamental understanding of solid-state reaction processes and continue to expand the capabilities of mechanochemical synthesis.[21]

The experimental studies presented throughout this thesis employ mechanochemistry as the principal synthetic route for preparing halogen- and chalcogen-bonded molecular solids. Two complementary techniques—ball milling and RAM—were investigated, each offering distinct advantages depending on the objectives of the synthesis. These approaches are discussed in the following sections.

3.2.1 Ball Milling

Ball milling is the most widely established mechanochemical technique for laboratory-scale molecular synthesis and has become the benchmark against which many newer mechanochemical methodologies are evaluated. In a typical experiment, reactants are sealed within a milling vessel together with one or more grinding balls. Mechanical energy is transferred to the reaction mixture through repeated impact, friction, and shear generated by collisions between the milling media and the walls of the reaction vessel.[22,23]

These localized mechanical events simultaneously reduce particle size, increase the contact area between reactants, and generate transient regions of elevated pressure and temperature that

facilitate chemical transformation. As a result, ball milling has proven highly effective for the preparation of pharmaceutical cocrystals, coordination compounds, metal-organic frameworks, and a wide variety of supramolecular solids.

Despite its versatility, ball milling possesses several practical limitations that become increasingly important as reactions are scaled or optimized. Continuous collisions between the milling media and the reaction vessel may introduce trace contamination arising from abrasion of the balls or jar materials. Furthermore, energy transfer is inherently localized and may become non-uniform for larger reaction volumes, potentially leading to incomplete mixing or reduced reproducibility. Product recovery can also require additional handling steps because material frequently adheres to both the milling balls and the interior surfaces of the reaction vessel.

Nevertheless, ball milling remains an indispensable mechanochemical technique and serves throughout this thesis as a well-established benchmark against which the performance of newer mechanochemical methodologies is evaluated.

3.2.2 Resonant Acoustic Mixing (RAM)

RAM represents a more recent development in mechanochemical synthesis that addresses several practical limitations associated with conventional ball milling. Rather than relying on collisions between grinding media and the reaction vessel, RAM transfers mechanical energy through low-frequency, high-intensity acoustic vibrations that induce rapid and homogeneous mixing of the reaction mixture. [24–26]

Because no grinding media are required, the risk of contamination arising from abrasion of milling balls is eliminated. Mechanical energy is instead distributed more uniformly throughout the reaction vessel, promoting efficient mixing while simplifying product recovery and reducing

equipment wear. These characteristics have attracted considerable interest for pharmaceutical manufacturing and process scale-up, where contamination, reproducibility, and scalability are critical considerations.

An additional advantage of RAM lies in its flexibility with respect to reaction scale. Unlike ball milling, where increasing reaction size often requires modification of both milling media and vessel geometry, RAM readily accommodates a broad range of reaction volumes while maintaining efficient energy transfer. This feature makes the technique particularly attractive for translation from laboratory-scale synthesis to larger-scale manufacturing.

The growing importance of RAM is reflected by its increasing application to pharmaceutical cocrystal preparation, metal-organic framework synthesis, and supramolecular materials. Recent studies have demonstrated that RAM can achieve reaction efficiencies comparable to or exceeding those obtained by conventional ball milling while substantially simplifying experimental workflows.

For these reasons, RAM occupies a central role throughout this thesis. In addition to serving as the primary synthetic methodology for several halogen-bonded molecular solids, it provides an experimentally simple, scalable, and solvent-minimized platform that complements the cryogen-free characterization strategies developed in the subsequent chapters. The integration of RAM with Zp-NQR therefore represents a key component of the sustainable experimental workflow established in this dissertation.

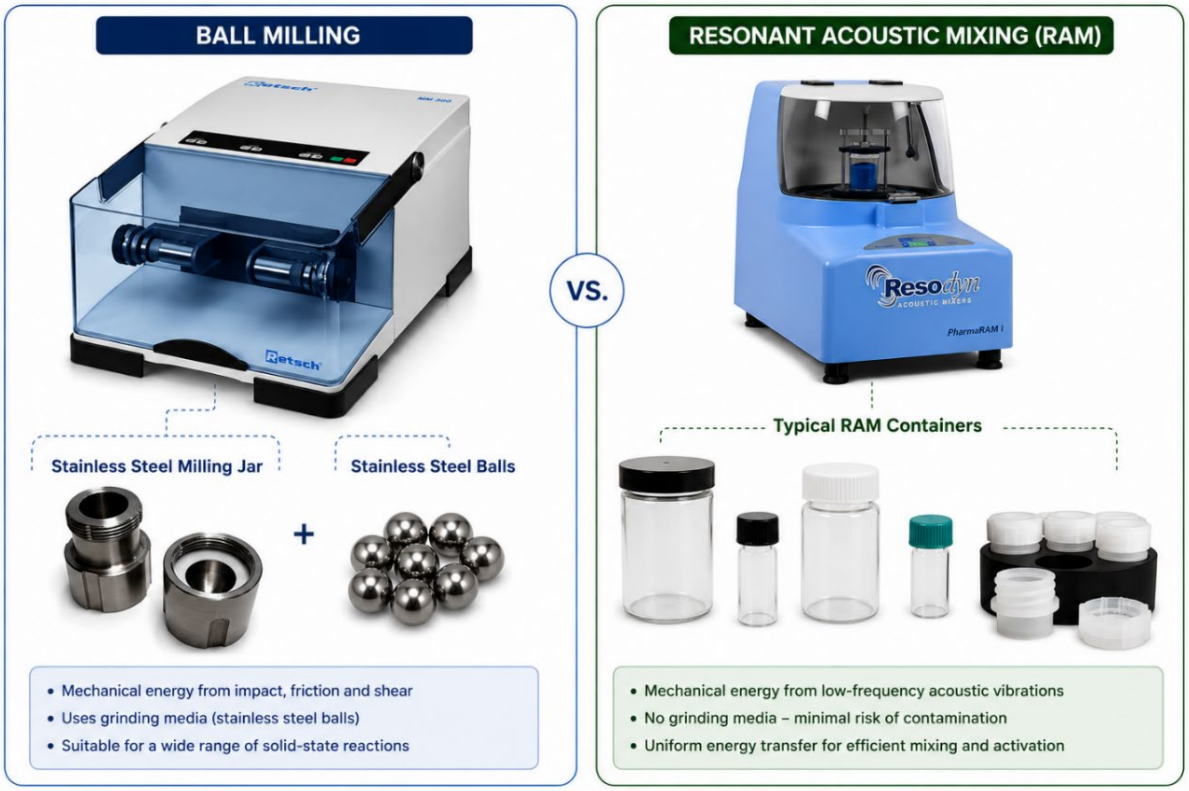


Figure 1.3.3. Mechanochemical synthesis platforms used throughout this thesis. *Left:* Laboratory-scale ball mill (Retsch MM 200) with stainless steel milling jars and grinding balls employed for conventional ball-milling reactions. Mechanical energy is transferred through repeated impact, friction, and shear generated by the milling media. *Right:* Resodyn PharmaRAM I resonant acoustic mixer with representative reaction vessels used for resonant acoustic mixing experiments. Photographs of the Retsch MM 200 ball mill and the Resodyn PharmaRAM I were adapted from the official product images provided by Retsch GmbH and Resodyn Acoustic Mixers, Inc., respectively.

3.3 Integrating Sustainable Synthesis with Cryogen-Free Zp-NQR

Scientific advances in molecular materials depend equally on the ability to prepare new compounds and to characterize their local structure with sufficient precision. Historically, these two objectives have evolved largely independently. Synthetic methodologies have focused on improving reaction efficiency and product quality, whereas characterization techniques have

emphasized increasing spectroscopic resolution and structural detail. Consequently, significant improvements in one area have not always been accompanied by comparable advances in the overall sustainability of the experimental workflow.

The research presented in this thesis adopts a different perspective by considering synthesis and characterization as complementary components of a unified methodology. Mechanochemical synthesis minimizes solvent consumption, reduces chemical waste, and simplifies sample preparation, while cryogen-free Zp-NQR substantially reduces reliance on superconducting magnets, liquid-helium cryogens, and the associated infrastructure required for conventional solid-state magnetic resonance spectroscopy. Together, these approaches establish an integrated workflow that reduces resource consumption without compromising the quality of structural information obtained from molecular solids.

An additional advantage of this integration arises from the natural compatibility between the two techniques. Mechanochemical reactions typically produce polycrystalline powders that are immediately suitable for Zp-NQR analysis, eliminating the need for single-crystal growth or extensive sample preparation. Conversely, the site-specific sensitivity of Zp-NQR to local electric field gradients enables direct characterization of the crystalline products generated by mechanochemistry, including halogen-bonded and chalcogen-bonded cocrystals containing chlorine, bromine, iodine, and antimony nuclei. The two methodologies therefore complement one another not only in terms of sustainability but also with respect to experimental practicality.

This integrated strategy forms one of the central themes of the present thesis. Rather than treating sustainable synthesis and sustainable characterization as independent objectives, the work demonstrates that combining modern mechanochemistry with cryogen-free quadrupolar spectroscopy establishes a coherent experimental framework for investigating molecular solids.

The studies presented in the following chapters illustrate how this approach enables efficient preparation, detailed structural characterization, and site-resolved analysis of supramolecular materials while substantially reducing dependence on organic solvents and cryogenic infrastructure.

3.4 Chapter Summary

This chapter has established mechanochemistry as a sustainable and practical synthetic platform for the preparation of molecular solids investigated throughout this thesis. Following a brief introduction to the principles of green chemistry and the quantitative metrics used to evaluate the environmental performance of synthetic methodologies, mechanochemistry was presented as an efficient alternative to conventional solution-based synthesis. Particular emphasis was placed on its ability to reduce solvent consumption, simplify experimental workflows, and improve the reproducibility of cocrystal preparation.

The fundamental principles of ball milling and RAM were then discussed, highlighting their respective advantages for the synthesis of supramolecular materials. While ball milling remains the most widely established mechanochemical technique, RAM offers several practical benefits, including the elimination of grinding media, reduced contamination, improved scalability, and more homogeneous energy transfer. These characteristics make RAM particularly well suited for the preparation of pharmaceutical and supramolecular molecular solids.

Finally, the complementary relationship between mechanochemical synthesis and cryogen-free Zp-NQR spectroscopy was examined. Together, these methodologies establish a resource-efficient experimental workflow in which sustainable synthesis is coupled with advanced structural

characterization, providing the methodological foundation for the experimental investigations presented in the following chapters.

Summary of Part 1

Part 1 has established the scientific and methodological framework that underpins the research presented throughout this thesis. Collectively, the first three chapters have introduced the supramolecular interactions, spectroscopic principles, and sustainable synthetic methodologies that form the basis of the integrated experimental strategy developed in this work.

Chapter 1 introduced the fundamental concepts of crystal engineering, with particular emphasis on halogen and chalcogen bonding as versatile non-covalent interactions for constructing functional molecular solids. The chapter further highlighted the growing importance of sustainable chemistry and motivated the development of experimental workflows that reduce environmental impact while maintaining high-quality structural characterization.

Building upon this foundation, Chapter 2 established the theoretical principles governing quadrupolar interactions and nuclear quadrupole resonance spectroscopy. The discussion progressed from the fundamental properties of quadrupolar nuclei and the electric field gradient tensor to the limitations of conventional NQR, ultimately motivating the development of Zp-NQR. The historical evolution of the technique, together with advances in exact Hamiltonian simulations and whole-spectrum fitting, demonstrated how modern Zp-NQR enables quantitative characterization of quadrupolar interactions in polycrystalline molecular solids.

Chapter 3 complemented these spectroscopic developments by introducing mechanochemistry as a sustainable synthetic platform for molecular solid preparation. Ball milling and resonant acoustic mixing were presented as efficient mechanochemical methodologies that

reduce solvent consumption while providing robust and reproducible access to supramolecular materials. When combined with cryogen-free Zp-NQR spectroscopy, these synthetic approaches establish an integrated workflow that emphasizes sustainability throughout both material preparation and structural characterization.

Together, these three chapters define the conceptual framework that unifies the research presented in this dissertation. Rather than treating synthesis and characterization as independent stages of materials research, this thesis demonstrates how they can be integrated into a coherent experimental strategy for the investigation of molecular solids. The following chapters build upon this foundation to develop, validate, and apply modern Zeeman-perturbed NQR methodologies to the site-resolved characterization of halogen- and antimony-containing materials, while simultaneously demonstrating the advantages of sustainable mechanochemical synthesis for the preparation of these systems.

References for Chapter 3.

(1) Friščić, T.; Mottillo, C.; Titi, H. M. Mechanochemistry for Synthesis. *Angew. Chem.* **2020**, *132* (3), 1030–1041. https://doi.org/10.1002/ange.201906755.

(2) L. James, S.; J. Adams, C.; Bolm, C.; Braga, D.; Collier, P.; Friščić, T.; Grepioni, F.; M. Harris, K. D.; Hyett, G.; Jones, W.; Krebs, A.; Mack, J.; Maini, L.; Guy Orpen, A.; P. Parkin, I.; C. Shearouse, W.; W. Steed, J.; C. Waddell, D. Mechanochemistry: Opportunities for New and Cleaner Synthesis. *Chem. Soc. Rev.* **2012**, *41* (1), 413–447. https://doi.org/10.1039/C1CS15171A.

(3) Fantozzi, N.; Volle, J.-N.; Porcheddu, A.; Virieux, D.; García, F.; Colacino, E. Green Metrics in Mechanochemistry. *Chem. Soc. Rev.* **2023**, *52* (19), 6680–6714. https://doi.org/10.1039/D2CS00997H.

(4) Anastas, P. T.; Warner, J. C. *Green Chemistry: Theory and Practice*; Oxford University Press, 2000. https://doi.org/10.1093/oso/9780198506980.001.0001.

(5) Raymond, M. J.; Slater, C. S.; Savelski, M. J. LCA Approach to the Analysis of Solvent Waste Issues in the Pharmaceutical Industry. *Green Chem.* **2010**, *12* (10), 1826–1834. https://doi.org/10.1039/c003666h.

(6) Constable, D. J. C.; Jimenez-Gonzalez, C.; Henderson, R. K. Perspective on Solvent Use in the Pharmaceutical Industry. *Org. Process Res. Dev.* **2007**, *11* (1), 133–137. https://doi.org/10.1021/op060170h.

(7) Zhang, R.; Tao, C.-A.; Chen, R.; Wu, L.; Zou, X.; Wang, J. Ultrafast Synthesis of Ni-MOF in One Minute by Ball Milling. *Nanomaterials* **2018**, *8* (12), 1067. https://doi.org/10.3390/nano8121067.

(8) Egorov, I. N.; Santra, S.; Kopchuk, D. S.; Kovalev, I. S.; Zyryanov, G. V.; Majee, A.; Ranu, B. C.; Rusinov, V. L.; Chupakhin, O. N. Ball Milling: An Efficient and Green Approach for Asymmetric Organic Syntheses. *Green Chem.* **2020**, *22* (2), 302–315. https://doi.org/10.1039/c9gc03414e.

(9) Tao, C.-A.; Wang, J.-F. Synthesis of Metal Organic Frameworks by Ball-Milling. *Crystals* **2021**, *11* (1), 15. https://doi.org/10.3390/cryst11010015.

(10) Dong, L.; Li, L.; Chen, H.; Cao, Y.; Lei, H. Mechanochemistry: Fundamental Principles and Applications. *Adv. Sci.* **2025**, *12* (24), 2403949. https://doi.org/10.1002/advs.202403949.

(11) Xiao, Y.; Wu, C.; Hu, X.; Chen, K.; Qi, L.; Cui, P.; Zhou, L.; Yin, Q. Mechanochemical Synthesis of Cocrystal: From Mechanism to Application. *Cryst. Growth Des.* **2023**, *23* (6), 4680–4700. https://doi.org/10.1021/acs.cgd.3c00183.

(12) Delori, A.; Friščić, T.; Jones, W. The Role of Mechanochemistry and Supramolecular Design in the Development of Pharmaceutical Materials. *CrystEngComm* **2012**, *14* (7), 2350–2362. https://doi.org/10.1039/c2ce06582g.

(13) Xu, Y.; Viger-Gravel, J.; Korobkov, I.; Bryce, D. L. Mechanochemical Production of Halogen-Bonded Solids Featuring P═O···I–C Motifs and Characterization via X-Ray Diffraction, Solid-State Multinuclear Magnetic Resonance, and Density Functional Theory. *J. Phys. Chem. C* **2015**, *119* (48), 27104–27117. https://doi.org/10.1021/acs.jpcc.5b09737.

(14) Mittapalli, S.; Sravanakumar Perumalla, D.; Nangia, A. Mechanochemical Synthesis of N-Salicylidene-aniline: Thermosalient Effect of Polymorphic Crystals. *IUCrJ* **2017**, *4* (3), 243–250. https://doi.org/10.1107/S2052252517004043.

(15) Friščić, T.; Jones, W. Recent Advances in Understanding the Mechanism of Cocrystal Formation via Grinding. *Cryst. Growth Des.* **2009**, *9* (3), 1621–1637. https://doi.org/10.1021/cg800764n.

(16) Salami, S. A.; Manyeruke, M. H.; Ezekiel, C. I.; Ndagano, U. N.; Safari, J. B.; Amusat, S. O.; Krause, R. W. M. Recent Advances in Liquid Assisted Grinding Chemistry: Towards Sustainable Synthesis. *Results Chem.* **2025**, *18*, 102675. https://doi.org/10.1016/j.rechem.2025.102675.

(17) Ying, P.; Yu, J.; Su, W. Liquid-Assisted Grinding Mechanochemistry in the Synthesis of Pharmaceuticals. *Adv. Synth. Catal.* **2021**, *363* (5), 1246–1271. https://doi.org/10.1002/adsc.202001245.

(18) Bedeković, N.; Stilinović, V.; Friščić, T.; Cinčić, D. Comparison of Isomeric Meta- and Para-Diiodotetrafluorobenzene as Halogen Bond Donors in Crystal Engineering. *New J. Chem.* **2018**, *42* (13), 10584–10591. https://doi.org/10.1039/c8nj01368c.

(19) Cinčić, D.; Friščić, T.; Jones, W. A Stepwise Mechanism for the Mechanochemical Synthesis of Halogen-Bonded Cocrystal Architectures. *J. Am. Chem. Soc.* **2008**, *130* (24), 7524–7525. https://doi.org/10.1021/ja801164v.

(20) Cinčić, D.; Friščić, T.; Jones, W. Isostructural Materials Achieved by Using Structurally Equivalent Donors and Acceptors in Halogen-Bonded Cocrystals. *Chem. – Eur. J.* **2008**, *14* (2), 747–753. https://doi.org/10.1002/chem.200701184.

(21) Katsenis, A. D.; Puškarić, A.; Štrukil, V.; Mottillo, C.; Julien, P. A.; Užarević, K.; Pham, M.-H.; Do, T.-O.; Kimber, S. A. J.; Lazić, P.; Magdysyuk, O.; Dinnebier, R. E.; Halasz, I.; Friščić, T. In Situ X-Ray Diffraction Monitoring of a Mechanochemical Reaction Reveals a

Unique Topology Metal-Organic Framework. *Nat. Commun.* **2015**, *6* (1), 6662. https://doi.org/10.1038/ncomms7662.

(22) Yadav, T. P.; Yadav, R. M.; Singh, D. P. Mechanical Milling: A Top down Approach for the Synthesis of Nanomaterials and Nanocomposites. *Nanosci. Nanotechnol.* **2012**, *2* (3), 22–48.

(23) Speight, I. R.; Ardila-Fierro, K. J.; Hernández, J. G.; Emmerling, F.; Michalchuk, A. A. L.; García, F.; Colacino, E.; Mack, J. Ball Milling for Mechanochemical Reactions. *Nat. Rev. Methods Primer* **2025**, *5* (1), 29. https://doi.org/10.1038/s43586-025-00401-2.

(24) Titi, H. M.; Do, J.-L.; Howarth, A. J.; Nagapudi, K.; Friščić, T. Simple, Scalable Mechanosynthesis of Metal–Organic Frameworks Using Liquid-Assisted Resonant Acoustic Mixing (LA-RAM). *Chem. Sci.* **2020**, *11* (29), 7578–7584. https://doi.org/10.1039/d0sc00333f.

(25) Andrews, M. R.; Collet, C.; Wolff, A.; Hollands, C. Resonant Acoustic® Mixing: Processing and Safety. *Propellants Explos. Pyrotech.* **2020**, *45* (1), 77–86. https://doi.org/10.1002/prep.201900280.

(26) Osorio, J. G.; Muzzio, F. J. Evaluation of Resonant Acoustic Mixing Performance. *Powder Technol.* **2015**, *278*, 46–56. https://doi.org/10.1016/j.powtec.2015.02.033.

Part 2 – Methodological Development and Applications of Cryogen-Free Zeeman-Perturbed Nuclear Quadrupole Resonance

The theoretical concepts introduced in Part 1 establish the foundation for the principal scientific contributions of this thesis, namely the development and application of a practical, quantitative, and cryogen-free Zp-NQR methodology for the characterization of quadrupolar nuclei in molecular solids. While the fundamental principles of Zp-NQR have been known for several decades, the technique has remained underutilized due to experimental complexity, limited instrumentation, and the absence of robust analysis tools capable of extracting quantitative structural information from powder spectra. Consequently, Zp-NQR has historically been regarded as a specialized spectroscopic technique rather than a routine method for solid-state characterization.

The research presented in this part addresses these limitations through a series of methodological developments that collaboratively transform Zp-NQR into an accessible and broadly applicable characterization technique. Beginning with the establishment of a practical laboratory workflow based on an adjustable electromagnet and exact Hamiltonian simulations, subsequent chapters expand the capabilities of the technique by introducing methods for isotopic identification in complex spectra, quantitative determination of halogen bond strength, and, ultimately, site-resolved characterization of pharmaceutically relevant molecular solids. Each development builds directly upon the preceding work, illustrating the progressive evolution of Zp-NQR from an experimental methodology into a versatile analytical tool for modern solid-state chemistry.

A central theme throughout this part is the combination of methodological innovation with sustainability. By replacing superconducting magnets with adjustable electromagnets and eliminating the need for liquid-helium cryogens, the cryogen-free Zp-NQR platform developed in this thesis provides a resource-efficient alternative to conventional high-field magnetic resonance methods for the study of quadrupolar nuclei. When combined with exact Hamiltonian simulations and whole-spectrum fitting, the technique enables accurate determination of electric field gradient parameters while maintaining a comparatively simple and accessible experimental infrastructure.

The four chapters comprising Part 2, document this methodological progression. Chapter 4 establishes the practical and experimental framework required for routine Zp-NQR measurements. Chapter 5 demonstrates how Zeeman perturbation enables unambiguous isotopic identification in complex and multi-component systems. Chapter 6 extends the methodology beyond structural characterization by showing that Zp-NQR can directly quantify halogen bond strength through changes in the electric field gradient tensor. Finally, Chapter 7 presents the capstone application of the methodology to pharmaceutical cocrystals and chlorine-containing drug degradation products, demonstrating that the cryogen-free Zp-NQR platform developed throughout this thesis is capable of addressing structurally complex and industrially relevant problems in pharmaceutical materials science. Together, these studies establish Zp-NQR as a practical, quantitative, and sustainable tool for the characterization of quadrupolar nuclei in molecular solids.

Chapter 4 – Practical Aspects of Zeeman-Perturbed NQR Spectroscopy Using an Adjustable Electromagnet: Establishing a Routine, Cryogen-Free Laboratory Workflow

Based on: Nari, A.; Szell, P. M. J.; Bryce, D. L. Practical aspects of Zeeman-perturbed NQR spectroscopy using an adjustable electromagnet. Solid State Nucl. Magn. Reson. 2025, 138, 102014.

4.1 Chapter Overview and Thesis Context

The previous chapters established the theoretical foundations of quadrupolar magnetic resonance spectroscopy and highlighted the need for sustainable characterization methods capable of providing detailed structural information without relying on resource-intensive instrumentation. Although Zp-NQR has been recognized for decades as a powerful approach for determining complete EFG tensors from polycrystalline samples, its practical implementation remained largely limited to specialized research laboratories. Consequently, despite its considerable potential, Zp-NQR never evolved into a routine characterization technique comparable to conventional solid-state NMR.

One of the principal reasons for this limited adoption was the experimental and analytical methodology available during the early development of the technique. Historically, Zp-NQR experiments relied on relatively simple instrumentation, most commonly low-precision Helmholtz coils, to generate weak static magnetic fields, typically below 10 mT. While these pioneering studies successfully demonstrated the fundamental principles of Zeeman perturbation, the limited field strength and magnetic-field homogeneity were frequently insufficient to fully resolve the characteristic inner and outer shoulders of Zp-NQR powder spectra. Because the positions and

relative intensities of these spectral features are highly sensitive to the electric field gradient asymmetry parameter, η, poor spectral resolution often introduced significant uncertainty into the determination of quadrupolar interaction parameters.

Equally important were the computational limitations of the time. In the absence of modern simulation software, spectral analysis was primarily based on identifying individual spectral singularities and applying analytical expressions derived mostly from first-order perturbation theory. These approaches generally assumed relatively small asymmetry parameters and were valid only within the weak-field approximation. Consequently, quantitative analysis became increasingly unreliable for systems exhibiting larger asymmetry parameters, overlapping resonances, multiple crystallographic sites, or higher-spin nuclei. These limitations significantly restricted the applicability of Zp-NQR to the increasingly complex molecular solids encountered in modern crystal engineering, supramolecular chemistry, and pharmaceutical materials science.

The work presented in this chapter addresses these longstanding limitations through the development of a practical, quantitative, and accessible Zp-NQR methodology. The experimental approach here, employs a high-quality adjustable electromagnet capable of generating stable and homogeneous magnetic fields over the range required for weak-field Zeeman perturbation. The improved field quality enables complete resolution of the characteristic Zp-NQR powder line shapes, thereby substantially improving the precision with which quadrupolar parameters can be extracted. Also, the methodology integrates exact Hamiltonian simulations using the QUEST, replacing approximate analytical treatments with rigorous numerical calculations of the complete nuclear spin Hamiltonian. Instead of extracting information from only a limited number of spectral features, the entire experimental powder spectrum is reproduced through iterative whole-spectrum fitting, yielding accurate and reliable values of the quadrupolar coupling constant, C_Q, and η.

This chapter therefore establishes the experimental and computational framework upon which all subsequent developments presented in Part 2 are built. The practical aspects described here directly enables the isotopic identification strategy introduced in Chapter 5, the quantitative evaluation of halogen bond strength presented in Chapter 6, and the site-resolved characterization of pharmaceutical cocrystals and chlorine-containing drug degradation products described in Chapter 7. Consequently, this work represents the methodological foundation of the entire thesis and marks the transition of cryogen-free Zp-NQR from a proof-of-concept spectroscopic technique to a robust and broadly applicable analytical platform for modern solid-state chemistry.

4.2. Statement of Authenticity

I certify that I have prepared the following article featuring my own work.

4.3 Permissions

I declare that I have obtained permission from the coauthor to include this article in my thesis. Chapter 4 has been reprinted with permission from Solid State Nuclear Magnetic Resonance.

4.4 Published manuscript

Solid State Nuclear Magnetic Resonance 138 (2025) 102014

Contents lists available at ScienceDirect

Solid State Nuclear Magnetic Resonance

journal homepage: www.elsevier.com/locate/ssnmr

Practical aspects of Zeeman-perturbed NQR spectroscopy using an adjustable electromagnet

Alireza Nari, Patrick M.J. Szell, David L. Bryce *

Department of Chemistry and Biomolecular Sciences, Centre for Catalysis Research and Innovation, and Nexus for Quantum Technologies, University of Ottawa, Ottawa, Ontario, Canada, K1N6N5

ARTICLE INFO

Handling Editor: Prof S Ashbrook

Keywords:
Nuclear quadrupole resonance
Solid-state NMR
Zeeman interaction
Iodine
NQR

ABSTRACT

Quadrupolar-perturbed solid-state NMR spectroscopy is a highly useful and well-established method for studying quadrupolar nuclei. This method relies on a high ratio of the Larmor frequency to the quadrupolar frequency and is limited, therefore, by the available magnetic field strengths suitable for NMR, which are on the order of 10^1 T. Nuclear quadrupole resonance (NQR) provides an approach to studying strongly quadrupolar isotopes, but there are technical challenges associated with measuring high-frequency transitions, and with measuring both the quadrupolar coupling constant, C_Q, and asymmetry parameter, η, with good precision. We describe here the technical and practical aspects of a modern implementation of Zeeman-perturbed NQR spectroscopy using an adjustable electromagnet, which overcomes the aforementioned challenges. This approach flips the quadrupolar-perturbed solid-state NMR method upside down, so that the quadrupolar interaction is dominant and the Zeeman interaction is the perturbation. ^{79}Br and ^{127}I Zeeman-perturbed NQR spectra are recorded for some solid bromo- and iodobenzene powders using applied magnetic fields on the order of 10^{-2} T. Various experimental considerations are discussed, including the optimal magnetic field to be used, the optimization of the coil angle, frequency stepping, the simulation of spectra using an exact diagonalization of the Zeeman-quadrupolar Hamiltonian, and how to ensure high precision in the resulting quadrupolar parameters. As an example, a $C_Q(^{127})$ value of 2077.25 ± 1.49 MHz (with $\eta = 0.114 \pm 0.008$) is measured for *sym*-triiodotrifluorobenzene in less than an hour at room temperature. The approach holds promise for studying strongly quadrupolar isotopes in a range of materials and obviates the need for ultrahigh magnetic fields in many situations of interest.

1. Introduction

Nuclear quadrupole resonance (NQR) spectroscopy of crystalline powders can provide the magnitude of the electric field gradient (EFG) tensor by characterizing the quadrupolar interaction (QI), allowing for a direct probe into the local electronic configuration about a nucleus. The EFG at the nuclear site is described by a second-rank tensor with principal components V_{11}, V_{22}, and V_{33}, where $|V_{11}| \leq |V_{22}| \leq |V_{33}|$. V_{33} is the largest EFG component and may also be written as eq_{33} or simply eq. The degree of deviation of the EFG from cylindrical symmetry is captured by the asymmetry parameter, which is defined as $\eta = (V_{11} - V_{22})/V_{33}$, and ranges from 0 (cylindrically symmetric) to 1. The quadrupolar coupling constant (C_Q) is defined as $\frac{eQV_{33}}{h}$, where e is the electronic charge and Q is the nuclear electric quadrupole moment. Overall, the EFG serves as a sensitive probe of the electronic environment at the nuclear site, reflecting variations due to changes in molecular structure, chemical bonding, crystal structure, and through-space interactions [1–4].

To determine the full EFG tensor magnitude using pure NQR (NQR measured in the absence of an external magnetic field) in the traditional 1-dimensional experiment, multiple NQR transitions must be measured. However, this is not possible for spin $I = 3/2$ nuclei which exhibit only a single NQR transition ($1/2 \leftrightarrow 3/2$), or in cases of spin $I > 3/2$ where only one NQR transition is within the spectral range of the transmitter and/or receiver [3]. More generally, the EFG tensor cannot be fully characterized from a single NQR transition under the pure NQR regime without the use of additional experimental techniques. For instance, nutation NQR experiments may lead to the full description of the EFG tensor magnitude from a single NQR transition but can at times require the application of prohibitive radio frequency (rf) powers to adequately resolve spectral features [5,6].

The application of a weak magnetic field (B_0) to the sample, typically

* Corresponding author.
E-mail address: dbryce@uottawa.ca (D.L. Bryce).

https://doi.org/10.1016/j.ssnmr.2025.102014
Received 28 April 2025; Received in revised form 29 May 2025; Accepted 30 May 2025
Available online 3 June 2025
0926-2040/© 2025 The Authors. Published by Elsevier Inc. This is an open access article under the CC BY license (http://creativecommons.org/licenses/by/4.0/).

<50 mT, introduces the Zeeman interaction to the spin system, a technique known as Zeeman-perturbed NQR (Zp-NQR) spectroscopy [7–14]. The interplay between the Zeeman interaction and the QI broadens the NQR signal, enabling the determination of the EFG tensor through spectral line shape fitting. Under a perturbative Zeeman field, the quadrupolar line shape splits into four distinct transitions, commonly referred to as the inner (α) and outer (β) pairs (*vide infra*). This splitting allows for the extraction of EFG parameters using perturbation theory expansion [11,13] or an exact Hamiltonian treatment [12,15]. Additionally, Zp-NQR can be applied to single crystals to establish the orientation of the EFG tensor relative to the crystalline frame [15–21].

Zp-NQR has been the subject of interest since the pioneering work of Toyama [7,8]. This attention stems from the power of Zp-NQR to measure the full EFG parameters in both polycrystalline powders [13,22] and in single crystals [17,19]. Early studies focused on the variations in energy level splitting of spin 3/2 systems in single crystals, where the orientation of the crystal was varied with respect to an external applied magnetic field [23,24]. Morino and Toyama [8] conducted the first investigations on powder samples, demonstrating that similar effects are also observable in polycrystalline materials.

To the best of our knowledge, Zp-NQR has been most commonly applied to spin $I = 3/2$ nuclei, where it offers clear advantages in measuring quadrupolar parameters. However, there are instances where this method has been extended to other spin systems. A notable example is the work by Ege et al. [25], who conducted Zp-NQR experiments on spin-5/2 nuclei using a Helmholtz coil to generate the B_0 magnetic field and a super-regenerative receiver to acquire the resulting spectrum. However, the accuracy of their measurements of η was significantly limited by the poor signal-to-noise (S/N) ratio of the Zp-NQR spectrum, even at 77 K, which was a consequence of the limits of their instrumentation. Furthermore, the low S/N ratio also restricted the authors from using higher B_0 magnetic fields in order to improve their measurements. This constraint has also prevented other authors from making accurate measurements of η for higher-spin nuclei, such as spin-7/2 nuclei [26]. Similarly, in the work of Ramaprabhu on spin-5/2 nuclei, η was estimated for covalently bonded iodine in H_5IO_6 powder and has considerable associated uncertainty [27].

The benefits of Zp-NQR for investigating chemical systems exhibiting large quadrupolar interactions [28] prompted us to take a closer look at the practical aspects of performing Zp-NQR using more modern instrumentation available in our laboratory. NQR spectroscopy can be performed using a solid-state NMR spectrometer console and a broadband NMR probe, provided that both the NMR console and NMR probe can operate within the intended spectral range of the NQR experiment. Further, magnetic resonance facilities may be equipped with an electromagnet that can be used to generate weaker B_0 magnetic fields suitable for Zp-NQR, which can be achieved, for example, using the electromagnet of an electron paramagnetic resonance (EPR) spectrometer. EPR magnets are particularly advantageous because they allow for convenient adjustments of the applied B_0 field and can generate field strengths well beyond what is required for Zp-NQR. While EPR magnets do not provide the same level of field homogeneity as high-resolution NMR magnets, they offer sufficient homogeneity to acquire Zp-NQR spectra with acceptable broadening, enabling the extraction of EFG parameters via spectral fitting. We recently showed how the weak B_0 fields generated by the electromagnet of an EPR spectrometer are of sufficient quality to acquire Zp-NQR spectra suitable to extract EFG parameters by means of spectral fitting, and how these data may be used to measure C_Q and η for $^{79/81}$Br and ^{127}I in a series of halogen-bonded cocrystals featuring C-Br···X and C-I···X motifs [29].

Here, we describe the practical aspects of combining a solid-state NMR spectrometer with an electromagnet intended for EPR spectroscopy for the purpose of performing Zp-NQR experiments. We demonstrate this experimental arrangement on two distinct spins: the spin $I = 3/2$ nuclei of ^{79}Br in 1,4-dibromobenzene (*p*-DBB), and the spin $I = 5/2$ ^{127}I nuclei in 1,4-diiodobenzene (*p*-DIB), 1,4-diiodotetrafluorobenzene (*p*-DITFB), and 1,3,5-trifluoro-2,4,6-triiodobenzene (*sym*-TFTIB). Scheme 1 illustrates the molecular structures of the studied compounds. The quadrupolar coupling parameters of $^{79/81}$Br and ^{127}I in these systems were previously well-established in the literature [29–33], and provide greater context on the power and versatility of Zp-NQR for studying complex chemical systems.

2. Theory

In this study, we aim to probe the transitions that occur in Zp-NQR experiments when the quadrupole energy levels are perturbed by a small Zeeman field. To illustrate the Zp-NQR line shapes of the $|m| = 1/2 \leftrightarrow 3/2$ transition, here we recapitulate the known method of calculating the frequency splitting for a half-integer-spin quadrupolar nucleus in an external magnetic field. When both nuclear quadrupole and Zeeman interactions are present, the total Hamiltonian is given by:

$$H_t = H_Q + H_Z \tag{1}$$

where

$$H_Q = \left[\frac{e^2qQ}{4I(2I-1)}\right]\left[3I_z^2 - I^2 + \eta\left(I_x^2 - I_y^2\right)\right] \tag{2}$$

and

$$H_Z = -\hbar\gamma B_0\left(I_z\cos\theta + I_x\sin\theta\cdot\cos\phi + I_y\sin\theta\cdot\sin\phi\right) \tag{3}$$

In this context, I represents the nuclear spin, the x, y, and z coordinates correspond to the principal axes of the laboratory frame, and θ and ϕ specify the orientation of the static magnetic field relative to this frame. Here, we use $eq = V_{33}$, where V_{33} is the largest principal component of the EFG tensor, as defined earlier in the introduction.

It is worth noting that θ and ϕ define the orientation of the static magnetic field B_0 relative to the principal axes of the EFG tensor. The direction of the radiofrequency (rf) field B_1 is determined by the orientation of the solenoid coil, which lies along the coil axis of the NQR probe. The angle between B_0 and B_1, which governs the transition probabilities in Zp-NQR, is therefore experimentally controlled by rotating the probe head (i.e., changing the coil orientation relative to the magnet's field direction). While the Hamiltonian above is written in the molecular frame with respect to the EFG, the influence of the relative orientation between B_0 and B_1 on the observed spectra is further discussed in the experimental and discussion sections.

In Zp-NQR, the quadrupolar interaction is considered much stronger than the Zeeman interaction, i.e., $|H_Q| \gg |H_Z|$. A magnetic field applied to the sample removes the degeneracy of the $\pm m$ spin states for half-integer spins. For a non-axially symmetric EFG tensor ($\eta \neq 0$), solving the secular problem to first order yields the energy levels for spins $I = 5/2$, 7/2, and 9/2 as:

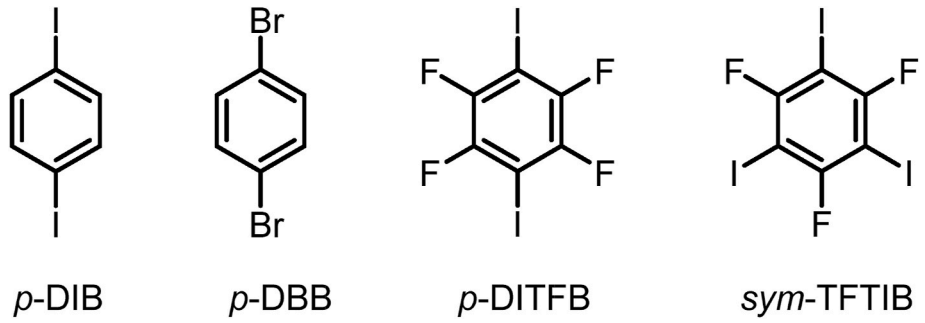
$$E_{\pm m} = E^0_{\pm m} \mp \hbar\gamma B_0\left[A_{\eta,I,m}\cos^2\theta + \frac{\sin^2\theta}{4}\cdot\left(B_{\eta,I,m} + 2C_{\eta,I,m}\cos 2\phi\right)\right]^{1/2} \tag{4}$$

Here, $E^0_{\pm m}$ represents the eigenvalues of the degenerate energy levels in the absence of an applied magnetic field. The Zeeman splitting parameters, $A_{\eta,I,m}$, $B_{\eta,I,m}$, and $C_{\eta,I.m}$ for $0.1 < \eta < 1.0$, for nuclear spins $I = 5/2$, 7/2, and 9/2, are provided in reference [34]. The transition frequencies between these energy states are [27]:

$$\nu = \nu_Q(m_1 \leftrightarrow m_2) \pm \frac{\gamma B_0}{2}[\varphi(m_1) \pm \varphi(m_2)] \tag{5}$$

where

$$\varphi(m_i) = \left[A_{\eta,I,m}\cos^2\theta + \frac{\sin^2\theta}{4}\left(B_{\eta,I,m} + 2C_{\eta,I,m}\cos 2\phi\right)\right]^{1/2} \tag{6}$$



Scheme 1. Molecular structures of 1,4-diiodobenzene (*p*-DIB), 1,4-dibromobenzene (*p*-DBB), 1,4-diiodotetrafluorobenzene (*p*-DITFB), and 1,3,5-trifluoro-2,4,6-triiodobenzene (*sym*-TFTIB).

In this context, $\nu_Q(m_1 \leftrightarrow m_2)$ represents the quadrupolar frequency in the absence of an external magnetic field. The transition pair with the larger frequency separation is referred to as the outer (β) pair. Conversely, the pair with the smaller frequency separation is known as the inner (α) pair [27].

To illustrate the nuclear quadrupolar energy levels and the corresponding Zeeman splitting observed in the Zp-NQR experiment, we adopt the convention introduced by Toyama [7] where the pure quadrupole states are labeled $\pm m$. These states are degenerate in the absence of an external magnetic field, with mQ denoting the eigenvalues of the quadrupole Hamiltonian, H_Q. As depicted in Fig. 1, applying a relatively small Zeeman magnetic field lifts this degeneracy due to the interaction with the magnetic field, H_Z. A line corresponding to the transition between $|mQ| = m'Q \leftrightarrow m''Q$ (where m', $m'' > 0$) splits into two pairs of transitions: $\pm m'M \leftrightarrow \pm m''M$, known as the α and β pairs. Here, mM represents the eigenstates of the total Hamiltonian, $H_t = H_Q + H_Z$, whereby the Zeeman interaction splits the degenerate quadrupole states, leading to new energy levels and transitions that depend on the orientation of the magnetic field relative to the EFG tensor.

In Zp-NQR of a spin-3/2 system, where only one absorption for transitions between $|m| = 1/2 \leftrightarrow 3/2$ is observed, the approximate solutions for the energy levels in the presence of a small magnetic field, i.e., $|H_Q| \gg |H_Z|$, can be obtained by treating the Zeeman term as a perturbation to the quadrupole energy levels. Consequently, the perturbed energy levels for transitions between $|m| = 1/2 \leftrightarrow 3/2$, which can be calculated exactly, are given by [7]:

$$E_{4,3} = \frac{h\nu_Q\rho}{2} \pm \frac{h\nu_0}{2\rho B_0}\left[(\rho - 1 + \eta)B_x^2 + (\rho - 1 - \eta)B_y^2 + (2 + \rho)B_z^2\right]^{1/2} \quad (7)$$

and

$$E_{2,1} = -\frac{h\nu_Q\rho}{2} \pm \frac{h\nu_0}{2\rho B_0}\left[(\rho + 1 - \eta)B_x^2 + (\rho + 1 + \eta)B_y^2 + (2 - \rho)B_z^2\right]^{1/2} \quad (8)$$

where

$$\rho = \left(1 + \frac{1}{3}\eta^2\right)^{1/2} \quad (9)$$

and ν_Q is the pure NQR frequency, ν_0 is the Larmor frequency, and B_x, B_y, and B_z are the components of the applied field along the EFG principal axes. These transitions are symmetrically centered about the pure quadrupolar frequency.

In this context, we note that while the above treatment for spin-3/2 nuclei is valid for all cases we have studied, i.e., where $\nu_Q = C_Q\rho/2$, this is not the case for spin-5/2 nuclei. For spin-5/2 nuclei, the exact treatment implemented in the QUEST software must be used. Perturbation theory, which is sometimes good enough for $\eta < 0.1$, generally fails when $\eta > 0.1$. For this reason, we cannot provide a simple formula relating the C_Q and ν_Q values measured in this work (*vide infra*).

2.1. Experimental details

In practice, Zp-NQR, like NMR, requires a homogeneous (having the same magnitude and direction at every point within the region of interest) and stable (constant over time without fluctuations) static magnetic field. The optimal field strength to be used is determined by both the pure NQR frequency (ν_Q) and the Larmor frequency (ν_0). An optimal setting will ensure sufficient frequency separation between the α and β pairs relative to the inherent spectral broadening (equations (5), (7) and (8)). A critical threshold for the applied Zeeman magnetic field must be

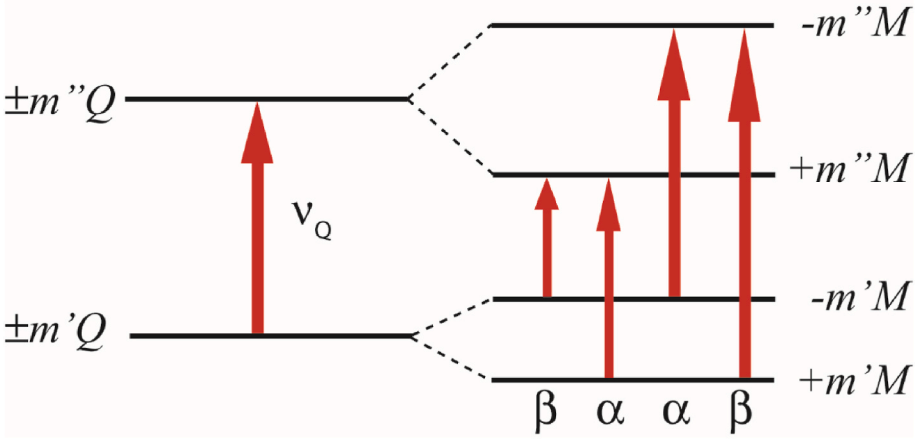


Fig. 1. Zp-NQR energy levels and the Zeeman splitting for a spin 3/2 system. Inspired by references [1,7,34].

met to achieve adequate resolution of the line shape features corresponding to the α and β pairs. The required field strength is dictated by multiple factors in addition to the NQR and Larmor frequencies, including the intrinsic broadening caused by sample crystallinity, the random orientation of powder particles, and the inhomogeneity of the external magnetic field, which in this work was generated by an EPR electromagnet.

To characterize the relative strength of the quadrupolar interaction, a useful dimensionless parameter can be defined as ν_Q/ν_0. Experimentally, achieving well-resolved spectral features in Zp-NQR, which are crucial for accurately determining η, typically requires that this ratio does not exceed approximately 1500. For example, in a ^{127}I system with an NQR frequency of 330 MHz, an optimal static magnetic field of at least 25 mT (250 Gauss) was necessary to meet this condition.

Higher B_0 fields also improve the accuracy of C_Q and η measurements, particularly for low-γ nuclei. However, it should be noted that increasing the magnetic field significantly reduces the signal-to-noise ratio (SNR) as a result of broadening the Zp-NQR spectral envelope (*vide infra*). Consequently, longer signal averaging is required, making data acquisition more time-consuming. Additionally, a broader envelope necessitates the accumulation of more subspectra to reconstruct the full Zp-NQR spectrum, further increasing the experimental workload.

Moreover, we found that the resolution and broadening of the Zp-NQR spectral features are influenced by several factors beyond the external magnetic field strength, including the imperfections in our setup, particularly the probe, powder grain size, and the magnitude of η — with larger η values leading to less resolved features of line shape. In our experience with $^{79/81}$Br and ^{127}I isotopes, a static Zeeman field as high as ~30–40 mT was necessary to achieve adequate definition of spectral features of interest.

In studying powder Zp-NQR as a perturbation of the Zeeman interaction over the quadrupolar interaction, it is assumed that the sample consists of a large number of randomly oriented single crystals and that the external Zeeman field is uniform across the entire sample. To satisfy these conditions, we use finely ground microcrystalline powders to ensure an even distribution of all crystallite orientations.

(i) EPR electromagnet field setting

In this study, we utilize an EMXplus electromagnet, which can generate magnetic fields up to 1.7 T (17000 G) with a field stability of approximately 10 mG per hour. The system operates using Bruker's Xenon interface software. To achieve a more uniform magnetic field, the field modulation amplitude was kept at its minimum value of 0.01 G, as any modulation could introduce field fluctuations. Additionally, the field modulation frequency setting was disabled to maintain a steady field.

The cavity of these electromagnets is sufficiently wide to allow narrow-bore (54 mm) NMR probes to fit (Fig. 2). A homebuilt narrow-bore NQR probe capable of operating from 200 MHz to 400 MHz was constructed, which covers the spectral range for $^{79/81}$Br (spin $I = 3/2$) in the C-Br motif, as well as the $3/2 \rightarrow 1/2$ transition of ^{127}I in the C-I motif. The effective excitation bandwidth was empirically determined to be approximately 310 kHz. As EPR magnets generally employ field modulation, this feature must be disabled in order to minimize any disruptions to the Zp-NQR experiment. As shown in Fig. 2, the homebuilt narrow-bore NQR probe was placed within the cavity of an electromagnet of an EPR spectrometer.

Since the homogeneity and quality of the applied static magnetic field are crucial in Zp-NQR experiments, we first calibrated the EPR electromagnetic field and mapped out the optimal position for placing the sample coil. Using *p*-DIB as a reference compound — owing to its well-known quadrupole parameters [35] — we systematically evaluated different regions within the electromagnet poles. We found that the center of the electromagnet provided the most uniform and stable magnetic field, making it the optimal location for conducting Zp-NQR experiments. This positioning yielded a well-defined envelope shape and the best resolution of the Zp-NQR spectral features relative to other areas between the poles, enabling more accurate spectral simulations. Fig. 3 presents a top-view illustration of the proper placement of the coil containing the sample tube at this optimal position.

(ii) NMR console and NQR pulse program

The Zp-NQR experiments were conducted after finding the $|m| = 1/2$ to 3/2 transition of the pure (zero-field) NQR spectrum using our custom-built NQR probe. This probe was placed on a bench, away from stray magnetic fields. Notably, Earth's stray field (~50 μT) was sufficiently small to be considered negligible. For zero-field NQR measurements, the probe — fitted with a solenoid coil of 7 mm inner diameter — was connected to a proton preamplifier in a Bruker Avance III 400 MHz NMR spectrometer. The proton preamplifier allows rf signals within the

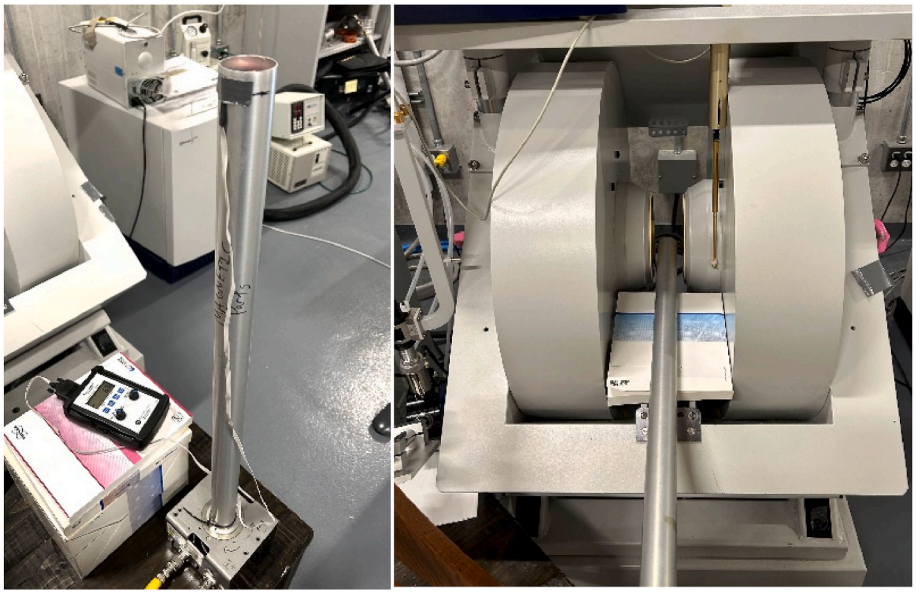


Fig. 2. The home-built NQR probe, capable of tuning in the 200–400 MHz range (left), and the probe positioned within the EPR electromagnetic field, supported by a useful Bruker manual (right).

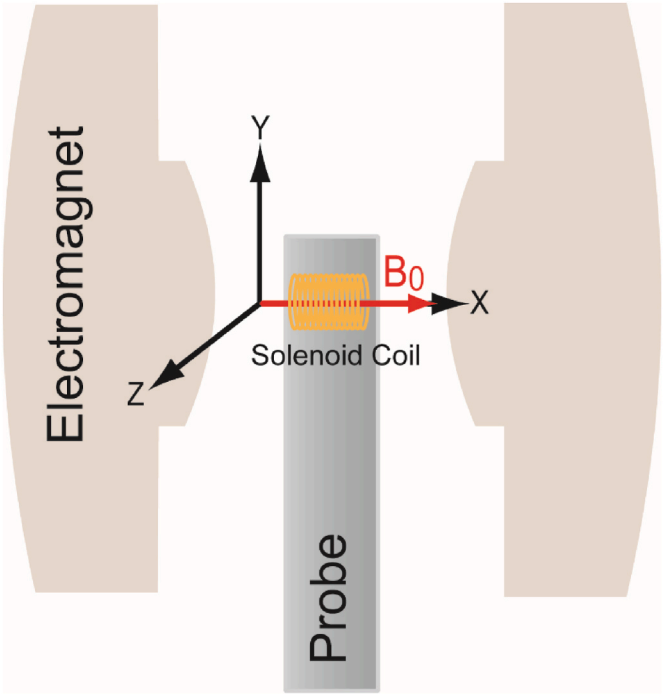


Fig. 3. Illustration of the NQR probe and solenoid coil aligned with the static magnetic field at the center of the electromagnet poles.

desired frequency range, typically 270 MHz–400 MHz, to pass through. To search for unknown NQR resonances, the rf frequency was incremented in 150 kHz steps. A Hahn-echo pulse sequence was used, with typical π/2 and π pulse lengths of 4 μs and 8 μs, respectively.

The optimal pulse length and power level for the Hahn echo experiment were determined by calibrating the π/2 and π pulses for the ^{127}I nuclei in *p*-DIB. Initially, the transmitter power was set based on prior experiments [35] or estimated using the gyromagnetic ratio. The π/2 pulse was optimized through a nutation experiment by applying a series of pulse lengths and identifying the first maximum in signal intensity, with the π pulse set to twice this duration. Fine-tuning was performed by varying pulse power and duration in Hahn echo experiments, adjusting parameters to maximize echo intensity while minimizing distortions.

For the Zp-NQR experiments, the same probe was placed between the poles of a Bruker EMXplus EPR electromagnet to introduce a weak, adjustable static magnetic field and thus perturb the NQR transitions. The EPR resonator and microwave waveguide remained disconnected, and the microwave bridge was removed from the magnet. Although the electromagnet is capable of generating fields up to 1.7 T, in our Zp-NQR measurements we applied fields in the range of 20–40 mT. This range was chosen based on the Morino lower limit condition, which requires the Zeeman splitting to exceed the natural NQR linewidth for the splitting to be resolvable. It also reflects practical considerations, including line broadening due to field inhomogeneity and the optimization of signal-to-noise ratio for accurate QUEST-based line shape simulations.

Due to the broad Zp-NQR spectral envelopes observed for our samples —up to ~2 MHz for systems with C_Q values of 1.8–2.1 GHz for ^{127}I and 0.6 GHz for ^{79}Br — the probe's bandwidth was insufficient to capture the full spectrum in a single acquisition. To overcome this limitation, data were collected as multiple subspectra with frequency offsets incremented in 50 and 100 kHz steps. These subspectra were subsequently combined using the variable offset cumulative spectrum (VOCS) [36] technique to reconstruct the final envelope. The total number of subspectra depended on both the applied field strength and the chosen frequency increments, typically ranging from 8 (at 5 mT) to 37 (at 40 mT) subspectra when using 100 kHz steps for *p*-DITFB and 50 kHz frequency steps for other compounds (Table 1). The acquisition of the complete envelope for the compounds studied here took between 30 and 90 min. An alternative approach for broadband excitation, such as WURST-QCPMG, could potentially improve efficiency in these types of broad-spectrum acquisitions by reducing the overall acquisition time [37]. We note that a recycle delay of 0.25 s was used, which could probably be shortened in future work to reduce overall experimental times. Presently we chose this delay to facilitate complete relaxation and to reduce possible sample heating.

(iii) Spectral simulation

Early Zp-NQR experiments often relied on assigning peak frequencies using simplified formulas and extrapolation procedures restricted to low η values. These approaches were constrained by first-order quadrupolar approximations, leading to significant uncertainties in determining quadrupolar parameters. By employing the QUEST software [42], which utilizes exact Hamiltonian diagonalization, we remove the dependence on first-order approximations and achieve robust, reliable spectral analyses of Zp-NQR data. Exact simulation allows for a more accurate reproduction of experimental spectra, even in cases of high η values where first- and second-order approximations fail. This ensures a precise determination of quadrupolar parameters, reducing ambiguities in spectral assignment and improving the overall reliability of Zp-NQR as a tool for characterizing the EFG tensor.

In QUEST, the fitting procedure requires specifying key parameters, including the coil angle which represents the orientation of the external Zeeman magnetic field, B_0, relative to the rf field, B_1. Additionally, the

Table 1
Experimental conditions for Zp-NQR measurements, including the applied magnetic field, coil angle, and resulting whole spectral breadth for each compound studied herein.

compound and CSD refcode	B_0/mT	coil angle/°	π/2 pulse /μs	recycle delay/s	subspectra/scans (#)	breadth/kHz	total expt time[a](min)	sample mass (g)
p-DIB: ZZZPRO01 [38]	30	0	6.0	0.25	27/128	1348 ± 40	60	0.41
		45	6.0	0.25	27/256	1372 ± 36	60	0.41
		90	4.0	0.25	27/256	1460 ± 42	60	0.41
p-DBB: CISTON01 [39]		0	4.8	0.25	37/256	1875 ± 50	90	0.38
	40	45	4.8	0.25	37/256	2014 ± 46	90	0.38
		90	4.8	0.25	37/256	1912 ± 48	90	0.38
sym-TFTIB: UCEPEY [40]	0	0	6.0	0.25	1/128	58 ± 4	1	0.47
	5		6.0	0.25	8/256	312 ± 11	20	0.47
	10		6.0	0.25	12/256	520 ± 18	30	0.47
	30		6.4	0.25	27/256	1383 ± 52	60	0.47
p-DITFB: ZZZAVM02 [41]	20	0	4.0	0.25	11[b]/256	869 ± 21	30	0.42

[a] Total experiment time includes the duration required to acquire the entire spectral envelope, including setting up new experiments and tuning the probe between each step (subspectra).
[b] The frequency step increment for this sample was 100 kHz, whereas it was maintained at 50 kHz for the other compounds.

Larmor frequency, determined by the gyromagnetic ratio and the applied magnetic field, and the nuclear spin quantum number (e.g., 3/2, 5/2, etc.) (Table 2) must be defined. Next, by iteratively adjusting the input values of C_Q and η, we determine the combination that best reproduces the experimental Zp-NQR spectrum. The final fit is assessed through visual inspection, allowing for a confident assignment of the quadrupolar parameters. The reliability of the fit is further enhanced by optimizing the fitting settings to ensure accurate determination of C_Q and η. As with high-field quadrupolar-perturbed solid-state NMR, fitting separate datasets obtained in more than one applied magnetic field improves the accuracy of the results.

3. Results and discussion

In the following paragraphs, experimental and simulated spectra are presented and discussed with the goal of demonstrating some of the practical aspects of our implementation of Zp-NQR spectroscopy. The quadrupolar coupling parameters measured in this section are summarized in Table 3 and the relevant spectra and simulations are shown in the figures that follow.

Calculations of transition probabilities between nuclear quadrupole energy levels perturbed by a weak static magnetic field, supported by experimental evidence, show a characteristic angular dependence on the orientation of the static field relative to the RF field, in agreement with previous investigations [8,17,42]. This angular dependence manifests in the two pairs of Zeeman components within the Zp-NQR envelope associated with $|m| = 1/2 \leftrightarrow 3/2$ transitions in quadrupolar nuclei. In single-crystal Zp-NQR experiments, the Zeeman splitting depends on the relative orientation between the applied magnetic field and the EFG tensor. By systematically varying the crystal orientation relative to the static field, one can determine the orientation of the EFG principal axes with respect to the crystallographic frame, as demonstrated in previous studies [43,44].

As shown in Fig. 4, the shape of the spectral envelope near the splitting frequencies ($\pm\nu_0$), derived from the product of the NQR frequency and the gyromagnetic ratio of the resonant nuclei, is significantly influenced by the relative orientation of the static magnetic field, B_0, to the radiofrequency field, B_1. In polycrystalline samples, when $B_0 \| B_1$, the nuclear quadrupole resonance transitions are generally modulated by the rf field component perpendicular to the principal z-axis of the EFG.

According to Morino and Toyama, the determination of η is most distinct when the magnetic field is aligned parallel to the principal xy plane of the EFG [8]. Their study demonstrated that when $B_0 \| B_1$, no spectral components appear at the splitting frequencies ($\pm\nu_0$). Instead, the intensities of the components at $\pm(1-\eta)\ \nu_0$ and $\pm(1+\eta)\ \nu_0$ increase proportionally to the decrease at $\pm\nu_0$. In a polycrystalline powder, this configuration produces sharp minima at $\pm\nu_0$ (troughs) and two pairs of sharp maxima (peaks) at $\pm(1-\eta)\nu_0$ and $\pm(1+\eta)\nu_0$ on the spectral envelope.

In contrast, when B_0 is perpendicular to B_1, specifically in the case where $B_0 \| z$, the situation differs significantly from the parallel alignment of B_0 and B_1. Under this configuration, a strong pair of components is produced at $\pm\nu_0$ because the rf field lies parallel to the xy-plane, rendering the transitions corresponding to the inner pair $\pm(1-\eta)\nu_0$ forbidden. Consequently, the Zeeman components at $\pm(1-\eta)\nu_0$ are not observed. We refer the readers to ref. [8] for more detailed information.

In Fig. 5, we illustrate the experimental dependence of the Zp-NQR line shape on the coil angle of the NQR probe. The coil angle (the orientation of the static magnetic field, B_0, relative to the rf field, B_1) is an adjustable parameter in QUEST and must be adjusted during spectral fitting to achieve the best results. In the Zp-NQR setup, the coil angle is adjusted by rotating the probe head, and consequently the solenoid coil containing the sample vial. The angle is physically measured using a bevel protractor, with reference to the direction of the static magnetic field (defined by the axis connecting the centers of the EPR magnet's pole faces). The probe baseplate is aligned manually relative to the magnet housing to reproducibly achieve coil angles of 0°, 45°, and 90°. As discussed above, the best results are achieved when the two fields are aligned parallel to each other, i.e., $B_0 \| B_1$, corresponding to a zero-angle of the solenoid coil relative to the Zeeman magnetic field. In this configuration, the spectral envelope is influenced by the relative orientation of B_0 and B_1, modulating the nuclear quadrupole transitions. The alignment ensures well-defined spectral features, enabling precise determination of the quadrupolar parameters. Deviations from this alignment result in distinct changes to the spectral line shape, as demonstrated by the variation in coil angle shown in Fig. 4.

Table 2
Gyromagnetic ratios (γ), quadrupole moments (Q), and natural abundances (NA) of the nuclei discussed in this work.

Nucleus	I	NA	γ (10^7 rad T^{-1} s^{-1})	Q (mb)
^{127}I	5/2	100	5.389573	−688.22
^{79}Br	3/2	50.69	6.725616	308.7

Table 3
Experimentally measured ^{79}Br/^{127}I quadrupole coupling constants, frequencies, and asymmetry parameters at room temperature.

compound	C_Q/MHz	η	ν_Q^b/MHz
p-DIB (^{127}I)	1841.42 ± 0.85	0.044 ± 0.004	276.68 ± 0.03
p-DBB (^{79}Br)	533.78 ± 0.12	0.16 ± 0.04	268.02 ± 0.03
sym-TFTIB (^{127}I)	2077.25 ± 1.49[a]	0.114 ± 0.008	315.97 ± 0.03
p-DITFB (^{127}I)	2145.14 ± 1.64	0.120 ± 0.004	326.80 ± 0.03

a: The data reported here correspond to the first crystallographic site (lower NQR frequency) of *sym*-TFTIB.
b: Lower frequency ½ → 3/2 transition for ^{127}I.

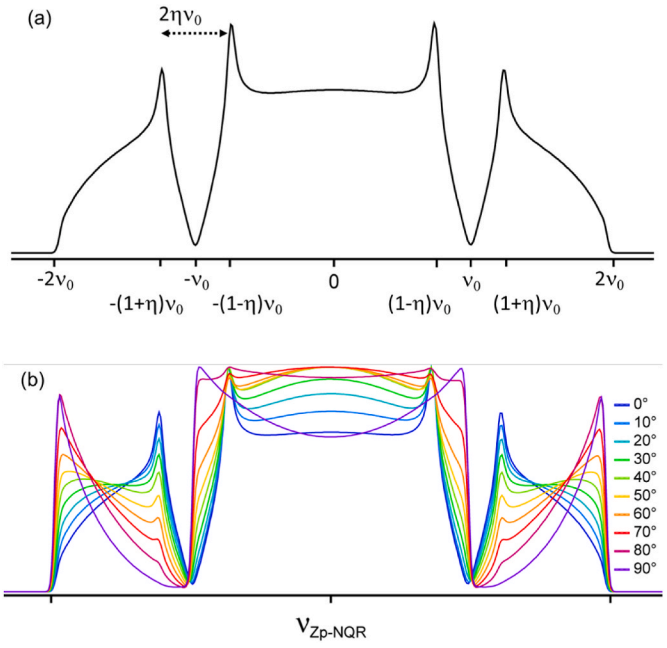


Fig. 4. QUEST simulated Zp-NQR spectrum of the $|m| = 1/2 \leftrightarrow 3/2$ transitions in a spin-3/2 system with $\eta = 0.25$ (a slightly asymmetric EFG), (a) at a coil angle of 0° (i.e., $B_0 \| B_1$). The observed peaks and troughs are assigned to corresponding spectral components, which are used in spectral fitting to determine the quadrupolar parameters. (Inspired by Morino and Toyama [8].) This configuration serves as the basis for the Zp-NQR studies presented here. (b) The dependence of the Zp-NQR envelope on coil angle, represented as a colour gradient from 0° ($B_0 \| B_1$) to 90° ($B_0 \perp B_1$) in 10° increments. (For interpretation of the references to colour in this figure legend, the reader is referred to the Web version of this article.)

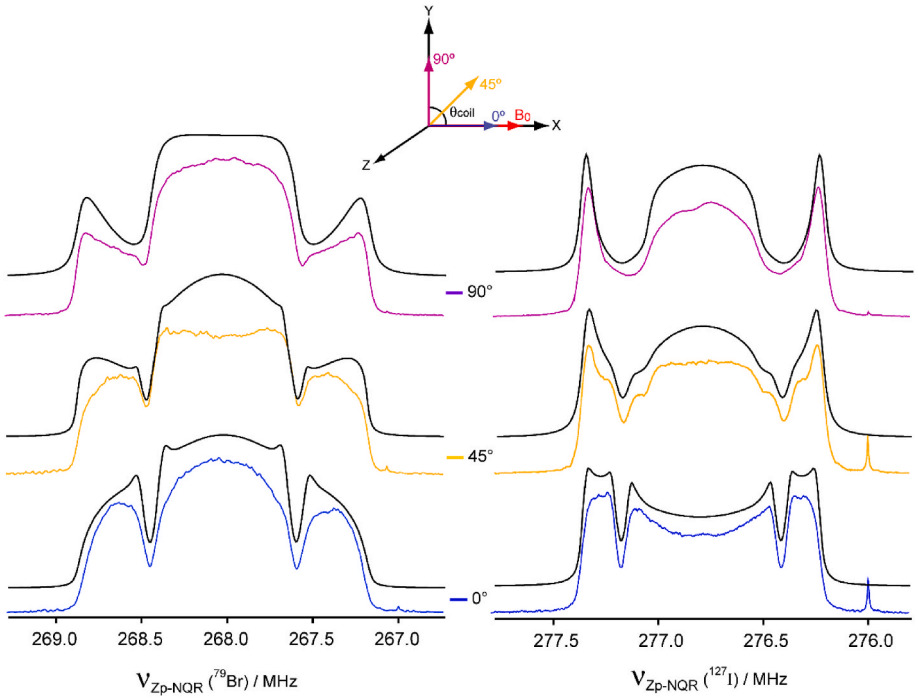


Fig. 5. Experimental Zp-NQR spectra at varying coil angles (B_0 relative to B_1) for (left) *p*-DBB at 40 mT and (right) *p*-DIB at 30 mT. Simulated spectra from QUEST are overlaid in black above each experimental spectrum. The corresponding quadrupole coupling constants and asymmetry parameters are summarized in Table 1. We tentatively assign spurious resonances at 267 and 276 MHz as artifacts of unknown origin.

Our experiments, which aimed to determine η with high precision, revealed that a carefully calibrated EPR magnetic field, accurate to within ±1 Gauss (0.1 mT), is crucial. This level of accuracy ensures precise calculation of the Larmor frequency (ν_0) of the nucleus, which is necessary for the reliable determination of η using the QUEST simulation software. To confirm the actual field experienced by the sample, the magnetic field set in the EPR software was externally verified using a Gaussmeter (AlphaLab model GM-2), showing agreement within ±1 G. Additionally, the accuracy was validated using a reference compound (DIB), where the experimentally observed NQR spectra and the simulated spectra based on known Larmor and quadrupolar parameters matched closely. The probe was positioned at the center of the electromagnet, where the field is most uniform and stable, and alignment was carried out reproducibly using Bruker's guidelines. The relationship is given by:

$$\nu_0 = \gamma B_0 / 2\pi \tag{10}$$

Here, γ is the gyromagnetic ratio (γ), and B_0 is the applied magnetic field. γ values and quadrupole moments (Q) of the quadrupolar nuclei studied herein are summarized in Table 2.

Based on the procedure described by Morino [8] on the Zeeman effect in polycrystalline powders, the applied static magnetic field must be strong enough to produce a splitting greater than the NQR linewidth, as shown in the following formula:

$$B_0 \gtrsim \frac{2\pi\Delta\nu}{\eta|\gamma|} \tag{11}$$

However, satisfying this condition significantly reduces the S/N ratio of each slice of the spectrum due to line broadening. This reduction hampered the accurate determination of η and prevented the examination of nuclei with high C_Q when using the basic equipment available at that time. Furthermore, the first-order perturbation treatment employed in the procedure outlined by Morino and Toyama, along with the frequent neglect of the sufficient static field limitations by many subsequent researchers, has hampered the accurate determination of the value of η up to now, particularly for nuclei with high quadrupole coupling. These limitations were pointed out previously by Darville [10].

Herein, we addressed this limitation by increasing the static magnetic field to a level where the deflections due to η became distinctly observable, particularly for the inner transitions. Furthermore, we utilized exact spectral simulations using the QUEST software, which involves diagonalization of the combined Zeeman-quadrupolar Hamiltonian without resorting to approximations when treating the

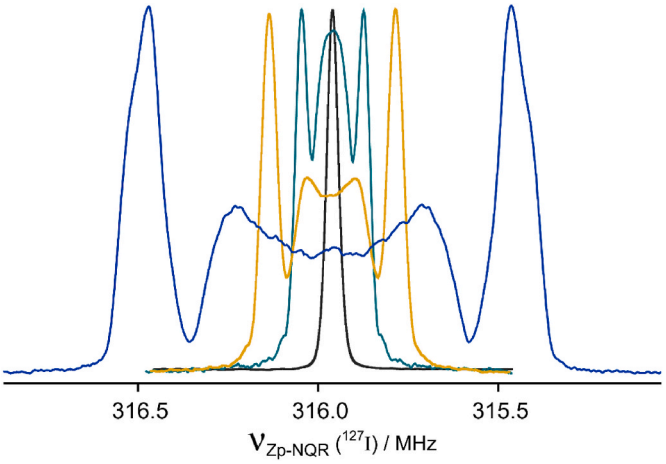


Fig. 6. Experimental zero-field ^{127}I NQR transition (Earth's magnetic field ~50 μT) is shown in black at the center, along with three ^{127}I Zp-NQR spectra corresponding to the $m = \pm 1/2$ to $\pm 3/2$ transition at applied magnetic fields of 5 (teal green), 10 (goldenrod), and 30 mT (deep blue), respectively, for *sym*-TFTIB. If the magnetic field is too low, spectral features are not resolved (teal green). If the magnetic field is too high, the spectrum broadens and takes longer to acquire; furthermore, each subspectrum will have a lower SNR. (For interpretation of the references to colour in this figure legend, the reader is referred to the Web version of this article.)

quadrupolar interaction. This exact approach, coupled with the enhanced resolution from the stronger magnetic field, allowed us to determine η with greater accuracy and precision.

Fig. 6 illustrates a pure NQR spectrum and various Zp-NQR spectra at different Zeeman field strengths, comparing cases where the field is insufficient versus sufficiently strong in a spin-5/2 system. By optimizing the field strength, we overcame challenges related to a reduced S/N ratio and successfully determined η even for nuclei with high C_Q.

To capture the entire envelope of broad Zp-NQR spectra, we employed the VOCS method. As shown in Fig. 7, the ^{127}I Zp-NQR spectrum of *p*-DITFB was constructed by summing 11 sub-spectra in a magnetic field of 20 mT, with frequency steps of 100 kHz.

Comparing the transitions between the $m = ½$ and 3/2 energy levels with those between the 3/2 and 5/2 levels for nuclei with spin $I = 5/2$ reveals that only the inner transitions (1/2↔3/2) are directly useful for determining the value of η. Varty demonstrated that the line shape associated with the ±3/2↔±5/2 transitions exhibits a minimal dependence on η, which is insufficient for accurately determining the asymmetry of the EFG tensor from experimental data [22].

In 1986, Bryant demonstrated that the line shapes in Zp-NQR spectra depend on the spin quantum number, with spectral widths increasing as the spin increases. Using computer simulations and perturbative approximations based on Toyama's formula, they showed that the optimal transitions for experimentally determining the asymmetry parameter η are the 1/2↔3/2 transitions for spins 3/2, 5/2, and 7/2, and the 3/2↔5/2 transition for spin 9/2 systems [13].

In Fig. 8, we present the Zp-NQR line shape simulations for various values of the asymmetry parameter η for nuclear spins $I = 3/2$ and 5/2 separately. The line shapes generated by exact simulations using QUEST are in good agreement with the classification proposed by Ege et al., who categorized η into three types: very small ($\eta = 0$), small ($0 < \eta < 0.01$), and not small ($\eta > 0.01$) [25].

In our experimental approach to determine η, we aligned the rf field parallel to the applied electromagnetic field (coil angle = 0°) within the EPR system, thereby maximizing sensitivity to variations in η. Ege et al. [25] previously mapped out simulations of lower-level Zeeman-perturbed transitions for spin-5/2 nuclei, examining coil angles from 0° to 90°. They observed that when the rf field is parallel to the magnetic field, the line shape undergoes significant changes as η increases. These findings reinforce the conclusions drawn from the work of Morino and Toyama (*vide supra*), supporting the relationship between coil angle, η, and the resulting Zp-NQR line shapes.

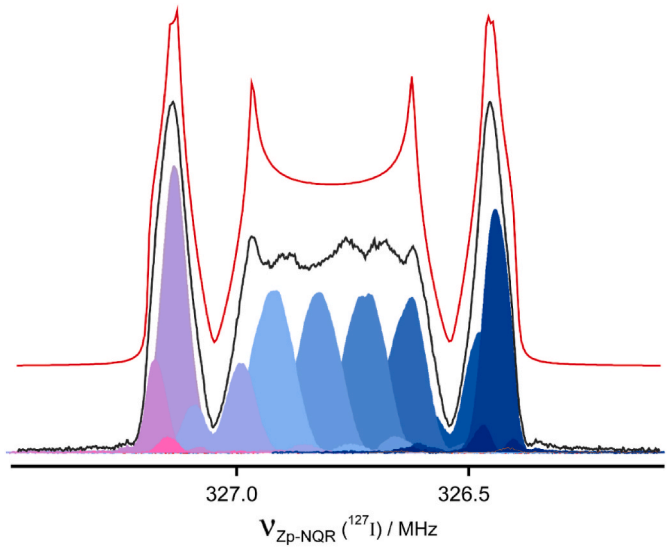


Fig. 7. Experimental Zp-NQR spectrum of a spin 5/2 nucleus (^{127}I in *p*-DITFB) at a magnetic field strength of 20 mT (black trace). Individual spectra acquired by frequency stepping, shown in various colours, were coadded to generate the full spectrum. Simulated spectrum is shown in red. (For interpretation of the references to colour in this figure legend, the reader is referred to the Web version of this article.)

As seen in Fig. 8, the evolution of the Zp-NQR line shapes for nuclear spins $I = 3/2$ and $I = 5/2$ demonstrates distinct changes as the asymmetry parameter η increases. For very small η, the line shape exhibits two symmetric peaks at the spectrum's edges, with less pronounced dips at $\pm\nu_0$ relative to higher values of η. As η increases to $0.01 < \eta < 0.4$, the spectrum transitions to showing more pronounced peaks and troughs, forming two inner pairs and two outer pairs. With further increases in η within the range $0.4 < \eta < 0.8$, the troughs become more pronounced, reaching maximum prominence. However, at η values close to 1, the dips diminish, and the outer features disappear, leaving only the inner pairs distinguishable.

While Zp-NQR is particularly well-suited for spin-3/2 systems, it also offers key advantages for quadrupolar nuclei with spins other than 3/2, including spin-1 and higher. This is especially relevant when additional NQR transitions are either inaccessible or fall outside the operational frequency range of the probe and preamplifier. In such cases, Zp-NQR enables the use of the first, lower-frequency transition (e.g., $\nu_1 \approx$ 250–350 MHz for ^{127}I in aryl iodides), thereby avoiding the challenges posed by conventional NQR methods that typically require detection of higher-frequency transitions (e.g., $\nu_2 \approx$ 500–700 MHz in aryl iodides) [29].

Another advantage of Zp-NQR is its adaptability to complex systems, particularly in aiding the identification of spectral transitions. For example, applying a Zeeman field to ^{14}N NQR lines in polycrystalline samples enhances the ability to assign transition frequencies, as demonstrated with aminopyridine [45].

4. Concluding remarks

We must acknowledge the current limitations in solid-state NMR approaches to studying strongly quadrupolar spin systems, where quadrupolar line broadening for strongly quadrupolar isotopes in asymmetric environments can result in intractable spectra, even in the highest available applied magnetic fields. In such instances, Zp-NQR emerges as a crucial alternative. By implementing a comprehensive approach — including the use of a high-quality adjustable magnetic field, precise calibration of the EPR electromagnetic field to perturb the quadrupolar interaction, optimization of the radiofrequency field orientation relative to the magnetic field (coil angle), and advanced data analysis with QUEST software — we showed how spectra characterized by quadrupolar coupling constants in the GHz regime can be recorded, and how these spectra can lead to a reliable measurement of η. The improved precision provided by Zp-NQR with exact spectral fitting positions this technique as a compelling alternative to conventional methods for studying spins exhibiting large quadrupolar coupling.

By targeting a single, accessible transition and leveraging the Zeeman effect, Zp-NQR enables the accurate and straightforward determination of C_Q and η, particularly in systems where conventional SSNMR approaches are impractical. These advancements simplify experimental setups and reduce limitations typically associated with operating in the ultra-high frequency range, such as instrumentation complexity and increased demands on tuning and probe design. In addition to our own recent application of the method to halogen-bonded systems [29], a recent study on automated wide-line NQR acquisition in lead halide perovskites alluded to the potential of Zeeman-perturbed NQR spectroscopy [46]. While Zp-NQR does not overcome the fundamental challenge of locating unknown NQR resonances, it serves as a powerful tool for refining the determination of quadrupolar parameters, particularly in cases where conventional NQR methods are limited by the inability to access multiple transitions.

Overall, Zp-NQR offers a practical method for characterizing materials featuring quadrupolar nuclei exhibiting strong quadrupolar



Fig. 8. QUEST-simulated Zp-NQR spectra of the $|m| = 1/2 \leftrightarrow 3/2$ transitions for different EFG asymmetry (η) values. The spectra correspond to a spin-5/2 system with $C_Q = 2150$ MHz (left) and a spin-3/2 system with $C_Q = 617$ MHz (right), both in applied magnetic fields of 30 mT with the static magnetic field aligned parallel to the RF field (0° coil angle). These spectra illustrate the effect of η on the Zp-NQR patterns for two distinct spin systems.

interaction. Its ability to provide precise and reliable data in scenarios where traditional SSNMR is impractical could help to make Zp-NQR an important tool for researchers across materials science, solid-state physics, and related fields, supporting the development of materials with unique electronic and structural properties.

Declaration of competing interest

The authors declare that they have no known competing financial interests or personal relationships that could have appeared to influence the work reported in this paper.

Acknowledgements

The authors thank Dr. Volodymyr Semeniuchenko for technical assistance. D. L. B. is grateful to the Natural Sciences and Engineering Research Council of Canada for funding.

Data availability

Data will be made available on request.

References

[1] G.K. Semin, T.A. Babushkina, G. Iakobson, Nuclear Quadrupole Resonance in Chemistry, Wiley, New York, 1972.

[2] T.P. Das, E.L. Hahn, Solid State Physics: Supplement 1: Nuclear Quadrupole Resonance Spectroscopy, Academic Press, New York, 1958.
[3] R.V. Pound, Nuclear electric quadrupole interactions in crystals, Phys. Rev. 79 (1950) 685–702, https://doi.org/10.1103/PhysRev.79.685.
[4] E.A. Lucken, Nuclear Quadrupole Coupling Constants, Academic Press, London, 1969.
[5] G.S. Harbison, A. Slokenbergs, Two-dimensional Nutation Echo Nuclear Quadrupole Resonance Spectroscopy, vol. 45, 1990, pp. 575–580, https://doi.org/10.1515/zna-1990-3-464.
[6] G.S. Harbison, A. Slokenbergs, T.M. Barbara, Two-dimensional zero-field nutation nuclear quadrupole resonance spectroscopy, J. Chem. Phys. 90 (1989) 5292–5298, https://doi.org/10.1063/1.456433.
[7] M. Toyama, Relative intensities of Zeeman components in nuclear quadrupole resonance spectrum, J. Phys. Soc. Jpn. 14 (1959) 1727–1738, https://doi.org/10.1143/JPSJ.14.1727.
[8] Y. Morino, M. Toyama, Zeeman effect of the nuclear quadrupole resonance spectrum in crystalline powder, J. Chem. Phys. 35 (1961) 1289–1296, https://doi.org/10.1063/1.1732041.
[9] J.D. Graybeal, P.J. Green, Nuclear quadrupole resonance Zeeman study of polycrystalline group IVa tetrachlorides, J. Phys. Chem. 73 (1969) 2948–2955, https://doi.org/10.1021/j100843a029.
[10] J. Darville, A. Gerard, M.T. Calende, Determination of the asymmetry parameter in nuclear quadrupole resonance for spin 3/2. A new computer simulation for powders, J. Magn. Reson. 16 (1969) 205–219, https://doi.org/10.1016/0022-2364(74)90044-4, 1974.
[11] H.R. Brooker, R.B. Creel, Zeeman nuclear quadrupole resonance line shapes in powders (I = 3/2), J. Chem. Phys. 61 (1974) 3658–3664, https://doi.org/10.1063/1.1682549.
[12] G.M. Muha, Exact solution of the eigenvalue problem for a spin 3/2 system in the presence of a magnetic field, J. Magn. Reson. 53 (1969) 85–102, https://doi.org/10.1016/0022-2364(83)90073-2, 1983.
[13] P. Bryant, S. Hacobian, Zeeman NQR powder line shapes for half integral spin nuclei, Z. Naturforsch. 41 (1986) 141–146, https://doi.org/10.1515/zna-1986-1-221.
[14] K.V. Raman, Asymmetry parameter studies for systems containing the ^{35}Cl nucleus from Zeeman NQR data, J. Mol. Struct. 345 (1995) 31–47, https://doi.org/10.1016/0022-2860(94)08378-U.
[15] R. Creel, D. Drabold, Exact analytic solution of the spin 3/2 combined Zeeman-quadrupole Hamiltonian, J. Mol. Struct. 111 (1983) 85–90, https://doi.org/10.1016/0022-2860(83)85101-1.
[16] H.G. Dehmelt, Quadrupol-resonanzfrequenzen von J^{127}-kernen in kristallinen kovalenten jodverbindungen, Z. Phys. 130 (1951) 356–370, https://doi.org/10.1007/BF01340172.
[17] Y. Morino, T. Chiba, T. Shimozawa, M. Toyama, Zeeman effect of nuclear quadrupole resonance spectrum in cyanuryl chloride, J. Phys. Soc. Jpn. 13 (1958) 869–879, https://doi.org/10.1143/JPSJ.13.869.
[18] R. Livingston, H. Zeldes, Zeeman effect on the quadrupole spectrum of iodic acid, J. Chem. Phys. 26 (1957) 351–358, https://doi.org/10.1063/1.1743297.
[19] H.C. Meal, Zeeman quadrupole spectra of p-chloroaniline and p-chlorobenzylchloride, J. Chem. Phys. 24 (1956) 1011–1017, https://doi.org/10.1063/1.1742668.
[20] S. Kojima, K. Tsukada, A. Shimauchi, Y. Hinaga, Zeeman splitting of nuclear quadrupole resonance line of bromine, J. Phys. Soc. Jpn. 9 (1954) 795–801, https://doi.org/10.1143/JPSJ.9.795.
[21] S. Kojima, K. Tsukada, Y. Hinaga, Zeeman splitting of nuclear quadrupole resonance in paradibromobenzene, J. Phys. Soc. Jpn. 10 (1955) 498–502, https://doi.org/10.1143/JPSJ.10.498.
[22] T. Varty, R.J.C. Brown, F.P. Temme, Optimal Zeeman-NQR powder lineshape calculations for $3/2 \leqq I \leqq 7/2$, Z. Naturforsch. 45 (1990) 550–558, https://doi.org/10.1515/zna-1990-3-459.
[23] C. Dean, Zeeman splitting of nuclear quadrupole resonances, Phys. Rev. 96 (1954) 1053–1059, https://doi.org/10.1103/PhysRev.96.1053.
[24] C. Dean, R. Pound, The temperature dependence of the chlorine quadrupole coupling in solid benzene compounds, J. Chem. Phys. 20 (1952) 195–196, https://doi.org/10.1063/1.1700174.
[25] O. Ege, S. Nishijima, E. Kimura, H. Akiyama, S. Hamai, H. Negita, Powder Zeeman NQR study on the absorption forms for nuclear spin 5/2, Z. Naturforsch. 53 (1998) 314–317, https://doi.org/10.1515/zna-1998-6-710.
[26] O. Ege, S. Maekawa, H. Negita, Powder zeeman NQR study on ^{123}Sb in $Sb(C_6H_5)_3$, Z. Naturforsch. 57 (2002) 304–306, https://doi.org/10.1515/zna-2002-6-703.
[27] S. Ramaprabhu, K.V.S.R. Rao, Powder Zeeman study of the nuclear quadrupole resonance lower transition spectrum for $I = 5/2$; application to orthoperiodic acid, Z. Naturforsch. 40 (1985) 112–115, https://doi.org/10.1515/zna-1985-0202.
[28] S. Segel, R.G. Barnes, Catalog of Nuclear Quadrupole Interactions and Resonance Frequencies in Solids. Part I, elements and inorganic compounds., Ames Lab., Ames, IA ,United States, 1968.
[29] A. Nari, M. Rahman, P.M.J. Szell, V. Semeniuchenko, D.L. Bryce, Halogen bond strength in solids quantified via Zeeman-perturbed nuclear quadrupole resonance spectroscopy, J. Am. Chem. Soc. 147 (2025) 9528–9543, https://doi.org/10.1021/jacs.4c17321.
[30] P. Bucci, P. Cecchi, A. Colligiani, The Zeeman effect of nuclear quadrupole resonance in single crystals of sodium bromate and p-dibromobenzene, J. Am. Chem. Soc. 86 (1964) 2513–2514, https://doi.org/10.1021/ja01066a040.
[31] K. Shimomura, Zeeman study of nuclear quadrupole resonance spectrum in p-dibromobenzene, J. Phys. Soc. Jpn. 14 (1959) 235–236, https://doi.org/10.1143/JPSJ.14.235.
[32] G.W. Ludwig, Some bromine, iodine, and indium nuclear quadrupole interaction frequencies, J. Chem. Phys. 25 (1956) 159–171.
[33] P. Bucci, P. Cecchi, A. Colligiani, The Zeeman effect of nuclear quadrupole resonance in single crystals of sodium bromate and *p*-dibromobenzene, J. Am. Chem. Soc. 86 (1964) 2513–2514.
[34] M.H. Cohen, Nuclear quadrupole spectra in solids, Phys. Rev. 96 (1954) 1278–1284, https://doi.org/10.1103/PhysRev.96.1278.
[35] P.M.J. Szell, L. Grébert, D.L. Bryce, Rapid identification of halogen bonds in co-crystalline powders via ^{127}I nuclear quadrupole resonance spectroscopy, Angew. Chem. Int. Ed. 58 (2019) 13479–13485, https://doi.org/10.1002/anie.201905788.
[36] D. Massiot, I. Farnan, N. Gautier, D. Trumeau, A. Trokiner, J.P. Coutures, ^{71}Ga and ^{69}Ga nuclear magnetic resonance study of β-Ga_2O_3: resolution of four- and six-fold coordinated Ga sites in static conditions, Solid State Nucl. Magn. Reson. 4 (1995) 241–248, https://doi.org/10.1016/0926-2040(95)00002-8.
[37] A.J. Rossini, H. Hamaed, R.W. Schurko, The application of frequency swept pulses for the acquisition of nuclear quadrupole resonance spectra, J. Magn. Reson. 206 (2010) 32–40, https://doi.org/10.1016/j.jmr.2010.05.018.
[38] A. Hinchliffe, R.W. Munn, R.G. Pritchard, C.J. Spicer, The structure of a solution-grown crystal of 1,4-diiodobenzene, J. Mol. Struct. 130 (1985) 93–96, https://doi.org/10.1016/0022-2860(85)85024-9.
[39] S. Saha, G.R. Desiraju, Crystal engineering of hand-twisted helical crystals, J. Am. Chem. Soc. 139 (2017) 1975–1983, https://doi.org/10.1021/jacs.6b11835.
[40] C.M. Reddy, M.T. Kirchner, R.C. Gundakaram, K.A. Padmanabhan, G.R. Desiraju, Isostructurality, polymorphism and mechanical properties of some hexahalogenated benzenes: the nature of halogen···halogen interactions, Chem. Eur J. 12 (2006) 2222–2234, https://doi.org/10.1002/chem.200500983.
[41] S.Y. Oh, C.W. Nickels, F. Garcia, W. Jones, T. Friščić, Switching between halogen- and hydrogen-bonding in stoichiometric variations of a cocrystal of a phosphine oxide, CrystEngComm (Camb.) 14 (2012) 6110–6114, https://doi.org/10.1039/C2CE25653C.
[42] F.A. Perras, C.M. Widdifield, D.L. Bryce, QUEST—quadrupolar exact software: a fast graphical program for the exact simulation of NMR and NQR spectra for quadrupolar nuclei, Solid State Nucl. Magn. Reson. 45–46 (2012) 36–44, https://doi.org/10.1016/j.ssnmr.2012.05.002.
[43] F. Adrian, Zeeman quadrupole spectrum of cyanuric chloride, J. Chem. Phys. 29 (1958) 1381–1386, https://doi.org/10.1063/1.1744727.
[44] Y. Morino, M. Toyama, Zeeman effect of nuclear quadrupole resonance spectrum in 1, 3, 5-trichlorobenzene, J. Phys. Soc. Jpn. 15 (1960) 288–296, https://doi.org/10.1143/JPSJ.15.288.
[45] H. Negita, K. Shibata, T. Kubo, ^{14}N Nuclear quadrupole resonances of 2-aminopyrimidine, Bull. Chem. Soc. Jpn. 46 (1973) 110–113, https://doi.org/10.1246/bcsj.46.110.
[46] J.W. Wolffs, J. Gomez, G.E. Janssen, G.A. de Wijs, A.P.M. Kentgens, Automated wideline nuclear quadrupole resonance of mixed-cation lead halide perovskites, Magn. Reson. (2025), https://doi.org/10.5194/mr-2025-2 (in press).

Chapter 5 – Isotopic Identification of Quadrupolar Spin Resonance Lines by Zeeman Perturbation: Enabling Analysis of Complex, Impure, and Multi-Component Systems

Based on: Nari, A.; Szell, P. M. J.; Bryce, D. L. Isotopic Identification of Quadrupolar Spin Resonance Lines by Zeeman Perturbation. J. Phys. Chem. Lett. 2025, 16, 8752–8757.

5.1 Chapter Overview and Thesis Context

The previous chapter established a practical and quantitative workflow for performing cryogen-free Zp-NQR spectroscopy using an adjustable electromagnet and exact Hamiltonian simulations. By demonstrating that high-quality Zp-NQR measurements can be routinely acquired and quantitatively analyzed without superconducting magnets or liquid-helium cryogens, Chapter 4 transformed Zp-NQR from a specialized experimental technique into an accessible methodology for the characterization of quadrupolar nuclei in molecular solids. However, establishing a robust experimental workflow represents only the first step toward making Zp-NQR a broadly applicable analytical technique. Another important consideration is the ability to interpret increasingly complex spectra encountered in chemically realistic materials.

In many molecular solids, quadrupolar spectra are considerably more complicated than those obtained from well-defined model compounds. Pharmaceutical formulations, multicomponent crystals, reaction mixtures, and samples containing impurities frequently exhibit numerous resonance lines originating from different crystallographic sites, chemically distinct environments, or multiple quadrupolar isotopes. In such systems, assigning each observed resonance to its corresponding isotope is often challenging, particularly when different isotopes possess similar quadrupolar coupling constants and therefore resonate within overlapping

frequency ranges. This ambiguity complicates spectral interpretation and can limit the structural information extracted from both conventional NQR and SSNMR experiments.

Historically, isotopic assignment has relied primarily on indirect approaches, including comparison with DFT calculations, measurements on isotopically enriched materials, or assumptions based on known isotopic abundance and expected quadrupolar coupling constants. While these methods can often provide useful guidance, they are not universally applicable and may become unreliable for structurally complex materials, samples containing multiple chemically inequivalent sites, or systems where resonance overlap obscures individual spectral features. Consequently, the absence of a direct experimental method for isotopic identification has represented an important limitation in the broader application of quadrupolar spectroscopy.

The work presented in this chapter demonstrates that Zeeman perturbation itself provides the information required for unambiguous isotopic identification. Because the Zeeman splitting is governed by the nuclear gyromagnetic ratio, each quadrupolar isotope exhibits a characteristic magnetic-field response that is independent of the zero-field resonance frequency. By analysing the evolution of resonance line shapes under weak magnetic fields, isotopes possessing nearly identical NQR frequencies can be distinguished directly from experimental measurements without isotopic enrichment or prior structural assumptions. This capability introduces an additional analytical dimension to Zp-NQR that extends well beyond the determination of quadrupolar interaction parameters.

The methodology presented here significantly expands the scope of Zp-NQR for the characterization of complex molecular solids. Direct isotopic identification facilitates the analysis of overlapping spectra, multicomponent systems, and samples containing impurities, thereby

improving the reliability of spectral assignments and enabling quantitative interpretation of increasingly complicated quadrupolar resonance experiments.

Within the overall progression of this thesis, this chapter represents the second stage in the development of modern Zp-NQR spectroscopy. Having established a practical experimental and computational workflow in Chapter 4, the present work demonstrates how Zeeman perturbation can be exploited to extract new spectroscopic information that is inaccessible from conventional NQR measurements alone. This analytical capability provides an essential foundation for the subsequent chapters, where the methodology is extended beyond isotopic identification to the quantitative determination of halogen-bond strength (Chapter 6) and the site-resolved characterization of pharmaceutically relevant molecular solids (Chapter 7). In this way, Chapter 5 marks the transition from establishing the methodology to expanding its analytical capabilities, further demonstrating the versatility of Zp-NQR as a powerful tool for structural characterization.

5.2. Statement of Authenticity

I certify that I have prepared the following article featuring my own work.

5.3 Permissions

I declare that I have obtained permission from the coauthor to include this article in my thesis. Chapter 5 has been reprinted with permission from the American Chemical Society.

5.4 Published manuscript

THE JOURNAL OF PHYSICAL CHEMISTRY LETTERS
A JOURNAL OF THE AMERICAN CHEMICAL SOCIETY

pubs.acs.org/JPCL

Letter

Isotopic Identification of Quadrupolar Spin Resonance Lines by Zeeman Perturbation

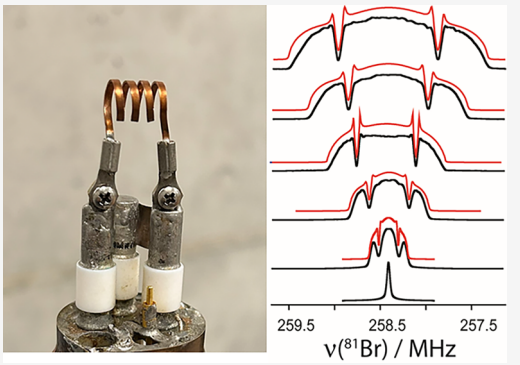
Alireza Nari, Patrick M. J. Szell, and David L. Bryce*

Cite This: J. Phys. Chem. Lett. 2025, 16, 8752−8757

Read Online

ACCESS | Metrics & More | Article Recommendations | Supporting Information

ABSTRACT: Quadrupolar spin resonance (QSR) is radio frequency spectroscopy that provides a chemical fingerprint in the absence of a magnetic field. Materials may present QSR spectra featuring multiple overlapping isotopic resonances, leading to ambiguous spectral assignments. We show how the application of a weak magnetic field (≤50 mT) enables measurement of the nuclear gyromagnetic ratio associated with each resonance with sufficient precision for isotopic identification. The method is demonstrated on pure and impure powdered samples, and the concept of multisite multinuclear QSR spectral fitting is introduced. New insights are thereby gained into the sensitivity of the Zeeman-QSR response and the characterization of complex samples. This approach creates new opportunities in QSR spectroscopy and provides a sustainable cryogen-free alternative to helium-cooled superconducting magnets associated with high-field NMR.



Downloaded via UNIV OF OTTAWA on May 1, 2026 at 18:37:26 (UTC).
See https://pubs.acs.org/sharingguidelines for options on how to legitimately share published articles.

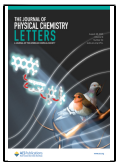
Quadrupolar spin resonance (QSR) spectroscopy, also known as nuclear quadrupole resonance (NQR) spectroscopy, is a form of radio spectroscopy that probes the spin quantum levels of quadrupolar nuclei (spin $I > 1/2$).[1−4] In chemically asymmetric environments, such as in the case of a halogen atom engaged in a single covalent bond, the electric field gradient (EFG) at the nucleus couples to the nuclear quadrupole moment (Q) via a quadrupolar interaction. The modulation of the spin quantum energy levels arising from the quadrupolar interaction allows for transitions to occur between spin states, typically at $\Delta m_I = 1$, upon the application of an oscillating radiofrequency field (B_1) at the correct frequency. For spin $I = 3/2$ nuclides such as ^{79}Br (Q = 308.7(2) mb) and ^{81}Br (Q = 257.9(2) mb), a single QSR transition is observed between the $m_I = 1/2$ and 3/2 states. For spin $I = 5/2$ nuclides such as ^{121}Sb (Q = 543(11) mb) and ^{127}I (Q = −688.22 mb), two transitions are typically observed, namely, the $1/2 \leftrightarrow 3/2$ and $3/2 \leftrightarrow 5/2$ transitions. For spin $I = 7/2$ nuclides such as ^{123}Sb (Q = −692(14) mb), three transitions are typically observed, i.e., the $1/2 \leftrightarrow 3/2$, $3/2 \leftrightarrow 5/2$, and $5/2 \leftrightarrow 7/2$ transitions.

Pure QSR spectroscopy is a nondestructive technique that spans the radiofrequency ranges from kHz to a few GHz, with typically sharp line widths of kHz to 10s of kHz for crystalline substances.[5−7] Consequently, QSR spectroscopy is a challenging technique, as it requires searching across broad spectral ranges for sparse, narrow resonances. In the cases of ^{79}Br, ^{81}Br, and ^{127}I in C-X moieties (X = Br, I), the QSR transitions are typically in the 200−320 MHz range ($1/2 \rightarrow 3/2$; ^{79}Br, ^{81}Br), the 250−400 MHz range ($3/2 \rightarrow 1/2$; ^{127}I), and 500−800 MHz range ($5/2 \rightarrow 3/2$; ^{127}I). Beyond providing information about chemical bonds, QSR spectral lines are extremely sensitive to the local chemical and electronic environment, with small changes to the crystal packing affording frequency changes on the order of MHz. As a result, the observation of a QSR line provides a definitive spectral identifier of a substance with polymorphic specificity.[8] The method is currently enjoying a renaissance, with key insights having been provided into the structure and properties of perovskites, halogen-bonded cocrystals, and related materials.[9−13]

QSR spectroscopy is performed by placing the sample of interest within an oscillating magnetic field (B_1), i.e., a radiofrequency (RF) field, either in the absence of an applied static magnetic field (B_0), known as pure quadrupolar spin resonance, or in a very low (∼mT) applied magnetic field, known as Zeeman-perturbed QSR spectroscopy (Zp-QSR).[14−16] In the case of Zp-QSR, the Zeeman effect broadens the QSR lines, thereby introducing spectral features that can be interpreted by means of spectral fitting to provide the full quadrupolar coupling tensor.

In addition to the sparsity problem, a challenge with QSR spectroscopy lies in assigning a given spectral line to a particular resonant nucleus. For instance, complex substances, such as cocrystals, mixed crystals, and physical mixtures, may

Received: July 18, 2025
Revised: August 13, 2025
Accepted: August 14, 2025
Published: August 19, 2025



ACS Publications
© 2025 American Chemical Society

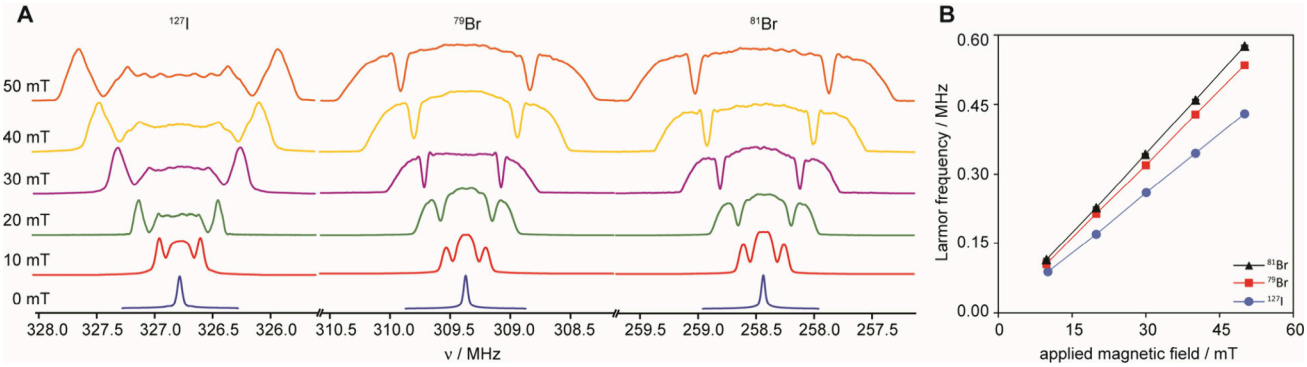


Figure 1. Isotopic identification via Zeeman-perturbed QSR of the resonant nucleus. (**A**) Pure quadrupolar signals (0 mT) and Zp-QSR lines for ^{127}I of **2** (left), ^{79}Br for **1** (middle), ^{81}Br for **1** (right), as a function of the applied external magnetic field ranging from 0 mT to 50 mT. The wobbling distortions are artifacts arising from undersampling the broad QSR lines. (**B**) The fitted Larmor frequencies obtained from the spectra shown in (A) as a function of the applied magnetic field, yielding experimental gyromagnetic ratios. The lines of best fit are [^{127}I, $y = 8.543 \times 10^{-3} \pm 5 \times 10^{-5})x + (1.896 \times 10^{-3} \pm 1.508 \times 10^{-3})$; $R^2 = 0.99992$], [^{79}Br: $y = (1.0650 \times 10^{-2} \pm 4 \times 10^{-5})x + (1.121 \times 10^{-3} \pm 1.2 \times 10^{-3})$; $R^2 = 0.99997$], [^{81}Br: $y = (1.147 \times 10^{-2} \pm 6 \times 10^{-5})x + (8.781 \times 10^{-4} \pm 2.017 \times 10^{-3})$; $R^2 = 0.99992$]. The error bars are displayed but are within the size of the markers. If the intercept is set to zero, the lines of best fit are [^{127}I, $y = 8.59 \times 10^{-3} \pm 2 \times 10^{-5})x$; $R^2 = 0.99998$], [^{79}Br: $y = (1.068 \times 10^{-2} \pm 2 \times 10^{-5})x$; $R^2 = 0.99999$], [^{81}Br: $y = (1.149 \times 10^{-2} \pm 2 \times 10^{-5})x$; $R^2 = 0.99998$].

feature a plurality of QSR lines that need to be properly assigned. Identifying a nucleus based on observing the QSR lines for multiple isotopes of the same atom is a good strategy, but it is limited to the cases where multiple QSR-active isotopes of the same element exist, and provided the instrumentation can access the spectral ranges of both isotopes, such as ^{79}Br and ^{81}Br. In contrast to NMR spectroscopy, correlation experiments in pulsed QSR spectroscopy may not be applicable, such as in the case of spin $I = 3/2$ nuclei that have a single transition, or they may require a highly specialized doubly tuned probe capable of broadband tuning across octaves (e.g., $\nu_1 = 300$ MHz and $\nu_2 = 600$ MHz). Recently, we have demonstrated the use of Zp-QSR for the interpretation of halogen bond strengths by leveraging exact theory to fit the resulting spectral line shapes, which requires the input of the Larmor frequency (ν_L) as part of the fitting process.[17,18] With knowledge of the value of B_0, the exact spectral fitting of the Zp-QSR lines can provide the gyromagnetic ratio (γ) of the nucleus under observation, as shown in eq 1.

$$\nu_L = \gamma B_0 / 2\pi \tag{1}$$

Here, we demonstrate how measurements of the nuclear gyromagnetic ratio through the application of a Zeeman perturbation field and exact spectral simulations can be leveraged in order to assign the identity of the resonant nucleus to each QSR spectral signal.

To establish the accuracy of measured nuclear gyromagnetic ratios from exact fitting, a series of QSR spectra were collected on 1,4-dibromotetrafluorobenzene (**1**) and 1,4-diiodotetrafluorobenzene (**2**) in the absence of a magnetic field (~0 mT) and in magnetic fields ranging from 10 to 50 mT, as shown in Figure 1. These magnetic field strengths were readily obtained using an electromagnet intended for electron spin resonance (ESR) spectroscopy. **1** and **2** are ideal cases to demonstrate the approach, as they feature only a single 3/2 → 1/2 transition for ^{127}I in **2**, a single 1/2 → 3/2 transition for ^{79}Br in **1**, and a single 1/2 → 3/2 transition for ^{81}Br in **1**. As the ^{79}Br nucleus has a value of $Q(^{79}\text{Br})$ which is approximately 19.7% larger than that of $Q(^{81}\text{Br})$,[19] QSR frequencies can be easily assigned to ^{79}Br, which are 19.7% higher than the resonances assigned to ^{81}Br, thereby providing confidence in assignments made based on the gyromagnetic ratios. All experimental QSR spectra with their simulated fits can be found in Figure S1.

As shown in Figure 1, the fitted Larmor frequency as a function of the applied magnetic field, which was measured at the sample position in the absence of a probe by an external gaussmeter, provides linear trends in agreement with eq 1. We report excellent fits in all cases with R^2 values above 0.999. The measured nuclear gyromagnetic ratios are 8.54 ± 0.05 MHz T^{-1} for ^{127}I, 10.65 ± 0.04 MHz T^{-1} for ^{79}Br, and 11.47 ± 0.06 MHz T^{-1} for ^{81}Br. In comparison, the literature values, which are typically measured using far more accurate methods, such as atomic beam experiments, are 8.5638(43) MHz T^{-1} for ^{127}I, 10.6950(30) MHz T^{-1} for ^{79}Br, and 11.5284(30) MHz T^{-1} for ^{81}Br,[20,21] and are each within the uncertainties of the measurements reported here.

While these measurements do not provide the sign of the gyromagnetic ratio or an improvement over the literature values, this approach demonstrates that the accuracy of the extracted nuclear gyromagnetic ratio is sufficient to identify the resonant isotope. The value of γ among quadrupolar nuclei spans from 0.7379(10) MHz T^{-1} in ^{197}Au to 16.548177(61) MHz T^{-1} in ^{7}Li, providing the variance needed to differentiate most pairs of nuclear isotopes beyond the measured uncertainty of 0.05 MHz T^{-1}. Differentiating pairs of low-γ nuclei, where the uncertainty may compete with the inherent differences in gyromagnetic ratios, may pose challenges and will benefit from increased values of B_0. It is noted that the instrument used for this work can generate fields of up to 1.7 T, which should enable clear differentiation of most isotopes.

Analysis of the data in Figure 1 consistently underestimates the true values of the gyromagnetic ratios. This has been determined to arise from an inaccuracy in the measurement of the magnetic field on the order of 0.1 to 0.3 mT, which may arise in part due to the effect of placing the QSR probe head within the bore of the electromagnet. Consequently, using accepted literature values of the gyromagnetic ratios of ^{127}I, ^{79}Br, and ^{81}Br, the data from Figure 1 were used to correct the magnetic field strength as a method of calibrating the measurements from the gaussmeter (Table S1). However, we note that this correction resulted in values that remained

https://doi.org/10.1021/acs.jpclett.5c02214
J. Phys. Chem. Lett. 2025, 16, 8752−8757

within the uncertainties of our original measurements, and it is not necessary to apply this correction to be able to differentiate and assign isotopes to resonances (Table S1). We further note that by fixing the intercept of the plots in Figure 1 to exactly zero, gyromagnetic ratios of 8.59 ± 0.05 MHz T^{-1} for ^{127}I, 10.68 ± 0.04 MHz T^{-1} for ^{79}Br, and 11.49 ± 0.06 MHz T^{-1} for ^{81}Br are obtained directly and are in better agreement with the literature data.

While the Larmor frequency was sampled at several magnetic field strengths in Figure 1, sufficient accuracy of the gyromagnetic ratio can be obtained from fitting a single Zp-QSR spectrum. With the Zp-QSR spectral acquisition often taking ~0.5 to 2.0 h in the cases explored here, the single-shot method provides a rapid way of identifying the isotope undergoing resonance. Improvements in the accuracy of γ can be obtained by repeating the measurement at multiple fields, but performing the measurement at a single field provided sufficient accuracy in these cases for the application of identifying the nuclear isotope. A single field can be used, owing to the simple relationship between B_0, ν_L, and γ (eq 1).

Several attempts were made to prepare a ternary cocrystal featuring halogen bond donors **1** and 1,3,5-triiodo-2,4,6-trifluorobenzene (**3**) and various halogen bond acceptors. **1** and **3** were selected by virtue of the proximity of their ^{127}I and ^{79}Br QSR resonances. In the case of mechanochemical grinding of the halogen bond acceptor 4,4′-bipyridine (**a**) with halogen bond donors **3** and **1** in a single jar, an interesting product was obtained which consists of a physical mixture of cocrystals **1a** and **3a** along with unreacted starting materials **1** and **3**. As a result, the QSR spectrum of this mixture featured a crowded spectral region with QSR signals of both ^{127}I and ^{79}Br, which cannot be obviously assigned without also searching for and observing the ^{81}Br QSR signals. As shown in Figure 2, QSR spectra were reacquired individually on pure **1**, **3**, **1a**, and **3a** in order to assign the resonances to each material. Upon the application of a low magnetic field of 30.0 ± 0.1 mT, the Zp-QSR line shapes allowed for the measurement of the gyromagnetic ratio of each QSR line with an uncertainty of ± 0.07 MHz T^{-1} in addition to the quadrupolar coupling constant (C_Q), and quadrupolar asymmetry parameter (η), as reported in Table S2. The measured gyromagnetic ratios allowed for the assignment of the signals corresponding to ^{127}I and ^{79}Br.

A strong overlap of the Zp-QSR signals for the ^{79}Br and ^{127}I isotopes in the physical mixture of cocrystals **1a** and **3a** was observed at approximately 320 MHz, along with the spectral overlap near 316 MHz of **1a** and unreacted starting material **3**. As shown in Figure 2, a complex line shape at approximately 320 MHz was observed due to the combination of both ^{127}I and ^{79}Br Zp-QSR signals; this is overlaid above the Zp-QSR spectra of the pure components. This line shape was successfully fit using a two-site model and exact simulations to extract the quadrupolar coupling parameters describing the EFG tensor (C_Q, η), the Larmor frequency, and consequently, the nuclear gyromagnetic ratio, which is possible using the QUEST software.[22] To our knowledge, this is the first instance of fitting complex QSR line shapes using exact methods and is reminiscent of fitting multisite solid-state NMR line shapes of quadrupolar nuclei. Ramachandran and Oldfield observed the overlap of ^{35}Cl Zp-QSR powder patterns for 2,4,6-trichloro-1,3,5-triazine and noted the difficulties in extracting information from this spectrum.[23]

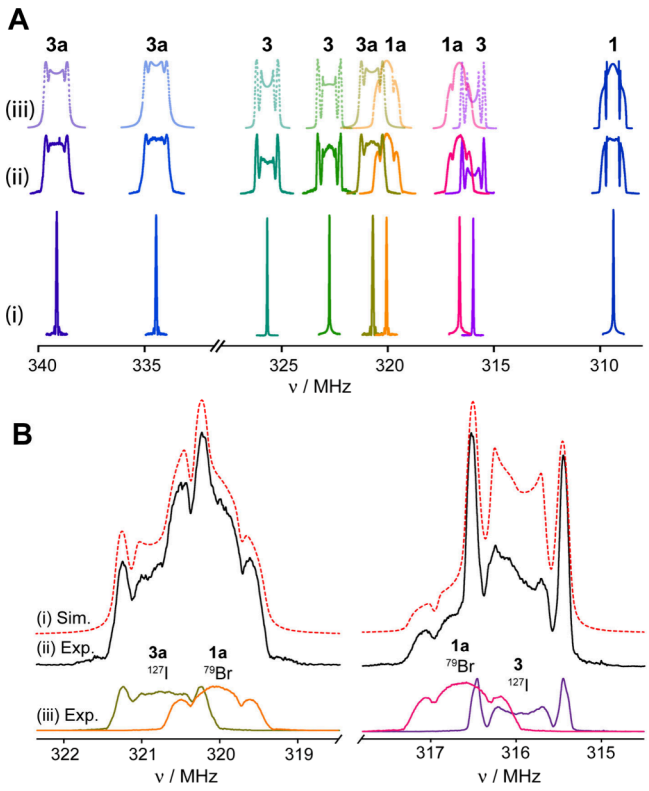


Figure 2. Experimental QSR spectra of pure crystalline materials, cocrystals, and mixtures. (**A**) Experimental QSR spectra of **1**, **3**, **1a**, and **3a** under (i) the pure QSR regime and (ii) Zp-QSR regime (B_0 = 30.0 ± 0.1 mT). (iii) The simulated Zp-QSR spectra. (**B**) (ii) Experimental and (i) simulated Zp-QSR spectra of the physical mixture of **3a**, **1a**, and **3** featuring the spectral overlap of ^{127}I and ^{79}Br QSR signals. The experimental Zp-QSR spectra of the pure substances are shown in (iii) for comparison.

To further demonstrate the approach of using Zp-QSR to identify the resonant nucleus, a novel cocrystal of **2** with 1-bromo-4-nitrobenzene (**b**) was identified by screening **2** with brominated halogen bond acceptors. A full description of the X-ray crystal structure and parameters can be found in the Supporting Information (Figure S4; Table S6). QSR spectroscopy was used to rapidly survey the preparations for successful cocrystallization by monitoring for the absence of starting materials. Interestingly, the QSR spectrum of **2b** featured two resonances at 276.34 ± 0.02 MHz and 330.38 ± 0.02 MHz. As shown in Figure S2, and summarized in Table S2, the fitted Zp-QSR spectrum provided a nuclear gyromagnetic ratio of 8.61 ± 0.04 MHz T^{-1} for the QSR signal at 330.38 ± 0.02 MHz, and 10.71 ± 0.07 MHz T^{-1} for the signal at 276.34 ± 0.02 MHz T^{-1}. These measurements support the assignment of ^{127}I and ^{79}Br, respectively, and were later bolstered by comparing the QSR spectrum of **2b** to those of their individual starting materials, **2** and **b** (see the SI), and confirmed by observing the ^{81}Br resonance of **2b**.

Zeeman-perturbed QSR was extended to antimony tribromide (**4**) in order to validate the application of this method to elements apart from the halogens, to include higher spin quantum numbers and across a wider spectral range. **4** was chosen as it features the ^{79}Br, ^{81}Br, ^{121}Sb, and ^{123}Sb isotopes, and two crystallographically unique bromine sites.[24] Consequently, nine QSR lines are expected for this compound with frequencies spanning from 170 to 30 MHz. In order to perform

https://doi.org/10.1021/acs.jpclett.5c02214
J. Phys. Chem. Lett. 2025, 16, 8752−8757

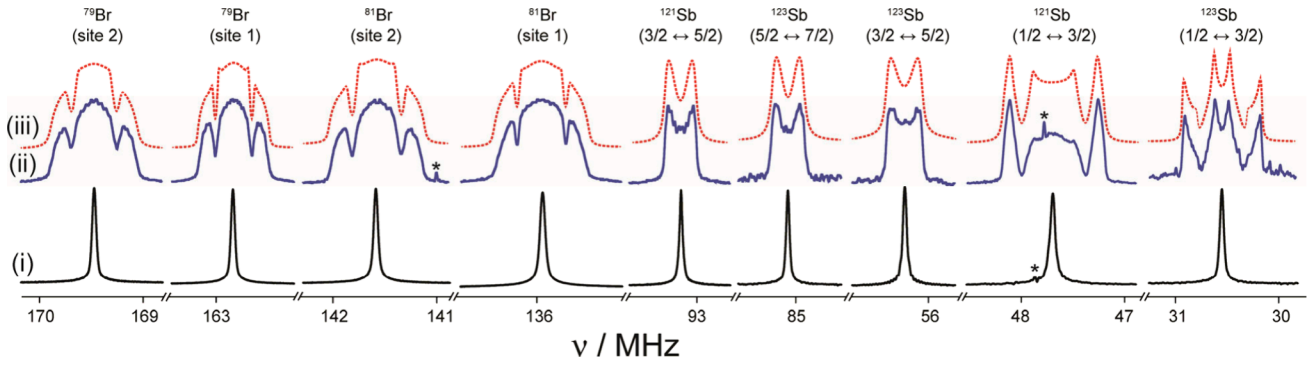


Figure 3. Spectral resolution and isotopic identification of nine unique resonances. Experimental QSR spectrum of **4** under (i) the pure QSR regime and (ii) the Zp-QSR regime (B_0 = 20.0 ± 0.1 mT). (iii) The simulated Zp-QSR spectrum.

Table 1. QSR Spectral Fitting Parameters for 4 Acquired in a Magnetic Field of B_0 = 20.0 ± 0.1 mT[a]

QSR Frequency (ν_Q)/MHz	C_Q/MHz	η	Larmor Frequency (ν_L)/MHz	Experimental Gyromagnetic ratio (MHz T^{-1})	Isotope and Assignment
169.47 ± 0.02	335.47 ± 0.027	0.25 ± 0.01	0.214 ± 0.001	10.55 ± 0.05	^{79}Br (site 2)[b] 1/2 → 3/2
162.77 ± 0.02	324.19 ± 0.018	0.16 ± 0.01	0.219 ± 0.001	10.78 ± 0.05	^{79}Br (site 1)[b] 1/2 → 3/2
141.57 ± 0.02	280.47 ± 0.22	0.24 ± 0.01	0.234 ± 0.001	11.51 ± 0.06	^{81}Br (site 2)[b] 1/2 → 3/2
135.97 ± 0.02	270.96 ± 0.16	0.15 ± 0.01	0.234 ± 0.001	11.53 ± 0.06	^{81}Br (site 1)[b] 1/2 → 3/2
93.21 ± 0.02	311.95 ± 0.89	0.14 ± 0.01	0.207 ± 0.002	10.23 ± 0.08	^{121}Sb 3/2 → 5/2
85.05 ± 0.02	397.81 ± 3.1	0.15 ± 0.01	0.110 ± 0.001	5.47 ± 0.05	^{123}Sb 7/2 → 5/2
56.17 ± 0.02	397.96 ± 3.2	0.15 ± 0.01	0.111 ± 0.001	5.49 ± 0.05	^{123}Sb 5/2 → 3/2
47.92 ± 0.02	312.74 ± 0.86	0.14 ± 0.01	0.209 ± 0.001	10.27 ± 0.05	^{121}Sb 1/2 → 3/2
30.54 ± 0.02	400.4 ± 3.1	0.14 ± 0.01	0.117 ± 0.001	5.76 ± 0.03	^{123}Sb 3/2 → 1/2

[a]Spectral fits were performed using exact theory using QUEST. [b]The assignment of the QSR signals to their crystallographic site is based on ref 30.

these measurements, four coils were designed to tune the QSR probe across the spectral areas of interest (Table S3). As shown in Figure 3, all nine QSR signals were successfully observed, revealing a complex spectrum. The application of a 20 mT field on the sample broadened the resonances and, as summarized in Table 1, allowed for the quadrupolar coupling and the Larmor frequency to be extracted for each nucleus. The average measured nuclear gyromagnetic ratios were 10.66 ± 0.05 MHz T^{-1} for ^{79}Br, 11.52 ± 0.06 MHz T^{-1} for ^{81}Br, 10.25 ± 0.06 MHz T^{-1} for ^{121}Sb, and 5.57 ± 0.04 MHz T^{-1} for ^{123}Sb. These values are in excellent agreement with the accepted values of 10.6950(30) MHz T^{-1} for ^{79}Br, 11.5284(30) MHz T^{-1} for ^{81}Br, 10.2387(49) MHz T^{-1} for ^{121}Sb, and 5.5442(26) MHz T^{-1} for ^{123}Sb. Importantly, despite the similarities in the values of the nuclear gyromagnetic ratios of ^{79}Br and ^{121}Sb, these isotopes can be unambiguously distinguished using the Zeeman-perturbed QSR results obtained here.

Interestingly, while an angle of 0° between the coil and the Zeeman field was best suited to perturb the lowest frequency transitions, including those of ^{79}Br and ^{81}Br, a coil angle of 90° was best suited for the higher frequency transitions, such as the 3/2 ↔ 5/2 and 5/2 ↔ 7/2 transitions. A coil angle of 0° for the higher frequency transitions provided a featureless broadening, which was difficult to fit with any useful degree of precision in the final parameters. This featureless broadening is simply attributable to the inherent line shape resulting from the orientational dependence of the various spectral discontinuities. Further discussion of the role of coil angle in the spectral line shape, along with experimental and simulated data, are given in reference 18.

The total experimental times for each complete spectrum ranged from approximately 25 to 110 min for the resonances studied in this work. Further optimization and exploitation of signal enhancement techniques[25] are likely to improve the signal-to-noise ratio and reduce experimental times, concomitantly rendering these QSR approaches amenable to a broad swath of quadrupolar isotopes. It is noted that the successful use of a Hahn echo, as used presently, depends on sufficiently long T_2 values, and that for systems with shorter T_2 values, alternative pulse schemes may be necessary. The ability to differentiate and assign resonances to particular isotopes could be particularly useful for sets of isotopes that have the same spin angular momentum (I) and similar natural abundances; an example includes the ^{25}Mg/^{67}Zn/^{95}Mo tuple, all isotopes of importance either as key components or as dopants in functional compounds such as metal−organic frameworks

https://doi.org/10.1021/acs.jpclett.5c02214
J. Phys. Chem. Lett. 2025, 16, 8752−8757

and perovskite-type energy materials. The use of density functional theory computations of quadrupolar parameters measured by the present approach will likely prove to be as valuable as they are for data measured from conventional high-field quadrupolar-perturbed solid-state NMR spectroscopy.[17] The most innovative and informative solid-state NMR studies of strongly quadrupolar nuclei currently can only be done in the highest applied magnetic fields using magnets which require cryogenic cooling.[26−29] Therefore, in light of the impact of an ongoing helium shortage, the cryogen-free low-field isotopic assignment Zp-QSR approach advanced here offers a powerful, sustainable, and environmentally friendly alternative to high-field NMR spectroscopy.

EXPERIMENTAL SECTION

1,4-Dibromotetrafluorobenzene (99%, **1**), 1,4-diiodotetrafluorobenzene (98%, **2**), 4,4′-bipyridine (98%, **a**), and 1-bromo-4-nitrobenzene (99%, **b**) were obtained from Sigma-Aldrich. 1,3,5-Triiodo-2,4,6-trifluorobenzene (98%+, **3**) was sourced from Alfa Aesar. Antimony(III) bromide (99.5%, **4**) was purchased from Fisher Scientific. All reagents were used as received without further purification. Cocrystals investigated in this study were prepared via mechanochemical synthesis by using a Retsch MM 400 benchtop ball mill.

Equimolar amounts of the starting materials were transferred to a 10 mL stainless steel jar to obtain approximately 500 mg of solid material. A liquid additive was then added at a ratio of 0.03 μL/mg: $CHCl_3$ was used for the preparation of **1a**, **3a**, and their physical mixture, while THF was used for the novel cocrystal of **2b**. Two stainless steel balls (5.0 mm diameter) were placed in the jar, and the mixture was subjected to ball milling for 30 min at room temperature.

To grow single crystals suitable for SCXRD analysis, equimolar amounts of compounds **2** (50 mg) and **b** (25 mg) were dissolved in 1 mL of THF in a 1 dram glass vial. The vial was covered with aluminum foil with two small holes to allow slow evaporation of the solvent, and it was stored in a dark place at room temperature. After 3 days, white crystals of **2b** were obtained and analyzed by SCXRD for crystal structure determination.

All QSR experiments were performed using the X channel of a Bruker Avance III 400 MHz solid-state NMR spectrometer console for frequencies below 200 MHz, and the ^{1}H channel for frequencies above 200 MHz. A home-built probe equipped with one of four custom-made solenoid coils was used (Table S3). The search for pure QSR resonances was conducted by stepping the receiver at increments of 150 kHz using a Hahn-echo (90-τ-180-acq) pulse sequence with a $\pi/2$ pulse length of 4 μs. The Zeeman-perturbed QSR experiments were subsequently acquired by placing the NQR probe head in the electromagnet of a Bruker EMX Plus EPR spectrometer with the microwave waveguide and bridge removed. A secondary magnetometer was used to ensure accurate magnetic field strengths, which were found to be within 0.1 mT of the reported magnetic field with the EMX Plus software. All Zp-QSR spectra were acquired as subspectra at steps of 50 kHz increments and later coadded in the frequency domain (VOCS)[31] to produce the final spectrum, using a Hahn echo pulse sequence with $\pi/2$ pulse lengths between 3 and 8 μs, adjusted for maximal signal-to-noise. All Zeeman-perturbed QSR spectra were fit using QUEST[22] to extract the Larmor frequency, C_Q, and η. Further practical aspects of the experiments and the spectral analysis are given in reference 18.

Single-crystal X-ray diffraction (SCXRD) data for compound **2b** were collected at 150 K from a shock-cooled crystal by using a Bruker Venture Metaljet diffractometer with κ-geometry. The instrument was equipped with a Metal Jet X-ray source, Helios MX Mirror Optics for monochromatization, and a Bruker Photon III CMOS detector. Gallium Kα radiation (λ = 1.34139 Å) was employed for data acquisition. Data integration was carried out using SAINT (2013), followed by a multiscan absorption correction using SADABS 2016/2.[32,33] The structure was solved using dual-space methods with XT 2018/2 and refined by full-matrix least-squares refinement against F^2 using the XL program.[34] All structure solution and refinement procedures were performed within the OLEX2 graphical user interface.[35] Non-hydrogen atoms were refined anisotropically, while hydrogen atoms were positioned using a riding model, refined isotropically, and assigned U_{iso} values equal to 1.2 times the equivalent isotropic displacement parameter (U_{eq}) of their parent atoms. The final report and CIF file were prepared using FinalCif.[36]

Powder X-ray diffraction (PXRD) was performed at room temperature using a Bruker D8 Endeavor diffractometer featuring a sealed-tube Cu Kα radiation source (λ = 1.54056 Å, 1 kW) and a fast LynxEye XE-T detector. Samples were loaded into a well plate and continuously rotated at 15 rpm throughout the data collection to ensure uniform exposure.

ASSOCIATED CONTENT

Data Availability Statement

Data are available in the main text or the Supporting Information; spectra have been deposited at Zenodo (Nari, A., Szell, P. M. J. & Bryce, D. L. (2025). Isotopic Identification of Quadrupolar Spin Resonance Lines by Zeeman Perturbation [Data set]. Zenodo. 10.5281/zenodo.15676433); the crystallographic information file for **2b** has been deposited with the Cambridge Crystallographic Data Centre (cif 2445917).

Supporting Information

The Supporting Information is available free of charge at https://pubs.acs.org/doi/10.1021/acs.jpclett.5c02214.

Description of X-ray crystal structure of **2b**; additional spectra; additional data; additional experimental details (PDF)

AUTHOR INFORMATION

Corresponding Author

David L. Bryce − *Department of Chemistry and Biomolecular Sciences, Centre for Catalysis Research and Innovation, and Nexus for Quantum Technologies Institute, University of Ottawa, Ottawa, Ontario K1N 6N5, Canada*; orcid.org/0000-0001-9989-796X; Email: dbryce@uottawa.ca

Authors

Alireza Nari − *Department of Chemistry and Biomolecular Sciences, University of Ottawa, Ottawa, Ontario K1N 6N5, Canada*

Patrick M. J. Szell − *Quadrufy Inc., Ottawa, Ontario K1N 6N5, Canada*

Complete contact information is available at: https://pubs.acs.org/10.1021/acs.jpclett.5c02214

Author Contributions

Conceptualization: AN, PMJS, DLB. Methodology: AN, PMJS, DLB. Investigation: AN, PMJS. Funding acquisition: DLB.

Project administration: DLB. Supervision: DLB. Writing—original draft: AN, PMJS, DLB. Writing—review and editing: AN, PMJS, DLB.

Funding

Natural Sciences and Engineering Research Council of Canada

Notes

The authors declare the following competing financial interest(s): PMJS is founder and CEO of Quadrufy, Inc. DLB serves on the Scientific Board of Quadrufy, Inc. AN declares no competing interests.

REFERENCES

(1) Cohen, M. H.; Reif, F. Nuclear Quadrupole Effects in Nuclear Magnetic Resonance Studies of Solids. *Solid State Phys.* **1957**, *5*, 321–438.
(2) Nierenberg, W.; Ramsey, N. F.; Brody, S. B. Measurements of Nuclear Quadrupole Moment Interactions. *Phys. Rev.* **1946**, *70*, 773–775.
(3) Pound, R. V. Nuclear Electric Quadrupole Interactions in Crystals. *Phys. Rev.* **1950**, *79*, 685–702.
(4) Dehmelt, H. G.; Krüger, H. Kernquadrupolfrequenzen in festem Dichloräthylen. *Naturwiss.* **1950**, *37*, 111–112.
(5) Das, T. P.; Hahn, E. L. *Solid State Physics: Supplement 1: nuclear quadrupole resonance spectroscopy*; Academic Press: New York, 1958.
(6) Lucken, E. A. *Nuclear Quadrupole Coupling Constants*; Academic Press: London, 1969.
(7) Semin, G. K.; Babushkina, T. A.; Iakobson, G. *Nuclear Quadrupole Resonance in Chemistry*; Wiley: New York, 1972.
(8) Wren, S. A. C.; Szell, P. M. J. Nuclear Quadrupole Resonance Spectroscopy in Pharmaceuticals. In *Magnetic Resonance and its Applications in Drug Formulation and Delivery*; Mantle, M. D., Hughes, L. P., Eds.; Royal Society of Chemistry, 2024; Vol. 33, pp 149–178.
(9) Szell, P. M. J.; Grébert, L.; Bryce, D. L. Rapid Identification of Halogen Bonds in Cocrystalline Powders via ^{127}I Nuclear Quadrupole Resonance Spectroscopy. *Angew. Chem., Int. Ed.* **2019**, *58*, 13479–13485.
(10) Henshaw, J.; Kehayias, P.; Saleh Ziabari, M.; Titze, M.; Morissette, E.; Watanabe, K.; Taniguchi, T.; Li, J. I. A.; Acosta, V. M.; Bielejec, E. S.; Lilly, M. P.; Mounce, A. M. Nanoscale Solid-State Nuclear Quadrupole Resonance Spectroscopy Using Depth-Optimized Nitrogen-Vacancy Ensembles in Diamond. *Appl. Phys. Lett.* **2022**, *120*, No. 174002.
(11) Hooper, R. W.; Lin, K.; Veinot, J. G. C.; Michaelis, V. K. 3D to 0D Cesium Lead Bromide: A $^{79/81}$Br NMR, NQR And Theoretical Investigation. *J. Magn. Reson.* **2023**, *352*, No. 107472.
(12) Piveteau, L.; Morad, V.; Kovalenko, M. V. Solid-State NMR and NQR Spectroscopy of Lead-Halide Perovskite Materials. *J. Am. Chem. Soc.* **2020**, *142*, 19413–19437.
(13) Doherty, T. A. S.; Nagane, S.; Kubicki, D. J.; Jung, Y.-K.; Johnstone, D. N.; Iqbal, A. N.; Guo, D.; Frohna, K.; Danaie, M.; Tennyson, E. M.; Macpherson, S.; Abfalterer, A.; Anaya, M.; Chiang, Y.-H.; Crout, P.; Ruggeri, F. S.; Collins, S.; Grey, C. P.; Walsh, A.; Midgley, P. A.; Stranks, S. D. Stabilized Tilted-Octahedra Halide Perovskites Inhibit Local Formation Of Performance-Limiting Phases. *Science* **2021**, *374*, 1598–1605.
(14) Toyama, M. Relative Intensities of Zeeman Components in Nuclear Quadrupole Resonance Spectrum. *J. Phys. Soc. Jpn.* **1959**, *14*, 1727–1738.
(15) Morino, Y.; Toyama, M. Zeeman Effect of The Nuclear Quadrupole Resonance Spectrum in Crystalline Powder. *J. Chem. Phys.* **1961**, *35*, 1289–1296.
(16) Brooker, H. R.; Creel, R. B. Zeeman Nuclear Quadrupole Resonance Line Shapes in Powders (I = 3/2). *J. Chem. Phys.* **1974**, *61*, 3658–3664.
(17) Nari, A.; Rahman, M.; Szell, P. M. J.; Semeniuchenko, V.; Bryce, D. L. Halogen Bond Strength in Solids Quantified Via Zeeman-Perturbed Nuclear Quadrupole Resonance Spectroscopy. *J. Am. Chem. Soc.* **2025**, *147*, 9528–9543.
(18) Nari, A.; Szell, P. M. J.; Bryce, D. L. Practical Aspects of Zeeman-Perturbed NQR Spectroscopy using an Adjustable Electromagnet. *Solid State Nucl. Magn. Reson.* **2025**, *138*, No. 102014.
(19) Pyykkö, P. Year-2017 Nuclear Quadrupole Moments. *Mol. Phys.* **2018**, *116*, 1328–1338.
(20) Stone, N. J. *Table of Recommended Nuclear Magnetic Dipole Moments: Part I, Long-Lived States, INDC International Nuclear Data Committee, IAEA Nuclear Data Section*, Vienna International Centre, P.O. Box 100, 1400 Vienna, Austria (2019). DOI: 10.61092/iaea.yjpc-cns6.
(21) Tiesinga, E.; Mohr, P. J.; Newell, D. B.; Taylor, B. N. CODATA recommended values of the fundamental physical constants: 2018. *Rev. Mod. Phys.* **2021**, *93*, No. 025010.
(22) Perras, F. A.; Widdifield, C. M.; Bryce, D. L. QUEST—QUadrupolar Exact Software: A Fast Graphical Program for The Exact Simulation Of NMR And NQR Spectra For Quadrupolar Nuclei. *Solid State Nucl. Magn. Reson.* **2012**, *45–46*, 36–44.
(23) Ramachandran, R.; Oldfield, E. Two Dimensional Zeeman Nuclear Quadrupole Resonance Spectroscopy. *J. Phys. Chem.* **1984**, *80*, 674–677.
(24) Cushen, D. W.; Hulme, R. 427. The Crystal And Molecular Structure Of Antimony Tribromide: β-Antimony Tribromide. *J. Chem. Soc.* **1962**, *0*, 2218–2222.
(25) Rossini, A. J.; Hamaed, H.; Schurko, R. W. The Application of Frequency Swept Pulses for The Acquisition of Nuclear Quadrupole Resonance Spectra. *J. Magn. Reson.* **2010**, *206*, 32–40.
(26) Zhang, W.; Xu, Y.; Venkatesh, A.; Hung, I.; Li, S.; Gan, Z.; Huang, Y. Pushing Limits of Ultra-wideline Solid-State NMR Spectroscopy: NMR Signatures of ^{209}Bi and ^{127}I in Metal–Organic Frameworks at Ultra-high Magnetic Fields. *J. Am. Chem. Soc.* **2025**, *147*, 10823–10828.
(27) Madsen, R.; Qiao, A.; Sen, J.; Hung, I.; Chen, K.; Gan, Z.; Sen, S.; Yue, Y. Ultrahigh-field ^{67}Zn NMR Reveals Short-Range Disorder in Zeolitic Imidazolate Framework Glasses. *Science* **2020**, *367*, 1473–1476.
(28) Zhao, Z.; Xiao, D.; Chen, K.; Wang, R.; Liang, L.; Liu, Z.; Hung, I.; Gan, Z.; Hou, G. Nature of Five-Coordinated Al in γ-Al_2O_3 Revealed by Ultra-High-Field Solid-State NMR. *ACS Cent. Sci.* **2022**, *8*, 795–803.
(29) Xu, Y.; Calabrese, M.; Demitri, N.; Pizzi, A.; Nag, T.; Hung, I.; Gan, Z.; Resnati, G.; Bryce, D. L. Non-Covalent Matere Bonds in Perrhenates Probed via Ultrahigh Field Rhenium-185/187 NMR and Zero-Field NQR Spectroscopy. *Chem. Commun.* **2023**, *59*, 12609–12612.
(30) Poleschuk, O. K.; Maksyutin, Y. K. NQR Study of $SbBr_3$, $BiBr_3$, And their Complexes with $AlBr_3$. *Theor. Exp. Chem.* **1976**, *11*, 345–348.
(31) Massiot, D.; Farnan, I.; Gautier, N.; Trumeau, D.; Trokiner, A.; Coutures, J. P. ^{71}Ga and ^{69}Ga Nuclear Magnetic Resonance Study Of β-Ga_2O_3: Resolution of Four- and Six-Fold Coordinated Ga Sites In Static Conditions. *Solid State Nucl. Magn. Reson.* **1995**, *4*, 241–248.
(32) Bruker *SAINT*; Bruker AXS Inc.: Madison, Wisconsin, USA, 2020.
(33) Krause, L.; Herbst-Irmer, R.; Sheldrick, G. M.; Stalke, D. Comparison Of Silver And Molybdenum Microfocus X-Ray Sources For Single-Crystal Structure Determination. *J. Appl. Crystallogr.* **2015**, *48*, 3–10.
(34) Sheldrick, G. M. SHELXT—Integrated Space-Group And Crystal Structure Determination. *Acta Crystallogr.* **2015**, *A71*, 3–8.
(35) Dolomanov, O. V.; Bourhis, L. J.; Gildea, R. J.; Howard, J. A. K.; Puschmann, H. OLEX2: A Complete Structure Solution, Refinement And Analysis Program. *J. Appl. Crystallogr.* **2009**, *42*, 339–341.
(36) Kratzert, D. *FinalCif, V144* (2023). See the following: https://dkratzert.de/finalcif.html . Accessed August 12, 2025.

Chapter 6 – Direct Quantification of Halogen Bond Strength in Solids via Zeeman-Perturbed NQR: The Electric Field Gradient as a Reporter of Interaction Energetics

Based on: Nari, A.; Rahman, M.; Szell, P. M. J.; Semeniuchenko, V.; Bryce, D. L. Halogen Bond Strength in Solids Quantified via Zeeman-Perturbed Nuclear Quadrupole Resonance Spectroscopy. J. Am. Chem. Soc. 2025, 147, 9528–9543.

6.1 Chapter Overview and Thesis Context

The previous chapters established Zp-NQR spectroscopy as a practical and versatile technique for the characterization of quadrupolar nuclei in molecular solids. Chapter 4 demonstrated a robust experimental workflow capable of accurately determining quadrupolar interaction parameters using weak magnetic fields and exact Hamiltonian simulations. Chapter 5 subsequently showed that the magnetic-field dependence of NQR spectra provides a direct experimental means of identifying quadrupolar isotopes, thereby extending the analytical capabilities of the technique to complex, multicomponent, and impure systems.

Having developed the methodology, the next logical question is whether the measured quadrupolar interaction parameters can be used to quantify chemically meaningful properties. In particular, intermolecular interactions govern the stability, packing, and physical properties of molecular solids, yet their experimental characterization remains challenging. Among these interactions, halogen bonding, XB, has emerged as one of the most important noncovalent forces in supramolecular chemistry, crystal engineering, pharmaceutical materials, and functional molecular design. The strength of a XB influences crystal packing, polymorphism, molecular

recognition, and reactivity, making its accurate quantification essential for understanding and rationally designing molecular solids.

Most experimental methods used to evaluate XB strength rely on indirect structural or spectroscopic observables. X-ray diffraction provides geometric information such as intermolecular distances and bond angles, while vibrational spectroscopy, calorimetry, and computational methods offer complementary measures of interaction strength. Although these approaches have proven highly valuable, they do not directly probe the local electronic environment surrounding the halogen nucleus itself. Since halogen bonding fundamentally arises from redistribution of electron density around the participating atoms, a technique capable of directly sensing these electronic changes offers an attractive route toward experimentally quantifying interaction strength.

NQR is uniquely sensitive to the EFG at the nucleus, which is determined by the surrounding electron density distribution. Because formation of a XB perturbs this distribution, the quadrupolar coupling constant, C_Q, and asymmetry parameter, η, become direct experimental observables that reflect changes in the local electronic environment. Conventional NQR, however, has been limited by the inability to determine these parameters uniquely for many systems. The development of Zp-NQR overcomes this limitation by enabling accurate extraction of the complete quadrupolar tensor, thereby allowing subtle electronic perturbations induced by intermolecular interactions to be quantified experimentally.

The work presented in this chapter demonstrates that the quadrupolar interaction measured by Zp-NQR serves as a quantitative reporter of halogen bond strength. By combining precise experimental measurements with relativistic DFT calculations across an extensive family of halogen-bonded molecular solids, clear correlations are established between experimentally

determined quadrupolar coupling constants, electronic descriptors of bonding, and interaction energies. These relationships reveal that Zp-NQR is capable of directly probing the electronic consequences of halogen-bond formation and provides a practical experimental method for quantifying interaction strength.

Within the overall progression of this thesis, this chapter represents the maturation of Zp-NQR into a tool for quantitative chemical analysis. After demonstrating how Zeeman perturbation enables accurate parameter determination (Chapter 4) and direct isotopic identification (Chapter 5), the methodology is now employed to address a fundamental problem in supramolecular chemistry: the experimental quantification of intermolecular interaction strength. This capability establishes the foundation for the final chapter of Part 2, where the methodology is extended to pharmaceutically relevant molecular solids containing multiple chemically distinct chlorine sites, demonstrating how the analytical framework developed throughout this thesis can resolve increasingly complex crystallographic and spectroscopic challenges.

6.2. Statement of Authenticity

I certify that I have prepared the following article featuring my own work.

6.3 Permissions

I declare that I have obtained permission from the coauthor to include this article in my thesis. Chapter 6 has been reprinted with permission from the American Chemical Society.

6.4 Published manuscript

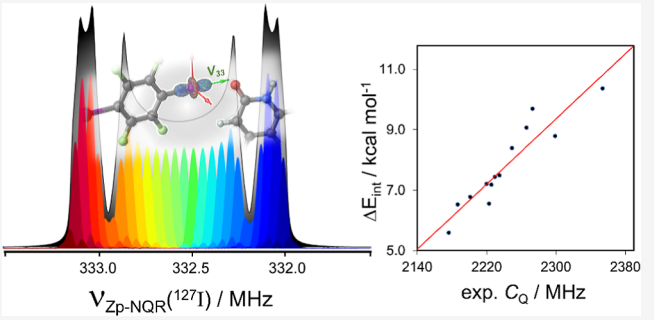
JACS
JOURNAL OF THE AMERICAN CHEMICAL SOCIETY
pubs.acs.org/JACS
Article

Halogen Bond Strength in Solids Quantified via Zeeman-Perturbed Nuclear Quadrupole Resonance Spectroscopy

Alireza Nari, Mubassira Rahman, Patrick M. J. Szell, Volodymyr Semeniuchenko, and David L. Bryce*

Cite This: J. Am. Chem. Soc. 2025, 147, 9528−9543
Read Online
ACCESS | Metrics & More | Article Recommendations | Supporting Information

ABSTRACT: Proton NMR is a ubiquitous and valuable probe of hydrogen bonds. Conversely, ^{127}I NMR of strong halogen bond (XB) donors is hopeless due to quadrupolar coupling constants (C_Q) on the order of GHz. We report here an innovative implementation of Zeeman-perturbed nuclear quadrupole resonance (Zp-NQR) spectroscopy, employing adjustable magnetic fields on the order of mT, which renders possible the acquisition and analysis of spectra of ^{127}I and ^{79}Br nuclei subject to quadrupolar couplings of up to 2.3 GHz in solid powders. This approach is demonstrated on three series of halogen-bonded cocrystals based on so-called "iconic" strong XB donors *p*-diiodotetrafluorobenzene, *sym*-trifluorotriiodobenzene, and *p*-dibromotetrafluorobenzene (27 compounds). Analysis of the spectra using a diagonalization of the Zeeman-quadrupolar Hamiltonian provides C_Q values and quadrupolar asymmetry parameters, thereby overcoming various limitations encountered in pure NMR and pure NQR. Inspection of the data reveals strong correlations with geometrical and structural features of the halogen bond, including its length. Dispersion-corrected zeroth-order regular approximation relativistic DFT computations of the interaction energies of the XB donor are strongly correlated with experimental and computed values of $C_Q(^{127}I)$ and $C_Q(^{79}Br)$. It is concluded that the electric field gradient at the XB donor site is a useful metric for quantifying XB strength in solids. The XB interaction energies range from ∼5 to 10 kcal mol^{-1} for the systems studied herein. The Zp-NQR approach is amenable to widespread application to diverse problems in the chemical and materials sciences related to energy materials, crystal engineering, and many systems comprising strongly quadrupolar isotopes.



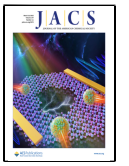
Downloaded via UNIV OF OTTAWA on May 1, 2026 at 18:28:27 (UTC).
See https://pubs.acs.org/sharingguidelines for options on how to legitimately share published articles.

1. INTRODUCTION

A halogen bond (XB) is a highly directional, tunable, noncovalent interaction characterized by an attractive force between the electrophilic region of a halogen atom and a nucleophilic species.[1−6] By enabling the assembly of complex supramolecular architectures at ambient temperatures and pressures,[7] halogen bonds play critical roles in fields such as crystal engineering and molecular recognition,[8,9] in the stabilization of protein structures and drug-receptor interactions,[10,11] in the development of advanced materials and selective catalysts,[12,13] and in the creation of effective pharmaceutical agents.[14−18] Despite this plethora of applications, quantifying XB strength in solid-state systems remains a considerable experimental challenge. While solution-phase techniques like NMR spectroscopy and isothermal titration calorimetry have provided valuable insights into XB energetics,[19−21] the quantification of XB strength in solid-state systems has lagged. Traditional spectroscopic techniques such as infrared (IR), Raman, and UV/vis spectroscopy can sometimes be used to assess bond strength but often lack the sensitivity to distinguish halogen bonds from other noncovalent interactions within the crystal lattice.[22,23] X-ray diffraction (XRD) provides detailed structural information but does not directly measure interaction strengths.[24] Although computational chemistry has offered estimates of halogen bond strengths,[25] experimental validation in solids remains elusive, particularly for systems with multiple competing intermolecular forces. This lack of direct experimental methods to quantify XB strength in solid-state systems hinders a complete understanding of halogen bond behavior and limits the rational design of materials for specific applications.

Solid-state NMR (SSNMR) spectroscopy has been extensively applied to characterize structure and bonding in halogen-bonded systems. Many early studies relied on either the indirect characterization of the XB via the observation of remote spin-1/2 isotopes like ^{13}C and ^{31}P, or on observation of the XB acceptor moiety.[26−30] Halogen bond donor atoms (X = Cl, Br, I) possess quadrupolar nuclei (spin $I > 1/2$)

Received: December 4, 2024
Revised: February 21, 2025
Accepted: February 24, 2025
Published: March 4, 2025



© 2025 American Chemical Society

https://doi.org/10.1021/jacs.4c17321
J. Am. Chem. Soc. 2025, 147, 9528−9543

characterized by an electric quadrupole moment (eQ) that arises from their nonspherical nuclear charge distribution and which interacts with the electric field gradient (EFG) at the nucleus.[31,32] The strength of this quadrupolar interaction may be quantified by the quadrupolar coupling constant (C_Q) and asymmetry parameter (η).[33] Direct observation of ^{35}Cl SSNMR spectra of the covalently bonded chlorine atoms in weakly halogen-bonded single-component chloronitriles has been reported,[34] but the much larger nuclear quadrupole interactions of the spin-active isotopes of bromine (^{79}Br and ^{81}Br with natural abundances (N.A.) of 50.69 and 49.31%, respectively) and iodine (^{127}I, N. A. 100%), when covalently bonded to carbon, render their observation impractical by SSNMR, even in the highest available applied magnetic fields.[35−39] However, chlorine only forms weak halogen bonds while the so-called iconic or prototypical perfluorinated halogen bond donors from which a wellspring of research activity has arisen in the past two decades rely instead on covalently bonded iodine or bromine donor atoms.[1,40,41] Rapid quadrupolar relaxation of covalently bonded $^{35/37}$Cl, $^{79/81}$Br, and ^{127}I renders their observation using solution NMR futile. There are therefore unmet needs to develop spectroscopic tools (i) to directly probe these strongly quadrupolar XB donor sites and (ii) to quantify the strength of XB in solids.

As a first step, our laboratory has reported $^{79/81}$Br and ^{127}I nuclear quadrupole resonance [NQR; also known as quadrupolar spin resonance (QSR)] studies of covalently bonded bromine and iodine atoms which act as halogen bond donors in two series of cocrystals.[42,43] In pure NQR spectroscopy, conducted without an external applied magnetic field, the degeneracy of the nuclear spin states is lifted by the quadrupolar interaction rather than the Zeeman interaction.[44] Applications extend across various disciplines including materials science, where measurements aid in characterizing the electronic properties of novel materials such as perovskites, superconductors, and nanomaterials.[45−54] NQR may also be employed for noninvasive drug testing and quality control, providing a unique method for identifying polymorphic forms.[55−59] However, NQR spectroscopy faces challenges that limit its effectiveness in determining precise quadrupolar parameters for many cases (see Table 1). In the case of spin-3/2 systems (e.g., $^{79/81}$Br), only one frequency is observed in the NQR spectrum, meaning that only a product depending on C_Q and η is generally accessible.[60] For spin-5/2 nuclei (e.g., ^{127}I), the measurement of the two nondegenerate NQR transitions allows for the determination of both quadrupolar parameters. However, for the most widely used halogen bond donors which feature strong electron withdrawing groups (i.e., perfluoroiodobenzenes), the higher energy transitions are experimentally inaccessible due to limited instrumentation that can operate across broad frequency bands, thereby hindering the extraction of quadrupolar parameters from NQR spectra.[61] In such cases, accessing the higher NQR transitions would require tuning to very high frequencies—exceeding 600 MHz for *p*-diiodotetrafluorobenzene halogen-bonded cocrystals. Unfortunately, operating in this ultrahigh-frequency range presents significant challenges including the requirement for a broadband high-frequency NQR probe capable of tuning across large ranges above 600 MHz, along with the required radiofrequency instrumentation (e.g., an NMR console and preamplifier) that can function in this region, both of which are costly and not generally available for NQR experiments.

Table 1. NQR Frequencies for the Single Transition in Spin 3/2 Nuclei and the Two Transitions for Spin 5/2 Nuclei (Approximate; Valid for η < 0.25)

spin no	NQR transition frequency
3/2	$\nu = {}^{1}/_{2}(C_Q)\left(1 + {}^{\eta^2}/_{3}\right)^{1/2}$
5/2	$\nu_1 = {}^{3}/_{20}(C_Q)(1 + 0.09259\eta^2 - 0.63403\eta^4)$
	$\nu_2 = {}^{3}/_{10}(C_Q)(1 - 0.20370\eta^2 + 0.16215\eta^4)$

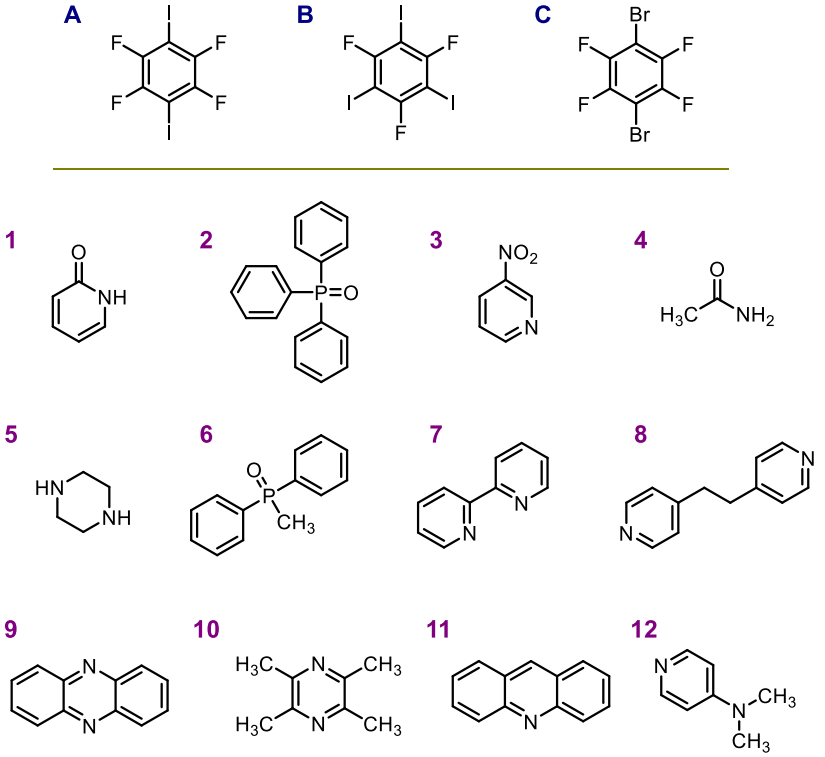
To overcome these limitations, we report here a novel experimental implementation of Zeeman-perturbed nuclear quadrupole resonance (Zp-NQR) spectroscopy[62] to directly observe strongly quadrupolar bromine and iodine sites in powdered perfluorinated halogen bond donors. Much of the early work on Zp-NQR focused on single crystals or systems with limited η values (below 0.4) and relied on first-order approximations for spectral interpretation. These methods often resulted in lower accuracy in determining quadrupolar parameters and, to our knowledge, did not address the challenges associated with the high-frequency transitions observed in the compounds of interest.[63−67] By applying a modest static magnetic field, Zp-NQR resolves the degeneracy of energy levels in spin-3/2 systems, enabling the simultaneous determination of C_Q and η.[62,67] For nuclei with spins greater than 3/2, Zp-NQR extends access to previously inaccessible transitions, significantly enhancing spectral resolution and facilitating accurate extraction of quadrupolar parameters. Our work addresses these challenges by introducing an electron paramagnetic resonance (EPR) electromagnet as a versatile, adjustable magnetic field source, enhancing signal-to-noise ratios and spectral resolution in magnetic fields of up to 500 gauss (0.05 T). The experiment is applied to a series of 27 halogen-bonded cocrystals featuring strong perfluoroiodo- and bromo-benzene donor molecules, followed by a meticulous analysis of the obtained quadrupolar coupling data. By correlating these experimental Zp-NQR data with zeroth-order regular approximation (ZORA) DFT results, we establish the quadrupolar coupling constants as novel reporters on halogen bond strength in solids.

2. RESULTS AND DISCUSSION

2.1. NQR and Zp-NQR Spectroscopy. The donor and acceptor molecules involved in this study, resulting in a total of 27 compounds, are depicted in Scheme 1. We selected three widely used perfluorinated halobenzenes—*p*-diiodotetrafluorobenzene (*p*-DITFB, **A**), *sym*-trifluorotriiodobenzene (*sym*-TFTIB, **B**), and *p*-dibromotetrafluorobenzene (*p*-DBTFB, **C**)—as halogen bond donors paired with a range of nitrogen- and oxygen-containing halogen bond acceptors. Assessment of these compounds enables a systematic investigation of both the effects of donor type and the influence of the nucleophilic acceptors on the XB interaction parameters. By analyzing data from these three series, we aim to discern patterns in interaction strengths and assess whether the XB donors exhibit consistent behavior with similar acceptors or demonstrate unique variations. To ensure a comprehensive and unbiased data set for comparison and to systematically investigate the quadrupolar parameters of the **A**, **B**, and **C** cocrystal series, we included all cocrystals that could be successfully synthesized

https://doi.org/10.1021/jacs.4c17321
J. Am. Chem. Soc. 2025, 147, 9528−9543

Scheme 1. Molecular Structures of the Halogen Bond Donors, A, B, and C, and Acceptors (1−12) Studied in This Work, with Their Corresponding Codes



via mechanochemistry. This approach ensures that the data set captures the full range of cocrystals achievable under the experimental conditions.

Shown in Figure 1 are the pure ^{127}I and ^{79}Br NQR spectra of the three series of cocrystals. For the iodine-containing **A** and **B** series, our custom-built high-frequency NQR probe, combined with a dedicated preamplifier and connected to a Bruker AVANCE III 400 MHz NMR console, was able to acquire only the first transition line, which occurs in the 316−355 MHz range. While our probe is one of the rare high-frequency NQR probes capable of reaching up to 500 MHz, operating at these extreme frequencies presents significant challenges, including difficulties in tuning the probe and sourcing high-frequency components in a cost-effective manner.

We next employed a weak magnetic field (∼mT) to perturb the pure NQR transitions in both ^{127}I and ^{79}Br systems to be able to extract the quadrupole parameters. When a weak external magnetic field is applied, the resonance conditions for the transition between energy levels of $m_I = \pm 1/2$ and $m_I = \pm 3/2$ (the lower frequency line for $I = 5/2$ and the sole transition for spin $I = 3/2$ nuclei) are perturbed, resulting in frequency shifts. Experimentally, these shifts yield a four-line spectrum, known as the inner (α) pair and outer (β) pair (see Figure 2).[60,68] The measurement of the splitting between the α and β components, when an RF field is applied along the magnetic field, facilitates the determination of the value of η. Further details describing our implementation of Zp-NQR will be reported in a forthcoming technical publication (see also Supporting Information). It may be noted that in the pure NQR experiments as well as the Zp-NQR experiments it is clear that the $m_I = \pm 1/2 \leftrightarrow m_I = \pm 3/2$ transitions are being observed rather than the $m_I = \pm 3/2 \leftrightarrow m_I = \pm 5/2$ transitions, in this case most obviously on the basis of the known experimental and computed quadrupolar coupling frequency ranges for covalently bonded iodine atoms (i.e., C_Q is known to be on the order of GHz and this places limitations on the possible ranges for the first and second transitions).

As depicted in the Zp-NQR spectra for the $m_I = \pm 1/2 \leftrightarrow m_I = \pm 3/2$ transitions of ^{79}Br in **C5** and ^{127}I in **A5** (Figure 2), spin 3/2 and spin 5/2 nuclei yield clearly different line shapes. Specifically, for ^{127}I, the inner and outer pairs of transitions are more resolved, with the outer pair being more intense. Generally, the envelope shape obtained for $\eta \neq 0$ consists of two peaks on each side of the unperturbed frequency position separated by the frequency difference $\Delta\nu$, which is defined by the equation $\Delta\nu = 2\eta\nu_0$, where $\nu_0 = \frac{\gamma B_0}{2\pi}$.[60] Exact Zeeman-quadrupolar diagonalization line shape simulations performed with QUEST software,[69] alongside experimental data, revealed that the spin-3/2 Zp-NQR line shape is more sensitive than spin 5/2 to changes in η. Even slight variations in η can cause significant shifts in the apparent value of C_Q. As shown in Tables 2 and 3, the range of η values observed for the Br-based (spin-3/2) cocrystals (0.123−0.230) is notably wider than that for the I-based (spin-5/2) cocrystals (0.048−0.102). This wider variation in η for Br-based cocrystals reflects the greater sensitivity of the Br system to asymmetry in the electric field gradient, which likely arises due to differences in bonding and the local environment around Br in these halogen-bonded systems.

The observed NQR lines typically have a full width at half-maximum (fwhm) of up to 60 kHz (Figure 1), while the breadth of the Zp-NQR spectrum is influenced by the strength of the applied static magnetic field used to perturb the pure NQR transition. A typical Zp-NQR spectrum, acquired at magnetic field strengths ranging from 20 to 40 mT, spans

https://doi.org/10.1021/jacs.4c17321
J. Am. Chem. Soc. 2025, 147, 9528−9543

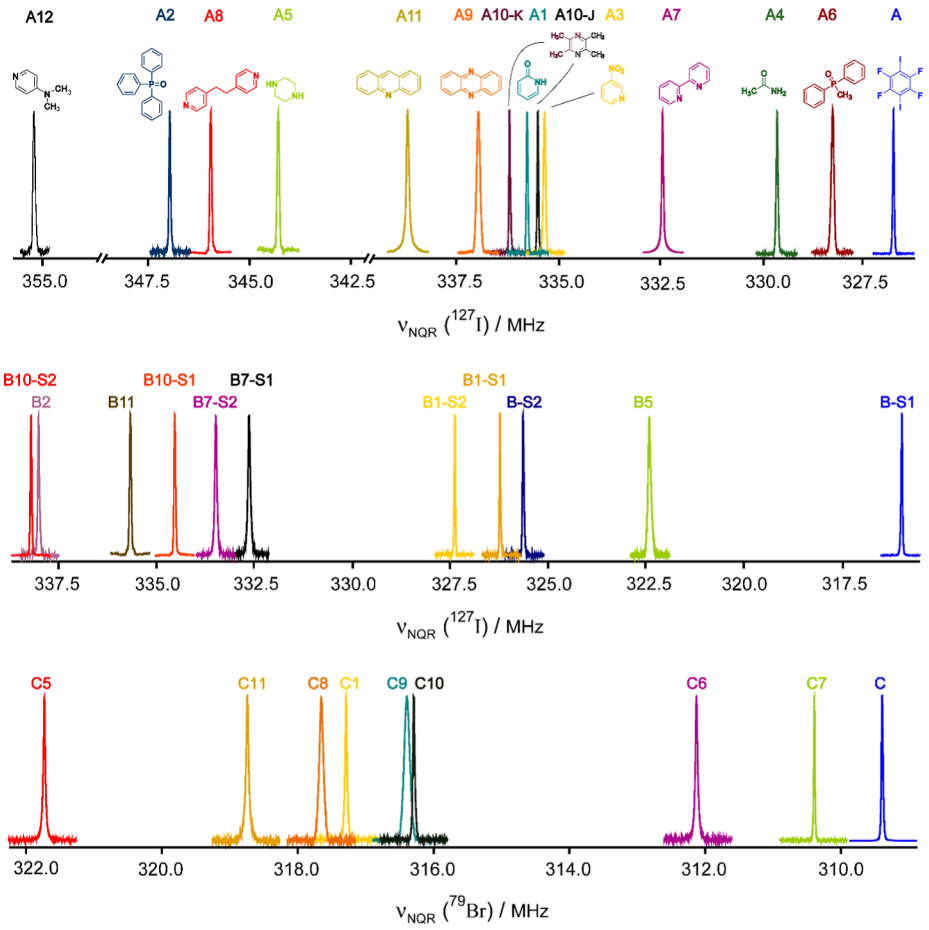


Figure 1. Top: ^{127}I NQR spectra for the first transitions ($m_I = \pm 1/2 \leftrightarrow m_I = \pm 3/2$) of **A** (the XB donor, appearing at the lowest frequency) and its series of XB cocrystals. Each peak represents a distinct cocrystal, with the molecular structures of compound **A** and each XB acceptor displayed above their respective spectra, labeled with the compound code. Middle: ^{127}I NQR lines for the first transitions ($m_I = \pm 1/2 \leftrightarrow m_I = \pm 3/2$) for XB donor **B** and its associated cocrystals, with crystallographically distinct iodine sites labeled as S1 and S2. Bottom: ^{79}Br NQR spectra of XB donor **C** and its corresponding XB cocrystals, with each spectrum labeled with the compound code. Only the crystallographic halogen sites relevant to this study are shown; for a complete list of NQR frequencies for all possible sites, see Table S1 in the Supporting Information.

approximately 0.9−2 MHz and consists of multiple subspectra (Figure 2 and Supporting Information). Given that each pure NQR line exhibits a substantial line width, adherence to the Morino static magnetic field condition, which requires that $B_0 \gtrsim {}^{2\pi\Delta\nu}/_{|\eta|\gamma|}$, is essential.[60] This necessitates a sufficiently strong static field such that the splitting, $\Delta\nu$, exceeds the breadth of the subspectra.

Upon conducting Zp-NQR analysis and extracting the EFG parameters, all the η and C_Q values for the three groups of our XB cocrystals, which include *p*-DITFB, *sym*-TFTIB, and *p*-DBTFB as halogen bond donors, are compiled in Tables 2 and 3. In addition to the examples shown in Figure 2, all Zp-NQR spectra are provided in the Supporting Information.

An important aspect of the **B** series cocrystals, where *sym*-TFTIB acts as the XB donor, is the presence of three iodine atoms per molecule, each serving as a σ-hole donor site. These electrophilic sites allow for multiple distinct halogen-bond interactions within the asymmetric unit, leading to unique quadrupolar parameters. For some cocrystals in the **B** series, two distinct crystallographic sites are reported, with Zp-NQR effectively distinguishing and assigning these sites (Table 2). This trivalency adds complexity to site assignments but also enhances the structural diversity and symmetry observed within the **B** series. By comparing the data in Table 2, it is evident that cocrystals featuring *p*-DITFB as the XB donor (series **A**) exhibit higher $C_Q(^{127}I)$ values compared to those in series **B**. For example, cocrystals with the same XB acceptor moieties in both series consistently show higher C_Q values in series **A**. This trend is further supported by Figure 3a, where the average C_Q for series **A** is 51.5 MHz higher than that of series **B**. Notably, this pattern is also observed for the pure donors of series **A** and **B**. This baseline enhancement in quadrupolar coupling can be largely attributed to the role of substituent effects, where the donor has either three (donor **B**) or four (donor **A**) electron-withdrawing fluorine substituents. These electron-withdrawing groups modulate the depth of the σ-hole on the iodine XB donor atoms. A stronger σ-hole on iodine, with an elevated electrostatic potential, strengthens both the electrostatic attraction and the charge-transfer component of the halogen bond, leading to stronger XB interactions and concomitantly higher ^{127}I quadrupole coupling constants observed in Zp-NQR measurements. The **C** series of cocrystals (*p*-DBTFB acting as XB donor) exhibit lower C_Q values due to the inherently smaller quadrupole moment of ^{79}Br, making it less sensitive to variations in the electric field gradient. Interestingly, the asymmetry of the quadrupolar interaction is consistently higher for the brominated halogen bond donor (series **C**) than for the two iodinated series (**A**, **B**)

https://doi.org/10.1021/jacs.4c17321
J. Am. Chem. Soc. 2025, 147, 9528−9543

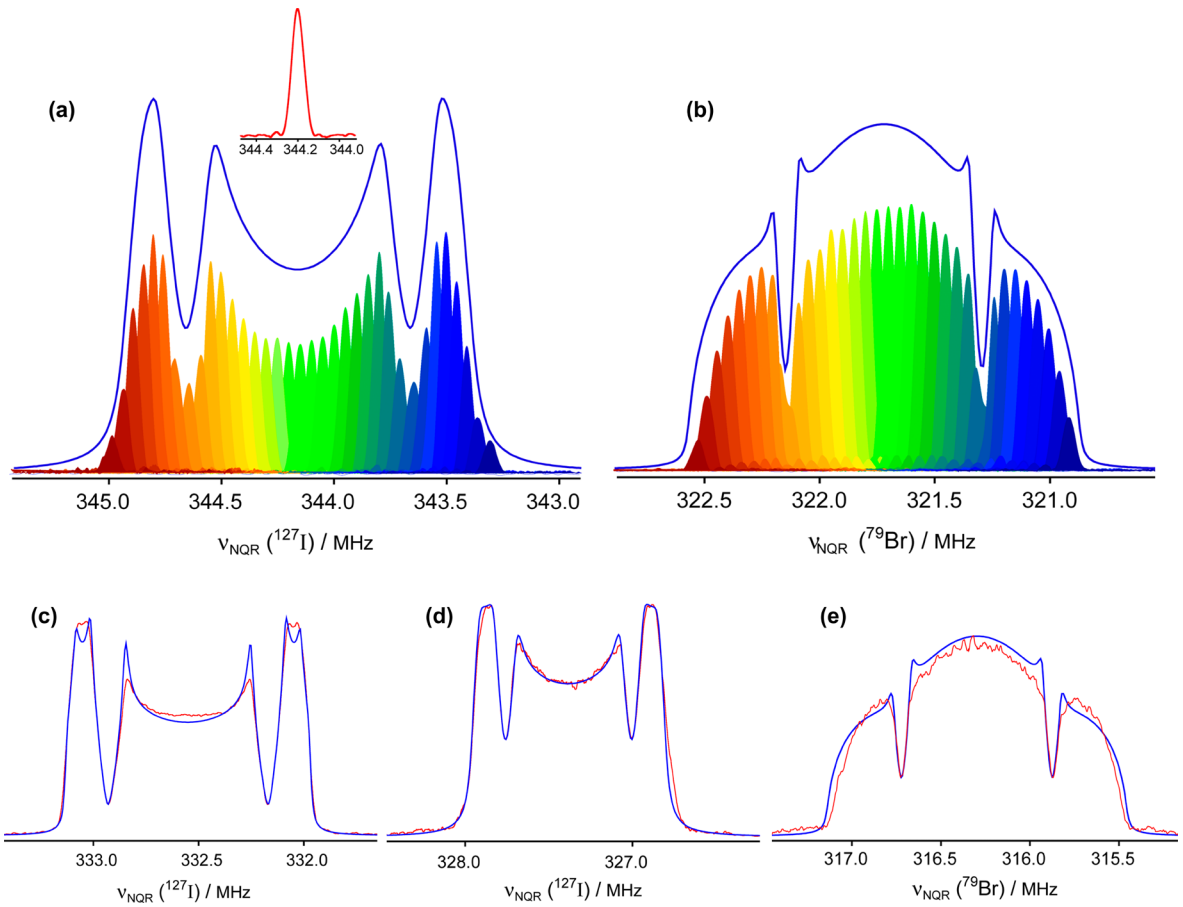


Figure 2. Zp-NQR spectral envelopes for two distinct spin systems both measured at a static magnetic field of 40 mT (400 gauss) generated using an EPR electromagnet: (a) ^{127}I, a spin-5/2 nucleus, **A5**. The inset displays the pure NQR spectrum of **A5**, with a full width at half-maximum (fwhm) of 60 kHz in red; (b) ^{79}Br, a spin-3/2 nucleus, **C5**. The experimental spectrum (color gradient) is constructed by summing 35 subspectra using the VOCS method, with the best-fit simulation generated using QUEST shown in blue. Exemplar experimental (in red) and best fit simulated spectra using QUEST (blue) for (c) **A7** at 30 mT, (d) **B1** (site 2) at 30 mT, and (e) **C10** at 40 mT. Slight discrepancies between experimental and simulated spectra may arise from the crystallinity of the sample and/or the homogeneity of the field.

(Figure 3e). This trend is evident in Figure 3e, where the acceptor is held constant and the donor molecule is switched from **A** to **B** to **C**. These findings are consistent with the weaker XB observed for bromine halogen bond donors. A weaker, longer XB exerts less influence over the electric field gradient at Br, thereby allowing the effects of the surrounding crystal lattice to also impact the EFG and to cause asymmetry. In the case of stronger, more highly linear XB to iodine in series **A** and **B**, the EFG tensor is more strongly dominated by the influence of the linear XB, resulting in η values approaching 0.

Each quadrupolar halogen nuclide (X) has a distinct quadrupole moment, meaning that direct comparisons of C_Q(X) values between different halogens are not straightforward. The nuclear quadrupole coupling constant is defined as $C_Q = eV_{33}Q/h$, where V_{33}, by convention, is the largest component of the EFG tensor. To enable a more meaningful comparison across different spin systems, the C_Q values for the iodine-based and bromine-based cocrystals were normalized by dividing by their respective Q value (Figure 3b). This adjustment makes it possible to compare C_Q values more accurately across halogen types, highlighting the relative strengths of quadrupolar interactions without the confounding influence of quadrupole moment variations. It is also worth considering the Sternheimer antishielding factor, expressed as $(1 - \gamma_\infty)$.[70] This factor adjusts the EFG at the nucleus by accounting for the polarization of inner-shell electrons,[71,72] modifying the lattice EFG ($eq_{lattice}$) to produce the observed EFG (eq_{obs}) according to the relationship $eq_{obs} = (1 - \gamma_\infty) \cdot eq_{lattice}$.[73,74] Plotting the average C_Q(lattice) values—corrected for the Sternheimer factor and Q—yielded more comparable values across the series than the observed C_Q values (Figure 3c). This correction highlights the significant quadrupolar interactions in these systems, even after accounting for inner-shell electron polarization effects.

2.2. Correlation of Quadrupolar Coupling Parameters with Halogen Bond Geometry and Strength. The intermolecular short contact distances in XBs are generally considered to be proportional to the interaction strength.[1,75,76] This follows from the generally accepted notion in chemistry that bond strength and bond length are inversely correlated, albeit with some exceptions.[77] For example, some researchers argue that distances are not directly indicative of bond strength because they also depend on other factors, such as the compressibility limits between atoms, bond stretching frequencies, atomic masses, and other related quantities.[78,79] In the following sections, correlations between quadrupolar coupling parameters and the halogen bond geometry and DFT-computed interaction energies are explored.

https://doi.org/10.1021/jacs.4c17321
J. Am. Chem. Soc. 2025, 147, 9528−9543

Table 2. Experimental ^{127}I NQR Frequencies (ν_{NQR}) for the First Transition (between Energy Levels $m = \pm 1/2$ and $m = \pm 3/2$) for Series A and B[a]

compound	I site	ν_{NQR}/MHz	expt $\lvert C_Q \rvert$/MHz	calc $\lvert C_Q \rvert$/MHz	expt η	calc η
A	_	326.80 ± 0.03	2145.14 ± 1.64	2174.80	0.120 ± 0.004	0.122
A1	_	335.80 ± 0.03	2229.49 ± 0.90	2295.90	0.062 ± 0.004	0.080
A2	_	347.23 ± 0.03	2266.14 ± 1.49	2302.58	0.048 ± 0.008	0.053
A3	_	335.42 ± 0.02	2223.44 ± 2.16	2266.92	0.072 ± 0.008	0.079
A4	_	329.79 ± 0.03	2186.51 ± 1.01	2248.60	0.071 ± 0.004	0.090
A5	_	344.18 ± 0.03	2273.03 ± 1.37	2292.28	0.093 ± 0.004	0.090
A6	_	328.46 ± 0.02	2176.27 ± 1.61	2233.16	0.075 ± 0.006	0.090
A7	_	332.63 ± 0.02	2201.01 ± 1.17	2256.18	0.082 ± 0.004	0.089
A8	_	346.21 ± 0.02	2299.04 ± 0.96	2301.82	0.064 ± 0.004	0.080
A9	_	336.98 ± 0.02	2234.85 ± 1.29	2265.14	0.070 ± 0.004	0.080
A10-J	_	335.56 ± 0.03	2219.98 ± 2.43	2260.72	0.084 ± 0.008	0.090
A10-K	_	336.26 ± 0.03	2225.45 ± 1.19	2270.07	0.082 ± 0.004	0.094
A11	_	338.70 ± 0.03	2249.27 ± 0.89	2280.22	0.060 ± 0.004	0.080
A12	_	355.33 ± 0.03	2353.74 ± 2.40	2355.52	0.078 ± 0.008	0.088
B	1	315.97 ± 0.03	2077.25 ± 1.49	2209.67	0.114 ± 0.008	0.088
B	2	325.66 ± 0.03	2150.48 ± 1.31	2185.81	0.094 ± 0.004	0.088
B1	1	326.20 ± 0.03	2158.38 ± 1.17	2226.92	0.080 ± 0.004	0.089
B1	2	327.41 ± 0.03	2171.65 ± 0.93	2227.76	0.068 ± 0.004	0.088
B2	_	338.02 ± 0.03	2238.09 ± 1.16	2270.42	0.080 ± 0.004	0.104
B5	_	322.42 ± 0.03	2125.57 ± 1.12	2191.97	0.102 ± 0.006	0.092
B7	1	332.63 ± 0.03	2204.68 ± 1.07	2254.32	0.074 ± 0.004	0.081
B7	2	333.50 ± 0.03	2206.39 ± 1.20	2248.24	0.084 ± 0.004	0.083
B10	1	334.58 ± 0.02	2214.93 ± 1.14	2266.24	0.080 ± 0.004	0.081
B10	2	338.22 ± 0.02	2244.15 ± 0.96	2254.16	0.066 ± 0.004	0.073
B11	_	335.68 ± 0.02	2221.60 ± 1.19	2268.55	0.082 ± 0.004	0.097

[a]Quadrupole coupling parameters (C_Q and η) were determined experimentally via Zp-NQR at room temperature (298 ± 3 K) and compared with theoretical values calculated via relativistic-ZORA DFT at 0 K.

Table 3. Experimental ^{79}Br NQR Frequencies (ν_{NQR}) for C and Its Halogen-Bonded Cocrystals, With Quadrupole Coupling Parameters (C_Q and η) Obtained Experimentally via Zp-NQR at Room Temperature (298 ± 3 K) and Theoretical Values Calculated via Relativistic-ZORA DFT at 0 K

compound	ν_{NQR}/MHz	expt $\lvert C_Q \rvert$/MHz	calc C_Q/MHz	expt η	calc η
C	309.32 ± 0.03	617.66 ± 0.52	635.41	0.105 ± 0.030	0.125
C1	315.60 ± 0.04	628.87 ± 0.78	639.16	0.202 ± 0.028	0.101
C5	321.75 ± 0.03	641.82 ± 0.49	643.28	0.123 ± 0.014	0.117
C6	312.11 ± 0.04	619.27 ± 1.38	638.51	0.220 ± 0.040	0.101
C7	310.40 ± 0.03	617.29 ± 0.87	637.28	0.185 ± 0.030	0.110
C8	317.65 ± 0.03	629.76 ± 2.18	637.82	0.230 ± 0.060	0.119
C9	316.28 ± 0.04	630.46 ± 1.90	642.83	0.140 ± 0.060	0.093
C10	316.39 ± 0.04	631.04 ± 0.66	644.15	0.126 ± 0.016	0.119
C11	318.75 ± 0.05	634.77 ± 1.05	645.80	0.160 ± 0.040	0.111

Shown in Figure 4 are plots of XB distances against C_Q for iodine−nitrogen (I···N) and iodine−oxygen (I···O) interactions in the **A** and **B** series, as well as the **C** series (analyzed separately). These plots demonstrate a clear inverse relationship: within each series, as the XB interaction distance decreases, the value of C_Q increases. To further validate the relationship between experimental C_Q values and crystallographically obtained XB distances, we conducted a leave-one-out cross-validation (LOOCV) analysis.[80] This analysis, combined with the R^2 values from the C_Q vs XB distance plots (Figure 4), offers a comprehensive perspective on how well C_Q, as determined through Zp-NQR, may be used to predict halogen bond geometry across various halogen bond donors and nucleophiles. In the **A** and **B** series, both iodine−nitrogen (I···N) and iodine−oxygen (I···O) interactions show a strong correlation between C_Q and XB distances, with R^2 values of 0.81 and 0.85, respectively. The low mean absolute error (MAE) of 0.044 Å and root-mean-square-error (RMSE) of 0.054 Å for the I···N interactions, alongside similar reliability for I···O, confirm C_Q as a consistent predictor of bond distances in these systems.

In the **C** series, where bromine interacts with both nitrogen and oxygen nucleophiles, the correlation is much weaker (R^2 = 0.34), with higher MAE (0.065 Å) and RMSE (0.078 Å) (Figure 4c). This clearly weak correlation indicates that C_Q is less effective in predicting XB distances in systems involving bromine, a less polarizable and weaker halogen bond donor than iodine. The data are nevertheless fit to a linear function on the basis of what was observed for the iodine data. The smaller σ-hole and reduced influence of bromine[81] on the EFG result in less pronounced changes in C_Q, limiting its ability to predict bond distances accurately. However, even in bromine-

https://doi.org/10.1021/jacs.4c17321
J. Am. Chem. Soc. 2025, 147, 9528−9543

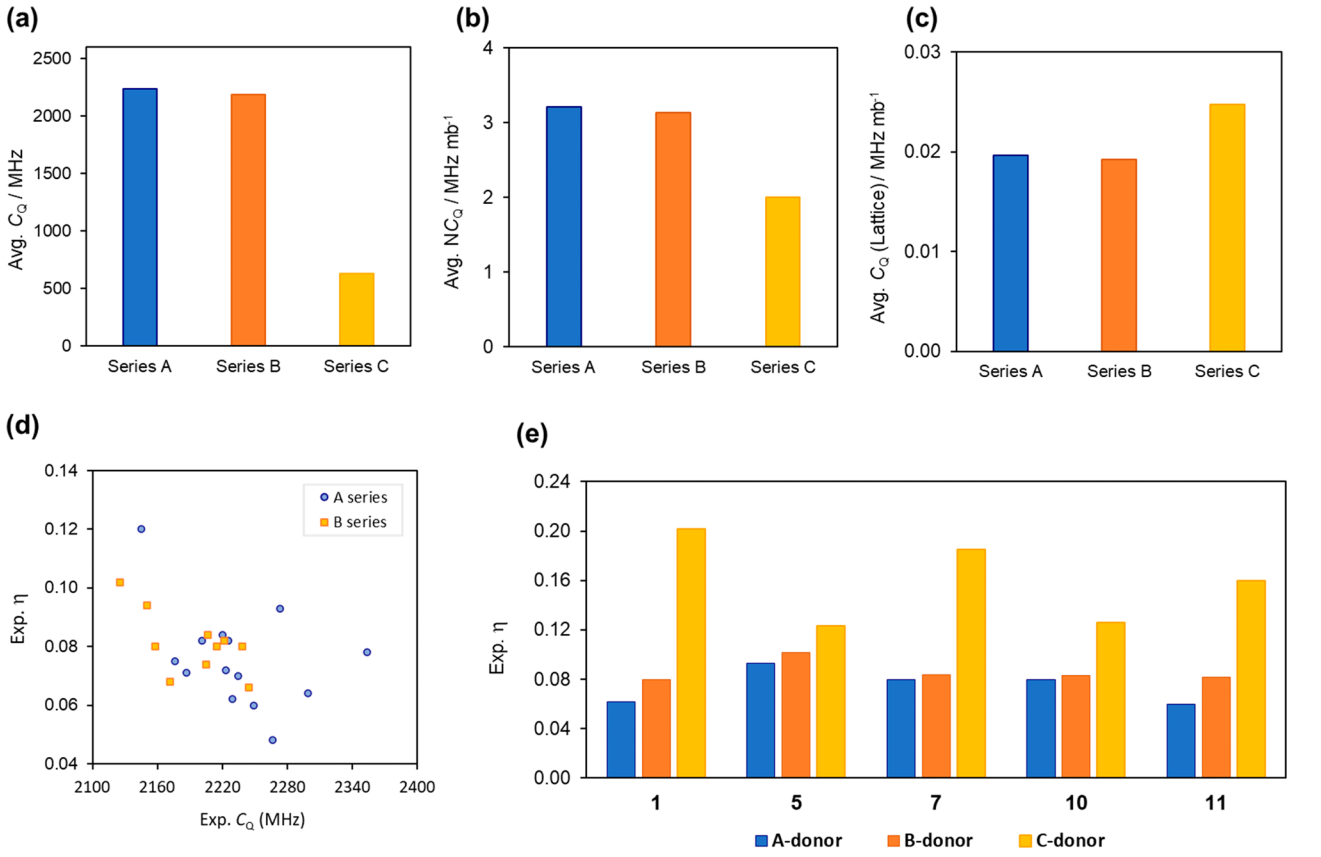


Figure 3. Comparison of average quadrupolar parameters for cocrystals in three XB donor series (**A**: *p*-DITFB, **B**: *sym*-TFTIB, **C**: *p*-DBTFB) obtained via Zp-NQR. (a) Average observed C_Q values for the three series of cocrystals. (b) Average normalized C_Q values ($NC_Q = C_Q/Q$, where Q is the quadrupole moment) for each series. (c) Average C_Q (lattice) values, calculated by normalizing the observed C_Q for Q and for the Sternheimer antishielding factor using the equation C_Q (lattice) = C_Q (observed)/(Q) ($1 - \gamma_\infty$). (d) Scatter plot of C_Q versus η for **A** and **B** series of cocrystals. (e) Variation in η across five groups of cocrystals (with **1**, **5**, **7**, **10**, and **11** as XB acceptors), where each group contains the same XB acceptor moiety paired with three different XB donors (Note: the average η value for **A10-J** and **A10-K** is used to account for both polymorphs of **A10**).

based systems, Zp-NQR still provides valuable insights into halogen bond interactions, reinforcing the utility of C_Q in studying noncovalent interactions. Overall, these results underscore the strength of Zp-NQR in determining C_Q as a powerful tool for assessing halogen bond geometry. The high correlation in the **A** and **B** series highlights the potential of NQR crystallography to capture and predict halogen bonding characteristics across different nucleophiles and halogen donors, with the strongest correlations observed in systems involving iodine.

The relationship between C_Q and XB distance observed in this study is supported by some previous literature. For instance, a $^{79/81}$Br NQR study on bromine halogen bonds shows a strong linear correlation between C_Q and halogen bond length, with C_Q increasing as the bond length decreases, emphasizing the sensitivity of C_Q to XB geometry.[42] Additionally, research on relativistic effects in halogen-bonded complexes highlights the significant influence of iodine and bromine's electronic properties on C_Q values, reinforcing the role of halogen type in modulating XB interactions.[82]

The relationship between C_Q and XB distance may be justified from a theoretical and computational perspective as well. For example, the EFG is a property that depends on r^{-3}, where r is the distance from the nucleus. Thus, an inherent distance dependence of the value of C_Q on the distance to the nearest atoms in the crystal structure is expected. Several works have reported DFT calculations which demonstrate a highly linear relationship over short variations in r in nonhalogen-bonded systems. These include results for $^{79/81}$Br and ^{127}I isotopes studied herein, i.e., the value of C_Q ($^{79/81}$Br) was shown to linearly depend on the position of the bromide ion in $MgBr_2$[83] and the value of C_Q (^{127}I) was shown to vary linearly with the position of the iodine ion in alkaline earth iodides.[70]

The observed elongation of the iodine−carbon (C−I) covalent bond upon halogen bond formation at iodine is a complementary indicator of the interaction strength between the halogen bond donor and acceptor.[84,85] As shown in Figure 4d for I···N halogen bonds, a strong positive correlation between C_Q and the C−I bond length (R^2 = 0.80) is observed. The elongation of the I−C bond reflects a weakening of this bond due to charge transfer from the acceptor's lone pair into the σ^* antibonding orbital of the I−C bond. This electron donation leads to partial depopulation of the bonding σ orbital, weakening the covalent I−C bond and resulting in an extended bond length.[86,87] Consequently, the charge-transfer interaction enhances the overall halogen bond strength, resulting in shorter halogen bond distances (vide supra). The relationship observed here aligns with three-center four-electron (3c−4e) bonding,[88] where the charge transfer component enhances halogen bond strength, leading to shorter halogen bond distances and increased C_Q values, reinforcing the inverse relationship between C_Q and XB distance.

https://doi.org/10.1021/jacs.4c17321
J. Am. Chem. Soc. 2025, 147, 9528−9543

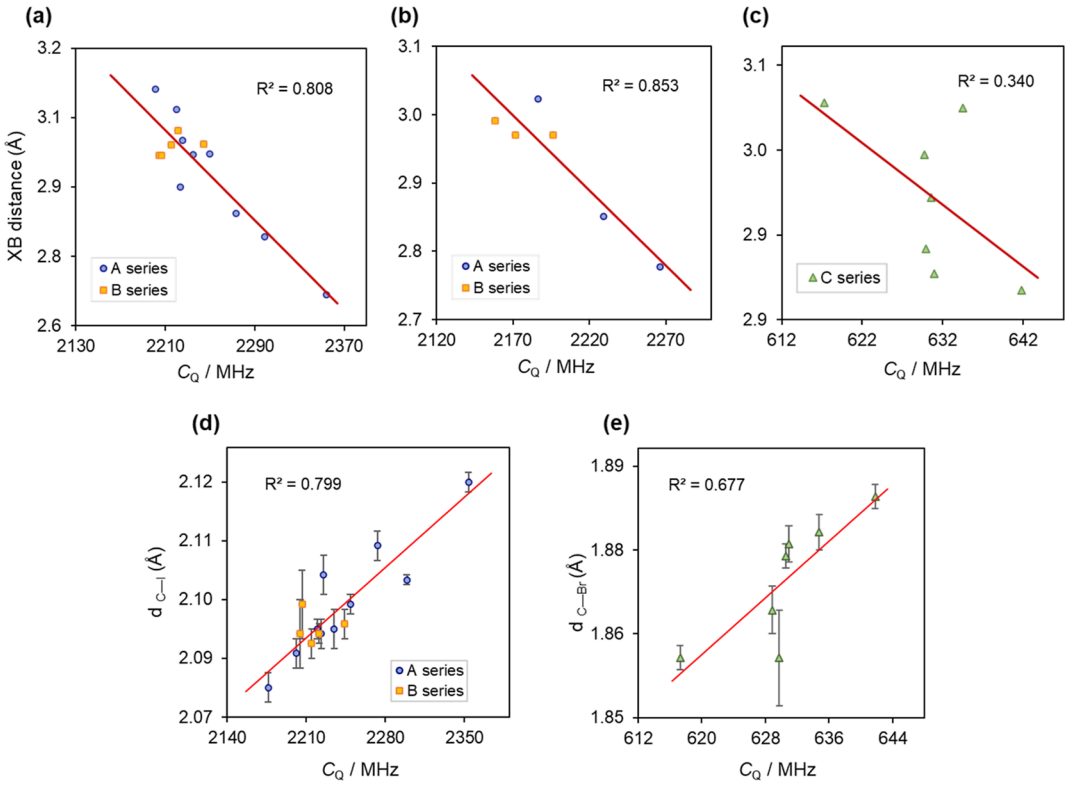


Figure 4. Plots of XB interaction geometries (Table S10) versus experimental C_Q values: for (a) XB interaction distance (XB_d) of I···N vs C_Q, $XB_d = -2.43 \times 10^{-3} C_Q + 8.40$, $R^2 = 0.808$, and (b) XB_d of I···O, $XB_d = -2.20 \times 10^{-3} C_Q + 7.73$, $R^2 = 0.853$, interactions in series **A** and **B**, and (c) the corresponding XB_d plot for Br···Lewis-base interactions in series **C**, $XB_d = -6.56 \times 10^{-3} C_Q + 7.12$, $R^2 = 0.340$. The bottom plots show C_Q versus the C−X covalent σ bond distance for the XB cocrystals studied here: (d) **A** and **B** series with I···N XB interaction, $d_{C\_I} = 2.05 \times 10^{-4} C_Q + 1.64$, $R^2 = 0.799$, and (e) the **C** series of cocrystals, $d_{C\_Br} = 1.19 \times 10^{-3} C_Q + 1.12$, $R^2 = 0.677$. Cocrystals **A6** and **C6** are excluded because they exhibit halogen bonds to the π ring systems rather than X···N/O interactions. Cocrystal **B5** is excluded because the iodine which engages in a halogen bond to N also has short contacts to carbon and hydrogen.

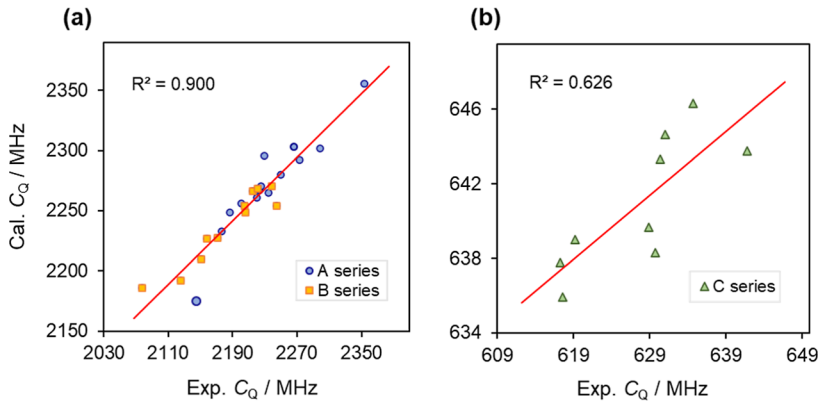


Figure 5. Comparison of experimentally obtained C_Q values from the Zp-NQR method with theoretically determined C_Q values via ZORA-DFT for (a) **A** and **B** series of cocrystals, cal $C_Q = 0.662$ exp $C_Q + 791$, $R^2 = 0.900$, and (b) **C** series of cocrystals, cal $C_Q = 0.343$ exp $C_Q + 425$, $R^2 = 0.626$. Absolute values are plotted in the case of C_Q (^{127}I); its sign is negative.

In contrast, the length of the C−Br covalent bond in the **C** series cocrystals shows a weaker correlation ($R^2 = 0.68$) with quadrupolar coupling constant (Figure 4e). This lower correlation can be attributed to the inherently weaker Br-based halogen bonds, where charge transfer is less pronounced, resulting in a reduced influence on the C−Br bond elongation and a more modest increase in C_Q. This difference highlights the distinctive bonding characteristics of iodine versus bromine in halogen-bonded systems and the corresponding impact on C_Q and bond elongation, which is explored below through NLMO analysis (vide infra).

2.3. Density Functional Theory Calculations. DFT calculated quadrupolar parameters obtained using the hybrid PBE0 functional with consideration of the ZORA spin−orbit relativistic effect for optimized geometries (while keeping the XB geometry fixed) and experimental geometries (directly extracted from X-ray diffraction data) are summarized in Tables 2, 3, and S5 (see Supporting Information). Shown in Figure 5 are plots of experimental vs calculated (with

https://doi.org/10.1021/jacs.4c17321
J. Am. Chem. Soc. 2025, 147, 9528−9543

Table 4. Calculated XB Energies (ΔE_{int}) From DFT

cocrystal	XB ΔE_{int} (kcal/mol)	cocrystal	site	XB ΔE_{int} (kcal/mol)	cocrystal	XB ΔE_{int} (kcal/mol)
A1	7.44	**B1**	1	6.66	**C1**	4.70
A2	9.07	**B1**	2	6.26	**C5**	6.57
A3	6.56	**B2**	_	8.90	**C6**	4.24
A4	6.53	**B5**	_	6.20	**C7**	4.51
A5	9.69	**B7**	1	7.23	**C8**	4.89
A6	5.59	**B7**	2	7.37	**C9**	5.54
A7	6.78	**B10**	1	7.37	**C10**	5.01
A8	8.79	**B10**	2	7.39	**C11**	5.33
A9	7.49	**B11**		7.94		
A10-J	7.21					
A10-K	7.18					
A11	8.39					
A12	10.36					

optimized geometry) C_Q values for all compounds. For the **A** and **B** series of cocrystals, which utilize *p*-DITFB and *sym*-TFTIB as halogen bond donors, there is a strong agreement between the experimental C_Q values and those calculated from the optimized geometries, with R^2 values of 0.90 (Figure 5a). The calculated root-mean-square deviation (RMSD) of 48.92 MHz represents about 2% of the magnitude of C_Q, while the RMSE of 12.4 MHz and the LOOCV RMSE of 9.645 MHz indicate that the model reliably captures the relationship between experimental and calculated C_Q values, despite some inherent variability. It is noted here that the DFT calculations show that the sign of C_Q (^{127}I) is negative and the sign of C_Q (^{79}Br) is positive.

Overall, the agreement between the calculated quadrupole parameters for series **A**, based on optimized geometries, outperforms those calculated using experimental geometries (Figure S8). Specifically, the R^2 value for the optimized geometry is 0.90 with an RMSD of 48.92 MHz, compared to an R^2 of 0.89 and a higher RMSD of 57.66 MHz when using the experimental geometry (Table S5 and Figure S8). The LOOCV analysis for experimental C_Q versus DFT-calculated C_Q values across the **A**, **B**, and **C** series provides valuable insights into the predictive strength of C_Q as determined by Zp-NQR for noncovalent interactions. This good correlation reinforces the predictive power of the Zp-NQR technique in capturing the EFG parameters for iodine-based systems, where the halogen bonds tend to be stronger and more directional.

In the **C** series, the R^2 value is lower at 0.63, but both the RMSD (13.76 MHz) and RMSE (2.08 MHz) are much lower than in the iodine-based XB cocrystals. This situation can occur when the range of C_Q values in the **C** series is smaller, resulting in lower absolute errors even though the relative correlation is weaker. The LOOCV RMSE is 2.65 MHz, further indicating a smaller range of variation in C_Q values. In the **C** series, which involves bromine as the halogen bond donor, the interactions are weaker, and the variation in C_Q values between the experimental and DFT-calculated results is less pronounced. Therefore, the lower error values can coexist with a weaker overall correlation. This highlights that, although C_Q can still be used to predict halogen bond interactions in weaker systems like those involving bromine, the accuracy of the prediction is reduced compared to systems with stronger halogen donors like iodine.

Even with the ZORA spin−orbit relativistic approximation, DFT overestimates EFG values due to inherent limitations, particularly in handling electron correlation and exchange interactions. As DFT calculations are performed at 0 K, they neglect temperature effects like thermal vibrations, leading to discrepancies compared to data acquired under real conditions. Relative to the experimental values obtained at room temperature, the computed C_Q and η values are slightly higher. This overestimation of EFG values arises because the simulation does not account for lattice dynamics at room temperature (Tables 1 and 2). Additionally, commonly used functionals such as PBE and PBE0 may not fully capture long-range interactions, especially in halogen bonded systems, resulting in elevated EFGs compared to experimental NQR data.[89,90] Nevertheless, as shown in Figure 5, the strong correlation between DFT-calculated and experimentally derived EFG parameters confirms the utility of the ZORA relativistic DFT approach, even in systems with strong quadrupole interactions (GHz range).

2.4. Measures of Halogen Bond Strength. The interaction energy (ΔE_{int}), also referred to as total binding energy or formation energy—and referred to in this paper as the halogen bonding (XB) energy—quantifies the strength of halogen bonds in cocrystals.[2,91] Interaction energies calculated via DFT represent the specific strength of these halogen bonds, as shown in Table 4. These values are calculated using basis set superposition error (BSSE) corrections via the counterpoise (CP) method[92] within the ADF 2019 package. According to the equation $\Delta E_{int} = E_{cocrystal} - (E_{donor} + E_{acceptor})$, the halogen bonding energy for each Lewis acid−base pair is the difference between the energy of the cocrystal and the sum of the energies of the individual donor and acceptor subunits, each optimized in the geometry they adopt within the cocrystal. Values range from 4.24 kcal mol^{-1} for **C6** to 10.36 kcal mol^{-1} for **A12**, slightly larger than experimental values measured in solution and computed gas-phase values reported by Taylor and co-workers for C_6F_5I and C_4F_9I-based systems.[20]

Within the I···Lewis-base cocrystals, **A6** exhibits the lowest XB energy (Table 4), with the iodine atom forming a close interaction with the π-system of the aromatic benzene ring in the methyldiphenylphosphine oxide.[93] π-Systems are generally weaker halogen bond acceptors compared to heteroatoms with lone pairs, likely due to the electron density being more delocalized within the π-cloud, which reduces the availability of localized electron density for halogen bonding. One of the most notable yet weakest XB interactions is observed in **A4**, which exhibits a low XB energy of 6.53 kcal/mol with acetamide. In this system, the nucleophilic carbonyl oxygen of acetamide, which is sp^2 hybridized, is expected to interact

https://doi.org/10.1021/jacs.4c17321
J. Am. Chem. Soc. 2025, 147, 9528−9543

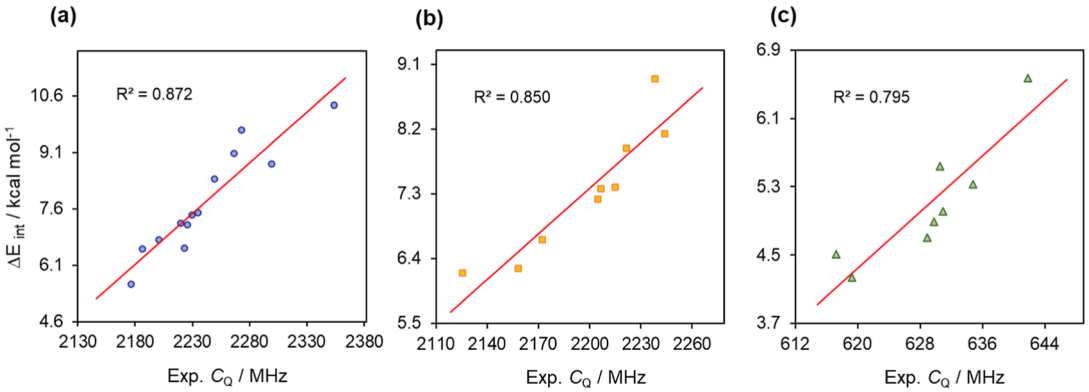


Figure 6. Plots of experimentally obtained C_Q values from the Zp-NQR technique versus DFT-calculated XB energies (ΔE_{int}) for (a) the **A** series, $\Delta E_{int} = 2.69 \times 10^{-2} C_Q - 52.6$, $R^2 = 0.872$, (b) **B** series, $\Delta E_{int} = 2.11 \times 10^{-2} C_Q - 39.1$, $R^2 = 0.850$, and (c) the **C** series of cocrystals, $\Delta E_{int} = 8.22 \times 10^{-2} C_Q - 46.6$, $R^2 = 0.795$.

Table 5. NLMO Analysis of the Halogen Atom Contributions to the V_{33} EFG Component in A, B, and C Halogen Bond Donor Moieties and Their Corresponding Cocrystals with 1 as the XB Acceptor (Atomic Units)

	A-donor	**A1**-cocrystal	**B**-donor	**B1**-cocrystal	**C**-donor	**C1**-cocrystal
σ (C−X)	−13.489	−13.813	−13.606	−13.290	−10.273	−10.287
X Lp	26.505	27.247	26.434	26.794	18.769	19.000
X core	1.027	0.889	1.003	1.065	0.573	1.019
sum	14.043	14.323	13.831	14.569	9.069	9.732

moderately with the electrophilic σ-hole of iodine but forms only a weak XB interaction. This weakness is attributed to the carbonyl oxygen also participating in hydrogen bonding with a nearby amine hydrogen in the amide group, which further diminishes the XB strength. This dual interaction leads to one of the weakest XBs in the series and explains why acetamide does not serve as an effective XB acceptor in the other two series, preferring instead to form hydrogen bonds within its own network.[94]

Strong correlations were observed between the experimentally determined C_Q and the DFT-calculated XB energies (Figure 6). These results suggest that C_Q can be a reliable predictor of intermolecular interaction strength in halogen-bonded systems. This correlation is particularly pronounced for the **A** and **B** series, with R^2 values of 0.87 and 0.85, respectively. The results from the LOOCV and R^2 values for the **A**, **B**, and **C** series further highlight the strong correlation. In the **A** series (*p*-DITFB as the XB donor), a R^2 value of 0.87, along with a low LOOCV error (MAE: 0.46 kcal/mol) and RMSE of 0.59 kcal/mol, confirms that C_Q accurately reflects the strength of XB interactions. The **C** series (*p*-DBTFB donor) shows a R^2 of 0.80 and the lowest errors (MAE: 0.41 kcal/mol, RMSE: 0.47 kcal/mol), reinforcing the reliability of C_Q as a consistent predictor of interaction energies, even for weaker bromine halogen donors.

The underlying basis for this connection between the value of C_Q and the interaction energies may be rationalized by realizing that, (i) as discussed above, the value of C_Q is known to vary with distance in ideal systems and (ii) halogen bond strength is also known to depend on distance in ideal systems where other factors are held constant (vide supra). Thus, the scatter in the correlation obtained presently reflects some of the nonidealities in the real systems studied presently, namely other differences in local geometry as well as differences in overall crystal packing and the long-range contacts that accompany this.

2.5. Natural Localized Molecular Orbital Visualization. A natural localized molecular orbital (NLMO) analysis of the EFG contributions in halogen-bonded cocrystals reveals trends consistent with the nature of the halogen atoms (iodine vs bromine) and the differing fluorine substitutions on the XB donors (Table 5). Key contributions to the V_{33} component of the EFG tensor include the σ(C−X) bond, the lone pair (Lp) on the halogen atom (X), and the core electron contribution of the halogen, X. Upon cocrystallization, both **A** and **B** systems (which involve iodine) exhibit an increase in the V_{33} value, primarily driven by an increase in the Lp contribution of iodine, which signifies enhanced polarization and electron density redistribution upon halogen bond formation.

In system **A**, for example, the Lp contribution of iodine to V_{33} increases from 26.505 to 27.247 au upon forming the **A1** cocrystal, while the σ(C−I) contribution shifts slightly more negative from −13.489 to −13.813 au, indicating a partial depopulation of the bonding electron density as it is redistributed toward the acceptor oxygen. This redistribution results in a stronger V_{33} component, reflecting the enhanced halogen bond strength in the cocrystal form. Similar but slightly less pronounced behavior is observed in system **B**, where the lone pair contribution of iodine also increases (from 26.434 to 26.794 au), with a slight adjustment in the σ(C−I) contribution from −13.606 to −13.290 au. The presence of only three fluorine atoms in **B** leads to a slightly reduced electron-withdrawing effect compared to **A**, resulting in a marginally weaker halogen bond and a smaller increase in the V_{33} component upon cocrystallization. In contrast, in system **C**, the σ(C−Br) contribution to V_{33} remains nearly unchanged upon formation of **C1**, and the Lp contribution of bromine increases modestly from 18.769 to 19.000 au. This limited change indicates a weaker Br···O interaction compared to the I···O interactions observed in **A** and **B**, consistent with bromine's lower polarizability and halogen-bonding capability.

https://doi.org/10.1021/jacs.4c17321
J. Am. Chem. Soc. 2025, 147, 9528−9543

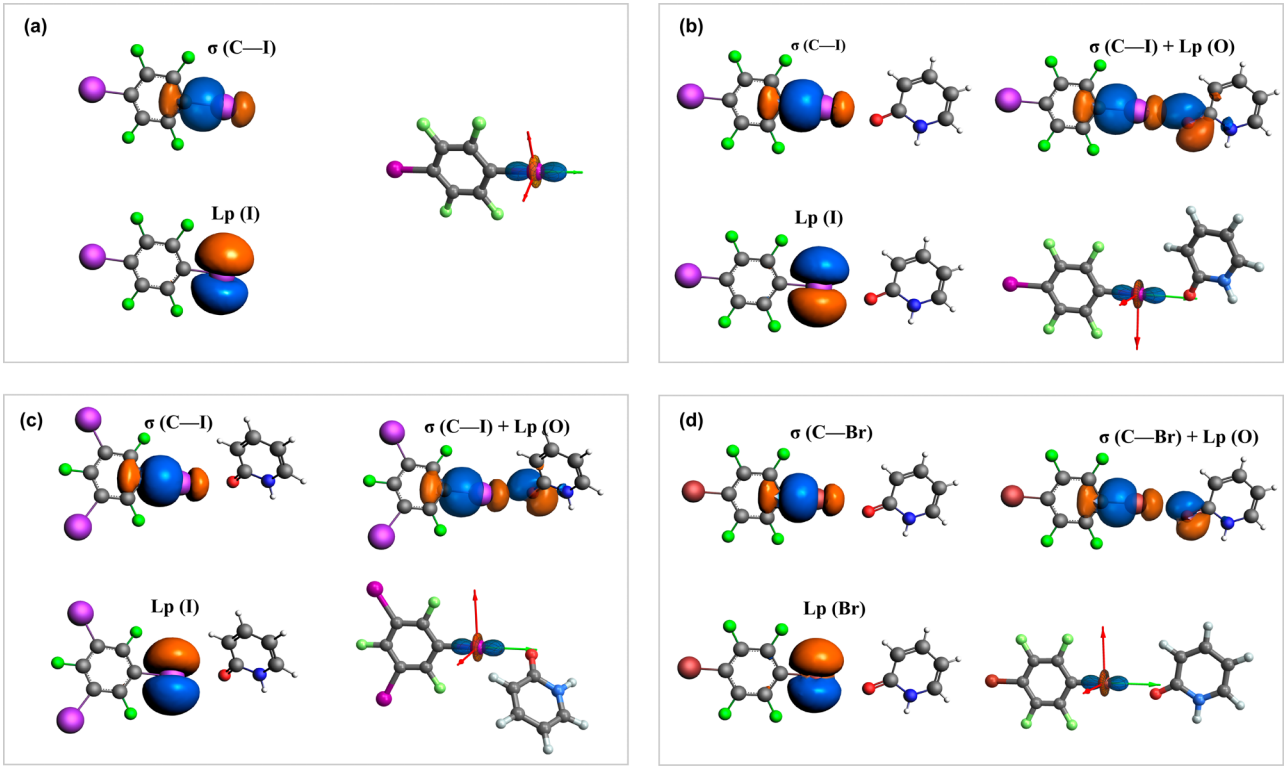


Figure 7. Visualization of the NLMOs calculated using AMS NBO5 package, visualized with AMS-view software,[95] and the electric field gradient (EFG) tensors visualized using Mathematica version14 notebook, for (a) the XB donor **A** (*p*-DITFB), and (b–d) corresponding to the cocrystals **A1**, **B1**, and **C1**, respectively. Each NLMO is labeled according to Table 5. The EFG tensor is displayed as a surface to visually convey its sign and symmetry, with orange indicating negative principal values and blue indicating positive ones (the green arrow indicates the V_{33} direction, and red arrows indicate the V_{11} and V_{22} directions).

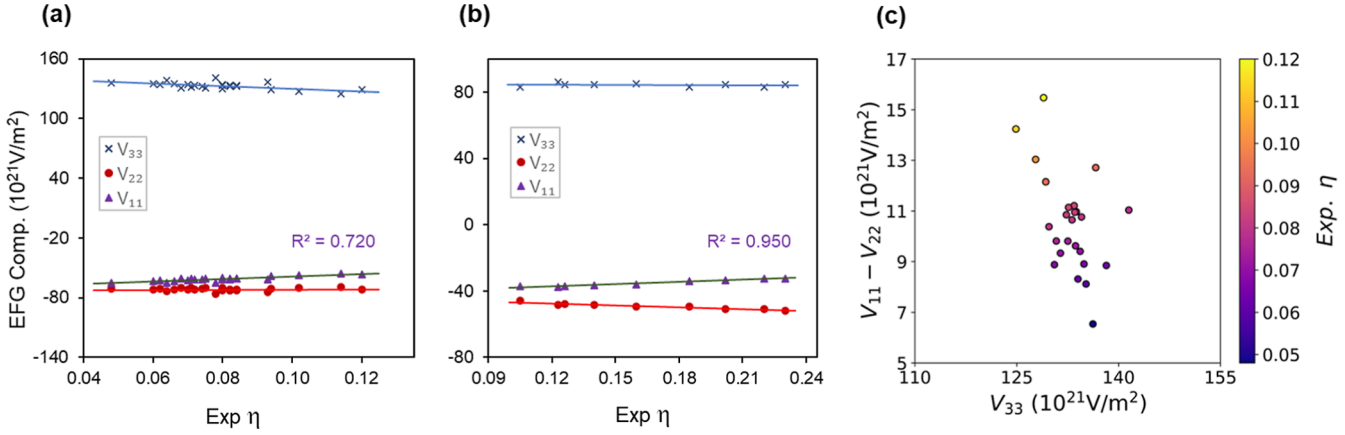


Figure 8. Plots illustrating the relationship between experimental EFG tensor components and quadrupolar parameters obtained via Zp-NQR. (a) EFG components plotted against η for ^{127}I systems in the **A** and **B** series of cocrystals; (b) EFG components versus η for the **C** series of cocrystals (^{79}Br); (c) Scatter plot of $(V_{11} - V_{22})$ versus V_{33} with a color gradient representing η values for **A** and **B** series of cocrystals.

Consequently, the total sum of the V_{33} component for **C** remains significantly lower than in **A** and **B**, highlighting the inherently weaker nature of bromine-based halogen bonds.

Figure 7b illustrates the NLMO of the halogen bond in the **A1** cocrystal, showing an antibonding character across the C–X covalent bond. This antibonding orbital facilitates the mixing of the lone pair electrons from the nucleophilic atom with the σ^* orbital of the C–X bond, making the $n \rightarrow \sigma^*$ charge transfer evident. Similar patterns are observed across other halogen-bonded cocrystals (**B1** and **C1**), where the NLMOs consistently reveal the interactions responsible for charge transfer from the nucleophile to the halogen bond donor.

The Lp and σ(C–X) MO shapes remain roughly the same in the XB donor moieties and their corresponding cocrystals (see Supporting Information for detailed MO orbitals of the other two XB donors and selected cocrystals). This suggests that the electronic structure of the halogen donor is largely preserved upon halogen bond formation, contrasting with the behavior observed in hydrogen bonding, such as in imidazole, where significant changes occur in the nitrogen MOs and their

https://doi.org/10.1021/jacs.4c17321
J. Am. Chem. Soc. 2025, 147, 9528–9543

contributions upon cocrystallization from the monomer to the crystalline state.[96]

EFG tensor plots illustrate the magnitude and orientation of the EFG at the X nucleus (Figure 7). Due to the traceless nature of the EFG tensor, it inherently possesses both positive and negative components. As shown in Figure 7a, in the XB donor **A**, the principal axis V_{33} aligns along the C−X bond direction. In the cocrystals, the EFG tensor maintains a similar orientation but shifts slightly to align along the vector between the X atom and the lone pair of the nucleophile. For all XB cocrystals, the sign of V_{33} is positive, as indicated by the blue arrows pointing toward the Lp, reinforcing the influence of the halogen bond on the EFG. This change in tensor orientation of the donor atom is consistent with similar changes seen from single-crystal NMR experiments on XB acceptor atoms.[97]

The role of the individual EFG tensor components on the value of the quadrupolar asymmetry parameter, $\eta = (V_{11} - V_{22})/V_{33}$, was analyzed for both iodine (^{127}I) and bromine (^{79}Br) systems (Figure 8). In Figure 8a and b, the strong positive correlation between V_{11} and η for both ^{127}I and ^{79}Br systems (R^2 = 0.72 and 0.95, respectively) indicates that V_{11} is a primary factor influencing quadrupolar asymmetry. Since V_{11} reflects the EFG along one of the principal axes, structural or electronic changes affecting it directly impact the overall asymmetry, emphasizing the importance of bonding environments and charge distribution along this axis in governing quadrupolar interactions.

Figure 8c shows a plot of $V_{11} - V_{22}$ versus V_{33}, with color coding based on the asymmetry parameter η. Here, η is primarily driven by differences between V_{11} and V_{22}, rather than by variations in V_{33}. The color gradient shows that higher η values align with greater $V_{11} - V_{22}$ differences, while V_{33} remains relatively constant. For the halogen-bonded cocrystals analyzed, V_{11} and V_{22} are thus key indicators of the local asymmetry, with V_{33} acting as a stable reference. Overall, the results suggest that while some EFG trends are consistent across both halogens, the larger size and polarizability of iodine introduce subtler variations in how the EFG components influence C_Q and η.

3. CONCLUSIONS

A novel implementation of Zeeman-perturbed NQR spectroscopy using an adjustable external magnetic field has been employed to measure quadrupolar frequencies, and the derived quadrupolar coupling constants and asymmetry parameters, for three series of halogen-bonded cocrystals. It is concluded that Zp-NQR offers a facile and sensitive method for accurately and precisely measuring these data for chemical sites subject to strong quadrupolar coupling interactions, thereby overcoming limitations encountered with more traditional high-field solid-state NMR approaches and pure NQR approaches. Such limitations include (i) insufficiently high applied magnetic fields to overcome the strong quadrupolar interactions (~GHz) in the case of solid-state NMR and (ii) a lack of generally available broadbanded instrumentation to record the high-frequency pure NQR resonances of spin-5/2 nuclei such as ^{127}I. When paired with exact spectral simulations employing a diagonalization of the Zeeman-quadrupolar Hamiltonian, the method was shown to provide easy access to spectra for sites featuring ^{127}I quadrupolar coupling constants of up to 2.3 GHz, far beyond what is accessible using solid-state NMR approaches even in the highest available applied magnetic fields. These advances may find application to a range of chemical problems where the spectroscopy of strongly quadrupolar systems currently presents challenges, including e.g., in the study of perovskites and related energy materials.[49,50]

The ^{127}I and ^{79}Br quadrupolar coupling constants and asymmetry parameters measured for three series of halogen-bonded cocrystals have been shown to correlate with various geometrical and structural features associated with the halogen bond, including halogen bond length. The correlations established are comparable to those reported previously on the basis of NMR studies of more remote probe nuclei.[30,39,98] The ^{127}I and ^{79}Br quadrupolar coupling data have also been shown to correlate linearly with ZORA relativistic computations of the halogen bond interaction energies, at least over the ranges covered by our data set. It is therefore concluded that experimental measurements of quadrupolar coupling constants in these systems may be taken as a proxy for halogen bond strength. To be clear, this does not imply a one-to-one correspondence between a measured quadrupolar coupling constant and a bond strength. For example, the relationships uncovered are a function of the identity of the halogen bond donor molecule, each of which has its own baseline quadrupolar coupling constant.

These findings lay the groundwork for future studies involving the measurement of interaction energies in other solid cocrystals and salt cocrystals featuring a range of noncovalent interactions involving spins subject to strong quadrupolar interactions, including e.g., halogen bonds,[99] pnictogen bonds,[100,101] and matere bonds.[102]

4. EXPERIMENTAL SECTION

4.1. Sample Preparation. 1,4-Diiodotetrafluorobenzene (*p*-DITFB, **A**) and 1,4-dibromotetrafluorobenzene (*p*-DBTFB, **C**) were purchased from Sigma-Aldrich, and 1,3,5-trifluoro-2,4,6-triiodobenzene (*sym*-TFTIB, **B**) was purchased from SynQuest Laboratories. The halogen bond acceptors 2-hydroxypyridine (**1**; note that the tautomeric form 2-pyridone is observed in the cocrystals), triphenylphosphine oxide (**2**), 3-nitropyridine (**3**), phenazine (**9**), 2,3,5,6-tetramethylpyrazine (**10**), acetamide (**4**), piperazine (**5**), 2,2′-bipyridine (**7**), and acridine (**11**), were all purchased from Sigma-Aldrich. Methyldiphenylphosphine oxide (**6**), 1,2-di(4-pyridyl)ethane (**8**), and 4-(dimethylamino)pyridine (**12**) were purchased from ChemCruz, TCI, and Merck, respectively.

Halogen-bonded cocrystals were synthesized mechanochemically, following the method outlined in other work.[103] In brief, equimolar amounts of the halogen bond donor and acceptor were weighed and placed in a 10 mL stainless-steel milling jar containing two stainless steel balls (5.0 mm diameter). The mixture was milled using a benchtop ball mill (Retsch MM 400). Some cocrystals were prepared using liquid-assisted grinding (LAG), where a small quantity of liquid (0.03 to 0.1 μL/mg of the solvents listed in Table S4) was added to facilitate cocrystal formation. Detailed milling conditions and the type and amount of liquid used for each cocrystal are provided in Table S4 in the Supporting Information.

4.2. NQR and Zp-NQR Experiments. The pure NQR experiments were carried out using the proton channel of a Bruker AVANCE III 400 MHz NMR spectrometer. A one-channel home-built NQR probe consisting of a 7 mm (inner) diameter solenoid coil was employed, and all samples were packed into 7 mm outer diameter glass tubes before being placed inside the RF coil of the probe. The NQR spectra were recorded using a Hahn-echo pulse sequence, with $\pi/2$ and π pulse lengths of 4 and 8 μs, respectively. Depending on the signal-to-noise ratio, either 256 or 512 transients were averaged, with a recycle delay of 0.25 s. To locate the NQR frequencies, the RF frequency was incremented in steps of 150 kHz. The pure NQR frequencies of the second bromine isotope, ^{81}Br, for compound **C** and

https://doi.org/10.1021/jacs.4c17321
J. Am. Chem. Soc. 2025, 147, 9528−9543

its series of XB cocrystals were obtained using an autotuning tabletop probe (with a tuning range of 30−300 MHz) interfaced with a Scout LF1 benchtop NMR/NQR console (NMR Service GmbH, Germany) and are listed in Table S2 in the Supporting Information.

For the Zp-NQR experiments, the home-built probe was positioned between the poles of a Bruker EMXplus EPR electromagnet, which introduced a weak, adjustable magnetic field to perturb the pure NQR transitions. The EPR resonator and microwave guide were left unconnected, and the microwave bridge remained off during the experiment. The applied magnetic field ranged from 20 to 40 mT, depending on the specific sample requirements. Each Zp-NQR spectrum was collected using the variable offset cumulative spectrum (VOCS) method,[104] where multiple subspectra were combined to produce the final spectral envelope. The number of subspectra varied from 15 to 37 (see Supporting Information, Table S3), with VOCS frequency steps of 50 kHz. The Hahn-echo pulse sequence was employed with pulse lengths between 3 and 7 μs, adjusted based on the frequency range of each sample. Further technical details regarding the optimization of this experimental setup will be described in a forthcoming publication. The resulting Zp-NQR spectra were fitted using exact spectral simulations performed with the QUEST software,[69] allowing for the precise extraction of quadrupolar parameters.

4.3. Density Functional Theory Calculations. DFT calculations of EFG tensors and interaction energies were performed using the Amsterdam Density Functional (ADF) 2019 package.[105,106] The calculations were carried out with the PBE0 hybrid functional and the triple-ζ doubly polarized (TZ2P) basis set. Interaction energies were computed using the counterpoise method to correct for basis set superposition error (BSSE) implemented in the ADF 2019 package, ensuring accurate energy values for the halogen-bonded systems. The zeroth-order regular approximation (ZORA) spin−orbit (in case of the EFG tensor calculations) and scalar (in case of the interaction energy calculations) relativistic method was employed to account for relativistic effects,[107] and dispersion corrections were applied using Grimme's D4 dispersion model.[108]

All coordinates were taken from available crystallographic information files (cifs). The geometries were optimized employing the PBE0 functional in combination with the TZ2P basis set. The ADF package was also used to analyze the electronic structure and bonding characteristics, with natural localized molecular orbital (NLMO) analyses performed through the adfnbo interface. This interface links to NBO version 5.0, enabling detailed insights into the electronic environment surrounding the quadrupolar nuclei.

Nuclear quadrupole moments were taken from Pyykkö as follows: −688.22 mb for ^{127}I and +308.7 mb for ^{79}Br.[109] Sternheimer antishielding factors $1 - \gamma_\infty$ of 163 and 81 for iodine and bromine, respectively, were used.[74]

■ ASSOCIATED CONTENT

Supporting Information

The Supporting Information is available free of charge at https://pubs.acs.org/doi/10.1021/jacs.4c17321.

Powder X-ray diffractograms. Additional Zp-NQR spectra and frequency tables. Results of DFT calculations and orbital analyses. Mechanochemical syntheses (PDF)

■ AUTHOR INFORMATION

Corresponding Author

David L. Bryce − *Department of Chemistry and Biomolecular Sciences, Centre for Catalysis Research and Innovation, and Nexus for Quantum Technologies, University of Ottawa, Ottawa, Ontario K1N6N5, Canada;* orcid.org/0000-0001-9989-796X; Phone: 613-562-5800; Email: dbryce@uottawa.ca

Authors

Alireza Nari − *Department of Chemistry and Biomolecular Sciences, Centre for Catalysis Research and Innovation, University of Ottawa, Ottawa, Ontario K1N6N5, Canada*

Mubassira Rahman − *Department of Chemistry and Biomolecular Sciences, Centre for Catalysis Research and Innovation, University of Ottawa, Ottawa, Ontario K1N6N5, Canada*

Patrick M. J. Szell − *Department of Chemistry and Biomolecular Sciences, Centre for Catalysis Research and Innovation, University of Ottawa, Ottawa, Ontario K1N6N5, Canada*

Volodymyr Semeniuchenko − *Department of Chemistry and Biomolecular Sciences, Centre for Catalysis Research and Innovation, University of Ottawa, Ottawa, Ontario K1N6N5, Canada*

Complete contact information is available at: https://pubs.acs.org/10.1021/jacs.4c17321

Notes

The authors declare no competing financial interest.

■ ACKNOWLEDGMENTS

We are grateful to the solid-state NMR group at the University of Ottawa for helpful feedback and discussions. D.L.B. thanks the Natural Sciences and Engineering Research Council of Canada for funding. This research was enabled in part by support provided by Compute Ontario (computeontario.ca) and the Digital Research Alliance of Canada (alliancecan.ca). The authors thank anonymous referees for their meticulous and constructive review of our manuscript.

■ REFERENCES

(1) Cavallo, G.; Metrangolo, P.; Milani, R.; Pilati, T.; Priimagi, A.; Resnati, G.; Terraneo, G. The Halogen Bond. *Chem. Rev.* **2016**, *116* (4), 2478−2601.

(2) Politzer, P.; Murray, J. S.; Clark, T. Halogen Bonding and Other σ-Hole Interactions: A Perspective. *Phys. Chem. Chem. Phys.* **2013**, *15* (27), 11178−11189.

(3) Gilday, L. C.; Robinson, S. W.; Barendt, T. A.; Langton, M. J.; Mullaney, B. R.; Beer, P. D. Halogen Bonding in Supramolecular Chemistry. *Chem. Rev.* **2015**, *115* (15), 7118−7195.

(4) Politzer, P.; Lane, P.; Concha, M. C.; Ma, Y.; Murray, J. S. An Overview of Halogen Bonding. *J. Mol. Model.* **2007**, *13* (2), 305−311.

(5) Clark, T.; Hennemann, M.; Murray, J. S.; Politzer, P. Halogen Bonding: The σ-Hole. *J. Mol. Model.* **2007**, *13* (2), 291−296.

(6) Desiraju, G. R.; Ho, P. S.; Kloo, L.; Legon, A. C.; Marquardt, R.; Metrangolo, P.; Politzer, P.; Resnati, G.; Rissanen, K. Definition of the Halogen Bond (IUPAC Recommendations 2013). *Pure Appl. Chem.* **2013**, *85* (8), 1711−1713.

(7) Catalano, L.; Pérez-Estrada, S.; Terraneo, G.; Pilati, T.; Resnati, G.; Metrangolo, P.; Garcia-Garibay, M. A. Dynamic Characterization of Crystalline Supramolecular Rotors Assembled through Halogen Bonding. *J. Am. Chem. Soc.* **2015**, *137* (49), 15386−15389.

(8) Molina, P.; Zapata, F.; Caballero, A. Anion Recognition Strategies Based on Combined Noncovalent Interactions. *Chem. Rev.* **2017**, *117* (15), 9907−9972.

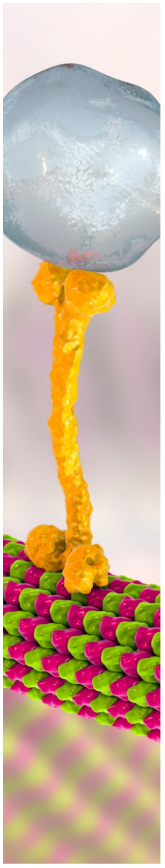
(9) Ravi, A.; Oshchepkov, A. S.; German, K. E.; Kirakosyan, G. A.; Safonov, A. V.; Khrustalev, V. N.; Kataev, E. A. Finding a Receptor Design for Selective Recognition of Perrhenate and Pertechnetate: Hydrogen vs. Halogen Bonding. *Chem. Commun.* **2018**, *54* (38), 4826−4829.

(10) Scholfield, M. R.; Zanden, C. M. V.; Carter, M.; Ho, P. S. Halogen Bonding (X-bonding): A Biological Perspective. *Protein Sci.* **2013**, *22* (2), 139−152.

(11) Valadares, N. F.; Salum, L. B.; Polikarpov, I.; Andricopulo, A. D.; Garratt, R. C. Role of Halogen Bonds in Thyroid Hormone Receptor Selectivity: Pharmacophore-Based 3D-QSSR Studies. *J. Chem. Inf. Model.* **2009**, *49* (11), 2606−2616.
(12) Gliese, J.-P.; Jungbauer, S. H.; Huber, S. M. A Halogen-Bonding-Catalyzed Michael Addition Reaction. *Chem. Commun.* **2017**, *53* (88), 12052−12055.
(13) Carreras, L.; Serrano-Torné, M.; van Leeuwen, P. W. N. M.; Vidal-Ferran, A. XBphos-Rh: A Halogen-Bond Assembled Supramolecular Catalyst. *Chem. Sci.* **2018**, *9* (15), 3644−3648.
(14) Wilcken, R.; Zimmermann, M. O.; Lange, A.; Joerger, A. C.; Boeckler, F. M. Principles and Applications of Halogen Bonding in Medicinal Chemistry and Chemical Biology. *J. Med. Chem.* **2013**, *56* (4), 1363−1388.
(15) Lu, Y.; Liu, Y.; Xu, Z.; Li, H.; Liu, H.; Zhu, W. Halogen Bonding for Rational Drug Design and New Drug Discovery. *Expert Opin. Drug Discovery* **2012**, *7* (5), 375−383.
(16) Parisini, E.; Metrangolo, P.; Pilati, T.; Resnati, G.; Terraneo, G. Halogen Bonding in Halocarbon−Protein Complexes: A Structural Survey. *Chem. Soc. Rev.* **2011**, *40* (5), 2267−2278.
(17) Sirimulla, S.; Bailey, J. B.; Vegesna, R.; Narayan, M. Halogen Interactions in Protein−Ligand Complexes: Implications of Halogen Bonding for Rational Drug Design. *J. Chem. Inf. Model.* **2013**, *53* (11), 2781−2791.
(18) Poznański, J.; Winiewska, M.; Czapinska, H.; Poznańska, A.; Shugar, D. Halogen Bonds Involved in Binding of Halogenated Ligands by Protein Kinases. *Acta Biochim. Polym.* **2016**, *63* (2), 203−214.
(19) Metrangolo, P.; Panzeri, W.; Recupero, F.; Resnati, G. Perfluorocarbon−Hydrocarbon Self-Assembly: Part 16. ^{19}F NMR Study of the Halogen Bonding between Halo-Perfluorocarbons and Heteroatom Containing Hydrocarbons. *J. Fluorine Chem.* **2002**, *114* (1), 27−33.
(20) Sarwar, M. G.; Dragisic, B.; Salsberg, L. J.; Gouliaras, C.; Taylor, M. S. Thermodynamics of Halogen Bonding in Solution: Substituent, Structural, and Solvent Effects. *J. Am. Chem. Soc.* **2010**, *132*, 1646−1653.
(21) Walter, S. M.; Kniep, F.; Rout, L.; Schmidtchen, F. P.; Herdtweck, E.; Huber, S. M. Isothermal Calorimetric Titrations on Charge-Assisted Halogen Bonds: Role of Entropy, Counterions, Solvent, and Temperature. *J. Am. Chem. Soc.* **2012**, *134* (20), 8507−8512.
(22) Oliveira, V.; Kraka, E.; Cremer, D. Quantitative Assessment of Halogen Bonding Utilizing Vibrational Spectroscopy. *Inorg. Chem.* **2017**, *56* (1), 488−502.
(23) Niemann, R. G.; Kontos, A. G.; Palles, D.; Kamitsos, E. I.; Kaltzoglou, A.; Brivio, F.; Falaras, P.; Cameron, P. J. Halogen Effects on Ordering and Bonding of $CH_3NH_3^+$ in $CH_3NH_3PbX_3$ (X = Cl, Br, I) Hybrid Perovskites: A Vibrational Spectroscopic Study. *J. Phys. Chem. C* **2016**, *120* (5), 2509−2519.
(24) Gavezzotti, A. Comparing the Strength of Covalent Bonds, Intermolecular Hydrogen Bonds and Other Intermolecular Interactions for Organic Molecules: X-Ray Diffraction Data and Quantum Chemical Calculations. *New J. Chem.* **2016**, *40* (8), 6848−6853.
(25) McKinnon, J. J.; Jayatilaka, D.; Spackman, M. A. Towards Quantitative Analysis of Intermolecular Interactions with Hirshfeld Surfaces. *Chem. Commun.* **2007**, No. 37, 3814−3816.
(26) Xu, Y.; Szell, P. M. J.; Kumar, V.; Bryce, D. L. Solid-State NMR Spectroscopy for the Analysis of Element-Based Non-Covalent Interactions. *Coord. Chem. Rev.* **2020**, *411*, 213237.
(27) Vioglio, P. C.; Catalano, L.; Vasylyeva, V.; Nervi, C.; Chierotti, M. R.; Resnati, G.; Gobetto, R.; Metrangolo, P. Natural Abundance ^{15}N and ^{13}C Solid-State NMR Chemical Shifts: High Sensitivity Probes of the Halogen Bond Geometry. *Chem.—Eur. J.* **2016**, *22* (47), 16819−16828.
(28) Szell, P. M. J.; Gabriel, S. A.; Gill, R. D. D.; Wan, S. Y. H.; Gabidullin, B.; Bryce, D. L. ^{13}C and ^{19}F Solid-State NMR and X-Ray Crystallographic Study of Halogen-Bonded Frameworks Featuring Nitrogen-Containing Heterocycles. *Acta Crystallogr., Sect. C:Struct. Chem.* **2017**, *73*, 157−167.
(29) Szell, P. M. J.; Gabriel, S. A.; Caron-Poulin, E.; Jeannin, O.; Fourmigué, M.; Bryce, D. L. Cosublimation: A Rapid Route toward Otherwise Inaccessible Halogen-Bonded Architectures. *Cryst. Growth Des.* **2018**, *18* (10), 6227−6238.
(30) Viger-Gravel, J.; Leclerc, S.; Korobkov, I.; Bryce, D. L. Correlation between ^{13}C Chemical Shifts and the Halogen Bonding Environment in a Series of Solid Para-Diiodotetrafluorobenzene Complexes. *CrystEngComm* **2013**, *15* (16), 3168−3177.
(31) Pound, R. V. Nuclear Electric Quadrupole Interactions in Crystals. *Phys. Rev.* **1950**, *79* (4), 685−702.
(32) Autschbach, J.; Zheng, S.; Schurko, R. W. Analysis of Electric Field Gradient Tensors at Quadrupolar Nuclei in Common Structural Motifs. *Concepts Magn. Reson., Part A* **2010**, *36A* (2), 84−126.
(33) Lucken, E. A. C. *Nuclear Quadrupole Coupling Constants*; Academic Press: New York, 1969.
(34) Szell, P. M. J.; Bryce, D. L. ^{35}Cl Solid-State NMR and Computational Study of Chlorine Halogen Bond Donors in Single-Component Crystalline Chloronitriles. *J. Phys. Chem. C* **2016**, *120* (20), 11121−11130.
(35) Segel, S.; Barnes, R. G. *Catalog of Nuclear Quadrupole Interactions and Resonance Frequencies in Solids. Part I*; Elements And Inorganic Compounds; Ames Lab.: Ames, IA (United States), 1968.
(36) Szell, P. M. J.; Bryce, D. L. Solid-State Nuclear Magnetic Resonance and Nuclear Quadrupole Resonance as Complementary Tools to Study Quadrupolar Nuclei in Solids. *Concepts Magn. Reson., Part A* **2016**, *45A* (6), No. e21412.
(37) Perras, F. A.; Bryce, D. L. Direct Investigation of Covalently Bound Chlorine in Organic Compounds by Solid-State ^{35}Cl NMR Spectroscopy and Exact Spectral Line-Shape Simulations. *Angew. Chem., Int. Ed.* **2012**, *51* (17), 4227−4230.
(38) Nag, T.; Terskikh, V. V.; Bryce, D. L. Experimental Evidence for Non-Fermi-Contact J Coupling Across Chalcogen Bonds in Ionic Salt Cocrystal Polymorphs. *Angew. Chem., Int. Ed.* **2024**, *63* (21), No. e202402441.
(39) Viger-Gravel, J.; Leclerc, S.; Korobkov, I.; Bryce, D. L. Direct Investigation of Halogen Bonds by Solid-State Multinuclear Magnetic Resonance Spectroscopy and Molecular Orbital Analysis. *J. Am. Chem. Soc.* **2014**, *136* (19), 6929−6942.
(40) Aakeröy, C. B.; Baldrighi, M.; Desper, J.; Metrangolo, P.; Resnati, G. Supramolecular Hierarchy among Halogen-Bond Donors. *Chem.—Eur. J.* **2013**, *19*, 16240−16247.
(41) Troff, R. W.; Mäkelä, T.; Topić, F.; Valkonen, A.; Raatikainen, K.; Rissanen, K. Alternative Motifs for Halogen Bonding. *Eur. J. Org Chem.* **2013**, *2013*, 1617−1637.
(42) Vioglio, P. C.; Szell, P. M. J.; Chierotti, M. R.; Gobetto, R.; Bryce, D. L. $^{79/81}$Br Nuclear Quadrupole Resonance Spectroscopic Characterization of Halogen Bonds in Supramolecular Assemblies. *Chem. Sci.* **2018**, *9* (20), 4555−4561.
(43) Szell, P. M. J.; Grébert, L.; Bryce, D. L. Rapid Identification of Halogen Bonds in Cocrystalline Powders via ^{127}I Nuclear Quadrupole Resonance Spectroscopy. *Angew. Chem., Int. Ed.* **2019**, *58*, 13479−13485.
(44) Pang, L.; Lucken, E. A. C.; Bernardinelli, G. The Application of Nuclear Quadrupole Resonance to the Study of Clathrates. Chlorine-35 NQR and Crystallography of Clathrated Carbon Tetrachloride. *J. Am. Chem. Soc.* **1990**, *112* (24), 8754−8764.
(45) Mali, M.; Brinkmann, D.; Pauli, L.; Roos, J.; Zimmermann, H.; Hulliger, J. Cu and Y NQR and NMR in the Superconductor $YBa_2Cu_3O_7$-δ. *Phys. Lett. A* **1987**, *124* (1−2), 112−116.
(46) Henshaw, J.; Kehayias, P.; Ziabari, M. S.; Titze, M.; Morissette, E.; Watanabe, K.; Taniguchi, T.; Li, J. I. A.; Acosta, V. M.; Bielejec, E. S.; Lilly, M. P.; Mounce, A. M. Nanoscale Solid-State Nuclear Quadrupole Resonance Spectroscopy Using Depth-Optimized Nitrogen-Vacancy Ensembles in Diamond. *Appl. Phys. Lett.* **2022**, *120* (17), 174002.

(47) Hooper, R. W.; Lin, K.; Veinot, J. G. C.; Michaelis, V. K. 3D to 0D cesium lead bromide: A $^{79/81}$Br NMR, NQR and theoretical investigation. *J. Magn. Reson.* **2023**, *352*, 107472.
(48) Senocrate, A.; Moudrakovski, I.; Maier, J. Short-range ion dynamics in methylammonium lead iodide by multinuclear solid state NMR and ^{127}I NQR. *Phys. Chem. Chem. Phys.* **2018**, *20*, 20043−20055.
(49) Piveteau, L.; Morad, V.; Kovalenko, M. V. Solid-State NMR and NQR Spectroscopy of Lead-Halide Perovskite Materials. *J. Am. Chem. Soc.* **2020**, *142*, 19413−19437.
(50) Doherty, T. A. S.; Nagane, S.; Kubicki, D. J.; Jung, Y.-K.; Johnstone, D. N.; Iqbal, A. N.; Guo, D.; Frohna, K.; Danaie, M.; Tennyson, E. M.; Macpherson, S.; Abfalterer, A.; Anaya, M.; Chiang, Y.-H.; Crout, P.; Ruggeri, F. S.; Collins, S. M.; Grey, C. P.; Walsh, A.; Midgley, P. A.; Stranks, S. D. Stabilized Tilted-Octahedra Halide Perovskites Inhibit Local Formation Of Performance-Limiting Phases. *Science* **2021**, *374*, 1598−1605.
(51) Aebli, M.; Porenta, N.; Aregger, N.; Kovalenko, M. V. Local Structure of Multinary Hybrid Lead Halide Perovskites Investigated by Nuclear Quadrupole Resonance Spectroscopy. *Chem. Mater.* **2021**, *33*, 6965−6973.
(52) Piveteau, L.; Aebli, M.; Yazdani, N.; Millen, M.; Korosec, L.; Krieg, F.; Benin, B. M.; Morad, V.; Piveteau, C.; Shiroka, T.; Comas-Vives, A.; Copéret, C.; Lindenberg, A. M.; Wood, V.; Verel, R.; Kovalenko, M. V. Bulk and Nanocrystalline Cesium Lead-Halide Perovskites as Seen by Halide Magnetic Resonance. *ACS Cent. Sci.* **2020**, *6*, 1138−1149.
(53) Mozur, E. M.; Hope, M. A.; Trowbridge, J. C.; Halat, D. M.; Daemen, L. L.; Maughan, A. E.; Prisk, T. R.; Grey, C. P.; Neilson, J. R. Cesium Substitution Disrupts Concerted Cation Dynamics in Formamidinium Hybrid Perovskites. *Chem. Mater.* **2020**, *32*, 6266−6277.
(54) Fabini, D. H.; Honasoge, K.; Cohen, A.; Bette, S.; McCall, K. M.; Stoumpos, C. C.; Klenner, S.; Zipkat, M.; Hoang, L. P.; Nuss, J.; Kremer, R. K.; Kanatzidis, M. G.; Yaffe, O.; Kaiser, S.; Lotsch, B. V. Noncollinear Electric Dipoles in a Polar Chiral Phase of $CsSnBr_3$ Perovskite. *J. Am. Chem. Soc.* **2024**, *146*, 15701−15717.
(55) Wren, S. A. C.; Szell, P. M. J. Nuclear Quadrupole Resonance Spectroscopy in Pharmaceuticals. In *Magnetic Resonance and its Applications in Drug Formulation and Delivery*; Mantle, M. D., Hughes, L. P., Eds.; Royal Society of Chemistry, 2024; Vol. *33*, pp 149−178.
(56) Pérez, S. C.; Cerioni, L.; Wolfenson, A.; Faudone, S.; Cuffini, S. Utilization of Pure Nuclear Quadrupole Resonance Spectroscopy for the Study of Pharmaceutical Crystal Forms. *Int. J. Pharm.* **2005**, *298* (1), 143−152.
(57) Barras, J.; Murnane, D.; Althoefer, K.; Assi, S.; Rowe, M. D.; Poplett, I. J. F.; Kyriakidou, G.; Smith, J. A. S. Nitrogen-14 Nuclear Quadrupole Resonance Spectroscopy: A Promising Analytical Methodology for Medicines Authentication and Counterfeit Anti-malarial Analysis. *Anal. Chem.* **2013**, *85* (5), 2746−2753.
(58) Balchin, E.; Malcolme-Lawes, D. J.; Poplett, I. J. F.; Rowe, M. D.; Smith, J. A. S.; Pearce, G. E. S.; Wren, S. A. C. Potential of Nuclear Quadrupole Resonance in Pharmaceutical Analysis. *Anal. Chem.* **2005**, *77* (13), 3925−3930.
(59) Apih, T.; Žagar, V.; Seliger, J. NMR and NQR Study of Polymorphism in Carbamazepine. *Solid State Nucl. Magn. Reson.* **2020**, *107*, 101653.
(60) Morino, Y.; Toyama, M. Zeeman Effect of the Nuclear Quadrupole Resonance Spectrum in Crystalline Powder. *J. Chem. Phys.* **1961**, *35* (4), 1289−1296.
(61) Ramaprabhu, S.; Rao, K. V. S. R. Powder Zeeman Study of the Nuclear Quadrupole Resonance Lower Transition Spectrum for I = 5/2; Application to Orthoperiodic Acid. *Z. Naturforsch.* **1985**, *40* (2), 112−115.
(62) Dehmelt, H. G. Quadrupol-Resonanzfrequenzen von J127-Kernen in Kristallinen Kovalenten Jodverbindungen. *Z. Phys.* **1951**, *130* (3), 356−370.
(63) Morino, Y.; Chiba, T.; Shimozawa, T.; Toyama, M. Zeeman Effect of Nuclear Quadrupole Resonance Spectrum in Cyanuryl Chloride. *J. Phys. Soc. Jpn.* **1958**, *13*, 869−879.
(64) Meal, H. C. Zeeman Quadrupole Spectra of p-Chloroaniline and p-Chlorobenzylchloride. *J. Chem. Phys.* **1956**, *24*, 1011−1017.
(65) Kojima, S.; Tsukada, K.; Shimauchi, A.; Hinaga, Y. Zeeman splitting of nuclear quadrupole resonance line of bromine. *J. Phys. Soc. Jpn.* **1954**, *9*, 795−801.
(66) Raman, K. V. Asymmetry parameter studies for systems containing the ^{35}Cl nucleus from Zeeman NQR data. *J. Mol. Struct.* **1995**, *345*, 31−47.
(67) Livingston, R.; Zeldes, H. Zeeman Effect on the Quadrupole Spectrum of Iodic Acid. *J. Chem. Phys.* **1957**, *26* (2), 351−358.
(68) Toyama, M. Relative Intensities of Zeeman Components in Nuclear Quadrupole Resonance Spectrum. *J. Phys. Soc. Jpn.* **1959**, *14* (12), 1727−1738.
(69) Perras, F. A.; Widdifield, C. M.; Bryce, D. L. QUEST—QUadrupolar Exact SofTware: A Fast Graphical Program for the Exact Simulation of NMR and NQR Spectra for Quadrupolar Nuclei. *Solid State Nucl. Magn. Reson.* **2012**, *45*−*46*, 36−44.
(70) Widdifield, C. M.; Bryce, D. L. Solid-State ^{127}I NMR and GIPAW DFT Study of Metal Iodides and Their Hydrates: Structure, Symmetry, and Higher-Order Quadrupole-Induced Effects. *J. Phys. Chem. A* **2010**, *114* (40), 10810−10823.
(71) Sternheimer, R. On Nuclear Quadrupole Moments. *Phys. Rev.* **1950**, *80* (1), 102.
(72) Sternheimer, R. On Nuclear Quadrupole Moments. *Phys. Rev.* **1951**, *84* (2), 244.
(73) Wu, G.; Terskikh, V. A Multinuclear Solid-State NMR Study of Alkali Metal Ions in Tetraphenylborate Salts, $M[BPh_4]$ (M = Na, K, Rb and Cs): What Is the NMR Signature of Cation−π Interactions? *J. Phys. Chem. A* **2008**, *112* (41), 10359−10364.
(74) Bryce, D. L.; Widdifield, C. M.; Chapman, R. P.; Attrell, R. J. *Chlorine, Bromine, and Iodine Solid-State NMR*; eMagRes, 2011.
(75) Cavallo, G.; Metrangolo, P.; Pilati, T.; Resnati, G.; Sansotera, M.; Terraneo, G. Halogen Bonding: A General Route in Anion Recognition and Coordination. *Chem. Soc. Rev.* **2010**, *39*, 3772−3783.
(76) Wang, W.; Zhang, Y.; Ji, B.; Tian, A. On the correlation between bond-length change and vibrational frequency shift in halogen-bonded complexes. *J. Chem. Phys.* **2011**, *134*, 224303.
(77) Kaupp, M.; Danovich, D.; Shaik, S. Chemistry is About Energy and its Changes: A Critique of Bond-Length/Bond-Strength Correlations. *Coord. Chem. Rev.* **2017**, *344*, 355−362.
(78) Cremer, D.; Wu, A.; Larsson, A.; Kraka, E. Some Thoughts about Bond Energies, Bond Lengths, and Force Constants. *Mol. Model. Annu.* **2000**, *6*, 396−412.
(79) Cremer, D.; Kraka, E. From Molecular Vibrations to Bonding, Chemical Reactions, and Reaction Mechanism. *Curr. Org. Chem.* **2010**, *14* (15), 1524−1560.
(80) Lachenbruch, P. A.; Mickey, M. R. Estimation of Error Rates in Discriminant Analysis. *Technometrics* **1968**, *10* (1), 1−11.
(81) Aubert, E.; Espinosa, E.; Nicolas, I.; Jeannin, O.; Fourmigué, M. Toward a Reverse Hierarchy of Halogen Bonding between Bromine and Iodine. *Faraday Discuss.* **2017**, *203*, 389−406.
(82) Alkorta, I.; Elguero, J.; Yáñez, M.; Mó, O.; Montero-Campillo, M. M. Relativistic Effects on NMR Parameters of Halogen-Bonded Complexes. *Molecules* **2019**, *24* (23), 4399.
(83) Widdifield, C. M.; Bryce, D. L. Crystallographic structure refinement with quadrupolar nuclei: a combined solid-state NMR and GIPAW DFT example using $MgBr_2$. *Phys. Chem. Chem. Phys.* **2009**, *11*, 7120−7122.
(84) Lambert, E. C.; Williams, A. E.; Fortenberry, R. C.; Hammer, N. I. Probing Halogen Bonding Interactions between Heptafluoro-2-Iodopropane and Three Azabenzenes with Raman Spectroscopy and Density Functional Theory. *Phys. Chem. Chem. Phys.* **2022**, *24* (19), 11713−11720.
(85) Scheiner, S.; Hunter, S. Influence of Substituents in the Benzene Ring on the Halogen Bond of Iodobenzene with Ammonia. *ChemPhysChem* **2022**, *23* (6), No. e202200011.

(86) Michalczyk, M.; Kizior, B.; Zierkiewicz, W.; Scheiner, S. Factors Contributing to Halogen Bond Strength and Stretch or Contraction of Internal Covalent Bond. *Phys. Chem. Chem. Phys.* **2023**, *25* (4), 2907−2915.
(87) Angarov, V.; Kozuch, S. On the σ, π and δ Hole Interactions: A Molecular Orbital Overview. *New J. Chem.* **2018**, *42* (2), 1413−1422.
(88) Wolters, L. P.; Schyman, P.; Pavan, M. J.; Jorgensen, W. L.; Bickelhaupt, F. M.; Kozuch, S. The Many Faces of Halogen Bonding: A Review of Theoretical Models and Methods. *Wiley Interdiscip. Rev. Comput. Mol. Sci.* **2014**, *4* (6), 523−540.
(89) Choudhary, K.; Ansari, J. N.; Mazin, I. I.; Sauer, K. L. Density Functional Theory-Based Electric Field Gradient Database. *Sci. Data* **2020**, *7* (1), 362.
(90) Reina, J. V.; Civaia, F.; Harper, A. F.; Scheurer, C.; Köcher, S. S. The EFG Rosetta Stone: Translating between DFT Calculations and Solid State NMR Experiments. *Faraday Discuss.* **2025**, *255*, 266−287.
(91) Clark, T. σ-Holes. *Wiley Interdiscip. Rev. Comput. Mol. Sci.* **2013**, *3* (1), 13−20.
(92) Ziegler, T.; Rauk, A. A Theoretical Study of the Ethylene-Metal Bond in Complexes between Copper(1+), Silver(1+), Gold(1+), Platinum(0) or Platinum(2+) and Ethylene, Based on the Hartree-Fock-Slater Transition-State Method. *Inorg. Chem.* **1979**, *18* (6), 1558−1565.
(93) Oh, S. Y.; Nickels, C. W.; Garcia, F.; Jones, W.; Friščić, T. Switching between Halogen- and Hydrogen-Bonding in Stoichiometric Variations of a Cocrystal of a Phosphine Oxide. *CrystEngComm* **2012**, *14* (19), 6110−6114.
(94) Takemura, A.; McAllister, L. J.; Hart, S.; Pridmore, N. E.; Karadakov, P. B.; Whitwood, A. C.; Bruce, D. W. Halogen- and Hydrogen-Bonded Salts and Co-Crystals Formed from 4-Halo-2,3,5,6-Tetrafluorophenol and Cyclic Secondary and Tertiary Amines: Orthogonal and Non-Orthogonal Halogen and Hydrogen Bonding, and Synthetic Analogues of Halogen-Bonded Biological Systems. *Chem.—Eur. J.* **2014**, *20* (22), 6721−6732.
(95) AMS GUI 2024.1, SCM, Amsterdam, The Netherlands. http://www.scm.com (accessed Feb 21, 2025).
(96) O'Dell, L. A.; Schurko, R. W.; Harris, K. J.; Autschbach, J.; Ratcliffe, C. I. Interaction Tensors and Local Dynamics in Common Structural Motifs of Nitrogen: A Solid-State ^{14}N NMR and DFT Study. *J. Am. Chem. Soc.* **2011**, *133* (3), 527−546.
(97) Xu, Y.; Gabidullin, B.; Bryce, D. L. Single-Crystal NMR Characterization of Halogen Bonds. *J. Phys. Chem. A* **2019**, *123*, 6194−6209.
(98) Viger-Gravel, J.; Meyer, J. E.; Korobkov, I.; Bryce, D. L. Probing Halogen Bonds With Solid-State NMR Spectroscopy: Observation And Interpretation Of J(^{77}Se,^{31}P) Coupling In Halogen-Bonded P = Se···I Motifs. *CrystEngComm* **2014**, *16*, 7285−7297.
(99) Griffin, L. P.; Streit, T.-N.; Sievers, R.; Aldridge, S.; Gomila, R. M.; Frontera, A.; Malischewski, M. Crystallographic Evidence for Bi(I) as the Heaviest Halogen Bond Acceptor. *J. Am. Chem. Soc.* **2024**, *146*, 29877−29882.
(100) Leroy, C.; Johannson, R.; Bryce, D. L. $^{121/123}$Sb Nuclear Quadrupole Resonance Spectroscopy: Characterization of Non-Covalent Pnictogen Bonds and NQR Crystallography. *J. Phys. Chem. A* **2019**, *123*, 1030−1043.
(101) Scilabra, P.; Terraneo, G.; Daolio, A.; Baggioli, A.; Famulari, A.; Leroy, C.; Bryce, D. L.; Resnati, G. 4,4'-Dipyridyl dioxide•SbF_3 Co-crystal: Pnictogen Bond Prevails over Halogen and Hydrogen Bonds in Driving Self-Assembly. *Cryst. Growth Des.* **2020**, *20*, 916−922.
(102) Xu, Y.; Calabrese, M.; Demitri, N.; Pizzi, A.; Nag, T.; Hung, I.; Gan, Z.; Resnati, G.; Bryce, D. L. Non-Covalent Matere Bonds in Perrhenates Probed via Ultrahigh-Field Rhenium-185/187 NMR and Zero-Field NQR Spectroscopy. *Chem. Commun.* **2023**, *59*, 12609−12612.
(103) Nari, A.; Ovens, J. S.; Bryce, D. L. Halogen-Bonded Cocrystals via Resonant Acoustic Mixing. *RSC Mechanochem.* **2024**, *1* (1), 50−62.
(104) Massiot, D.; Farnan, I.; Gautier, N.; Trumeau, D.; Trokiner, A.; Coutures, J. P. ^{71}Ga and ^{69}Ga Nuclear Magnetic Resonance Study of β-Ga_2O_3: Resolution of Four- and Six-Fold Coordinated Ga Sites in Static Conditions. *Solid State Nucl. Magn. Reson.* **1995**, *4* (4), 241−248.
(105) van Lenthe, E.; Jan Baerends, E. Density Functional Calculations of Nuclear Quadrupole Coupling Constants in the Zero-Order Regular Approximation for Relativistic Effects. *J. Chem. Phys.* **2000**, *112* (19), 8279−8292.
(106) ADF 2019, SCM. http://www.scm.com (accessed Feb 21, 2025).
(107) Van Lenthe, E.; Ehlers, A.; Baerends, E.-J. Geometry Optimizations in the Zero Order Regular Approximation for Relativistic Effects. *J. Chem. Phys.* **1999**, *110* (18), 8943−8953.
(108) Caldeweyher, E.; Ehlert, S.; Hansen, A.; Neugebauer, H.; Spicher, S.; Bannwarth, C.; Grimme, S. A Generally Applicable Atomic-Charge Dependent London Dispersion Correction. *J. Chem. Phys.* **2019**, *150* (15), 154122.
(109) Pyykkö, P. Year-2017 Nuclear Quadrupole Moments. *Mol. Phys.* **2018**, *116*, 1328−1338.



CAS BIOFINDER DISCOVERY PLATFORM™
BRIDGE BIOLOGY AND CHEMISTRY FOR FASTER ANSWERS
Analyze target relationships, compound effects, and disease pathways
Explore the platform
CAS
A division of the American Chemical Society

https://doi.org/10.1021/jacs.4c17321
J. Am. Chem. Soc. 2025, 147, 9528−9543

Chapter 7 – Resolving Chlorine Sites in Pharmaceuticals by Integrated Site-Resolved Zeeman-Perturbed NQR, Solid-State NMR, and Electron Diffraction Crystallography

Based on: Nari, A.; Ngo-Minh Rusimovic, J.; Szell, P. M. J.; Jasil, M.; Terskikh, V.; Bryce, D. L.; Thomas, B. Resolving Chlorine Sites in Pharmaceuticals by Integrated Site-Resolved Zeeman-Perturbed NQR, Solid-State NMR, and Electron Diffraction Crystallography. (Manuscript under revision in J. Am. Chem. Soc. 2026.)

7.1 Chapter Overview and Thesis Context

The previous chapters established Zp-NQR spectroscopy as a versatile experimental platform for the structural characterization of quadrupolar nuclei in molecular solids. Beginning with the development of a practical experimental methodology (Chapter 4), the technique was subsequently shown to enable direct isotopic identification of quadrupolar resonance lines (Chapter 5) and, more importantly, to provide quantitative measurements of quadrupolar interactions that could be directly correlated with intermolecular interaction energies in halogen-bonded materials (Chapter 6). Together, these studies demonstrated that Zp-NQR extends beyond conventional NQR spectroscopy by providing complete quadrupolar interaction tensors that serve as experimentally accessible descriptors of local electronic structure.

The logical next step is to determine whether these capabilities can be extended to chemically and structurally complex materials of direct practical importance. Pharmaceutical solids provide an ideal test bed for this purpose because they frequently contain halogen atoms, structural disorder, hydration-dependent polymorphism, and microcrystalline phases that cannot

readily be characterized by conventional crystallographic methods. These factors complicate structural determination and often require several complementary analytical techniques to establish the relationship between local molecular structure and macroscopic solid-state properties.

Among pharmaceutical materials, chlorine-containing active pharmaceutical ingredients (APIs) are particularly attractive systems for investigation. Covalently bonded chlorine atoms play important roles in controlling molecular conformation, crystal packing, polymorphism, solubility, chemical stability, and biological activity. Because the quadrupolar interaction of ^{35}Cl is governed by the local EFG, chlorine nuclei provide exceptionally sensitive probes of changes in intermolecular packing, hydrogen bonding, halogen interactions, hydration, and structural disorder. Despite this intrinsic sensitivity, extracting quantitative, site-specific structural information from chlorine-containing molecular solids has remained a longstanding challenge, particularly for powdered samples containing multiple crystallographically inequivalent chlorine environments.

Traditional characterization methods each possess important limitations in addressing these problems. Powder X-ray diffraction often struggles with severe peak overlap and provides only average structural information, while single-crystal diffraction requires crystals that are frequently unavailable for pharmaceutical materials. Although high-field ^{35}Cl solid-state NMR provides access to chlorine quadrupolar interactions, the extremely broad powder patterns produced by large quadrupolar couplings frequently hinder the resolution of chemically similar sites. Likewise, 3D ED has recently emerged as a powerful technique for solving structures from nanocrystalline powders, but structural models obtained from diffraction alone may remain ambiguous in the presence of disorder, multiple conformations, or hydration-dependent transformations. These limitations motivate the development of integrated characterization strategies in which

complementary spectroscopic and crystallographic techniques collectively constrain structural models.

The work presented in this chapter extends the methodologies developed in the previous chapters to structurally complex pharmaceutical solids through an integrated characterization strategy combining cryogen-free ^{35}Cl Zp-NQR, zero-field NQR, high-field ^{35}Cl SSNMR, 3D ED, and first-principles DFT calculations. By integrating complementary spectroscopic, crystallographic, and computational techniques, this approach enables site-resolved characterization of chlorine-bearing molecular solids directly from powder samples.

The methodology is demonstrated using three representative pharmaceutical systems that highlight distinct structural challenges. Ketoconazole is investigated as a model of conformational disorder, chloramine-T illustrates the sensitivity of chlorine quadrupolar interactions to hydration-dependent structural transformations, and a series of chlorzoxazone cocrystals demonstrates the ability of the combined approach to resolve multiple crystallographically distinct chlorine environments and relate local crystal packing to experimentally measured quadrupolar parameters. Together, these case studies establish an integrated workflow for the structural characterization of chlorine-containing pharmaceutical materials and illustrate the broad applicability of Zp-NQR when combined with complementary diffraction and computational methods.

7.2. Statement of Authenticity

This work was carried out in collaboration with Jonathan Ngo-Minh Rusimovic, Patrick M. J. Szell, Mohammed Jasil, Victor Terskikh, David L. Bryce, and Brijith Thomas. I conceived and led the Zp-NQR experiments, performed the spectroscopic and computational measurements, data analysis, and interpretation, and prepared the initial manuscript draft. Contributions from the co-

authors are acknowledged throughout the manuscript and in accordance with their respective roles in the project.

7.3 Introduction

Chlorine-containing molecular solids are widespread in pharmaceutically relevant materials,[1–3] yet direct site-resolved structural characterization from powders remains challenging, especially in systems exhibiting multiple chemically or crystallographically nonequivalent sites, disorder, or hydration sensitivity. In the solid state, the ^{35}Cl quadrupole moment couples to the EFG tensors,[4–6] making chlorine NQR,[7–9] Zp-NQR[10–15] and NMR observables exceptionally sensitive to the local crystallographic and electronic environment, including intermolecular packing, hydrogen and halogen bonding interactions, and degree of hydration.[16,17] This sensitivity makes ^{35}Cl an attractive local probe of pharmaceutical solids, where subtle changes in supramolecular organization can strongly influence solid form behavior. However, translating chlorine spectral fingerprints into site resolved quantitative quadrupolar parameters (quadrupolar coupling constant and the EFG asymmetry parameter) that can function as crystallographic constraints has remained particularly challenging in structurally complex organic powders containing multiple inequivalent chlorine sites, conformational disorder, or hydration-sensitive motifs. Recent work from Bryce[18–23] and coworkers has reintroduced NQR and Zp-NQR as practical and unique approaches for studying quadrupolar nuclei with large quadrupolar coupling constants. The introduction of QUEST software[23] has further facilitated the analysis of Zp-NQR spectra, making this approach more accessible for extracting quadrupolar parameters and connecting them to local structural environments.

Routine ^{1}H and ^{13}C solution NMR is indispensable for confirming molecular identity and purity but lacks information on the solid-state electrostatic environment that governs chlorine

quadrupolar interactions.[24] Likewise, conventional ^{1}H and ^{13}C SSNMR affords only indirect access to chlorine centered structure and generally cannot map chlorine-specific signatures onto individual atoms without extensive multidimensional correlation experiments. ^{35}Cl SSNMR could address many of the above mentioned challenges; however, much of the literature has focused on ionic inorganic chlorides and related hydrochloride salts, [25,26] and selected halide ionic liquids, whose spectra are often more tractable than those of covalent organic chlorides.[20–22,27] Prior ^{35}Cl SSNMR studies of hydrochloride pharmaceuticals,[28] halogen-bonded chlorinated solids,[29] and inorganic or organometallic chlorides clearly demonstrated the structural sensitivity of chlorine quadrupolar observables. However, a general approach for the conversion of covalently-bonded chlorine observables into structural constraints, in the cases of complex molecular solids exhibiting multiple inequivalent sites, hydration sensitivity or conformational disorder is lacking.

To monitor the effect of chlorine on crystal packing and to correlate spectroscopic observables with atomistic details, we have chosen ketoconazole (KTZ), chloramine-T (CAT), and chlorzoxazone (CHZ) molecules (Figure 2.7.1). KTZ contains multiple chlorine-bearing aromatic groups within a conformationally flexible framework.[30–32] The reported crystal structure of KTZ reveals a complex solid-state organization arising from racemic superposition of the *cis*-enantiomers, which gives rise to distinct chlorine environments. These features make KTZ an ideal benchmark for assessing whether an NQR/Zp-NQR approach can directly resolve site inequivalence and disorder in powdered samples. CAT[33–35] provides a second, chemically distinct candidate that extends the methodology beyond covalent aromatic C–Cl motifs to an ionic N–Cl environment with significant sensitivity towards hydration. Finally, 5-chloro-2-benzoxazolone (chlorzoxazone, CHZ)[36] and its cocrystals provide a chemically well-controlled platform for evaluating how ^{35}Cl observables respond systematically to supramolecular packing. Unlike KTZ

and CHZ, CAT contains highly polarized chlorine bound to nitrogen within an anionic sulfonamide framework and exists in both anhydrous and trihydrate forms. Here we introduce a site-resolved chlorine spectroscopic methodology (Figure 2.7.1) built around four complementary elements: (i) zero-field ^{35}Cl NQR for rapid site counting and initial differentiation, (ii) Zp-NQR for comprehensive resonance assignment and EFG (iii) high field ^{35}Cl WURST-QCPMG SSNMR for quantitative extraction of the quadrupolar coupling constant C_Q and asymmetry parameter η from ultra-broad powder patterns, and (iv) first principles DFT calculations of EFG tensors to support site assignment and structural interpretation. For these microcrystalline pharmaceutical cocrystals which do not easily produce single crystals, our approach is complemented by 3D ED along with DFT to refine structural models. [37–40] Recent studies have shown that 3D ED can be used to successfully solve pharmaceutical crystal structures from nanocrystals and even confirm API structures directly in formulated tablets, making it an ideal crystallographic counterpart to the site-resolved chlorine spectroscopy developed herein.[41,42]

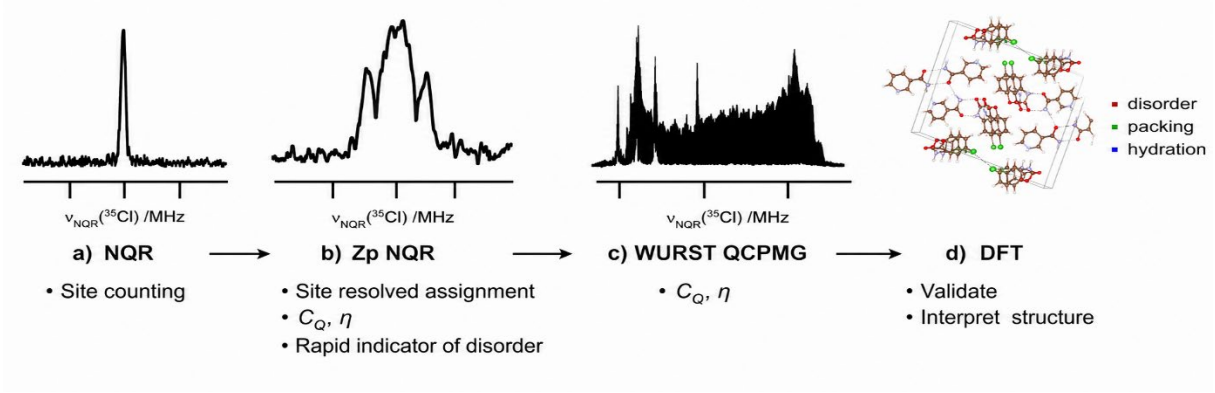


Figure 2.7.1. Site-resolved chlorine spectroscopy for pharmaceutical compounds. Pure ^{35}Cl NQR provides rapid site counting and compound-specific fingerprinting. Zp-NQR resolves near-degenerate resonances and enables extraction of C_Q and η. High-field static ^{35}Cl NMR WURST-QCPMG experiments validate the corresponding powder line shapes, while DFT EFG calculations support site assignment and enable discrimination among structural, disorder, and hydration models.

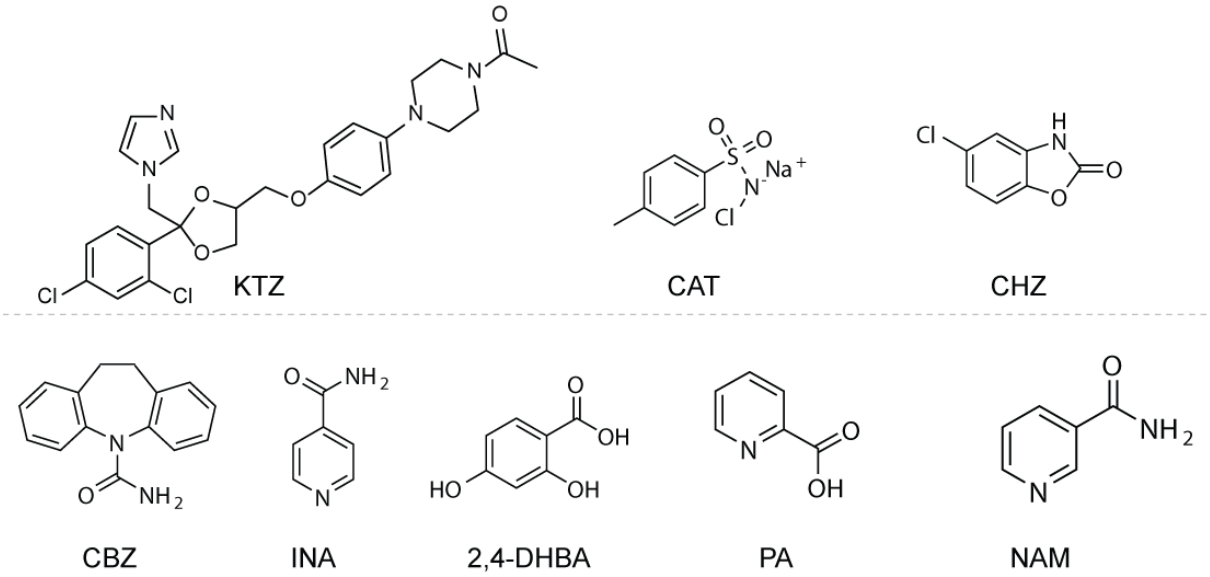


Figure 2.7.2. Molecular structures of the chlorine-containing compounds investigated in this chapter and the coformers used for pharmaceutical cocrystal preparation. *Top row:* Ketoconazole (KTZ), chloramine-T (CAT), and 5-chloro-2-benzoxazolone (CHZ), representing the three principal chlorine-containing systems examined in this work. *Bottom row:* Coformers employed for the preparation of CHZ cocrystals, including carbamazepine (CBZ), isonicotinamide (INA), 2,4-dihydroxybenzoic acid (2,4-DHB), picolinic acid (PA), and nicotinamide (NAM).

7.4 Experimental Methods

The KTZ, CAT**,** and CHZ samples were purchased from Sigma-Aldrich and used without further purification. The mechanochemistry synthesis of the cocrystal and CAT-dehydrated sample are explained in detail in the SI.

7.4.1 Powder X-ray diffraction

Powder X-ray diffraction (PXRD) data were obtained using a Bruker D8 Endeavor instrument equipped with a 1 kW Cu Kα radiation source (λ = 1.54056 Å) from a sealed tube and

a high-speed LynxEye XE-T detector. Measurements were performed at room temperature, with samples placed in a well plate and rotated at 15 RPM during data acquisition.

7.4.2 Single crystal X-ray diffraction

Data for cocrystals in this work were collected from a shock-cooled single cocrystal at 150 K on a Bruker Venture Metaljet k-geometry diffractometer with a Metal Jet using a Helios MX Mirror Optics as monochromator and a Bruker CMOS Photon III detector. The diffractometer used Ga Kα radiation (λ = 1.34139 Å). All data were integrated with SAINT (2013) and a multi-scan absorption correction using SADABS 2016/2 was applied.[43] The structure was solved by dual methods with XT 2018/2 and refined by full-matrix least-squares methods against F2 using SHELXL.[44]Structure solution and refinement cycles were performed within the graphical user interface of OLEX2.[45] All non-hydrogen atoms were refined with anisotropic displacement parameters. All C-bound hydrogen atoms were refined isotropic on calculated positions using a riding model with their U_{iso} values constrained to 1.2 times the U_{eq} of their pivot atoms. This report and the CIF file were generated using FinalCif.

7.4.3 3D Electron diffraction

Samples were deposited on standard TEM grids (amorphous carbon on Cu) as dry powder after gentle grinding between microscope slides and measured on an ELDICO *ED-1* electron diffractometer using the software ELDIX. Ketoconazole was measured at room temperature while the chlorzoxazone cocrystals were cryo plunged in liquid nitrogen, transferred to the diffractometer protected from air, and measured at 100 K. The diffractometer is equipped with a LaB_6 electron source operating at an acceleration voltage of 160 kV (λ = 0.02851 Å) and a hybrid-pixel detector (Dectris QUADRO). The grids were screened for suitable crystals in STEM (scanning transmission electron microscopy) mode and diffraction data were recorded in continuous rotation

mode with a pseudo-parallel beam of ca. 800 nm diameter. Parts of measurements affected by beam damage or shadowing by the grid were omitted. Measurement details for all datasets used are given in Tables II.3.3 to II.3.6 in Appendix II.3.

7.4.4 NQR and Zp-NQR Spectroscopy

Initial frequency searches were performed using powder samples packed into 4 mm outer-diameter glass tubes to a length of approximately 30 mm, corresponding to a total sample mass of 150–250 mg. Frequency sweeps were conducted using an autotuning tabletop probe (tuning range: 30–300 MHz) interfaced with a Scout LF1 benchtop NMR/NQR console (NMR Service GmbH, Germany).

Zero-field ^{35}Cl NQR measurements were subsequently carried out on a Bruker AVANCE III 400 MHz NMR spectrometer using the proton channel. A single-channel, home-built NQR probe equipped with a solenoidal coil (7 mm inner diameter) was used for all experiments. Samples were packed into 7 mm outer-diameter glass tubes (typically 400–700 mg of powder) and positioned within the radiofrequency coil. Spectra were acquired using a Hahn-echo pulse sequence with $\pi/2$ pulse lengths in the range of 6–9 μs. Depending on the signal-to-noise ratio, 256–512 transients were accumulated using a recycle delay of 0.20 s.

For Zp-NQR experiments, the same probe was placed between the poles of a Bruker EMXplus EPR electromagnet to apply a weak static magnetic field. During these measurements, the microwave bridge remained inactive, and the resonator assembly was disengaged. The applied magnetic field was varied between 20 and 30 mT, depending on the sample. Zp-NQR spectra were collected using the variable offset cumulative spectrum (VOCS) method[46], in which a series of frequency-stepped sub spectra were acquired and combined to generate the full spectral envelope, with typical frequency increments of 50 kHz. A Hahn-echo pulse sequence was used with pulse

lengths of 7–9 μs, optimized for each frequency range. The resulting spectra were analyzed using exact spectral simulations implemented in the QUEST software, enabling extraction of the C_Q and η.[23]

7.4.5 Solid State NMR Spectroscopy

The ^{35}Cl NMR experiments were performed at 21.1 T using a Bruker AVANCE II spectrometer at the National Ultrahigh-Field NMR Facility for Solids in Ottawa. For the chlorine NMR experiments, the samples were powdered and packed into 7 mm glass tubes which were then placed into the coil of a home-built 7 mm HX static probe. A WURST-QCPMG pulse sequence was used with proton decoupling using 50 μs WURST pulses that swept over a frequency range of 1 MHz.[47,48] The VOCS acquisition method was used, where a series of subspectra were collected, processed and then co-added in the frequency domain.[46] A QCPMG spikelet separation of 5 kHz was used in all cases with a VOCS stepping frequency of 150 kHz to ensure uniformly excited line shapes. 30 k scans were used to acquire each piece using a recycle delay of 0.5 s.[46] In most cases 128 echoes were collected for each QCPMG echo train (an acquisition time of 25.7 ms). All the spectra were simulated using QUEST written in the C programming language.

7.4.6 Periodic DFT calculations

All GIPAW-DFT calculations were performed using the CASTEP package (version 20.11) as implemented in BIOVIA Materials Studio 2023.[49] Geometry optimizations and ^{35}Cl EFG calculations were carried out with the revised Perdew–Burke–Ernzerhof (rPBE) exchange-correlation functional within the generalized gradient approximation (GGA), augmented with the Grimme D2 dispersion correction (s_6 = 1.0, d = 3.25). On-the-fly ultrasoft pseudopotentials were employed throughout.[50–53] Scalar relativistic effects were accounted for using the zero-order regular approximation (ZORA).[54] A plane-wave kinetic energy cutoff of 700 eV and a Monkhorst–

Pack k-point grid with a spacing of 0.06 $Å^{-1}$ were used. Geometry optimizations were performed using the BFGS algorithm until the energy, maximum force, and maximum displacement converged to 5×10^{-6} eV/atom, 0.01 eV/Å, and 5×10^{-4} Å, respectively. The ^{35}Cl EFG tensors were computed using the gauge-including projector augmented-wave (GIPAW) method as implemented in CASTEP.

7.4.7 Molecular DFT calculations and QTAIM/NCI analysis

Single-point energy calculations were performed on the CASTEP-optimized crystal geometries using the ORCA program (version 6.1.1).[55] The PBE0 hybrid functional was employed in combination with the def2-TZVP basis set for all atoms except chlorine, for which the ZORA-def2-QZVPP basis set was used to improve the description of the core region. Scalar relativistic effects were included via the ZORA approximation.[54] The resulting wavefunctions were subsequently analyzed using the Quantum QTAIM and NCI methods as implemented in the Multiwfn program (version 3.8).[56] Bond critical points (BCPs), electron densities (ρ), and Laplacian of the electron density ($\nabla^2\rho$) were extracted for all relevant intermolecular contacts involving chlorine. NCI isosurfaces were generated and visualized using VMD (version 1.9.3).[57]

7.5 Results and Discussion

7.5.1 Conformational Disorder in Ketoconazole

KTZ was selected as a benchmark system because it combines multiple covalent aryl C–Cl environments with substantial conformational flexibility and crystallographic disorder (Figure 2.7.3b).[58] Previous SCXRD (single crystal X-ray diffraction) studies reported that KTZ crystallizes as a racemically disordered structure containing two molecules in the asymmetric unit, giving rise to four crystallographically distinct chlorine environments associated with conformational disorder within aromatic region attached to piperazine ring of the molecule.[59] The experimental

^{35}Cl NQR spectrum displays two resonances at 34.89 and 35.40 MHz (Figure 2.7.3 and Table 2.7.1). The full-width at half maximum (FWHM) of the KTZ resonances is approximately 54 kHz, while the corresponding Zp-NQR spectra are comparatively smeared and show weakly defined shoulders and minima. These spectral characteristics are consistent with a distribution of chlorine EFG environments arising from conformational heterogeneity and subtle variations in local packing. The broad NQR lines and smeared Zp-NQR envelopes therefore suggest inhomogeneous broadening arising from a continuum of closely related local EFG environments rather than fully discrete and independently resolved chlorine sites. These findings motivated a detailed structural analysis to look at the origin of the broadened Zp-NQR response.

To investigate the structural origin of this behavior, 3D ED was employed directly on microcrystalline powder samples (Figures II.3.3-II.3.5). Measurements were performed using an ELDICO ED-1 diffractometer with a carbon-coated Cu TEM grid at ambient temperature (electron wavelength λ = 0.02851 Å). Approximately fifty nanocrystals were screened, of which sixteen crystals were selected and merged for structure solution and refinement, yielding a maximum resolution of 1.0 Å and full data completeness (100%). Crystal mapping of 325 particles showed that 196 could be indexed to a single consistent unit cell, with no evidence for additional crystalline phases. The structure was solved and refined within the kinematical approximation and revealed that KTZ crystallizes in the triclinic space group P^{-1} with conformational disorder arising from the superposition of both enantiomers at the same crystallographic position. The two independent refinements resolve the enantiomer-superimposed average structure into two discrete conformational models corresponding to the (2R,4S) and (2S,4R) enantiomers.

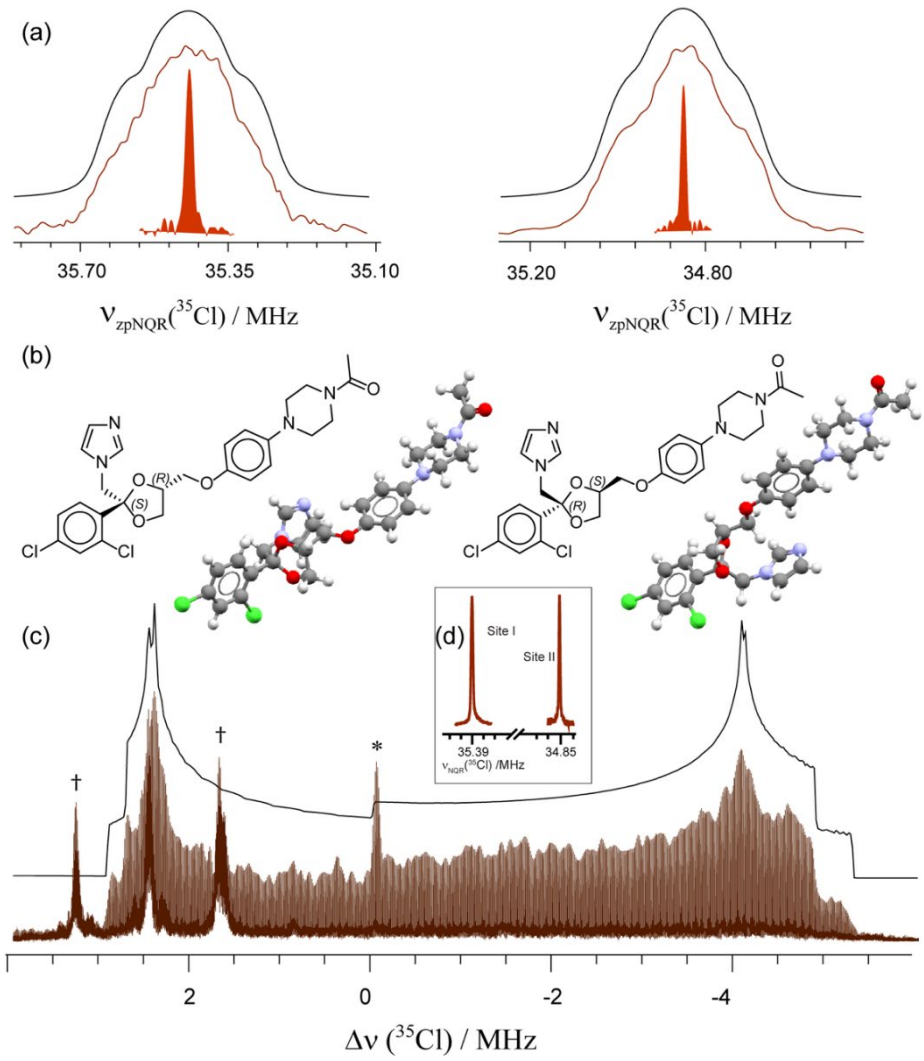


Figure 2.7.3. ^{35}Cl NQR, Zp-NQR, and SSNMR spectra of KTZ powder, together with the molecular structures of the two *cis*-enantiomers and the corresponding 3D ED derived crystal structures. **(a)** Experimental zero-field ^{35}Cl NQR spectra (filled solid red traces) and Zp-NQR spectra at 30 mT (brown traces) for the two spectroscopically distinct chlorine sites, with the corresponding QUEST simulated spectra shown in black above each experimental trace. The broadened NQR lines and featureless Zp-NQR envelopes reflect the inherent static conformational disorder. **(b)** ChemDraw representations of the (2R,4S) and (2S,4R) enantiomers (left and right, respectively) placed next to the ball-and-stick models extracted from the two independent 3D ED refinements, which resolve the enantiomer-superimposed average structure into the two discrete conformations. **(c)** ^{35}Cl WURST-QCPMG SSNMR spectrum acquired at 21.1 T (bottom trace)

with the QUEST simulated fit shown above. Asterisks mark trace $NaCl/NH_4Cl$ impurities; daggers indicate radiofrequency interference or artefacts. **(d)** The NQR spectra of the tablet.

To obtain further insights into the crystal packing of KTZ, GIPAW-DFT calculations were performed on the two structural models derived from 3D ED. From these calculations two sets of quadrupolar parameters (C_Q and η) that are similar between the corresponding chlorine sites in each conformer (Table 2.7.2) are obtained. For the site1 a C_Q value of 67.64 and 67.34 MHz and for site2 a C_Q value of 66.99 and 66.98 MHz were obtained respectively for two structural model. The overlap of the peaks from the four different C_Q results in the broad ^{35}Cl NQR signal and smeared Zp-NQR spectra. In short, the experimentally observed resonances (Figure 2.7.3a) correspond to averaged distributions of closely related four EFG tensors arising from the superposition of the disorder components. In the current approach insights from the DFT calculations enable us to distinguish subtle disorder induced variations in local electronic structure. This interpretation is further supported by the 21.1 T ^{35}Cl WURST-QCPMG spectra shown in Figure 2.7.3c, which also display substantial broadening characteristic of distributed quadrupolar environments. The NQR, Zp-NQR observations and the high-field ^{35}Cl solid-state NMR measurements agree with the disorder-induced broadening in the KTZ.

Table 2.7.1. Experimental ^{35}Cl NQR frequencies and quadrupolar parameters for KTZ and its commercial tablet formulation. NQR frequencies were measured under zero-field conditions, while quadrupolar coupling constants (C_Q) and asymmetry parameters (η) for the pure KTZ powder were extracted from Zp-NQR spectra acquired at 30 mT.

sample	NQR frequency / MHz	exp. C_Q / MHz	exp. η
KTZ (ETEXAC01 [a], site1)	35.39± 0.05	69.56 ± 0.12	0.10 ± 0.04
KTZ (ETEXAC01, site 2)	34.89 ± 0.04	70.80 ± 0.14	0.12 ± 0.04
KTZ (Tablet, site 1)	35.34 ± 0.04	_	_
KTZ (Tablet, site 2)	34.86 ± 0.04	_	_

[a] the CSD refcode for the ketoconazole molecule

KTZ system highlights a unique advantage of the site-resolved chlorine spectroscopic methodology in cases where PXRD and high-field ^{35}Cl solid-state NMR cannot unambiguously resolve local structural motifs, chlorine quadrupolar observables remain highly sensitive to subtle conformational and electronic heterogeneity directly from powdered materials. Here Zp-NQR guided us to use 3D ED to derive the two conformers, which will be applicable in many other crystal systems.

One of the practical applications of ^{35}Cl NQR spectroscopy is the development of method to detect the purity of the commercial tablet, and it is successfully demonstrated in the case of commercial ketoconazole tablet obtained from the pharmacy. The chlorine quadrupolar fingerprint is preserved upon pharmaceutical formulation (Figure 2.7.3.d) despite the presence of excipients and processing induced microstructural complexity. This observation underlines the important practical advantage of NQR for the ability to probe local structural motifs directly in formulated pharmaceutical solids without requiring single crystals, isotopic enrichment, or phase-pure recrystallization. The approach could be used for other chlorine-based tablet to find out the counterfeit and expired drug such as dimenhydrinate, efavirenz, lortadine and chlorpromazine.

Table 2.7.2. Calculated ^{35}Cl quadrupolar parameters for KTZ obtained from GIPAW-DFT (CASTEP) calculations using crystallographic models derived from 3D ED and the reported CSD structure. The 3D ED models each contain two inequivalent chlorine environments, while the CSD structure generates four crystallographically distinct chlorine sites due to conformational disorder.

structure	site	calc. C_Q / MHz	calc. η
3D ED (2R,4S)	site1	67.64	0.19
3D ED (2R,4S)	site2	66.99	0.13
3D ED (2S,4R)	site1	67.34	0.18
3D ED (2S,4R)	site2	66.98	0.14
CSD structure[58]	site1	67.30	0.18
CSD structure	site2	66.91	0.14
CSD structure	site3	67.71	0.19
CSD structure	site4	66.88	0.13

7.5.2 Degree of hydration in Chloramine-T

CAT (sodium *N*-chloro-*p*-toluenesulfonamide) was selected as a candidate to understand the sensitivity of site-resolved chlorine spectroscopy toward hydration-dependent structural transformations.[60] In contrast to the covalent aromatic C–Cl environments with conformational disorder in KTZ, CAT contains a highly polarized N–Cl functionality embedded within an ionic lattice containing Na^+ counterions and an extended hydrogen-bonding network.[33] The commercially available CAT (CSD refcode FABCOA) provides a well-defined structural reference for examining how dehydration perturbs the local electronic environment around chlorine. CAT crystalizes in the *P-1* space group and in the crystal structure the water molecules participate directly in Na^+ coordination. Even though the chlorine does not directly interact with H_2O molecules, a change in water environment around sodium results in a change in packing as shown in the PXRD pattern (Figure II.3.2).

Zero-field ^{35}Cl NQR measurements of the as-received CAT yielded a single, well-defined resonance at 44.59 MHz, confirming the presence of one crystallographically unique N–Cl environment and establishing a spectroscopic fingerprint for this trihydrate phase (Figure 2.7.4 and Table 2.7.3). The Zp-NQR spectra were collected at 30 mT and were fitted using QUEST simulations to extract the corresponding quadrupolar parameters, yielding C_Q = 88.95 MHz and η = 0.12. To further validate the observation, static ^{35}Cl WURST-QCPMG NMR spectra acquired at 21.1 T (Figure 2.7.4.b) and 11.7 T (Figure II.3.7) independently reproduced these parameters and confirmed the large quadrupolar interaction associated with the highly polarized N–Cl bond. The relatively large C_Q value is consistent with a strongly anisotropic chlorine electron density distribution arising from the combined effects of the covalent N–Cl bond, electrostatic interaction with Na^+, and the surrounding hydrogen-bonding network.

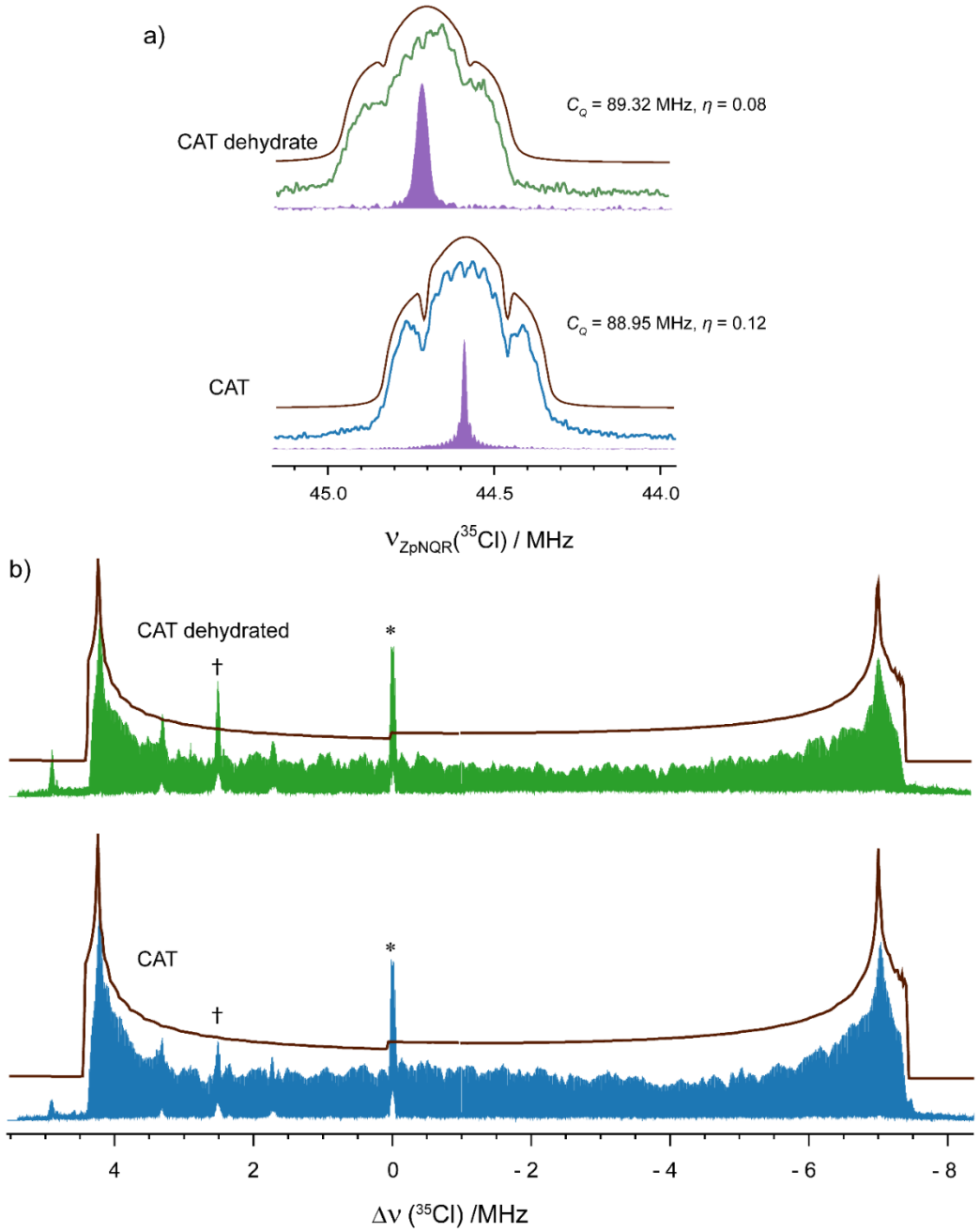


Figure 2.7.4. ^{35}Cl NQR, Zp-NQR, and WURST-QCPMG SSNMR spectra of CAT before and after dehydration. (a) Experimental zero field ^{35}Cl NQR spectra (solid purple traces), and Zp-NQR spectra recorded at 30 mT for the commercial trihydrate (blue) and the sample heated at 80 °C (green), with overlaid QUEST simulations (brown lines). (b) Corresponding static ^{35}Cl WURST-QCPMG spectra acquired at high magnetic field, with QUEST fits shown in brown. The shift in resonance frequency and change in spectral envelope upon heating demonstrate the high sensitivity

of the ^{35}Cl quadrupolar parameters to the hydration state of the N–Cl moiety. Asterisks mark trace NaCl/NH_4Cl impurities; daggers indicate radiofrequency interference or artefacts.

To probe the sensitivity of the chlorine EFG to changes in hydration, a portion of the trihydrate sample was heated at 80 °C for 8 h. Following thermal treatment, the original 44.59 MHz resonance disappeared completely and was replaced by a new sharp resonance at 44.72 MHz (Figure 2.7.4.a). This clean and quantitative spectral transformation demonstrates that ^{35}Cl NQR can rapidly distinguish hydration states directly from powder samples without requiring single crystals or extensive diffraction analysis. The increase in NQR frequency after heating indicates an increase in the magnitude of the principal EFG tensor component ($|V_{zz}|$) at chlorine following dehydration. Correspondingly, the Zp-NQR and WURST-QCPMG line shapes also changed after heating, confirming that dehydration modifies not only the resonance frequency but the overall quadrupolar interaction tensor.

The observed change in EFG tensor was further investigated using TGA (thermogravimetric analysis) and DSC (differential scanning calorimetry) measurements to establish the dehydration stoichiometry and correlate the thermal events with the observed quadrupolar tensor changes. As shown in Figure 2.7.5.a, the as-received chloramine-T trihydrate exhibits an initial mass-loss step of 12.4 % between approximately 25–75 °C, in close agreement with the theoretical loss of two H_2O molecules (12.79 % calculated for $C_7H_7ClNNaO_2S\cdot 3H_2O$). This dehydration event is accompanied by a broad DSC endotherm centered at 80.0 °C with an integrated enthalpy of 190.7 J g^{-1} (Figure 2.7.5.c). A second sharper endotherm centered at 115.15 °C (ΔH = 292.0 J g^{-1}) corresponds to removal of the remaining water molecule. Between these two events, the TGA profile displays a stable plateau extending to approximately 158 °C, indicating formation of a discrete intermediate phase.

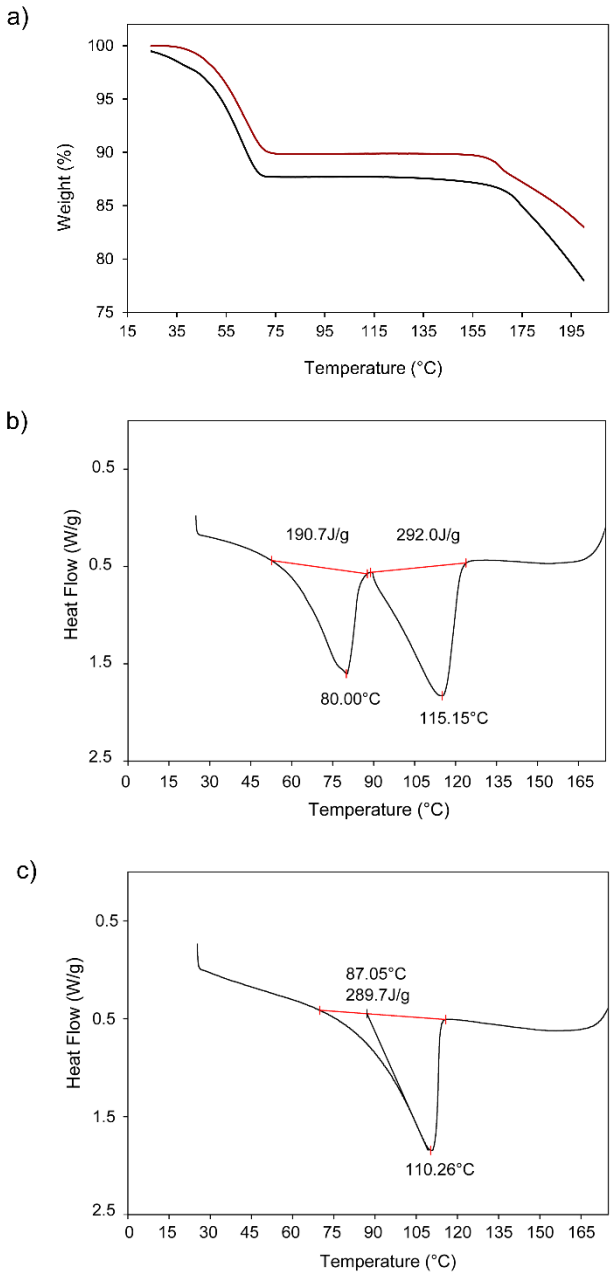


Figure 2.7.5. Thermogravimetric analysis (TGA) and differential scanning calorimetry (DSC) thermograms of commercial CAT trihydrate and the sample pre-heated at 80 °C. (a) TGA weight percent curves recorded at a heating rate of 5 °C min^{-1} under N_2 for (a) the as received trihydrate in black and the 80 °C heated sample in maroon. (b,c) DSC traces showing endothermic dehydration events (b) CAT trihydrate exhibits two well-resolved peaks with integrated enthalpies of 190.7 J g^{-1} (peak temperature 80.0 °C) and 292.0 J g^{-1} (115.15 °C); (c) dehydrated CAT displays a single dominant endotherm of 289.7 J g^{-1} at 110.26 °C (minor feature near 87 °C).

Consistent with this interpretation, the sample pre-heated at 80 °C exhibits a reduced first-step mass loss of 10.11% together with a single dominant DSC endotherm at 110.26 °C (ΔH = 289.7 J g^{-1}), closely matching the second dehydration event observed for the original trihydrate (Figure 2.7.5). These data indicate that heating at 80 °C removes the two most labile water molecules and generates a distinct partially dehydrated phase. The dominant DSC endotherm at 110.26 °C closely matches the second dehydration event of the parent trihydrate, suggesting that the heated material retains a monohydrate-like structural motif. However, the residual mass loss observed by TGA indicates that the hydration state of the heated phase may deviate from an ideal stoichiometric monohydrate. Importantly, the complete replacement of the original ^{35}Cl NQR resonance by a new signal at 44.72 MHz demonstrates that dehydration produces a distinct chlorine environment associated with a well-defined structural transformation.

To gain more insight into structural transformation during the dehydration, periodic DFT calculations of the EFG tensors were performed using GIPAW-DFT. The DFT calculations on the CAT (CSD refcode = FABCOA) give C_Q = 87.27 MHz and η = 0.069, in reasonable agreement with the experimental values of 88.95 MHz[61] and 0.12, respectively (Table 2.7.3). Among several plausible dehydration topologies, only one reproduced the experimentally observed increase in C_Q and NQR frequency. The optimized crystal structure and packing arrangement associated with this model are shown in the Appendix II.3 (Figure II.3.6). In this optimized model, removal of the two water molecules reorganizes the Na^+ coordination environment and modifies the surrounding hydrogen-bonding network, thereby redistributing the local electrostatic potential around the N–Cl moiety. This redistribution increases the anisotropy of the chlorine electron density distribution and consequently enhances the principal EFG tensor component V_{ZZ}, consistent with the experimentally observed increase in NQR frequency. Simultaneously, the lower calculated

asymmetry parameter suggests partial restoration of local symmetry around the chlorine site following dehydration. Further studies on the proposed model will open the possibility of using NQR/Zp-NQR crystallography to predict the structure when it is challenging to achieve by SCXRD or 3D ED.

Table 2.7.3. Experimental ^{35}Cl quadrupolar parameters and NQR frequencies compared with GIPAW calculations for CAT and the CAT-dehydrated obtained by thermal dehydration.

Chloramine T form	Method / Source	C_Q (MHz)	η	^{35}Cl NQR frequency (MHz)	Comment
CAT*	Experiment (Zp-NQR at 30 mT)	88.95	0.12	44.59	As-received commercial sample
CAT	CASTEP (CSD structure)	87.27	0.069	43.67	Reference calculation on experimental geometry
CAT-dehydrated**	Experiment (NQR)	89.32	0.06	44.72	After 80 °C for 8 h; original resonance disappeared
CAT-dehydrated	CASTEP (best optimized model)	88.68	0.04	44.36	Removal of two specific water molecules; best overall agreement with the experimental dehydrated quadrupolar parameters.

*CAT represents the commercial chloramine-T which is the trihydrate form.

**CAT-dehydrated is the commercial chloramine-T sample after heat treatment and in the proposed model it is monohydrate-like structural model

Importantly, alternative water-removal geometries either lowered C_Q or failed to reproduce the experimental η values, demonstrating that the quadrupolar observables are sensitive not only to the number of water molecules removed but also to their specific crystallographic positions within the hydrogen-bonding network. The agreement between experiment and the best-performing monohydrate model therefore provides strong evidence that the experimentally observed NQR transformation originates from a specific dehydration topology rather than from nonspecific lattice collapse or amorphization. As shown in Figure 2.7.4, the Zp-NQR and high-field SSNMR spectra of the heated sample are fully consistent with the monohydrate model. The quantitative agreement between experiment and the best-performing DFT model is summarized in

Table 2.7.3. The corresponding geometry optimized CIF file is provided in the Supporting Information.

The agreement between experiment and the proposed monohydrate model therefore provides strong evidence that the experimentally observed NQR transformation originates from a specific dehydration topology rather than from nonspecific lattice collapse or amorphization.

7.5.3 Packing Influence in Chlorzoxazone Cocrystal Series

Chlorzoxazone (CHZ) contains a single aromatic C–Cl bond embedded in a rigid benzoxazolone framework.[62,63] This structural rigidity makes CHZ an excellent model system for examining how intermolecular packing and hydrogen-bonding interactions modulate the ^{35}Cl electric field gradient without complications arising from molecular conformational changes. CHZ readily forms cocrystals with pharmaceutically relevant coformers, generating a systematic series in which the covalent C–Cl motif remains constant while the local electrostatic environment of chlorine is varied in a controlled manner. The acceptors used are PA, 2,4-DHBA, CBZ, NAM and INA (Figure 2.7.2). In the case of CHZ·CBZ and CHZ·NAM, the size of the cocrystals is in the microcrystalline range and it was difficult to grow single crystals. DFT calculations were performed on the 3D ED derived structural models of the CHZ·CBZ and CHZ·NAM co-crystals to predict C_Q values for crystallographically distinct chlorine sites. The calculated C_Q values show close agreement with the experimental values for all four independent chlorine environments across these two cocrystals. The agreement highlights the value of using C_Q as a sensitive metric for assessing the local structural accuracy.[64–66] The cocrystal series examined here includes two previously reported cocrystals and three novel cocrystals whose structures were determined from microcrystalline powders or single crystals. This chemical platform enables evaluation of how site-

resolved Zp-NQR, high-field SSNMR, and 3D ED or SCXRD can be integrated to characterize chlorine environments in pharmaceutical solids.

The zero-field NQR spectra of the CHZ, CHZ·PA, CHZ·2,4-DHBA, CHZ·CBZ, CHZ·NAM, and CHZ·INA (Figure 2.7.6a) appears within a small frequency window from 34.44 to 35.24 MHz. NQR easily reveals the precise number of crystallographically distinct sites, including near degenerate pairs separated by 0.11–0.16 MHz. Zp-NQR spectra acquired at 30 mT, analyzed with QUEST fitting, provide accurate site specific C_Q and η directly from powder samples (Figure 2.7.6b).

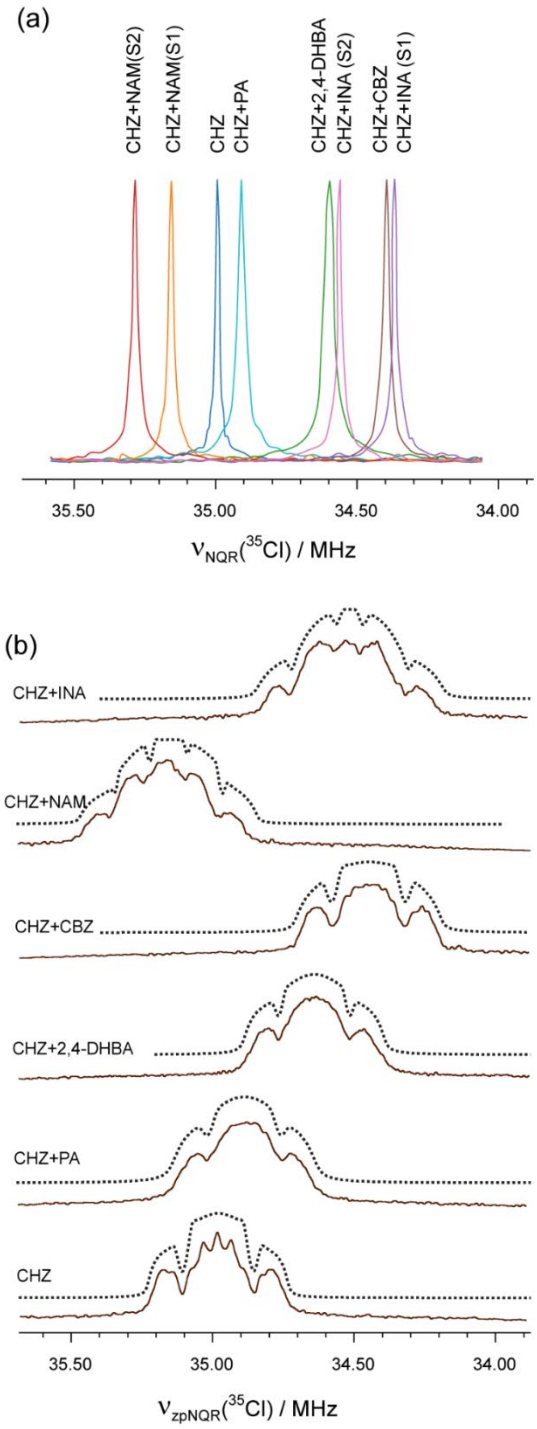


Figure 2.7.6. (a) Zero-field ^{35}Cl NQR spectra of CHZ and cocrystals with PA, 2,4-DHBA, CBZ, NAM, and INA. The NQR spectra are distributed from 34.44 to 35.24 MHz for the seven chlorine sites. The two independent sites in the CHZ·NAM and CHZ·INA cocrystals are labeled site1 and site2. (b) Experimental Zp-NQR spectra at 30 mT (bottom traces, brown) with QUEST simulated fits overlaid (top dotted traces, black).

Static ^{35}Cl WURST-QCPMG spectra were recorded at 21.1 T to validate the expected quadrupolar lineshapes (Figure 2.7.7). The experimental envelopes are well reproduced by simulations that employ the quadrupolar parameters obtained from Zp-NQR. However, even at this high magnetic field, the spectra do not reliably disclose the presence of multiple sites when the quadrupolar parameters are similar.[67] The two chlorine sites in the CHZ+NAM cocrystal, for example, appear as a single broadened pattern, whereas zero-field NQR in Figure 2.7.6.b clearly resolves two distinct resonances separated by only 0.11 MHz. These observations highlight the complementary strengths of the techniques: Zp-NQR excels at site counting and precise parameter extraction, while high-field SSNMR provides valuable lineshape information once the number and approximate parameters of the sites are known.

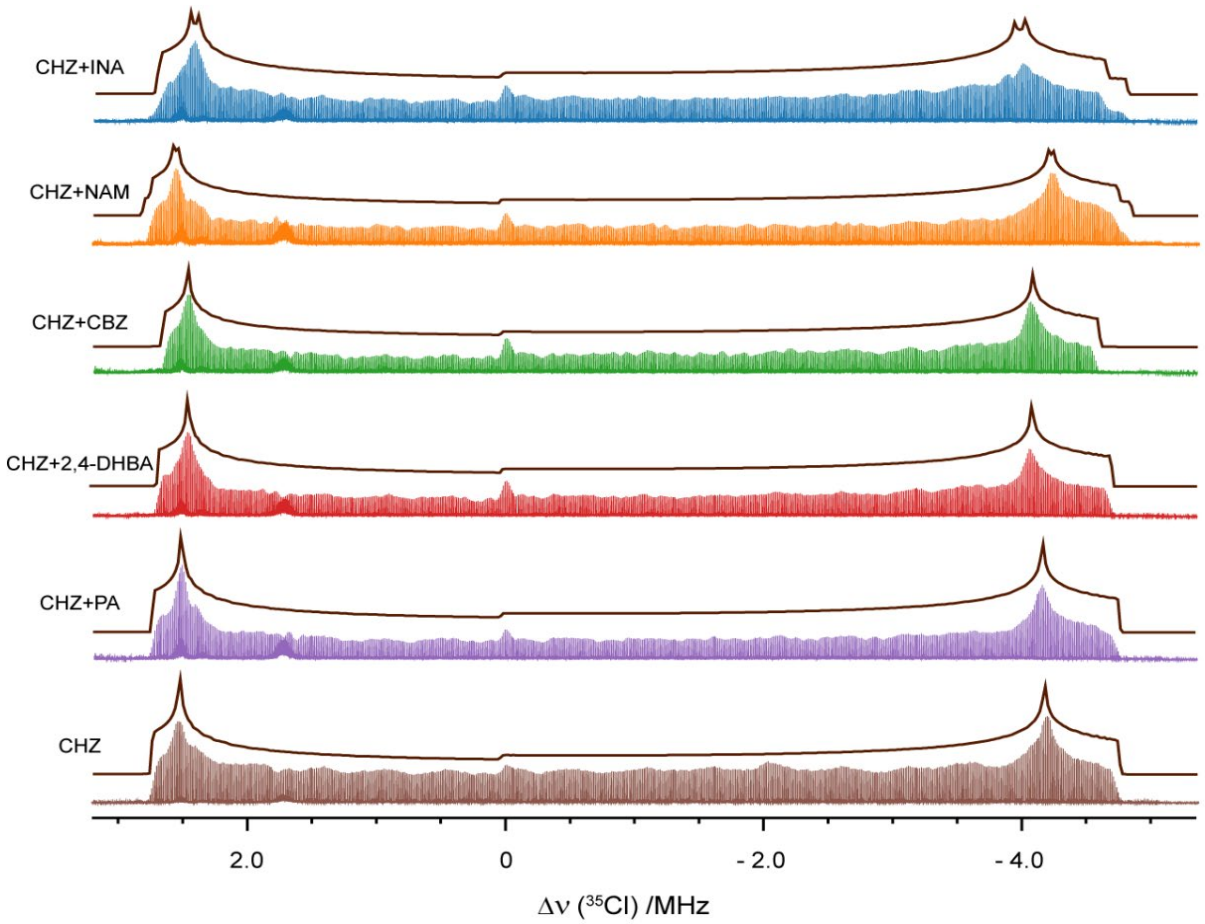


Figure 2.7.7. The static ^{35}Cl WURST-QCPMG solid-state NMR spectra of CHZ and its cocrystals with PA, 2,4-DHBA, CBZ, NAM and INA collected at 21.1 T. Experimental spectra are displayed with overlaid QUEST simulations (thick maroon lines). Spectra are shown with vertically offset for clarity.

High-quality structural models are essential for interpreting the spectroscopic observables. The crystal structures of CHZ+CBZ and CHZ+NAM were solved from nanocrystalline powders using 3D ED, which directly provided unit-cell parameters, space-group assignments, molecular stoichiometry, and overall packing arrangements (see Appendix II.3 for crystallographic data). The structure of CHZ+INA was determined by single-crystal X-ray diffraction. Together with the previously reported structures of CHZ+PA[68] and CHZ+2,4-DHBA [69], these models furnish a consistent structural framework for correlating local chlorine environments with the observed

quadrupolar parameters. Crystal packing diagrams of the CHZ cocrystal series showing the local coordination environment of each distinct chlorine site are presented in Figure 2.7.8.

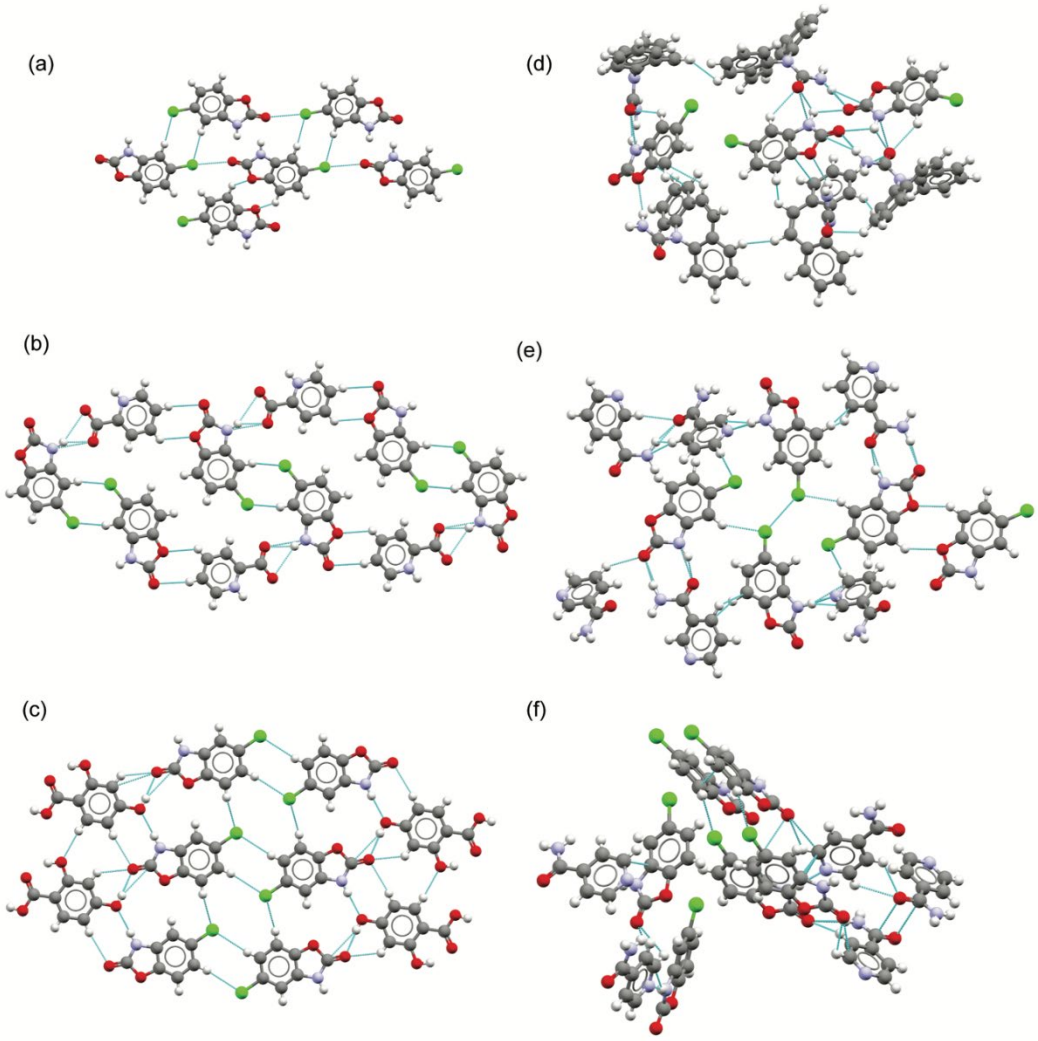


Figure 2.7.8. Crystal packing diagrams of the CHZ series illustrating the local coordination environment of each distinct chlorine site. Panels are presented in the same order as Table 2.7.4: (a) parent CHZ, (b) CHZ·PA, (c) CHZ·2,4-DHBA, (d) CHZ·CBZ, (e) CHZ·NAM, and (f) CHZ·INA. All structures are shown at identical scale. Short intermolecular contacts (< 3.8 Å) to each chlorine atom are highlighted by cyan dashed lines, with interatomic distances (Å) and C–Cl···X angles (°) indicated. These local packing interactions (Cl···O, Cl···H–C, Cl···Cl, or complete Cl isolation) modulate the electric field gradient tensor at chlorine and directly account

for the variations in experimental ^{35}Cl NQR frequencies, quadrupolar coupling constants C_Q, and η reported in Table 2.7.4.

Table 2.7.4 summarizes the experimental ^{35}Cl NQR frequencies, C_Q, and η values together with the dominant intermolecular contacts at each chlorine site. Two main structural factors govern the observed trends. Replacement of the parent Cl···O contact by weaker Cl···H interactions (CHZ·PA, CHZ·2,4-DHBA, and one site in CHZ·INA) reduces both the resonance frequency and C_Q. Complete isolation of chlorine, accompanied by strengthened oxazolone N–H···coformer hydrogen bonding (CHZ·CBZ and one site in CHZ·INA), produces the lowest C_Q values in the series. These results demonstrate that Zp-NQR not only resolves sites that are challenging to distinguish by SSNMR but also provides predictive insight into local structural features that can guide subsequent diffraction studies.

Table 2.7.4. Relationship between experimental ^{35}Cl quadrupolar parameters and local chlorine environments in the CHZ family.

Compound	ν_{NQR} (MHz)	C_Q (MHz)	η	Structural Hypothesis from NQR/Zp-NQR	Contacts Observed by SCXRD/3D ED	Dominant Cl Environment
CHZ	34.99	69.31	0.24	Mixed Cl···O / Cl···H environment	Cl···O 3.239 Å, Cl···H 2.95 Å	Cl···O + Cl···H
CHZ·PA	34.91	69.46	0.18	Reduced Cl···O contribution	Cl···H 2.94 Å	Cl···H
CHZ·2,4-DHBA	34.63	68.98	0.16	Increased Cl···H interactions	Cl···H 2.72, 2.89 Å	Two Cl···H contacts
CHZ·CBZ	34.45	68.26	0.20	Weakly interacting / isolated Cl site	No short Cl contacts	Isolated Cl
CHZ·NAM S1	35.13	70.38	0.10	Enhanced local EFG anisotropy	Cl···H 2.92 Å	Cl···H + packing effects
CHZ·NAM S2	35.24	70.02	0.14	Enhanced local EFG anisotropy	Cl···Cl 3.46 Å + Cl···H 2.73 Å	Cl···Cl + Cl···H

Compound	ν_{NQR} (MHz)	C_Q (MHz)	η	Structural Hypothesis from NQR/Zp-NQR	Contacts Observed by SCXRD/3D ED	Dominant Cl Environment
CHZ·INA S1	34.44	68.90	0.16	Weakly perturbed Cl environment	No short Cl contacts	Relatively isolated Cl
CHZ·INA S2	34.60	68.82	0.15	Weakly perturbed Cl environment	Cl···H 2.85 Å	Cl···H

Looking at NQR frequencies in Table 2.7.4, the CHZ+NAM cocrystal is a clear outlier. Both independent sites exhibit the highest resonance frequencies and the highest C_Q values, accompanied by unusually low asymmetry parameters. This behavior arises from the presence of a Cl···Cl contact (3.464 Å) on one site together with modified hydrogen bonding involving the pyridine nitrogen. Notably, the Zp-NQR parameters correctly indicated the presence of a Cl···Cl interaction on one site prior to structure determination by 3D ED. Even the small frequency difference (0.11 MHz) between the two sites in CHZ·INA was sufficient to distinguish an isolated chlorine from one participating in a single Cl···H contact. These results demonstrate that Zp-NQR not only resolves sites that are difficult to distinguish by SSNMR but also provides predictive insight into local structural features that can guide subsequent diffraction studies.

Periodic DFT calculations performed with full geometry optimization reproduce the experimental C_Q trends across the CHZ series. As shown in the plots in Figure 2.7.9 when only the CHZ cocrystals are considered, a good linear correlation is obtained (R^2=0.862) with an RMSD of 2.02 MHz for the C_Q. Inclusion of the chemically distinct KTZ (conformationally disordered) and CAT (polarized N–Cl) systems, which together span a significantly wider range of C_Q values, markedly improves the correlation to R^2=0.998. This result demonstrates that the computational protocol reliably captures the electric field gradient across diverse chlorine environments when high-quality structural models are employed. These findings are consistent with our recent work on halogen-bonded cocrystals, where experimental C_Q values obtained via Zp-NQR showed strong

linear correlations with both halogen bond distances and DFT computed interaction energies. Together, these studies indicate that the quadrupolar coupling constant serves as a sensitive and general experimental metric for non-covalent interaction strength in solids, whether arising from subtle packing effects or from directional halogen bonds.

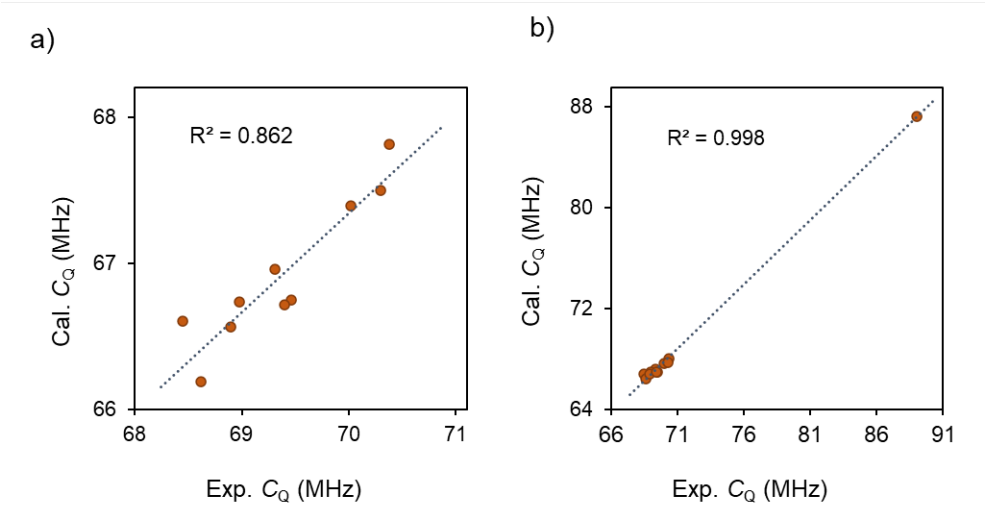


Figure 2.7.9. Correlation between experimental and GIPAW-DFT calculated ^{35}Cl C_Q obtained after full geometry optimization. (a) CHZ cocrystal series, (Cal C_Q = 0.683 Exp C_Q + 19.74, R^2 = 0.862). (b) All compounds studied in this work, encompassing the CHZ cocrystal family, ketoconazole, and chloramine-T. (Cal C_Q = 1.023 Exp C_Q - 3.847, R^2 = 0.998). Experimental and DFT calculated quadrupolar parameters can be found in Table II.3.1 in Appendix II.3.

To elucidate the electronic origin of the observed ^{35}Cl NQR frequency and quadrupolar parameter trends, we performed Quantum Theory of Atoms in Molecules (QTAIM)[52] and Non-Covalent Interaction (NCI)[53] analyses on representative systems selected to capture the main spectroscopic behaviors observed experimentally: the parent CHZ phase, CHZ·CBZ which exhibits one of the largest downward NQR shifts, and CHZ·NAM which behaves as an outlier and displays increased NQR frequency and C_Q. Complementary NCI analysis was used to visualize the spatial distribution and cooperativity of weak intermolecular interactions. Representative QTAIM parameters are summarized in Appendix II.3.

Importantly, the intermolecular interactions identified by QTAIM and NCI are not merely crystallographic packing features; rather, they perturb the electronic environment surrounding the chlorine nuclei and modify the EFG tensor components. Since the quadrupolar parameters are directly related to the EFG tensor, changes in crystal packing can be directly linked to the experimentally observed NQR behavior.

$$\nu_{NQR} \propto \frac{e^2 qQ}{h} \qquad Eq.7.1$$

$$eq = V_{zz} \qquad Eq.7.2$$

$$C_Q \propto V_{zz} \qquad Eq.7.3$$

Thus, a decrease in $|V_{ZZ}|$ leads to lower NQR frequencies and C_Q values, whereas an increase in $|V_{ZZ}|$ produces higher quadrupolar couplings.

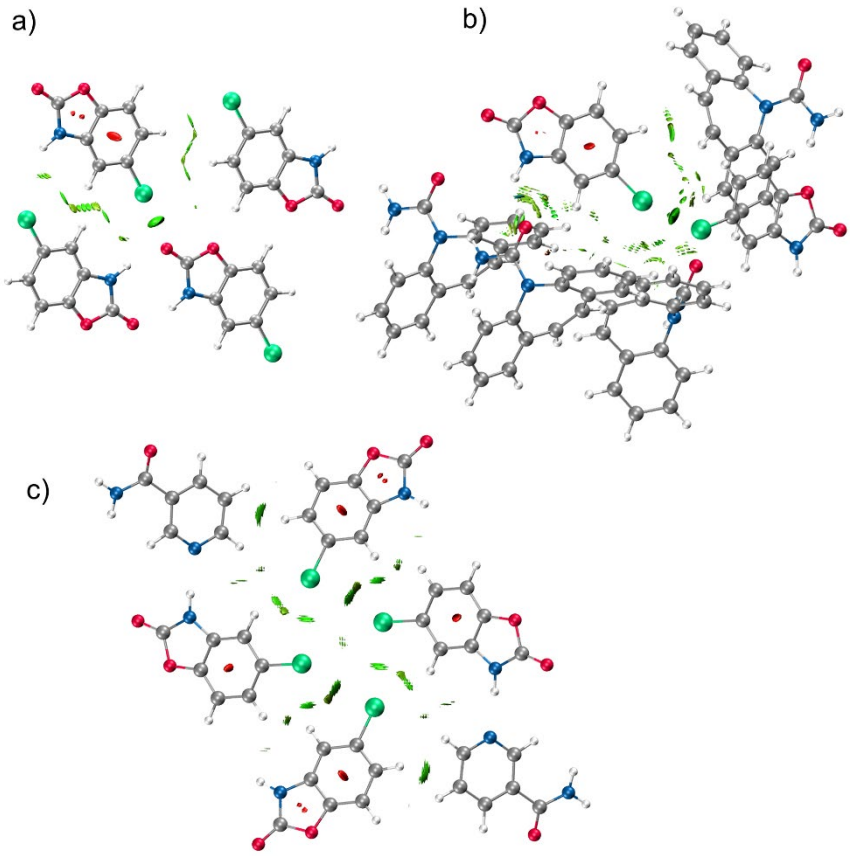


Figure 2.7.10. NCI plots for CHZ and its cocrystals highlighting the local interaction environment around the chlorine atom. Green isosurfaces indicate attractive non-covalent interactions (van der Waals' contacts, weak hydrogen bonds, and halogen bonds). (a) Parent CHZ; (b) CHZ·CBZ cocrystal; (c) CHZ·NAM cocrystal. The NCI surfaces reveal distinct changes in the supramolecular environment of the Cl atom upon cocrystallization. In particular, the CHZ·NAM cocrystal shows a localized Cl···Cl interaction that is absent in the parent compound and the CHZ·CBZ cocrystal, consistent with the observed increase in the ^{35}Cl quadrupolar coupling constant.

Shown in Figure 2.7.10 for the parent CHZ structure, the NCI analysis reveals relatively localized and weak intermolecular interactions involving primarily Cl···H, Cl···O, and π-associated contacts. The green NCI iso-surfaces are sparse and isolated, consistent with weak dispersion-dominated intermolecular interactions.

The QTAIM analysis supports this interpretation, showing low electron density values at the intermolecular bond critical points together with positive Laplacian and positive total energy density values, characteristic of closed-shell noncovalent interactions (Figure II.3.1, Table II.3.7-II.3.9). Consequently, the chlorine EFG in CHZ is only moderately perturbed by intermolecular interactions, and the observed NQR frequency (34.99 MHz) primarily reflects the intrinsic molecular electronic environment.

Among the investigated cocrystals, CHZ·CBZ exhibits one of the lowest NQR frequencies (34.45 MHz). The NCI analysis shows significantly more extended and interconnected green iso-surfaces compared with CHZ, indicating a highly cooperative intermolecular interaction network involving dispersion-assisted and π-associated contacts.

The QTAIM analysis similarly reveals enhanced intermolecular electronic coupling together with the presence of weak Cl···Cl interactions. Although these interactions remain closed-shell and noncovalent in nature, the overall crystal packing environment becomes substantially more electronically delocalized.

Importantly, CHZ·CBZ exhibits the most diffuse and cooperative intermolecular interaction topology within the studied systems. This extensive intermolecular delocalization electronically averages the charge distribution surrounding the chlorine nuclei, reducing the anisotropy of the local electronic environment and thereby decreasing the magnitude of V_{33}. Consequently, CHZ·CBZ displays one of the lowest experimentally observed NQR frequencies and C_Q values in the series.

In contrast, CHZ·NAM behaves as a distinct outlier and exhibits increased NQR frequencies and C_Q values relative to the parent CHZ structure. The NCI analysis reveals a less delocalized and more localized interaction topology compared with CHZ·CBZ, with intermolecular

interactions concentrated around specific directional contacts rather than forming an extensively cooperative network.

The QTAIM analysis reveals stabilizing Cl···H and Cl···Cl interactions in CHZ·NAM with higher electron densities at the bond critical points (0.0049–0.0059 and 0.0041 a.u., respectively) compared to CHZ·CBZ. In contrast to the cooperative, delocalized interaction network in CHZ·CBZ, the contacts in CHZ·NAM are more directional and localized around chlorine. Consequently, the crystal packing generates enhanced directional polarization and hence increases the anisotropy of the local environment at chlorine, leading to a larger $|V_{33}|$ and thus higher ^{35}Cl NQR frequencies and C_Q values.

7.6 Conclusions and Broader Perspective

This chapter demonstrates that the integration of cryogen-free ^{35}Cl Zp-NQR, zero-field NQR, ultra-wideline ^{35}Cl SSNMR, 3D ED, and first-principles DFT calculations provides a comprehensive strategy for the site-resolved characterization of chlorine-containing pharmaceutical solids directly from powders. By combining complementary spectroscopic, crystallographic, and computational methods, quantitative EFG tensors were determined and correlated with local molecular structure, crystal packing, hydration, conformational disorder, and intermolecular interactions.

The three pharmaceutical systems investigated highlight the versatility of this integrated methodology. In ketoconazole, Zp-NQR distinguished closely related chlorine environments arising from conformational disorder and guided the subsequent 3D ED analysis, while the successful detection of the active pharmaceutical ingredient directly within a commercial tablet demonstrated the potential of ^{35}Cl NQR as a rapid, non-destructive analytical tool for pharmaceutical identification. In chloramine-T, combined NQR, Zp-NQR, diffraction, thermal

analysis, and DFT calculations enabled the characterization of hydration-dependent structural transformations and supported the structural assignment of the previously unknown dehydrated phase. The chlorzoxazone cocrystal series provided the most comprehensive demonstration of the methodology, where Zp-NQR resolved multiple crystallographically distinct chlorine sites that were difficult to distinguish by ultra-wideline ^{35}Cl SSNMR alone. Integration with 3D ED and first-principles calculations further established direct relationships between experimentally determined quadrupolar parameters, crystal packing, and local electronic structure. These studies demonstrate that quadrupolar interactions serve as quantitative descriptors of the local electronic environment surrounding chlorine nuclei.

Beyond the individual case studies, this work represents the culmination of the methodological developments presented throughout Part 2 of this thesis. The Zp-NQR methodology, isotope-selective resonance assignment, quantitative determination of EFG tensors, and integration with complementary crystallographic and computational techniques have been unified into a practical workflow for the structural characterization of complex molecular solids. Importantly, this work demonstrates that Zp-NQR alone can provide sufficient experimental information to determine complete EFG tensors for spin-3/2 nuclei, while complementary techniques such as 3D ED, SSNMR, and DFT provide additional structural validation and chemical interpretation.

More broadly, the methodology developed here extends beyond the pharmaceutical systems investigated. Chlorine is present in approximately 20% of marketed pharmaceuticals and plays an important role in molecular conformation, crystal packing, polymorphism, chemical stability, and biological activity. The sensitivity of chlorine quadrupolar interactions to these structural features makes Zp-NQR a promising tool for pharmaceutical solid-form screening, polymorph

identification, cocrystal characterization, degradation studies, quality control, and drug authentication, particularly for materials available only as microcrystalline powders. Furthermore, the experimental and computational framework established in this work is readily applicable to other quadrupolar nuclei, including bromine, iodine, antimony, and nitrogen, as well as a wide range of molecular and inorganic materials.

Finally, the combination of cryogen-free quadrupolar spectroscopy with emerging crystallographic methods such as 3D ED establishes a framework for NQR-assisted crystallography, in which experimentally determined EFG tensors provide independent local structural constraints that complement diffraction-derived models. This chapter reinforces one of the central themes of this dissertation: quadrupolar interactions are not merely spectroscopic observables, but quantitative probes of local molecular structure and intermolecular interactions. By integrating accessible instrumentation, exact Hamiltonian simulations, complementary diffraction techniques, and first-principles electronic structure calculations, the methodology developed throughout this thesis establishes Zp-NQR as a practical, versatile, and sustainable platform for the atomistic characterization of complex molecular solids.

References for Chapter 7.

(1) Cavallo, G.; Metrangolo, P.; Milani, R.; Pilati, T.; Priimagi, A.; Resnati, G.; Terraneo, G. The Halogen Bond. *Chem. Rev.* **2016**, *116* (4), 2478–2601. https://doi.org/10.1021/acs.chemrev.5b00484.

(2) Chiodi, D.; Ishihara, Y. "Magic Chloro": Profound Effects of the Chlorine Atom in Drug Discovery. *J. Med. Chem.* **2023**, *66* (8), 5305–5331. https://doi.org/10.1021/acs.jmedchem.2c02015.

(3) Fang, W.-Y.; Ravindar, L.; Rakesh, K. P.; Manukumar, H. M.; Shantharam, C. S.; Alharbi, N. S.; Qin, H.-L. Synthetic Approaches and Pharmaceutical Applications of Chloro-Containing Molecules for Drug Discovery: A Critical Review. *Eur. J. Med. Chem.* **2019**, *173*, 117–153. https://doi.org/10.1016/j.ejmech.2019.03.063.

(4) Ashbrook, S. E.; Sneddon, S. New Methods and Applications in Solid-State NMR Spectroscopy of Quadrupolar Nuclei. *J. Am. Chem. Soc.* **2014**, *136* (44), 15440–15456. https://doi.org/10.1021/ja504734p.

(5) Smith, J. A. S. Nuclear Quadrupole Resonance Spectroscopy. General Principles. *J. Chem. Educ.* **1971**, *48* (1), 39. https://doi.org/10.1021/ed048p39.

(6) Pound, R. V. Nuclear Electric Quadrupole Interactions in Crystals. *Phys Rev* **1950**, *79* (4), 685–702. https://doi.org/10.1103/PhysRev.79.685.

(7) Brame, E. G. Chlorine-35 Nuclear Quadrupole Resonance Studies of Trichloromethyl Compounds. *Anal. Chem.* **1971**, *43* (1), 35–37. https://doi.org/10.1021/ac60296a008.

(8) Gallier, J.; Toudic, B.; Delugeard, Y.; Cailleau, H.; Gourdji, M.; Péneau, A.; Guibé, L. Chlorine-Nuclear-Quadrupole-Resonance Study of the Neutral-to-Ionic Transition in

Tetrathiafulvalene-Chloranil. *Phys Rev B* **1993**, *47* (18), 11688–11695. https://doi.org/10.1103/PhysRevB.47.11688.

(9) Le Cointe, M.; Gallier, J.; Cailleau, H.; Gourdji, M.; Péneau, A.; Guibé, L. ^{35}Cl NQR Study on TTF-CA Crystals: Symmetry Lowering and Hysteresis at the Neutral-to-Ionic Transition. *Solid State Commun.* **1995**, *94* (6), 455–459. https://doi.org/10.1016/0038-1098(95)00108-5.

(10) Graybeal, J. D.; Green, P. J. Nuclear Quadrupole Resonance Zeeman Study of Polycrystalline Group IVa Tetrachlorides. *J. Phys. Chem.* **1969**, *73* (9), 2948–2955. https://doi.org/10.1021/j100843a029.

(11) Ting, Y.; Manring, E. R.; Williams, D. Zeeman Effects in the Chlorine Nuclear Quadrupole Resonance in Sodium Chlorate. *Phys Rev* **1954**, *96* (2), 408–414. https://doi.org/10.1103/PhysRev.96.408.

(12) Ege, O.; Hamai, S.; Negita, H. Zeeman NQR Studies on Polycrystals of Copper Compounds, Arsenic Compounds, and Chlorine Compounds. **1992**, *47* (1–2), 401–408. https://doi.org/10.1515/zna-1992-1-267.

(13) Raman, K. V. Asymmetry Parameter Studies for Systems Containing the ^{35}Cl Nucleus from Zeeman NQR Data. *Nucl. Quadrupole Reson. Relat. Tech.* **1995**, *345*, 31–47. https://doi.org/10.1016/0022-2860(94)08378-U.

(14) Ramachandran, R.; Oldfield, E. Two Dimensional Zeeman Nuclear Quadrupole Resonance Spectroscopy. *J. Chem. Phys.* **1984**, *80* (2), 674–677. https://doi.org/10.1063/1.446763.

(15) Bucci, P.; Cecchi, P.; Colligiani, A. Zeeman Effect of the Nuclear Quadrupole Resonance of Chlorine-35 in 3,5- and 2,6-Dichloropyridine. *J. Am. Chem. Soc.* **1965**, *87* (13), 3027–3028. https://doi.org/10.1021/ja01091a056.

(16) Quarti, C.; Gautier, R.; Zacharias, M.; Gansmuller, A.; Katan, C. Nuclear Quadrupolar Resonance Structural Characterization of Halide Perovskites and Perovskitoids: A Roadmap from Electronic Structure Calculations for Lead–Iodide-Based Compounds. *J. Am. Chem. Soc.* **2025**, *147* (1), 278–291. https://doi.org/10.1021/jacs.4c09877.

(17) Scarperi, A.; Landi, N.; Costamagna, M.; Taddei, M.; Carignani, E.; Geppi, M.; Borsacchi, S. Probing Photoinduced Halide Segregation in $CH_3NH_3Pb(Br_xI_{1-x})_3$ Perovskites via in Situ Nuclear Quadrupole Resonance Spectroscopy. *J. Am. Chem. Soc.* **2025**, *147* (37), 33799–33811. https://doi.org/10.1021/jacs.5c10094.

(18) Nari, A.; Szell, P. M. J.; Bryce, D. L. Isotopic Identification of Quadrupolar Spin Resonance Lines by Zeeman Perturbation. *J. Phys. Chem. Lett.* **2025**, *16* (34), 8752–8757. https://doi.org/10.1021/acs.jpclett.5c02214.

(19) Nari, A.; Szell, P. M. J.; Bryce, D. L. Practical Aspects of Zeeman-Perturbed NQR Spectroscopy Using an Adjustable Electromagnet. *Solid State Nucl. Magn. Reson.* **2025**, *138*, 102014. https://doi.org/10.1016/j.ssnmr.2025.102014.

(20) Perras, F. A.; Bryce, D. L. Direct Investigation of Covalently Bound Chlorine in Organic Compounds by Solid-State 35Cl NMR Spectroscopy and Exact Spectral Line-Shape Simulations. *Angew. Chem. Int. Ed.* **2012**, *51* (17), 4227–4230. https://doi.org/https://doi.org/10.1002/anie.201200728.

(21) Chapman, R. P.; Bryce, D. L. A High-Field Solid-State $^{35/37}$Cl NMR and Quantum Chemical Investigation of the Chlorine Quadrupolar and Chemical Shift Tensors in Amino Acid Hydrochlorides. *Phys Chem Chem Phys* **2007**, *9* (47), 6219–6230. https://doi.org/10.1039/B712688C.

(22) Bryce, D. L.; Sward, G. D.; Adiga, S. Solid-State $^{35/37}$Cl NMR Spectroscopy of Hydrochloride Salts of Amino Acids Implicated in Chloride Ion Transport Channel Selectivity: Opportunities at 900 MHz. *J. Am. Chem. Soc.* **2006**, *128* (6), 2121–2134. https://doi.org/10.1021/ja057253i.

(23) Perras, F. A.; Widdifield, C. M.; Bryce, D. L. QUEST—QUadrupolar Exact SofTware: A Fast Graphical Program for the Exact Simulation of NMR and NQR Spectra for Quadrupolar Nuclei. *Solid State Nucl. Magn. Reson.* **2012**, *45–46*, 36–44. https://doi.org/10.1016/j.ssnmr.2012.05.002.

(24) Martin, G. E.; Sunseri, D. Establishing the Carbon Skeleton of Pharmaceutical Agents Using HSQC-ADEQUATE Spectra. *J. Pharm. Biomed. Anal.* **2011**, *55* (5), 895–901. https://doi.org/10.1016/j.jpba.2011.02.032.

(25) Holmes, S. T.; Vojvodin, C. S.; Veinberg, N.; Iacobelli, E. M.; Hirsh, D. A.; Schurko, R. W. Hydrates of Active Pharmaceutical Ingredients: A 35Cl and 2H Solid-State NMR and DFT Study. *Solid State Nucl. Magn. Reson.* **2022**, *122*, 101837. https://doi.org/10.1016/j.ssnmr.2022.101837.

(26) Namespetra, A. M.; Hirsh, D. A.; Hildebrand, M. P.; Sandre, A. R.; Hamaed, H.; Rawson, J. M.; Schurko, R. W. 35Cl Solid-State NMR Spectroscopy of HCl Pharmaceuticals and Their Polymorphs in Bulk and Dosage Forms. *CrystEngComm* **2016**, *18* (33), 6213–6232. https://doi.org/10.1039/C6CE01069E.

(27) Gordon, P. G.; Brouwer, D. H.; Ripmeester, J. A. ^{35}Cl Solid-State NMR of Halide Ionic Liquids at Ultrahigh Fields. *J. Phys. Chem. A* **2008**, *112* (49), 12527–12529. https://doi.org/10.1021/jp808524h.

(28) Hamaed, H.; Pawlowski, J. M.; Cooper, B. F. T.; Fu, R.; Eichhorn, S. H.; Schurko, R. W. Application of Solid-State ^{35}Cl NMR to the Structural Characterization of Hydrochloride Pharmaceuticals and Their Polymorphs. *J. Am. Chem. Soc.* **2008**, *130* (33), 11056–11065. https://doi.org/10.1021/ja802486q.

(29) Szell, P. M. J.; Bryce, D. L. ^{35}Cl Solid-State NMR and Computational Study of Chlorine Halogen Bond Donors in Single-Component Crystalline Chloronitriles. *J. Phys. Chem. C* **2016**, *120* (20), 11121–11130. https://doi.org/10.1021/acs.jpcc.6b02806.

(30) Rotstein, D. M.; Kertesz, D. J.; Walker, K. A. M.; Swinney, D. C. Stereoisomers of Ketoconazole: Preparation and Biological Activity. *J. Med. Chem.* **1992**, *35* (15), 2818–2825. https://doi.org/10.1021/jm00093a015.

(31) Chen, X.; Li, D.; Deng, Z.; Zhang, H. Ketoconazole: Solving the Poor Solubility via Cocrystal Formation with Phenolic Acids. *Cryst. Growth Des.* **2020**, *20* (10), 6973–6982. https://doi.org/10.1021/acs.cgd.0c01014.

(32) Peeters, O. M.; Blaton, N. M.; De Ranter, C. J. *cis*-1-acetyl-4-(4-{[2-(2,4-dichlorophenyl)-2-(1H-1-imidazolylmethyl)-1,3-dioxolan-4-yl]methoxy}phenyl)piperazine: Ketoconazole. A Crystal Structure with Disorder. *Acta Crystallogr. Sect. B* **1979**, *35* (10), 2461–2464. https://doi.org/10.1107/S0567740879009651.

(33) Olmstead, M. M.; Power, P. P. Crystal and Molecular Structure of Chloramine-T Trihydrate. Absence of a Sodium-Nitrogen Interaction in the Oxidant. N-Chloro-N-Sodiotoluene-p-Sulfonamide. *Inorg. Chem.* **1986**, *25* (22), 4057–4058. https://doi.org/10.1021/ic00242a047.

(34) Fairey, J. L.; Laszakovits, J. R.; Pham, H. T.; Do, T. D.; Hodges, S. D.; McNeill, K.; Wahman, D. G. Chloronitramide Anion Is a Decomposition Product of Inorganic Chloramines. *Science* **2024**, *386* (6724), 882–887. https://doi.org/10.1126/science.adk6749.

(35) Ozlem Sanli-Yurudu, N.; Kimiran-Erdem, A.; Cotuk, A. Studies on the Efficacy of Chloramine T Trihydrate (N-Chloro-p-Toluene Sulfonamide) against Planktonic and Sessile Populations of Different Legionella Pneumophila Strains. *Int. J. Hyg. Environ. Health* **2007**, *210* (2), 147–153. https://doi.org/10.1016/j.ijheh.2006.08.004.

(36) İde, S.; Topaçh, A. Tautomeric Investigations and Crystal Structure Analysis of Chlorzoxazone. *J. Chem. Crystallogr.* **1997**, *27* (5), 303–306. https://doi.org/10.1007/BF02575978.

(37) Gemmi, M.; Mugnaioli, E.; Gorelik, T. E.; Kolb, U.; Palatinus, L.; Boullay, P.; Hovmöller, S.; Abrahams, J. P. 3D Electron Diffraction: The Nanocrystallography Revolution. *ACS Cent. Sci.* **2019**, *5* (8), 1315–1329. https://doi.org/10.1021/acscentsci.9b00394.

(38) Mathew, R.; Mazumder, A.; Kumar, P.; Matula, J.; Mohamed, S.; Brazda, P.; Hariharan, M.; Thomas, B. Unveiling the Topology of Partially Disordered Micro-Crystalline Nitro-Perylenediimide with X-Aggregate Stacking: An Integrated Approach. *Chem Sci* **2024**, *15* (2), 490–499. https://doi.org/10.1039/D3SC05514K.

(39) Klar, P. B.; Krysiak, Y.; Xu, H.; Steciuk, G.; Cho, J.; Zou, X.; Palatinus, L. Accurate Structure Models and Absolute Configuration Determination Using Dynamical Effects in Continuous-Rotation 3D Electron Diffraction Data. *Nat. Chem.* **2023**, *15* (6), 848–855. https://doi.org/10.1038/s41557-023-01186-1.

(40) Vinod, K.; Mathew, R.; Jandl, C.; Thomas, B.; Hariharan, M. Electron Diffraction and Solid-State NMR Reveal the Structure and Exciton Coupling in a Eumelanin Precursor. *Chem Sci* **2024**, *15* (39), 16015–16024. https://doi.org/10.1039/D4SC05453A.

(41) Das, P. P.; Mugnaioli, E.; Nicolopoulos, S.; Tossi, C.; Gemmi, M.; Galanis, A.; Borodi, G.; Pop, M. M. Crystal Structures of Two Important Pharmaceuticals Solved by 3D Precession

Electron Diffraction Tomography. *Org. Process Res. Dev.* **2018**, *22* (10), 1365–1372. https://doi.org/10.1021/acs.oprd.8b00149.

(42) Karothu, D. P.; Alhaddad, Z.; Göb, C. R.; Schürmann, C. J.; Bücker, R.; Naumov, P. The Elusive Structure of Levocetirizine Dihydrochloride Determined by Electron Diffraction. *Angew. Chem. Int. Ed.* **2023**, *62* (26), e202303761. https://doi.org/https://doi.org/10.1002/anie.202303761.

(43) Krause, L.; Herbst-Irmer, R.; Sheldrick, G. M.; Stalke, D. Comparison of Silver and Molybdenum Microfocus X-Ray Sources for Single-Crystal Structure Determination. *J. Appl. Crystallogr.* **2015**, *48* (1), 3–10. https://doi.org/10.1107/S1600576714022985.

(44) Sheldrick, G. M. Crystal Structure Refinement with It SHELXL. *Acta Crystallogr. Sect. C* **2015**, *71* (1), 3–8. https://doi.org/10.1107/S2053229614024218.

(45) Dolomanov, O. V.; Bourhis, L. J.; Gildea, R. J.; Howard, J. A. K.; Puschmann, H. It OLEX2: A Complete Structure Solution, Refinement and Analysis Program. *J. Appl. Crystallogr.* **2009**, *42* (2), 339–341. https://doi.org/10.1107/S0021889808042726.

(46) Massiot, D.; Farnan, I.; Gautier, N.; Trumeau, D.; Trokiner, A.; Coutures, J. P. ^{71}Ga and ^{69}Ga Nuclear Magnetic Resonance Study of β-Ga_2O_3: Resolution of Four- and Six-Fold Coordinated Ga Sites in Static Conditions. *Solid State Nucl. Magn. Reson.* **1995**, *4* (4), 241–248. https://doi.org/10.1016/0926-2040(95)00002-8.

(47) O'Dell, L. A. The WURST Kind of Pulses in Solid-State NMR. *Solid State Nucl. Magn. Reson.* **2013**, *55–56*, 28–41. https://doi.org/10.1016/j.ssnmr.2013.10.003.

(48) O'Dell, L. A.; Schurko, R. W. QCPMG Using Adiabatic Pulses for Faster Acquisition of Ultra-Wideline NMR Spectra. *Chem. Phys. Lett.* **2008**, *464* (1), 97–102. https://doi.org/10.1016/j.cplett.2008.08.095.

(49) Clark, S. J.; Segall, M. D.; Pickard, C. J.; Hasnip, P. J.; Probert, M. I. J.; Refson, K.; Payne, M. C. First Principles Methods Using CASTEP. **2005**, *220* (5–6), 567–570. https://doi.org/10.1524/zkri.220.5.567.65075.

(50) Perdew, J. P.; Burke, K.; Ernzerhof, M. Generalized Gradient Approximation Made Simple. *Phys Rev Lett* **1996**, *77* (18), 3865–3868. https://doi.org/10.1103/PhysRevLett.77.3865.

(51) Perdew, J. P.; Burke, K.; Ernzerhof, M. Generalized Gradient Approximation Made Simple [Phys. Rev. Lett. 77, 3865 (1996)]. *Phys Rev Lett* **1997**, *78* (7), 1396. https://doi.org/10.1103/PhysRevLett.78.1396.

(52) Grimme, S.; Hansen, A.; Brandenburg, J. G.; Bannwarth, C. Dispersion-Corrected Mean-Field Electronic Structure Methods. *Chem. Rev.* **2016**, *116* (9), 5105–5154. https://doi.org/10.1021/acs.chemrev.5b00533.

(53) Grimme, S.; Ehrlich, S.; Goerigk, L. Effect of the Damping Function in Dispersion Corrected Density Functional Theory. *J. Comput. Chem.* **2011**, *32* (7), 1456–1465. https://doi.org/10.1002/jcc.21759.

(54) Green, T. F. G.; Yates, J. R. Relativistic Nuclear Magnetic Resonance J-Coupling with Ultrasoft Pseudopotentials and the Zeroth-Order Regular Approximation. *J. Chem. Phys.* **2014**, *140* (23), 234106. https://doi.org/10.1063/1.4882678.

(55) Neese, F.; Wennmohs, F.; Becker, U.; Riplinger, C. The ORCA Quantum Chemistry Program Package. *J. Chem. Phys.* **2020**, *152* (22), 224108. https://doi.org/10.1063/5.0004608.

(56) Lu, T.; Chen, F. Multiwfn: A Multifunctional Wavefunction Analyzer. *J. Comput. Chem.* **2012**, *33* (5), 580–592. https://doi.org/https://doi.org/10.1002/jcc.22885.

(57) Humphrey, W.; Dalke, A.; Schulten, K. VMD: Visual Molecular Dynamics. *J. Mol. Graph.* **1996**, *14* (1), 33–38. https://doi.org/10.1016/0263-7855(96)00018-5.

(58) Martin, F. A.; Pop, M. M.; Borodi, G.; Filip, X.; Kacso, I. Ketoconazole Salt and Co-Crystals with Enhanced Aqueous Solubility. *Cryst. Growth Des.* **2013**, *13* (10), 4295–4304. https://doi.org/10.1021/cg400638g.

(59) Campbell, M. M.; Johnson, Graham. Chloramine T and Related N-Halogeno-N-Metallo Reagents. *Chem. Rev.* **1978**, *78* (1), 65–79. https://doi.org/10.1021/cr60311a005.

(60) Hung, I.; Altenhof, A. R.; Schurko, R. W.; Bryce, D. L.; Han, O. H.; Gan, Z. Field-Stepped Ultra-Wideline NMR at up to 36 T: On the Inequivalence between Field and Frequency Stepping. *Magn. Reson. Chem.* **2021**, *59* (9–10), 951–960. https://doi.org/10.1002/mrc.5128.

(61) Childs, S. L.; Hardcastle, K. I. Cocrystals of Chlorzoxazone with Carboxylic Acids. CrystEngComm; **2007**, *9* (5), 364–367. https://doi.org/10.1039/B703292G.

(62) Roy, P.; Ghosh, A. Mechanochemical Cocrystallization to Improve the Physicochemical Properties of Chlorzoxazone. *CrystEngComm* **2020**, *22* (27), 4611–4620. https://doi.org/10.1039/D0CE00635A.

(63) Mathew, R.; Thomas, B. Deciphering the Topology of Sitagliptin Using an Integrated Approach. *ACS Omega* **2025**, *10* (2), 2289–2295. https://doi.org/10.1021/acsomega.4c09930.

(64) Guzmán-Afonso, C.; Hong, Y.; Colaux, H.; Iijima, H.; Saitow, A.; Fukumura, T.; Aoyama, Y.; Motoki, S.; Oikawa, T.; Yamazaki, T.; Yonekura, K.; Nishiyama, Y. Understanding Hydrogen-Bonding Structures of Molecular Crystals via Electron and NMR Nanocrystallography. *Nat. Commun.* **2019**, *10* (1), 3537. https://doi.org/10.1038/s41467-019-11469-2.

(65) Thomas, B.; Dubey, R. K.; Clabbers, M. T. B.; Gupta, K. B. S. S.; van Genderen, E.; Jager, W. F.; Abrahams, J. P.; Sudholter, E. J. R.; de Groot, H. J. M. A Molecular Level Approach

to Elucidate the Supramolecular Packing of Light-Harvesting Antenna Systems. *Chem. – Eur. J.* **2018**, *24* (56), 14989–14993. https://doi.org/10.1002/chem.201802288.

(66) Perras, F.A. and Bryce, D.L., Direct Investigation of Covalently Bound Chlorine in Organic Compounds by Solid-State ^{35}Cl NMR Spectroscopy and Exact Spectral Line-Shape Simulations, *Angew.Chem* **2012**; 51 (17), 4227-4230. https://doi.org/10.1002/anie.201200728

(67) Roy, P.; Ghosh, A. Mechanochemical Cocrystallization to Improve the Physicochemical Properties of Chlorzoxazone. *CrystEngCom* **2020**; 22 (27): 4611–4620. https://doi.org/10.1039/d0ce00635a.

(68) Roy, P.; Ghosh, A. Mechanochemical Cocrystallization to Improve the Physicochemical Properties of Chlorzoxazone. *Cryst. Eng. Comm.* **2020**, *22* (27), 4611–4620. https://doi.org/10.1039/d0ce00635a

(69) Scott L. Childs, Kenneth I. Hardcastle; Cocrystals of chlorzoxazone with carboxylic acids. *CrystEngComm* **2007**; 9 (5), 364–367. https://doi.org/10.1039/b703292g.

Summary of Part 2

Part 2 presented the development and application of cryogen-free Zp-NQR spectroscopy as a quantitative methodology for the characterization of quadrupolar nuclei in molecular solids. Beginning with the establishment of a practical laboratory workflow using an adjustable electromagnet and exact Hamiltonian simulations, the methodology was subsequently expanded to enable direct isotopic identification in complex spectra, quantitative evaluation of halogen-bond strength through experimentally determined quadrupolar interaction parameters, and integrated structural characterization of chlorine-containing pharmaceutical materials using complementary spectroscopic, crystallographic, and computational techniques.

These studies demonstrate the versatility of Zp-NQR as a modern approach for probing the local electronic environments of quadrupolar nuclei and illustrate how advances in instrumentation, computation, and multimodal characterization can significantly expand the scope of nuclear quadrupole resonance spectroscopy. The following parts of this thesis present complementary investigations of molecular solids using alternative experimental and computational methodologies, further highlighting the range of approaches employed throughout this research to understand structure, bonding, and materials properties.

Part 3 – Complementary Solid-State Characterization by Solid-State NMR and First-Principles Calculations

Chapter 8 – Unraveling the Amphiphilic Nature of Selenium in Non-Covalent Interactions: Combined ^{77}Se MAS SSNMR and Quantum Chemical Analysis of Se–I Halogen and Chalcogen Bonds

Based on: Nari, A.; Thomas, S. P.; Bryce, D. L.; Thomas, B. Understanding Non-Covalent Interactions in Diphenyldiselenide and Diphenylselenide Cocrystals Using a Combined 77Se Magic-Angle Spinning Solid-State NMR and Quantum Chemical Analysis Approach. J. Phys. Chem. C 2025, 129, 13299–13311.

8.1 Chapter Overview and Thesis Context

Although the primary focus of this thesis is the development and application of Zp-NQR spectroscopy for the characterization of molecular solids, the research undertaken during this doctoral work also includes complementary investigations using alternative spectroscopic and computational methodologies. This chapter presents one such study, employing ^{77}Se magic-angle spinning (MAS) SSNMR spectroscopy together with first-principles quantum chemical calculations to investigate the electronic structure of selenium-containing molecular solids. While independent of the Zp-NQR studies presented in Part 2, this work addresses the same overarching scientific objective of relating experimentally measurable spectroscopic parameters to local electronic structure and intermolecular interactions.

Selenium occupies a unique position among the chalcogen elements owing to its amphiphilic electronic character, allowing it to function either as an electron donor or as an

electron acceptor depending on its local chemical environment. Consequently, selenium can participate in both halogen bonding and chalcogen bonding, two highly directional σ-hole interactions that have become increasingly important in supramolecular chemistry, crystal engineering, and functional materials design. Despite their growing importance, the electronic factors governing selenium-centered non-covalent interactions remain comparatively less understood than those associated with hydrogen- and halogen-bonded systems.

An important advantage of ^{77}Se NMR spectroscopy is its exceptional sensitivity to the local electronic environment. The ^{77}Se nucleus possesses a chemical shift range exceeding 3000 ppm, making it particularly responsive to subtle variations in oxidation state, coordination geometry, intermolecular interactions, and crystal packing. As a result, even relatively small changes in selenium's electronic environment arising from halogen bonding or chalcogen bonding can produce measurable changes in the ^{77}Se chemical shift tensor, providing a powerful experimental probe of selenium-centered non-covalent interactions.

The work presented in this chapter investigates a family of selenium-containing cocrystals prepared from diphenyldiselenide and diphenylselenide with iodine and 1,4-diiodotetrafluorobenzene as halogen-bond donors. Experimental ^{77}Se MAS SSNMR spectroscopy is integrated with single-crystal X-ray diffraction and periodic GIPAW-DFT calculations, together with complementary electronic structure analyses including electrostatic potential mapping (ESP), the Quantum Theory of Atoms in Molecules (QTAIM), Non-Covalent Interaction (NCI) analysis, Extended Transition State–Natural Orbitals for Chemical Valence (ETS-NOCV), and Interacting Quantum Atoms (IQA) energy decomposition. These complementary methods establish direct relationships between experimentally observed ^{77}Se NMR parameters, electron density redistribution, and the nature of selenium-centered halogen and chalcogen bonding.

8.2. Statement of Authenticity

I certify that I have prepared the following article featuring my own work.

8.3 Permissions

I declare that I have obtained permission from the coauthor to include this article in my thesis. Chapter 8 has been reprinted with permission from the American Chemical Society.

8.4 Published manuscript

THE JOURNAL OF PHYSICAL CHEMISTRY C
A JOURNAL OF THE AMERICAN CHEMICAL SOCIETY

Open Access
This article is licensed under CC-BY 4.0

pubs.acs.org/JPCC
Article

Understanding Non-Covalent Interactions in Diphenyldiselenide and Diphenylselenide Cocrystals Using a Combined ^{77}Se Magic-Angle Spinning Solid-State NMR and Quantum Chemical Analysis Approach

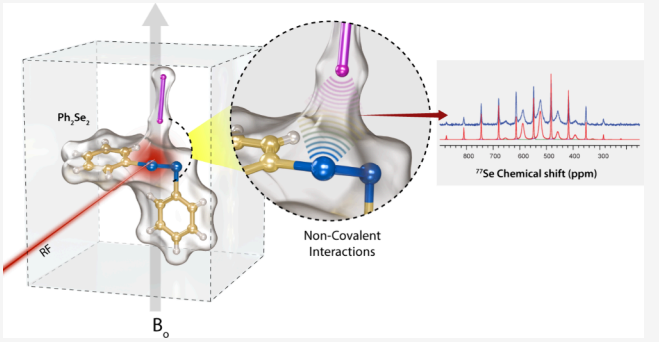
Alireza Nari, Sajesh P. Thomas, David L. Bryce,* and Brijith Thomas*

Cite This: J. Phys. Chem. C 2025, 129, 13299−13311

Read Online

ACCESS | Metrics & More | Article Recommendations | Supporting Information

ABSTRACT: Chalcogen bonds are σ-hole interactions that arise from the net attractive forces between an electron-deficient chalcogen atom (such as selenium) and a Lewis base. In recent years, chalcogen bonds have become important noncovalent interactions, playing a key role in building supramolecular structures and functional materials. Given their significance, there is a continuous interest in gaining a deeper understanding of chalcogen interactions. In this study, we examined systems involving Se−I interactions, where diphenyldiselenide and diphenylselenide serve as selenium sources, while molecular iodine and 1,4-diiodotetrafluorobenzene act as iodine donors. We explore the intricate interplay between selenium's chemical environment and its role in noncovalent interactions, with a focus on Se···I chalcogen bonds and halogen bonds. An interdisciplinary approach combining solid-state NMR, single-crystal X-ray diffraction, and advanced quantum chemical analyses, such as the Quantum Theory of Atoms in Molecules (QTAIM), Non-Covalent Interactions analysis (NCI), the Extended Transition-State Method with Natural Orbitals for Chemical Valence (ETS-NOCV), and Interactive Quantum Atoms (IQA), were used to investigate the electronic and structural factors influencing selenium's behavior. By analyzing the chemical shift tensors, we demonstrate how they are influenced by both halogen and chalcogen bonding roles, in addition to the effects of crystal packing and weak interactions.

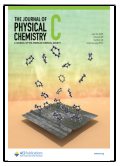


INTRODUCTION

The adaptability of selenium, enabled by its wide range of accessible oxidation states from −2 to +6, makes it a versatile element in both covalent and noncovalent interactions.[1,2] This chemical flexibility enables its crucial roles across a range of areas, including synthetic chemistry, medicinal chemistry, and materials science.[3−7] Selenium is not only central to bioactive compounds but also emerges as a key player in noncovalent interactions, such as selenium-halogen (Se···X) (X: Cl, Br, I) interactions, which are integral to supramolecular and materials chemistry.[3−7] These interactions exhibit unique versatility: in some cases, halogen atoms (X) function as σ-hole donors with selenium as the halogen bond (XB) acceptor, while in other instances, selenium itself can function as a σ-hole donor, forming chalcogen bonds (ChBs) with halogen acceptors.[8,9] The broad chemical shift range of ^{77}Se NMR provides a powerful tool for discerning subtle variations in bonding and geometry, enabling precise characterization of selenium-containing cocrystals. By examining chemical shift tensors, it is possible to reveal the dependence on halogen and chalcogen bonding roles, as well as the influence of crystal packing and weak interactions. The interaction between selenium and N-heterocyclic carbene ligands provides valuable insights into the electronic properties of these ligands, often probed through selenium solution state NMR chemical shifts.[10−12]

A XB is a directional, noncovalent interaction involving an attractive force between a halogen atom and a nucleophile. This interaction is driven by electrostatic attraction between the nucleophile and a region of elevated electrostatic potential (σ-hole) on the halogen, oftentimes alongside a charge-transfer from the nucleophilic lone pair to the antibonding σ^* orbital of the halogen.[7−11] Halogen bonding closely parallels hydrogen bonding in many respects. The σ-hole in halogen bonds functions similarly to the proton in hydrogen bonds (HBs), enabling precise and tunable noncovalent interactions.[12,13]

Received: March 25, 2025
Revised: July 3, 2025
Accepted: July 8, 2025
Published: July 16, 2025

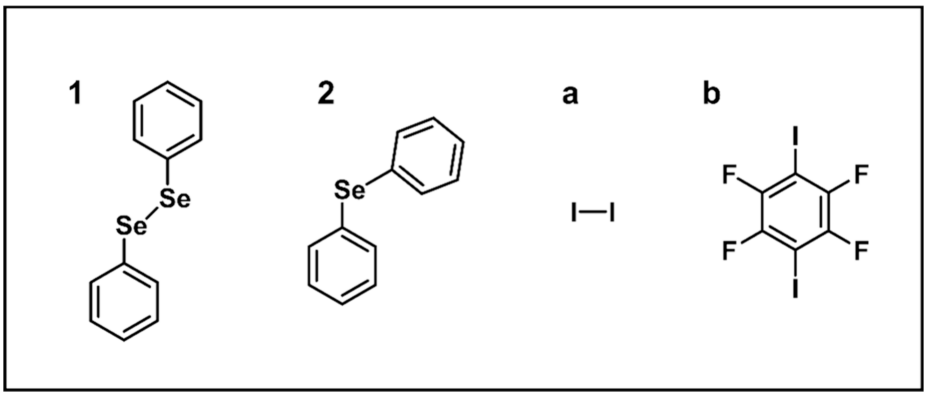


Downloaded via UNIV OF OTTAWA on May 1, 2026 at 18:30:15 (UTC).
See https://pubs.acs.org/sharingguidelines for options on how to legitimately share published articles.

ACS Publications
© 2025 The Authors. Published by American Chemical Society

https://doi.org/10.1021/acs.jpcc.5c01979
J. Phys. Chem. C 2025, 129, 13299−13311

Scheme 1. Molecular Structures of the Donors and Acceptors Used in This Study



Well-known XB acceptors include nitrogen, oxygen, sulfur, and halogens themselves,[14−21] along with some less common acceptors like phosphorus[22] and halide anions. Selenium, however, is among the less-studied XB acceptors.[23] Belonging to Group 16, known as the chalcogens, selenium can exhibit amphiphilic Lewis character, playing a dual role in the noncovalent interaction world as both a Lewis acid and a Lewis base when interacting with halogen atoms.[24,25] In ChB, the σ-hole is positioned along the extension of the R−Se covalent bond.[26] This property can be a powerful tool in the design of (supra)molecular materials, bearing specific properties similar to other well-known σ-hole interactions like HB and XB. The presence of electron withdrawing groups (EWGs) on potential σ-hole donors plays a crucial role in defining the interaction characteristics, determining which component acts as the Lewis acid and which as the Lewis base, considering the amphiphilic nature of both halogen and chalcogen atoms.[27,28]

Selenium−halogen (Se···X) noncovalent interactions cover a broad range of applications in supramolecular design, biochemistry, catalysis, and optoelectronics, where selenium can act as either a σ-hole donor or acceptor.[24,29] Certain chalcogen-containing compounds, such as 1,2,5-chalcogenadiazoles (Ch = S, Se, Te), are especially recognized as robust and versatile Lewis bases; substituent variations allow fine-tuning of σ-hole strength and, consequently, the strength of ChB interactions.[30−34] Gaining a deeper understanding of the Se−I interaction is therefore crucial for advancing knowledge across various domains. Herein, we investigate the Se−I interaction in a series of molecular systems, as depicted in Scheme 1. Specifically, diphenyldiselenide (**1**) and diphenylselenide (**2**) serve as selenium sources, while iodine (**a**) and 1,4-diiodotetrafluorobenzene (*p*-DITFB) (**b**) act as iodine sources. Through a combination of experimental solid-state NMR (SSNMR), single-crystal X-ray diffraction (SCXRD), and advanced quantum chemical analyses such as the Quantum Theory of Atoms in Molecules (QTAIM), noncovalent interaction (NCI) analyses, and Extended Transition State−Natural Orbitals for Chemical Valence (ETS-NOCV) analyses, we investigate the electronic and structural factors influencing selenium's behavior and its role in Se···I chalcogen bonding and halogen bonding. This work highlights the dual role of selenium as a ChB donor and XB acceptor, as well as shedding light on Se−Se and Se−Ph interactions, enhancing our understanding of selenium's reactivity and its significance in noncovalent chemistry.

RESULTS AND DISCUSSION

X-ray Diffraction and Structural Features. Cocrystals **1a**, **1b**, and **2b** were synthesized via mechanochemical methods and subsequently characterized to confirm their phase purity and crystallographic integrity. Specifically, **1a** is a cocrystal formed from diphenyldiselenide (**1**) and iodine (**a**) in a **1:1** ratio, **1b** is a cocrystal of diphenyldiselenide (**1**) and *p*-DITFB (**b**) in a **1:2** ratio, and **2b** consists of diphenylselenide (**2**) and *p*-DITFB (**b**) in a **1:1.5** ratio.

As shown in Figure 1, the experimental powder X-ray diffraction (PXRD) patterns of the bulk samples closely match the simulated patterns derived from SCXRD data, confirming that the synthesized samples retained the expected crystallographic structure. This detailed comparison ensures the absence of significant impurities or secondary phases and

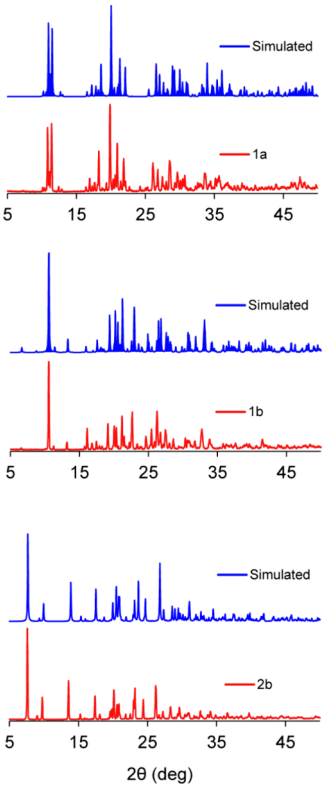


Figure 1. Comparison between experimental PXRD patterns of cocrystals prepared in this work (red) and their corresponding simulated diffractograms (blue).

https://doi.org/10.1021/acs.jpcc.5c01979
J. Phys. Chem. C 2025, 129, 13299−13311

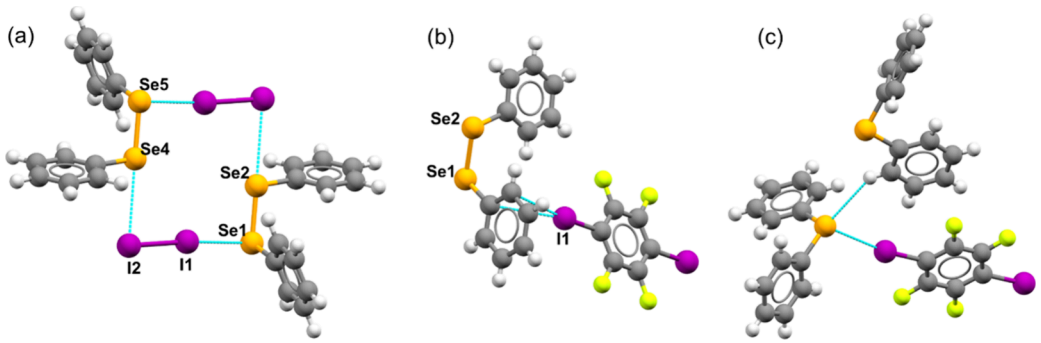


Figure 2. Crystal structures of (a) **1a**, (b) **1b**, and (c) **2b**, with selected atoms labeled, highlighting the diversity of bonding environments observed for selenium.

verifies that the observed structural and interaction data, including those involving selenium and iodine, are intrinsic to the intended crystalline form.

In the cocrystal of diphenyldiselenide and molecular iodine (**1a**), a previously reported structure,[35] distinct Se···I interactions illustrate the versatile donor–acceptor roles of selenium and iodine. In this structure, one selenium atom (Se1 or Se5, Figure 2a) acts as an electron donor to an iodine atom within the diiodine molecule, engaging in a XB interaction. This interaction involves selenium providing electron density toward the σ-hole of iodine, stabilizing the noncovalent bonding. Simultaneously, the other selenium atom in **1** plays an acceptor role by interacting with an iodine atom of a neighboring diphenyldiselenide moiety, here participating in a ChB. In this second interaction, selenium accepts electron density from the electron-rich region of the iodine atom, facilitated by the linear I···Se—Se and Se···I—I arrangements characteristic of hypervalent bonding, as discussed further in the QTAIM analysis section (vide infra). These dual donor–acceptor interactions exemplify selenium's amphiphilic nature and underscore the importance of selenium–iodine noncovalent bonding in supramolecular assembly.

In cocrystal **1b**, two selenium atoms are present: one (Se1, Figure 2b) is bonded to the phenyl ring involved in a XB with *p*-DITFB, while the other Se, (Se2) is attached to a phenyl ring with no halogen bond interaction. The electronic environment of these two Se atoms, influenced by their respective phenyl rings, warrants further investigation to elucidate their roles. This analysis is crucial for determining whether each Se atom acts as a ChB σ-hole donor or a ChB acceptor in interactions with adjacent diphenyldiselenide molecules. This will be further analyzed in the upcoming sections.

Table 2 summarizes critical bond distances, interaction angles, and interaction types for compounds **1**, **1a**, **1b**, and **2b**, illustrating the influence of various cocrystallized molecules on the Se–Se covalent bond in **1**, diphenyldiselenide. In **1**, the Se–Se bond distance is 2.307 Å, reflecting a typical value for a diselenide. Upon cocrystallization with iodine (cocrystal **1a**), this distance increases to 2.347 Å. This elongation can be rationalized by considering orbital interactions and charge-transfer effects: the selenium lone pair orbitals donate electron density into the electrophilic region of the iodine moiety, likely involving the σ^* orbitals of the I–I bond or other vacant orbitals on iodine. This electron donation depletes electron density from the Se–Se bond, weakening and lengthening it. The ETS-NOCV analysis quantifies these interactions, revealing significant orbital contributions in **1a**: $\Delta E_{\sigma 1}$= −23.99 kcal/mol, $\Delta E_{\sigma 2}$ = −3.85 kcal/mol, and $\Delta E_{\pi 1}$ = −1.75 kcal/mol (see Figure S1(i) in the Electronic Supporting Information, ESI). The dominant $\Delta E_{\sigma 1}$ term reflects a strong σ-type charge-transfer interaction, consistent with the observed XB and ChB (at 2.99 and 3.59 Å), which redistributes electron density away from the Se–Se bond. This is shown in Figure S1(i), where the NOCV orbital pairs show significant electron depletion (blue lobes) around the Se–Se bond and accumulation (red lobes) toward the iodine acceptor, directly corroborating the bond elongation from 2.307 to 2.347 Å. In **1a**, the partial redistribution of electron density associated with these interactions reduces the electron density localized in the Se–Se bond, subtly weakening and elongating it, as reflected by its length of 2.35 Å in Table 2, which is longer than in **1** and **1b**.

In contrast, for the **1b** cocrystal with *p*-DITFB, no direct Se···I short contacts are observed. Instead, the halogen bond interacts with the π-system of the phenyl ring. Although electron redistribution still occurs, the electrophilic demand from the π-system is lower than that from I_2, resulting in a minimal increase in the Se–Se bond distance to 2.313 Å, only slightly longer than in pure **1**. The ETS-NOCV analysis for **1b** supports this weaker interaction, with $\Delta E_{\sigma 1}$ = −1.25 kcal/mol, $\Delta E_{\sigma 2}$ = −0.46 kcal/mol, and $\Delta E_{\pi 1}$ = −0.72 kcal/mol (see Figure S1(ii)). These smaller ΔE values indicate less significant charge transfer compared to **1a**, consistent with the reduced impact on the Se–Se bond. Figure S1(ii) further illustrates this, showing less pronounced electron depletion around the Se–Se bond compared to **1a**, aligning with the weaker influence of the π-system interaction.

The crystal structure of cocrystal **2b,** reported here for the first time (Figure 2c) was solved in the monoclinic space group $P2_1/n$ with cell dimensions a = 13.011 Å, b = 6.148 Å, c = 18.166 Å and a cell volume of 1422.46 Å^3 (Table 1). The structure reveals notable selenium–iodine (Se···I) and selenium–hydrogen (Se···H) interactions. The Se···I interaction, with a distance of 3.551 Å, falls within the range typical of XB, where iodine acts as a σ-hole donor and selenium serves as a XB acceptor. Additionally, the selenium atom forms a secondary interaction with a hydrogen atom from a neighboring diphenylselenide molecule, with a Se···H distance of 3.053 Å, indicating a weak hydrogen bond. These dual interactions — Se···I as a halogen bond and Se···H as a weak hydrogen bond (Figure 2c)— highlight selenium's amphiphilic nature, allowing it to participate in both chalcogen bonds and hydrogen bonding-like interactions (vide infra), which collectively enhance the stability of the cocrystal structure.

Solid-State NMR Spectroscopy. Selenium-77 (^{77}Se) stands out among selenium isotopes as NMR-active (I = 1/

https://doi.org/10.1021/acs.jpcc.5c01979
J. Phys. Chem. C 2025, 129, 13299−13311

Table 1. Crystallographic Data for 2b

compound	2b
chemical formula	$C_{30}H_{20}F_4I_2Se_2$
CCDC number	2416743
FW/g mol	868.18
crystal color	clear
crystal system	monoclinic
crystal space group	$P2_1/n$
temperature/K	100
a, *b*, *c*/A°	13.0111(5), 6.1482(2), 18.1659(6)
α, *β*, *γ*/°	90, 101.802(2), 90
V/A°^{3}	1422.46 (9)
Z	2
R_1 (final)	0.0258
wR_2 (final)	0.0534

2) and naturally abundant at 7.58%. Notably, its NMR receptivity relative to ^{13}C is approximately 2.9, making ^{77}Se nearly three times more sensitive than ^{13}C. This heightened sensitivity, combined with its broad chemical shift range of over 3000 ppm,[39,40] renders ^{77}Se NMR an invaluable tool for probing noncovalent interactions involving selenium. Such an extensive range allows for precise detection of subtle variations in oxidation states, coordination geometries, and ChB environments. Consequently, ^{77}Se SSNMR is exceptionally well-suited for distinguishing nuanced electronic differences in organoselenium compounds. The sensitivity of ^{77}Se chemical shifts to variations in local geometry and intermolecular interactions makes it challenging to assign ^{77}Se solid-state NMR spectra based solely on chemical or molecular structure. To address this complexity, computational methods for calculating ^{77}Se NMR parameters offer valuable insights for interpreting experimental data. In this study, density functional theory (DFT) calculations of ^{77}Se magnetic shielding tensors were performed for all the compounds. A comparison of experimental and calculated selenium chemical shifts is presented in Table 4. Due to the presence of different short contacts in each molecule and the high sensitivity of ^{77}Se chemical shifts to the local environment, a degree of scatter is observed between experimental and calculated values. Notably, a significant shift in the δ_{22} component of the chemical shift tensor is attributed to the short Se···I distance, with this contribution diminishing as the Se···I distance decreases. The $^1H \rightarrow {}^{77}Se$ cross-polarization magic-angle spinning NMR spectra for **1**, **1a**, **1b**, and **2b** are shown in Figure 3 (see also Figures S2 and S3). Diphenylselenide (**2**) was not included in Figure 3 as it is a liquid. The ^{77}Se chemical shifts were referenced to solid $(NH_4)_2SeO_4$ at δ_{iso} = 1040.2 ppm and are listed in Table 3.

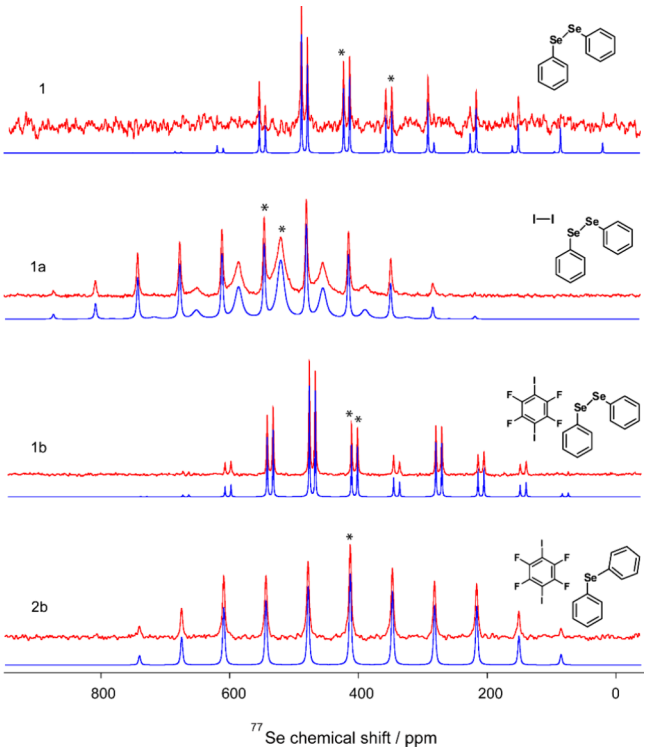


Figure 3. Experimental $^1H \rightarrow {}^{77}Se$ CP/MAS NMR spectra of diphenyldiselenide (**1**) and the studied cocrystals, collected at a spinning speed of 5 kHz (top, red), overlaid on their corresponding SOLA-simulated spectra (bottom, blue). The molecular structures of the selenium-containing species and each iodinated counterpart are shown above their respective spectra. Isotropic peaks are indicated with asterisks.

In the spectra of compounds **1**, **1a**, and **1b**, two distinct selenium sites are observed, indicating the presence of two crystallographically unique selenium environments. This differentiation is further supported by DFT calculations, which assist in assigning the two selenium sites in these compounds (vide infra).

In the parent compound, diphenyldiselenide (**1**), two distinct crystallographic selenium sites are observed due to intermolecular ChB interactions. One selenium atom (Site 1) acts as a *σ*-hole donor in the ChB interaction, exhibiting a higher chemical shift (424.5 ppm), while the other selenium atom (Site 2) acts as a ChB acceptor (electron density donor) and shows a lower chemical shift (349.6 ppm). Initially, this chemical shift difference highlights the role of subtle structural

Table 2. Selected Non-Covalent Interaction Distances to Se, Se−Se Covalent Bond Lengths (in Å), and Interaction Angles (in Degrees) for Compounds, 1, 1a, 1b, and 2b

compound/CSD refcode	Se−Se covalent bond length	noncovalent interaction distance/interacting atom	noncovalent interaction angle
1/DPHDSE02[36]	2.307(1)	3.778/Se	122.66[C−Se···Se]
		3.664/Se	172.35[C−Se···Se]
1a / GIHZIG[37]	2.347(2)	2.992/I	174.21[I−I···Se]
		3.588/I	176.50 [Se−Se···I]
1b/POGZOD[38]	2.313(1)	3.606/Se	94.76[C−Se···Se]
		3.752/Se	171.85[C−Se···Se]
2b/This work[a]		3.551/I	167.86[C−I···Se]

[a]CSD deposition number 2416743.

https://doi.org/10.1021/acs.jpcc.5c01979
J. Phys. Chem. C 2025, 129, 13299−13311

Table 3. Experimental Isotropic Chemical Shifts (δ_{iso}) and Chemical Shift Tensors[a] for Diphenyldiselenide (1), and the Cocrystals Studied Herein. All shift values are in ppm

compound	Se site	δ_{iso} [a]	δ_{CSA} [b]	δ_{11}	δ_{22}	δ_{33}	η [c]
1	1	424.5(0.2)	−239(5.8)	577(6)	511(4)	185.2(4)	0.28(0.03)
1	2	349.6(0.2)	−350(9.9)	526(10)	523(8)	−0.4(7)	0.01(0.04)
1a	1	548.1(0.2)	281(2)	829(2)	521(1)	294(1)	0.81(0.01)
1a	2	521.9(0.3)	−151(4)	660(2)	534(1)	371(1)	0.84(0.01)
1b	1	412.2(0.1)	−275.3(2)	566(2)	534(2)	137(1)	0.12(0.01)
1b	2	402.9(0.1)	−289.1(2)	550(2)	545(2)	114(1)	0.02(0.01)
2b		414.1(0.1)	−312(5)	720(3)	420(3)	102(2)	0.96(0.01)

[a] $\delta_{11} \geq \delta_{22} \geq \delta_{33}$; $\delta_{iso} = (\delta_{11} + \delta_{22} + \delta_{33})/3$. [b] Chemical shift anisotropy. [c] Asymmetry parameter

features and directional electron-density flow induced by ChB interactions in influencing shielding and deshielding effects at the selenium centers.

To further clarify the relative contributions of intrinsic molecular geometry and intermolecular interactions (XB/ChB), additional gauge-including projector-augmented wave (GIPAW)-DFT calculations were performed on both the isolated molecule and its crystalline geometry. Calculated shifts for the isolated molecule (423.3 ppm for Se1 and 343.2 ppm for Se2) and for the crystalline geometry (439.9 ppm for Se1 and 339.5 ppm for Se2) revealed a relatively modest difference of approximately 16.6 ppm for Se1 and −3.7 ppm for Se2. This indicates that the intrinsic molecular geometry—particularly internal torsion angles and electron distribution—primarily dictates the selenium chemical shifts, while the intermolecular ChB interactions present in the crystal packing contribute in a subtle, yet discernible manner. Thus, the distinct chemical shift environments observed experimentally in the solid-state ^{77}Se CP/MAS NMR spectrum predominantly reflect intrinsic molecular conformations, with intermolecular interactions serving as secondary contributors.

Upon cocrystallization with iodine (**a**) to form **1a**, these selenium environments are further modulated by the introduction of strong Se···I halogen bonding and accompanying chalcogen bonding. In **1a**, both selenium sites experience significant deshielding, with their chemical shifts increasing to 548.1 ppm (Site 1 or Se1 in Figure 2a) and 521.9 ppm (Site 2 or Se2 in Figure 2a). Here, Se1 donates electron density to iodine atom, reinforcing the XB interaction, while Se2 maintains its role as a ChB donor (σ-hole donor) in the altered crystal environment. This trend deviates from the observations in **1**, where the σ-hole acceptor site (electron density donor) exhibited a lower chemical shift. A possible explanation is that, despite Se1 acting as an electron density donor in the XB interaction, its close proximity to iodine (2.99 Å) and the strong electronic influence of the iodine atom led to a higher chemical shift compared to Se2. The pronounced shift in both selenium sites underscore the significant impact of σ-hole interactions on the local electronic and magnetic environments, effectively enhancing polarization and reducing electron density around the selenium nuclei.

In contrast, cocrystallization with *p*-DITFB to form **1b** introduces weaker interactions that do not involve direct Se···I contacts. Although the selenium environments are still influenced by ChB interactions, the overall effect is less pronounced. The chemical shifts change from 424.5 and 349.6 ppm in **1** to approximately 412.2 (Site 1 or Se1 in Figure 2b) and 402.9 (Site2 or Se2 in Figure 2b) ppm in **1b**. Although both selenium sites are affected, the absence of a strong direct XB interaction leads to comparatively smaller deshielding effects.

In this case, Se1 acts as a σ-hole donor and Se2 as a σ-hole acceptor in ChB interactions within the unit cell with other selenium atoms. This trend aligns with the observations in **1**, where only Se···Se ChB interactions are present, and the electron density acceptor (σ-hole donor) site exhibits a higher chemical shift. Notably, in the absence of interactions with high-electron-density species—such as the iodine-mediated interaction observed in **1a**—this trend holds: the σ-hole donor site, which accepts electron density, consistently exhibits a higher chemical shift compared to the electron density donor Se site.

A notable observation is that the solid-state ^{77}Se CP/MAS NMR spectrum of **1** (Figure 3a) exhibits two distinct resonances at δ_{iso} = 424.5 and 349.6 ppm, whereas only a single signal at δ = 463 ppm is observed in solution.[41] This discrepancy highlights the influence of the solid-state environment, where intermolecular noncovalent interactions (such as XB and ChB) and crystal packing result in distinct selenium sites, each characterized by a unique local electronic environment. To clarify the relative contributions of intrinsic molecular geometry and intermolecular interactions, additional GIPAW-DFT calculations were conducted on both the isolated molecule and its crystalline geometry. The calculated shifts for the isolated molecule (423.3 ppm for Se1 and 343.2 ppm for Se2) and the crystalline geometry (439.9 ppm for Se1 and 339.5 ppm for Se2) showed relatively modest differences of approximately 16.6 ppm and−3.7 ppm, respectively. This indicates that intrinsic molecular geometry—specifically internal torsion angles and electron distribution—predominantly determines the observed chemical shifts, while intermolecular ChB interactions in the crystal structure have a subtle yet detectable influence. Therefore, the significant 75 ppm chemical shift difference between solid-state and solution spectra primarily arises from conformational changes upon crystallization, further underscoring the exceptional analytical power of ^{77}Se SSNMR to probe subtle structural and electronic variations in selenium-containing solids.

^{13}C SSNMR spectroscopy (Figures S5 and S6) has proven to be an effective indirect probe for investigating noncovalent interactions, with chemical shift changes providing evidence of cocrystallization through interactions such as XB and ChB.[42−44] This technique allows us to gain insights into the changes in the crystallographic and electronic environment surrounding carbon atoms, particularly those covalently bonded to selenium (C−Se) in the acceptor moieties. Although the ^{13}C nucleus is indirectly involved in each XB or ChB (one bond removed), it is still sensitive to subtle alterations in the electronic and crystallographic environment

https://doi.org/10.1021/acs.jpcc.5c01979
J. Phys. Chem. C 2025, 129, 13299−13311

induced by cocrystallization. These interactions result in observable shifts in the ^{13}C NMR spectra, as demonstrated in Figure S5 for compound **1** and cocrystals (Figures S4–S6). Note that compound **2** was not included, as it is a liquid. The ^{13}C SSNMR spectra show distinct chemical shifts for the starting materials compared to the cocrystals, reflecting differences in the local electronic environment and confirming the formation of new noncovalent interactions.

Computational Studies. *ESP MAP.* To understand the σ-hole interactions, electrostatic potential (ESP) maps[45,46] are frequently used in conjunction with ^{77}Se NMR spectroscopy (Figure 4).[47] The ESP analysis allows one to visualize charge distribution within a molecule, highlighting potential electrophilic or nucleophilic sites. By mapping the electrostatic potential around a molecule, it is possible to pinpoint areas likely to engage in ChBs, offering a visual representation of interaction sites. These maps are particularly valuable for interpreting NMR data, as they correlate observed chemical shifts with specific regions of charge density and potential ChB formation. The integration of ^{77}Se NMR spectroscopy and ESP maps provide a comprehensive approach to studying ChBs, providing both experimental and theoretical insights into the chemical and electronic structures of selenium-containing compounds.

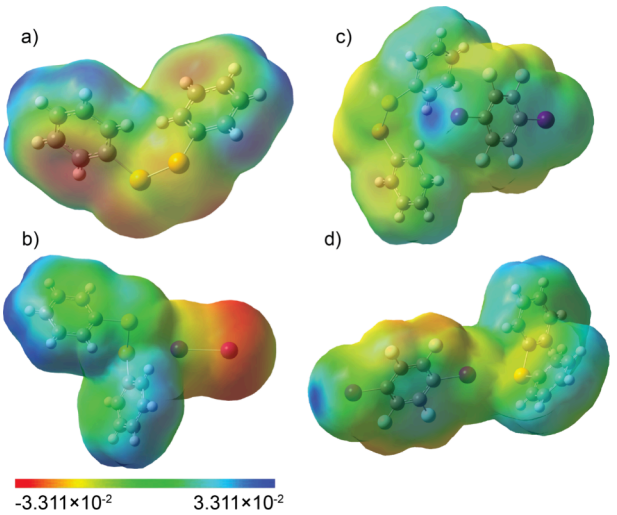


Figure 4. ESP maps of (a) diphenyldiselenide (**1**), (b) its cocrystal with iodine (**1a**), (c) its cocrystal with *p*-DITFB (**1b**), and (d) the cocrystal of diphenylselenide (**2**) with *p*-DITFB (**2b**). The maps illustrate the charge distribution across the molecular surfaces, highlighting regions of electron density (blue) and electron deficiency (red), which correspond to nucleophilic and electrophilic sites, respectively.

In the case of diphenyldiselenide, the chemical shift of selenium appears at 424.5 ppm for the σ-hole donor and 349.6 ppm for the σ-hole acceptor, which is evident from the ESP map of **1**. In the case of cocrystal **1b**, the σ-hole donor appears at 412.2 ppm and the acceptor appears at 349.6 ppm. In the case of cocrystal **1a** the σ-hole acceptor comes at 548.1 ppm, which is more deshielded and is engaged in the halogen bond. In the case of **2b**, the σ-hole acceptor appears at 414.1 ppm, showing a moderated deshielding due to the weaker halogen interaction.

The GIPAW-DFT calculations exhibit a linear correlation between the experimental ^{77}Se isotropic chemical shifts (δ_{iso}) and the calculated isotropic shielding constants (σ_{iso}), as illustrated in Figure 5. For the fully optimized structures (Figure 5a), the correlation is particularly robust, yielding an R^2 value of 0.982 and demonstrating excellent agreement between the computed and experimental data. The resulting regression equation, Cal. $\sigma_{iso} = -1.188$ Exp. $\delta_{iso} + 1.692 \times 10^3$, underscores the method's predictive capabilities. The calculated chemical shift components derived from the regression equation based on fully optimized structures are summarized in Table 4.

The differences between calculated and experimental chemical shifts are generally small in Table 4. For example, **1a**(1) and **1a**(2) exhibit deviations of only 2.6 and −10.2 ppm, respectively. While a larger discrepancy of 56.9 ppm is observed for **2b**, this may reflect the influence of specific intermolecular interactions or structural constraints not fully captured in the model. Further, this difference represents only 1% of the total ^{77}Se chemical shift range. Overall, the GIPAW approach employed here is sufficiently accurate for computing ^{77}Se NMR parameters in the studied systems. These results are consistent with previous work using GIPAW and (Zeroth

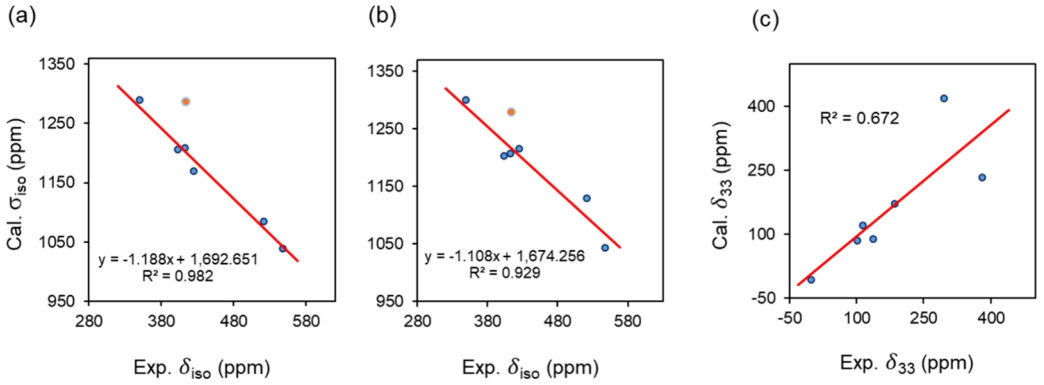


Figure 5. Correlation plots comparing calculated and experimental ^{77}Se NMR parameters: (a) isotropic chemical shielding constants (σ_{iso}) vs experimental isotropic chemical shifts (δ_{iso}) for fully optimized structures. The linear regression excluding the outlier (**2b**, shown as an orange dot) yields Cal. $\sigma_{iso} = -1.188$ Exp. $\delta_{iso} + 1.692 \times 10^3$ ($R^2 = 0.982$), while including the outlier gives Cal. $\sigma_{iso} = -1.260$ Exp. $\delta_{iso} + 1.737 \times 10^3$ ($R^2 = 0.872$). (b) σ_{iso} vs δ_{iso} for hydrogen-optimized structures. Excluding the outlier (**2b**), the regression is Cal. $\sigma_{iso} = -1.108$ Exp. $\delta_{iso} + 1.674 \times 10^3$ ($R^2 = 0.929$); including it: Cal. $\sigma_{iso} = -1.162$ Exp. $\delta_{iso} + 1.707 \times 10^3$ ($R^2 = 0.866$). (c) Calculated δ_{33} vs experimental δ_{33} for all selenium sites: Cal. $\delta_{33} = 0.873$ Exp. $\delta_{33} + 7.470$ ($R^2 = 0.672$).

https://doi.org/10.1021/acs.jpcc.5c01979
J. Phys. Chem. C 2025, 129, 13299−13311

Table 4. Experimental Isotropic Chemical Shifts (δ_{iso}) and GIPAW-DFT (Fully Optimized Structure) Calculated ^{77}Se SSNMR Parameters for the Compounds Studied Herein[a]. All values are in ppm

compound	Se site	$\delta_{iso,expt}$	$\sigma_{iso,calc}$	$\delta_{iso,calc}$	$\delta_{11,calc}$	$\delta_{22,calc}$	$\delta_{33,calc}$	$\delta_{iso,calc}-\delta_{iso,expt}$
1	1	424.5	1170.0	439.9	650.3	497.1	172.2	15.3
1	2	349.6	1289.3	339.5	622.4	401.7	−5.6	−10.1
1a	1	548.1	1038.3	550.7	705.1	528.9	418.2	2.6
1a	2	521.9	1084.6	511.7	859.6	442.8	232.8	−10.2
1b	1	412.2	1208.3	407.6	669.6	464.5	88.8	−4.6
1b	2	402.9	1205.6	409.9	686.4	422.8	120.7	7.0
2b	_	414.1	1286.3	357.2	625.6	360.5	85.6	−56.9

[a]Cal.σ_{iso} = −1.188 Exp. δ_{iso} + 1.692 × 10^3

Order Regular Approximation) ZORA-DFT methods to accurately predict ^{77}Se NMR parameters,[48,49] confirming the reliability and transferability of such computational strategies.

The GIPAW algorithm,[50] which reconstructs the all-electron wave function in the presence of a magnetic field, has proven to be an accurate and reliable method for simulating the ^{77}Se chemical shift. The principal components of the chemical shift tensor, δ_{11}, δ_{22}, and δ_{33}, are reported following the Maryland convention,[51] where they are arranged in descending order such that $\delta_{11} > \delta_{22} > \delta_{33}$. The δ_{iso}, is calculated as the average of the three principal components:

$$\delta_{iso} = \frac{\delta_{11} + \delta_{22} + \delta_{33}}{3} \quad \text{(i)}$$

A strong agreement between the experimental and calculated values across a wide chemical shift range enables the precise assignment of experimental ^{77}Se NMR spectra for compounds containing multiple crystallographically distinct Se sites. The calculated ^{77}Se NMR parameters effectively differentiate these selenium sites, as demonstrated in compounds, and **1b** (Figure S7), where clear variations in the calculated chemical shifts correlate well with experimental results.

For example, in cocrystal **1a**, two distinct selenium sites exhibit different roles within the XB and ChB interactions. Selenium site 1 (Se1), which participates as a Lewis base in a XB by donating electron density to iodine, exhibits a higher experimental chemical shift of 548.1 ppm, consistent with the calculated GIPAW-DFT value of 550.7 ppm. Conversely, site 2 (Se2), which acts as a Lewis acid in a ChB by interacting with iodine, shows a lower chemical shift in both experimental and calculated values, reflecting its role as an electron density acceptor (vide infra, Figure 6a). A similar trend is observed for compounds **1** and **1b**, where distinct selenium sites are clearly resolved due to their differing bonding roles and electronic environments.

QTAIM and NCI Analysis. The nature of intermolecular interactions within the studied systems was investigated using the The Quantum Theory of Atoms in Molecules (QTAIM). QTAIM provides a powerful framework for analyzing noncovalent interactions, such as XB and ChB, as well as covalent bonds, by evaluating key topological parameters at the bond critical point (BCP). Key descriptors include the electron density (ρ_{BCP}) and the Laplacian of electron density ($\nabla^2\rho_{BCP}$), which indicate interaction strength and bonding type. A positive $\nabla^2\rho$ typically signifies closed-shell interactions (e.g., hydrogen or ionic bonds), while a negative value is associated with shared-shell, covalent interactions. The electron density (ρ_{BCP}) and the Laplacian of electron density ($\nabla^2\rho_{BCP}$) are particularly informative, as they allow for the characterization of bond strength and bonding type.[52,53] These data,

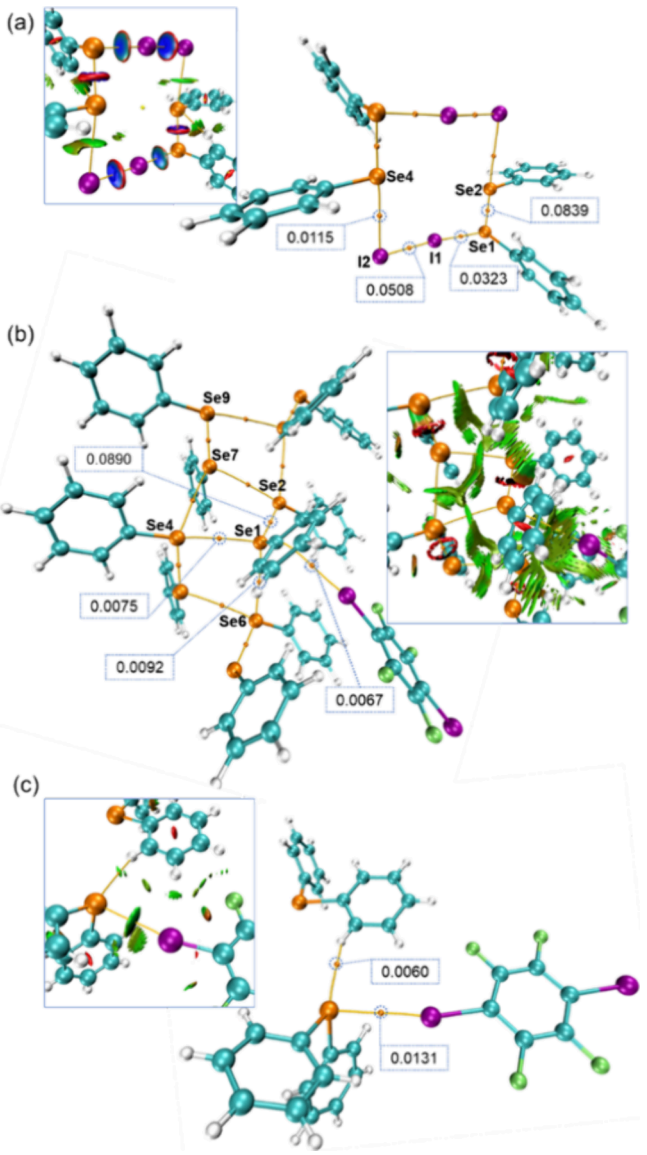


Figure 6. QTAIM and NCI graphs illustrating the selected interactions in the cocrystals of **1a** (a), **1b** (b), and **2b** (c). The NCI graphs are displayed as insets within each QTAIM plot, highlighting the regions of noncovalent interactions. In the NCI plots, green isosurfaces represent weakly attractive interactions (e.g., van der Waals forces, XB, and ChB), red regions indicate repulsive interactions, and blue regions denote strong attractive interactions. The values of electron density at the BCPs are provided in atomic units (a.u.) at selected BCPs, corresponding to data in Table 5.

https://doi.org/10.1021/acs.jpcc.5c01979
J. Phys. Chem. C 2025, 129, 13299−13311

summarized in Table 5 and illustrated in Figure 6, provide insight into bonding characteristics across the studied systems.

Table 5. QTAIM Analysis of the Selected Interactions at the BCPs in the Cocrystals Studied, Highlighting Electron Density (ρ), Laplacian of Electron Density ($\nabla^2\rho$), and Total Energy Density ($H(r)$) Values

cocrystal	interaction (BCP)	ρ (a.u.)	$\nabla^2\rho$ (a.u.)	$H(r)$ (a.u.)
1a	Se1−Se2 (covalent)	0.0585	0.0478	−0.0121
	I−I (Covalent)	0.0340	0.0514	−0.0025
	I1···Se1 (XB)	0.0336	0.0603	−0.0020
	Se4···I2 (ChB)	0.0115	0.0297	0.0010
1b	Se1−Se2 (covalent)	0.0716	0.0282	−0.0204
	I1···π(C) (XB)	0.0075	0.0259	0.0142
	Se1···Se4 (ChB)	0.0089	0.0243	0.0009
	Se1···Se6 (ChB)	0.0123	0.0330	0.0011
2b	I···Se (XB)	0.0135	0.0349	0.0011
	Se···H (HB)	0.0060	0.0226	0.0015

To more accurately describe weak chalcogen-bonding interactions, dispersion effects were explicitly included in our QTAIM and NCI analyses using Grimme's D3-BJ correction scheme. Dispersion interactions are now well-established as essential contributors to chalcogen bonding, particularly in systems involving heavy atoms, as demonstrated in theoretical studies by Bleiholder et. al[54] and by Huber and co-workers.[55]

In cocrystal **1a**, the bonding environment is multifaceted, involving both covalent and noncovalent interactions. Specifically, Se1 and Se2 are covalently bonded, while Se1 also participates in a XB with iodine, and Se4 forms a ChB with a different iodine moiety. The I−I bond represents the covalent linkage between the iodine atoms within the halogen bond donor. The inclusion of dispersion corrections in the QTAIM analysis slightly altered the electron density parameters, providing a more accurate picture of these interactions.

The Se1−Se2 covalent bond shows the highest electron density at the bond critical point (BCP), with ρ = 0.0585 au, $\nabla^2\rho$ = 0.0478 au, and $H(r)$ = −0.0121 au, confirming its covalent character. This is consistent with expectations for a typical Se−Se bond, where the negative energy density ($H(r)$) reflects strong electron sharing. The I−I covalent bond exhibits an electron density of ρ = 0.0340 au, with a Laplacian of $\nabla^2\rho$ = 0.0514 au, and $H(r)$ = −0.0025 au The positive Laplacian coupled with a small negative $H(r)$ suggests a closed-shell covalent interaction, common for halogen−halogen bonds.

The I···Se1 halogen bond has a slightly lower electron density at the BCP (ρ = 0.0336 au) but still shows a comparable Laplacian ($\nabla^2\rho$ = 0.0603 au) and $H(r)$ = −0.0020 au These parameters support the partially covalent nature of the halogen bond, with meaningful charge accumulation and some degree of electron sharing between the iodine and selenium atoms.

Finally, the Se···I2 chalcogen bond is characterized by the weakest interaction, with ρ = 0.0115 au, $\nabla^2\rho$ = 0.0297 au, and a positive energy density ($H(r)$ = +0.0010 au). The positive $H(r)$ and lower ρ values confirm that this is a typical noncovalent chalcogen bond, dominated by electrostatic attraction and polarization rather than electron sharing.

In cocrystal **1b**, the I1···π(C) interaction (ρ = 0.0075 au, $\nabla^2\rho$ = +0.2586 au, $H(r)$ = +0.0142 au) reflects a typical weak halogen bond, dominated by electrostatic interactions, consistent with the characteristics of halogen−π interactions. Despite the low electron density, the positive Laplacian and Hamiltonian energy density confirm its noncovalent, closed-shell nature.

The Se1−Se2 covalent bond shows a significant electron density (ρ = 0.0716 au, $\nabla^2\rho$ = +0.2819 au, $H(r)$ = −0.0204 au), demonstrating a shared-shell interaction with weak covalent character. Compared to **1a**, the slightly lower ρ and more positive $\nabla^2\rho$ suggest a marginally more polarized Se−Se bond in **1b**, reflecting a subtle difference in selenium's bonding environment.

The Se1···Se4 chalcogen bond (ρ = 0.0089 au, $\nabla^2\rho$ = +0.2428 au, $H(r)$ = +0.0009 au) lies within the weak, closed-shell interaction regime. The presence of a bond path and a BCP confirms the interaction, with the positive Laplacian indicating a net depletion of electron density at the BCP. Se1 again acts as a σ-hole donor, evidenced by angular directionality and its dual role in XB and ChB interactions.

Geometrical and topological data further distinguish the bonding roles of selenium centers: Se1 participates in both halogen and chalcogen bonding as a σ-hole donor, while Se2 primarily serves as an electron donor. The directional Se1···Se4 interaction (C−Se1−Se4 = 87°) and the relative location of the BCP reinforce Se1's electrophilic nature, while Se2's interactions remain more nucleophilic. Altogether, these features support selenium's adaptable bonding behavior across different interaction types in **1b**.

From the QTAIM data (Figure 6c and Table 5), the I···Se interaction in the **2b** cocrystal exhibits features consistent with a halogen bond. The electron density at the bond critical point (ρ_{BCP} = 0.0135 au) is above the typical threshold for noncovalent interactions, indicating a significant interaction between the iodine and selenium atoms. The positive Laplacian ($\nabla^2\rho_{BCP}$ = +0.0349 au) reflects electron density depletion in the bonding region, which is characteristic of closed-shell interactions such as halogen bonds. Importantly, the total energy density ($H(r)$ = +0.0011 au) is slightly positive, suggesting that although the interaction is stabilizing, it lacks significant covalent character and remains within the regime of noncovalent, electrostatic-dominated bonding.

The Se···H interaction also presents a detectable electron density (ρ_{BCP} = 0.0060 au) and a positive Laplacian ($\nabla^2\rho_{BCP}$ = +0.0226 au), consistent with weak hydrogen bonding. Its $H(r)$ = +0.0015 au, again slightly positive, indicates a weakly stabilizing, closed-shell interaction, likely contributing modestly to the crystal packing.

Taken together, these QTAIM parameters confirm that the I···Se interaction is the more prominent noncovalent force in cocrystal **2b**, while the Se···H interaction provides secondary stabilization. The positive total energy densities in both cases indicate noncovalent but energetically favorable interactions, dominated by electrostatics rather than covalency.

The Non-Covalent Interaction (NCI) analysis[56,57] provides complementary insights into the nature of the interactions within the cocrystals beyond what is revealed by QTAIM. As shown in the insets of Figure 6, NCI plots visualize weak noncovalent interactions, such as van der Waals forces, XB, and ChB, by highlighting regions of low electron density and low reduced density gradient (RDG). The green isosurfaces in the NCI plots represent weakly attractive interactions, while the red and blue regions indicate repulsive and strong attractive interactions, respectively. For example, in **1a**, the NCI analysis captures the weak dispersive interactions between neighboring phenyl rings, which play a key role in stabilizing the crystal

https://doi.org/10.1021/acs.jpcc.5c01979
J. Phys. Chem. C 2025, 129, 13299−13311

packing. Similarly, in **1b**, the NCI plots reveal the dispersion interactions in the Se···π and Se···Se contacts, aligning with the QTAIM-detected bond critical points. In **2b**, the isosurfaces emphasize the strong XB interactions between iodine and selenium atoms, further corroborating the QTAIM findings. These visualizations illustrate the spatial extent and distribution of noncovalent interactions, offering a qualitative perspective that complements the quantitative parameters obtained from QTAIM analysis.

IQA Analysis. To complement the QTAIM and NCI findings, the Interacting Quantum Atoms (IQA)[58,59] approach was employed to decompose the total interaction energy between atomic basins into classical electrostatic and quantum mechanical exchange-correlation components. This method provides a quantitative measure of the stabilizing (or destabilizing) contributions to bonding, particularly valuable for noncovalent interactions where electron density-based descriptors may be ambiguous. The results are summarized in Table S1 of the Supporting Information, and are discussed below.

The IQA analysis of cocrystal **1a** provides further insight into the nature of bonding interactions involving selenium and iodine, complementing the QTAIM and NCI findings. For the Se1−Se2 bond in diphenyldiselenide, the IQA-derived total interaction energy (−129.37 kcal/mol) confirms a stabilizing interaction, with the covalent contribution (−144.94 kcal/mol) overwhelmingly dominating (112%), and a small destabilizing noncovalent component (+15.56 kcal/mol), consistent with the QTAIM description of weak covalent character and significant electrostatic influence due to diffuse selenium orbitals. The I1···Se1 halogen bond, identified as moderate by QTAIM, also shows a predominantly covalent character (98.4%) with an interaction energy of−52.87 kcal/mol, reinforcing its partially covalent and stabilizing nature despite low electron density at the bond critical point. In contrast, the Se4···I2 interaction, suspected to be a chalcogen bond, exhibits a much weaker interaction energy (−13.56 kcal/mol) with a nearly pure covalent contribution (100.5%), yet the overall weak and slightly destabilizing nature observed in QTAIM (positive $H(r)$) suggests that the IQA "covalency" arises from minimal orbital interactions rather than strong electron sharing. Taken together, these IQA metrics align with the QTAIM interpretation: both Se−Se and I−I are weak covalent bonds with substantial electrostatic contributions, while the I···Se and Se···I contacts show gradations in bond strength and covalency, reflecting their classification as halogen and chalcogen bonds respectively, and illustrating the nuanced bonding behaviors typical of heavy element systems.

The IQA results for the **1b** cocrystal offer quantitative support for the nature and relative strengths of the noncovalent and covalent interactions identified via QTAIM and NCI analysis. The Se1−Se2 interaction, with a total interaction energy of −138.65 kcal/mol and a dominant covalent contribution (112.1%), aligns with the QTAIM indication of a weak covalent bond, reinforcing the conclusion that this is a genuine covalent Se−Se bond with some delocalization due to selenium's diffuse orbitals. In contrast, the Se1···Se4 chalcogen bond, with an interaction energy of only −5.78 kcal/mol and a similarly dominant covalent contribution (110.7%), is much weaker but still shows signs of orbital overlap, supporting its classification as a directional, σ-hole-driven interaction. Finally, the I···π halogen bond between iodine and the aromatic carbon C9 shows a modest interaction energy of −11.24 kcal/mol, with a larger electrostatic (noncovalent) component (63.7%) compared to the covalent part (36.3%). This energetic profile is consistent with the QTAIM and NCI evidence pointing to a closed-shell, electrostatically dominated halogen bond. Overall, the IQA data corroborate the dual role of selenium as both a σ-hole donor and electron donor in the crystal and reinforce the complementary nature of electrostatics and covalency in stabilizing the halogen and chalcogen bonding motifs in **1b**.

For **2b** cocrystal, IQA analysis quantifies the Se···I interaction energy at−13.90 kcal/mol, with a notably high covalent contribution (−16.90 kcal/mol, 121.6%), partially offset by a small destabilizing noncovalent component (+3.00 kcal/mol, −21.6%), further underscoring the strongly polarized, partially covalent nature of this halogen bond. A secondary interaction between selenium and a neighboring hydrogen atom (Se···H = 3.05 Å) was also detected. Though weaker (−5.32 kcal/mol), this contact is still significant and shows a covalent contribution of 62.6%, suggesting a stabilizing influence through a directional Se···H hydrogen-type contact. Collectively, these results confirm the Se···I halogen bond as the primary interaction driving the cocrystal formation in **2b**, with additional stabilization provided by weaker intermolecular contacts.

CONCLUSIONS

This study offers a detailed and multifaceted understanding of noncovalent interactions in diphenyldiselenide and diphenylselenide cocrystals formed with iodine-based halogen bond donors (I_2 and *p*-DITFB). Using a combination of experimental SSNMR, X-ray diffraction, and advanced quantum chemical analyses—including GIPAW-DFT, QTAIM, NCI, ETS-NOCV, and IQA energy decomposition—we examined in detail the interplay of halogen and chalcogen bonding in the **1**, **1a**, **1b** and **2b** systems.

The ^{77}Se SSNMR chemical shifts provide significant evidence of selenium's amphiphilic character, revealing a tunable balance between its σ-hole donor and acceptor roles. In diphenyldiselenide (**1**), the σ-hole donor (ChB, δ_{iso} = 424.5 ppm) is significantly more deshielded than the σ-hole acceptor (ChB, δ_{iso} = 349.6 ppm), a 74.9 ppm difference. This trend persists in cocrystal **1b** (with *p*-DITFB), where the σ-hole donor (δ_{iso} = 412.2 ppm) remains more deshielded than the acceptor (δ_{iso} = 402.9 ppm) by 9.3 ppm. In contrast, cocrystal **1a** (with I_2) exhibits an inversion: the σ-hole acceptor site engaged in a halogen bond (XB, δ_{iso} = 548.1 ppm) is more deshielded than the donor site (ChB, δ_{iso} = 521.9 ppm) by 26.2 ppm. In **2b**, the lone σ-hole acceptor site (XB, δ_{iso} = 414.1 ppm) shows moderate deshielding, consistent with a weaker XB interaction. GIPAW-DFT chemical shift calculations incorporating dispersion correction (PBE0-D3(BJ)) closely track experimental values (R^2 = 0.901), confirming the accuracy of the electronic structure modeling.

The QTAIM analysis corroborates these spectroscopic trends, revealing both the partially covalent nature of Se−Se bonding (e.g., ρ = 0.0839 au, $\nabla^2\rho$ = +0.0264 au in **1a**) and the moderate strength of Se···I halogen bonds (e.g., ρ = 0.0323 au in **1a**). The NCI plot visualizations further highlight the role of stabilizing dispersive interactions, including Se···I contacts and π···π stacking between phenyl rings.

Notably, the implementation of IQA energy decomposition allowed us to understand the interatomic interaction energies into covalent and noncovalent components, enabling quantitative benchmarking of interaction types. For example, Se···I

https://doi.org/10.1021/acs.jpcc.5c01979
J. Phys. Chem. C 2025, 129, 13299−13311

halogen bonds were shown to possess non-negligible covalent contributions (up to ∼30% covalency), while Se···H−C and $\pi-\pi$ interactions were dominated by electrostatics and dispersion. These insights underscore how even ostensibly weak interactions contribute significantly to crystal stability and supramolecular organization.

Together, these findings demonstrate that subtle variations in XB or ChB partners profoundly influence the selenium chemical environment, which is sensitively captured by ^{77}Se SSNMR. The comprehensive integration of experimental and computational approaches—augmented by dispersion-corrected DFT and quantitative IQA analysis—provides a robust framework for understanding and rationally tuning selenium-based noncovalent interactions. This work lays the groundwork for the deliberate design of supramolecular materials leveraging selenium's dual σ-hole behavior in diverse applications, from molecular electronics to functional crystalline materials.

EXPERIMENTAL SECTION

Materials. Diphenyldiselenide, **1** and diphenylselenide, **2** were purchased from Alfa Aesar. 1,4-diiodotetrafluorobenzene (*p*-DITFB), **b**, and iodine, **a**, were obtained from Sigma-Aldrich. All compounds were used as received without further purification. Reagent-grade solvents and doubly distilled water were used.

Sample Preparation. Powder crystalline samples of compounds **1a**, **1b**, and **2b** were prepared mechanochemically using a benchtop ball mill (Retsch MM 400). Equimolar amounts of starting materials were used for the cocrystallization process. For the liquid-assisted grinding (LAG) method, small amounts of liquid were added: 0.05 μL/mg of CH_2Cl_2 for **1a** and $CHCl_3$ for **1b**, while **2b** was prepared without any liquid additive. The ball milling process was conducted at room temperature with a milling frequency of 30 Hz for 40 min, utilizing a 10 mL grinding jar and two stainless steel balls (5 mm outer diameter).

A single crystal of **2b** suitable for SCXRD analysis was obtained by slowly adding a solution of **b** (0.4 mmol) in 2 mL of chloroform to a solution of **2** (0.4 mmol) in chloroform, dropwise. The solvent was allowed to evaporate gradually at room temperature, resulting in the formation of bright white to colorless crystals.

Powder X-ray Diffraction. PXRD data were acquired using a Bruker D8 Endeavor instrument equipped with a 1 kW Cu Kα radiation source (λ = 1.54056 Å) and a LynxEye XE-T high-speed detector. The measurements were performed at room temperature. Samples were placed securely in a well plate and rotated at a speed of 15 rpm during data collection to ensure even exposure.

Single-Crystal X-ray Diffraction. A single crystal of compound **2b** was mounted on a thin glass fiber using Parabar oil. SCXRD analysis was carried out on a Bruker AXS SMART diffractometer, which used a Mo Kα radiation source (λ = 0.71073 Å) from a sealed tube. The measurements were conducted at a temperature of 213 K. Raw data were collected and processed using the Bruker ApexIII software.[60] Unit cell parameters were determined from 36 frames obtained via specific ω scans, with semiempirical absorption corrections applied based on equivalent reflections. The systematic absences and unit cell parameters confirmed the assigned space group. Initial structural solutions were obtained using ShelxT direct methods,[61] and the structures were refined through full-matrix least-squares techniques using F^2, aided by ShelXL and ShelXle software.[62] Hydrogen atoms were positioned geometrically and refined using a riding model.

Solid-State NMR Spectroscopy. *Experiments at 60 kHz MAS Rate.* Solid-state NMR spectra were measured with a Bruker Avance HD 600 WB NMR spectrometer at B_0 = 14.1 T ($\nu_0(^1H)$ = 600 MHz) with a triple resonance 1.3 mm MAS NMR probe. Samples were gently ground into fine powders and packed in 1.3 mm o.d. zirconium oxide rotors prior to data collection. The ^{1}H and ^{13}C chemical shifts are quoted relative to neat tetramethylsilane (TMS) using adamantane as a secondary chemical shift standard. Single-pulse ^{1}H NMR spectra were recorded using 90° rf pulses operating at the ^{1}H nutation frequency $\nu_H \approx$ 185 kHz, 16 accumulated NMR-signal transients, and relaxation delays of 2.0 s. The ^{13}C NMR spectra were recorded using ^{1}H → ^{13}C CP at the double quantum Hartmann−Hahn condition,[63] $\nu_H + \nu_C = \nu_r$, which involved ramped CP of ν_H = 20 ± 5 kHz for ^{1}H (ν_C = 40 kHz), a 1.5 μs 90° ^{1}H pulse, and spinal-64 ^{1}H decoupling[64] at ν_H = 150 kHz.

Experiments at 10 kHz MAS Rate. A Bruker Avance III spectrometer operating at B_0 = 9.4 T [$\nu(^1H)$ = 400 MHz] with a triple resonance 4 mm MAS NMR probe was used for the ^{77}Se NMR experiments. ^{77}Se SSNMR chemical shifts were referenced to solid $(NH_4)_2SeO_4$, (δ_{iso} = 1040.2 ppm). Samples were gently ground into fine powders and packed in 4 mm o.d. zirconium oxide rotors prior to data collection. The spectra were generally obtained at room temperature. A standard ^{1}H → ^{77}Se CP pulse sequence with proton decoupling was employed. The $\pi/2$ pulse length was optimized to be 3.70 μs, and the CP contact time used was 5000 μs. The recycle delay varied from 10 to 60 s. All solid-state NMR spectra were processed using the TopSpin (version 4.3.0) software package developed by Bruker BioSpin GmbH. Chemical shift tensor components were obtained from ^{77}Se SSNMR spectra simulated via the Sola module in Topspin (version 4.3.0).

The ^{77}Se chemical shift parameters, including the isotropic chemical shift (δ_{iso}), the chemical shift anisotropy parameters based on the Maryland convention, and the principal components of the chemical shift tensor (δ_{11}, δ_{22}, and δ_{33}), were obtained by fitting the spinning sideband patterns using the Solid Lineshape Analysis (SOLA) module within TopSpin and the HBA 1.8.1 software.[40]

Computational Chemistry. Molecular electrostatic potential (ESP) maps were computed using the B3LYP/LANL2DZ level of theory with Gaussian 03, Revision C.02.[65] The Cartesian coordinates of the individual ChB donor molecules were derived from their crystallographic information files and used as input data. Electrostatic surface potentials were plotted with isovalues set at MO = 0.02 au and density = 0.0004 au, allowing for the determination of maxima and minima at specific points on the molecule.

DFT calculations were performed to determine the ^{77}Se magnetic shielding tensors using periodic boundary conditions as implemented in the CASTEP package (version 20.11).[66−68] Input files were generated using Materials Studio 5.0. Geometry optimizations and NMR calculations employed the PBE exchange-correlation (XC) functional within the generalized gradient approximation (GGA) framework, augmented with the Grimme D3(BJ) dispersion correction to account for long-range dispersion interactions.[54,55,69−71] On the fly pseudopotentials were used in all simulations. Two types of geometry optimizations were performed: (i) full atomic relaxation and (ii) hydrogen-only relaxation, both carried out

https://doi.org/10.1021/acs.jpcc.5c01979
J. Phys. Chem. C 2025, 129, 13299−13311

while keeping the unit cell parameters fixed to the experimental values. The resulting geometries were then used to compute and compare NMR parameters. All CASTEP-based DFT calculations were performed using the ZORA scalar relativistic approach to account for relativistic effects.

Plane-wave cutoff energies and k-point meshes were chosen based on system-specific convergence tests. A cutoff of 600 eV was used for geometry optimization, and 700 eV for NMR shielding calculations. The following Monkhorst−Pack k-point grids were employed:

- Compound **1**: 13 × 9 × 3 grid (70 total points)
- Cocrystal **1a**: 8 × 9 × 8 grid (288 total points)
- Cocrystal **1b**: 8 × 14 × 3 grid (84 total points)
- Cocrystal **2b**: 7 × 14 × 5 grid (126 total points)

All initial crystal structures were obtained from SCXRD data. Calculated GIPAW shielding values were converted to chemical shifts (δ) by linear regression using the best-fit line between experimental $\delta(^{77}\mathrm{Se})$ values and computed $\sigma(^{77}\mathrm{Se})$ values across the data set. This calibration accounts for systematic deviations and ensures accurate prediction of chemical shifts. The optimized CIF files, along with the corresponding CASTEP input files and selected output data, are provided in the data repository referenced in the data availability section.

The Energy Decomposition Analysis, including ETS-NOCV and IQA analyses, was performed using the Amsterdam Density Functional (ADF) 2019 software package.[72] All calculations employed the PBE0 hybrid functional with the triple-ζ doubly polarized (TZ2P) basis set and included Grimme's D3-BJ dispersion correction to accurately account for long-range van der Waals interactions. Scalar relativistic effects were treated using the ZORA (Zero-Order Regular Approximation) method. The ETS-NOCV analysis provided insights into the orbital and electrostatic components of Se···Se, Se···I, Se···H, and $\pi\cdots\pi$ interactions, while the IQA analysis, extracted from the "Interatomic Contributions" section of the output file, enabled quantitative decomposition of the interaction energy into electrostatic, exchange−correlation (covalent), and dispersion terms. Orbital and energy visualizations were rendered using (Amsterdam Modeling Suite) AMS-View within the AMS-GUI interface.[73]

QTAIM and NCI-RDG analyses were carried out using the Gaussian 09 software package.[74] Geometry optimizations were performed without symmetry constraints using the B3LYP functional in conjunction with Grimme's D3-BJ dispersion correction to account for long-range van der Waals interactions. The LANL2DZ basis set was used for heavy atoms (Se and I). The optimized wave functions were subsequently analyzed using the QTAIM to identify bond critical points (BCPs), electron densities (ρ), and to visualize dispersive and noncovalent interactions, including halogen and chalcogen bonding. The resulting isosurfaces were rendered using VMD software.[75]

■ ASSOCIATED CONTENT

Data Availability Statement

Representative input and output files from CASTEP-DFT and QTAIM calculations, and optimized structure files are available in the Zenodo repository at: 10.5281/zenodo.15620208. All experimental/computational data and procedures are available in the ESI.

Supporting Information

The Supporting Information is available free of charge at https://pubs.acs.org/doi/10.1021/acs.jpcc.5c01979.

Additional solid-state NMR spectra; additional visualizations of orbital interactions; and additional X-ray crystallographic details (PDF)

■ AUTHOR INFORMATION

Corresponding Authors

David L. Bryce − *Department of Chemistry and Biomolecular Sciences, Centre for Catalysis Research and Innovation, and Nexus for Quantum Technologies, University of Ottawa, Ottawa, Ontario KIN6N5, Canada;* orcid.org/0000-0001-9989-796X; Phone: 613-562-5800; Email: dbryce@uottawa.ca

Brijith Thomas − *Chemistry Program, Science Division and Mubadala Arabian Center for Climate and Environmental Sciences, New York University Abu Dhabi, Abu Dhabi 129188, United Arab Emirates;* orcid.org/0000-0003-3590-0992; Phone: 971-2628-4238; Email: brijiththomas@nyu.edu

Authors

Alireza Nari − *Department of Chemistry and Biomolecular Sciences, Centre for Catalysis Research and Innovation, and Nexus for Quantum Technologies, University of Ottawa, Ottawa, Ontario KIN6N5, Canada*

Sajesh P. Thomas − *Department of Chemistry, Indian Institute of Technology Delhi, New Delhi 110016, India;* orcid.org/0000-0003-3552-8625

Complete contact information is available at: https://pubs.acs.org/10.1021/acs.jpcc.5c01979

Author Contributions

A.N. prepared compounds, conducted the SCXRD and data analysis, carried out solid-state NMR measurements, performed quantum chemical and NMR parameters calculations, cowrote the first draft of the manuscript, and contributed to its subsequent editing. S.P.T. provided input on the nature of bonding during project discussion. B.T. cowrote the first draft of the manuscript, carried out solid-state NMR measurements, performed data analysis and contributed to its subsequent editing. D.L.B. supervised the project and edited the manuscript. All authors have given approval to the final version of the manuscript.

Notes

The authors declare no competing financial interest.

■ ACKNOWLEDGMENTS

The research was funded by New York University Abu Dhabi (NYUAD, UAE) by Tamkeen. The research was partially carried out using the Core Technology Platforms at New York University Abu Dhabi. Part of the computer simulations were carried out on the High-Performance Computing Resources at New York University, Abu Dhabi. DLB thanks the Natural Sciences of Engineering Research Council of Canada for funding. We thank Dr. Jeffrey Ovens for technical support on SCXRD analysis.

REFERENCES

(1) Rocha, J. B.; Piccoli, B. C.; Oliveira, C. S. Biological and Chemical Interest in Selenium: A Brief Historical Account. *ARKIVOC* **2017**, *2017* (2), 457−491.

(2) Bleiholder, C.; Werz, D. B.; Köppel, H.; Gleiter, R. Theoretical Investigations on Chalcogen−Chalcogen Interactions: What Makes These Nonbonded Interactions Bonding? *J. Am. Chem. Soc.* **2006**, *128* (8), 2666−2674.

(3) Hu, Y. X.; Miao, J.; Hua, T.; Huang, Z.; Qi, Y.; Zou, Y.; Qiu, Y.; Xia, H.; Liu, H.; Cao, X.; Yang, C. Efficient Selenium-Integrated TADF OLEDs with Reduced Roll-Off. *Nat. Photo.* **2022**, *16* (11), 803−810.

(4) Chen, S.; Fan, C.; Xu, Z.; Pei, M.; Wang, J.; Zhang, J.; Zhang, Y.; Li, J.; Lu, J.; Peng, C.; Wei, X. Mechanochemical Synthesis of Organoselenium Compounds. *Nat. Commun.* **2024**, *15* (1), 769.

(5) Rayman, M. P. Selenium and Human Health. *Lancet* **2012**, *379* (9822), 1256−1268.

(6) Fan, B.; Lin, F.; Wu, X.; Zhu, Z.; Jen, A. K.-Y. Selenium-Containing Organic Photovoltaic Materials. *Acc. Chem. Res.* **2021**, *54* (20), 3906−3916.

(7) Hoover, G. C.; Seferos, D. S. Photoactivity and Optical Applications of Organic Materials Containing Selenium and Tellurium. *Chem. Sci.* **2019**, *10* (40), 9182−9188.

(8) Aakeroy, C. B.; Bryce, D. L.; Desiraju, G. R.; Frontera, A.; Legon, A. C.; Nicotra, F.; Rissanen, K.; Scheiner, S.; Terraneo, G.; Metrangolo, P.; Resnati, G. Definition of the Chalcogen Bond (IUPAC Recommendations 2019). *Pure Appl. Chem.* **2019**, *91* (11), 1889−1892.

(9) Desiraju, G. R.; Ho, P. S.; Kloo, L.; Legon, A. C.; Marquardt, R.; Metrangolo, P.; Politzer, P.; Resnati, G.; Rissanen, K. Definition of the Halogen Bond (IUPAC Recommendations 2013). *Pure Appl. Chem.* **2013**, *85* (8), 1711−1713.

(10) Mames, A.; Pietrzak, M.; Bernatowicz, P.; Kubas, A.; Luboradzki, R.; Ratajczyk, T. NMR Crystallography Enhanced by Quantum Chemical Calculations and Liquid State NMR Spectroscopy for the Investigation of Se-NHC Adducts. *Chem.—Eur. J.* **2021**, *27* (66), 16477−16487.

(11) Vummaleti, S. V. C.; Nelson, D. J.; Poater, A.; Gómez-Suárez, A.; Cordes, D. B.; Slawin, A. M. Z.; Nolan, S. P.; Cavallo, L. What Can NMR Spectroscopy of Selenoureas and Phosphinidenes Teach Us about the π-Accepting Abilities of N-Heterocyclic Carbenes? *Chem. Sci.* **2015**, *6* (3), 1895−1904.

(12) Pruschinski, L.; Kahnert, S. R.; Herzberger, C.; Namyslo, J. C.; Schmidt, A. Studies on the Effect of Positive and Negative Charges on the ^{77}Se NMR Shifts of Selenones and Selenenyls of N-Heterocyclic Carbenes of Imidazolium-4,5-Dicarboxylates. *J. Org. Chem.* **2025**, *90* (6), 2201−2213.

(13) Clark, T.; Hennemann, M.; Murray, J. S.; Politzer, P. Halogen Bonding: The σ-Hole. *J. Mol. Mod.* **2007**, *13* (2), 291−296.

(14) Metrangolo, P.; Meyer, F.; Pilati, T.; Resnati, G.; Terraneo, G. Halogen Bonding in Supramolecular Chemistry. *Angew. Chem., Int. Ed.* **2008**, *47* (33), 6114−6127.

(15) Cavallo, G.; Metrangolo, P.; Milani, R.; Pilati, T.; Priimagi, A.; Resnati, G.; Terraneo, G. The Halogen Bond. *Chem. Rev.* **2016**, *116* (4), 2478−2601.

(16) Politzer, P.; Murray, J. S.; Clark, T. Halogen Bonding and Other σ-Hole Interactions: A Perspective. *Phys. Chem. Chem. Phys.* **2013**, *15* (27), 11178−11189.

(17) Gilday, L. C.; Robinson, S. W.; Barendt, T. A.; Langton, M. J.; Mullaney, B. R.; Beer, P. D. Halogen Bonding in Supramolecular Chemistry. *Chem. Rev.* **2015**, *115* (15), 7118−7195.

(18) Terao, H.; Hashimoto, M.; Hashimoto, S.; Furukawa, Y. Studies of Structure and Phase Transition in $[C(NH_2)_3]HgBr_3$ and $[C(NH_2)_3]HgI_3$ by Means of Halogen NQR, 1H NMR, and Single Crystal X-Ray Diffraction. *Z. Naturforsch.* **2000**, *55* (1−2), 230−236.

(19) Metrangolo, P.; Neukirch, H.; Pilati, T.; Resnati, G. Halogen Bonding Based Recognition Processes: A World Parallel to Hydrogen Bonding. *Acc. Chem. Res.* **2005**, *38* (5), 386−395.

(20) Ford, M. C.; Saxton, M.; Ho, P. S. Sulfur as an Acceptor to Bromine in Biomolecular Halogen Bonds. *J. Phys. Chem. Lett.* **2017**, *8* (17), 4246−4252.

(21) Costa, P. J. The Halogen Bond: Nature and Applications. *Phys. Sci. Rev.* **2017**, *2* (11), 136.

(22) Xu, Y.; Huang, J.; Gabidullin, B.; Bryce, D. L. A Rare Example of a Phosphine as a Halogen Bond Acceptor. *Chem. Commun.* **2018**, *54* (78), 11041−11043.

(23) Arman, H. D.; Rafferty, E. R.; Bayse, C. A.; Pennington, W. T. Complementary Selenium···Iodine Halogen Bonding and Phenyl Embraces: Cocrystals of Triphenylphosphine Selenide with Organoiodides. *Cryst. Grow. Desi.* **2012**, *12* (9), 4315−4323.

(24) Kumar, V.; Triglav, M.; Morin, V. M.; Bryce, D. L. Predictability of Chalcogen-Bond-Driven Crystal Engineering: An X-Ray Diffraction and Selenium-77 Solid-State NMR Investigation of Benzylic Selenocyanate Cocrystals. *ACS Org. Inorg. Au* **2022**, *2* (3), 252−260.

(25) Chernysheva, M. V.; Haukka, M. The S ··· Hal and Se ··· Hal Chalcogen Bonding in a Series of Thiourea, Selenourea and Their Derivatives. *J. Solid State Chem.* **2021**, *293*, No. 121759.

(26) Resnati, G.; Bryce, D. L.; Desiraju, G. R.; Frontera, A.; Krossing, I.; Legon, A. C.; Metrangolo, P.; Nicotra, F.; Rissanen, K.; Scheiner, S.; Terraneo, G. Definition of the Pnictogen Bond (IUPAC Recommendations 2023). *Pure Appl. Chem.* **2024**, *96* (1), 135−145.

(27) Politzer, P.; Murray, J. S.; Clark, T. Halogen Bonding and Other σ-Hole Interactions: A Perspective. *Phys. Chem. Chem. Phys.* **2013**, *15* (27), 11178−11189.

(28) Cozzolino, A. F.; Vargas-Baca, I.; Mansour, S.; Mahmoudkhani, A. H. The Nature of the Supramolecular Association of 1,2,5-Chalcogenadiazoles. *J. Am. Chem. Soc.* **2005**, *127* (9), 3184−3190.

(29) Kumar, V.; Xu, Y.; Bryce, D. L. Double Chalcogen Bonds: Crystal Engineering Stratagems via Diffraction and Multinuclear Solid-State Magnetic Resonance Spectroscopy. *Chem.—Eur. J.* **2020**, *26* (15), 3275−3286.

(30) Jeannin, O.; Huynh, H.-T.; Riel, A. M. S.; Fourmigué, M. Chalcogen Bonding Interactions in Organic Selenocyanates: From Cooperativity to Chelation. *New J. Chem.* **2018**, *42* (13), 10502−10509.

(31) Georges, T.; Beaudoin, J.; Rahman, M.; Nari, A.; Ovens, J. S.; Bryce, D. L. 77Se Solid-State NMR Investigation of Selenium Chemical Shift Tensors of Chalcogen Bonds in Selenadiazole Cocrystals. *J. Phys. Chem. C* **2025**, *129*, 5483−5492.

(32) Cosby, G. E.; Iftemie, T.; Nari, A.; Bryce, D. L. Chalcogen-Bonded Cocrystals and Salt Cocrystals via Automated Resonant Acoustic Mixing with a Button Operative Bot. *RSC Mechanochem.* **2025**, *2* (2), 201−208.

(33) Wonner, P.; Vogel, L.; Kniep, F.; Huber, S. M. Catalytic Carbon−Chlorine Bond Activation by Selenium-Based Chalcogen Bond Donors. *Chem.—Eur. J.* **2017**, *23* (67), 16972−16975.

(34) Wonner, P.; Vogel, L.; Düser, M.; Gomes, L.; Kniep, F.; Mallick, B.; Werz, D. B.; Huber, S. M. Carbon−Halogen Bond Activation by Selenium-Based Chalcogen Bonding. *Angew. Chem., Int. Ed.* **2017**, *56* (39), 12009−12012.

(35) Thomas, S. P.; Singh, A.; Grosjean, A.; Alhameedi, K.; Grønbech, T. B. E.; Piltz, R.; Edwards, A. J.; Iversen, B. B. The Ambiguous Origin of Thermochromism in Molecular Crystals of Dichalcogenides: Chalcogen Bonds versus Dynamic Se−Se/Te−Te Bonds. *Angew. Chem., Int. Ed.* **2023**, *62* (45), No. e202311044.

(36) Fuller, A. L.; Scott-Hayward, L. A. S.; Li, Y.; Bühl, M.; Slawin, A. M. Z.; Woollins, J. D. Automated Chemical Crystallography. *J. Am. Chem. Soc.* **2010**, *132* (16), 5799−5802.

(37) Kubiniok, S.; du Mont, W.-W.; Pohl, S.; Saak, W. The Reagent Diphenyldiselane/Iodine: No Phenylselenenyl Iodide but a Charge Transfer Complex with Cyclic Moieties. *Angew. Chem., Int. Ed.* **1988**, *27* (3), 431−433.

(38) Torubaev, Y. V.; Rai, D. K.; Skabitsky, I. V.; Pakhira, S.; Dmitrienko, A. Energy Framework Approach to the Supramolecular Reactions: Interplay of the Secondary Bonding Interaction in Ph_2E_2

(E = Se, Te)/p-I-C_6F_4-I Co-Crystals. *New J. Chem.* **2019**, *43* (21), 7941−7949.
(39) Duddeck, H. Selenium-77 Nuclear Magnetic Resonance Spectroscopy. *Prog. Nucl. Magn. Reson. Spectrosc.* **1995**, *27* (1), 1−323.
(40) Duddeck, H. ^{77}Se NMR Spectroscopy and Its Applications in Chemistry. In *Annu. Rep. NMR Spectrosc.*; Academic Press, 2004; Vol. *52*, pp 105−166.
(41) Balzer, G.; Duddeck, H.; Fleischer, U.; Röhr, F. 77Se Shielding Tensors of Diphenyl Diselenide, Comparison of the Results from CP/MAS NMR Spectroscopy and IGLO Calculations. *Fresenius' J. Anal. Chem.* **1997**, *357* (5), 473−476.
(42) Eichele, K. *WSolids1*, 2013.
(43) Szell, P. M. J.; Gabriel, S. A.; Gill, R. D. D.; Wan, S. Y. H.; Gabidullin, B.; Bryce, D. L. 13C and 19F Solid-State NMR and X-Ray Crystallographic Study of Halogen-Bonded Frameworks Featuring Nitrogen-Containing Heterocycles. *Acta Crystallogr., Sect. C: Struct. Chem.* **2017**, *73*, 157−167.
(44) Nari, A.; Ovens, J. S.; Bryce, D. L. Halogen-Bonded Cocrystals via Resonant Acoustic Mixing. *RSC Mechanochem.* **2024**, *1* (1), 50−62.
(45) Politzer, P.; Laurence, P. R.; Jayasuriya, K. Molecular Electrostatic Potentials: An Effective Tool for the Elucidation of Biochemical Phenomena. *Environ. Health Perspect.* **1985**, *61*, 191−202.
(46) De Vleeschouwer, F.; Denayer, M.; Pinter, B.; Geerlings, P.; De Proft, F. Characterization of Chalcogen Bonding Interactions via an In-Depth Conceptual Quantum Chemical Analysis. *J. Comput. Chem.* **2018**, *39* (10), 557−572.
(47) Georges, T.; Ovens, J. S.; Bryce, D. L. Electrostatic Surface Potentials and Chalcogen-Bonding Motifs of Substituted 2,1,3-Benzoselenadiazoles Probed via ^{77}Se Solid-State NMR Spectroscopy. *Chem.—Eur. J.* **2024**, *30* (51), No. e202402254.
(48) Griffin, J. M.; Knight, F. R.; Hua, G.; Ferrara, J. S.; Hogan, S. W. L.; Woollins, J. D.; Ashbrook, S. E. ^{77}Se Solid-State NMR of Inorganic and Organoselenium Systems: A Combined Experimental and Computational Study. *J. Phys. Chem. C* **2011**, *115* (21), 10859−10872.
(49) Demko, B. A.; Eichele, K.; Wasylishen, R. E. A Combined Experimental and Quantum Chemistry Study of Selenium Chemical Shift Tensors. *J. Phys. Chem. A* **2006**, *110* (50), 13537−13550.
(50) Pickard, C. J.; Mauri, F. All-Electron Magnetic Response with Pseudopotentials: NMR Chemical Shifts. *Phys. Rev. B* **2001**, *63* (24), No. 245101.
(51) Mason, J. Conventions for the Reporting of Nuclear Magnetic Shielding (or Shift) Tensors Suggested by Participants in the NATO ARW on NMR Shielding Constants at the University of Maryland, College Park, July 1992. *Solid State Nucl. Magn. Reson.* **1993**, *2* (5), 285−288.
(52) Bader, R. F. W. Atoms in Molecules. *Acc. Chem. Res.* **1985**, *18* (1), 9−15.
(53) Grabowski, S. J. Non-Covalent Interactions−QTAIM and NBO Analysis. *J. Mol. Model.* **2013**, *19* (11), 4713−4721.
(54) Bleiholder, C.; Werz, D. B.; Köppel, H.; Gleiter, R. Theoretical Investigations on Chalcogen−Chalcogen Interactions: What Makes These Nonbonded Interactions Bonding? *J. Am. Chem. Soc.* **2006**, *128* (8), 2666−2674.
(55) Haberhauer, G.; Gleiter, R. The Nature of Strong Chalcogen Bonds Involving Chalcogen-Containing Heterocycles. *Angew. Chem., Int. Ed.* **2020**, *59* (47), 21236−21243.
(56) Johnson, E. R.; Keinan, S.; Mori-Sánchez, P.; Contreras-García, J.; Cohen, A. J.; Yang, W. Revealing Noncovalent Interactions. *J. Am. Chem. Soc.* **2010**, *132* (18), 6498−6506.
(57) Otero-de-la-Roza, A.; Johnson, E. R.; Contreras-García, J. Revealing Non-Covalent Interactions in Solids: NCI Plots Revisited. *Phys. Chem. Chem. Phys.* **2012**, *14* (35), 12165−12172.
(58) Blanco, M. A.; Martín Pendás, A.; Francisco, E. Interacting Quantum Atoms: A Correlated Energy Decomposition Scheme Based on the Quantum Theory of Atoms in Molecules. *J. Chem. Theory Comput.* **2005**, *1* (6), 1096−1109.
(59) Bickelhaupt, F. M.; Baerends, E. J. Kohn-Sham Density Functional Theory: Predicting and Understanding Chemistry. In *Reviews in Computational Chemistry*. *Reviews in Computational Chemistry* **2000**, *15*, 1−86.
(60) Blessing, R. An Empirical Correction for Absorption Anisotropy. *Acta Crystallogr., Sect. A* **1995**, *51*, 33−38.
(61) Sheldrick, G. A Short History of SHELX. *Acta Crystallogr., Sect. A* **2008**, *64*, 112−122.
(62) Hubschle, C. B.; Sheldrick, G. M.; Dittrich, B. ShelXle: A Qt Graphical User Interface for SHELXL. *J. Appl. Crystallogr.* **2011**, *44*, 1281−1284.
(63) Kolodziejski, W.; Klinowski, J. Kinetics of Cross-Polarization in Solid-State NMR: A Guide for Chemists. *Chem. Rev.* **2002**, *102* (3), 613−628.
(64) Fung, B. M.; Khitrin, A. K.; Ermolaev, K. An Improved Broadband Decoupling Sequence for Liquid Crystals and Solids. *J. Magn. Reson.* **2000**, *142* (1), 97−101.
(65) Frisch, M. J.; Trucks, G. W.; Schlegel, H. B.; Scuseria, G. E.; Robb, M. A.; Cheeseman, J. R.; Montgomery, J. A.; Vreven, T.; Kudin, K. N.; Burant, J. C. *Gaussian 03, Revision C. 02*; Gaussian Inc.: Wallingford, CT, 2004.
(66) Pickard, C. J.; Mauri, F. All-Electron Magnetic Response with Pseudopotentials: NMR. *Phys. Rev. B* **2001**, *63*, No. 245101.
(67) Yates, J. R.; Pickard, C. J.; Mauri, F. Calculation of NMR Chemical Shifts for Extended Systems Using Ultrasoft Pseudopotentials. *Phys. Rev. B* **2007**, *76* (2), No. 024401.
(68) Clark, S. J.; Segall, M. D.; Pickard, C. J.; Hasnip, P. J.; Probert, M. I. J.; Refson, K.; Payne, M. C. *First Principles Methods Using CASTEP.* **2005**, *220* (5−6), 567−570.
(69) Perdew, J. P.; Burke, K.; Ernzerhof, M. Generalized Gradient Approximation Made Simple. *Phys. Rev. Lett.* **1996**, *77* (18), 3865−3868.
(70) Perdew, J. P.; Burke, K.; Ernzerhof, M. Generalized Gradient Approximation Made Simple [Phys. Rev. Lett. 77, 3865 (1996)]. *Phys. Rev. Lett.* **1997**, *78* (7), 1396−1396.
(71) Grimme, S.; Ehrlich, S.; Goerigk, L. Effect of the Damping Function in Dispersion Corrected Density Functional Theory. *J. Comput. Chem.* **2011**, *32* (7), 1456−1465.
(72) ADF. *SCM*, 2019. http://www.scm.com.
(73) AMS GUI 2024.1. Available at: http://www.scm.com.
(74) Frisch, M. J. *Gaussian 09, Revision D. 01*; Gaussian Inc., 2009.
(75) Humphrey, W.; Dalke, A.; Schulten, K. VMD: Visual Molecular Dynamics. *J. Mol. Graph* **1996**, *14* (1), 33−38.

Summary of Part 3

Part 3 presented a complementary investigation of non-covalent interactions in selenium-containing molecular solids using the combined capabilities of ^{77}Se MAS SSNMR spectroscopy and first-principles quantum chemical calculations. By correlating experimental chemical shielding tensors with electronic structure analyses, this work provides detailed insight into the amphiphilic behavior of selenium and its participation in halogen and chalcogen bonding within crystalline materials.

Part 4 – Sustainable Mechanochemical Synthesis of Halogen-Bonded Molecular Solids

Chapter 9 – Resonant Acoustic Mixing as a Gentle, Scalable, and Solvent-Efficient Route to Halogen-Bonded Cocrystals: Accessing Novel Polymorphs and Stoichiometries

Based on: Nari, A.; Ovens, J. S.; Bryce, D. L. Halogen-bonded cocrystals via resonant acoustic mixing. RSC Mechanochemistry 2024, 1, 50–62.

9.1 Chapter Overview and Thesis Context

The preceding chapters of this thesis have focused primarily on understanding molecular solids through advanced spectroscopic characterization and computational modeling. Complementing these studies, the present chapter addresses another important aspect of molecular solid research: the sustainable preparation of supramolecular materials. As discussed in Chapter 3, mechanochemistry has emerged as an environmentally responsible alternative to conventional solution-based synthesis by minimizing solvent consumption, reducing waste generation, and providing rapid access to crystalline materials. Among recent mechanochemical methodologies, RAM has attracted increasing attention as a gentle, scalable, and media-free technique capable of promoting solid-state reactions without the grinding media required in conventional ball milling.

Although mechanochemical synthesis has been widely applied to pharmaceutical cocrystals, metal-organic frameworks, and coordination compounds, at the time this work was undertaken, systematic investigations of halogen-bond-directed cocrystallization by RAM had not been

reported, leaving open important questions regarding the ability of acoustic mixing to efficiently generate XB architectures while maintaining precise control over crystal form and stoichiometry.

The work presented in this chapter demonstrates that RAM provides an effective and reproducible route for the preparation of XB cocrystals. A family of eleven iodine-based XB cocrystals was synthesized using neat and liquid-assisted RAM conditions and compared directly with products obtained by conventional ball milling. The resulting materials were characterized by X-ray diffraction, and ^{13}C and ^{19}F SSNMR spectroscopy. These complementary techniques confirm that RAM reliably produces phase-pure halogen-bonded cocrystals while providing synthetic outcomes comparable to, and in some cases extending beyond, those accessible through conventional mechanochemical methods.

A particularly significant finding of this study is the discovery that RAM can access regions of the cocrystal landscape that are inaccessible through ball milling alone. In addition to producing two previously unknown XB crystal structures, RAM enabled the selective preparation of a new stoichiomorphic form of the *p*-DITFB/TMP cocrystal that could not be obtained under comparable ball-milling conditions. These results demonstrate that RAM is not simply an alternative mechanochemical technique but rather a complementary synthetic methodology capable of expanding polymorphic and stoichiometric space for supramolecular materials.

Although this study was conducted independently of the spectroscopic developments presented in Parts 2 and 3, it shares the same broader objective of advancing the understanding and design of molecular solids. Whereas the earlier chapters focused on characterizing local electronic structure and intermolecular interactions, the present work demonstrates how sustainable mechanochemical synthesis can provide efficient access to those same supramolecular architectures.

9.2. Statement of Authenticity

I certify that I have prepared the following article featuring my own work.

9.3 Permissions

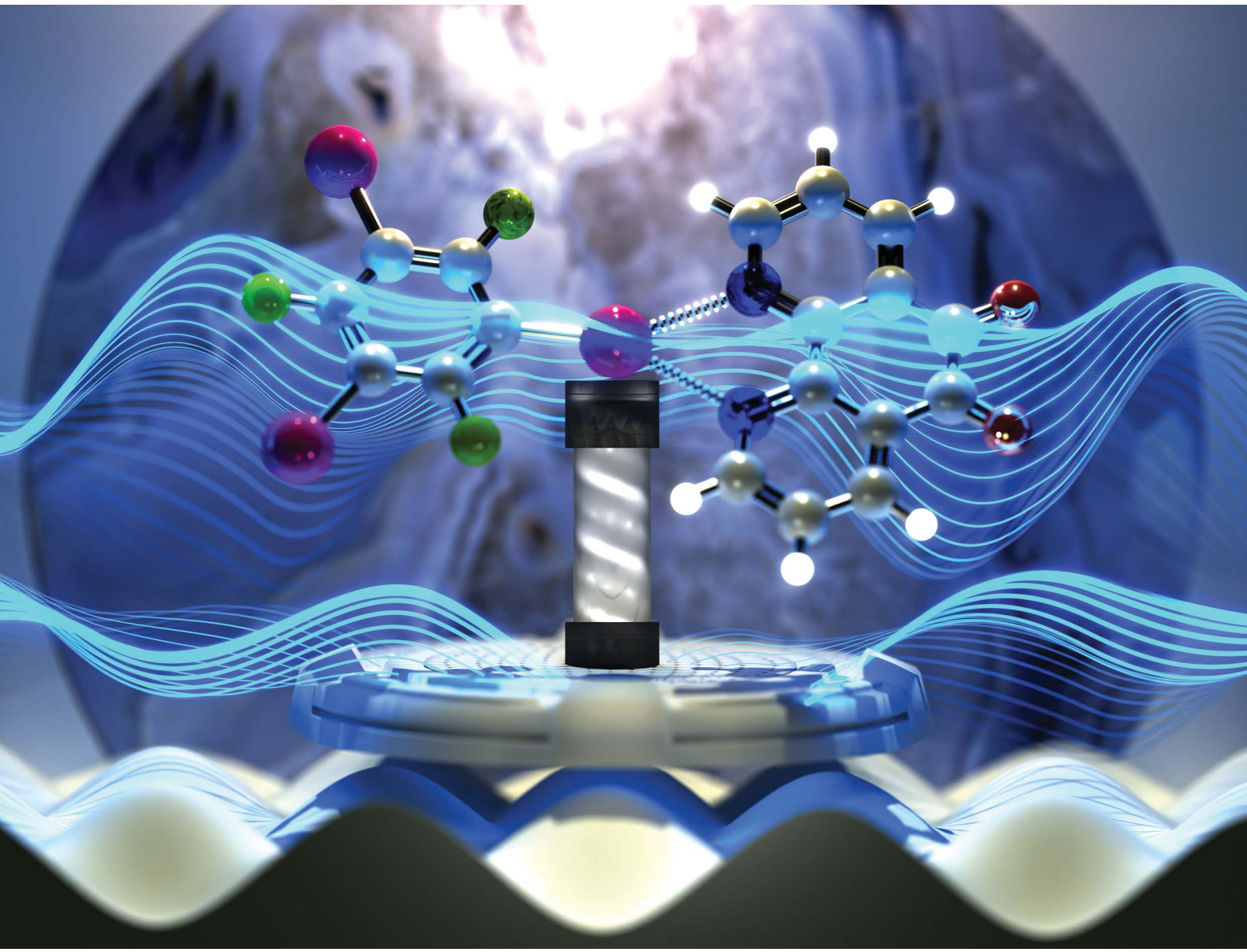
I declare that I have obtained permission from the coauthor to include this article in my thesis. Chapter 9 has been reprinted with permission from the Royal Society of Chemistry.

9.4 Published manuscript

Volume 1
Number 1
March 2024
Pages 1–146

RSC Mechanochemistry

rsc.li/RSCMechanochem



ISSN 2976-8683

ROYAL SOCIETY OF CHEMISTRY

PAPER
David L. Bryce *et al.*
Halogen-bonded cocrystals *via* resonant acoustic mixing

RSC Mechanochemistry

ROYAL SOCIETY OF CHEMISTRY

PAPER

View Article Online
View Journal | View Issue

Check for updates

Cite this: *RSC Mechanochem.*, 2024, **1**, 50

Halogen-bonded cocrystals *via* resonant acoustic mixing†

Alireza Nari, Jeffrey S. Ovens and David L. Bryce *

Resonant acoustic mixing is a relatively gentle mechanochemical technology that employs pressure waves to induce chemical and morphological transformations. We report here on the production of eleven halogen-bonded (XB) cocrystalline architectures *via* neat and liquid-assisted resonant acoustic mixing (RAM). Two strong iodinated XB donors, namely 1,4-diiodotetrafluorobenzene (*p*-DITFB, **1**) and 1,3,5-trifluoro-2,4,6-triiodobenzene (*sym*-TFTIB, **2**) each react with five XB donors, namely 2,3,5,6-tetramethylpyrazine (TMP, **a**), 4-dimethylaminopyridine (DMAP, **b**), 1,10-phenanthroline (*o*-Ph, **c**), 1,10-phenanthroline-5,6-dione (PheDON, **d**), and 4,5-diazafluoren-9-one (DIZFON, **e**) to form ten cocrystals. For these systems, it is shown that RAM is capable of producing the same products as are obtained *via* ball milling. Two novel cocrystals are obtained (of **2d** featuring bifurcated XBs, and **2e** featuring monofurcated XBs) and their single-crystal X-ray structures are reported. However, an eleventh stoichiomorphic cocrystal of *p*-DITFB and TMP is obtained exclusively *via* RAM, suggesting that the combination of RAM and milling approaches may afford a broader exploration of the polymorphic and stoichiomorphic landscape than the use of a single technique in isolation. All products are characterized *via* powder X-ray diffraction, and ^{13}C cross-polarization magic angle spinning (CP/MAS) and ^{19}F MAS NMR spectroscopy, providing further evidence for the phase purity of samples obtained from RAM experiments and for the degree of polymorphic control available when small volumes of liquid are employed in mechanochemical reactions. This work demonstrates the potential of RAM for the production of known and novel halogen-bonded cocrystalline assemblies, including polymorphic and stoichiomorphic structures.

Received 8th December 2023
Accepted 16th January 2024

DOI: 10.1039/d3mr00028a

rsc.li/RSCMechanochem

Open Access Article. Published on 31 January 2024. Downloaded on 5/1/2026 7:25:08 PM.
This article is licensed under a Creative Commons Attribution 3.0 Unported Licence.

Introduction

Halogen bonding (XB), a distinctive noncovalent interaction, has surged in interest due to its directional and tunable characteristics,[1,2] enabling the deliberate design of frameworks[3,4] and control of biomolecular structure.[5,6] This interaction involves the electrophilic region of a covalently bonded halogen (termed the σ-hole)[7] on the halogen bond donor engaging with a Lewis base as the halogen bond acceptor.[8] The presence of this interaction is often assessed using the normalized contact distance ratio, R_{XB},[9] which gauges the halogen bond distance ($d_{X\cdots Y}$) relative to the sum of the van der Waals radii of the atoms involved ($\sum d_{vdw}$):[10]

$$R_{XB} = \frac{d_{X\cdots Y}}{\sum d_{vdw}}.$$

Over the past two decades, halogen bonding has emerged as a versatile tool, finding applications across diverse domains such as crystal engineering, medicinal chemistry,[11,12] anion recognition,[13,14] supramolecular systems,[15] and catalysis.[16,17] Its adaptable nature and the potential for precise modulation make halogen bonding an intriguing avenue for innovative molecular design and tailored interactions.

Mechanochemistry, a dynamic and evolving field, has emerged as an innovative approach to chemical synthesis and materials discovery. This methodology harnesses mechanical force, such as grinding or milling, as a key driver in chemical reactions, replacing or complementing traditional solution-based processes.[18,19] The concept of mechanochemistry dates back to the 19th century when it was first noted that certain reactions occurred more readily under mechanical action.[20–22] However, it wasn't until recent decades that the full potential of mechanochemistry began to be realized. Today, this field offers a versatile platform for green and sustainable chemistry,[23,24] with applications ranging from pharmaceuticals[25–27] to catalysis,[28–33] and materials science.[34,35]

Department of Chemistry and Biomolecular Sciences, Centre for Catalysis Research and Innovation, and Nexus for Quantum Technologies, University of Ottawa, Ottawa, Ontario, Canada K1N6N5. E-mail: dbryce@uottawa.ca; Fax: +1-613-562-5170; Tel: +1-613-562-5800

† Electronic supplementary information (ESI) available: Further synthetic details; additional NMR spectra; powder X-ray diffractograms. Crystallographic information files for compounds **2d** and **2e** have been deposited with the CCDC with cif numbers 2305189 and 2305188. For ESI and crystallographic data in CIF or other electronic format see DOI: https://doi.org/10.1039/d3mr00028a

© 2024 The Author(s). Published by the Royal Society of Chemistry

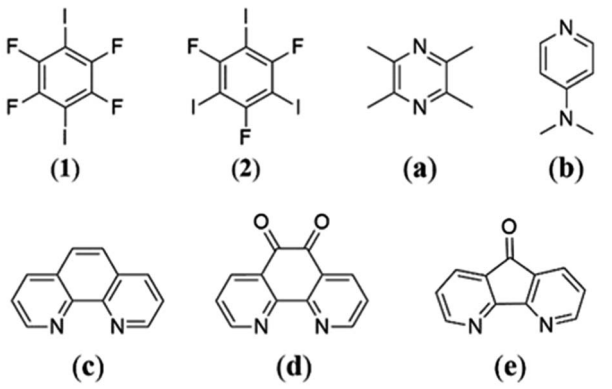
Open Access Article. Published on 31 January 2024. Downloaded on 5/1/2026 7:25:08 PM.
This article is licensed under a Creative Commons Attribution 3.0 Unported Licence.

In addition to the absence of solvents offering advantages, solid-state reactions frequently yield highly pure products and can be conducted using uncomplicated equipment, such as basic manual grinding[36] or mechanical milling.[37–39] Occasionally, a small quantity of liquid is introduced into mechanochemical reactions to expedite the transformation or facilitate the reaction, which, in certain instances, may induce polymorphic variations.[40] These reactions can be categorized as "minimal solvent" rather than purely "solvent-free",[18] and they are often referred to as kneading, solvent drop grinding, or, in a more comprehensive and contemporary context, liquid-assisted grinding (LAG).[41,42]

Mechanochemical reactions are often characterized by their unique ability to access reaction pathways and product formations that are often elusive through traditional methods.[43] The fundamental principles behind mechanochemistry involve the application of mechanical energy to overcome activation barriers and promote bond cleavage, facilitating the synthesis of complex molecules and materials. As a result, mechanochemistry has garnered increasing interest within the scientific community for its potential to revolutionize the way we approach chemical synthesis and discover new materials. Recent advances in the field have demonstrated its efficacy in preparing cocrystals,[44–49] polymorphs,[50] and metal–organic frameworks,[51,52] highlighting its versatility and potential in various applications.

Here, we provide a proof of principle study of direct mechanochemical halogen bond-induced cocrystallization by resonant acoustic mixing (RAM), focusing on the reduction of reaction time and the engineering of cocrystals featuring I···N and I···O interactions (Fig. 1). We show that acoustic mechanochemistry with RAM, leveraging acoustic wave pressure as the driving force, can efficiently provide the energy required for promoting halogen bond-induced cocrystallization. Cocrystal synthesis *via* RAM has been reported previously,[53–58] but to our knowledge the production of halogen-bonded systems has not been systematically explored.

Furthermore, our ongoing work focuses on fine-tuning the coordination of XB interactions using RAM methodology. Notably, in a recent study by Michalczyk *et al.*,[59] it was reported that only 2% of XB cocrystals exhibit bifurcated interactions, underscoring the rarity of such configurations obtained *via* traditional methods. The efficiency of RAM in forging XB interactions may hold the potential to unlock bifurcated and multi-coordinated XB interactions, thus broadening the possibilities for tailoring cocrystals in ways that were previously inaccessible through traditional mechanochemical approaches.



Cocrystals Obtained:

4(p-DITFB).1.5(TMP): **1a(ii)**	(p-DITFB).2(TMP): **1a(i)**
(p-DITFB).2(DMAP): **1b**	(sym-TFTIB).(TMP): **2a**
2(p-DITFB).(o-Phe): **1c**	(sym-TFTIB).3(DMAP): **2b**
(p-DITFB).(PheDON): **1d**	(sym-TFTIB).(o-Phe): **2c**
(p-DITFB).(DIZFON): **1e**	(sym-TFTIB).(PheDON): **2d**
	(sym-TFTIB).(DIZFON): **2e**

Fig. 1 Molecular structure of halogen bond donors and acceptors studied herein with the cocrystals obtained.

Experimental section

(i) General

1,4-Diiodotetrafluorobenzene (*p*-DITFB, **1**), 2,3,5,6-tetramethylpyrazine (TMP, **a**), and 4-dimethylaminopyridine (DMAP, **b**), were purchased from Sigma-Aldrich. 1,10-Phenanthroline (*o*-Ph, **c**) and 1,10-phenanthroline-5,6-dione (PheDON, **d**) were purchased from Fisher Scientific. 4,5-Diazafluoren-9-one (DIZFON, **e**) was purchased from TCI. 1,3,5-Trifluoro-2,4,6-triiodobenzene (*sym*-TFTIB, **2**) was purchased from SynQuest Laboratories. These compounds were utilized in their as-received state without further purification. Reagent grade solvents and doubly distilled water were used.

(ii) Mechanochemistry and sample preparation

Mechanochemical transformations were performed using ball milling (Retsch MM 400) and resonant acoustic mixing (Resodyn PharmaRAM 1) devices.

Ball milling. The production of each cocrystal was upscaled to generate 300 to 400 mg of the intended product. Both the halogen bond donor and the halogen bond acceptor at the indicated ratios were introduced into a 10 mL stainless steel milling jar. For cocrystallization using liquid assisted grinding (LAG), a small quantity (ranging from 0.1 to 0.5 μL mg^{-1}) of chloroform, acetonitrile, tetrahydrofuran, or methanol was added. The ball milling procedure was carried out at room temperature with a milling frequency of 30 Hz, spanning a duration of 30 to 45 min. This process utilized two stainless steel grinding balls, each with a diameter of 5 mm. The specific synthesis conditions for each cocrystal *via* ball milling are outlined in Table 1 and detailed procedures are explained in the ESI.†

Resonant acoustic mixing. In a standard procedure, specific amounts of finely powdered halogen bond donor and halogen bond acceptor were transferred into a 1-dram glass vial, securely mounted within a lab-built sample holder, and positioned on the RAM platform. To this reactant mixture, a liquid additive such as tetrahydrofuran, chloroform, or methanol was added within the range of 0 to 1.0 μL mg^{-1}. The blend was mixed vigorously using the PharmaRAM 1 instrument for a duration of 45 to 50 min, employing an acceleration of 80 *g* (*g*: acceleration of gravity). The

Open Access Article. Published on 31 January 2024. Downloaded on 5/1/2026 7:25:08 PM. This article is licensed under a Creative Commons Attribution 3.0 Unported Licence.

Table 1 Experimental synthesis conditions of cocrystals in this work

			Ball milling			RAM			
Compound	Molar ratio (donor : acceptor)	Masses (donor : acceptor) (mg)	Time (min)	Liquid	η (μL mg^{-1})	Time (min)	Liquid	η (μL mg^{-1})	Refcode
1a(i)	(1 : 1)	(241 : 82)	45	$CHCl_3$	0.10	50	$CHCl_3$	0.20	JAQMAQ[60]
1a(ii)	(2 : 1)	(402 : 68)	*NA*[a]	*NA*	*NA*	45	None	—	KIHRAX[61]
1b	(1 : 2)	(321 : 196)	45	None	—	45	None	—	RUYHID[62]
1c	(1 : 1)	(241 : 108)	45	$CHCl_3$	0.05	50	$CHCl_3$	0.10	JAQMIY[60]
1d	(1 : 1)	(205 : 105)	30	$CHCl_3$	0.10	50	THF	0.5	EXIFEX[63]
1e	(1 : 1)	(205 : 91)	30	$CHCl_3$	0.10	50	THF	0.5	EXIFAT[63]
2a	(1 : 1)	(357 : 95)	30	THF	0.05	50	THF	0.1	SAJCUE[9]
2b	(1 : 3)	(255 : 183)	45	None	—	50	None	—	RUYJAX[64]
2c	(1 : 1)	(255 : 90)	45	$CHCl_3$	0.05	50	THF	0.10	SAJDEP[9]
2d	(1 : 1)	(255 : 105)	45	$CHCl_3$	0.05	50	$CHCl_3$	0.7	This work
2e	(1 : 1)	(255 : 94)	45	$CHCl_3$	0.10	50	$CHCl_3$	0.7	This work

[a] Not achievable.

specific RAM synthesis conditions for each cocrystal are outlined in Table 1 and detailed procedures are explained in the ESI.†

Slow evaporation. To grow cocrystals of **2d** and **2e** suitable for single crystal X-ray diffraction (SCXRD), a solution of *sym*-TFTIB (0.15 mmol) dissolved in 2 mL of chloroform was added dropwise to a solution of PheDON or DIZON (0.15 mmol) also dissolved in 2 mL of chloroform. The solvent was allowed to gradually evaporate at room temperature, resulting in the formation of yellow and orange cocrystals for **2d** and **2e**, respectively, over the course of one week. Vials were tightly sealed as soon as single cocrystals were observed by eye.

(iii) Powder X-ray diffraction

Powder X-ray diffraction (PXRD) data were collected using a Bruker D8 Endeavor instrument that features a 1 kW Cu Kα radiation source from a sealed tube and a LynxEye XE-T high-speed detector operating at a wavelength of $\lambda = 1.54056$ Å. These measurements were conducted under standard room temperature conditions. The samples were securely positioned within a well plate and underwent a rotational motion at 15 revolutions per minute throughout the data collection process.

(iv) Single-crystal X-ray diffraction

Single cocrystals of compounds **2d** and **2e** were affixed onto a thin glass fiber using parabar oil. SCXRD analysis was conducted employing a Bruker AXS SMART single crystal diffractometer equipped with a sealed Mo tube source emitting radiation at a wavelength of 0.71073 Å. This analysis was carried out at a temperature of 213 K.

The diffraction dataset revealed systematic absences, and the unit cell parameters were in accordance with the monoclinic $P2_1/c$ crystal system for both compounds **2d** and **2e**. See ESI† for further details.

(v) Solid-state NMR spectroscopy

$^1H \rightarrow {}^{13}C$ cross-polarization magic-angle spinning (CPMAS) SSNMR experiments were conducted using a Bruker Avance III spectrometer operating at 9.4 T. A Bruker 4 mm HXY MAS probe was employed, and the spinning frequency was typically set to 11 kHz (see ESI† for further details). The CPMAS technique involved a 6 to 8 ms contact time, a proton $\pi/2$ pulse duration of 3.60 μs, and ^1H decoupling at a nutation frequency of 54.3 kHz. To determine chemical shifts, referencing was done relative to glycine at 176.4 ppm ($^{13}C = O$) with respect to TMS.

^{19}F MAS SSNMR experiments were conducted at 11.7 T, utilizing a Bruker Avance III spectrometer. For these experiments, a Bruker 2.5 mm HX MAS probe was employed, with a spinning frequency set at 25 kHz. The data acquisition employed a Bloch decay sequence with a $\pi/2$ pulse duration of 1.75 μs and a recycle delay of 60–90 seconds. Chemical shifts are reported with respect to polytetrafluoroethylene at −122.2 ppm.

Results and discussion

(i) Mechanochemistry and PXRD

The preparation of XB cocrystals can typically be achieved through both solution crystal growth and solid-state mechanochemistry. Nevertheless, mechanochemistry offers a rapid and efficient means of cocrystal synthesis while minimizing solvent usage and by-product formation. However, for obtaining molecular structural information and geometry, the use of single crystals is indispensable, which can be achieved through solvent-based crystallization. Herein, the employed cocrystallization techniques encompass neat solid-state and liquid-assisted ball milling and RAM. Additionally, solution growth methods were employed to produce single cocrystals of two novel compounds, *i.e.*, *sym*-TFTIB with PheDON and DIZFON (cocrystals **2d** and **2e**).

We describe here the mechanochemical preparation, *via* ball milling and RAM, of cocrystals **1a**, **2a**, **1b**, **2b**, **1c**, **2c**, **1d**, **2d**, **1e**, and **2e** (Fig. 1). Except for two novel cocrystals (**2d** and **2e**), the rest of these compounds had previously been cocrystallized through solution growth and characterized *via* SCXRD. This work therefore focusses on minimizing solvent usage and on exploring the potential of environmentally friendly and low energy consumption RAM mechanochemical methods for producing halogen-bonded compounds.

© 2024 The Author(s). Published by the Royal Society of Chemistry

Open Access Article. Published on 31 January 2024. Downloaded on 5/1/2026 7:25:08 PM.
This article is licensed under a Creative Commons Attribution 3.0 Unported Licence.

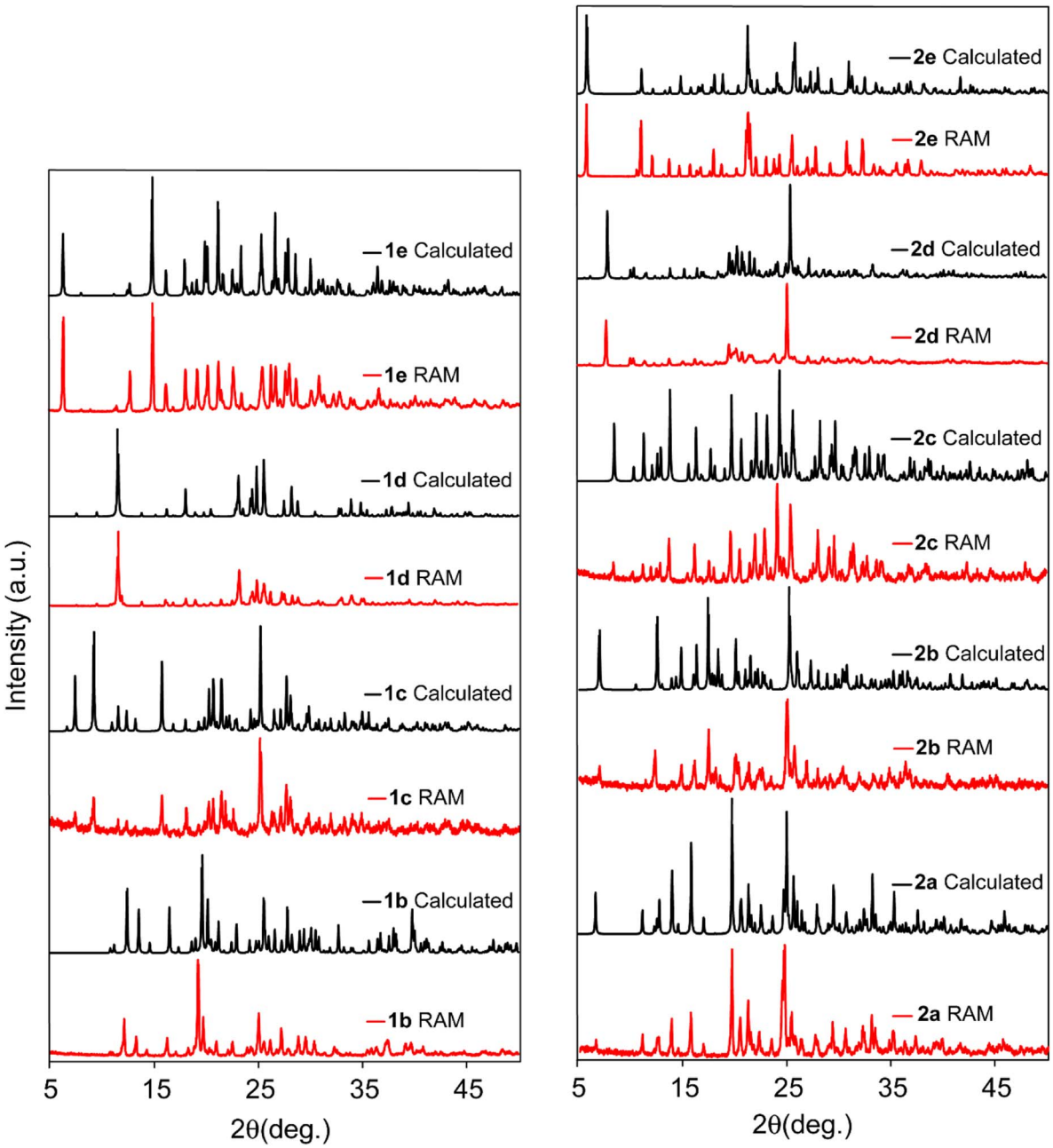


Fig. 2 Comparison between experimental PXRD patterns of cocrystals prepared *via* RAM (red) and the simulated X-ray powder patterns (black).

In all cases, the PXRD patterns depicted in Fig. 2 and in the ESI† reveal a notable similarity between the products obtained through ball milling and RAM methods when the same stoichiometry of reactants and identical synthesis conditions (*e.g.*, reaction time and liquid additive) were applied. Pure and stable forms of these cocrystals were obtained using RAM, typically within less than an hour (in most cases, around 40 min), under both neat and LAG conditions.

In the investigation of the application of RAM in the mechanochemical synthesis of halogen bonded cocrystals, eleven cocrystals were prepared, as outlined in Table 1. Specifically, cocrystal **1b** was prepared *via* RAM by introducing a 1 : 2 molar ratio of the donor to the acceptor into a 1-dram glass vial, and subjecting it to pressure waves of 80 g for a duration of 45 min. The resulting PXRD pattern, as illustrated in Fig. 2, confirms the successful formation of the RUYHID cocrystal (Table 1) using the pristine solvent-free resonance acoustic mixing approach. To validate the reproducibility and versatility of RAM in producing halogen-bonded cocrystals and to make a comparative assessment with conventional mechanochemistry methods, we employed ball milling under identical synthesis conditions for the preparation of cocrystal **1b**. Remarkably, the PXRD data indicate a striking similarity between the cocrystals obtained through

© 2024 The Author(s). Published by the Royal Society of Chemistry

Open Access Article. Published on 31 January 2024. Downloaded on 5/1/2026 7:25:08 PM.
This article is licensed under a Creative Commons Attribution 3.0 Unported Licence.

these two distinct methods, confirming the formation of a pure and stable phase of cocrystal **1b**.

Subsequently, cocrystal **2b** was synthesized using RAM, employing a 1 : 3 molar ratio of donor **2** to acceptor **b**, with an 80 g acceleration for a duration of 50 min. Additionally, a parallel synthesis was carried out using ball milling with a frequency of 30 kHz and a duration of 45 min. The PXRD patterns, depicted in Fig. 2 (and ESI†), provide compelling evidence for the formation of a pure and stable RUYJAX phase in both cases.

It should be noted that our optimization process for RAM synthesis commenced with neat powders to avoid the use of solvents. Additionally, we explored various preparation times, including 15, 30, and 45 min. The results presented herein encompass the optimized synthesis conditions for each cocrystal *via* both RAM and ball milling techniques. It was observed that the exclusion of liquid additives yielded pure cocrystals only in the case of **1a(ii)**, **1b**, and **2b**. This phenomenon can be attributed to the superior properties of acceptors TMP(**a**) and DMP(**b**), characterized by their enhanced nucleophilicity and reduced steric hindrance, facilitating efficient halogen bond formation. This distinction is expected to result in shorter bond lengths and stronger XB interactions within these compounds. This is evident in the geometric parameters obtained from SCXRD data where the R_{XB} values of 0.85, 0.76 and 0.78 were determined for the I···N interactions in **1a(ii)**, **1b**, and **2b** cocrystals, respectively.

To address this issue, we adopted a strategy involving the introduction of liquid additives[33] within the range of 0.05 to 0.7 μL per milligram of reactants ($\eta = 0.05$ to 0.7) in the reaction jar. In this context, the RAM of **1** and **c** reactants in a 1 : 2 molar ratio, supplemented with chloroform at an $\eta = 0.1$ μL mg^{-1} ratio, yielded the pure and stable cocrystal **1c** (refcode: JAQMIY). Similarly, the syntheses of cocrystals **1d** and **1e**, as confirmed by their PXRD patterns displayed in Fig. 2, were achieved by introducing equimolar quantities of starting materials, along with an $\eta = 0.5$ μL mg^{-1} of THF. Applying an 80 g acceleration for 50 min *via* RAM yielded the EXIFEX and EXIFAT phases for **1e** and **1d**, respectively. Comparison with the simulated PXRD pattern alongside those of the RAM and ball mill products unequivocally establishes the production of a pure phase of cocrystal **1e** through both mechanochemical methods.

To further investigate the influence of the type and quantity of liquid additives on RAM-synthesized XB cocrystals, a screening experiment was conducted on cocrystal **2c**. Samples were prepared under neat conditions, with 0.1 μL mg^{-1} $CHCl_3$, and with 0.1 μL mg^{-1} THF in the RAM process. Fig. 3 showcases the PXRD results, revealing incomplete conversion in the neat and $CHCl_3$ experiments while highlighting the formation of a pure SAJDEP phase when employing THF as the liquid additive in RAM cocrystallization for cocrystal **2c**. This comprehensive exploration of mechanochemical synthesis conditions and the influence of liquid additives underscores the versatility and effectiveness of RAM in the preparation of diverse halogen-bonded cocrystals, offering valuable insights into the optimization of this synthesis approach. Friščić and co-workers have

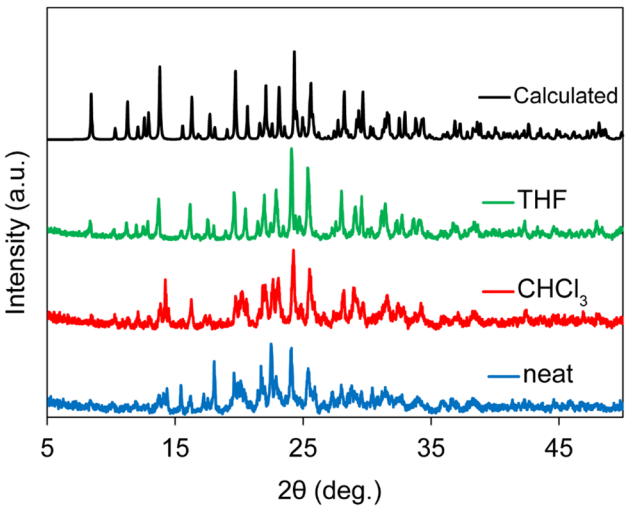


Fig. 3 Powder X-ray diffractograms for samples of **2c** produced using different RAM conditions: neat RAM (blue), 0.1 μL mg^{-1} $CHCl_3$ RAM (red), and 0.1 μL mg^{-1} THF RAM (green). The calculated PXRD pattern based on the SCXRD structure is shown in black.

discussed the optimization of the η value in liquid-assisted RAM applied to catalysis.[33]

In the preparation of cocrystals **2d** and **2e**, equimolar quantities of the starting materials were introduced into the reaction vessel, accompanied by the addition of 0.7 μL mg^{-1} of $CHCl_3$. The resulting PXRD patterns, as illustrated in Fig. 2, unequivocally demonstrate the successful formation of these novel cocrystals after a reaction duration of 50 min at 80 g acceleration. This is in excellent agreement with the simulated pattern derived using Mercury 4.2.0 software[65] based on newly acquired SCXRD data (*vide infra*). It is noteworthy that RAM proved to be an efficient and viable mechanochemical approach for the synthesis of these two novel XB cocrystals, eliminating the necessity for milling media and extensive mechanical grinding or abrasion processes.

During the RAM screening for cocrystal formation, with the compound **1a**, we observed intriguing results. Neat RAM for 45 min with a 1 : 2 ratio (donor : acceptor) led to the formation of the stable phase of the **1a(ii)** stoichiomorph (refcode: KIHRAX)[61] which was not achievable with other mechanochemical methods like ball milling. Addition of 85 μL of chloroform ($\eta = 0.2$ μL mg^{-1}) and mixing time of 50 min, however, transform the reactants (1 : 2 ratio (donor : acceptor)) instead to the **1a(i)** stoichiomorph (refcode = JAQMAQ),[60] the same product as obtained when ball milling for 45 min with same liquid additive. These results are presented in Fig. 4, showcasing PXRD patterns acquired for both neat and liquid-added RAM products. This finding affirms that varying RAM conditions can yield distinct stoichiomorphs of compound **1a** and highlights the remarkable potential of RAM as a tool for controlling and influencing stoichiomorphism and polymorphism. Notably, our attempts to prepare the **1a(ii)** stoichiomorph using ball milling were unsuccessful. It is important to mention that previous applications of mechanochemical ball milling, involving neat grinding and LAG, have resulted in the formation of different

© 2024 The Author(s). Published by the Royal Society of Chemistry

Open Access Article. Published on 31 January 2024. Downloaded on 5/1/2026 7:25:08 PM.
This article is licensed under a Creative Commons Attribution 3.0 Unported Licence.

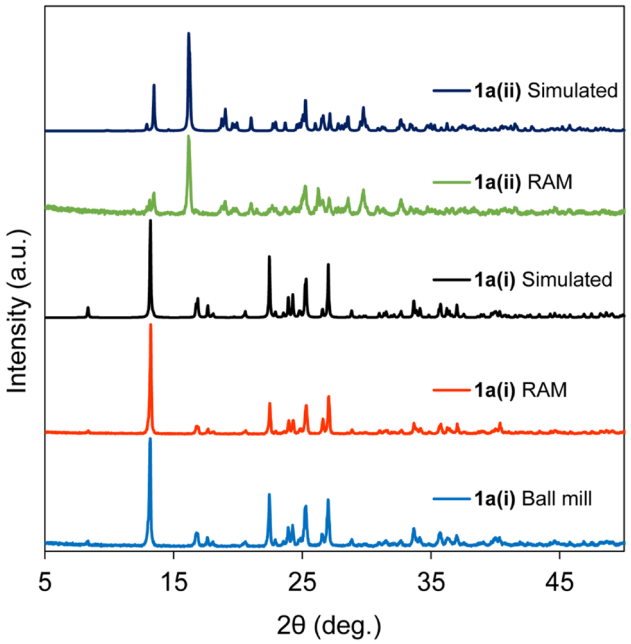


Fig. 4 X-ray diffractograms of **1a(i)** and **1a(ii)** cocrystalline powders prepared under ball milling and RAM conditions. See Table 1 and the main text for details. Simulated diffractograms are generated from the known single-crystal X-ray structures with refcodes JAQMAQ (**1a(i)**) and KIHRAX (**1a(ii)**).

polymorphs, as reported elsewhere.[66] To the best of our knowledge, the present work represents the first instance where the formation of different stable cocrystalline phases can be controlled using RAM; related work on controlling polymorphism with RAM has recently been reported.[33]

While the exact mechanism underlying this phenomenon remains incompletely understood, two distinct factors appear to influence the formation of different products *via* RAM. Firstly, in the liquid-assisted approach, the presence of a liquid component can enhance the reaction rate by introducing degrees of orientational and conformational freedom to the molecules at various interfaces.[67] Additionally, adding liquid may lead to the formation of a mobile surface layer at the molecule interface, which can enhance the reactivity of the reactants[68] and affect the resulting polymorphs. The second factor could be particularly apposite for RAM, which operates as a milder mechanochemical methodology where the reaction occurs through the direct impact of the reactant particles.

(ii) Single crystal X-ray diffraction

The crystal structures of **1a(i)** (CCDC 259702),[60] **1a(ii)** (CCDC 1854044),[61] **2a** (CCDC 1505893),[9] **1b** (CCDC 773127),[64] **2b** (CCDC 773130),[64] **1c** (CCDC 259705),[60] **2c** (CCDC 1505895),[9] **1d** (CCDC 824297),[63] and **1e** (CCDC 824296)[63] have been previously documented. In this study, we determined the single crystal X-ray diffraction (SCXRD) structures for compounds **2d** and **2e** to enhance our comprehension of halogen bonding interactions within these supramolecular assemblies.

SCXRD analysis revealed a 1 : 1 stoichiometry of *sym*-TFTIB to PheDON in **2d**. This compound crystallizes in a monoclinic crystal system, belonging to the $P2_1/c$ space group. The volume of the unit cell is determined to be 15 288(7) Å^3, and the crystal contains 32 molecules in the unit cell. The unit cell parameters and the other relevant information are presented in Table 2. As can be seen in Fig. 5(C), in **2d**, both nitrogen atoms of the bidentate PheDON interact with one of the *sym*-TFTIB iodine atoms, resulting in the observation of a slightly asymmetrical bifurcated halogen bond (XB) with I–N bond lengths of 2.997 and 3.297 Å (for example; there are 7 other pairs with similar distances as shown in Table 3). A straightforward layered packing arrangement is formed, where I–C and π—π interactions lead to a parallel stacking arrangement between *sym*-TFTIB and PheDON molecules as shown in Fig. 5(A), with intermolecular distances of 3.557 Å and 3.393 Å, respectively. Furthermore, the crystal structure reveals the presence of C–H···I and F···F interactions, which play a crucial role in extending the one-dimensional (1D) layer structures throughout the crystal network.

sym-TFTIB and DIZFON were cocrystallized to form the 1 : 1 cocrystal **2e** in the monoclinic space group $P2_1/c$. The supramolecular structure of **2e** is characterized by a monocoordinated XB of one *sym*-TFTIB with two acceptor moieties featuring one I–N and one I–O XB interaction (Fig. 5(D)). As is

Table 2 Crystallographic data and details

Compound	**2d**	**2e**
Chemical formula	$C_{18}H_6F_3I_3N_2O_2$	$C_{17}H_6F_3I_3N_2O$
CCDC number	2305189	2305188
FW (g mol^{-1})	719.95	691.94
Crystal colour	Orange	Yellow
Crystal system	Monoclinic	Monoclinic
Crystal space group	$P2_1/c$	$P2_1/c$
Temperature (K)	100 K	200 K
a, b, c (Å)	29.938(8), 18.399(5), 28.189(7)	8.3178(7), 30.472(2), 7.4150(5)
α, β, γ (deg)	90, 100.074(3), 90	90, 94.297(4), 90
V (Å^3)	15 288(7)	1874.1(2)
Z	32	4
R_1 (final)	0.1051	0.0504
wR_2 (final)	0.2484	0.0999

Open Access Article. Published on 31 January 2024. Downloaded on 5/1/2026 7:25:08 PM.
This article is licensed under a Creative Commons Attribution 3.0 Unported Licence.

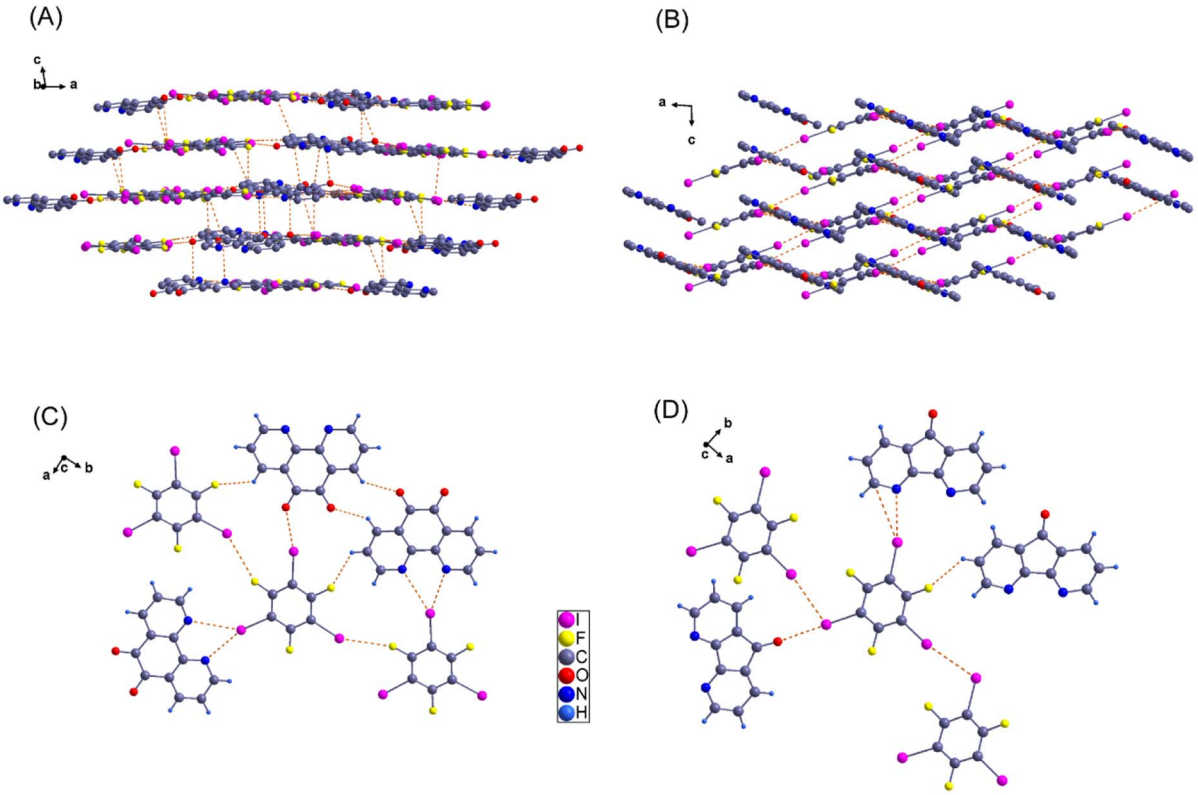


Fig. 5 Two novel crystal structures of compound **2d** (left, parts (A) and (C)) and **2e** (right, parts (B) and (D)) showing halogen bonds (dashed lines) in compounds **2d** and **2e**. In cocrystal **2d**, the iodine interacts with two nitrogen atoms making a bifurcated halogen bond and one oxygen with a monocoordinated interaction. In compound **2e**, the iodine of the donor interacts with two crystallographically distinct acceptor moieties.

Table 3 Selected halogen bond geometrical parameters, including contact distance, angle, and normalized contact distance ratio (R_{XB})

Cocrystal	$d_{I\cdots N}$ (Å)	$\theta_{C-N\cdots I}$	$R_{XB\ (I)}$	$d_{I\cdots O}$ (Å)	$\theta_{C-N\cdots O}$	$R_{XB\ (O)}$
1a(i) (*p*-DITFB)·(TMP)	3.067	177.15	0.869	—	—	—
1a(ii) (*p*-DITFB)·(TMP)	3.001	177.51	0.850	—	—	—
2a (*sym*-TFTIB)·(TMP)	2.991	178.90	0.847	—	—	—
	2.993	179.81	0.849			
1b (*p*-DITFB)·(DMAP)	2.677	179.25	0.756	—	—	—
2b (*sym*-TFTIB)·(DMAP)	2.766	176.15	0.784	—	—	—
	2.886	168.58	0.818			
1c (*p*-DITFB)·(*o*-Phe)	3.01	159.03	0.853	—	—	—
	3.274	149.76	0.927			
2c (*sym*-TFTIB)·(*o*-Phe)	3.02	175.68	0.856	—	—	—
	3.148	164.18	0.892			
1d (*p*-DITFB)·(PheDON)	3.149	154.93	0.892	3.214	155.14	0.918
2d (*sym*-TFTIB)·(PheDON)	3.297, 3.011, 3.215, 3.047, 3.225, 3.097, 2.997, 3.326, 3.316, 3.026, 3.406, 3.029, 3.039, 3.259, 3.094, 3.230	144.8, 165.1, 166.7, 143.3, 165.6, 143.9, 159.0, 149.5, 160.8, 149.0, 162.4, 146.5, 158.7, 149.9, 144.6, 164.1	0.934, 0.853, 0.911, 0.863, 0.914, 0.877, 0.849, 0.942, 0.939, 0.857, 0.965, 0.858, 0.861, 0.923, 0.876, 0.91	2.884[a]	177.52	0.824
1e (*p*-DITFB)·(DIZFON)	2.924	165.10	0.828	3.036	163.02	0.867
2e (*p*-DITFB)·(PheDON)	2.968	158.66	0.841	2.931	177.52	0.824

[a] For this compound, we avoid detailing the entire list of I···O XB interactions and instead provide one example in this table.

depicted in Fig. 5(B), the **2e** cocrystal structure propagates in zigzag chains where each 1D chain is packed on the next *via* I–I intermolecular interactions between donor moieties, generating a 2D layered structure.

It is not surprising that the structure of **2e** lacks a bifurcated XB, consistent with conclusions reached in the study by Ji *et al.* on similar acceptor moieties.[63] This finding can be attributed to the relatively greater distance between the two electron-rich

© 2024 The Author(s). Published by the Royal Society of Chemistry

Open Access Article. Published on 31 January 2024. Downloaded on 5/1/2026 7:25:08 PM.
This article is licensed under a Creative Commons Attribution 3.0 Unported Licence.

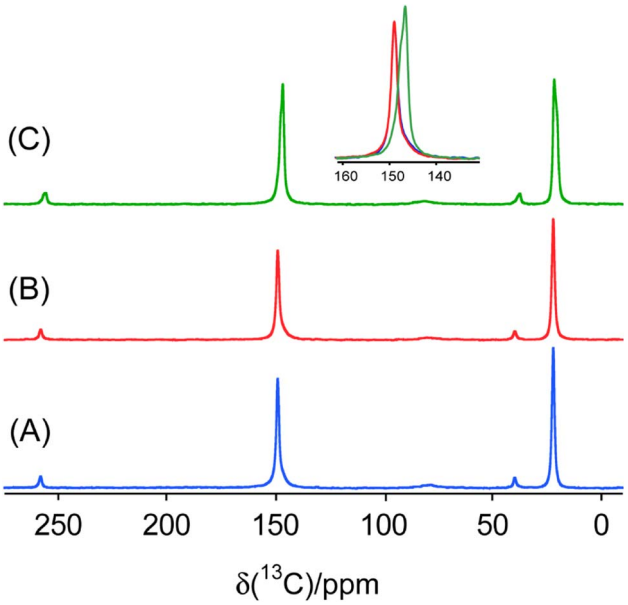


Fig. 6 $^{1}H \rightarrow {}^{13}C$ CP/MAS solid-state NMR spectra of sample **1a(i)** obtained by ball milling (blue, A), RAM (red, B), and the second stoichiomorph **1a(ii)** obtained by RAM (green, C). Inset: overlay of peak for the C covalently bonded to N in these three products to illustrate the identical ^{13}C chemical shifts for the ball milled and RAM products for **1a(i)**, but different chemical shift for the second stoichiomorph **1a(ii)**.

atoms (N) in DIZFON molecules, exceeding the threshold for the formation of a three-centered XB involving I and two N atoms. The distance between I and N in the XB interaction is measured at 2.968 Å, which is shorter than the corresponding bifurcated I–N XB in the **2d** cocrystal. This observation aligns with the concept that a monocoordinated XB is expected to be stronger than a bifurcated XB.[63]

(iii) Solid-state NMR spectroscopy

To further characterize the halogen-bonded cocrystals produced *via* RAM, we conducted ^{13}C CP/MAS SSNMR spectroscopy on all of the samples. The use of $^{1}H \rightarrow {}^{13}C$ cross-polarization has been demonstrated as a reliable and effective indirect method for characterizing the formation of XB cocrystals.[9] This technique allows us to gain insights into changes in the crystallographic and electronic environment surrounding the carbon atom covalently bonded to the nitrogen atom (C–N) in the acceptor moieties. The principle underlying this technique lies in the polarization transfer from protons to the carbon atom covalently bonded to the nitrogen atom. This ^{13}C nucleus is indirectly engaged in each XB (*i.e.*, one bond removed), and is subjected to small changes in electronic and crystallographic environment upon cocrystallization. Consequently, this involvement results in changes in the chemical shifts, exemplified in Fig. 6 for the two stoichiomorphs of **1a** (**1a(i)** and **1a(ii)**). The distinct ^{13}C chemical shifts observed for the two samples reflect differences in the local nuclear environment.

Fig. 7 and 8 depict the ^{13}C CP/MAS NMR spectra of XB acceptor moieties alongside all cocrystals formed with the two XB donors, **1** and **2**. Notable changes in chemical shifts are evident upon the formation of XB cocrystals, with their corresponding δ_{iso} values listed in Table 4. Strikingly, these NMR data also provide clear evidence that products generated *via* RAM and *via* ball milling are isomorphic; this is consistent with the PXRD data presented above and in the ESI.† In some cases, ball milling gives broader NMR lines which could be indicative of partial amorphization of the product (see ESI†). This effect

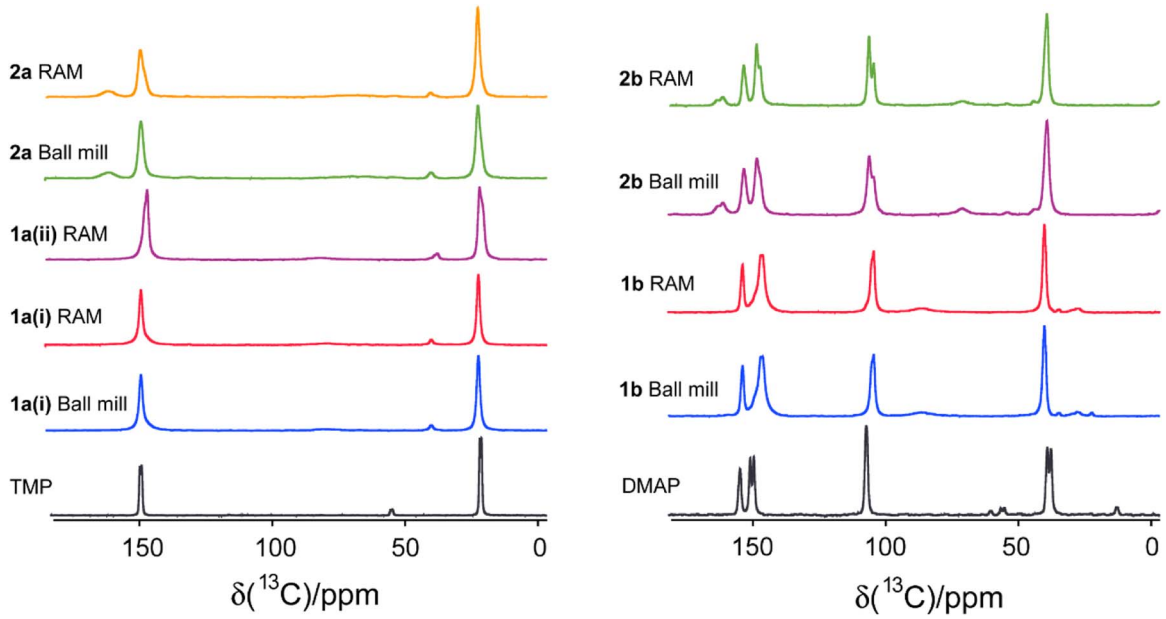


Fig. 7 Comparison of ^{13}C CP/MAS NMR spectra for monotopic XB acceptors (TMP and DMAP) and their respective cocrystals produced *via* ball milling and RAM. The corresponding chemical shifts are listed in Table 4.

© 2024 The Author(s). Published by the Royal Society of Chemistry

Open Access Article. Published on 31 January 2024. Downloaded on 5/1/2026 7:25:08 PM.
This article is licensed under a Creative Commons Attribution 3.0 Unported Licence.

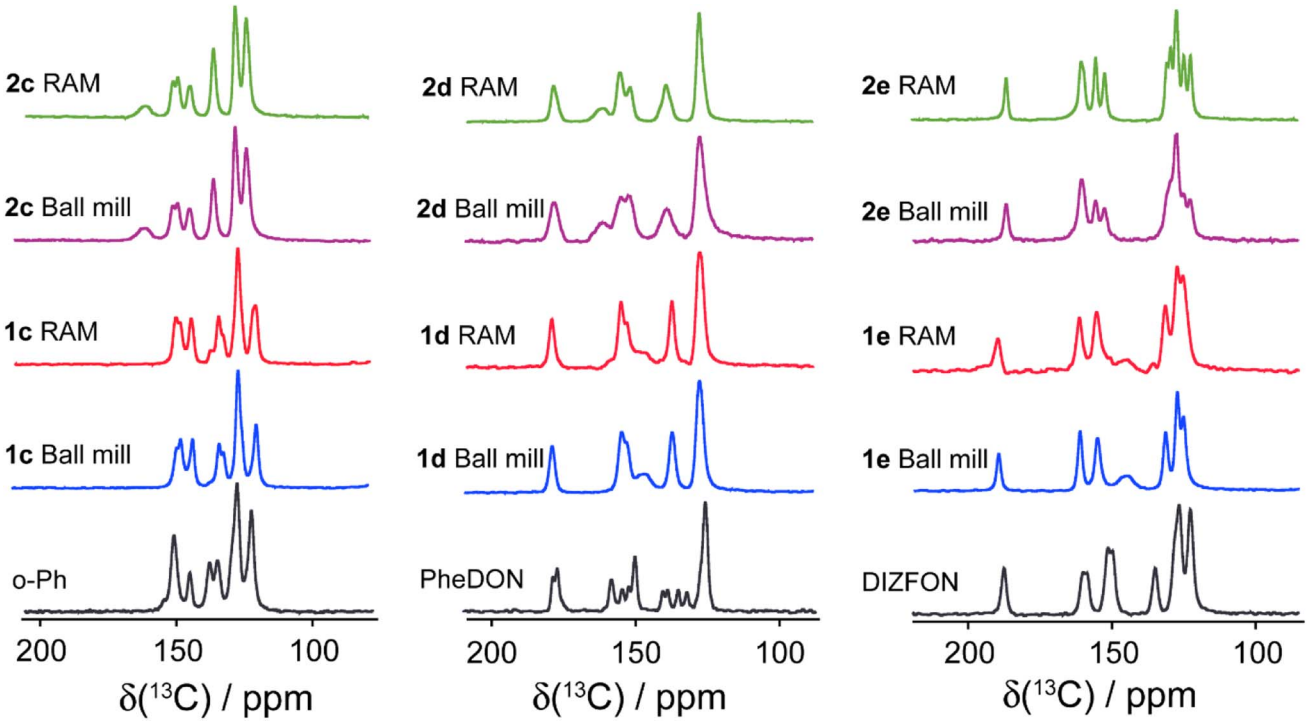


Fig. 8 Comparison of ^{13}C CP/MAS NMR spectra of ditopic XB acceptors (*o*-Ph, PheDON, and DIZFON) and their cocrystals produced *via* ball milling and RAM. The chemical shifts are detailed in Tables 4 and 5.

Table 4 Experimental ^{13}C chemical shifts of the carbon covalently bonded to the nitrogen in the XB acceptor moieties, based on ^{1}H → ^{13}C CP/MAS NMR experiments[a]

Cocrystal	XB acceptor	δ_{iso}/ppm XB acceptor	δ_{iso}/ppm cocrystal
1a(i)	TMP	142.7 & 149.1 ± 0.1	149.3 ± 0.3[b]
1a(ii)	TMP	142.7 & 149.1 ± 0.1	147.1 ± 0.5
2a	TMP	142.7 & 149.1 ± 0.1	149.5 ± 0.6
1b	DMAP	150.9 & 149.5 ± 0.1	146.6 ± 0.6
2b	DMAP	150.9 & 149.5 ± 0.1	147.8 ± 0.7
1c	*o*-Ph	150.8 & 145.1 ± 0.3	149.8 & 148.4 & 144.0 ± 0.3
2c	*o*-Ph	150.8 & 145.1 ± 0.3	151.2 & 149.5 & 145.1 ± 0.4
1d	PheDON	158.4 & 154.7 152.5 & 150.3 ± 0.4	154.8 & 153.2 & 147.1 ± 0.6
2d	PheDON	158.4 & 154.7 152.5 & 150.3 ± 0.4	161.4 & 155.5 & 152.0 ± 0.5
1e	DIZFON	160.7 & 152.0 ± 0.4	162.5 & 156.4 ± 0.4
2e	DIZFON	160.7 & 152.0 ± 0.4	162.1 & 157.1 & 154.0 ± 0.4

[a] Chemical shifts of donor molecules are also evident; these are marked on spectra shown in the ESI. [b] Errors in chemical shift measurements are attributed to the lack of certainty regarding the quantitative impact of residual ^{13}C–^{14}N dipolar coupling on peak positions.

could possibly be reduced by using shorter milling times, but these experiments were not pursued presently.

In a statistical and computational analysis conducted by Allen *et al.* on NO_2–X synthons involving both monocoordinate and bifurcated XB, it was observed that as the interaction distance decreased, the XB angles tended to become more directional and linear.[69] This observation suggests that bifurcated halogen bonding interactions, where one halogen atom interacts with two Lewis bases, will correlate with smaller C–X···O angles. Conversely, smaller angles correlate with weaker interactions when compared to more linear monocoordinated XB interactions. In the cocrystals involving acceptor molecules **c** and **d** with donors **1** and **2**, which engage in bifurcated halogen-bonded interactions, the contact lengths between I and N atoms are relatively long, corresponding to weaker XB interactions. Consequently, the C–N covalent bond in the acceptor molecule will be

Table 5 Experimental ^{13}C chemical shifts of the carbon covalently bonded to I and F in the XB donor moieties, based on ^{1}H → ^{13}C CP/MAS experiments

Cocrystal	XB donor	δ_{iso}/ppm C–I	δ_{iso}/ppm C–F
1a(i)	*p*-DITFB	78.7 ± 0.8	—
1a(ii)	*p*-DITFB	82.3 ± 0.8	—
2a	*sym*-TFTIB	68.6 ± 2.2	161.9 ± 0.9
1b	*p*-DITFB	86.7 ± 1.4	—
2b	*sym*-TFTIB	71.2 ± 0.9	163.4 ± 0.6
1c	*p*-DITFB	77.4 ± 1.4	—
2c	*sym*-TFTIB	67.1 ± 1.2	161.5 ± 0.8
1d	*p*-DITFB	73.8 ± 1.2	—
2d	*sym*-TFTIB	63.2 ± 1.4	161.6 ± 0.6
1e	*p*-DITFB	76.8 ± 1.2	—
2e	*sym*-TFTIB	68.6 ± 1.4	—[a]

[a] In **2e**, the resonance frequency of the C atom bonded to F is obscured by the intense and distinct signals from the acceptor moieties' carbon. Therefore, we are unable to report the chemical shift of the C–F carbon.

© 2024 The Author(s). Published by the Royal Society of Chemistry

Open Access Article. Published on 31 January 2024. Downloaded on 5/1/2026 7:25:08 PM.
This article is licensed under a Creative Commons Attribution 3.0 Unported Licence.

weakened less than it is in the presence of a stronger monocoordinated XB, resulting in a lower ^{13}C chemical shift for the C atom covalently bonded to the N atom within the acceptor moiety. More generally, the data in Table 4 show that the ^{13}C chemical shifts of the acceptor molecules can increase or decrease upon cocrystallization; increases are generally noted for TMP and DIZFON, while decreases are noted for DMAP and more subtle changes are noted for *o*-Ph and PheDON.

In another study conducted by our group,[70] it was shown that an increase in the C–I bond length of halogen bond donor **1** as a result of XB formation corresponded to an increase in the ^{13}C chemical shift. The δ_{iso} values for ^{13}C covalently bonded to iodine and fluorine in the XB donor moieties are listed in Table 5. Consistent with previous work, increases in the C–I chemical shifts relative to that for pure donor **1** (76.50(0.50) ppm)[70] and for pure donor **2** (67.6 ± 2.4 ppm)[9] are generally observed. Interestingly, exceptions are seen in both cases for cocrystals formed with acceptor **d**, which forms bifurcated halogen bonds; such exceptions could therefore possibly be NMR signatures of bifurcated XB, but more data are needed to confirm the generality of this finding.

Fluorine-19 SSNMR spectroscopy is a powerful technique that has found extensive utility in characterizing halogen-bonded compounds due to the high receptivity of fluorine nuclei, high natural abundance, and the wide chemical shift range.[9,71] Fig. 9 illustrates the ^{19}F MAS SSNMR spectra acquired for all cocrystals and the perfluorinated XB donor starting materials. Importantly, changes in the ^{19}F chemical shift upon the formation of halogen-bonded cocrystals serve as valuable independent indicators of cocrystallization events. These

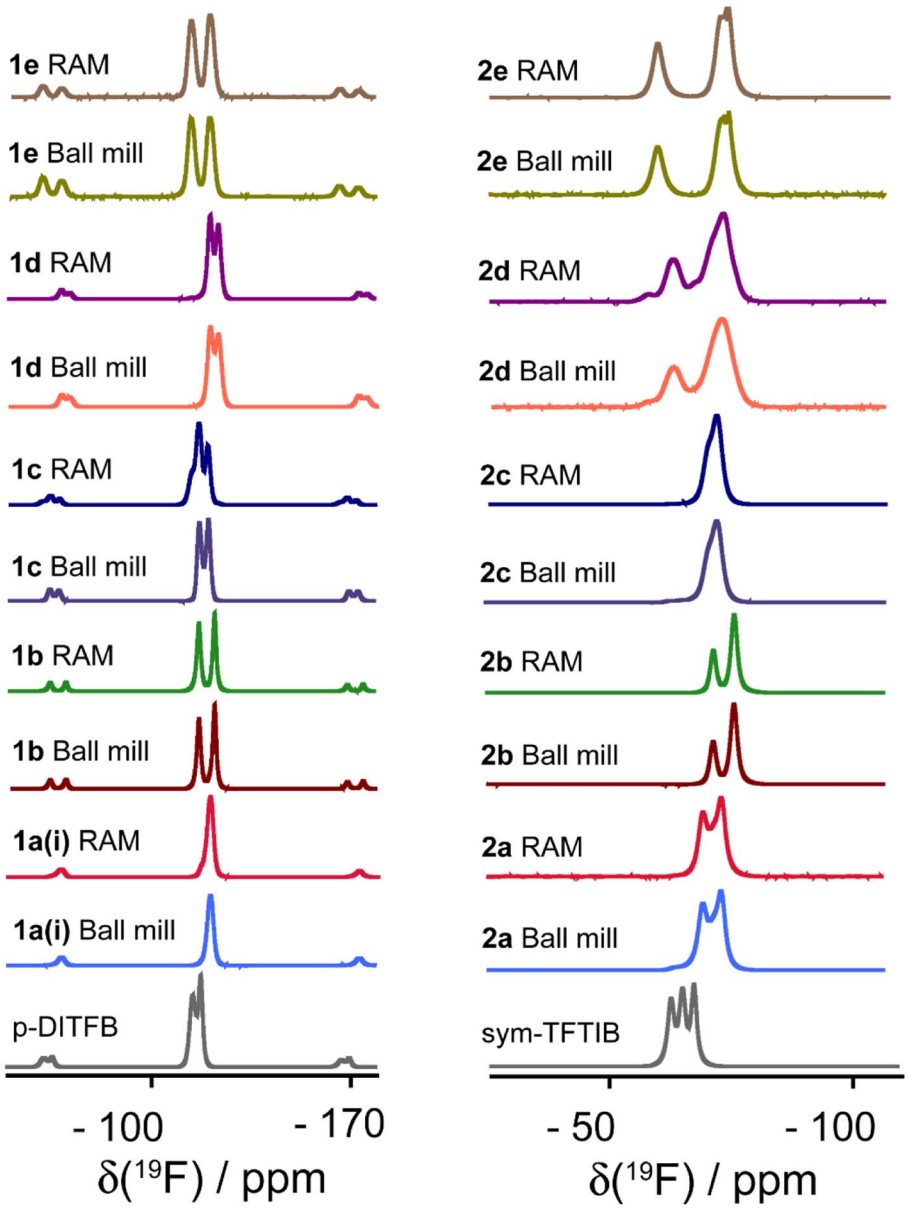


Fig. 9 Comparison of ^{19}F MAS SSNMR spectra of XB donors (*p*-DITFB and *sym*-TFTIB) and their cocrystals produced *via* ball milling and RAM. The chemical shifts are detailed in Table 6.

© 2024 The Author(s). Published by the Royal Society of Chemistry

Open Access Article. Published on 31 January 2024. Downloaded on 5/1/2026 7:25:08 PM.
This article is licensed under a Creative Commons Attribution 3.0 Unported Licence.

Table 6 Experimental ^{19}F chemical shifts of the halogen-bond donor moieties

Cocrystal	δ_{iso}/ppm cocrystal	XB donor	δ_{iso}/ppm XB donor
1a(i)	−118.9 ± 0.5	*p*-DITFB	−112.6 & −115.5 ± 0.6
1b	−114.8 & −120.4 ± 0.3		
1c	−115.0 & −118.3 ± 0.6		
1d	−118.8 & −121.7 ± 0.6		
1e	−121.2 & −118.8 ± 0.7		
2a	−68.3 & −72.1 ± 0.7	*sym*-TFTIB	−61.8 & −64.1 & −66.5 ± 0.3
2b	−70.4 & −74.8 ± 0.3		
2c	−71.2 ± 0.8		
2d	−62.2 & −72.6 ± 0.7		
2e	−59.1 & −72.0 & −73.4 ± 0.4		

spectra also provide an additional independent perspective that the products obtained *via* RAM and *via* ball milling are identical.

The ^{19}F chemical shifts are listed in Table 6, and the results demonstrate a consistent and notable decrease in the ^{19}F chemical shift for all samples upon the formation of halogen-bonded cocrystals. Since the crystallographic and electronic environment encountered by ^{19}F nuclei are highly sensitive to XB and certain short interactions involving ^{19}F nuclei with I or H atoms, as revealed by XRD, the extent of chemical shift changes exhibits variability across the compounds. Shifts on the order of up to −8 ppm are observed as a result of cocrystallization. These findings highlight the sensitivity of ^{19}F SSNMR as a probe to detect structural changes associated with XB cocrystallization. It is noted that while the ^{19}F NMR resonances for cocrystal **2d**, which features a large number of crystallographically non-equivalent molecules, are somewhat broader than for the other cocrystals, there is no clear spectral resolution of these multiple sites.

Conclusions

We have demonstrated that resonant acoustic mixing can consistently promote halogen-bond-induced cocrystallization of donor and acceptor molecules. Eleven halogen-bonded cocrystals have been prepared *via* RAM, including two novel structures which were characterized by single-crystal X-ray diffraction and one novel stoichiomorphic product which is inaccessible *via* ball milling. One of the notable advantages of RAM-based cocrystallization is its capacity to transform reactants into halogen-bonded interaction products through direct interactions, both under neat mixing conditions and when aided by the addition of small amounts of polar or moderately polar solvents. For most cocrystals studied herein, the inclusion of even a minimal quantity of these solvents serves to significantly enhance the cocrystallization process and increase the completeness of the transformation, further highlighting the potential of RAM in optimizing cocrystal synthesis. Powder X-ray diffraction and ^{13}C CP/MAS and ^{19}F MAS NMR spectroscopy have provided compelling evidence for the phase purity of samples obtained from RAM experiments and for the degree of polymorphic control available when small volumes of liquid are employed in mechanochemical reactions. Overall, this work demonstrates the potential of RAM for the production of known and novel cocrystalline assemblies, including polymorphic and stoichiomorphic structures.

Data availability

Data are available upon reasonable request from the authors.

Author contributions

A. N. prepared samples, carried out PXRD and SSNMR experiments, analysed all data, and wrote the first draft of the manuscript, and edited the manuscript. J. S. O. solved the single-crystal X-ray structures. D. L. B. directed research, secured funding, analysed data, and wrote and edited the manuscript.

Conflicts of interest

The authors declare they have no conflicts of interest.

Acknowledgements

D. L. B. is grateful to the Natural Sciences and Engineering Research Council of Canada for funding. The authors thank the solid-state NMR group at the University of Ottawa for helpful comments, and Dr Patrick Szell and Dr Tristan Georges for technical assistance.

References

1 P. Politzer, J. S. Murray and T. Clark, *Phys. Chem. Chem. Phys.*, 2010, **12**, 7748–7757.
2 L. C. Gilday, S. W. Robinson, T. A. Barendt, M. J. Langton, B. R. Mullaney and P. D. Beer, *Chem. Rev.*, 2015, **115**, 7118–7195.
3 A. Priimagi, G. Cavallo, P. Metrangolo and G. Resnati, *Acc. Chem. Res.*, 2013, **46**, 2686–2695.
4 A. Mukherjee, S. Tothadi and G. R. Desiraju, *Acc. Chem. Res.*, 2014, **47**, 2514–2524.
5 P. Auffinger, F. A. Hays, E. Westhof and P. S. Ho, *Proc. Natl. Acad. Sci. U. S. A.*, 2004, **101**, 16789–16794.
6 M. R. Scholfield, C. M. Vander Zanden, M. Carter and P. S. Ho, *Prot. Sci.*, 2013, **22**, 139–152.
7 T. Clark, M. Hennemann, J. S. Murray and P. Politzer, *J. Mol. Model.*, 2007, **13**, 291–296.
8 G. R. Desiraju, P. S. Ho, L. Kloo, A. C. Legon, R. Marquardt, P. Metrangolo, P. Politzer, G. Resnati and K. Rissanen, *Pure Appl. Chem.*, 2013, **85**, 1711–1713.
9 P. M. J. Szell, S. A. Gabriel, R. D. D. Gill, S. Y. H. Wan, B. Gabidullin and D. L. Bryce, *Acta Crystallogr., Sect. C: Struct. Chem.*, 2017, **73**, 157–167.
10 A. Bondi, *J. Phys. Chem.*, 1964, **68**, 441–451.
11 P. S. Ho, *Future Med. Chem.*, 2017, **9**, 637–640.

© 2024 The Author(s). Published by the Royal Society of Chemistry

Open Access Article. Published on 31 January 2024. Downloaded on 5/1/2026 7:25:08 PM. This article is licensed under a Creative Commons Attribution 3.0 Unported Licence.

12 R. Wilcken, M. O. Zimmermann, A. Lange, A. C. Joerger and F. M. Boeckler, *J. Med. Chem.*, 2013, **56**, 1363–1388.
13 P. Molina, F. Zapata and A. Caballero, *Chem. Rev.*, 2017, **117**, 9907–9972.
14 A. Ravi, A. S. Oshchepkov, K. E. German, G. A. Kirakosyan, A. V. Safonov, V. N. Khrustalev and E. A. Kataev, *Chem. Commun.*, 2018, **54**, 4826–4829.
15 L. Catalano, S. Perez-Estrada, H.-H. Wang, A. J.-L. Ayitou, S. I. Khan, G. Terraneo, P. Metrangolo, S. Brown and M. A. Garcia-Garibay, *J. Am. Chem. Soc.*, 2017, **139**, 843–848.
16 J.-P. Gliese, S. H. Jungbauer and S. M. Huber, *Chem. Commun.*, 2017, **53**, 12052–12055.
17 L. Carreras, M. Serrano-Torné, P. W. N. M. van Leeuwen and A. Vidal-Ferran, *Chem. Sci.*, 2018, **9**, 3644–3648.
18 S. L. James, C. J. Adams, C. Bolm, D. Braga, P. Collier, T. Friščić, F. Grepioni, K. D. M. Harris, G. Hyett, W. Jones, A. Krebs, J. Mack, L. Maini, A. G. Orpen, I. P. Parkin, W. C. Shearouse, J. W. Steed and D. C. Waddell, *Chem. Soc. Rev.*, 2012, **41**, 413–447.
19 K. Horie, M. Barón, R. B. Fox, J. He, M. Hess, J. Kahovec, T. Kitayama, P. Kubisa, E. Maréchal, W. Mormann, R. F. T. Stepto, D. Tabak, J. Vohlídal, E. S. Wilks and W. J. Work, *Pure Appl. Chem.*, 2004, **76**, 889–906.
20 L. Takacs, *JOM*, 2000, **52**, 12–13.
21 L. Takacs, *J. Therm. Anal. Calorim.*, 2007, **90**, 81–84.
22 L. Takacs, *J. Mater. Sci.*, 2004, **39**, 4987–4993.
23 *Ball Milling towards Green Synthesis: Applications, Projects, Challenges*, ed. A. Stolle and B. Ranu, Royal Society of Chemistry, Cambridge, UK, RSC Green Chemistry Series, No. 31, 2015, p. 303.
24 I. Huskić, C. B. Lennox and T. Friščić, *Green Chem.*, 2020, **22**, 5881–5901.
25 M. Solares-Briones, G. Coyote-Dotor, J. C. Páez-Franco, M. R. Zermeño-Ortega, C. M. de la O Contreras, D. Canseco-González, A. Avila-Sorrosa, D. Morales-Morales and J. M. Germán-Acacio, *Pharmaceutics*, 2021, **13**, 790.
26 D. E. Crawford, A. Porcheddu, A. S. McCalmont, F. Delogu, S. L. James and E. Colacino, *ACS Sustain. Chem. Eng.*, 2020, **8**, 12230–12238.
27 P. Cerreia Vioglio, M. R. Chierotti and R. Gobetto, *Adv. Drug Delivery Rev.*, 2017, **117**, 86–110.
28 D. Braga and F. Grepioni, *Angew. Chem., Int. Ed.*, 2004, **43**, 4002–4011.
29 T. Stolar, A. Prašnikar, V. Martinez, B. Karadeniz, A. Bjelić, G. Mali, T. Friščić, B. Likozar and K. Užarević, *ACS Appl. Mater. Interfaces*, 2021, **13**, 3070–3077.
30 L. Gonnet, C. B. Lennox, J.-L. Do, I. Malvestiti, S. G. Koenig, K. Nagapudi and T. Friščić, *Angew. Chem., Int. Ed.*, 2022, **61**, e202115030.
31 F. Effaty, L. Gonnet, S. G. Koenig, K. Nagapudi, X. Ottenwaelder and T. Friščić, *Chem. Commun.*, 2023, **59**, 1010–1013.
32 C. B. Lennox, T. H. Borchers, L. Gonnet, C. J. Barrett, S. G. Koenig, K. Nagapudi and T. Friščić, *Chem. Sci.*, 2023, **14**, 7475–7481.
33 L. Gonnet, T. H. Borchers, C. B. Lennox, J. Vainauskas, Y. Teoh, H. M. Titi, C. J. Barrett, S. G. Koenig, K. Nagapudi and T. Friščić, *Faraday Discuss.*, 2023, **241**, 128–149.
34 A. Pichon, A. Lazuen-Garay and S. L. James, *CrystEngComm*, 2006, **8**, 211–214.
35 K. Kubota, Y. Pang, A. Miura and H. Ito, *Science*, 2019, **366**, 1500–1504.
36 F. Toda, K. Tanaka and A. Sekikawa, *J. Chem. Soc., Chem. Commun.*, 1987, 279–280.
37 G. Kaupp, in *Organic Solid State Reactions*, ed. F. Toda, Springer Berlin Heidelberg, Berlin, Heidelberg, 2005, pp. 95–183.
38 K. Tanaka and F. Toda, *Chem. Rev.*, 2000, **100**, 1025–1074.
39 G. Kaupp, in *Encyclopedia of Physical Organic Chemistry*, John Wiley & Sons, Inc., 2017, pp. 1–80.
40 A. V. Trask, N. Shan, W. D. S. Motherwell, W. Jones, S. Feng, R. B. H. Tan and K. J. Carpenter, *Chem. Commun.*, 2005, 880–882.
41 T. Friščić, S. L. Childs, S. A. A. Rizvi and W. Jones, *CrystEngComm*, 2009, **11**, 418–426.
42 A. V. Trask, W. D. S. Motherwell and W. Jones, *Chem. Commun.*, 2004, 890–891.
43 A. O. Patil, D. Y. Curtin and I. C. Paul, *J. Am. Chem. Soc.*, 1984, **106**, 348–353.
44 M. C. Etter, Z. Urbanczyk-Lipkowska, M. Zia-Ebrahimi and T. W. Panunto, *J. Am. Chem. Soc.*, 1990, **112**, 8415–8426.
45 M. C. Etter and D. A. Adsmond, *J. Chem. Soc., Chem. Commun.*, 1990, 589–591.
46 V. R. Pedireddi, W. Jones, A. P. Chorlton and R. Docherty, *Chem. Commun.*, 1996, 987–988.
47 K. Lisac, S. Cepić, M. Herak and D. Cinčić, *Chem.: Methods*, 2022, **2**, e202100088.
48 X. Ding, A. W. Crawford, W. P. Derrick, D. K. Unruh, R. H. Groeneman and K. M. Hutchins, *Chem.–Eur. J.*, 2021, **27**, 16329–16333.
49 C. Schumacher, K.-N. Truong, J. S. Ward, R. Puttreddy, A. Rajala, E. Lassila, C. Bolm and K. Rissanen, *Org. Chem. Front.*, 2024, DOI: 10.1039/D3QO01512B.
50 D. Braga, G. Palladino, M. Polito, K. Rubini, F. Grepioni, M. R. Chierotti and R. Gobetto, *Chem.–Eur. J.*, 2008, **14**, 10149–10159.
51 A. Pichon and S. L. James, *CrystEngComm*, 2008, **10**, 1839–1847.
52 H. M. Titi, J.-L. Do, A. J. Howarth, K. Nagapudi and T. Friščić, *Chem. Sci.*, 2020, **11**, 7578–7584.
53 D. J. am Ende, S. R. Anderson and J. S. Salan, *Org. Process Res. Dev.*, 2014, **18**, 331–341.
54 K. Nagapudi, E. Y. Umanzor and C. Masui, *Int. J. Pharm.*, 2017, **521**, 337–345.
55 R. Tanaka, S. Osotprasit, J. Peerapattana, K. Ashizawa, Y. Hattori and M. Otsuka, *Pharmaceutics*, 2021, **13**, 56.
56 M. Bui, P. Chakravarty and K. Nagapudi, *Faraday Discuss.*, 2022, **241**, 357–366.
57 S. R. Anderson, P. Dubé, M. Krawiec, J. S. Salan, D. J. am Ende and P. Samuels, *Propellants, Explos., Pyrotech.*, 2016, **41**, 783–788.

© 2024 The Author(s). Published by the Royal Society of Chemistry

Open Access Article. Published on 31 January 2024. Downloaded on 5/1/2026 7:25:08 PM.
This article is licensed under a Creative Commons Attribution 3.0 Unported Licence.

58 S. R. Anderson, D. J. am Ende, J. S. Salan and P. Samuels, *Propellants, Explos., Pyrotech.*, 2014, **39**, 637–640.
59 M. Michalczyk, W. Zierkiewicz and S. Scheiner, *Cryst. Growth Des.*, 2022, **22**, 6521–6530.
60 J. L. Syssa-Magale, K. Boubekeur, P. Palvadeau, A. Meerschaut and B. Schöllhorn, *CrystEngComm*, 2005, **7**, 302–308.
61 P. M. J. Szell, S. A. Gabriel, E. Caron-Poulin, O. Jeannin, M. Fourmigué and D. L. Bryce, *Cryst. Growth Des.*, 2018, **18**, 6227–6238.
62 R. Wang, D. Hartnick and U. Englert, *Z. Kristallogr.*, 2018, **233**, 733–744.
63 B. Ji, W. Wang, D. Deng and Y. Zhang, *Cryst. Growth Des.*, 2011, **11**, 3622–3628.
64 L. C. Roper, C. Präsang, V. N. Kozhevnikov, A. C. Whitwood, P. B. Karadakov and D. W. Bruce, *Cryst. Growth Des.*, 2010, **10**, 3710–3720.
65 C. F. Macrae, I. Sovago, S. J. Cottrell, P. T. A. Galek, P. McCabe, E. Pidcock, M. Platings, G. P. Shields, J. S. Stevens, M. Towler and P. A. Wood, *J. Appl. Crystallogr.*, 2020, **53**, 226–235.
66 A. V. Trask, W. D. S. Motherwell and W. Jones, *Cryst. Growth Des.*, 2005, **5**, 1013–1021.
67 N. Shan, F. Toda and W. Jones, *Chem. Commun.*, 2002, 2372–2373.
68 J.-L. Do and T. Friščić, *ACS Cent. Sci.*, 2017, **3**, 13–19.
69 F. H. Allen, J. P. M. Lommerse, V. J. Hoy, J. A. K. Howard and G. R. Desiraju, *Acta Crystallogr., Sect. B: Struct. Sci.*, 1997, **53**, 1006–1016.
70 J. Viger-Gravel, S. Leclerc, I. Korobkov and D. L. Bryce, *CrystEngComm*, 2013, **15**, 3168–3177.
71 C. M. Widdifield, G. Cavallo, G. A. Facey, T. Pilati, J. Lin, P. Metrangolo, G. Resnati and D. L. Bryce, *Chem.–Eur. J.*, 2013, **19**, 11949–11962.

© 2024 The Author(s). Published by the Royal Society of Chemistry

Part 5 – Conclusions and Future Outlook

5.1 Summary of Major Scientific Contributions

The research presented in this dissertation explores complementary approaches to the characterization and sustainable synthesis of molecular solids through the development and application of experimental and computational methodologies. The work demonstrates how modern magnetic resonance spectroscopy, crystallographic techniques, first-principles calculations, and green synthetic methodologies can be integrated to investigate the relationship between local electronic structure, intermolecular interactions, and solid-state properties.

The principal contribution of this thesis is the development of cryogen-free Zp-NQR spectroscopy as a practical and quantitative methodology for studying quadrupolar nuclei in molecular solids. Through the establishment of a routine laboratory workflow, the development of reliable simulation strategies, direct isotopic identification of quadrupolar resonance lines, quantitative determination of quadrupolar interaction parameters, and their application to pharmaceutical materials, this work significantly broadens the analytical capabilities and accessibility of NQR spectroscopy.

Beyond methodological development, this dissertation demonstrates that experimentally determined quadrupolar interaction parameters provide sensitive probes of local electronic structure and intermolecular interactions. Their successful application to halogen-bonded molecular solids establishes new opportunities for employing quadrupolar spectroscopy to investigate halogen-bond interactions, crystal packing, pharmaceutical cocrystals, and chemically complex materials.

Complementary investigations employing ^{77}Se solid-state NMR spectroscopy and quantum chemical calculations further expanded the understanding of selenium-centered non-covalent interactions, while mechanochemical synthesis through resonant acoustic mixing demonstrated environmentally responsible routes toward the preparation of halogen-bonded molecular solids. Together, these studies illustrate how multiple experimental methodologies can be combined to address common scientific questions from different but complementary perspectives.

5.2 Assessing the Green Chemistry Footprint of This Thesis

A recurring theme throughout this dissertation is the consideration of sustainability in both the synthesis and characterization of molecular solids. Rather than focusing solely on environmentally responsible synthesis, the studies presented here illustrate how sustainable practices can be incorporated into multiple stages of the experimental workflow, from materials preparation to structural characterization.

Mechanochemical synthesis significantly reduces the dependence on organic solvents traditionally employed during cocrystal preparation. Both ball milling and resonant acoustic mixing provide rapid, efficient, and scalable routes toward supramolecular materials while substantially decreasing solvent consumption and chemical waste. Resonant acoustic mixing further eliminates the need for grinding media, providing additional practical advantages for scale-up and industrial implementation.[1–3]

Similarly, the development of cryogen-free Zp-NQR spectroscopy eliminates the dependence on superconducting magnets and liquid helium that characterizes conventional high-field magnetic resonance techniques. Although complementary high-field NMR measurements remain valuable for specific applications, many of the quadrupolar characterization experiments

presented in this thesis were performed under ambient laboratory conditions using compact instrumentation and adjustable electromagnets.[4–6] These developments demonstrate that improvements in both synthesis and characterization contribute toward more resource-efficient molecular solid research.

5.3 Zp-NQR in the Post-Helium Era: A Practical Model for Sustainable Magnetic Resonance

The increasing cost and limited availability of liquid helium continue to motivate the development of alternative magnetic resonance methodologies that reduce dependence on cryogenic infrastructure.[4] Although superconducting NMR spectrometers remain indispensable for numerous applications, there exists a growing need for complementary techniques capable of providing high-quality structural information using simpler and more accessible instrumentation.

The cryogen-free Zp-NQR methodology developed throughout this thesis addresses this need by combining adjustable electromagnets with exact Hamiltonian simulations to determine complete quadrupolar interaction parameters directly from powder samples.[7] This approach substantially lowers the experimental barrier to quadrupolar spectroscopy while maintaining quantitative sensitivity to local electronic structure. Consequently, Zp-NQR has the potential to expand access to advanced magnetic resonance techniques for research laboratories, educational institutions, and industrial environments where conventional high-field instrumentation may be unavailable or impractical.

As instrumentation, automation, and computational analysis continue to advance, Zp-NQR spectroscopy may become an increasingly important component of the modern magnetic resonance toolbox for solid-state chemistry.

5.4 The Realized Synergy: Green Mechanochemistry + Cryogen-Free Zp-NQR

One theme that emerges from this dissertation is the value of combining sustainable synthesis with complementary characterization techniques. As illustrated in Figure 5.1, mechanochemical preparation of molecular solids can be integrated with magnetic resonance spectroscopy, crystallographic methods, and first-principles calculations to provide a comprehensive framework for investigating supramolecular materials. Together, these complementary approaches contribute to a more resource-efficient workflow while providing detailed insight into crystal structures, local electronic environments, and intermolecular interactions.

Figure 5.1 highlights the integrated workflow developed throughout this thesis. Halogen-bonded molecular solids are prepared using either conventional ball milling or resonant acoustic mixing before being characterized using complementary experimental and computational techniques, including Zp-NQR spectroscopy, high-field SSNMR, and first-principles quantum chemical calculations. Collectively, these methods provide detailed insight into crystal structures, local electronic environments, and intermolecular interactions while reducing reliance on solvent-intensive synthesis and cryogenic characterization.

Although each research project presented in this dissertation was motivated by distinct scientific questions, together they illustrate a broader strategy for molecular solid research in which sustainable synthesis, advanced spectroscopy, crystallography, and computational chemistry function as complementary components of a unified experimental framework.

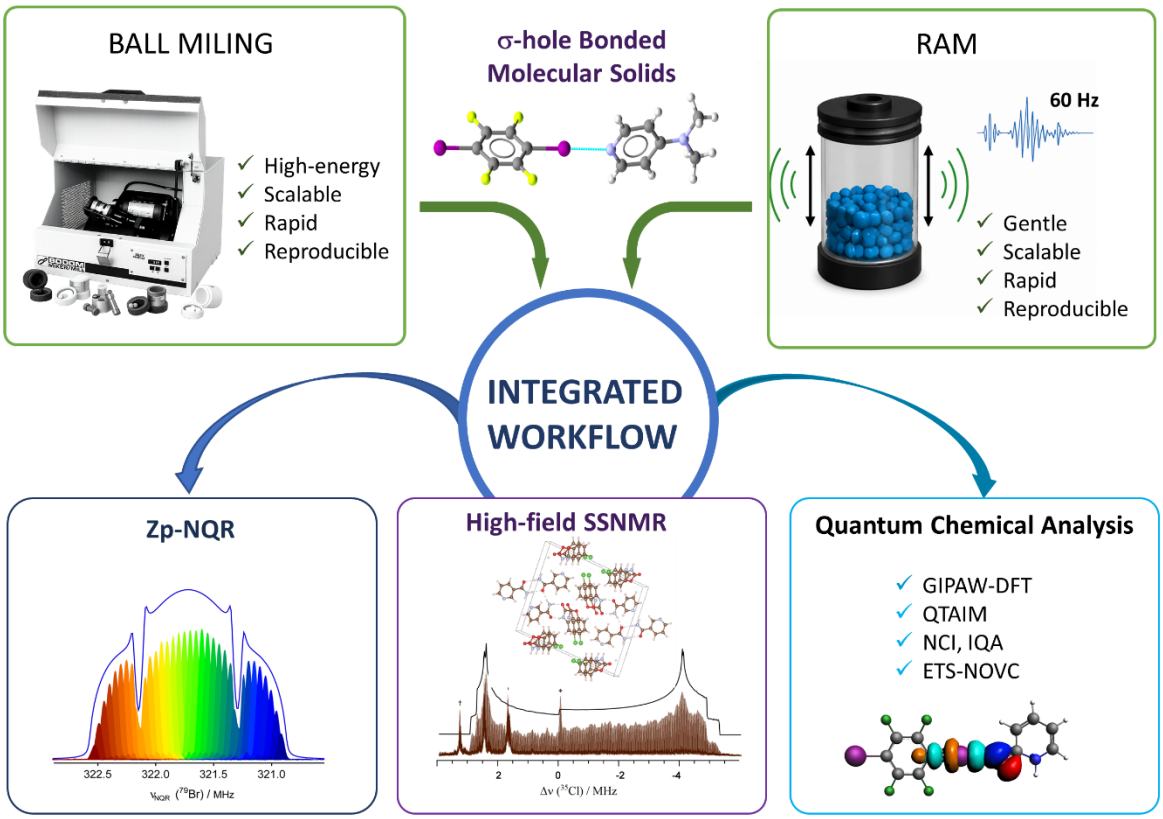


Figure 5.1. Integrated workflow developed throughout this thesis for the sustainable preparation and comprehensive characterization of molecular solids. Halogen-bonded molecular solids are prepared using complementary mechanochemical approaches, including conventional ball milling and RAM. The resulting materials are subsequently characterized through an integrated suite of experimental and computational techniques including Zp-NQR, high-field SSNMR, and first-principles quantum chemical calculations.

5.5 Limitations and Critical Reflections

Despite the advances presented in this dissertation, several limitations remain. Unlike conventional NMR spectroscopy, NQR resonance frequencies are not known *a priori* and must first be located experimentally through a frequency search over a potentially broad spectral range. Consequently, identifying resonance frequencies can be time-consuming, particularly for compounds containing multiple quadrupolar sites or when little prior spectroscopic information is

available. Furthermore, Zp-NQR is inherently restricted to quadrupolar nuclei and, in its current implementation, is best suited for systems exhibiting moderate to high NQR resonance frequencies. For the instrumentation employed in this work, resonance frequencies below approximately 20 MHz often exhibit reduced signal-to-noise ratios owing to increased environmental electromagnetic interference, probe ringing, and radiofrequency noise, making reliable signal detection and the acquisition of well-resolved Zeeman-perturbed spectra more challenging. Continued improvements in probe design, radiofrequency electronics, shielding, and noise suppression strategies are expected to enhance sensitivity and extend the applicability of Zp-NQR to lower-frequency quadrupolar systems.

Similarly, mechanochemical synthesis is not universally applicable to every molecular system, and successful cocrystal formation frequently requires optimization of milling conditions, liquid additives, or acoustic mixing parameters. Quantum chemical calculations likewise depend on the chosen computational methodology and may become computationally demanding for large molecular systems.

Recognizing these limitations provides opportunities for future methodological improvements while emphasizing the importance of combining multiple complementary characterization techniques when investigating complex molecular solids.

5.6 Future Directions

The methodologies developed throughout this dissertation open several promising directions for future research. From an instrumentation perspective, continued improvements in probe design, radiofrequency electronics, electromagnetic shielding, and noise suppression are expected to enhance the sensitivity of Zp-NQR spectroscopy and extend its operational frequency

range toward lower NQR frequencies. Such advances would enable the investigation of a broader range of quadrupolar nuclei, particularly those exhibiting low NQR resonance frequencies, including ^{14}N, whose resonance frequencies in molecular solids often lie between a few hundred kilohertz and several megahertz. Expanding the accessible frequency range would significantly broaden the applicability of Zp-NQR to pharmaceutical compounds, energetic materials, organic molecular crystals, and numerous nitrogen-containing systems that are currently difficult to study using the present instrumentation.

Beyond pharmaceuticals, Zp-NQR has considerable potential for the characterization of emerging functional materials. One particularly promising area is the investigation of halide-based solid-state electrolytes, where quadrupolar nuclei such as ^{35}Cl, ^{79}Br, and ^{127}I can provide site-specific information on local structure, disorder, phase transformations, and ion transport pathways. Similarly, Zp-NQR could offer valuable insight into heterogeneous catalysts and catalytic materials containing quadrupolar nuclei by probing changes in the local electronic environment associated with catalyst activation, adsorption processes, and reaction intermediates.

The integration of Zp-NQR with complementary experimental and computational techniques also presents exciting opportunities for future research. Combined with SSNMR spectroscopy, diffraction methods, and first-principles calculations, Zp-NQR can provide increasingly comprehensive structural and electronic information for complex molecular solids, including pharmaceutical polymorphs, multicomponent cocrystals, degradation products, and disordered crystalline materials. Continued development of multimodal characterization strategies will further strengthen the ability to relate experimentally determined quadrupolar interaction parameters to local electronic structure and material properties.

Finally, resonant acoustic mixing represents a promising platform for the scalable and sustainable synthesis of molecular solids. Future studies may explore continuous manufacturing, automated process optimization, and the preparation of increasingly complex supramolecular materials, further advancing the role of mechanochemistry in green pharmaceutical and materials synthesis.

5.7 Final Remarks

This dissertation has demonstrated that meaningful advances in molecular solid science arise from the integration of complementary methodologies rather than from any single experimental technique. By combining cryogen-free quadrupolar spectroscopy, solid-state NMR, crystallography, first-principles quantum chemical calculations, and sustainable mechanochemical synthesis, this work has established new approaches for investigating the structural and electronic properties of molecular solids while promoting more resource-efficient research practices.

More broadly, this thesis illustrates that sustainability and scientific innovation are not competing objectives but can instead reinforce one another. The methodologies developed and applied throughout this work contribute to a growing movement toward accessible, quantitative, and environmentally responsible approaches for the preparation and characterization of molecular materials. It is hoped that these advances will encourage wider adoption of cryogen-free magnetic resonance techniques and sustainable synthetic methodologies while supporting future developments in supramolecular chemistry, pharmaceutical materials science, and solid-state spectroscopy.

References for Part 5.

(1) Osorio, J. G.; Muzzio, F. J. Evaluation of Resonant Acoustic Mixing Performance. *Powder Technol.* **2015**, *278*, 46–56. https://doi.org/10.1016/j.powtec.2015.02.033.

(2) Friščić, T.; Mottillo, C.; Titi, H. M. Mechanochemistry for Synthesis. *Angew. Chem.* **2020**, *132* (3), 1030–1041. https://doi.org/10.1002/ange.201906755.

(3) L. James, S.; J. Adams, C.; Bolm, C.; Braga, D.; Collier, P.; Friščić, T.; Grepioni, F.; M. Harris, K. D.; Hyett, G.; Jones, W.; Krebs, A.; Mack, J.; Maini, L.; Guy Orpen, A.; P. Parkin, I.; C. Shearouse, W.; W. Steed, J.; C. Waddell, D. Mechanochemistry: Opportunities for New and Cleaner Synthesis. *Chem. Soc. Rev.* **2012**, *41* (1), 413–447. https://doi.org/10.1039/C1CS15171A.

(4) Anderson, S. T. Economics, Helium, and the U.S. Federal Helium Reserve: Summary and Outlook. *Nat. Resour. Res.* **2018**, *27* (4), 455–477. https://doi.org/10.1007/s11053-017-9359-y.

(5) Fantozzi, N.; Volle, J.-N.; Porcheddu, A.; Virieux, D.; García, F.; Colacino, E. Green Metrics in Mechanochemistry. *Chem. Soc. Rev.* **2023**, *52* (19), 6680–6714. https://doi.org/10.1039/D2CS00997H.

(6) Tundo, P.; Anastas, P.; Black, D. S.; Breen, J.; Collins, T. J.; Memoli, S.; Miyamoto, J.; Polyakoff, M.; Tumas, W. Synthetic Pathways and Processes in Green Chemistry. Introductory Overview. *Pure Appl. Chem.* **2000**, *72* (7), 1207–1228. https://doi.org/10.1351/pac200072071207.

(7) Nari, A.; Szell, P. M. J.; Bryce, D. L. Practical Aspects of Zeeman-Perturbed NQR Spectroscopy Using an Adjustable Electromagnet. *Solid State Nucl. Magn. Reson.* **2025**, *138*, 102014. https://doi.org/10.1016/j.ssnmr.2025.102014.

Appendix I – List of Publications and Conference Presentations

List of publications.

- **A. Nari**, J. N. Rusimovic , P. M. J. Szell, M. Jasil, Terskikh, V. D. L. Bryce, and B. Thomas Integrated Site-Resolved Zeeman-Perturbed NQR, Solid-State NMR, and 3D Electron Diffraction Crystallography of Chlorine-Bearing Molecules in Powders. *Under preparation.*

- **A. Nari**, P. M. J. Szell, and D. L. Bryce, "Isotopic Identification of Quadrupolar Spin Resonance Lines by Zeeman Perturbation", *J. Phys. Chem. Lett.*, **2025**,*16*, 8752-8757.

- **A. Nari**, S. J. Thomas, D. L. Bryce, and B. Thomas, "Understanding Non-Covalent Interactions in Diphenyldiselenide and Diphenylselenide Cocrystals Using a Combined 77Se Magic-Angle Spinning Solid-State NMR and Quantum Chemical Analysis Approach", *J. Phys. Chem. C*, **2025**, *129*, 13299-13311.

- **A. Nari**, P. M. J. Szell, and D. L. Bryce, "Practical Aspects of Zeeman-Perturbed NQR Spectroscopy using an Adjustable Electromagnet", *Solid State Nucl. Magn. Reson*. **2025**, *138*, 102014

- **A. Nari**, M. Rahman, P. M. J. Szell, V. Semeniuchenko, and D. L. Bryce, ″Halogen Bond Strength in Solids Quantified via Zeeman-Perturbed Nuclear Quadrupole Resonance Spectroscopy″, *J. Am. Chem. Soc.* **2025**, *147*, 9528-9543.

- G. Cosby, T. Iftimie, **A. Nari**, and D. L. Bryce, ″Chalcogen-Bonded Cocrystals and Salt Cocrystals via Automated Resonant Acoustic Mixing with a Button Operative Bot″, *RSC Mechanochem.,* **2025**, *2*, 201-208 **(Cover article)**.

- T. Georges, J. Beaudoin, M. Rahman, **A. Nari**, J. S. Ovens, and D. L. Bryce, "^{77}Se Solid-State NMR Investigation of Selenium Chemical Shift Tensors of Chalcogen Bonds in Selenadiazole Cocrystals", *J. Phys. Chem. C*, **2025**, *129*, 5483-5492.

- **A. Nari**, J. S. Ovens, and D. L. Bryce, "Halogen-Bonded Cocrystals via Resonant Acoustic Mixing", *RSC Mechanochem.*, **2024**, *1*, 50-62 **(Cover article)**.

List of conference presentations.

1. Oral Presentation, Physical and Theoretical Chemistry – Magnetic Resonance Section, CSC 2026 Conference, May 24, 2026, Toronto, Canada.
2. Promoted Oral presentation at the Alpine Conference on Magnetic Resonance in Solids, September 14, 2025, Chamonix, France
3. Accepted Oral presentation at the Joint ENC - ISMAR Conference, April 19, 2025, California, USA. *(Received the JMR Award for outstanding paper submitted by a graduate student or postdoc)*
4. Oral presentation at the CSC 2025, June 15, 2025, Ottawa, Canada.
5. Oral presentation at the 35th MOOT NMR Symposium, October 19–20, 2024, Montreal, Canada.
6. Oral presentation at the PANACEA Solid-State NMR School, June 16–21, 2024, Venice, Italy.
7. Oral presentation at the OCCI 2024, May 24, 2024, Ottawa, Canada.
8. Poster presentation at the 65th ICASS Seminar, July 26–28, 2023, Ottawa, Canada.
9. Oral presentation at the OCCI 2023, May 31, 2023, Ottawa, Canada.

Appendix II – Supporting Information

II.1 Supporting Information for Chapter 5

Supplementary Text

Single crystal X-ray structure of **2b**

The single crystal X-ray diffraction analysis of compound **2b**, a cocrystal formed between 1,4-diiodotetrafluorobenzene (**2**) and 1-bromo-4-nitrobenzene (**b**), revealed a 1:2 donor–acceptor stoichiometry. The structure crystallized in the triclinic space group $P\bar{1}$ (no. 2), which is centrosymmetric. In the asymmetric unit, one molecule of **2** is halogen-bonded to two molecules of **b** through I···O contacts involving the nitro group. The I···O halogen bonds are nearly linear, with C–I···O angles close to 170°, and the I···O distances fall well within the range expected for strong halogen bonding (ca. 2.84 Å), shorter than the sum of van der Waals radii.

The crystal packing is dominated by a network of directional halogen bonds and additional weak interactions involving bromine atoms. Each iodine atom in **2** participates in a halogen bond with a different **b** molecule, resulting in a discrete trimeric motif. These trimers are extended into layers via intermolecular I···O and I···π interactions, while Br···O and Br···π contacts from **b** molecules further stabilize the three-dimensional architecture. The absence of high symmetry in $P\bar{1}$ permits subtle distortions and flexibility in packing, accommodating the various non-covalent interactions. The overall crystal structure highlights a synergistic combination of halogen bonding from both iodine and bromine donors, reflecting the importance of multi-site recognition in halogen-bonded solids.

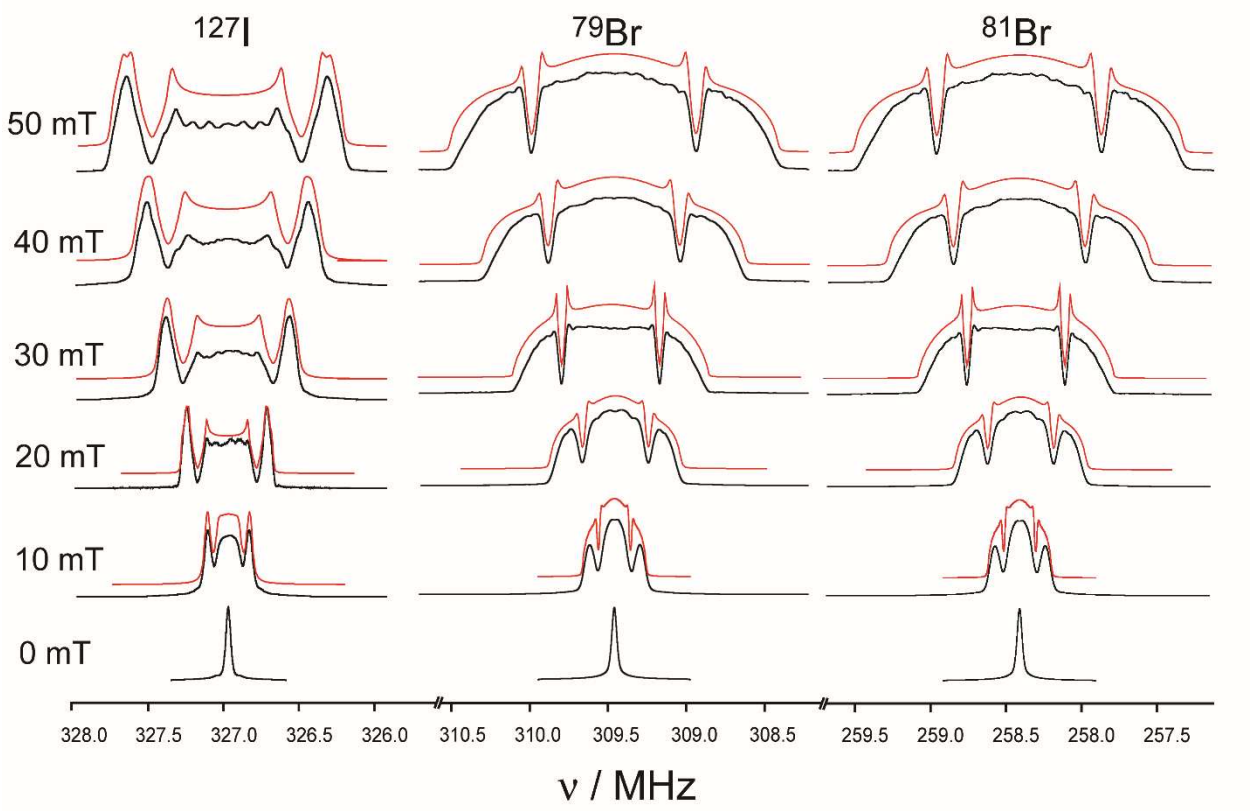


Fig. S1. Pure quadrupolar signals and Zp-QSR lines of ^{127}I in **2** (left), ^{79}Br in **1** (middle), ^{81}Br in **1** (right), as a function of the applied external magnetic field ranging from 0 mT to 50 mT. The wobbling distortions are artifacts arising from undersampling the broad QSR lines. The experimental spectra are shown in black, and the simulated spectra are shown in red. These are the same data as shown in Fig. 1, but with spectral simulations overlaid.

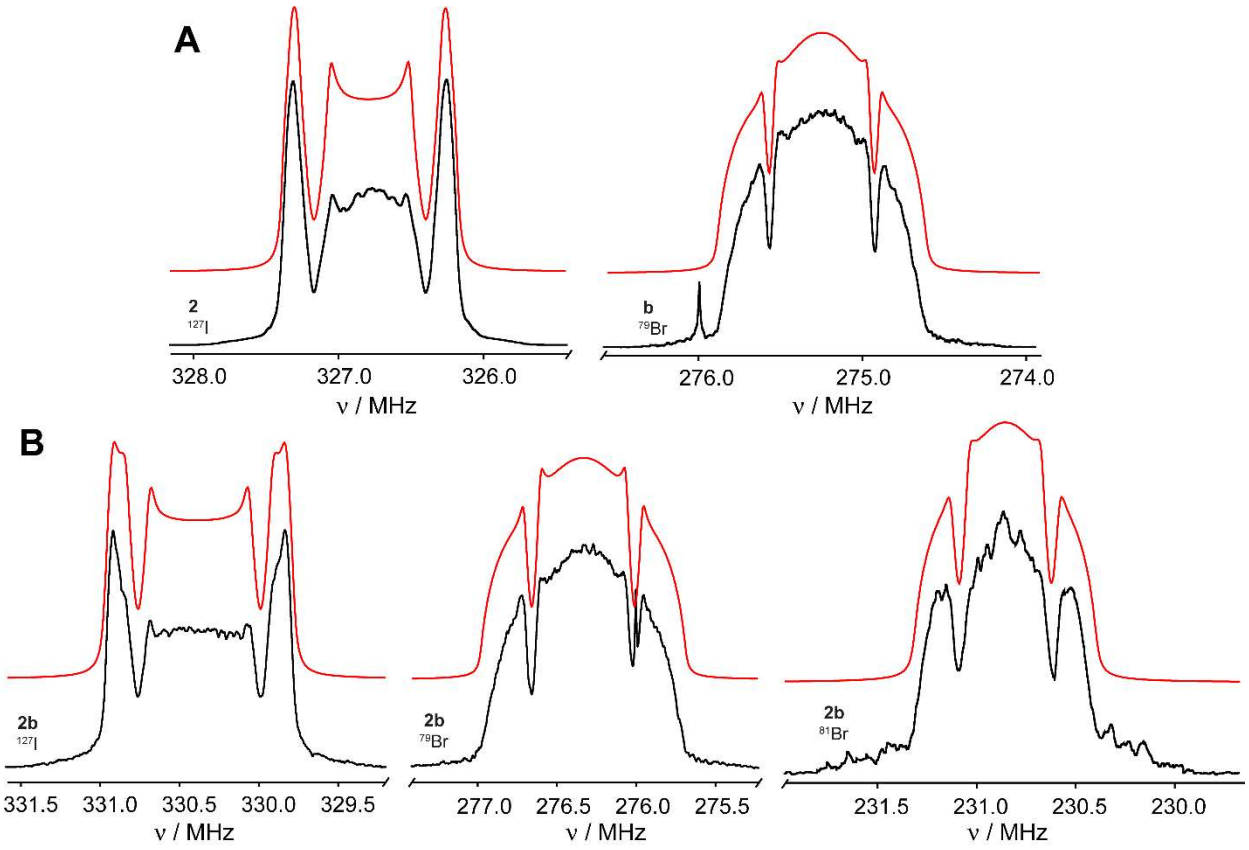


Fig. S2. (A) Zp-NQR spectra of starting materials: ^{127}I in **2** and ^{79}Br in **b**. (**B**) Zp-NQR spectra of product **2b.** Experimental spectra are in black and the QUEST-simulated fits are overlaid in red. Acquisition details are given in Table S4.

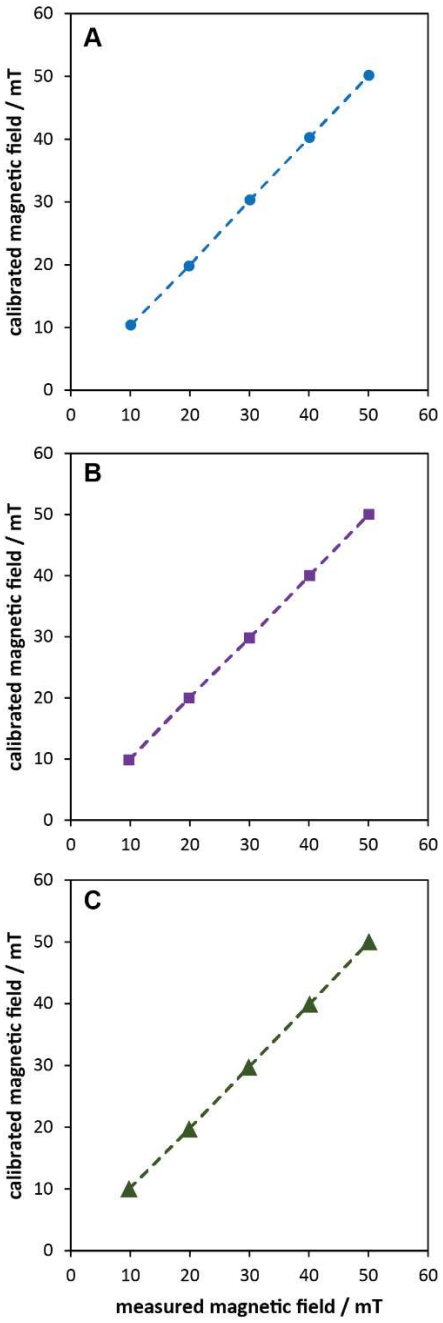


Fig. S3. (A) Calibration of the applied magnetic field B_0 for the ^{127}I nucleus. The equation for the line of best fit is: $B_{0,corr} = (1.0024 \pm 5.323 \times 10^{-3})B_{0,meas} + (-2.193 \times 10^{-1} \pm 1.775 \times 10^{-1})$; $R^2 = 0.99992$. (**B**) Calibration of the applied magnetic field B_0 using the ^{79}Br nucleus. The equation for the line of best fit is: $B_{0,corr} = (1.0042 \pm 3.408 \times 10^{-3})B_{0,meas} + (-1.043 \times 10^{-1} \pm 1.130 \times 10^{-1})$; $R^2 = 0.99997$. (**C**) Calibration of the applied magnetic field B_0 using the ^{81}Br nucleus. The equation for the line of best fit is: $B_{0,corr} = (1.0053 \pm 5.330 \times 10^{-3})B_{0,meas} + (-7.405 \times 10^{-2} \pm 1.763 \times 10^{-1})$; $R^2 = 0.99992$.

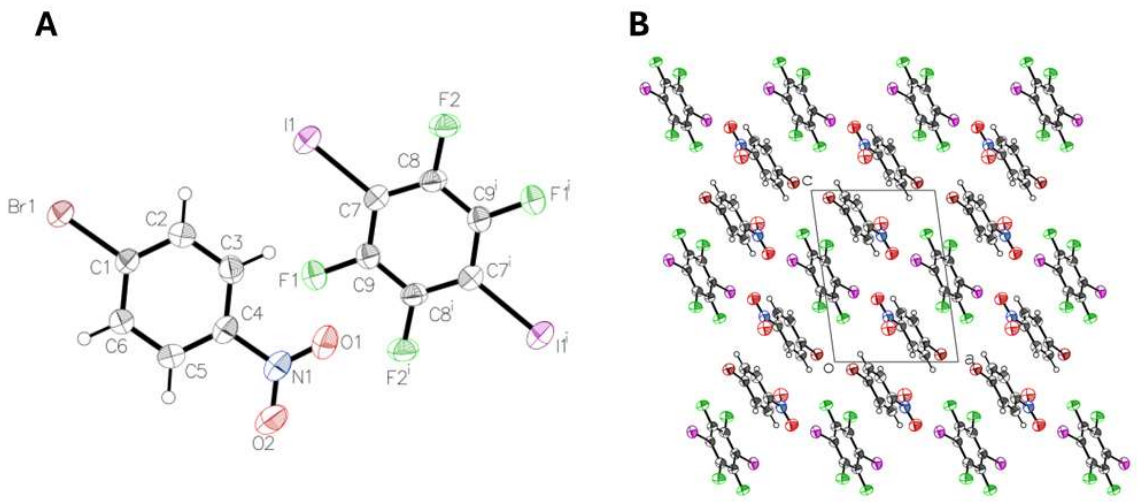


Fig. S4. (**A**) Thermal ellipsoid plot of compound **2b**, showing the atomic numbering scheme. Ellipsoids are drawn at the 50% probability level. Hydrogen atoms are depicted as spheres of arbitrary radius. Symmetry code: (i) 2 – X, 1 – Y, 1 – Z. (**B**) Crystal structure projection and molecular packing of compound **2b** viewed along the b-axis.

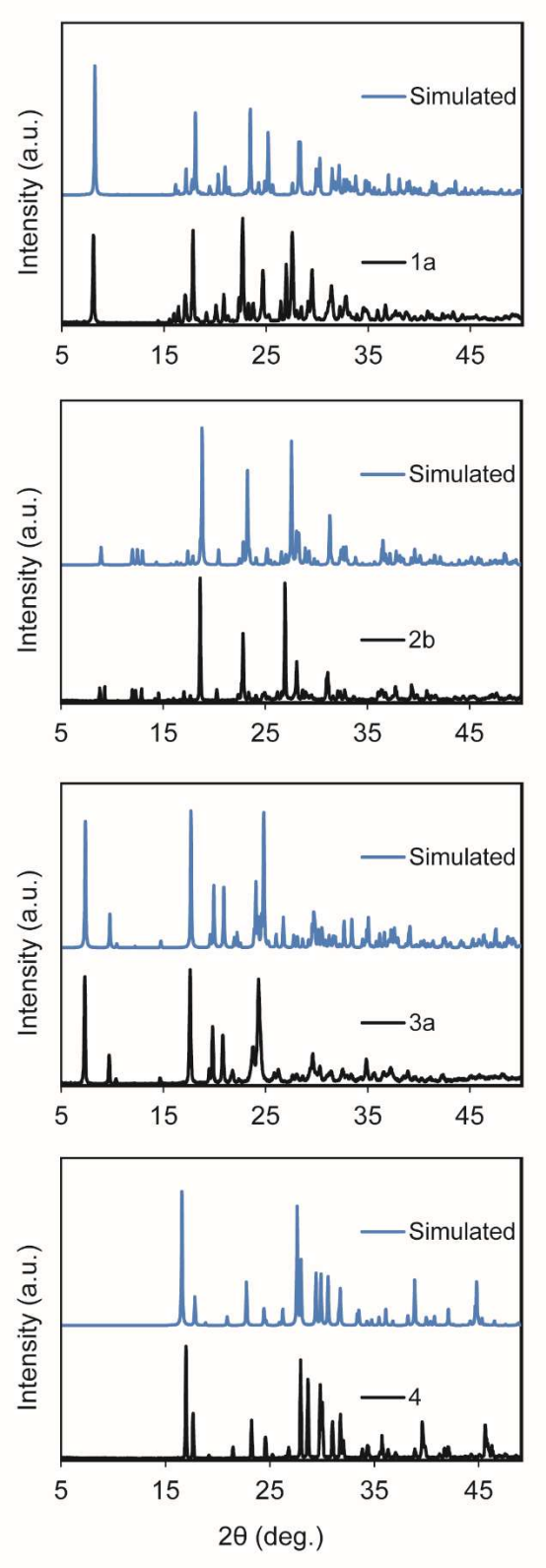


Fig. S5. Comparison of experimental (black) and simulated (blue) PXRD patterns for some compounds investigated in this study, from top to bottom: **1a**, **2b**, **3a**, and **4**.

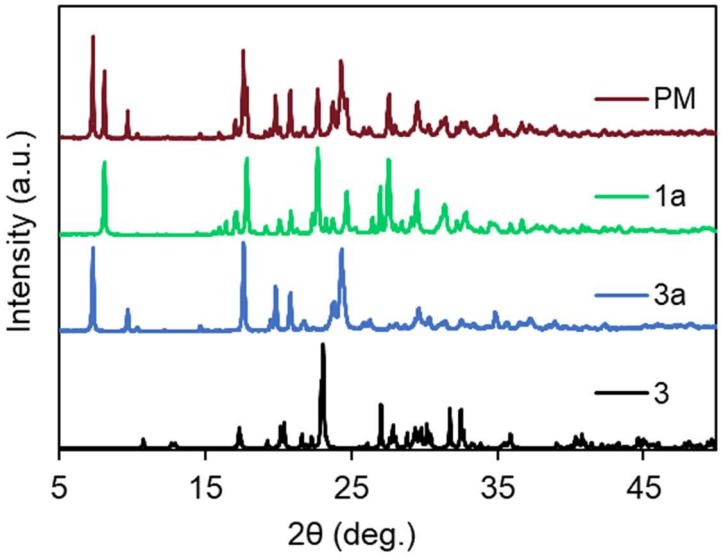


Fig. S6. Comparison of the PXRD patterns of the physical mixture (PM) with those of cocrystals **1a** and **3a**, and the starting material **3**. The PM pattern shows characteristic peaks from all three components, confirming the presence of **1a**, **3a**, and residual **3**. These phase assignments are consistent with the Zp-NQR results presented in Figure 2.

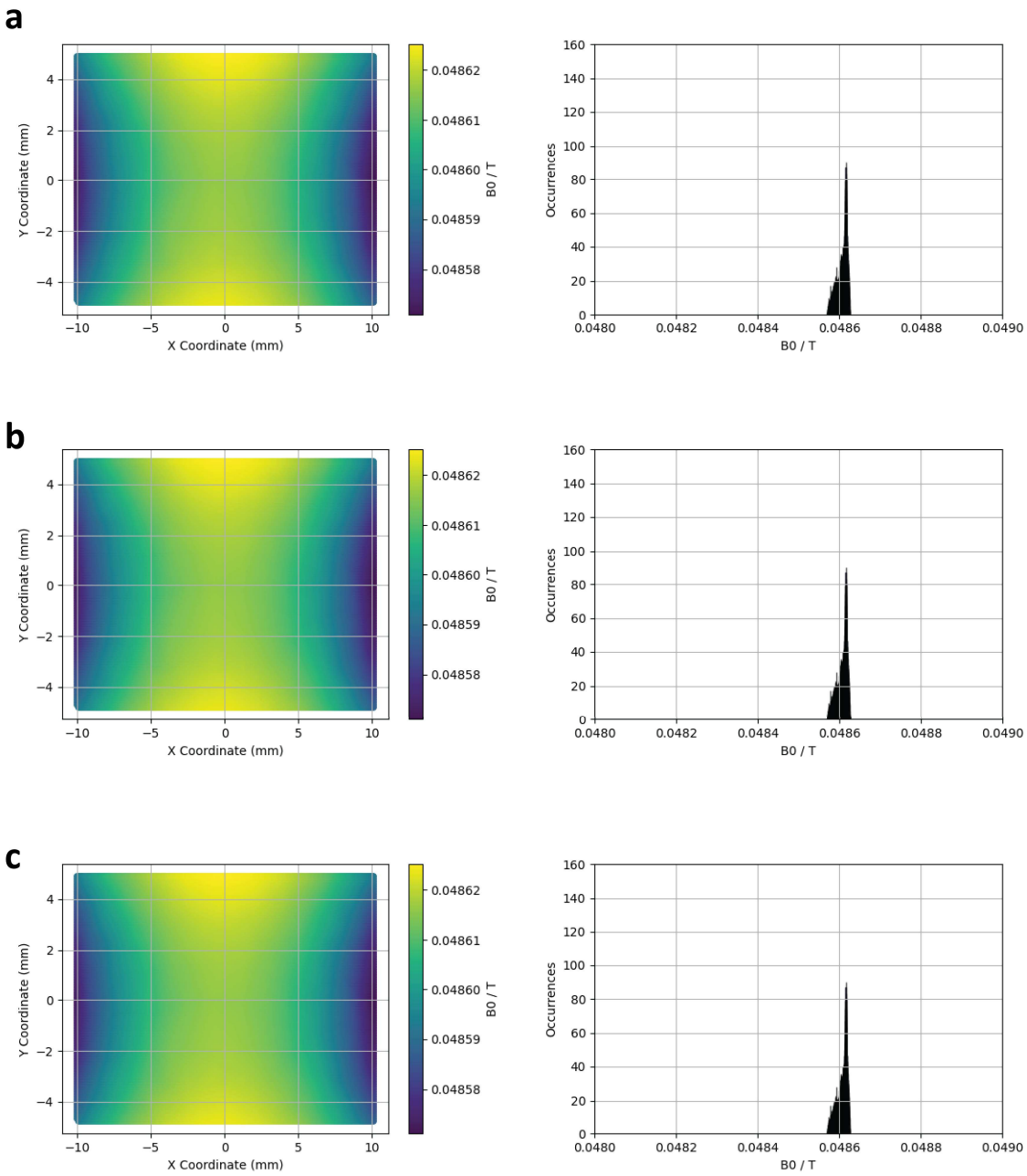


Fig. S7. Simulated magnetic field strength over the sample volume (9.64 mm diameter, 2 cm length) showing (left) the 2D plot and (right) the histogram when (a) the QSR probe is absent, (b) the QSR probe shell is present but the RF coil is absent, (c) both the QSR probe and RF coil are present. The simulation was performed with an external probe diameter of 39 mm and wall size of 1.22 mm wall size (aluminum 6061), an approximation of the RF coil (30 AWG copper cylinder of 20 mm in length, 10.64 mm outer diameter, 1 mm wall thickness), and an approximation of the EPR magnet maintaining a distance of 60 mm between the two poles. No notable differences are seen between the three plots, and the spread of B_0 values in each case is less than 0.1 mT.

Table S1. Raw and calibrated magnetic field data used in Figure 1.

Sample Information		Isotope	Zeeman Field Information					Calibrated Zeeman Field		QUEST Fitting Parameters										
Compound Label in Manuscript	Description	Isotope Under Observation	Applied magnetic field from software / G	Applied magnetic field from gaussmeter / G	Error on Field (Gauss)	Applied magnetic field from gaussmeter (in mT)	Error on Field (mT)	Calibrated Zeeman Field (mT)	Error on calibrated field (mT)	Fitted Larmor frq / MHz	Uncertainty on Larmor Frq	NQR frequency / MHz	Error on NQR frequency / MHz	Fitted CQ	Error on Fitted CQ	Fitted Eta	Error on Fitted Eta	Coil angle	LB	GB
2	p-DTFB	127I	100-102	101	1	10.1	0.1	10.42	0.10	0.08921	0.000578	326.78	± 0.03	2145.08	± 3.2	0.12	± 0.006	20	3400	2000
2	p-DTFB	127I	199-200	199	1	19.9	0.1	19.83	0.10	0.16984	0.000578	326.78	± 0.03	2145.14	± 2.4	0.12	± 0.006	12	8000	10000
2	p-DTFB	127I	301-302	301	1	30.1	0.1	30.35	0.10	0.2599	0.000578	326.78	± 0.03	2149.35	± 3.2	0.12	± 0.006	12	37000	10000
2	p-DTFB	127I	401-402	401	1	40.1	0.1	40.26	0.15	0.3448	0.001282	326.78	± 0.03	2155.2	± 3.3	0.1	± 0.006	8	40000	30000
2	p-DTFB	127I	501-502	501	1	50.1	0.1	50.18	0.15	0.4297	0.001282	326.78	± 0.03	2155.25	± 3.4	0.1	± 0.006	8	20000	30000
1	p-DBTFB	79Br	97-100	98	1	9.8	0.1	9.86	0.15	0.1055	0.001657	309.371	± 0.03	616.73	± 0.24	0.14	± 0.01	12	700	4000
1	p-DBTFB	79Br	199-200	199	1	19.9	0.1	20.02	0.15	0.2141	0.001657	309.371	± 0.03	617.26	± 0.24	0.12	± 0.01	10	9000	20000
1	p-DBTFB	79Br	300	300	1	30	0.1	29.83	0.15	0.319	0.001657	309.371	± 0.03	617.66	± 0.52	0.116	± 0.030	-5	6000	0
1	p-DBTFB	79Br	401-402	401	1	40.1	0.1	40.04	0.15	0.42819	0.001657	309.371	± 0.03	617.265	± 0.25	0.12	± 0.01	6	1100	23000
1	p-DBTFB	79Br	500-502	501	1	50.1	0.1	50.04	0.20	0.5352	0.002409	309.371	± 0.03	617.505	± 0.25	0.11	± 0.01	5	9500	22000
1	p-DBTFB	81Br	97-100	98	1	9.8	0.1	10.00	0.15	0.1153	0.001731	258.46	± 0.04	515.64	± 0.2	0.12	± 0.008	12	3000	8000
1	p-DBTFB	81Br	199-200	199	1	19.9	0.1	19.72	0.15	0.2273	0.001731	258.46	± 0.04	515.62	± 0.2	0.12	± 0.008	10	9000	5000
1	p-DBTFB	81Br	299-300	299	1	29.9	0.1	29.72	0.15	0.34268	0.001731	258.46	± 0.04	515.7	± 0.21	0.12	± 0.008	8	1000	15000
1	p-DBTFB	81Br	401-402	401	1	40.1	0.1	39.90	0.15	0.46	0.001731	258.46	± 0.04	515.695	± 0.21	0.12	± 0.008	2	6000	20000
1	p-DBTFB	81Br	500-502	501	1	50.1	0.1	50.04	0.15	0.5769	0.001731	258.46	± 0.04	515.885	± 0.22	0.11	± 0.008	2	5000	30000

Table S2. QSR spectral fitting parameters for 3a, 1a, and 2b acquired in a magnetic field of B_0 = 30.0 ± 0.1 mT.[a]

QSR Frequency (ν_Q) / MHz	C_Q / MHz	η	Larmor Frequency (ν_L) / MHz	Experimental Gyromagnetic ratio / MHz T^{-1}	Isotopic identity & Assignment
320.70 ± 0.02	2125.6 ± 2.1	0.074 ± 0.004	0.258 ± 0.001	8.61 ± 0.04[b] 8.63 ± 0.04[c]	^{127}I (**3a**)
334.45 ± 0.02	2214.2 ± 1.6	0.080 ± 0.004	0.257 ± 0.001	8.58 ± 0.04 8.60 ± 0.04	^{127}I (**3a**)
339.13 ± 0.02	2253.3 ± 1.1	0.056 ± 0.004	0.259 ± 0.001	8.61 ± 0.04 8.63 ± 0.04	^{127}I (**3a**)
316.62 ± 0.002	629.8 ± 0.3	0.180 ± 0.008	0.318 ± 0.002	10.70 ± 0.07 10.75 ± 0.07	^{79}Br (**1a**)
320.046 ± 0.002	638.0 ± 0.3	0.140 ± 0.008	0.321 ± 0.002	10.71 ± 0.07 10.75 ± 0.07	^{79}Br (**1a**)
276.34 ± 0.02	550.7 ± 0.3	0.148 ± 0.008	0.321 ± 0.002	10.71 ± 0.07 10.75 ± 0.07	^{79}Br (**2b**)
330.38 ± 0.02	2190.8 ± 1.9	0.070 ± 0.006	0.259 ± 0.001	8.61 ± 0.04 8.63 ± 0.04	^{127}I (**2b**)

a. Spectral fits were performed using exact theory using QUEST.
b. The first row of data result from fitting to raw data.
c. The second row of data are the results after correction to B_0 using known gyromagnetic ratios.

Table S3. Description of the QSR coils used in this work, including the approximate amount of sample used in each experiment.

Coil #	Length	Outer diameter	# turns	Wire size	Upper frequency[a]	Lower frequency[a]	Sample amount (mg)
Coil 1	10 mm	8 mm	4 turns	1.72 mm (flat ribbon)	214 ± 5 MHz	380 ± 5 MHz	300-400
Coil 2	17.4 mm	9.65 mm	9 turns	20 AWG (round wire)	167 ± 5 MHz	100 ± 5 MHz	700-800
Coil 3	20 mm	9.65 mm	21 turns	20 AWG (round wire)	91 ± 5 MHz	56 ± 5 MHz	700-800
Coil 4	26 mm	9 mm	39 turns	24 AWG (round wire)	50 ± 5 MHz	28 ± 3 MHz	700-800

[a] The uncertainties consider the possibility of adjusting the frequency ranges by slightly compressing or stretching the coil.

Table S4. Experimental Zp-QSR parameters for each isotope in the compounds studied in this work.

Compound	Isotope - site - transition	ν_Q / MHz	B_0 / mT	subspectra / #	Number of scans per transmitter offset	Expt. coil angle / °	breadth /kHz	π/2 pulse / μs	total expt time [a] / min
2	^{127}I [b]	326.80 ± 0.03	10.1 ± 0.1	13	256	0	535 ±41	5.6	25
	^{127}I	326.80 ± 0.03	20.0 ± 0.1	19	256	0	857±52	4.0	40
	^{127}I	326.80 ± 0.03	30.1 ± 0.1	29	256	0	1496 ±72	5.6	60
	^{127}I	326.80 ± 0.03	40.1 ± 0.1	36	256	0	1874 ±76	5.6	90
	^{127}I	326.80 ± 0.03	50.1 ± 0.1	31[c]	256	0	2193 ±74	3.0	80
1	^{79}Br	309.32 ± 0.03	9.9 ± 0.1	13	256	0	523 ±35	5.4	25
	^{79}Br	309.32 ± 0.03	19.9 ± 0.1	19	256	0	883 ±51	5.4	40
	^{79}Br	309.32 ± 0.03	30.1 ± 0.1	26	128	0	1318 ±33	6.0	40
	^{79}Br	309.32 ± 0.03	40.1 ± 0.1	36	256	0	1807 ±44	5.6	90
	^{79}Br	309.32 ± 0.03	50.1 ± 0.1	44	256	0	2223 ±46	5.6	100
1	^{81}Br	258.46 ± 0.04	9.9 ± 0.1	12	256	0	614 ±37	5.4	20
	^{81}Br	258.46 ± 0.04	19.9 ± 0.1	20	256	0	983 ±38	5.6	40
	^{81}Br	258.46 ± 0.04	29.9 ± 0.1	29	128	0	1415 ±30	5..6	45
	^{81}Br	258.46 ± 0.04	40.1 ± 0.1	37	256	0	1912 ±46	5.6	85
	^{81}Br	258.46 ± 0.04	50.1 ± 0.1	47	256	0	2364 ±50	5.4	110
1a	^{79}Br (S1)	316.62 ± 0.002	29.8 ± 0.1	27	256	0	1445 ±42	8	45
	^{79}Br (S2)	320.046 ± 0.002	30.0 ± 0.1	28	256	0	1462 ±35	7.4	45
3a	^{127}I (S1)	320.70 ± 0.02	30.0 ± 0.1	28	512	0	1482 ±38	5.6	95
	^{127}I (S2)	334.45 ± 0.02	29.9 ± 0.1	30	512	0	1660 ±46	6.6	105
	^{127}I (S3)	339.13 ± 0.02	30.1 ± 0.1	29	256	0	1546 ±40	6.4	60
3	^{127}I (S1)	315.97 ± 0.03	30.1 ± 0.1	27	256	0	1357 ±32	6.6	60

	^{127}I (S2)	322.75 ± 0.03	30.1 ± 0.1	27	256	0	1292 ±40	5.6	60
	^{127}I (S3)	325.66 ± 0.03	29.8 ± 0.1	27	256	0	1324 ±34	6.6	60
2b	^{79}Br	276.34 ± 0.02	30.0 ±0.1	27	256	0	1380 ±32	6.6	60
	^{81}Br	230.86 ± 0.02	19.9 ±0.1	19	512	0	1007 ±38	6.4	70
	^{127}I	330.38 ± 0.02	30.1 ±0.1	27	256	0	1407 ±46	6.8	60
b	^{79}Br	275.29 ± 0.02	30.0 ±0.1	27	256	0	1332 ±32	6.6	60
4	^{79}Br (site 2)	169.47 ± 0.02	20.3 ± 0.1	19	128	0	9628 ±42	7.1	30
	^{79}Br (site 1)	162.77 ± 0.02	20.2 ± 0.1	19	128	0	9652 ±40	7.1	30
	^{81}Br (site 2)	141.57 ± 0.02	20.2 ± 0.1	20	128	0	998 ± 30	6.2	30
	^{81}Br (site 1)	135.97 ± 0.02	20.1 ± 0.1	30	128	0	1054 ±35	5.6	30
	^{121}Sb (3/2 ↔ 5/2)	93.21 ± 0.02	20.1 ± 0.1	13	256	90	575 ± 38	6.6	30
	^{123}Sb (5/2 ↔ 7/2)	85.05 ± 0.02	19.9 ± 0.1	7	256	90	301 ± 18	7.3	20
	^{123}Sb (3/2 ↔ 5/2)	56.17 ± 0.02	20.5± 0.1	9	256	90	318 ± 20	4.8	25
	^{121}Sb (1/2 ↔ 3/2)	47.92 ± 0.02	20.2 ± 0.1	22	512	0	1118 ± 35	4.3	80
	^{123}Sb (1/2 ↔ 3/2)	30.54 ± 0.02	21.0 ± 0.1	9	1024	-5	472 ± 32	4.8	60

a: The total experiment time is approximate (± a few minutes) and does not include time spent on parameter optimization.

b: For the ^{127}I isotope, the (1/2↔3/2) transition was acquired in this study.

c: For the ^{127}I isotope at 50 mT, the frequency step increment was 70 kHz; for all other measurements, a 50 kHz step was used.

Table S5. QUEST simulation parameters for the isotopes studied in this work.

Compound/ CSD refcode	Isotope - site - transition	Larmor frq /MHz	C_Q /MHz	η	Coil angle/°	LB[a] /kHz	GB[b] /kHz
p-DITFB (***2***) / ZZZAVM02 (*1*)	^{127}I	0.08921 ± 0.001	2145.08 ± 3.2	0.12 ± 0.006	20	34	2
	^{127}I	0.16984 ± 0.002	2145.14 ± 2.4	0.12 ± 0.006	12	8	10
	^{127}I	0.2599 ± 0.002	2149.35 ± 3.2	0.112 ± 0.006	12	37	10
	^{127}I	0.3448 ± 0.002	2155.2 ±3.3	0.1 ± 0.006	8	40	30
	^{127}I	0.4297 ± 0.002	2155.25 ±3.4	0.1 ± 0.006	8	20	30
p-DBTFB (**1**) / ZZZAVJ01 (*2*)	^{79}Br	0.1055 ± 0.002	616.73 ±0.24	0.14 ± 0.01	12	7	4
	^{79}Br	0.2141 ± 0.002	617.26 ±0.24	0.12 ± 0.01	10	9	20
	^{79}Br	0.319 ± 0.002	617.66 ± 0.52	0.105 ± 0.030	-5	6	0
	^{79}Br	0.42819 ± 0.002	617.265 ±0.25	0.12 ± 0.01	6	11	23
	^{79}Br	0.5352 ± 0.002	617.505 ±0.25	0.11 ± 0.01	5	9.5	22
p-DBTFB (**1**) / ZZZAVJ01 (*2*)	^{81}Br	0.1153 ± 0.002	515.64 ±0.2	0.12 ± 0.008	12	3	8
	^{81}Br	0.2273 ± 0.002	515.62 ±0.2	0.12 ± 0.008	10	9	5
	^{81}Br	0.34268 ± 0.002	515.7 ±0.21	0.12 ± 0.008	8	1	15
	^{81}Br	0.4601 ± 0.002	515.695 ±0.21	0.12 ± 0.008	2	6	20
	^{81}Br	0.5769 ± 0.002	515.865 ±0.22	0.11 ± 0.008	2	5	30
1a / IKUJUT(*3*)	^{79}Br (S1)	0.318 ± 0.002	629.8 ± 0.3	0.180 ± 0.008	5	100	20
	^{79}Br (S2)	0.321 ± 0.002	638.0 ± 0.3	0.140 ± 0.008	4	58	20
3a / WEXWEC(*4*)	^{127}I (S1)	0.258 ± 0.001	2125.6 ± 2.1	0.074 ± 0.004	8	108	20
	^{127}I (S2)	0.257 ± 0.001	2214.2 ± 1.6	0.080 ± 0.004	6	160	20
	^{127}I (S3)	0.259 ± 0.001	2253.3 ± 1.1	0.056 ± 0.004	8	100	20

sym-TFTIB (**3**) / UCEPEY(*5*)	^{127}I (S1)	0.2616 ± 0.001	2077.25 ± 1.49	0.114 ± 0.008	0	14	2
	^{127}I (S2)	0.26076 ± 0.001	2135.30 ± 1.6	0.084 ± 0.004	14	20	10
	^{127}I (S3)	0.2548 ± 0.002	2150.48 ± 1.31	0.094 ± 0.004	5	39	2
2b / This work	^{79}Br	0.321 ± 0.002	550.7 ± 0.3	0.148 ± 0.008	4	24	10
	^{81}Br	0.231 ± 0.002	459.9 ± 0.7	0.154 ± 0.008	8	32	10
	^{127}I	0.259 ± 0.001	2190.8 ± 1.9	0.070 ± 0.006	10	35	10
b / ULEBOD(*6*)	^{79}Br	0.321 ± 0.002	549.47 ± 0.2	0.108 ± 0.08	4	30	10
4 (*7*)	^{79}Br (site 2)	0.214 ± 0.001	335.47 ± 0.027	0.25 ± 0.01	6	49	2
	^{79}Br (site 1)	0.219 ± 0.001	324.19 ± 0.18	0.16 ± 0.01	6	20	2
	^{81}Br (site 2)	0.234 ± 0.001	280.47 ± 0.22	0.24 ± 0.01	8	34	2
	^{81}Br (site 1)	0.234 ± 0.001	270.96 ± 0.16	0.15 ± 0.01	4	33	2
	^{121}Sb (3/2 ↔ 5/2)	0.207 ± 0.002	311.95 ± 0.89	0.14 ± 0.01	80	70	2
	^{123}Sb (5/2 ↔ 7/2)	0.110 ± 0.001	397.81 ± 3.1	0.15 ± 0.01	80	44	2
	^{123}Sb (3/2 ↔ 5/2)	0.111 ± 0.001	397.96 ± 3.2	0.15 ± 0.01	83	40	0
	^{121}Sb (1/2 ↔ 3/2)	0.209 ± 0.001	312.74 ± 0.86	0.14 ± 0.01	9	17	10
	^{123}Sb (1/2 ↔ 3/2)	0.117 ± 0.001	400.4 ± 3.1	0.14 ± 0.01	4	20	20

a: Gaussian line broadening
b: Lorentzian line broadening

Table S6. Crystal data and structure refinement for 2b.

Compound	**2b**
Empirical formula	$C_{18}H_8Br_2F_4I_2N_2O_4$
Formula weight	805.88
Temperature [K]	150
Crystal system	triclinic
Space group (number)	$P\overline{1}$ (2)
a [Å]	7.2254(5)
b [Å]	7.7123(5)
c [Å]	10.2903(7)
α [°]	103.904(3)
β [°]	95.483(3)
γ [°]	98.358(2)
Volume [Å^3]	545.60(6)
Z	1
ρ_{calc} [gcm^{-3}]	2.453
μ [mm^{-1}]	18.893
F(000)	374
Crystal size [mm^3]	0.04×0.13×0.26
Crystal colour	clear light colourless
Crystal shape	plate
Radiation	Ga K_α (λ=1.34139 Å)
2θ range [°]	10.87 to 126.95 (0.75 Å)
Index ranges	$-9 \le h \le 9$ $-10 \le k \le 10$ $-13 \le l \le 13$
Reflections collected	21727
Independent reflections	2691 R_{int} = 0.0430 R_{sigma} = 0.0297
Completeness to θ = 53.594°	99.4
Data / Restraints / Parameters	2691 / 0 / 145
Goodness-of-fit on F^2	1.138
Final *R* indexes	R_1 = 0.0281
[$I \ge 2\sigma(I)$]	wR_2 = 0.0806
Final *R* indexes	R_1 = 0.0284
[all data]	wR_2 = 0.0810
Largest peak/hole [eÅ^{-3}]	1.46/−0.62

References

1. Oh, S. Y.; Nickels, C. W.; Garcia, F.; Jones, W.; Friščić, T. Switching Between Halogen- and Hydrogen-Bonding in Stoichiometric Variations of A Cocrystal Of A Phosphine Oxide. *CrystEngComm* **2012**, *14*, 6110–6114. https://doi.org/10.1039/C2CE25653C
2. d'Agostino, S.; Spinelli, F.; Taddei, P.; Ventura, B.; Grepioni, F. Ultralong Organic Phosphorescence in the Solid State: The Case of Triphenylene Cocrystals with Halo- and Dihalo-penta/tetrafluorobenzene. *Cryst. Growth Des.* **2019**, *19*, 336–346. https://doi.org/10.1021/acs.cgd.8b01443
3. De Santis, A.; Forni, A.; Liantonio, R.; Metrangolo, P.; Pilati, T.; Resnati, G. N···Br Halogen Bonding: One-Dimensional Infinite Chains through the Self-Assembly of Dibromotetrafluorobenzenes with Dipyridyl Derivatives. *Chem. Eur. J.* **2003**, *9*, 3974–3983. https://doi.org/10.1002/chem.200204655
4. Lucassen, A. C. B.; Karton, A.; Leitus, G.; Shimon, L. J. W.; Martin, J. M. L; van der Boom, M. E. Co-Crystallization of Sym-Triiodo-Trifluorobenzene with Bipyridyl Donors: Consistent Formation of Two Instead of Anticipated Three N···I Halogen Bonds. *Cryst. Growth Des.* **2007**, *7*, 386–392. https://doi.org/10.1021/cg0607250
5. Reddy, C. M.; Kirchner, M. T.; Gundakaram, R. C.; Padmanabhan, K. A.; Desiraju, G. R. Isostructurality, Polymorphism and Mechanical Properties of Some Hexahalogenated Benzenes: The Nature of Halogen···Halogen Interactions. *Chem. Eur. J.* **2006**, *12*, 2222–2234. https://doi.org/10.1002/chem.200500983
6. Ali, Q.; Raza Shah, M.; Ng, S. W. 4-Bromo-1-nitrobenzene. *Acta Crystallogr. Sect. E.* **2011**, *67*, o548. https://doi.org/10.1107/S1600536811003394
7. Cushen, D. W.; Hulme, R. 427. The Crystal And Molecular Structure Of Antimony Tribromide: β-Antimony Tribromide. *J. Chem. Soc.* **1962**, 2218–2222. https://doi.org/10.1039/JR9620002218

II.2 Supporting Information for Chapter 6

1. Notes on our Implementation of Zp-NQR Spectroscopy

Early Zp-NQR experiments relied on rudimentary equipment, such as low-precision Helmholtz coils, to generate weak static magnetic fields (below 10 mT), which were inadequate for fully resolving the inner and outer shoulders of Zp-NQR spectra. Since the positions and shapes of these peaks are critical for determining η, these limitations introduced significant uncertainties in quadrupolar parameter estimation. Additionally, the absence of advanced spectral simulation methods required reliance on outdated approaches, such as assigning peak frequencies and using formulas limited to η values below 0.4, often constrained by first-order quadrupolar approximations. Our work addresses these limitations by introducing a modern Zp-NQR setup featuring a versatile EPR electromagnet capable of generating homogeneous, adjustable magnetic fields. We found that moderate fields, up to 50 mT, are necessary to achieve high resolution, well-resolved spectra suitable for spectral simulation and fitting, depending on the quadrupolar nucleus and interaction strength. This setup provides precise field control, significantly enhancing SNR and spectral resolution, enabling the assignment and differentiation of nuclei in distinct crystallographic sites. By leveraging exact Hamiltonian diagonalization, we eliminate reliance on first-order approximations, ensuring robust and reliable spectral analysis while removing the limitation of η values being restricted to below 0.4. These advancements allow for the clear resolution of inner and outer spectral shoulders, facilitating the accurate quantification of halogen bonding strengths in diverse chemical environments. Further technical details will be described in a forthcoming publication.

2. Powder X-ray Diffraction

Powder X-ray diffraction (PXRD) data were obtained using a Bruker D8 Endeavor instrument equipped with a 1 kW Cu Kα radiation source (λ = 1.54056 Å) from a sealed tube and a high-speed LynxEye XE-T detector. Measurements were performed at room temperature, with samples placed in a well plate and rotated at 15 RPM during data acquisition.

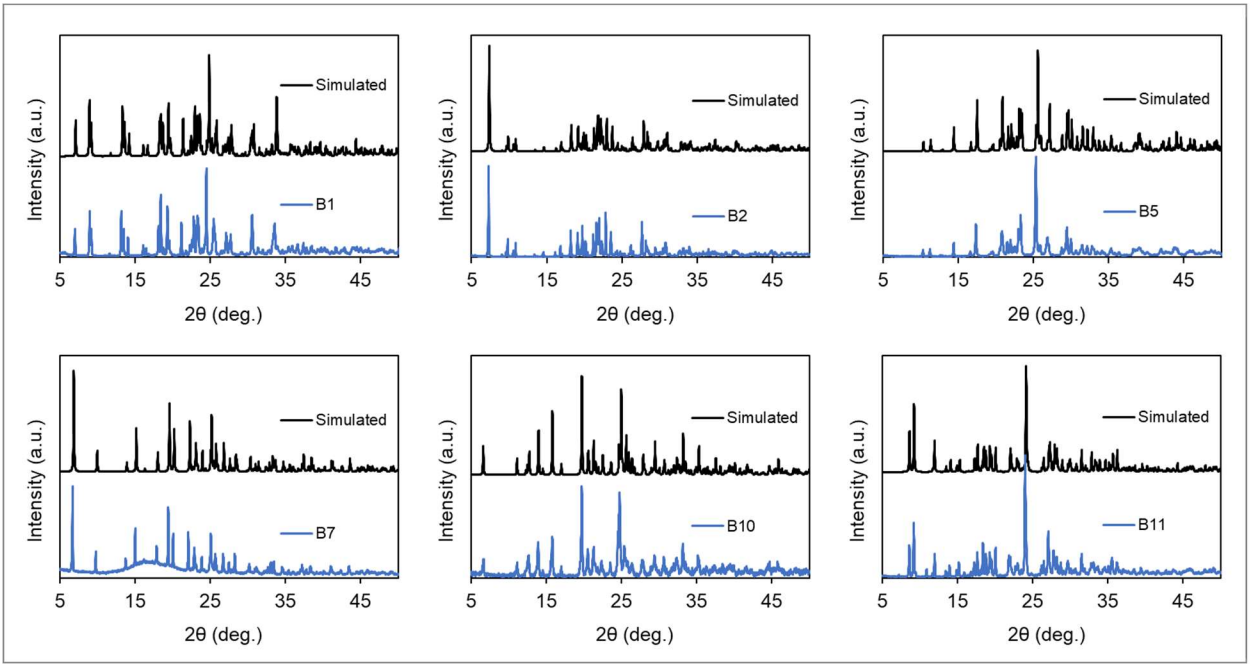


Figure S1. Comparison of experimental (blue) and simulated (black) PXRD patterns for the **B** series of cocrystals.

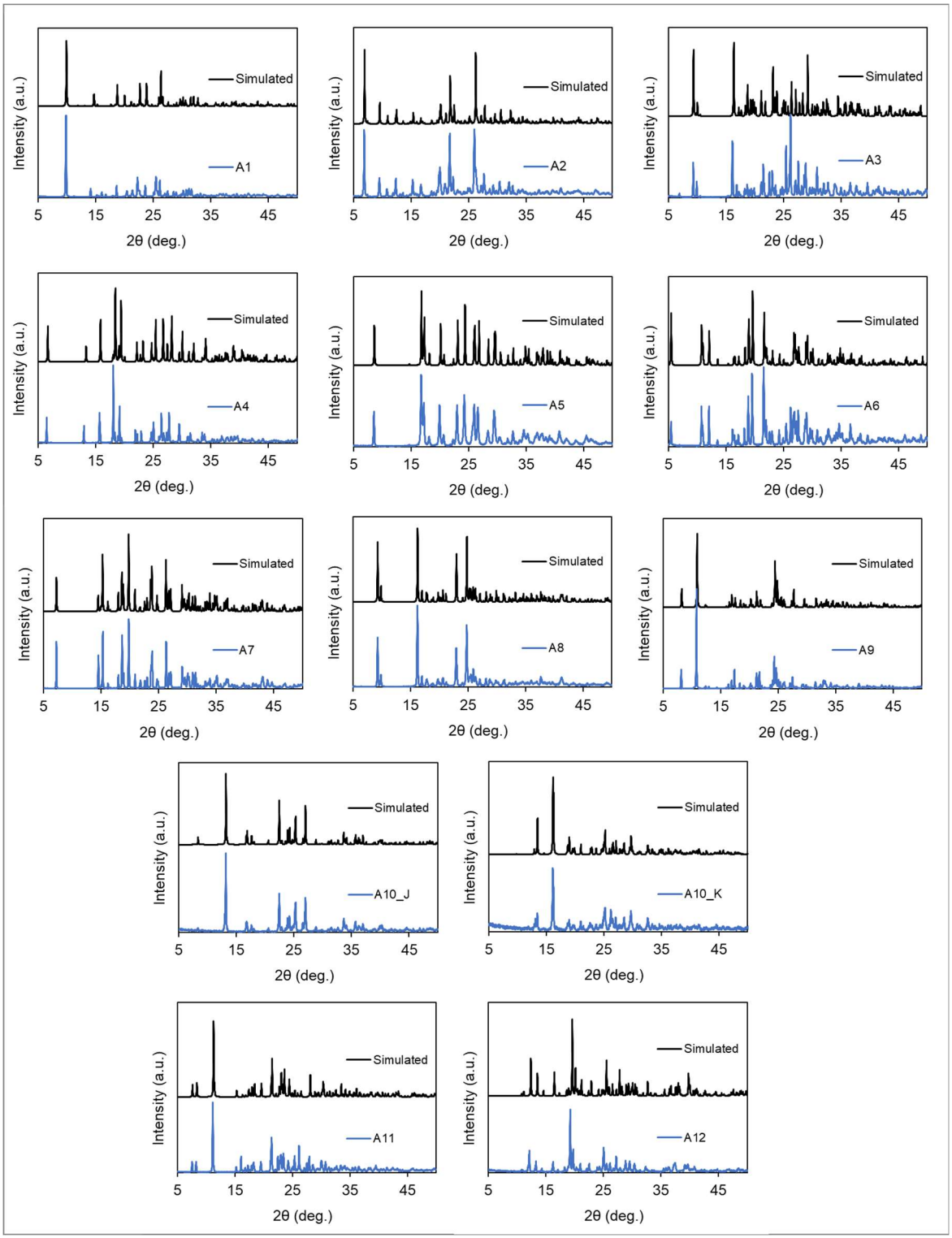


Figure S2. Comparison of experimental (blue) and simulated (black) PXRD patterns for the **A** series of cocrystals. Cocrystal **A10** has two polymorphs, with CSD refcodes JAQMAQ and KIHRAX, labeled as **A10-J** and **A10-K**, respectively.

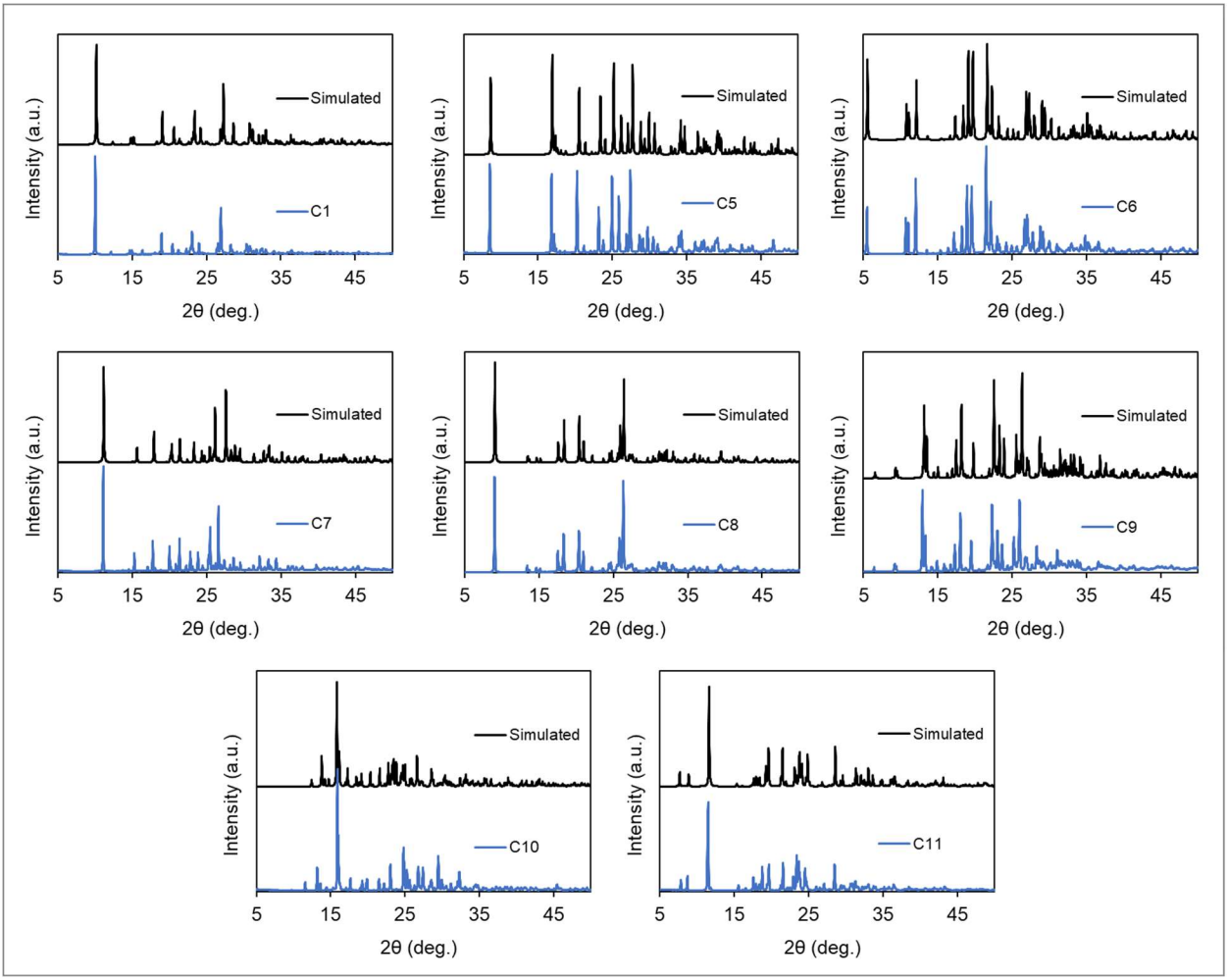


Figure S3. Comparison of experimental (blue) and simulated (black) PXRD patterns for the **C** series of cocrystals.

3. Zp-NQR Spectra

Overall uncertainties are estimated at less than 0.01% for C_Q and less than 5% for η (Table 2). This uncertainty is lower than that observed for η values determined by acquiring both NQR transition frequencies and using conversion tables.

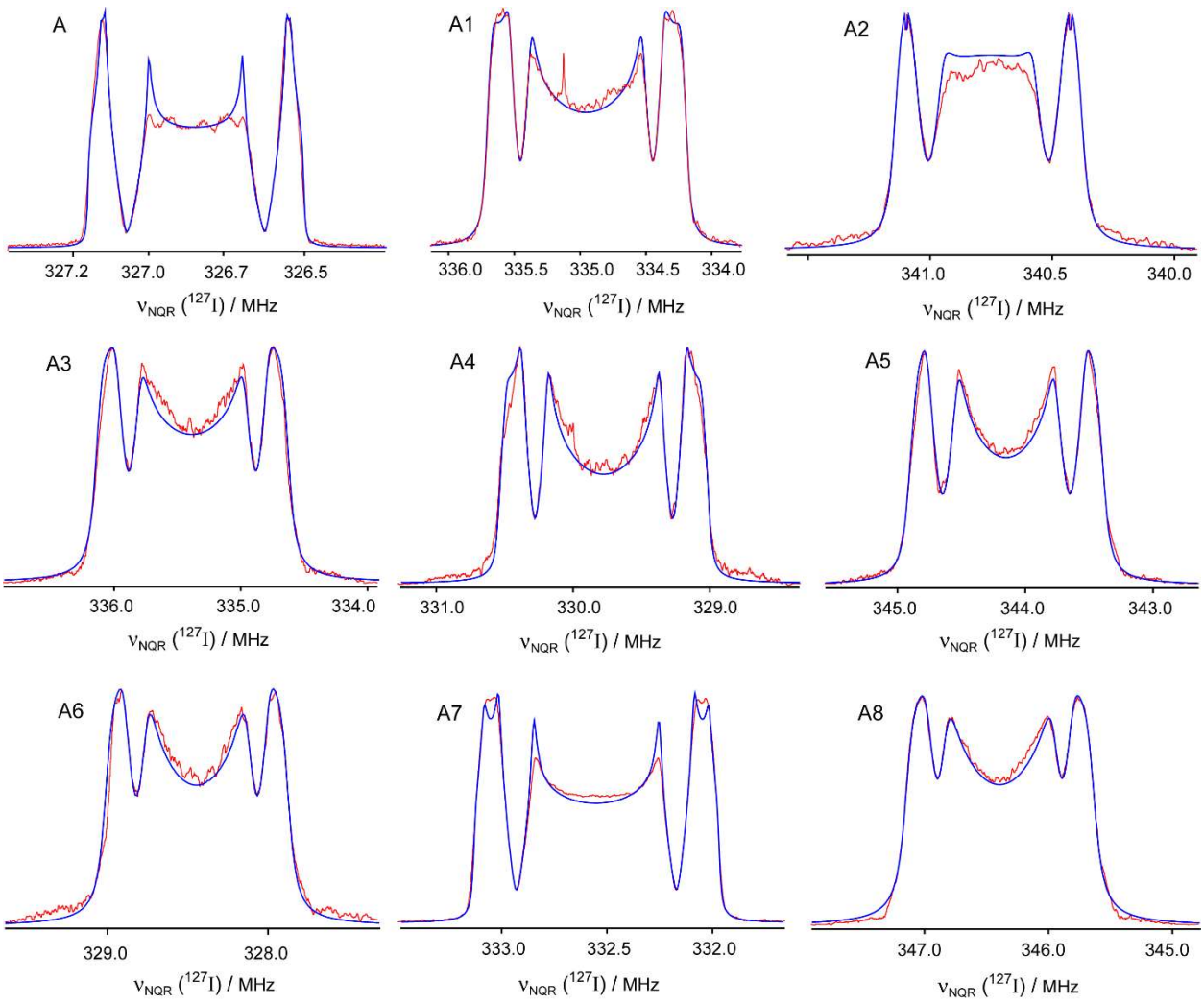


Figure S4. Experimental (in red) and best-fit simulated (in blue) Zp-NQR spectra for **A** (the XB donor) and its cocrystals, **A1** to **A8.** The experimental setup parameters and simulation parameters for QUEST are detailed in Table S1.

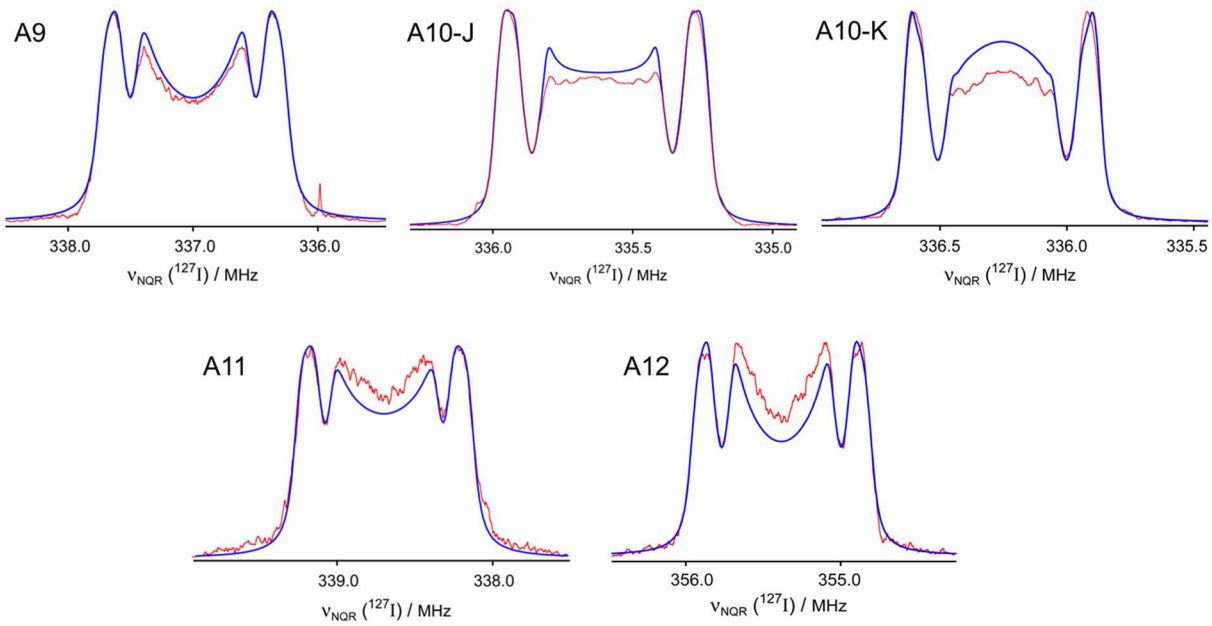


Figure S5. Experimental (in red) and best-fit simulated (in blue) Zp-NQR spectra for cocrystals **A9** to **A12**. Cocrystal **A10** has two polymorphs, with CSD refcodes JAQMAQ and KIHRAX, labeled as **A10-J** and **A10-K**, respectively. Details of the experimental setup and simulation parameters for QUEST can be found in Table S1.

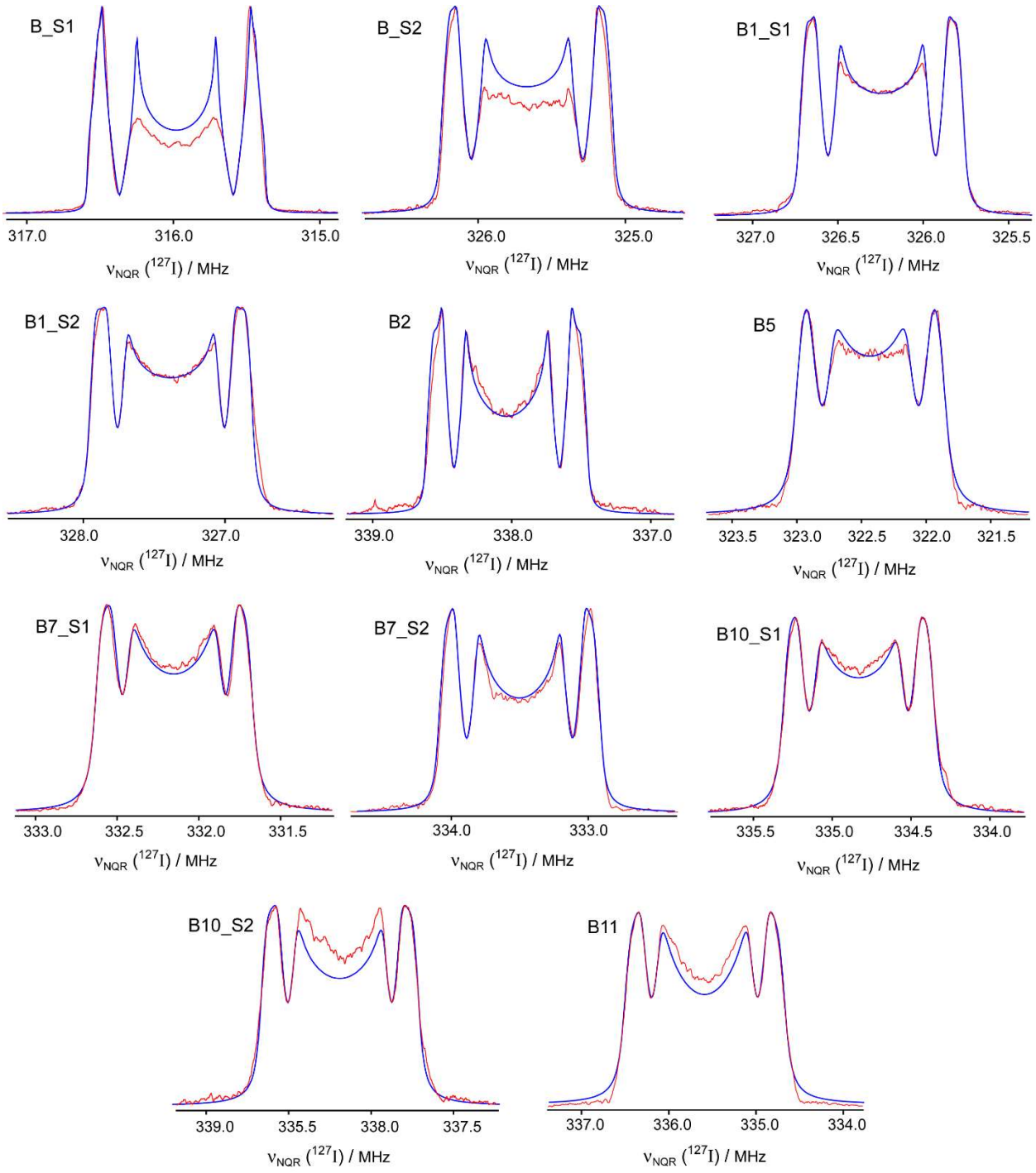


Figure S6. Experimental (in red) and best-fit simulated (in blue) Zp-NQR spectra for **B** (the XB donor) and its cocrystals. The Zp-NQR spectra for iodine sites 1 and 2 are labeled as S1 and S2, respectively. Detailed experimental setup parameters and simulation parameters for QUEST are provided in Table S1.

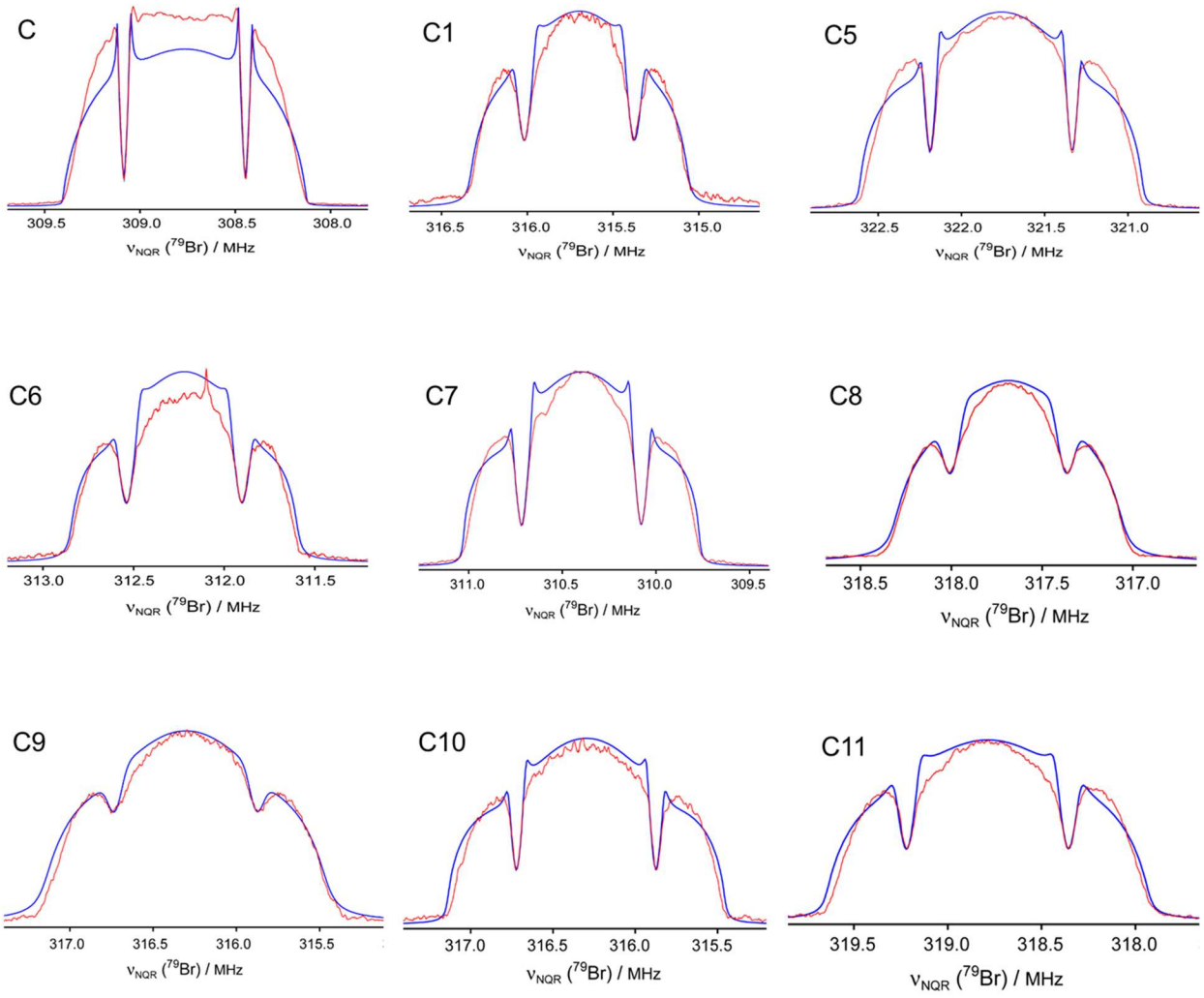


Figure S7. Experimental (in red) and best-fit simulated (in blue) Zp-NQR spectra for **C** (the XB donor) and its cocrystals. Detailed experimental setup parameters and simulation parameters for QUEST are provided in Table S1.

Table S1. ^{127}I NQR frequencies of **A**, **B**, and their XB cocrystals. The table details the number of distinct crystallographic iodine sites, their short contact types studied herein, and all measured NQR frequencies for the iodine sites.

CSD Ref.	Number of crystallographic sites	Site ID	I···O/N short contact	ν_{NQR}
A: ZZZAVM02 [1]	1	_	_	326.80 ± 0.03
A1: FAPKOA [2]	2	1	I···O	335.80 ± 0.03
		2	I···O/C	[a]
A2: JUZRUT [3]	4	1	I···O	347.23 ± 0.03
		2	_	340.75 ± 0.03
		3	_	337.45 ± 0.03
		4	_	336.88 ± 0.03
A3: AXOJUV [4]	1	1	I···N	335.42 ± 0.02
A4: BIYGIB [5]	1	1	I···O	329.79 ± 0.03
A5: DIVCUH [6]	1	1	I···N	344.18 ± 0.03
A6: LICBIK [1]	1	1	I···C	328.46 ± 0.02
A7: ISIJEZ [7]	1	1	I···N	332.63 ± 0.02
A8: MEKWOO[8]	1	1	I···N	346.21 ± 0.02
A9: VOMHAH [6]	1	1	I···N	336.98 ± 0.02
A10-J: JAQMAQ [7]	1	1	I···N	335.56 ± 0.03
A10-K: KIHRAX [9]	1	1	I···N	336.26 ± 0.03
A11: VOMHIP [10]	1	1	I···N	338.70 ± 0.03
A12: RUYHID [11]	1	1	I···N	355.33 ± 0.03
B: UCEPEY [12]	3	1	_	315.97 ± 0.03
		2	_	325.66 ± 0.03
		3	_	322.75 ± 0.03
B1: FAPKUG[2]	3	1	I···O	326.20 ± 0.03
		2	I···O	327.41 ± 0.03
		3	I···C/O [b]	330.54 ± 0.03
B2: JUZRON [3]	3	1	I···O	338.02 ± 0.03
		2	I···O/H [b]	332.20 ± 0.03
		3	_	314.17 ± 0.03
B5: ODEGAJ [13]	3	1	I···N/C/H/I [b]	322.42 ± 0.03
		2	_	324.78 ± 0.03
		3	_	[c]
B7: KIHREB [9]	3	1	I···N	332.63 ± 0.03
		2	I···N	333.50 ± 0.03
		3	_	318.39 ± 0.03
B10: SAJCUE [14]	3	1	I···N	334.58 ± 0.02
		2	I···N	338.22 ± 0.02

		3	_	320.02 ± 0.02
B11: SAJDAL [14]	3	1	I···N	335.68 ± 0.02
		2	_	323.01 ± 0.02
		3	_	313.71 ± 0.02

[a]As the two sites have very similar short contact distances (2.807 Å and 2.795 Å), their iodine resonances may occur at nearly identical frequencies. Therefore, in Figure 4(b), the average of these two distances has been considered.

[b]This site does not exhibit a distinct I···N or I···O contact and was therefore not included in the geometrical correlation graphs in Figure 4.

[c]The corresponding frequency could not be determined. It is possible there is spectral overlap with another site.

4. ^{79}Br and ^{81}Br NQR Frequencies

The difference in quadrupole moments (Q) between the two isotopes of bromine, ^{79}Br and ^{81}Br, results in distinct NQR frequencies. ^{79}Br, with a natural abundance of 50.67%, has Q = 308.7 mb, while ^{81}Br, with a natural abundance of 49.31%, has Q = 257.9 mb. Both isotopes are spin-3/2 nuclei, and since the electric field gradient at ^{79}Br and ^{81}Br is identical, they share the same asymmetry parameter (η). However, their differing quadrupole moments lead to distinct quadrupolar coupling constants (C_Q), resulting in different pure NQR frequencies. The frequencies for ^{81}Br are lower than those for ^{79}Br due to the former's smaller quadrupole moment. Some pure NQR frequencies for ^{81}Br were measured using an Autotune Scout LF1 NQR system (NMR Service GmbH, Germany) and are listed in Table S2.

Table S2. ^{79}Br and ^{81}Br NQR frequencies of *p*-DBTFB (**C**), and its XB cocrystals, measured using a homebuilt NQR probe connected to a Bruker Avance III NMR console (for ^{79}Br) and an autotune NQR system (for ^{81}Br). The table details the number of distinct crystallographic iodine sites, their short contact types studied herein, and all possible NQR frequencies for the existing iodine sites.

CSD Ref.	Number of crystallographic sites	Br···O/N short contact	^{79}Br ν_{NQR}	^{81}Br ν_{NQR}
C: ZZZAVJ01[15]	1	_	309.32 ± 0.03	258.46 ± 0.12
C1: FAPKIU[2]	2	Br···O/C	315.60 ± 0.04	263.65 ± 0.08
		Br···O/C [a]	317.28 ± 0.04	265.04 ± 0.08
C5: DIVDOC[6]	1	Br···N	321.75 ± 0.03	268.77 ± 0.09
C6: LICBAC[1]	1	Br···C	312.11 ± 0.04	260.76 ± 0.08
C7: OZEFEH[16]	1	Br···N	310.40 ± 0.03	259.32 ± 0.10
C8: QIHDAM[17]	1	Br···N	317.65 ± 0.03	265.34 ± 0.09
C9: JAYFUO[7]	2	Br···N	316.28 ± 0.04	264.27 ± 0.08
		Br···C	_ [b]	_ [b]
C10: OZAZUN[16]	1	Br···N	316.39 ± 0.04	264.24 ± 0.08
C11: VOMHEL[10]	1	Br···N	318.75 ± 0.05	266.28 ± 0.09

[a]This site was not studied in this work.

[b]The corresponding frequency could not be determined.

Table S3. Experimental conditions for Zp-NQR measurements, including the applied magnetic field, coil angle, and resulting spectral breadth for each compound studied herein, along with their respective CSD reference codes.

CSD Ref.	X site	B_0 (mT)	subspectra (#)	coil angle (°)	breadth (kHz)
A: ZZZAVM02 [1]	_	20	15	9	868.5 ± 20.5
A1: FAPKOA [2]	_	40	37	0	1855.0 ± 53.0
A2: JUZRUT [3]	_	30	26	4	1495.0 ± 52.0
A3: AXOJUV [4]	_	40	35	-4	1972.5 ± 86.5
A4: BIYGIB [5]	_	40	36	-6	1853.0 ± 60.0
A5: DIVCUH [6]	_	40	35	-5	1943.5 ± 82.5
A6: LICBIK [1]	_	30	29	-5	1561.5 ± 75.5
A7: ISIJEZ [7]	_	30	28	4	1337.0 ± 33.0
A8: MEKWOO[8]	_	40	37	-5	1912.5 ± 36.5
A9: VOMHAH [6]	_	40	36	-5	1920.5 ± 63.5
A10-J: JAQMAQ [7]	_	20	19	8	960.0 ± 36.0
A10-K: KIHRAX [9]	_	20	19	20	962.5 ± 31.5
A11: VOMHIP [10]	_	30	28	0	1592.0 ± 94.0
A12: RUYHID [11]	_	30	28	0	1432.0± 47.0
B: UCEPEY [12]	1	30	28	-2	1314.0 ± 58.0
	2	30	28	5	1326.0 ± 31.0
B1: FAPKUG[2]	1	25	23	4	1158.5 ± 37.5
	2	30	27	4	1466.0 ± 68.0
B2: JUZRON [3]	1	30	27	-3	1507.0 ± 96.0
B2	2	30	27	-3	1410.0 ± 65.0
B5: ODEGAJ [13]	_	30	28		1515.5 ± 90.5
B7: KIHREB [9]	1	25	24	0	1284.5 ± 62.5
B7	2	30	26	-2	1440.0 ± 64.0
B10: SAJCUE [14]	1	25	23	2	1287.5 ± 40.5
B10	2	25	23	0	1312.5 ± 64.5
B11: SAJDAL [14]	_	30	27	6	1511.0 ± 75.0
C: ZZZAVJ01 [15]	_	30	26	-4	1305.5 ± 21.5
C1: FAPKIU [2]	_	30	27	8	1414.5 ± 37.5
C5: DIVDOC [6]	_	40	34	8	1777.0 ± 29.0
C6: LICBAC [1]	_	30	27	12	1358.0 ± 38.0
C7: OZEFEH [16]	_	30	27	14	1434.5 ± 47.5
C8: QIHDAM [17]	_	30	27	6	1452.5 ± 37.5
C9: JAYFUO [7]	_	40	37	4	1918.5 ± 24.5
C10: OZAZUN [16]	_	40	29	10	1598.5 ± 63.5
C11: VOMHEL [10]	_	40	37	4	1957.0 ± 95.0

5. Mechanochemical Synthesis of Cocrystals

All cocrystals studied in this work were prepared mechanochemically using a Retsch MM400 ball mill, except for **A10-K**, which was synthesized following a previously reported method[18] utilizing a Pharma Ram 1 (Resodyn Inc.) resonant acoustic mixer (RAM). Detailed preparation conditions for each cocrystal are provided in Table S3.

Table S4. Experimental mechanochemical synthesis conditions of cocrystals in this work

cocrystal	molar ratio (donor: acceptor)	milling time (min)	milling frequency (Hz)	liquid	η* (μL/mg)
A1	(1:1)	40	30	$CHCl_3$	0.05
A2	(1:1)	40	30	CH_3OH	0.05
A3	(1:1)	40	30	THF	0.05
A4	(1:2)	40	30	None	_
A5	(1:1)	40	30	$CHCl_3$	0.05
A6	(1:1)	50	30	$CHCl_3$	0.05
A7	(1:1)	45	30	CH_3NO_2	0.1
A8	(1:1)	45	30	CH_3NO_2	0.1
A9	(1:2)	45	30	CH_3NO_2	0.1
A10-J	(1:1)	45	30	$CHCl_3$	0.1
A10-K	(2:1)	50 (RAM)**	(80g)** RAM	None	_
A11	(1:1)	45	30	$CHCl_3$	0.03
A12	(1: 2)	45	30	None	_
B1	(1:2)	45	30	$CHCl_3$	0.05
B2	(1:1)	45	30	$CHCl_3$	0.03
B5	(1:1)	45	30	$CHCl_3$	0.03
B7	(1:1)	45	30	$CHCl_3$	0.03
B10	(1:1)	45	30	$CHCl_3$	0.03
B11	(1:1)	45	30	$CHCl_3$	0.03
C1	(1:1)	45	30	$CHCl_3$	0.05
C5	(1:1)	45	30	$CHCl_3$	0.05
C6	(1:1)	45	30	$CHCl_3$	0.05
C7	(1:1)	45	30	$CHCl_3$	0.03
C8	(1:1)	45	30	$CHCl_3$	0.03
C9	(1:1)	45	30	$CHCl_3$	0.03
C10	(1:1)	45	30	$CHCl_3$	0.03
C11	(1:1)	45	30	$CHCl_3$	0.03

* Here, η is defined as the ratio of the volume of liquid added to the total mass of solids used in the experiment.

** The **A10-K** cocrystal was prepared using the RAM method, conducted at a high intensity of 80 g, where *g* represents Earth's gravitational acceleration (9.8 m/s²).

6. DFT Calculations

Table S5. Comparison of DFT-calculated quadrupolar parameters (C_Q and η) from two calculation sets: one with optimized geometry (maintaining the XB geometry) and another using unoptimized geometry directly from SCXRD data, alongside experimental results obtained via Zp-NQR.

	geometry optimized		no optimization		experimental	
compound	$\|C_Q\|$	η	$\|C_Q\|$	η	$\|C_Q\|$	η
A	2174.80	0.122	2190.53	0.128	2145.14 ± 1.64	0.120 ± 0.004
A1	2295.90	0.080	2310.50	0.096	2229.49 ± 0.90	0.062 ± 0.004
A2	2302.58	0.053	2316.43	0.053	2266.14 ± 1.49	0.048 ± 0.008
A3	2266.92	0.079	2281.77	0.085	2223.44 ± 2.16	0.072 ± 0.008
A4	2248.60	0.090	2259.29	0.107	2186.51 ± 1.01	0.071 ± 0.004
A5	2292.28	0.090	2306.51	0.089	2273.03 ± 1.37	0.093 ± 0.004
A6	2233.16	0.090	2255.02	0.089	2176.27 ± 1.61	0.075 ± 0.006
A7	2256.18	0.089	2262.03	0.096	2201.01 ± 1.17	0.082 ± 0.004
A8	2301.82	0.080	2318.60	0.081	2299.04 ± 0.96	0.064 ± 0.004
A9	2265.14	0.080	2279.56	0.085	2234.85 ± 1.29	0.070 ± 0.004
A10-J	2260.72	0.090	2277.42	0.091	2219.98 ± 2.43	0.084 ± 0.008
A10-K	2270.07	0.094	2283.37	0.091	2225.45 ± 1.19	0.082 ± 0.004
A11	2280.22	0.080	2294.20	0.087	2249.27 ± 0.89	0.060 ± 0.004
A12	2355.52	0.088	2370.52	0.091	2353.74 ± 2.40	0.078 ± 0.008

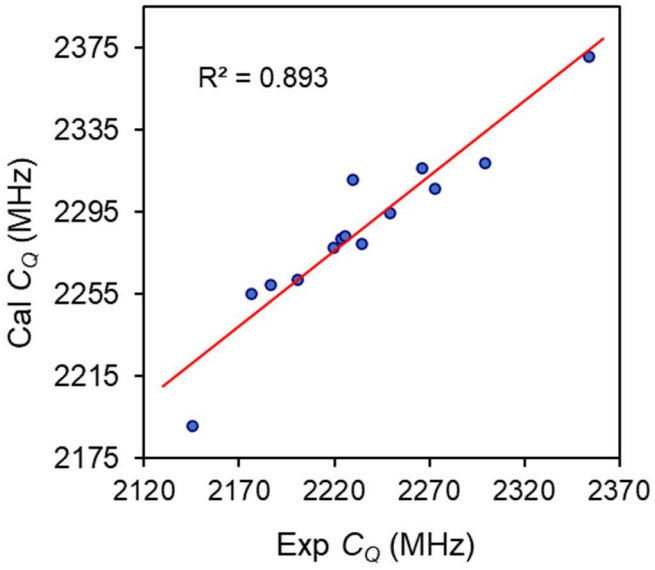


Figure S8. Comparison of experimentally obtained C_Q values from the Zp-NQR method with theoretically determined C_Q values via ZORA-DFT, using *unoptimized* geometries directly from SCXRD data, for the **A** series, Cal. $C_Q = 0.731\,\text{Exp. } C_Q + 653.3$, $R^2 = 0.893$. Absolute values are plotted.

7. EFG Tensor Visualization

The rank-2 electric field gradient (EFG) tensor, similar to other tensor quantities in NMR such as shielding and *J*-coupling tensors, can be effectively visualized using three-dimensional plots that display the orientation, sign, and relative magnitudes of its principal components. These visual representations are highly useful for interpreting both experimentally measured and theoretically computed EFG tensors. Since EFG calculations are typically conducted within an arbitrarily chosen Cartesian coordinate system, the orientation of the tensor relative to the molecular framework is not immediately evident from its 3×3 matrix form, especially in molecules lacking high symmetry. Visualizing the EFG tensor clarifies the orientation of its principal axes in relation to the molecular geometry (Figure S9).

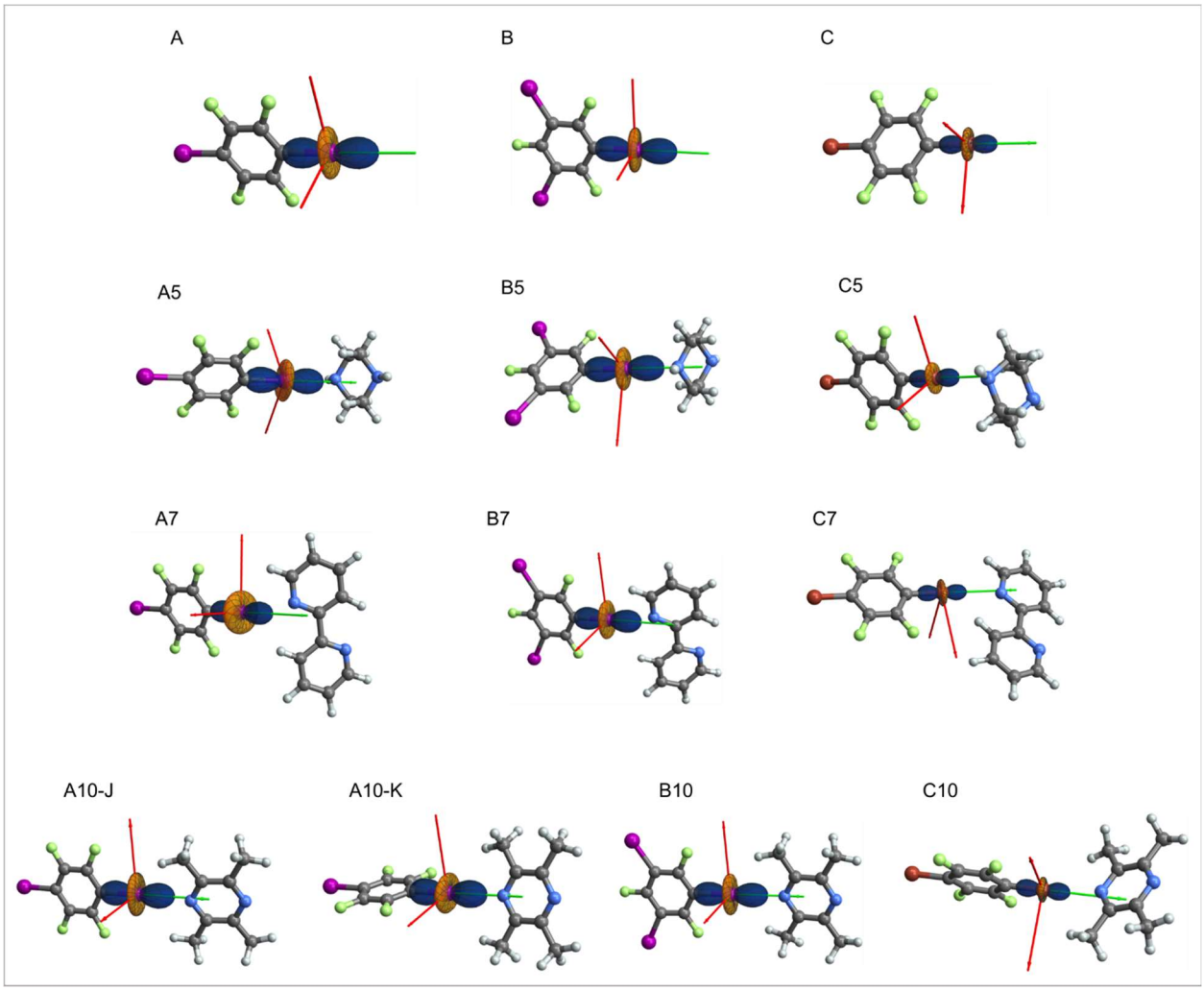


Figure S9. Visualization of halogen EFG tensors for the three XB donors (**A**, **B**, and **C**) and their corresponding cocrystals with XB acceptors **5**, **7**, and **10**. The two polymorphs of **A10** are labeled as **A10-J** (CSD ref: JAQMAQ) and **A10-K** (CSD ref: KIHRAX), respectively.

8. NLMO Analysis

As shown in Tables S5 to S8, in the XB donor molecules, the large positive contributions to V_{33} arise primarily from the X atom lone pair molecular orbital (MO), which are only partially counterbalanced by smaller negative field gradients from the σ(I–C) and negligible X core contribution.

Table S6. NLMO analysis of the halogen atom contributions (in a.u.) to the V_{33} EFG component in **A**, **B**, and **C** halogen bond donor moieties and their corresponding cocrystals with **5** (piperazine) as the XB acceptor.

	***A*-donor**	***A5*-cocrystal**	***B*-donor**	***B5*-cocrystal**	***C*-donor**	***C5*-cocrystal**
σ(C—X)	-13.489	-13.077	-13.606	-13.09	-10.273	-10.331
X Lp	26.505	27.027	26.434	27.028	18.769	19.049
X core	1.027	1.05	1.003	1.005	0.573	0.594
Sum	14.043	15	13.831	14.943	9.069	9.312

Table S7. NLMO analysis of the halogen atom contributions (in a.u.) to the V_{33} EFG component in **A**, **B**, and **C** halogen bond donor moieties and their corresponding cocrystals with **7** (2,2′-bipyridine) as the XB acceptor.

	***A**-donor*	***A7**-cocrystal*	***B**-donor*	***B7**-cocrystal*	***C**-donor*	***C7**-cocrystal*
σ(C—X)	-13.489	-13.335	-13.606	-13.329	-10.273	-10.373
X Lp	26.505	26.71	26.434	26.84	18.769	18.921
X core	1.027	1.312	1.003	1.208	0.573	0.583
Sum	14.043	14.687	13.831	14.719	9.069	9.131

Table S8. NLMO analysis of the halogen atom contributions (in a.u.) to the V_{33} EFG component in **A**, **B**, and **C** halogen bond donor moieties and their corresponding cocrystals with **10** (2,3,5,6-tetramethylpyrazine) as the XB acceptor.

	A *donor*	***A10-J*** *cocrystal*	***A10-K*** *cocrystal*	***B*** *donor*	***B10*** *cocrystal*	***C*** *donor*	***C10*** *cocrystal*
σ(C—X)	-13.489	-13.277	-13.28	-13.606	-13.285	-10.273	-10.392
X Lp	26.505	26.824	26.884	26.434	26.863	18.769	18.984
X core	1.027	1.072	1.366	1.003	1.06	0.573	0.596
Sum	14.043	14.619	14.97	13.831	14.638	9.069	9.188

Table S9. NLMO analysis of the halogen atom contributions (in a.u.) to the V_{33} EFG component in **A**, **B**, and **C** halogen bond donor moieties and their corresponding cocrystals with **11** (acridine) as the XB acceptor.

	***A**-donor*	***A11**-cocrystal*	***B**-donor*	***B11**-cocrystal*	***C**-donor*	***C11**-cocrystal*
σ(C—X)	-13.489	-13.194	-13.606	-13.318	-10.273	-10.19
X Lp	26.505	26.995	26.434	26.845	18.769	18.912
X core	1.027	1.094	1.003	1.057	0.573	0.623
Sum	14.043	14.895	13.831	14.584	9.069	9.345

9. Halogen bond geometrical parameters

Table S10. Halogen bond geometric parameters, including X···N/O short contact distances ($d_{X...N/O}$) and C–X covalent bond distances ($d_{C–X}$), investigated in this study. All values are given in angstroms (Å).

cocrystal	$d_{I\cdots N/O}$	$d_{C—I}$	cocrystal	site	$d_{I\cdots N/O}$	$d_{C—I}$	cocrystal	$d_{Br\cdots N/O}$	$d_{C—Br}$
A1	2.801[a]	2.088[a]	**B1**	1	2.920	2.088	**C1**	2.925	1.868
A2	2.727	2.092	**B1**	2	2.941	2.086	**C5**	2.881	1.887
A3	2.899	2.09	**B2**	_	2.920	2.091	**C6**	_[c]	1.874
A4	2.973	2.075	**B5**	_	_[b]	2.119	**C7**	3.080	1.860
A5	2.842	2.108	**B7**	1	2.968	2.090	**C8**	3.025	1.860
A6	_[b]	2.079	**B7**	2	2.969	2.096	**C9**	2.980	1.877
A7	3.111	2.086	**B10**	1	2.993	2.092	**C10**	2.899	1.879
A8	2.793	2.101	**B10**	2	2.991	2.088	**C11**	3.075	1.881
A9	2.970	2.091	**B11**	_	3.022	2.090			
A10-J	3.067	2.091							
A10-K	3.001	2.102							
A11	2.971	2.096							
A12	2.667	2.121							

[a] The average distances for the two sites, 2.807 and 2.795 Å for $d_{I\cdots N/O}$ (or 2.097 Å and 2.078 Å for $d_{C—I}$), were used as these sites were not resolved spectroscopically.

[b] Cocrystals **A6** and **C6** exhibit halogen bonds to the π ring systems rather than X···N/O interactions.

[c] Cocrystal **B5** is excluded because the iodine which engages in a halogen bond to N also has short contacts to carbon and hydrogen.

10. References

(1) Oh, S. Y.; Nickels, C. W.; Garcia, F.; Jones, W.; Friščić, T. Switching between Halogen- and Hydrogen-Bonding in Stoichiometric Variations of a Cocrystal of a Phosphine Oxide. *CrystEngComm* **2012**, *14* (19), 6110–6114. https://doi.org/10.1039/C2CE25653C.

(2) Bedeković, N.; Fotović, L.; Stilinović, V.; Cinčić, D. Conservation of the Hydrogen-Bonded Pyridone Homosynthon in Halogen-Bonded Cocrystals. *Crystal Growth & Design* **2022**, *22* (2), 987–992. https://doi.org/10.1021/acs.cgd.1c01424.

(3) Xu, Y.; Viger-Gravel, J.; Korobkov, I.; Bryce, D. L. Mechanochemical Production of Halogen-Bonded Solids Featuring P═O···I–C Motifs and Characterization via X-Ray Diffraction, Solid-State Multinuclear Magnetic Resonance, and Density Functional Theory. *J. Phys. Chem. C* **2015**, *119* (48), 27104–27117. https://doi.org/10.1021/acs.jpcc.5b09737.

(4) Jain, H.; Sutradhar, D.; Roy, S.; Desiraju, G. R. Synthetic Approaches to Halogen Bonded Ternary Cocrystals. *Angewandte Chemie International Edition* **2021**, *60* (23), 12841–12846. https://doi.org/10.1002/anie.202103516.

(5) Takemura, A.; McAllister, L. J.; Hart, S.; Pridmore, N. E.; Karadakov, P. B.; Whitwood, A. C.; Bruce, D. W. Halogen- and Hydrogen-Bonded Salts and Co-Crystals Formed from 4-Halo-2,3,5,6-Tetrafluorophenol and Cyclic Secondary and Tertiary Amines: Orthogonal and Non-Orthogonal Halogen and Hydrogen Bonding, and Synthetic Analogues of Halogen-Bonded Biological Systems. *Chemistry – A European Journal* **2014**, *20* (22), 6721–6732. https://doi.org/10.1002/chem.201402128.

(6) Cinčić, D.; Friščić, T.; Jones, W. Isostructural Materials Achieved by Using Structurally Equivalent Donors and Acceptors in Halogen-Bonded Cocrystals. *Chemistry – A European Journal* **2008**, *14* (2), 747–753. https://doi.org/10.1002/chem.200701184.

(7) Syssa-Magalé, J.-L.; Boubekeur, K.; Palvadeau, P.; Meerschaut, A.; Schöllhorn, B. The Tailoring of Crystal Structures via the Self-Assembly of Organic Coordination Compounds by N···I Non-Covalent Halogen Bonds: Co-Crystals of Sterically Hindered N-Heterocycles and 1,4-Diiodo-Tetrafluorobenzene. *CrystEngComm* **2005**, *7* (50), 302–308. https://doi.org/10.1039/B500009B.

(8) Corradi, E.; Meille, S. V.; Messina, M. T.; Metrangolo, P.; Resnati, G. Halogen Bonding versus Hydrogen Bonding in Driving Self-Assembly Processes. *Angewandte Chemie*

International Edition **2000**, *39* (10), 1782–1786. https://doi.org/10.1002/(SICI)1521-3773(20000515)39:10<1782::AID-ANIE1782>3.0.CO;2-5.

(9) Szell, P. M. J.; Gabriel, S. A.; Caron-Poulin, E.; Jeannin, O.; Fourmigue, M.; Bryce, D. L. Cosublimation: A Rapid Route toward Otherwise Inaccessible Halogen-Bonded Architectures. *Crystal Growth and Design* **2018**, *18* (10), 6227–6238. https://doi.org/10.1021/acs.cgd.8b01089.

(10) Cinčić, D.; Friščić, T.; Jones, W. Structural Equivalence of Br and I Halogen Bonds: A Route to Isostructural Materials with Controllable Properties. *Chem. Mater.* **2008**, *20* (21), 6623–6626. https://doi.org/10.1021/cm800923r.

(11) Wang, R.; Hartnick, D.; Englert, U. Short Is Strong: Experimental Electron Density in a Very Short N···I Halogen Bond. **2018**, *233* (9–10), 733–744. https://doi.org/10.1515/zkri-2018-2069.

(12) Reddy, C. M.; Kirchner, M. T.; Gundakaram, R. C.; Padmanabhan, K. A.; Desiraju, G. R. Isostructurality, Polymorphism and Mechanical Properties of Some Hexahalogenated Benzenes: The Nature of Halogen···Halogen Interactions. *Chemistry – A European Journal* **2006**, *12* (8), 2222–2234. https://doi.org/10.1002/chem.200500983.

(13) Hajjar, C.; Ovens, J. S.; Bryce, D. L. 1,3,5-Trifluoro-2,4,6-Triiodobenzene–Piperazine (2/1). *IUCrData* **2021**, *6* (10), x211044. https://doi.org/10.1107/S2414314621010440.

(14) Szell, P. M. J.; Gabriel, S. A.; Gill, R. D. D.; Wan, S. Y. H.; Gabidullin, B.; Bryce, D. L. ^{13}C and ^{19}F Solid-State NMR and X-Ray Crystallographic Study of Halogen-Bonded Frameworks Featuring Nitro\-Gen-Containing Heterocycles. *Acta Crystallographica Section C* **2017**, *73* (3), 157–167. https://doi.org/10.1107/S2053229616015023.

(15) d'Agostino, S.; Spinelli, F.; Taddei, P.; Ventura, B.; Grepioni, F. Ultralong Organic Phosphorescence in the Solid State: The Case of Triphenylene Cocrystals with Halo- and Dihalo-Penta/Tetrafluorobenzene. *Crystal Growth & Design* **2019**, *19* (1), 336–346. https://doi.org/10.1021/acs.cgd.8b01443.

(16) Peloquin, A. J.; McMillen, C. D.; Pennington, W. T. One Dimensional Halogen Bond Design: Br···N versus I···N with Fluoroarenes. *CrystEngComm* **2021**, *23* (35), 6098–6106. https://doi.org/10.1039/D1CE00864A.

(17) Walsh, R. B.; Padgett, C. W.; Metrangolo, P.; Resnati, G.; Hanks, T. W.; Pennington, W. T. Crystal Engineering through Halogen Bonding: Complexes of Nitrogen Heterocycles with

Organic Iodides. *Crystal Growth & Design* **2001**, *1* (2), 165–175. https://doi.org/10.1021/cg005540m.

(18) Nari, A.; Ovens, J. S.; Bryce, D. L. Halogen-Bonded Cocrystals via Resonant Acoustic Mixing. *RSC Mechanochem.* **2024**, *1* (1), 50–62. https://doi.org/10.1039/D3MR00028A.

II.3 Supporting Information for Chapter 7

Materials and sample preparation

5-Chloro-2-benzoxazolinone (CHZ), chloramine-T trihydrate (CAT), and ketoconazole (KTZ) were purchased from Sigma-Aldrich. The coformers carbamazepine (CBZ), picolinic acid (PA), and 2,4-dihydroxybenzoic acid (2,4DHBA) were purchased from Sigma Aldrich. Nicotinamide (NAM) and isonicotinamide (INA) were purchased from Acros Organics and Alfa Aesar, respectively.

The production of each cocrystal was intended to generate roughly 700 mg of product to fill a 7 mm glass tube rotor. Chlorine-based cocrystals were synthesized using liquid-assisted grinding (LAG) for 30-minute intervals. Equimolar amounts of halogen bond donor and acceptor were weighed and placed in a 10 mL stainless-steel milling jar containing two stainless steel balls (4 mm). The mixture was milled using a benchtop ball mill (Retsch MM 400) and a small quantity of liquid (0.05 – 0.1μL/mg) was added to catalyze crystal formation. The ball milling was conducted at room temperature at a frequency of 30 Hz. The specific synthesis conditions for each cocrystal via ball milling are outlined in Table II.3.2.

Solid state NMR 600 MHz

^{1}H and ^{13}C SSNMR spectra were collected on a Bruker Avance III HD spectrometer operating at a magnetic field strength of 14.1 T corresponding to a ^{1}H Larmor frequency of 600.5 MHz. Samples were packed on 1.3 mm zirconia rotors and spun at the magic angle at frequency of 60 kHz. The ^{1}H and ^{13}C NMR chemical shifts were externally referenced to adamantane. All data were processed using the Topspin software. All experiments were performed at room temperature.

The single pulse ^{1}H SSNMR spectra were recorded using 90° radiofrequency pulses with a ^{1}H nutation frequency (ν_H) of 185 kHz. Data acquisition involved the accumulation of 16 transients with a relaxation delay (τ_{relax}) varying from of 1.0 to 100.0 s.

The ^{13}C SSNMR spectra were recorded by $^{1}H \rightarrow ^{13}C$ cross-polarization (CP) at the double quantum Hartmann−Hahn condition,[1] $\nu_H + \nu_C = \nu_{rf}$, which involved ramped CP of $\nu_H = 20 \pm 5$ kHz for ^{1}H ($\nu_C = 40$ kHz), a 1.5 μs 90° ^{1}H pulse, and spinal-64 ^{1}H decoupling[2] at $\nu_H = 150$ kHz, with a contact time of (3 ms KTZ, 4 ms CAT, 1 ms CHZ), recycle delay (25 s KTZ, 50 s CAT, 1500 s CHZ) and number of scans (1000 KTZ, 256 CAT, 512 CHZ).[1,2]

The double-quantum to single-quantum (DQ–SQ) ^{1}H NMR correlation spectra were recorded using the 2D NMR protocol in the article by Fieke *et.al*.[3] This experiment probes dipolar couplings between ^{1}H nuclei, allowing for the identification of proximities and interactions between protons within the structure. Double-quantum coherence (2QC) excitation and reconversion were achieved using the BABA dipolar recoupling scheme, which spans two rotor periods ($2\tau_r$). This provided 2Q excitation (τ_{exc}) and reconversion (τ_{rec}) intervals of $\tau_{exc}=\tau_{rec}=2\tau_r=33.33$ μs. The ^{1}H BABA scheme ensures efficient recoupling under magic angle spinning conditions, enabling the generation and observation of double-quantum coherences.

The ^{1}H nutation frequency was $\nu_H \approx 185$ kHz, corresponding to 90° dipolar recoupling pulses with a duration of 1.35 μs. The 2D NMR acquisition parameters included a τ_{relax} of 2.0 s, with 48 (t_1) × 512 (t_2) time points acquired. Dwell times were set to $\Delta t_1=2\tau_r$ and $\Delta t_2=33.3$ μs, ensuring sufficient resolution in both dimensions. Each t_1 value accumulated 32 transients to enhance the signal to noise ratio. The 2D data sets were zero-filled to 256 × 2048 points to improve

digital resolution, and apodization with an exponential Lorentzian broadening of 50 Hz full width at half maximum (FWHM) was applied in both dimensions.

The ^{35}Cl NMR experiments in supporting information, were performed at 11.7 T using a Bruker AVANCE II spectrometer. A 7 mm static probe was used with samples packed in a 7 mm glass tube. A WURST-QCPMG pulse sequence was used which swept over a frequency range of 1 MHz. [3,4] The VOCS acquisition method was used, where a series of 20 spectra (10 each side) were collected, processed and then co-added in the frequency domain. A QCPMG spikelet separation of 10-15 kHz was used in all cases with a VOCS stepping frequency of 150 kHz to ensure uniformly excited line shapes. 30k scans were used to acquire each piece using a recycle delay of 0.5 s. In most cases 128 echoes were collected for each QCPMG echo train (an acquisition time of 25.7 ms).

Discussion of QTAIM data

For the pure CHZ phase, the selected model contained three neighboring CHZ molecules surrounding the target chlorine site. The Quantum Theory of Atoms in Molecules (QTAIM) analysis revealed several weak intermolecular Cl···H and Cl···O contacts characterized by low electron density values at the BCPs ($\rho(r) \approx 0.0028$ a.u.) and positive Laplacian values ($\nabla^2\rho(r) \approx 0.0093$ a.u.). The positive Laplacian together with positive total energy density H(r) indicates that these interactions are predominantly closed-shell and noncovalent in nature, which is consistent with weak electrostatic or dispersive contacts commonly observed in molecular crystals. The negative values of sign($\lambda 2)\rho$ further support the attractive nature of these interactions. Overall, the intermolecular contacts in pure CHZ are relatively weak and diffuse.

In the CHZ·CBZ cocrystal, the chlorine atom participates in multiple intermolecular interactions with neighboring CBZ molecules through Cl···H contacts. The electron density values at the BCPs increase slightly compared to the pure CHZ structure. For example, one representative Cl···H interaction exhibits $\rho(r) = 0.00293$ a.u. and $\nabla^2\rho(r) = 0.00936$ a.u., while stronger contacts show considerably larger values, reaching $\rho(r) = 0.00529$ a.u. with $\nabla^2\rho(r) = 0.0201$ a.u. These larger electron density values indicate enhanced intermolecular stabilization in the cocrystal phase. Similar to the pure CHZ structure, all interactions display positive Laplacian and positive H(r) values, confirming their closed-shell character. A Cl···Cl bond critical point was also detected between Cl45 and Cl150 with $\rho(r) = 0.00542$ a.u. and $\nabla^2\rho(r) = 0.0177$ a.u. Although the Cl···Cl separation is relatively long (~3.8 Å), the existence of a BCP suggests the presence of a weak attractive halogen–halogen interaction contributing to the crystal packing.

For the CHZ·NAM cocrystal, two crystallographically distinct chlorine sites were analyzed. The QTAIM results reveal significantly stronger intermolecular interactions compared to the other systems. Several Cl···H contacts display electron density values approaching 0.0049–0.0059 a.u. with Laplacian values between approximately 0.015 and 0.018 a.u. In addition, Cl···Cl interactions were identified with $\rho(r)$ values close to 0.0040–0.0041 a.u. and positive Laplacians around 0.0136–0.0138 a.u. The larger electron density values observed in the CHZ·NAM cocrystal indicate comparatively stronger intermolecular interactions and a more cooperative supramolecular environment around the chlorine atoms. Nevertheless, the positive Laplacian and positive H(r) values demonstrate that these contacts remain noncovalent closed-shell interactions dominated by electrostatic and dispersion contributions rather than covalent bonding.

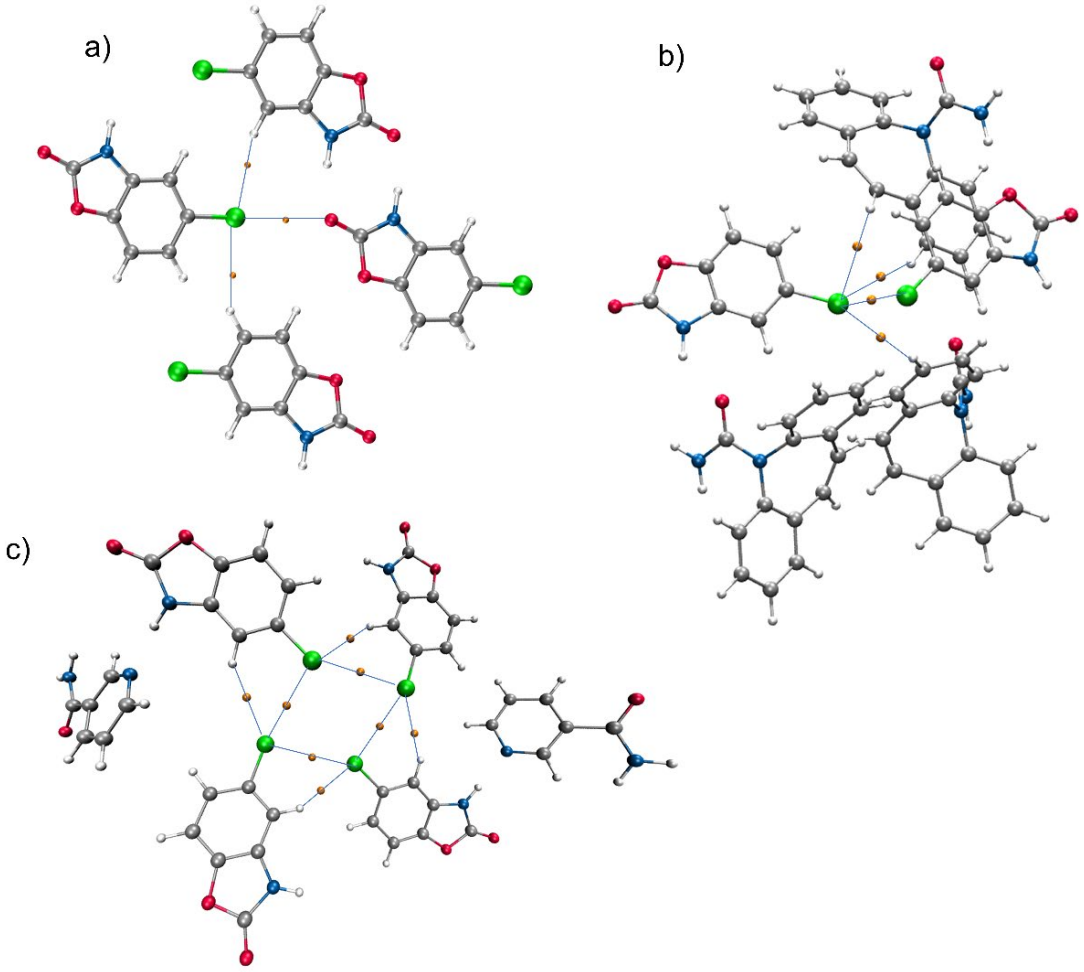


Figure II.3.1. QTAIM analysis of the chlorine local environments in the chlorzoxazone series. Bond critical points (BCPs) are shown as colored spheres (orange) connected by electron-density paths for (a) parent CHZ, (b) the CHZ·CBZ cocrystal, and (c) the CHZ·NAM cocrystal. The selected systems correspond to the QTAIM parameters (electron density ρ, Laplacian $\nabla^2\rho$, total energy density H(r), and |V(r)|/G(r) ratios) summarized in Table II.3.7 to II.3.9. All calculations were performed on the rPBE-D2 optimized geometries.

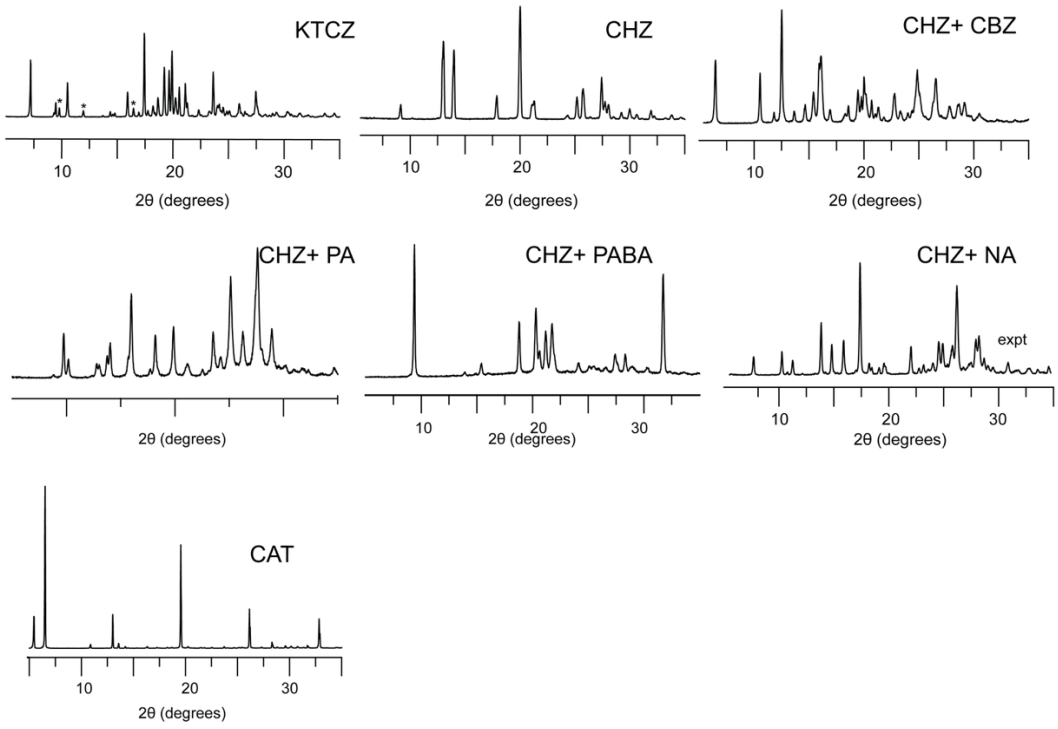


Figure II.3.2. The PXRD pattern of the chlorine-containing samples used in this study.

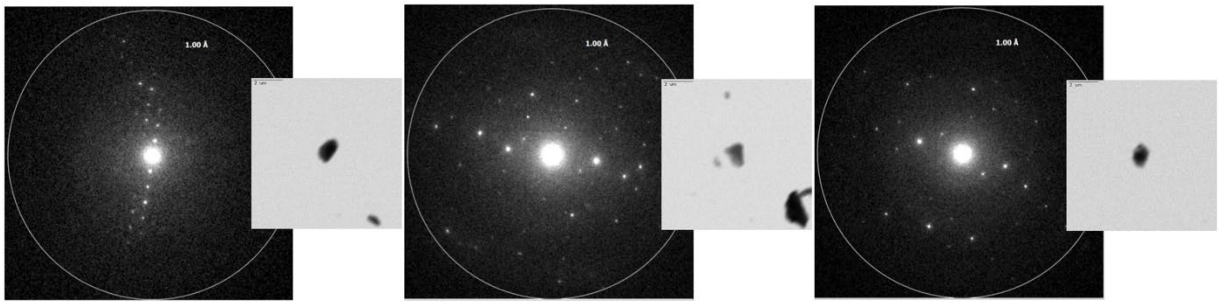


Figure II.3.3. The selected STEM and diffraction images of KTZ.

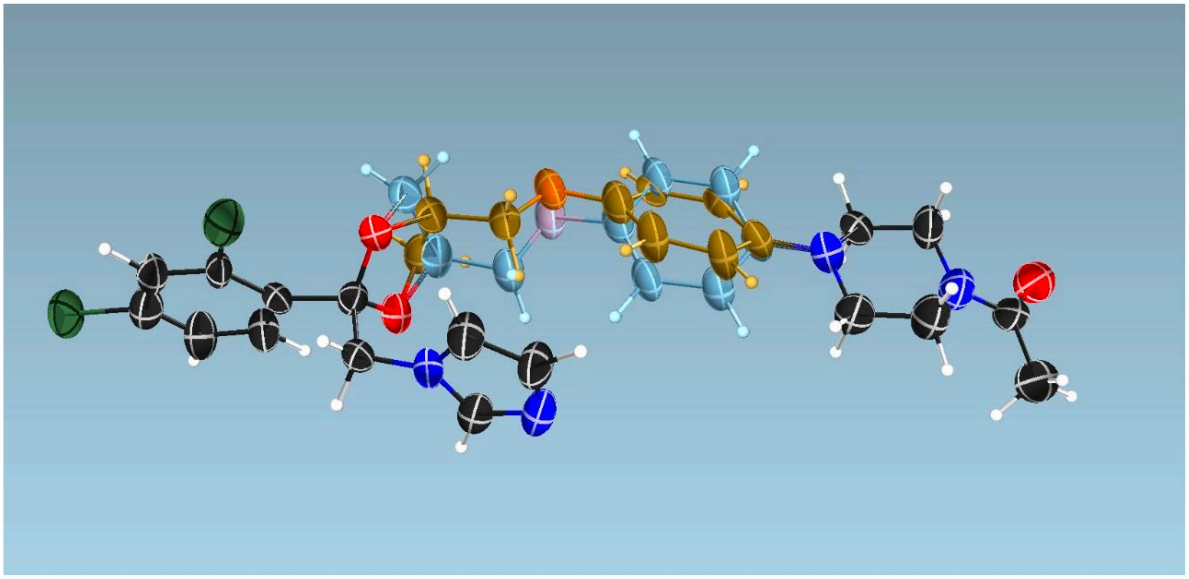


Figure II.3.4. The structure solution and kinematical refinement of 16 merged datasets on KTZ molecule.

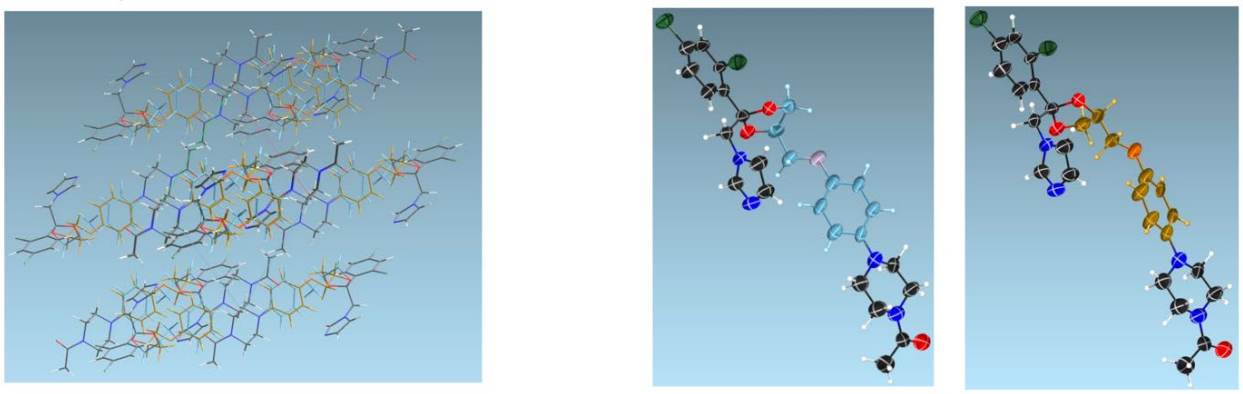


Figure II.3.5. The crystal packing and disorder in the KTZ molecule.

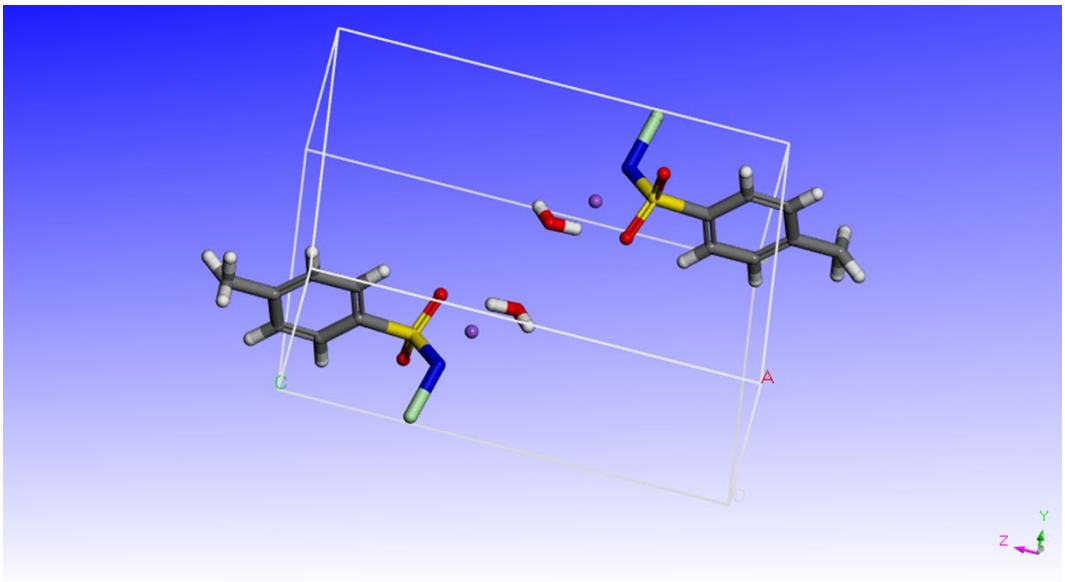


Figure II.3.6. The crystal structure of the CAT-dehydrated predicted by GIPAW calculation.

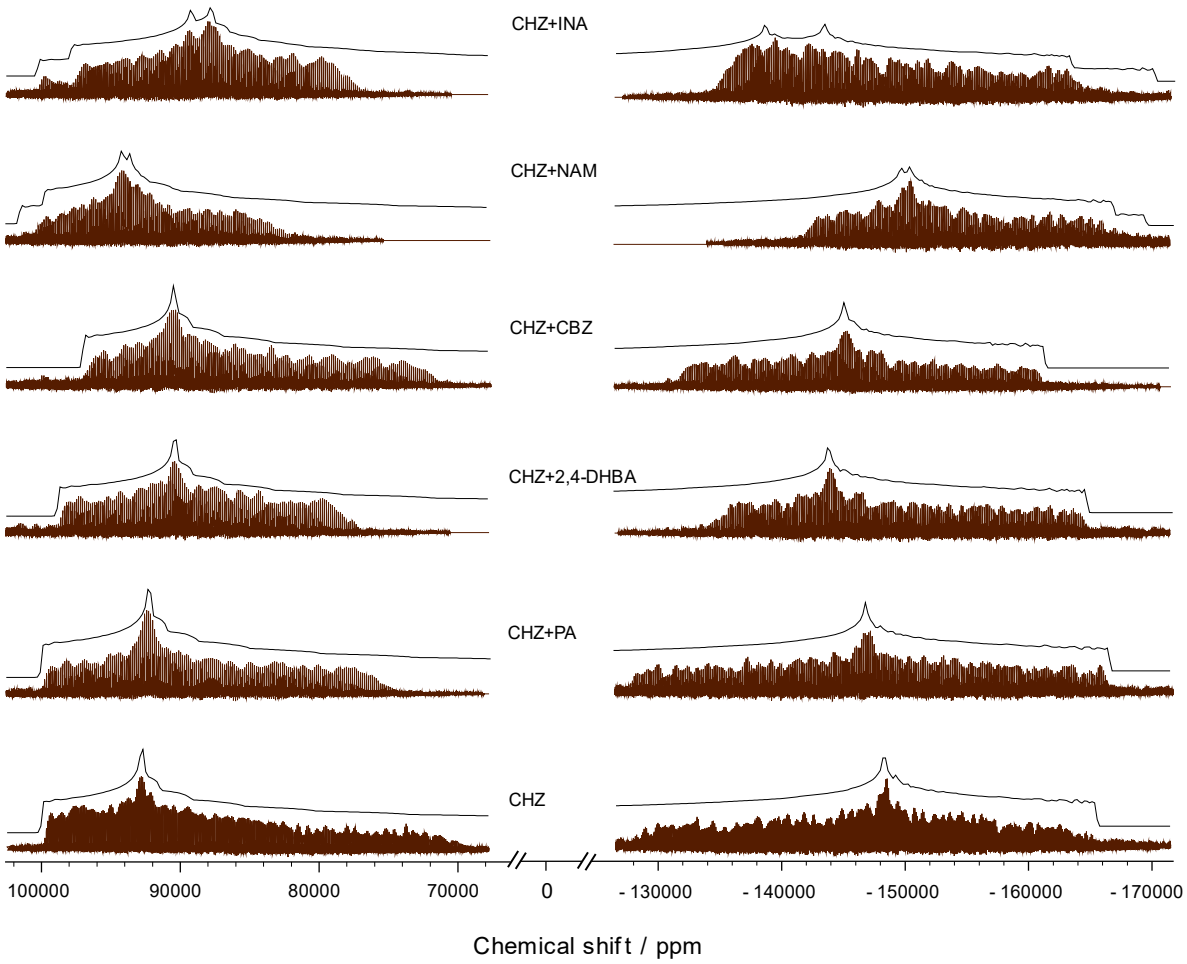


Figure II.3.7. ^{35}Cl SSNMR spectra of the CHZ family. Experimental ^{35}Cl WURST-QCPMG SSNMR spectra (edges only) acquired at 11.7 T (bottom traces, brown) with the corresponding QUEST simulated fits overlaid (top traces, black). The Zp-NQR spectra were simulated using QUEST to obtain the values of C_Q and η. These data guided the experimental search for the edges and key discontinuities of the WURST-QCPMG SSNMR spectra shown here.

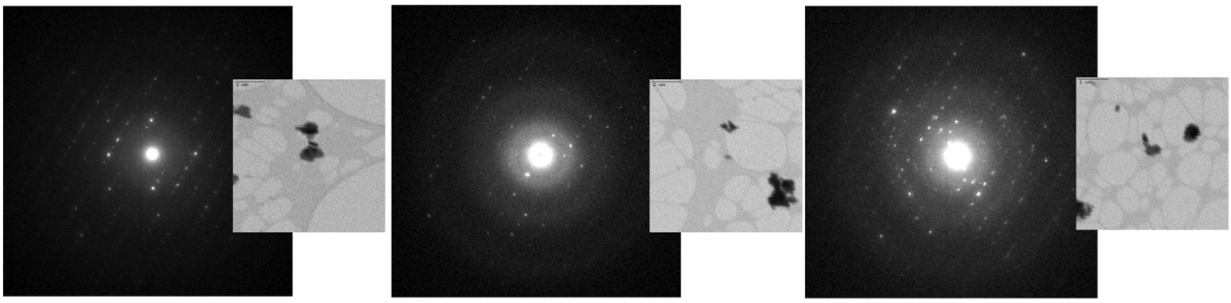


Figure II.3.8. Selected STEM (FOV 10x10 µm) and diffraction images of CHZ·CBZ cocrystal.

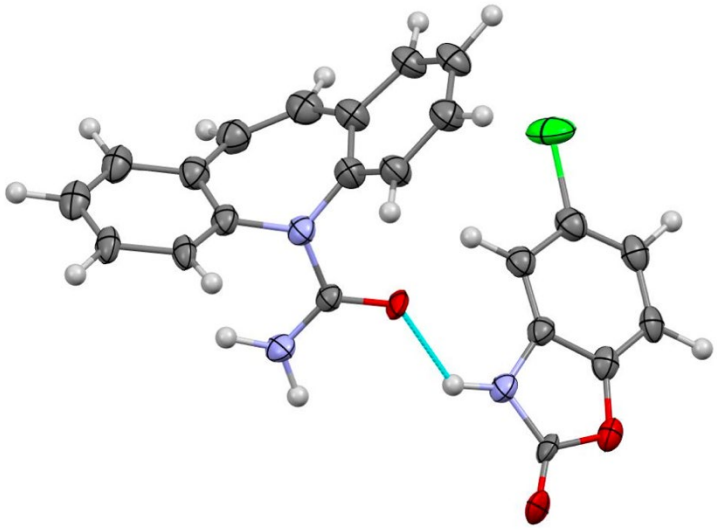


Figure II.3.9. The structure solution and kinematical refinement from eight merged datasets on CHZ·CBZ cocrystal.

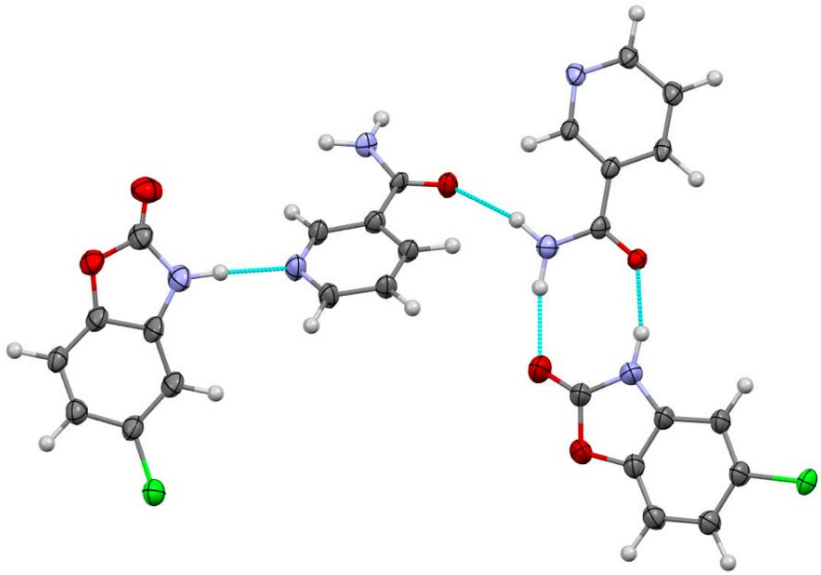


Figure II.3.10. The structural solution and kinematical refinement form eight merged datasets of CHZ·NAM cocrystals.

Table II.3.1. ^{35}Cl NQR frequencies and quadrupolar parameters for CHZ and its cocrystal series.

sample	NQR frequency / MHz	exp. C_Q / MHz	calc. C_Q / MHz	exp. η	calc. η
CHZ	34.99 ± 0.02	69.31 ± 0.23	67.16	0.24 ± 0.04	0.09
CHZ·PA	34.91 ± 0.04	69.46 ± 0.19	66.95	0.18 ± 0.04	0.09
CHZ·2,4-DHBA	34.63 ± 0.03	68.98 ± 0.12	66.94	0.16 ± 0.04	0.09
CHZ·CBZ	34.45 ± 0.03	68.45 ± 0.23	66.80	0.20 ± 0.04	0.07
CHZ·NAM (site1)	35.24 ± 0.02	70.38 ± 0.10	68.01	0.10 ± 0.03	0.09
CHZ·NAM (site2)	35.13 ± 0.02	70.02 ± 0.09	67.59	0.14 ± 0.02	0.08
CHZ·INA (site1)	34.44 ± 0.02	68.62 ± 0.13	66.40	0.14 ± 0.04	0.10
CHZ·INA (site2)	34.60 ± 0.02	68.90 ± 0.10	66.77	0.15 ± 0.04	0.14

[a] Experimental values are compared with periodic DFT calculations (GIPAW-DFT) based on H-only optimized crystal structures. For systems with two inequivalent chlorine environments (site1 and site2), both sites are reported.

Table II.3.2. Experimental conditions for cocrystal synthesis.

Donor	Acceptor	Milling Time (min)	Solvent	$\eta\,(\mu L\,mg^{-1})$
CHZ	**CBZ**	30	Chloroform	0.05
	PA	30	Chloroform	0.05
	2-4,DHBA	30	Acetonitrile	0.05
	NA	30	Chloroform	0.05
	INA	30	Methanol	0.10

Table II.3.3. 3D ED data collection details for the KTZ crystals used in refinement.

Crystal no.	Approximate size [µm]	Angular range [°]	Rotation per frame [°]	Exposure time [s]	Total exposure [s]	Frames measured	Frames used
1	2.2 x 1.5 x 0.8	−50 to +50	1	1	100	100	all
2	1.6 x 0.9 x 0.5	−60 to +40	1	1	100	100	all
3	0.9 x 0.5 x 0.3	−60 to +60	1	1	120	120	all
4	1.3 x 1.0 x 0.9	−60 to +60	1	1	120	120	all
5	1.4 x 1.2 x 0.8	−50 to +50	1	1	100	100	all
6	2.0 x 1.4 x 0.5	−60 to +60	1	1	120	120	all
7	1.1 x 1.1 x 0.6	−50 to +50	1	1	100	100	all
8	1.4 x 0.6 x 0.6	−50 to +50	1	1	100	100	all
9	3.0 x 1.2 x 0.7	−50 to +50	1	1	100	100	all
10	1.5 x 1.2 x 0.7	−60 to +60	1	1	120	120	all
11	1.2 x 1.0 x 0.4	−60 to +60	1	1	120	120	all
12	1.8 x 1.8 x 0.7	−60 to +50	1	1	110	110	all
13	3.1 x 1.2 x 0.8	−40 to +60	1	1	100	100	all
14	1.1 x 0.9 x 0.3	−40 to +60	1	1	100	100	all
15	1.1 x 0.8 x 0.7	−60 to +60	1	1	120	120	all
16	1.4 x 0.6 x 0.6	−50 to +50	1	1	100	100	all

Table II.3.4. Structure and refinement details for KTZ and the CHZ cocrystals.

	KTZ	**CHZ·CBZ**	**CHZ·NAM**
CCDC	2559789	2559788	2551009
	10.3907(7)	28.865(3)	3.8084(8)
a, b, c (Å)	10.9050(9)	7.2663(5)	17.069(3)
	13.2743(10)	18.1066(11)	19.811(3)
	67.582(6)	90	96.109(15)
α, β, γ (°)	79.429(7)	90	95.507(15)
	65.781(7)	90	91.92(2)
Volume ($Å^3$)	1267.41(19)	3797.7(5)	1273.4(4)
Space group	$P\bar{1}$	*Pbcn*	$P\bar{1}$
Formula	$C_{26}H_{28}Cl_2N_4O_4$	$C_{22}H_{16}ClN_3O_3$	$C_{26}H_{20}Cl_2N_6O_6$
Z	2	8	4
Independent reflections	2664	2307	2563
Parameters	418	263	362
Restraints	916	435	558
Resolution (Å)	1.0	0.95	1.0
Completeness (%)	100	99.4	96.5
R_{int} (%)	32.89	43.77	31.63
R_1 [$I > 2\sigma(I)$] (%)	11.46	21.03	22.62
wR_2 [all data] (%)	35.64	50.24	53.59
Goodness of fit	1.196	1.216	1.072
	$-10 \leq h \leq 10$	$-30 \leq h \leq 30$	$-3 \leq h \leq 3$
Index ranges	$-10 \leq k \leq 10$,	$-7 \leq k \leq 7$	$-17 \leq k \leq 17$
	$-13 \leq l \leq 13$	$-19 \leq l \leq 19$	$-19 \leq l \leq 19$
Min./max.diff.peaks($e^-/Å$)	-0.416, 0.386	-0.648, 0.888	-1.040, 0.951

Table II.3.5. 3D ED data collection details for the CHZ·CBZ cocrystals used in refinement.

Crystal no.	Approximate size [µm]	Angular range [°]	Rotation per frame [°]	Exposure time [s]	Total exposure [s]	Frames measured	Frames used
1	1.6 x 1.4 x 0.9	−60 to +40	0.5	0.5	100	200	all
2	1.6 x 1.2 x 0.6	−60 to +60	0.5	0.5	120	240	all
3	2.4 x 1.2 x 0.7	−50 to +50	0.5	0.5	100	100	all
4	1.4 x 1.0 x 0.9	−60 to +60	0.5	0.5	120	240	all
5	0.9 x 0.7 x 0.5	−40 to +40	0.5	0.5	80	160	all
6	0.5 x 0.4 x 0.3	−50 to +50	0.5	0.5	100	200	all
7	0.3 x 0.2 x 0.2	−60 to +50	0.5	0.5	110	220	all
8	1.0 x 0.8 x 0.6	−50 to +50	0.5	0.5	100	200	all

Table II.3.6. 3D ED data collection details for the CHZ·NAM cocrystals used in refinement.

Crystal no.	Approximate size [µm]	Angular range [°]	Rotation per frame [°]	Exposure time [s]	Total exposure [s]	Frames measured	Frames used
1	1.0 x 0.6 x 0.6	−50 to +60	0.5	0.5	110	220	1-109
2	0.8 x 0.4 x 0.3	−60 to +60	0.5	0.5	120	240	1-154
3	0.7 x 0.7 x 0.6	−50 to +50	0.5	0.5	100	200	1-196
4	0.2 x 0.2 x 0.2	−50 to +50	0.5	0.5	100	200	1-180
5	0.6 x 0.6 x 0.5	−60 to +60	0.5	0.5	120	240	1-205
6	0.9 x 0.6 x 0.5	−50 to +50	0.5	0.5	100	200	1-98
7	0.3 x 0.3 x 0.2	−60 to +60	0.5	0.5	120	240	1-194
8	0.4 x 0.2 x 0.2	−70 to +40	0.5	0.5	110	220	1-205

Table II.3.7. QTAIM Parameters of CHZ Parent (Cl15) molecule.

BCP	Interaction	ρ (a.u.)	∇²ρ (a.u.)	H(r) (a.u.)	|V(r)|/G(r)	Sign(λ₂)ρ (a.u.)
CP 99	Cl···H	0.00285	0.00931	+0.00054	0.696	-0.00285
CP 107	Cl···O	0.00512	0.02347	+0.00146	0.669	-0.00512
CP 119	Cl···H	0.00489	0.01541	+0.00078	0.746	-0.00489

Table II.3.8. QTAIM Parameters for CHZ·NAM (Cl15 / Cl35 Sites) cocrystal.

BCP	Interaction	ρ (a.u.)	∇²ρ (a.u.)	H(r) (a.u.)	|V(r)|/G(r)	Sign(λ₂)ρ (a.u.)
CP 148	Cl···Cl	0.00409	0.01382	+0.00082	0.689	-0.00409
CP 152	Cl···Cl	0.00409	0.01382	+0.00082	0.689	-0.00409
CP 159	Cl···H	0.00591	0.01821	+0.00088	0.761	-0.00591
CP 167	Cl···Cl	0.00398	0.01365	+0.00082	0.685	-0.00398
CP 175	Cl···H	0.00591	0.01821	+0.00088	0.761	-0.00591

Table II.3.9. QTAIM Parameters for CHZ·CBZ (Cl45) cocrystal.

BCP	Interaction	ρ (a.u.)	∇²ρ (a.u.)	H(r) (a.u.)	|V(r)|/G(r)	Sign(λ₂)ρ (a.u.)
CP 174	Cl···H	0.00293	0.00936	+0.00055	0.694	-0.00293
CP 175	Cl···H	0.00306	0.01001	+0.00057	0.708	-0.00306
CP 190	Cl···Cl	0.00542	0.01775	+0.00094	0.733	-0.00542

References for appendix II.3

(1) Kolodziejski, W.; Klinowski, J. Kinetics of Cross-Polarization in Solid-State NMR: A Guide for Chemists. Chem. Rev. 2002, 102 (3), 613–628.

(2) Fung, B. M.; Khitrin, A. K.; Ermolaev, K. An Improved Broadband Decoupling Sequence for Liquid Crystals and Solids. J. Magn. Reson. 2000, 142 (1), 97–101.

(3) Feike, M.; Demco, D. E.; Graf, R.; Gottwald, J.; Hafner, S.; Spiess, H. W. Broadband Multiple-Quantum NMR Spectroscopy. J. Magn. Reson. A 1996, 122 (2), 214–221.

(4) O'Dell, L. A.; Schurko, R. W. QCPMG Using Adiabatic Pulses for Faster Acquisition of Ultra-Wideline NMR Spectra. Chem. Phys. Lett. 2008, 464 (1), 97–102.

(5) O'Dell, L. A. The WURST Kind of Pulses in Solid-State NMR. Solid State Nucl. Magn. Reson. 2013, 55–56, 28–41.

II.4 Supporting Information for Chapter 8

ETS-NOCV Analysis: Qualitative and Quantitative Insights into Bonding

The ETS-NOCV (Extended Transition State-Natural Orbitals for Chemical Valence)[1] method provides a powerful tool for visualizing and quantifying chemical bonding interactions in molecular systems. This approach combines NOCV, which highlights the redistribution of electron density upon bond formation, with ETS, enabling the decomposition of total interaction energy (ΔE_{total}) into its contributing components. Specifically, ΔE_{orb}, the orbital interaction energy, quantifies the extent of electronic contributions to bonding, including both sigma (σ) donation from the Lewis base (nucleophile) to the Lewis acid (σ-hole), and pi (π) back-donation from the Lewis acid to the Lewis base.

The NOCV analysis visualizes regions of electron density accumulation (positive values) and depletion (negative values), illustrating the flow of electron density upon bond formation. By combining NOCV with ETS, the method provides a comprehensive understanding of bonding interactions, integrating qualitative insights from electron density maps with quantitative energy contributions.[2] The total interaction energy can be expressed as:

$$\Delta E_{\text{total}} = \Delta E_{\text{int}} + \Delta E_{\text{orb}} + \Delta E_{\text{Pauli}} + \Delta E_{\text{prep}} + \Delta E_{\text{elast}}$$

where each term represents a specific contribution to the bonding. This combined approach is particularly useful for exploring non-covalent interactions, such as chalcogen and halogen bonding, offering a detailed characterization of both their energetic and orbital nature.

The NCI analyses and orbital visualizations in Figure S1, combined with these quantitative ΔE values, thus demonstrate how the nature and strength of halogen bonding modulate the electron density distribution, influencing the bonding environment in these cocrystalline systems.

IQA data: Quantitative Insights into Interactions

Interacting Quantum Atoms (IQA) energy decomposition analysis was performed using the ADF software package at the PBE0/TZ2P level of theory. The data shown in Table S1 were extracted from the "Interatomic Contributions" section of the output files. Listed are selected pairwise interactions from compound **1**, cocrystals **1a**, **1b**, and **2b**, including interaction distances (in Å), energy components (in Hartree and kcal/mol), and the corresponding covalent and non-covalent contributions. Percent covalency was estimated by the ratio of the absolute covalent component to the total interaction energy.

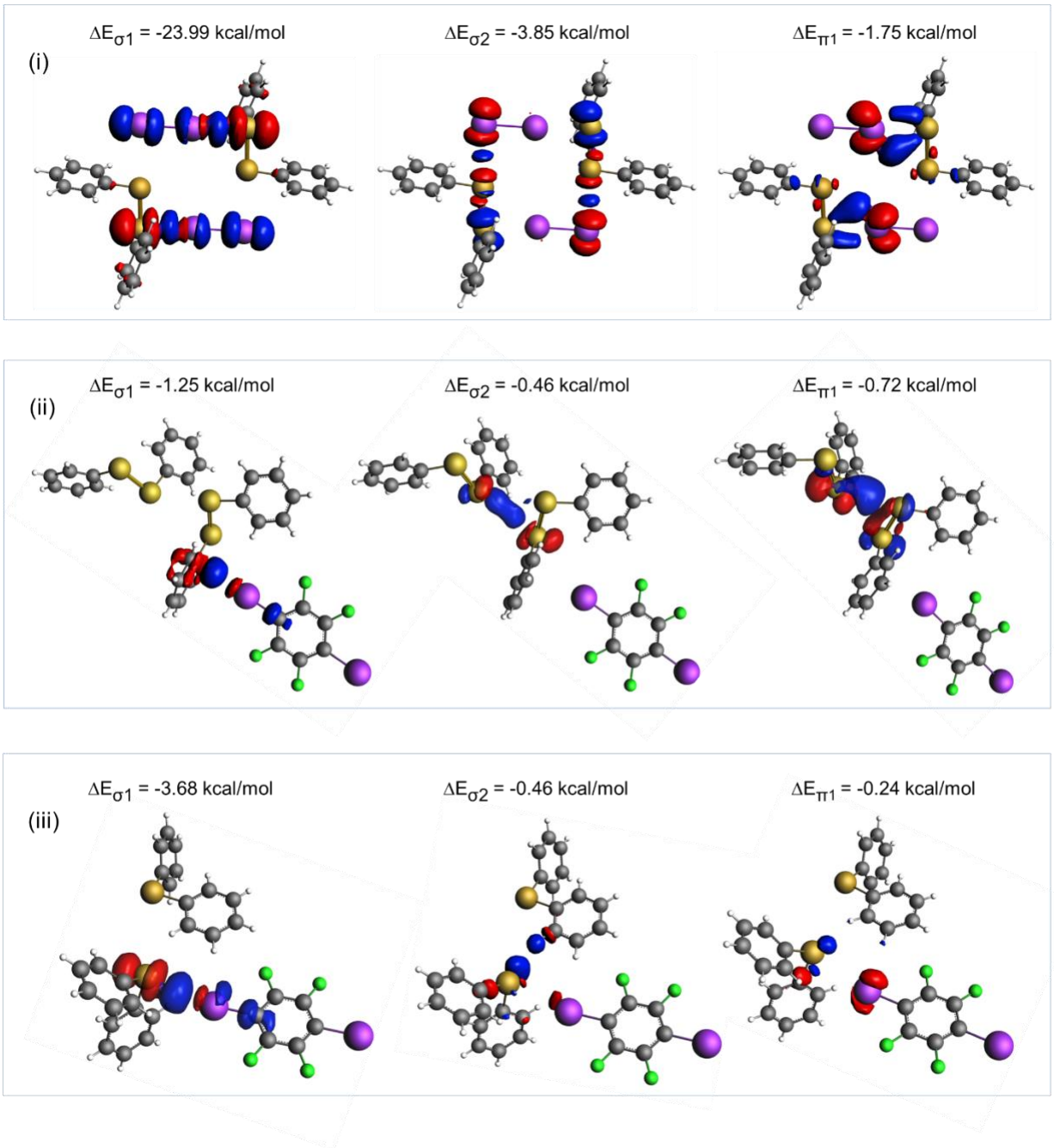


Figure S1. Visualization of the natural orbitals for chemical valence (NOCV) interactions in three cocrystals, analyzed using the ETS-NOCV method to quantify key orbital contributions to intermolecular interactions. Each diagram depicts the most significant NOCV orbital pairs associated with chalcogen and halogen bonding, with corresponding orbital interaction energies (ΔE_{orb}) displayed above each visualization. (i) **1a**, showing electron depletion around the Se–Se bond and accumulation toward the iodine acceptor, supporting the observed bond elongation; (ii) **1b**, illustrating weaker electron redistribution due to π-system interaction; and (iii) **2b**. The orbital interactions are color-coded, with red and blue lobes representing regions of electron accumulation and depletion, respectively.

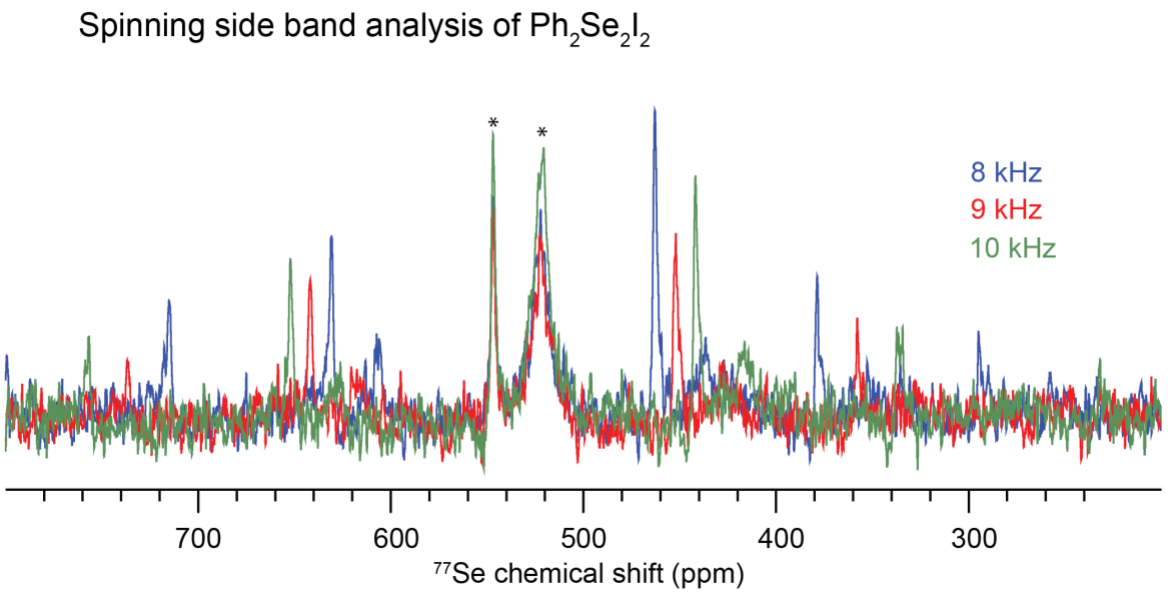


Figure S2. The 1D $^{1}H \rightarrow ^{77}Se$ CPMAS NMR spectra of **1a** at different spinning speeds. The isotropic chemical shifts are observed at 522 ppm and 547 ppm. The peak at 522 ppm is broad, while the peak at 547 ppm is sharp.

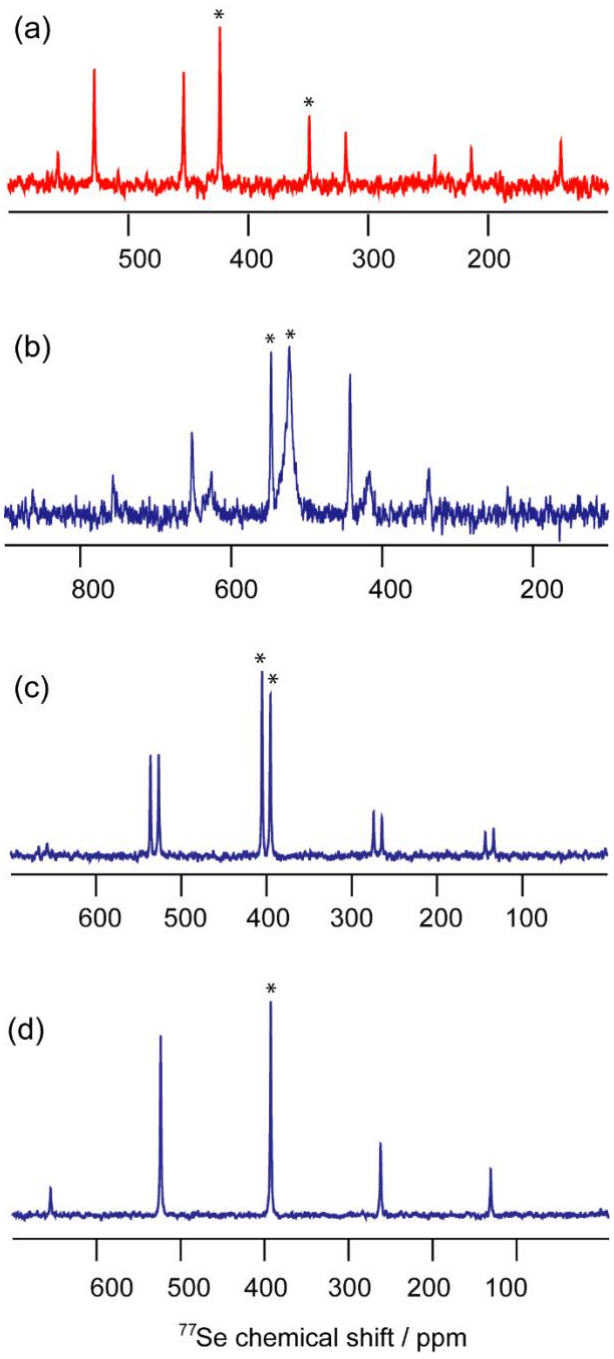


Figure S3. Experimental $^{1}H \rightarrow {}^{77}Se$ CP/MAS NMR spectra of diphenyldiselenide (**1**) and the studied cocrystals, collected at a spinning speed of 10 kHz. Isotropic peaks are indicated with asterisks.

High spinning frequency ^{1}H and ^{13}C SSNMR data

Single pulse ^{1}H SSNMR spectra were recorded using 90° radiofrequency (rf) pulses with a ^{1}H nutation frequency (ν_H) of 185 kHz. Data acquisition involved the accumulation of 16 transients with a relaxation delay (τ_{relax}) of 2.0 seconds.

The ^{13}C spectra were recorded by the $^{1}H \rightarrow {}^{13}C$ CP at the double quantum Hartmann−Hahn condition,$^{1}\nu_H + \nu_C = \nu_r$, which involved ramped CP of $\nu_H = 20 \pm 5$ kHz for ^{1}H ($\nu_C = 40$ kHz), a 1.5 μs 90° ^{1}H pulse, and spinal-64 ^{1}H decoupling[2] at $\nu_H = 150$ kHz.

The double-quantum to single-quantum (DQ–SQ) ^{1}H NMR correlation spectra were recorded using the 2D NMR protocol in the article by Fieke *et.al*.[3] This experiment probes dipolar couplings between ^{1}H nuclei, allowing for the identification of proximities and interactions between protons within the structure. Double-quantum coherence (2QC) excitation and reconversion were achieved using the BABA dipolar recoupling scheme, which spans two rotor periods ($2\tau_r$). This provided 2Q excitation (τ_{exc}) and reconversion (τ_{rec}) intervals of $\tau_{exc}=\tau_{rec}=2\tau_r=33.33$ μs. The BABA scheme ensures efficient recoupling under magic angle spinning conditions, enabling the generation and observation of double-quantum coherences.

The ^{1}H nutation frequency was $\nu_H \approx 185$ kHz, corresponding to 90° dipolar recoupling pulses with a duration of 1.35 μs. This setup ensures precise manipulation of the proton dipolar couplings, crucial for obtaining high-quality 2D NMR spectra.

The 2D NMR acquisition parameters included a τ_{relax} of 2.0 s, with 48 (t_1) × 512 (t_2) time points acquired. Dwell times were set to $\Delta t_1=2\tau_r$ and $\Delta t_2=33.3$ μs, ensuring sufficient resolution in both dimensions. Each t_1 value accumulated 32 transients to enhance the signal-to-noise ratio. The 2D data sets were zero-filled to 256 × 2048 points to improve digital resolution, and apodization

with an exponential Lorentzian broadening of 50 Hz full width at half maximum (FWHM) was applied in both dimensions.

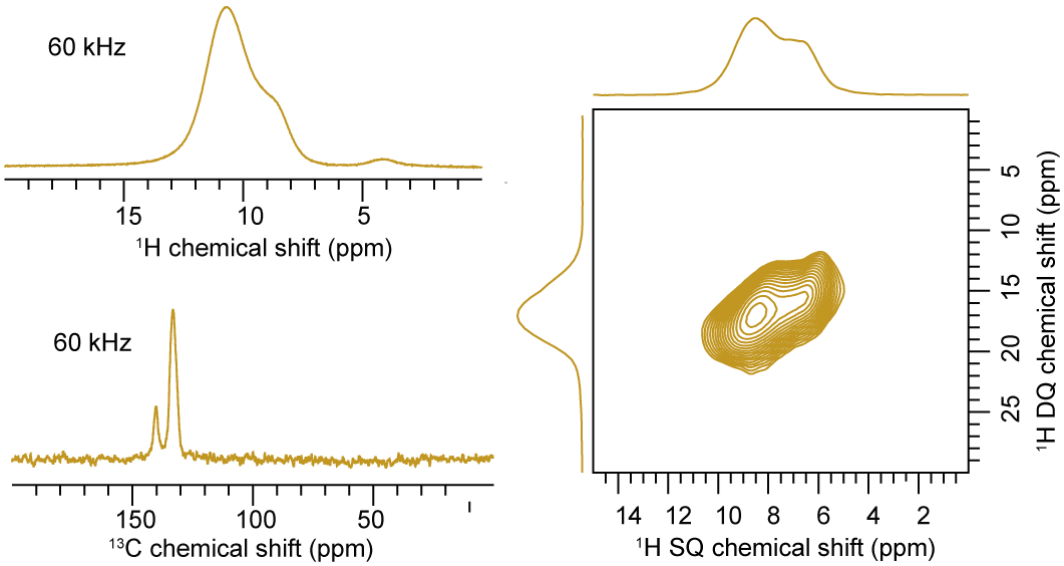


Figure S4. ^{1}H one pulse, ^{13}C CPMAS, and ^{1}H-^{1}H BABA 2D spectrum of **1a**, collected at a spinning speed of 60 kHz. The spectrum reveals correlations between neighboring protons within the aromatic ring.

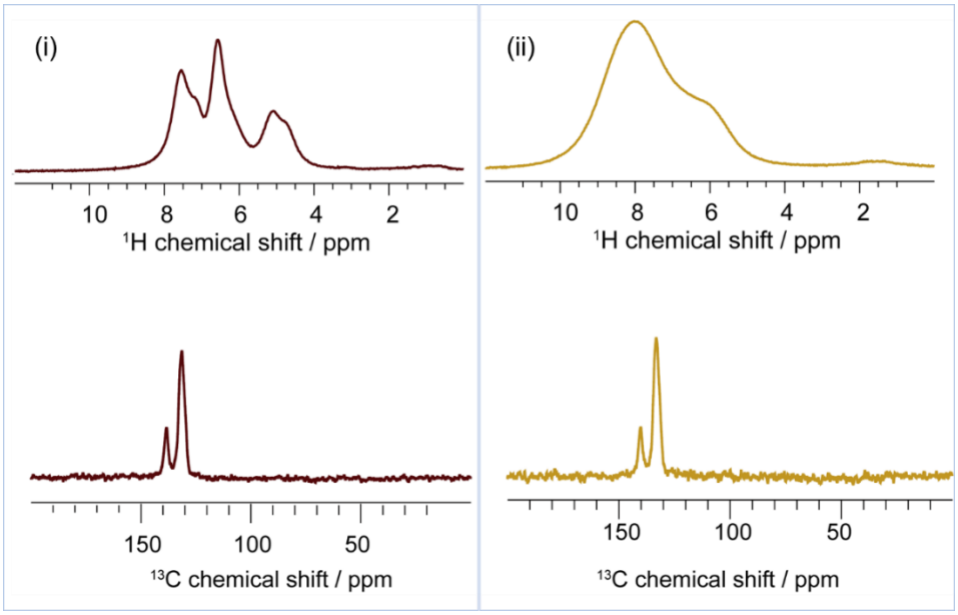


Figure S5. ^{1}H one pulse and ^{13}C CPMAS NMR spectra of (i) Ph_2Se_2 (**1**), and (ii) **1a** collected at a spinning speed of 60 kHz.

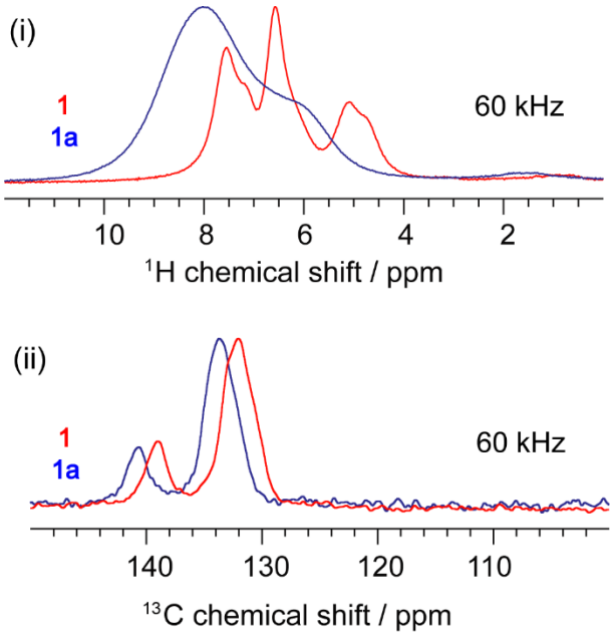


Figure S6. Comparison of the high spinning frequency (i) ^{1}H single-pulse and (ii) ^{13}C CP/MAS solid-state NMR spectra of compound **1** and its cocrystal, **1a**.

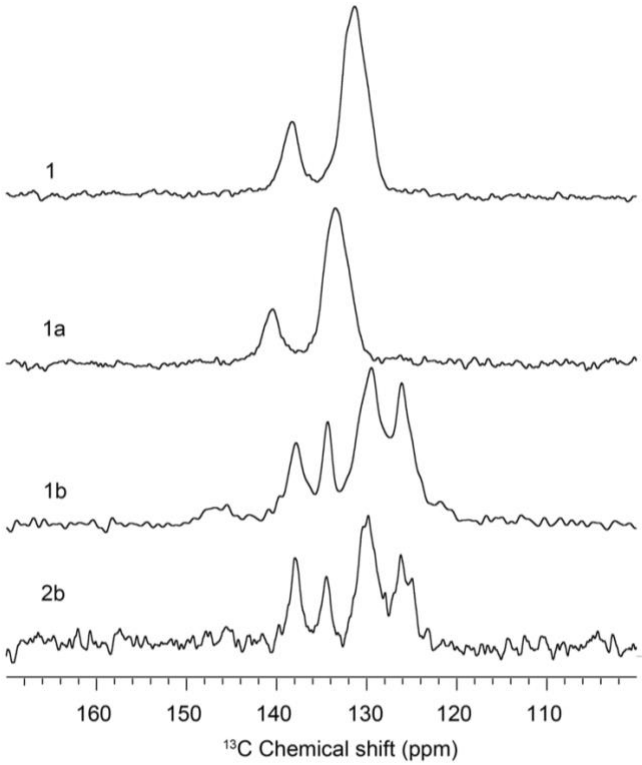


Figure S7. The ^{13}C CP/MAS NMR spectra of diphenyldiselenide (**1**), and cocrystals studied herein, collected at 60 kHz spinning speed. The ^{13}C peaks appearing from the *p*-DITFB moiety are evident in the spectra of **1b** and **2b**.

SCXRD

The crystallographic data for **1a** and **1b** reveal significant structural variations induced by different acceptors (Table S2). Ph_2Se_2 (**1**) crystallizes in the orthorhombic space group $P2_12_12_1$, characterized by a simple and highly symmetrical unit cell with dimensions of a = 5.65 Å, b = 8.29 Å, and c = 24.11 Å. In contrast, its cocrystal with I_2, **1a**, adopts a triclinic structure within the *P*-1 space group, indicative of a less symmetrical arrangement. The unit cell parameters (a = 9.57 Å, b = 9.84 Å, c = 9.98 Å) and the significant deviations of angles from 90° (α = 116.00°, β = 91.18°, γ = 115.57°) indicate a change in packing arrangement associated with the incorporation of iodine, resulting in a more complex molecular environment within the crystal lattice. Similarly, the introduction of *p*-DITFB in **1b** results in a monoclinic structure with the $P2_1/c$ space group, where the unit cell dimensions are a = 10.11 Å, b = 5.67 Å, and c = 26.65 Å, with the β angle slightly deviating from orthogonality at 94.61°, while α and γ remain at 90°. This slight monoclinic distortion indicates that *p*-DITFB influences the molecular packing differently than iodine. These structural changes highlight how the incorporation of different molecules can significantly alter the crystallographic symmetry and unit cell parameters of **1**, leading to variations in physical properties that are critical for potential applications.

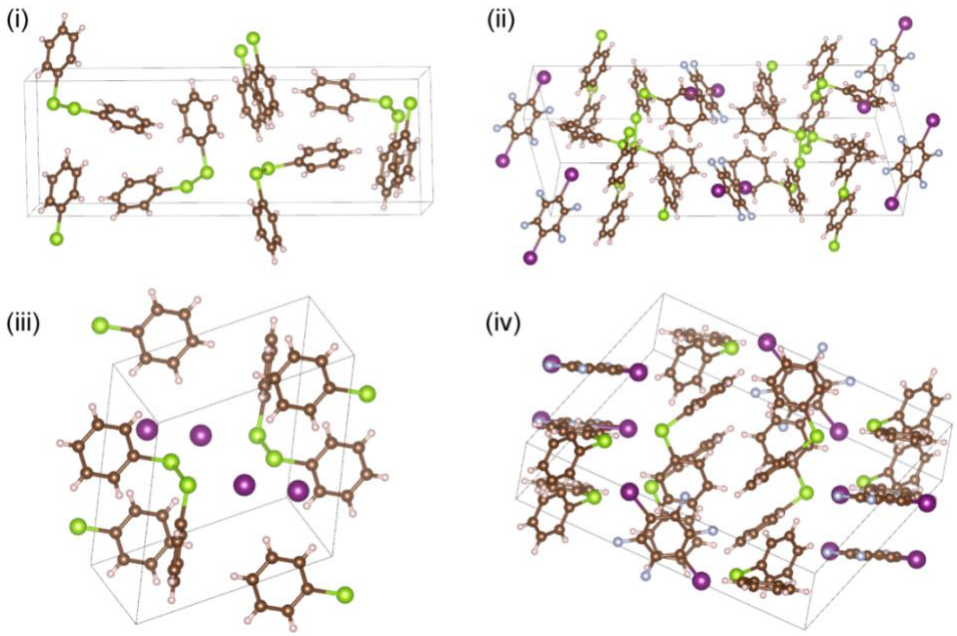


Figure S7. Crystal packing diagrams of **1** (i), and cocrystals **1a** (ii), **1b** (iii), **2b** (iv).

Table S1. Crystallographic parameters of Ph_2Se_2 and cocrystals studied herein.

compound	space group	*a* / Å	*b* / Å	*c* / Å	α / º	β / º	γ / º
1	$P2_12_12_1$	5.65	8.29	24.11	90.00	90.00	90.00
1a	*P*-1	9.57	9.84	9.98	116.00	91.18	115.57
1b	$P2_1/c$	10.11	5.67	26.65	90.00	94.61	90.00
2b	$P2_1/n$	13.01	6.15	18.17	90.00	101.80	90.00

Table S2. IQA for Key Se–Se, Se–I, Se–H, and π-Interactions in the Investigated Cocrystals.

Parameter	**1**[a]		**1a**			**1b**			**2b**	
	Se1–Se2	Se1–Se25	Se1–Se2	Se4–I2	I1–Se1	Se1–Se2	Se1–Se4	C9–I (π)	Se1–I24	Se1–H50
Distance (Å)	2.307	7.201	2.347	3.588	2.990	2.314	3.752	3.566	3.550	3.053
VeN[b]	-263.380	-160.264	-258.965	-264.305	-317.986	-262.405	-162.657	-49.406	-267.081	-5.868
VNe[c]	-263.014	-160.064	-258.339	-265.805	-317.966	-262.651	-162.576	-46.956	-267.302	-6.614

Vee (Coulomb)[d]	261.295	159.796	256.724	264.350	317.202	260.648	162.209	49.162	265.869	6.585
VNN[e]	265.127	160.532	260.605	265.760	318.748	264.435	163.025	47.188	268.520	5.894
VCoulomb (Total)[f]	0.0277	0.0003	0.0248	0.0001	-0.0013	0.0266	0.0010	-0.0114	0.0048	-0.0032
Vee (Exchange)[g]	-0.2492	-0.0104	-0.2310	-0.0217	-0.0829	-0.2476	-0.0102	-0.0065	-0.0269	-0.0053
Vee (Total)[h]	261.046	159.786	256.493	264.328	317.119	260.401	162.198	49.155	265.842	6.579
Einter (kcal/mol)[i]	-138.99	-6.31	-129.37	-13.56	-52.87	-138.65	-5.78	-11.24	-13.9	-5.32
Covalent part (kcal/mol)	-156.35	-6.51	-144.94	-13.63	-52.03	-155.36	-6.41	-4.08	-16.9	-3.33
Covalent part (%)	112.50%	103.10%	112.00%	100.50%	98.40%	112.10%	110.70%	36.30%	121.60%	62.60%
Non-Covalent part (kcal/mol)	17.36	0.19	15.56	0.07	-0.84	16.71	0.63	-7.17	3.00	-1.99
Non-Covalent part (%)	-12.50%	-3.10%	-12.00%	-0.50%	1.60%	-12.10%	-10.70%	63.70%	-21.60%	37.40%

a: The numbering are from the cif file from the crystallographic data. The optimized cife file is deposited align other manuscript data. All other numbering is corresponded to the Figure 7 in the main text.

b: Coulomb interaction between the electrons of A and the nucleus of B in Hartree

c: Coulomb interaction between the nucleus of A and the electrons of B in Hartree

d: Coulomb interaction between the electrons of A and B in Hartree

e: Coulomb interaction between the nuclei of A and B in Hartree

f: VeN+VNe+Vee(Coulomb)+VNN in Hartree

g: exchange interaction between the electrons of A and B in Hartree

h: Vee(Coulomb)+Vee(Exchange) in Hartree

i: total interaction energy between A and B, i.e. VCoulomb(total)+Vee(exchange) in kcal/mol

TEM image

High-resolution transmission electron microscopy (HRTEM) images were acquired using a Thermo Fisher Scientific (TFS) Talos F200X scanning/transmission electron microscope (S/TEM). This instrument offers a lattice-fringe resolution of 0.14 nm and operates at an accelerating voltage of 200 kV. Imaging was performed with a CETA 16M camera. The samples were prepared by placing a drop of diluted particle solution onto a holey carbon film supported by a copper grid, followed by drying overnight at room temperature (298 K).

TEM images of compound **2b** prepared by mechanochemical ball milling. The observed particle sizes range from ~1 × 2 × 1.5 µm to 3 × 5 × 2 µm and 3 × 2 × 4 µm, confirming the formation of micron-sized crystallites as expected from solid-state synthesis. These images provide direct evidence of the bulk morphology of the materials following the ball-milling process.

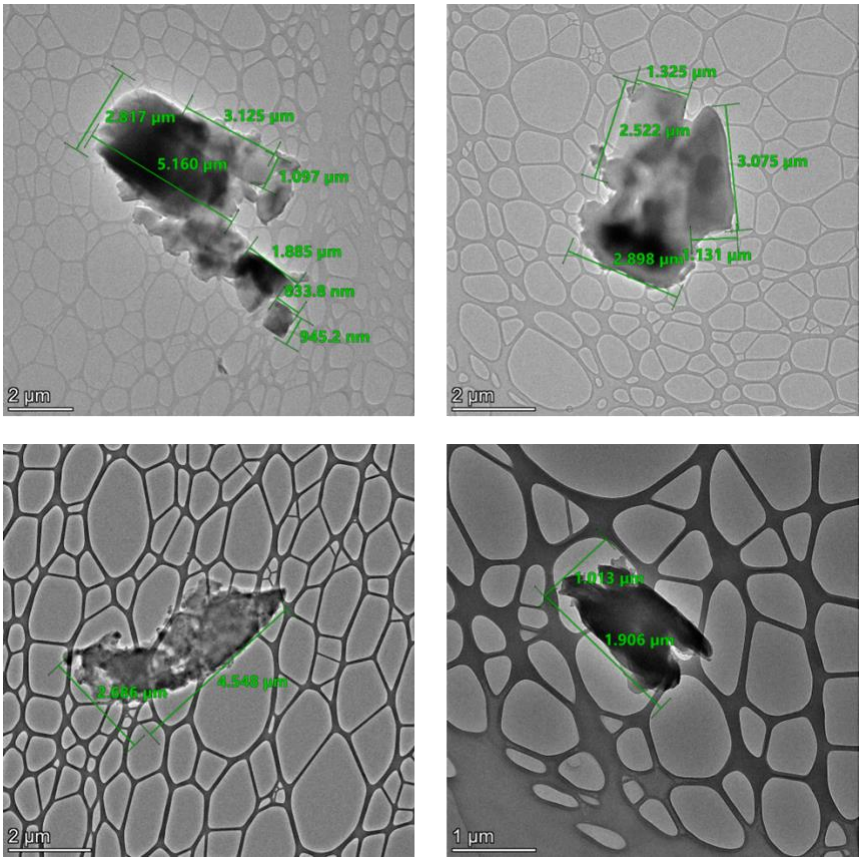


Figure S8. The TEM images of the 2b cocrystal, captured from various orientations showing the crystal size.

Reference

(1) Mitoraj, M.; Michalak, A. Natural Orbitals for Chemical Valence as Descriptors of Chemical Bonding in Transition Metal Complexes. *Journal of Molecular Modeling* **2007**, *13* (2), 347–355.

(2) Mitoraj, M. P.; Michalak, A.; Ziegler, T. A Combined Charge and Energy Decomposition Scheme for Bond Analysis. *J. Chem. Theory Comput.* **2009**, *5* (4), 962–975.

(3) Feike, M.; Demco, D. E.; Graf, R.; Gottwald, J.; Hafner, S.; Spiess, H. W. Broadband Multiple-Quantum NMR Spectroscopy. *Journal of Magnetic Resonance, Series A* **1996**, *122* (2), 214–221.

II.5 Supporting Information for Chapter 9

1: 1a(i), (p-DITFB)·2(TMP)[1]:

1-1: RAM mechanochemistry synthesis

241 mg (0.5 mmol) 1,4-diiodotetrafluorobenzene (*p*-DITFB) as halogen bond donor, 82 mg (0.5 mmol) 2,3,5,6-tetramethypyrazine (TMP) as an acceptor, and 260 µL chloroform were added to a 1-dram glass vial and securely mounted within a lab-built sample holder and positioned on the PharmaRAM 1 resonant acoustic mixer. The sample was oscillated for 50 minutes at an acceleration of 80g.

1.2: Ball milling preparation

The halogen bond donor, *p*-DITFB (241 mg, 0.5 mmol), and the halogen bond acceptor, TMP (82 mg, 0.5 mmol), were combined in a 10 mL stainless steel milling jar, with 50 µL of chloroform as a liquid additive. Subsequently, ball milling was conducted using a Retsch MM 400 ball mill at a frequency of 30 Hz for 45 minutes at room temperature. The milling process employed two stainless steel grinding balls with a diameter of 5 mm.

1.3: PXRD results

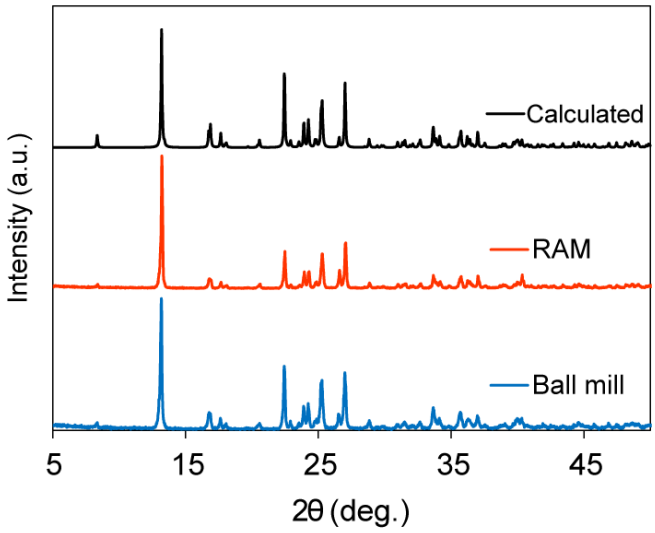


Figure S1. Experimental diffractograms for ball milled and RAM products, and calculated diffractogram for cocrystal **1a(i)**, (*p*-DITFB)·2(TMP).

1-3: ^{13}C CP/MAS SSNMR results

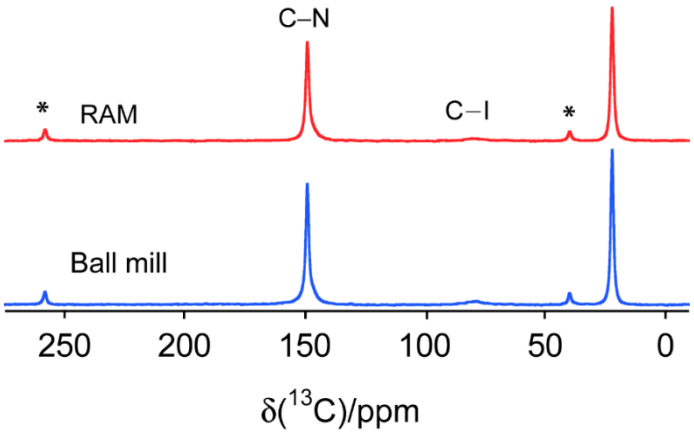


Figure S2. ^{13}C solid-state NMR spectra of cocrystal **1a(i)**, (*p*-DITFB).2(TMP): the ball mill product is depicted in blue (lower); RAM product in red (upper). The labels denote the C-N and C-I carbons of TMP and *p*-DITFB, respectively. The asterisks denote spinning sidebands.

2: 1a(ii), 4(p-DITFB)·1.5(TMP)[2]

2.1: RAM mechanochemistry synthesis

402 mg (1 mmol) 1,4-diiodotetrafluorobenzene (*p*-DITFB) as halogen bond donor and 68 mg (0.5 mmol) 2,3,5,6-tetramethypyrazine (TMP) as an acceptor were added to a 1-dram glass vial and securely mounted within a lab-built sample holder and positioned on the PharmaRAM 1 resonant acoustic mixer. The sample was oscillated for 45 minutes at an acceleration of 80g.

2.2: PXRD results

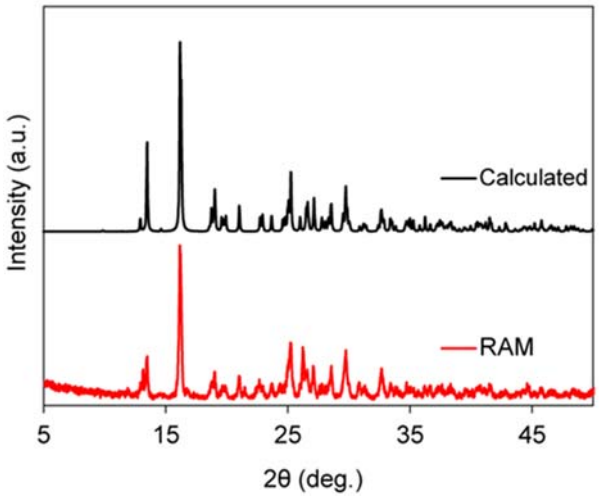


Figure S3. Diffractogram for the RAM product, and calculated diffractogram for cocrystal **1a(ii),** 4(*p*-DITFB)·1.5(TMP).

2.3: ^{13}C CP/MAS SSNMR results

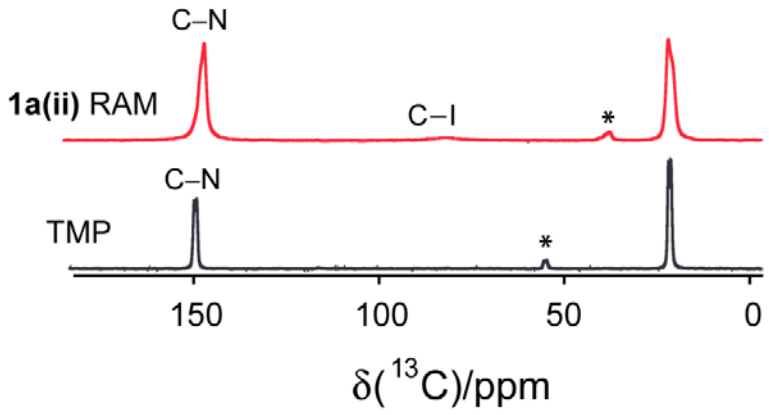


Figure S4. ^{13}C solid-state NMR spectra of XB acceptor TMP in black (lower) and cocrystal **1a(ii),** 4(*p*-DITFB)·1.5(TMP), prepared by RAM in red (upper). The labels denote the C-N and C-I carbons of TMP and *p*-DITFB, respectively. The asterisks denote spinning sidebands.

3: 2a, (*sym*-TFTIB)·(TMP)^3

3.1: RAM mechanochemistry synthesis

357 mg (0.7 mmol) 1,3,5-trifluoro-2,4,6-triiodobenzene (*sym*-FTIB) as halogen bond donor, 95 mg (0.7 mmol) 2,3,5,6-tetramethypyrazine (TMP) as an acceptor, and 45 µL THF were added to a 1-dram glass vial and securely mounted within a lab-built sample holder and positioned on the PharmaRAM 1 resonant acoustic mixer. The sample was oscillated for 50 minutes at an acceleration of 80g.

3.2: Ball milling preparation

The halogen bond donor, *sym*-TFTIB (357 mg, 0.7 mmol), and the halogen bond acceptor, TMP (95 mg, 0.7 mmol), were combined in a 10 mL stainless steel milling jar, supplemented with 23 µL of THF as a liquid additive. Subsequently, ball milling was conducted using a Retsch MM 400 ball mill at a frequency of 30 Hz for 40 minutes at room temperature. The milling process employed two stainless steel grinding balls with a diameter of 5 mm.

3.3: PXRD results

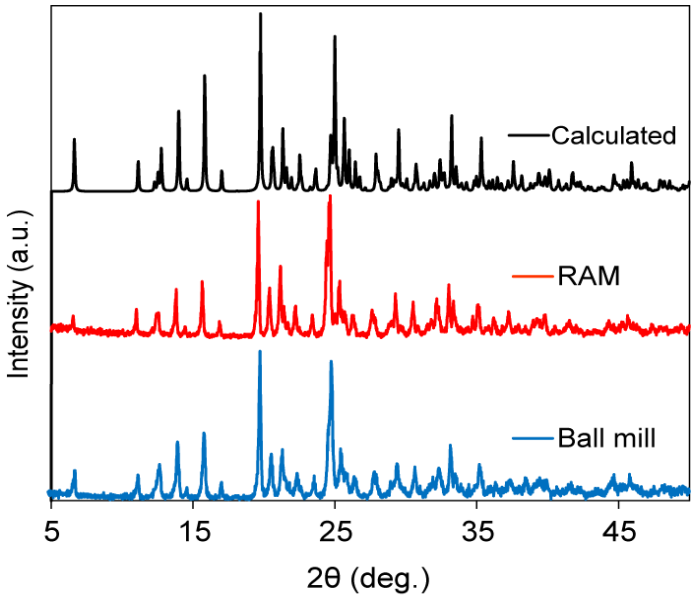


Figure S5. Diffractograms for ball mill and RAM products, and calculated powder X-ray diffraction pattern for cocrystal **2a,** (*sym*-TFTIB)·(TMP).

3.4: ^{13}C CP/MAS SSNMR results

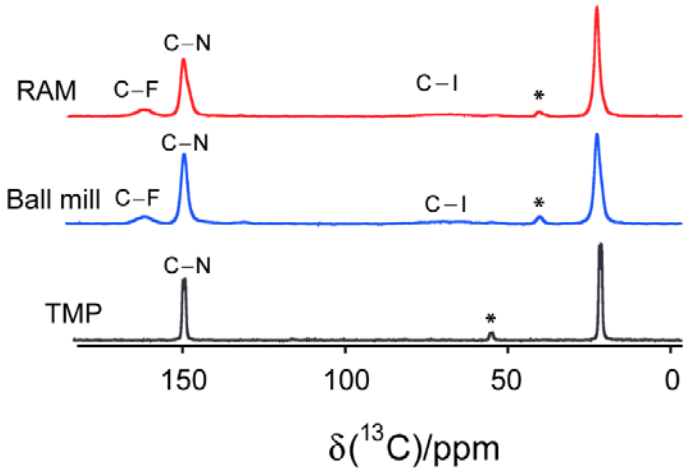


Figure S6. ^{13}C solid-state NMR spectra of XB acceptor TMP in black (lower) and cocrystal **2a,** (*sym*-TFTIB)·(TMP), prepared by ball milling in blue (middle), and by RAM in red (upper). The labels denote the C-N carbons of TMP, and C-I and C-F carbons of *sym*-TFTIB. The asterisks denote spinning sidebands.

4: 1b, (*p*-DITFB)·2(DMAP)[4]

4.1: RAM mechanochemistry synthesis

321 mg (0.8 mmol) 1,4-diiodotetrafluorobenzene (p-DITFB) as halogen bond donor and 196 mg (1.6 mmol) 4-dimethylaminopyridine (DMAP) as an acceptor were added to a 1-dram glass vial and securely mounted within a lab-built sample holder and positioned on the PharmaRAM 1 resonant acoustic mixer. The sample was oscillated for 45 minutes at an acceleration of 80g.

4.2: Ball milling preparation

The halogen bond donor, *p*-DITFB (321 mg, 0.8 mmol), and the halogen bond acceptor, DMAP (196 mg, 1.6 mmol), were combined in a 10 mL stainless steel milling jar. Subsequently, ball milling was conducted using a Retsch MM 400 ball mill at a frequency of 30 Hz for 30 minutes at room temperature. The milling process employed two stainless steel grinding balls with a diameter of 5 mm.

4.3: PXRD results

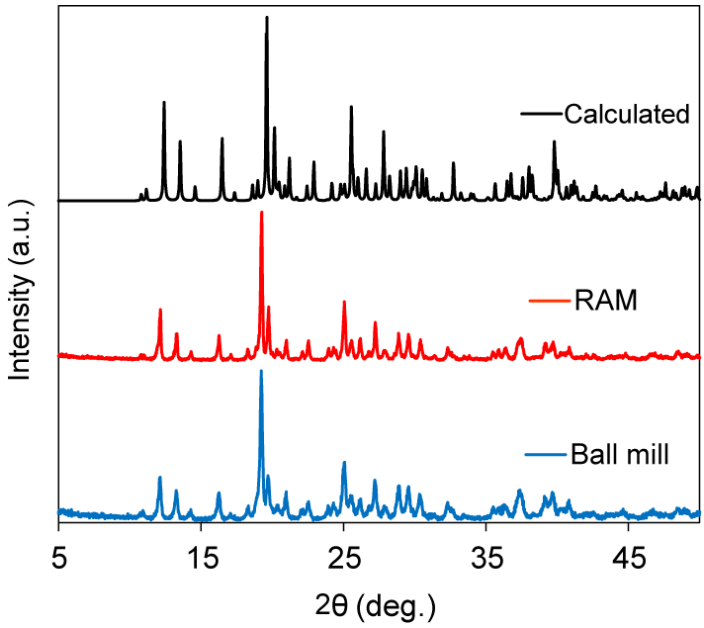


Figure S7. Diffractograms for ball mill and RAM products, and calculated powder X-ray diffraction pattern for cocrystal **1b,** (*p*-DITFB)·2(DMAP).

4.4: ^{13}C CP/MAS SSNMR results

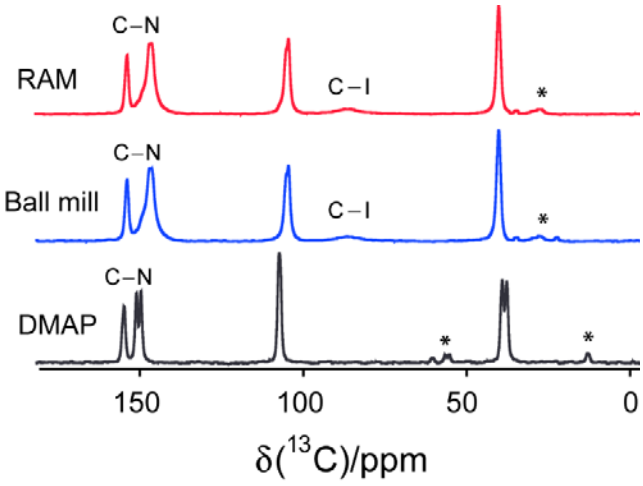


Figure S8. ^{13}C solid-state NMR spectra of XB acceptor DMAP in black (lower) and cocrystal **1b,** (*p*-DITFB)·2(DMAP) prepared by ball milling in blue (middle), and by RAM in red (upper). The labels denote the C-N and C-I carbons of DMAP and *p*-DITFB, respectively. The asterisks denote spinning sidebands.

5: 2b, (*sym*-TFTIB)·3(DMAP)[5]

5.1: RAM mechanochemistry synthesis

255 mg (0.5 mmol) 1,3,5-trifluoro-2,4,6-triiodobenzene (*sym*-TFTIB) as halogen bond donor and 183 mg (1.5 mmol) 4-dimethylaminopyridine (DMAP) as an acceptor were added to a 1-dram glass vial and securely mounted within a lab-built sample holder and positioned on the PharmaRAM 1 resonant acoustic mixer. The sample was oscillated for 50 minutes at an acceleration of 80g.

5.2: Ball milling preparation

The halogen bond donor, *sym*-TFTIB (255 mg, 0.5 mmol), and the halogen bond acceptor, DMAP (183 mg, 1.5 mmol), were added to a 10 mL stainless steel milling jar. Subsequently, ball milling was conducted using a Retsch MM 400 ball mill at a frequency of 30 Hz for 45 minutes at room temperature. The milling process employed two stainless steel grinding balls with a diameter of 5 mm.

5.3: PXRD results

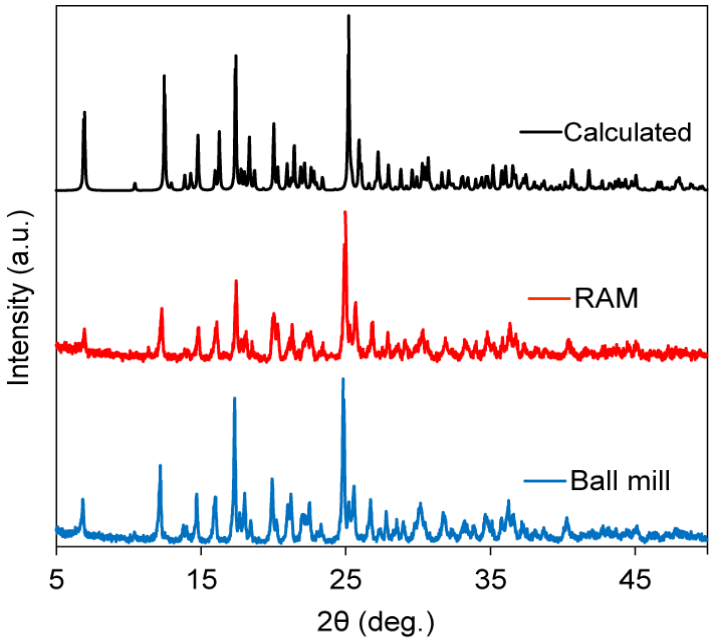


Figure S9. Diffractograms for ball mill and RAM products, and calculated powder X-ray diffraction pattern for cocrystal **2b,** (*sym*-TFTIB)·3(DMAP).

5.4: ^{13}C CP/MAS SSNMR results

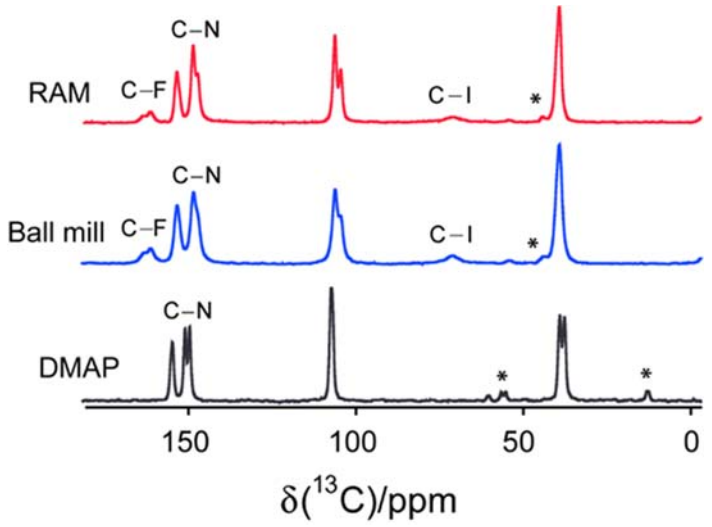


Figure S10. ^{13}C solid-state NMR spectra of XB acceptor DMAP in black (lower) and cocrystal **2b,** (*sym*-TFTIB)·3(DMAP) prepared by ball milling in blue (middle), and by RAM in red (upper). The labels denote the C-N carbons of DMAP, and C-I and C-F carbons of *sym*-TFTIB. The asterisks denote spinning sidebands.

6: 1c, 2(*p*-DITFB).(o-Phe)[1]

6.1: RAM mechanochemistry synthesis

321 mg (0.8 mmol) 1,4-diiodotetrafluorobenzene (*p*-DITFB) as halogen bond donor, 196 mg (1.6 mmol) 1,10-phenanthroline (o-Ph) as acceptor, and 35 µL chloroform were added were added to a 1-dram glass vial and securely mounted within a lab-built sample holder and positioned on the PharmaRAM 1 resonant acoustic mixer. The sample was oscillated for 50 minutes at an acceleration of 80g.

6.2: Ball milling preparation

The halogen bond donor, *p*-DITFB (241 mg, 0.6 mmol), and the halogen bond acceptor, o-Ph (108 mg, 0.6 mmol), were combined in a 10 mL stainless steel milling jar, supplemented with 18 µL of chloroform as a liquid additive. Subsequently, ball milling was conducted using a Retsch MM 400 ball mill at a frequency of 30 Hz for 45 minutes at room temperature. The milling process employed two stainless steel grinding balls with a diameter of 5 mm.

6.3: PXRD results

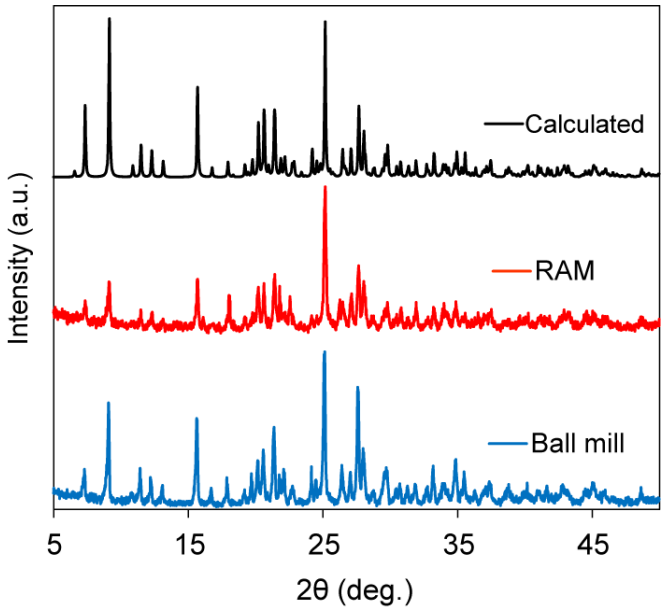


Figure S11. Diffractograms of ball mill and RAM products, and calculated powder X-ray diffraction pattern for cocrystal **1c,** 2(*p*-DITFB)·(o-Phe).

6.4: ^{13}C CP/MAS SSNMR results

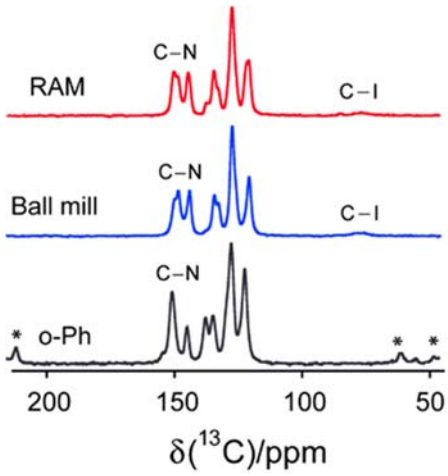


Figure S12. ^{13}C solid-state NMR spectra of XB acceptor o-Phe in black (lower) and cocrystal **1c,** 2(*p*-DITFB)·(o-Phe) prepared by ball milling in blue (middle), and by RAM in red (upper). The labels denote the C-N and C-I carbons of o-Phe and *p*-DITFB, respectively. The asterisks denote spinning sidebands.

7: 2c, (*sym*-TFTIB)·(o-Phe)^3

7.1: RAM mechanochemistry synthesis

255 mg (0.5 mmol) 1,3,5-trifluoro-2,4,6-triiodobenzene (*sym*-TFTIB) as halogen bond donor, 90 mg (0.5 mmol) 1,10-phenanthroline (o-Ph) as acceptor, and 35 µL THF were added were added to a 1-dram glass vial and securely mounted within a lab-built sample holder and positioned on the PharmaRAM 1 resonant acoustic mixer. The sample was oscillated for 50 minutes at an acceleration of 80g.

7.2: Ball milling preparation

The halogen bond donor, *sym*-TFTIB (255 mg, 0.5 mmol), and the halogen bond acceptor, o-Ph (90 mg, 0.5 mmol), were combined in a 10 mL stainless steel milling jar, supplemented with 18 µL of chloroform as a liquid additive. Subsequently, ball milling was conducted using a Retsch MM 400 ball mill at a frequency of 30 Hz for 45 minutes at room temperature. The milling process employed two stainless steel grinding balls with a diameter of 5 mm.

7.3: PXRD results

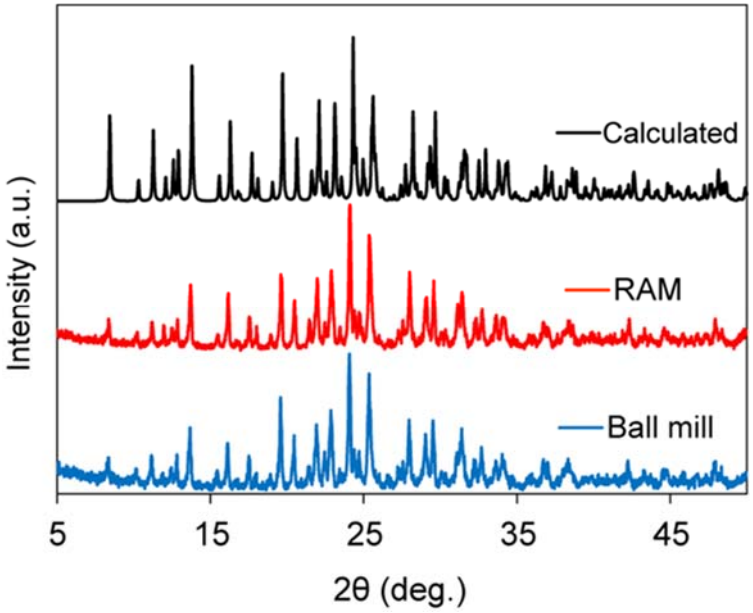


Figure S13. Diffractograms of ball mill and RAM products, and calculated powder X-ray diffraction pattern for cocrystal **2c,** (*sym*-TFTIB)·(o-Phe).

7.4: ^{13}C CP/MAS SSNMR results

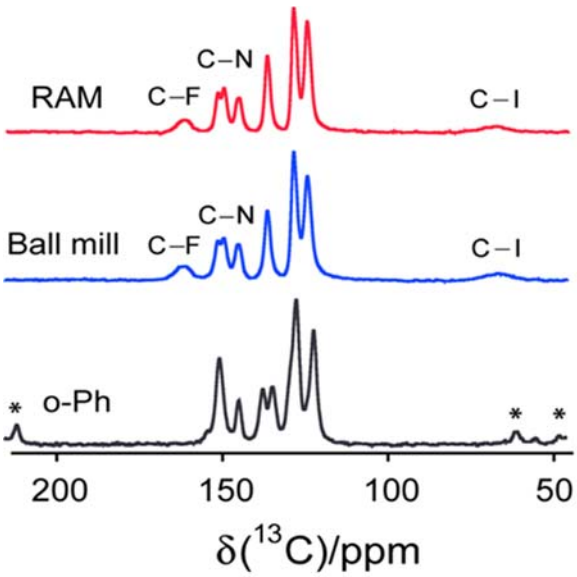


Figure S14. ^{13}C solid-state NMR spectra of XB acceptor o-Phe in black (lower) and cocrystal **2c,** (*sym*-TFTIB).(o-Phe) prepared by ball milling in blue (middle), and by RAM in red (upper). The labels denote the C-N carbons of o-Phe, and C-I and C-F carbons of *sym*-TFTIB. The asterisks denote spinning sidebands.

8: 1d, (*p*-DITFB)·(PheDON)[6]

8.1: RAM mechanochemistry synthesis

205 mg (0.5 mmol) 1,4-diiodotetrafluorobenzene (*p*-DITFB) as halogen bon donor, 105 mg (0.5 mmol) 1,10-phenanthroline-5,6-dione (PheDON) as acceptor, and 155 µL chloroform were added were added to a 1-dram glass vial and securely mounted within a lab-built sample holder and positioned on the PharmaRAM 1 resonant acoustic mixer. The sample was oscillated for 50 minutes at an acceleration of 80g.

8.2: Ball milling preparation

The halogen bond donor, *p*-DITFB (205 mg, 0.5 mmol), and the halogen bond acceptor, PheDON (105 mg, 0.5 mmol), were combined in a 10 mL stainless steel milling jar, supplemented with 31 µL of chloroform as a liquid additive. Subsequently, ball milling was conducted using a Retsch MM 400 ball mill at a frequency of 30 Hz for 30 minutes at room temperature. The milling process employed two stainless steel grinding balls with a diameter of 5 mm.

8.3: PXRD results

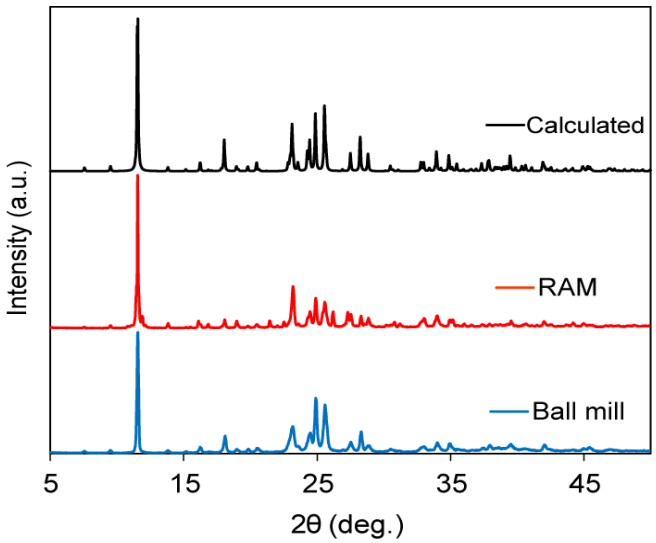


Figure S15. Diffractograms of ball mill and RAM products, and calculated powder X-ray diffraction pattern for cocrystal **1d,** (*p*-DITFB)·(PheDON).

8.4: ^{13}C CP/MAS SSNMR results

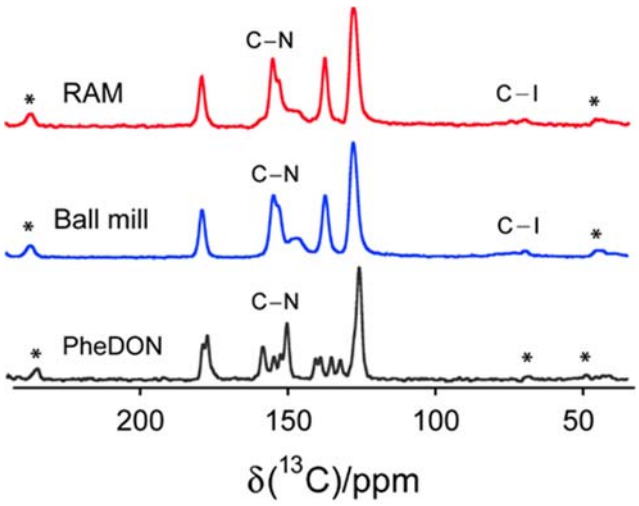


Figure S16. ^{13}C solid-state NMR spectra of XB acceptor o-Phe in black (lower) and cocrystal **1d,** (*p*-DITFB)·(PheDON) prepared by ball milling in blue (middle), and by RAM in red (upper). The labels denote the C-N and C-I carbons of PheDON and *p*-DITFB, respectively. The asterisks denote spinning sidebands.

9: 2d, (*sym*-TFTIB)·(PheDON)

9.1: RAM mechanochemistry synthesis

205 mg (0.5 mmol) 1,3,5-trifluoro-2,4,6-triiodobenzene (*sym*-TFTIB) as halogen bond donor, 105 mg (0.5 mmol) 1,10-phenanthroline-5,6-dione (PheDON) as acceptor, and 250 µL chloroform were added were added to a 1-dram glass vial and securely mounted within a lab-built sample holder and positioned on the PharmaRAM 1 resonant acoustic mixer. The sample was oscillated for 50 minutes at an acceleration of 80g.

9.2: Ball milling preparation

The halogen bond donor, *sym*-TFTIB (205 mg, 0.5 mmol), and the halogen bond acceptor, PheDON (105 mg, 0.5 mmol), were combined in a 10 mL stainless steel milling jar, supplemented with 31 µL of chloroform as a liquid additive. Subsequently, ball milling was conducted using a Retsch MM 400 ball mill at a frequency of 30 Hz for 45 minutes at room temperature. The milling process employed two stainless steel grinding balls with a diameter of 5 mm.

9.3: Crystal preparation by slow evaporation:

The halogen bond donor, *sym*-TFTIB (76 mg, 0.15 mmol), was dissolved in 2 mL of chloroform. The halogen bond acceptor, PheDON (32 mg, 0.15 mmol), was dissolved in 2mL of chloroform. The donor solution was added dropwise to the halogen bond acceptor solution. The solvent was allowed to gradually evaporate at room temperature, resulting in the formation of orange cocrystals of **2d.** The vial was tightly sealed as soon as single cocrystals were observed by eye.

9.4: PXRD results

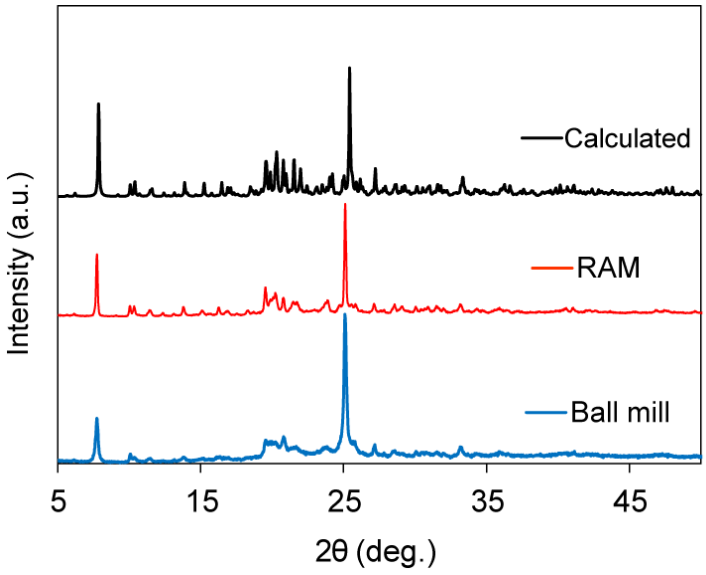


Figure S17. Diffractograms of ball mill and RAM products, and calculated powder X-ray diffraction pattern for cocrystal **2d,** (*sym*-TFTIB)·(PheDON).

9.5: ^{13}C CP/MAS SSNMR results

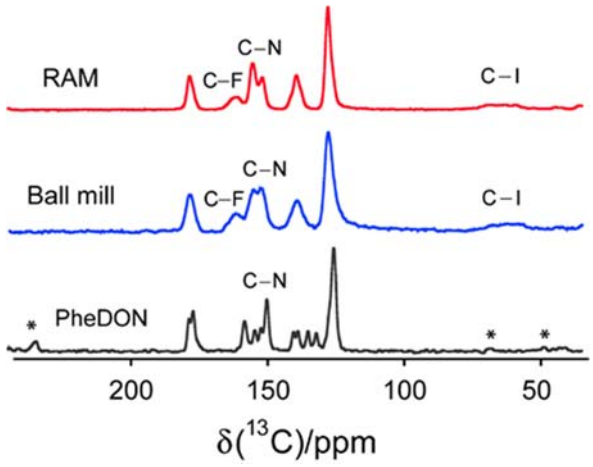


Figure S18. ^{13}C solid-state NMR spectra of XB acceptor o-Phe in black (lower) and cocrystal **2d**, (*sym*-TFTIB)·(PheDON) prepared by ball milling in blue (middle), and by RAM in red (upper). The labels denote the C-N carbons of PheDON, and C-I and C-F carbons of *sym*-TFTIB. The asterisks denote spinning sidebands.

10: 1e, (*p*-DITFB)·(DIZFON)[6]

10.1: RAM mechanochemistry synthesis:

205 mg (0.5 mmol) 1,4-diiodotetrafluorobenzene (*p*-DITFB) as halogen bond donor, 91 mg (0.5 mmol) 4,5-diazafluoren-9-one (DIZFON) as acceptor, and 150 µL THF were added were added to a 1-dram glass vial and securely mounted within a lab-built sample holder and positioned on the PharmaRAM 1 resonant acoustic mixer. The sample was oscillated for 50 minutes at an acceleration of 80g.

10.2: Ball milling preparation

The halogen bond donor, *p*-DITFB (205 mg, 0.5 mmol), and the halogen bond acceptor, DIZFON (91 mg, 0.5 mmol), were combined in a 10 mL stainless steel milling jar, supplemented with 30 µL of chloroform as a liquid additive. Subsequently, ball milling was conducted using a Retsch MM 400 ball mill at a frequency of 30 Hz for 30 minutes at room temperature. The milling process employed two stainless steel grinding balls with a diameter of 5 mm.

10.3: PXRD results

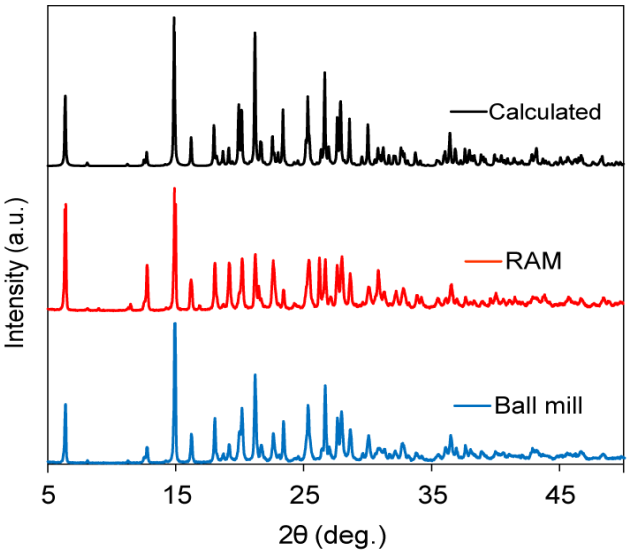


Figure S19. Diffractograms of ball mill and RAM products and calculated powder X-ray diffraction pattern for cocrystal **1e,** (*p*-DITFB)·(DIZFON).

10.4: ^{13}C CP/MAS SSNMR results

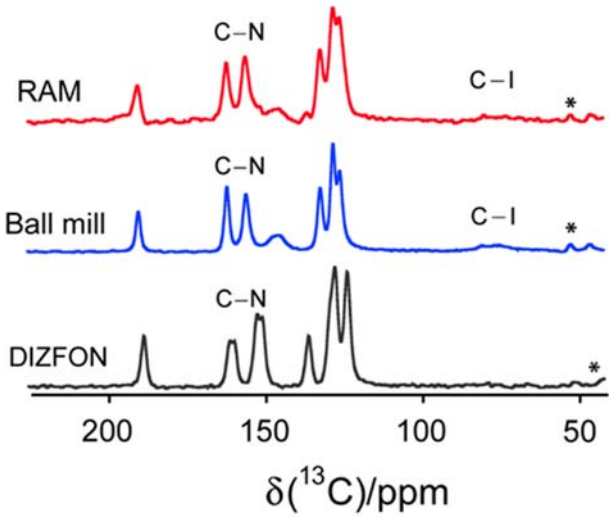


Figure S20. ^{13}C solid-state NMR spectra of XB acceptor o-Phe in black (lower) and cocrystal **1e,** (*p*-DITFB)·(DIZFON) prepared by ball milling in blue (middle), and by RAM in red (upper). The labels denote the C-N and C-I carbons of DIZFON and *p*-DITFB, respectively. The asterisks denote spinning sidebands.

11: 2e, (*sym*-TFTIB)·(DIZFON)

11.1: RAM mechanochemistry synthesis

255 mg (0.5 mmol) 1,3,5-trifluoro-2,4,6-triiodobenzene (*sym*-TFTIB) as halogen bond donor, 94 mg (0.5 mmol) 4,5-diazafluoren-9-one (DIZFON) as acceptor, and 223 µL THF were added were added to a 1-dram glass vial and securely mounted within a lab-built sample holder and positioned on the PharmaRAM 1 resonant acoustic mixer. The sample was oscillated for 50 minutes at an acceleration of 80g.

11.2: Ball milling preparation

The halogen bond donor, *sym*-TFTIB (255 mg, 0.5 mmol), and the halogen bond acceptor, DIZFON (94 mg, 0.5 mmol), were combined in a 10 mL stainless steel milling jar, supplemented with 32 µL of chloroform as a liquid additive. Subsequently, ball milling was conducted using a Retsch MM 400 ball mill at a frequency of 30 Hz for 45 minutes at room temperature. The milling process employed two stainless steel grinding balls with a diameter of 5 mm.

11.3: Crystal preparation by slow evaporation

The halogen bond donor, *sym*-TFTIB (76 mg), was dissolved in 2 mL of chloroform. The halogen bond acceptor, DIZFON (27 mg), was dissolved in 2 mL of chloroform. The donor solution was added dropwise to the acceptor solution. The solvent was allowed to gradually evaporate at room temperature, resulting in the formation of yellow cocrystals of **2e.** The vial was tightly sealed as soon as single cocrystals were observed by eye.

11.4: PXRD results

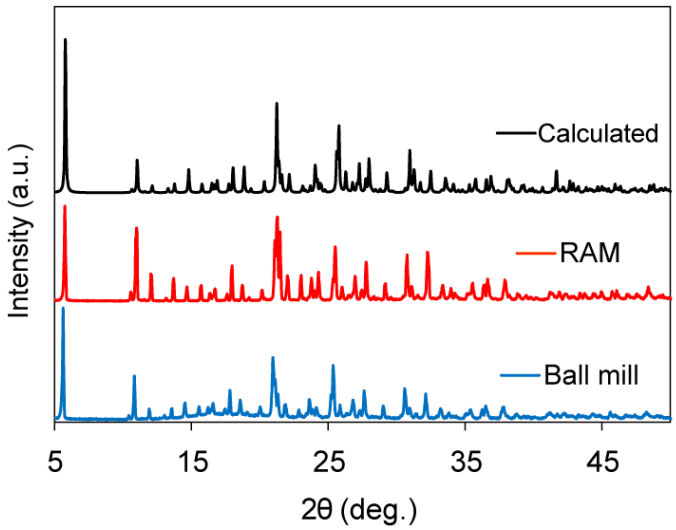


Figure S21. Diffractograms for ball mill and RAM products, and calculated powder X-ray diffraction pattern for cocrystal **2e,** (*sym*-TFTIB)·(DIZFON).

11.5: ^{13}C CP/MAS SSNMR results

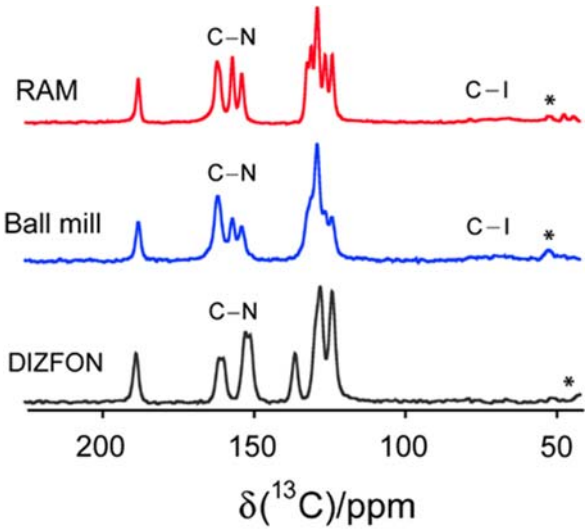


Figure S22. ^{13}C solid-state NMR spectra of XB acceptor DIZFON in black (lower) and cocrystal **2e,** (*sym*-TFTIB)·(DIZFON) prepared by ball milling in blue (middle), and by RAM in red (upper). The labels denote the C-N carbons of, and C-I carbons of sym-TFTIB. The asterisks denote spinning sidebands.

Table S1. $^{13}C[^{1}H]$ CPMAS solid-state NMR experimental conditions.

compound	number of scans	recycle delay / s	MAS frequency / kHz
a	2048	2	10
1a(i)	1024	30	11
1a(ii)	1024	30	11
2a	1024	30	11
b	2048	30	10
1b	1024	30	12
2b	1024	40	11
c	1024	60	4.5
1c	1024	60	12
2c	1024	90	12
d	512	100	11
1d	2048	30	11
2d	2048	40	12
e	1024	120	11
1e	1024	120	11
2e	1024	80	11

Additional Details on Single-Crystal X-Ray Diffraction for 2d and 2e

Raw data collection and processing were executed utilizing the ApexIII software package developed by Bruker.[7] Initial unit cell parameters were deduced from 36 data frames obtained from specific ***ω*** scans. Semi-empirical absorption corrections, based on equivalent reflections, were applied as part of the data processing.[8] The systematic absences observed in the diffraction dataset and the unit cell parameters were in line with the assigned space group.

Initial structural solutions were established employing ShelxT direct methods[9] and subsequently refined using full-matrix least-squares procedures based on F^2 with the assistance of ShelXL and ShelXle software.[10] Hydrogen atom positions were determined based on geometric considerations and further refined using a riding model.

The structure of **2d** (which contains 8 sets of crystallographically unique molecule pairs stacked in layers) is noteworthy as the difference map shows the presence of whole molecule disorder among some of the layers over a mirror plane. Attempts were made to model this behaviour both from a twinning or supercell standpoint, and through modelling of the disorder directly. In the former case, use of RLatt, cell_now, and other twin detection tools did not convincingly show the presence of any twinning. When disorder was modelled directly, the R value and general quality of the structure did not improve, the disorder fraction remained small, and it served only to muddy the interpretation of the structure. Thus the potential disorder was not included in the final model.

References

1 J. L. Syssa-Magalé, K. Boubekeur and B. Schöllhorn, *J. Mol. Struct.*, 2005, **737**, 103–107.

2 P. M. J. Szell, S. A. Gabriel, E. Caron-Poulin, O. Jeannin, M. Fourmigué and D. L. Bryce, *Cryst. Growth. Des.*, 2018, **18**, 6227–6238.

3 P. M. J. Szell, S. A. Gabriel, R. D. D. Gill, S. Y. H. Wan, B. Gabidullin and D. L. Bryce, *Acta Cryst. C*, 2017, **73**, 157–167.

4 R. Wang, D. Hartnick and U. Englert, *Z. Kristallogr.*, 2018, **233**, 733–744.

5 L. C. Roper, C. Präsang, V. N. Kozhevnikov, A. C. Whitwood, P. B. Karadakov and D. W. Bruce, *Cryst. Growth Des.*, 2010, **10**, 3710–3720.

6 B. Ji, W. Wang, D. Deng and Y. Zhang, *Cryst. Growth Des.*, 2011, **11**, 3622–3628.

7 Bruker, APEX3 Software Suite (version 218.7-2), Bruker AXS Inc. Madison Wisconsin USA, 2018.

8 R. H. Blessing, *Acta Cryst. A*, 1995, **51**, 33–38.

9 G. M. Sheldrick, *Acta Cryst. A*, 2008, **64**, 112–122.

10 C. B. Hübschle, G. M. Sheldrick and B. Dittrich, *J. Appl. Crystallogr.*, 2011, **44**, 1281–1284.